博士論文

Experimental Investigation on Water Film Characteristics and Droplets Formation around Cascade Blade

（翼列翼における液膜の特性と液滴形成に関する実験的研究）

Baber JAVED

ジャベッド　バーベール

Experimental Investigation on Water Film Characteristics and Droplets Formation around Cascade Blade

翼列翼における液膜の特性と液滴形成に関する実験的研究

Doctoral Thesis

By

Baber JAVED

ジャベッド　バーベール

Submitted in Partial fulfilment of the requirements

for the degree of

Doctoral of Engineering in Aeronautics & Astronautics Engineering

The University of Tokyo

Acknowledgement

I am greatly thankful to my parents and family members for their unconditional moral support and love have always been with me throughout my life. It's only because of their exceptional humanity and inestimable sacrifices, has made it all possible.

I would like to express my deepest sense of gratitude to my supervisor Prof. T. Watanabe, for giving me the opportunity to conduct this research and for constant encouragement during my studies. He has been very supportive throughout my studies (both academically and financially) with his patience, kindness and knowledge while allowing me to work in my own way. His profound leadership and vast knowledge in the field of gas turbine systems is the source of inspiration throughout the course of this work. His gentle personality and meticulous attitude in research will benefit my career as well as personal life.

I am also grateful to my co-supervisor Assoc. Prof. T. Himeno for being an extraordinary advisor throughout my Ph.D. course, who shared many ideas and helped me to get started on this degree. His enthusiasm, encouragement and faith in me throughout is extremely helpful. He was always available for any kind of discussion and had given his positive comments as well as vast knowledge. He always knew how to answer my academic questions while leading and guiding me to the correct source, theory and perspective.

I am thankful to my doctoral supervising committee members, Prof. Tanuma, Assoc. Prof. Teramoto and Assoc. Prof. Imamura for their kind feedback. I would also like to acknowledge Ass. Prof. C. Inoue for his generous feedbacks and advices on different topics to achieve the research objectives. He has also given valuable comments to improve the quality of this research work. I am equally grateful to my experimental supervisor Mr. S. Uzawa from whom I learnt a lot about the way of thinking and conducting experiments. His profound knowledge, creative thinking and consistent encouragement is a source of inspiration throughout my experimental work. Without his comments, it would be almost impossible to produce such experimental results. I am personally thankful to him for giving me consistent feedbacks to improve my test facility, while also help me in improving my Japanese language skills. I am also thankful to Assoc. Prof. Teramoto and Assoc. Prof. Okamoto for their feedbacks and comments during the joint lab seminars. Also, the support from Miss. Y. Yamada for helping me in dealing with different office work is also highly appreciated.

In my daily research routine, I am blessed with friendly seniors, Dr. Y. Sakuma and Dr. A. Tateishi. Both of them are always generous in giving their time for not only discussing and commenting on my research activities but also helping me in filling up various forms for my smooth stay in Japan. My seniors, Dr. R. Okada and Dr. Y. Umemura lively chat during my first 6 months in Japan will always be cherished. I am thankful to my doctoral research fellows Mr. Okamoto, Mr. Haba and Mr. Gan for their nice chat. I am also thankful to the master's and bachelor's student from the batch 2012 to 2016 for the light jokes throughout my studies. To say the least, all the members of University of Tokyo Jet Propulsion Lab made my staying over these years stimulating and enjoyable. Their constructive suggestions and assisting me with utter sincerity in dealing with side issues during this time will always be remembered and is highly appreciated, which greatly contributed to my research. I am also thankful to the lab members of Teramoto-Okamoto lab for their feedbacks during the joint lab seminars.

Finally, I would like to thanks my all teachers, friends and staff of The University of Tokyo with whom I spend a memorable time at The University of Tokyo, Japan.

Abstract

Power augmentation of gas turbines by fogging (ingestion of fine droplets from nozzles) have been gaining more interest among the gas turbine manufacturers mainly due to relatively being extremely simple and highly effective among the available augmentation techniques for gas turbines. The presence of water droplets ingestion due to fogging in gas turbine systems has shown significant improvement in the performances of gas turbine systems. Despite due to this positive effect, the presence of liquid phase in the gas turbine can cause damage to the components or may cause a change to the flow path of the working fluid, which can affect the flow physics of air around the compressor blades as well as can cause physical damages to the gas turbine system. In fact, the fundamental of the behaviour of the two-phase in gas turbines has not been completely understood, as our knowledge of the gas turbine systems is mainly limited from the single phase (i.e. air) point of view. Due to limited fundamental experimental study, the aim of this study is to get an insight about the fundamental phenomena involved due to the presence of liquid and how the characteristics of liquid phase are affected by different parameters.

Geometrically simple blade profile is used in this study to investigate the formation of the liquid film, water accumulation at the trailing edge, ligament formation, droplets shedding angle and the droplets size distribution aft the trailing edge region of the aerofoil. In the present study, extensive shadowgraph images were taken by using a high-speed camera with a back-lighting technique and an in-house code was developed to measure the above characteristics.

It was found that the water film formation on the blade surface was primarily governed by two parameters. Firstly, due to the external forces exerted by the air flow speed (i.e., depending on the Reynolds number of the air) and secondly, due to the liquid's restoring forces due to surface tension (i.e., Weber number of liquid film thickness). Based on these, in the present study, the appearance of the water film was categorized as wavy-film, intermediate and mirror-like smooth wave pattern for the high, intermediate and low air velocity respectively. The instability of the water film was found to be due to the Kelvin-Helmholtz instability and was evaluated by Craik's criteria for the instability of the thin liquid film. Moreover, a theoretical expression for the liquid film thickness was obtained based on the Couette flow with linear velocity profile.

At the trailing edge, the experimental study revealed that the amount of water accumulation is a function of many parameters, such as the air momentum ratio, liquid's flow rate, weber number and the thickness of the trailing edge. For thick trailing edge profile blades, a large amount of water gets accumulated due to the large surface area under the same aerodynamic and water load conditions to that of the thin trailing edge profile. From the visualization study, vortex shedding was found to be responsible for the stripping and breakup of ligaments at the trailing edge, and the shedding frequency was found to be relatively larger for thicker trailing edges and vice versa. The breakup of accumulated water occurs mainly due to the two modes. When the air momentum ratio is large, the surface waves formed due the aerodynamic forces plays an important role in the stripping of water droplets from the tip of the trailing edge. On the other hand, for low air momentum ratio, the surface tension forces get dominant which results in mainly the bag mode of the breakup of ligaments at the trailing edge. With the decrease in the air momentum ratio, the amount of accumulated liquid increases, which ultimately results in an increase in the length of the ligaments and ultimately resulted in the bag mode of the breakup of these ligaments. The length of ligament increases with an increase in liquid's flow rate and decrease in the air velocity and vice versa. It had also been observed that the water gets accumulated at a region of flow separation and the amount of water accumulated increases along the span direction of the blade if the relative difference between the liquid film velocity and the surrounding air flow becomes very large. The effect of angle of attack on the characteristics of two-phase phenomena around a cascade blade was also investigated. From these experiments, it was concluded that the liquid film thickness as well as the size of droplets formed aft the T.E. of the blade increases due to the reduced velocity effects.

The primary droplets size formed, due to the breakup of the ligament, aft the trailing edge region decreases with an increase in the air momentum and weber number (based on the trailing edge

thickness). Theoretical models were proposed to predict the size of primary droplets formed aft the T.E. of the blade, the shedding frequency and the wavelength of the accumulated water at the T.E.. It was measured experimentally and proven theoretically that greater the thickness of the blade is, larger would be the primary droplets formed under the same weber number (based on the thickness of the trailing edge). Furthermore, the theoretical investigation had shown that the primary droplets produced are inversely proportional to the square of the air velocity and vice versa. As the chord-wise distance aft the trailing edge increases the gradient of droplet size change. For high air momentum ratio cases, this change in the gradient was usually small, mainly due to the vibrational mode of a breakup. However, for low air momentum cases, the gradient of droplet size changes was large mainly due to the bag mode of a breakup. Additionally, the primary droplets size decreases with an increase in the air momentum ratio and vice versa. The results further showed that the droplets distribution angle in the pitch-wise direction, increases with a decrease in the air momentum ratio, due to the bag mode of a breakup, whereas, it decreases for high air momentum ratio, due to the dominance of vibrational breakup. However, for the droplets distribution angle in the span-wise direction, it increases with an increase in air momentum ratio and vice versa. The increase in the span-wise angle was mainly due to the accumulation of water over a large are in the span-wise direction.

Table of Contents

NOMENCLATURE

Latin Symbols

		Units
x	Spatial coordinate	[m]
y	Spatial coordinate	[m]
z	Spatial coordinate	[m]
u	Velocity in x-direction	[m/sec]
v	Velocity in x-direction	[m/sec]
w	Velocity in x-direction	[m/sec]
t	Time	[sec]
g	Acceleration due to gravity	[m/sec^2]
p	Pressure	[Pa] or [N/m^2]
U/V	Velocity	[m/sec]
$\bar{U}$	Mean (average) component of velocity	[m/sec]
U'	Fluctuating component of velocity	[m/sec]
Tu	Turbulence	
m	Mass	[kg]
C_D	Coefficient of drag	
f_D	Drag factor	
F	Force	[N]
D/d	Droplet diameter	[m]
C	Chord length	[m]
N	Number	
q	Rosin-Rammler droplet size distribution parameter	
X	Characteristic droplet diameter of the Rosin-Rammler equation	
C_p	Coefficient of pressure	
I	Electric current	[A]
R	Electric resistance	[Oh]
T	Temperature	[K]
h	Heat transfer coefficient (used in chapter 3 only)	[W/m^{2}K]
h	Height	[m]
w	Width	[m]
$\dot{Q}$	Volume flow rate	[m^3/sec]
c_f	Coefficient of friction	
A	Area	[m^2]
t	Thickness of the trailing edge	[m]
k	Dimensional wave number	[m]
$\dot{m}$	Mass flow rate	[kg/sec]
H	Height of the test section	[m]
f	Frequency	[Hz]
E	Energy	[J]
A_f	Factor A	[-]

Greek Symbols

		Units
ρ	Density	[kg/m^3]
μ	Dynamic viscosity	[Pa.sec] or [kg/m.sec]
υ	Kinematic viscosity	[m^2/sec]
λ	2nd viscosity or bulk viscosity	[Pa.sec] or [kg/m.sec]
τ	Response time	[sec]
σ/γ	Coefficient of surface tension	[N/m]
α	Non-dimensional wave number	[-]
δ	Boundary layer thickness	[m]
λ	Wavelength	[m]
Π	Complex Normal shear stress tensor	
Σ	Complex Tangential (shear) perturbation stress tensor	
θ	Droplets distribution angle or shedding angle	[degree]

Subscript

x	Component along x-direction
y	Component along y-direction
z	Component along z-direction
p	Dispersed phase (droplets/particles)
a/c	Continuous (air) phase
rel	Relative
vm	Virtual mass
$basset$	Basset
$staff$	Staffman
mag	Magnus
D	Drag
10	Average droplet diameter
32	Sauter Mean droplet diameter
T	Total
W	Wire
f	Fluid
ref	Reference
$film$	Thin liquid film
w	Water
i	Imaginary part
r	Real part
L	Longitudinal
$span$	Span-wise direction
in	Inlet
lig	Ligament

Dimensionless Number

MFR	Dimensionless mass flow rate	$MFR = \frac{\dot{m}_W}{\mu_W \, C}$
St	Strohaul number	$St = \frac{fL}{U}$
Re_a	Reynolds number of air	$Re_a = \frac{\rho_a \, C \, U_a}{\mu_a}$
Re_p	Reynolds number of particles	$Re_p = \frac{\rho_a \, d_p \, \lvert u_{rel} \rvert}{\mu_a}$
St	Stokes number	$St = \frac{\rho_p \, d_p^2 \, U}{18 \, \mu_a \, C}$
We	Weber number	$We = \frac{\rho_a \, d_p^2 \, u_{rel}^2}{\sigma}$
We_a	Weber number based on T.E. thickness (air phase)	$We_a = \frac{\rho_a \, U_a^2 \, t}{\sigma}$
We_t	Weber number based on T.E. thickness (liquid phase)	$We_t = \frac{\rho_l \, U_a^2 \, t}{\sigma}$
Re_{film}	Reynolds Number of liquid film	$Re_{film} = \frac{\rho_w V_{film} h_{film}}{\mu_w}$
T	Inverse Weber Number	$T = \frac{\gamma}{\rho_w h_{film} V_{film}^2}$
G	Inverse Froude Number	$G = \frac{g h_{film}}{V_{film}^2}$
M	Momentum ratio	$M = \frac{\rho_a \, U_a^2}{\rho_l \, U_l^2}$
ALR	Air to Liquid Ratio	$ALR = \frac{m_a}{m_l}$
t^*	Dimensional time	$t^* = \frac{t \, U}{C}$

Abbreviations

PDF	Probability distribution function
CDF	Cumulative distribution function
$T.E.$	Trailing edge
$L.E.$	Leading edge
CFD	Computational fluid dynamics
SMD	Sauter Mean Diameter
FFT	Fast Fourier Transformation
ALR	Air to Liquid Ratio
$const./k$	Constant
$m.sec$	Milli – second

List of Figures

CHAPTER 1: INTRODUCTION

CHAPTER 2: FUNDAMENTAL THEORETICAL BACKGROUND

CHAPTER 3: EXPERIMENTAL SETUP

CHAPTER 4: ELLIPTICAL PROFILE BLADE

APPENDIX A: FLAT BLADE

APPENDIX D: CIP-LSM (Cubic Interpolated Pseudo-particle with Level Set Method)

List of Tables

Part –I General Introduction, Objectives & Fundamental Study

Chapter No. 1: Introduction

Power generation across the world is undergoing rapid changes. Developing as well as developed countries are consistently increasing their electric power generation capacity in order to meet their increasing power demands. However, emission level of carbon dioxide from the power generation systems must also have to be reduced in order to avoid the increasing level of global climatic changes. Renewable energy sources cannot provide the continuous and reliable power output as their output efficiency changes with a change in time (or seasons etc.). At present our dependency on conventional thermal power systems is inevitable and a lot of researchers have focused on for not only improving the overall efficiency of these systems but also to make conventional power systems more environmentally friendly. Therefore, the power generation industry needs some major reforms for not only enhancing the efficiency of power generation systems but also to produce the environmentally friendly systems to avoid the threats of the global warming, as well as to meet the requirements of recently approved environmental policy on global climate changes in Paris, COP21.

1.1. The World Energy Resources

Earth's energy resources are limited and have been decreasing with more rapid pace than they are being reproduced due to mankind energy consumption. Human life is driven by energy and at present the main sources of energy which are used to fulfil human's electricity energy requirements can be summarized as follow;

- Fossil Fuels

Fossil fuels primarily contain liquids (petroleum and diesel), coal and natural gas. According to EIA [1], fossil fuels are the major source of supplying energy to the human life and contributes to 86.4% of humans' current energy requirements. Among fossil fuels, the shares of energy obtained from coal, petroleum and natural gas are 27.4%, 36% and 23% respectively [2]. Fossil fuels are formed via natural processes but are generally considered as non-renewable energy resources as it takes thousands (or millions) of years for them to form. Therefore, if these resources are not being consumed effectively and efficiently then human activities can be severely affected. Additionally, fossil fuels are also a major contributor to the world's environmental problems due to the production of CO_2 by burning them. CO_2 is one of the greenhouse gases which contributes to the increasing level of surface temperature of the earth.

- Nuclear Energy

Nuclear energy provides around 11% of the world's total electricity need. It is considered as a clean source of energy and poses no threats to the emission of greenhouse gases. However, such energy source is considered very dangerous and can cause enormous threats to the surrounding environment in case of an accident. According to [3], the worldwide nuclear output fell by almost 4.3% in the wake of Fukushima nuclear disaster accident.

- Wind Energy

Wind energy is very consistent from year to year and has significant variations over a shorter time scales. Wind farms are one of the fastest growing energy resources and presently contributes to about 4% of worldwide electricity usage [4].

- Hydroelectric Energy

Hydroelectricity is the most widely used renewable energy resource and contributes to around 16% of world's electricity requirements and is expected to increase by 3.1% in the next 25 years [5]. The cost of energy production from these systems is relatively low.

- Solar Energy

Solar energy is considered to be one of the most widely available renewables and free energy source. One of the biggest advantages of such energy is that it can be used to provide uninterrupted energy to small scales, such as street lights, traffic signals, etc. However, despite being available abundantly, such

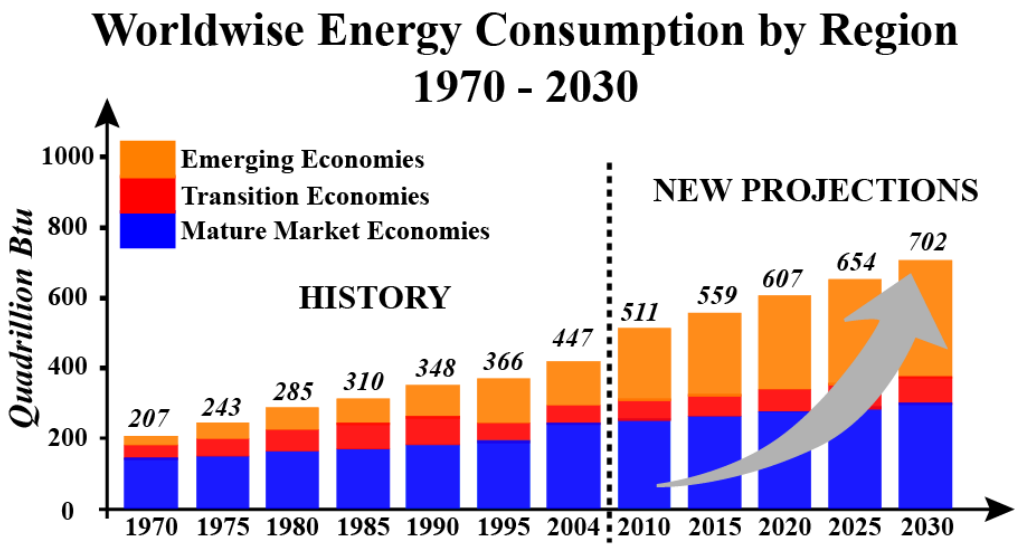

Figure 1.1 – World marketed energy consumption, 1990-2035 (quadrillion Btu) [8]

energy source is considered relatively expensive among the renewable energy resources mainly because the current technology is not capable of storing sun energy for longer time period.

- Wave Energy

Among the available renewable energy resources, wave energy has the maximum density (around 75% of the world is covered by ocean). However, sea waves are random in nature due to which harnessing energy from waves is not easy. Additionally, the cost of maintenance and the ability of wave devices to withstand in the extreme weather condition is a challenging task for energy extraction. Recently, many types of research have been conducted in this area to optimize the energy from the sea waves and different controlling strategies are proposed [6].

- Geothermal Energy

Geothermal energy sources are clean and do not contribute to the environmental pollution or greenhouse gas. However, due to the limited availability of sites, geothermal thermal plants has to be built at a specific location.

1.2. Future Energy Demand

Among the available major energy resources discussed above, fossil fuels will still continue to supply almost 80% of world energy sources by 2040 [7]. Therefore, there is a need to improve the efficiency of the presently available systems to get the maximum output by consuming the minimal energy. Since the start of the 21st century, the overall world's energy demand will become almost twice within 30 years, due to the high energy demands in the emerging economies [8], as shown in Fig. 1.1. Increasing demands of electricity creates a need for generating capacity. World's electricity demands are mainly fulfilled by the thermal power plants, and more commonly coal is used as fuel. Recently, gas turbines are also being used to meet the peak load demands. Figure 1.2 shows the key power production systems which are utilized to meet the world's electricity demand at present and in the near future.

1.3. Thermal Power Plants

Thermal Power is a general word used for the systems in which the heat energy of the working fluid is converted into a mechanical energy by driving a turbine. Figure 1.2 shows that the world primary electricity demands are being fulfilled mainly by the thermal energy sources. Based on the working fluid of the thermal power plants can be classified into following two categories;

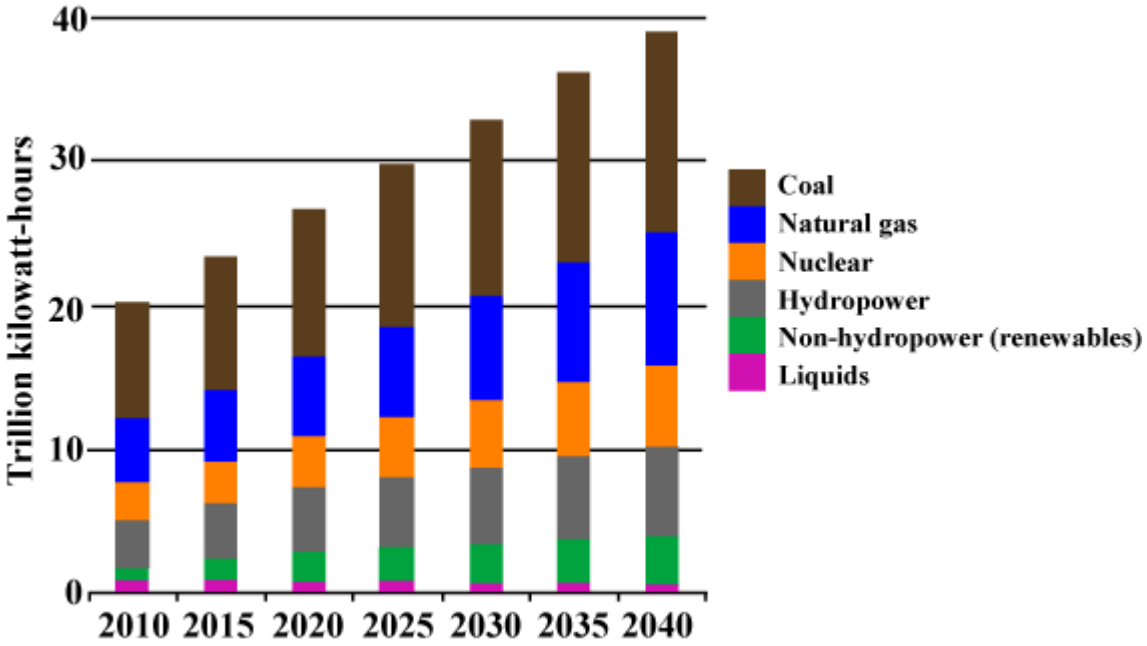

Figure 1.2 – World Net Electricity Generation by Energy Source (Trillion kilowatt-hours) [7]

- Air (or more specifically hot air) – Gas Turbines
- Water (or more specifically steam) – Steam Turbines

Steam turbines are being used since late 19th century for the production of electricity, whereas gas turbines are being used in the aviation industry since the mid of 20th century. However, from the last 50 years, gas turbines have also been commonly used for the electricity generation, due to more environmentally friendly compared to the steam turbine systems.

1.3.1. Steam Turbines

Among all the electricity production plants, steam turbines are the most widely thermal energy source of electricity production in the world. According to Starzmann et al. [9], the share of steam turbines in worldwide electricity generation is 70%. The demand of steam power plants continues to rise, especially in the newly developed countries as they can provide the base load for a longer period of time without any trouble. Nuclear or more commonly coal-based power plants fall into this category, which is commonly used as a fuel to produce steam. In a thermal power plant, a high-pressure and high-temperature steam are used to rotate the steam turbine and this rotational speed of the turbine is then transferred to a generator to produce electricity. When the turbine blades get rotated by high-pressure and high-temperature steam, the steam loses its energy. This, in turn, will result in a low-pressure and low-temperature steam at the outlet of the turbine. The steam is expanded until a saturation point is reached. Since there is no heat addition or removal from the steam, ideally, the entropy of the steam remains the same. Compressing a fluid which is in the gaseous state requires a huge amount of energy, so before compressing the fluid is converted into the liquid state. A condenser is used for this purpose, which rejects heat to the surrounding and converts steam into liquid. At the exit of the condenser, the fluid is in a liquid state, whose pressure can be easily raised by a compressor. During the compression process, the volume and temperature (2-3 ^{o}C rise) of fluid hardly changes, since it is in a liquid state. Now the fluid has regained its original pressure. At last, heat is added to the fluid in order to bring back the fluid to its original temperature. This heat is usually added through a heat exchanger, called boiler. Inside the boiler, the temperature of the fluid is raised and the fluid is transformed from the liquid state to the gaseous state. During this process, the pressure of the fluid remains the same as it is free to expand in heat exchanger tubes. This completes the thermodynamic cycle of a thermal power plant, called Rankine Cycle. This cycle can be repeated and continuous power production is possible, as shown in Fig. 1.3.

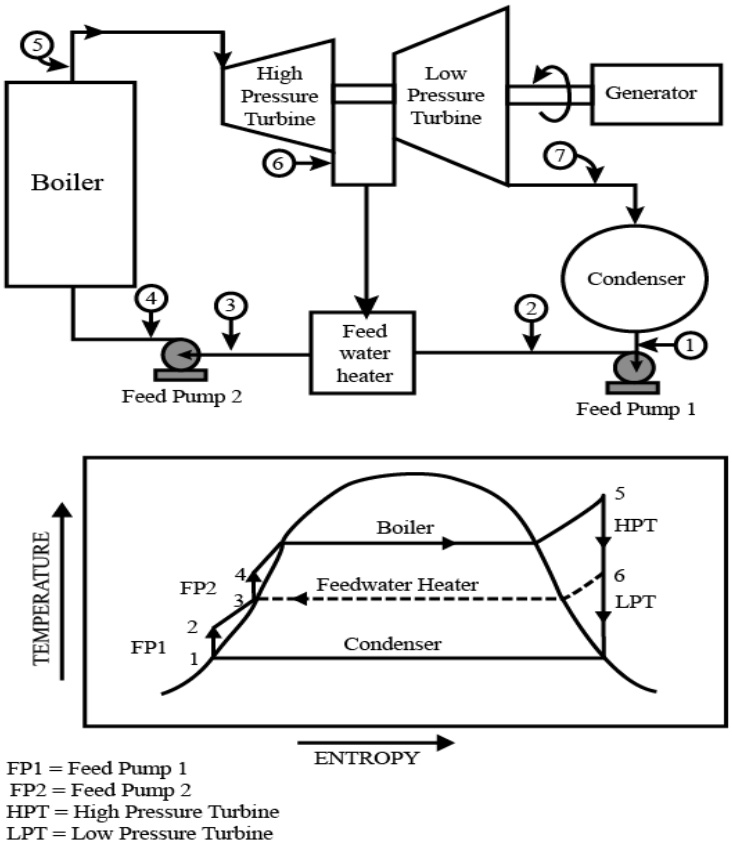

Figure 1.3 – Rankine cycle with a two-stage steam turbine and a single feedwater heater [10]

➢ Advantages

Steam turbines have been used since the 19th century and a lot of researches were conducted to improve their overall efficiency. Following are the major advantages of steam turbines, which are classified as follows;

- Overall highest cogeneration efficiency among the thermal power systems (up to 80%).
- A wide range of fuels can be used to produce steam (coal, nuclear etc.).
- Production of high pressure and temperature steam, which can be used for additional applications, such as heating etc.

➢ Disadvantages

- Condensation of steam leads to the generation of coarse droplets, which eventually causes erosion of the turbine blades, especially at the last (or near last) stage.
- Slow start up times.
- Poor part loads performance.

1.3.2. Gas Turbines – As Energy Production Unit

Due to the poor part-time load capability of steam turbines, gas turbines are commonly used to fulfil the peak load demands. The share of electricity generated from the natural gas grows steadily from more than half century. The shift to natural gas occurs primarily as a result of being relatively low cost compared to the steam turbines. According to EIA [11], natural gas plants account for more than 70% of all the new capacity in projection, as shown in Fig. 1.4. Additionally, gas turbines systems (including Gas Turbine Combined Cycles) are one of the most efficient thermal power systems (having efficiency as much as 60% or even higher). However, increasing stringent legislations have forces the gas turbines manufacturers to increase the Research and Development (R&D) phases in order to make such devices more efficient in design, cheaper and cleaner.

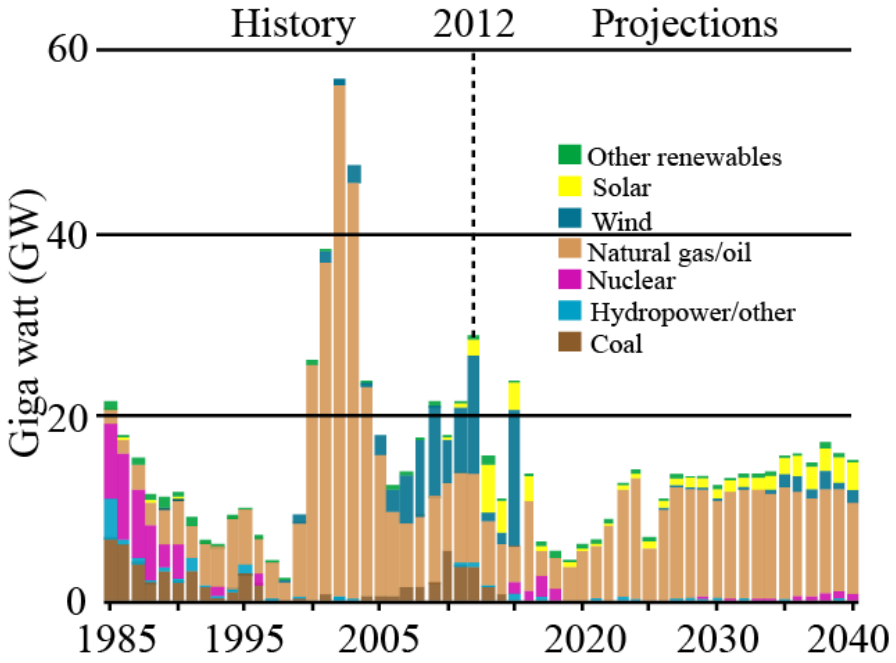

Figure 1.4 – Addition to Electricity Generating Capacity, 1985-2040 (Giga Watt (GW)) [11]

A gas turbine is a rotary machine designed to produce energy by combustion and it consists of three main components - a compressor, a combustion chamber and a turbine. Air after being compressed into the compressor is heated either by directly burning fuel in it or by burning fuel externally in a heat exchanger and mixed with the incoming air. The heated air with or without products of combustion is expanded in a turbine resulting in work output, a substantial part (about two-thirds) of energy is used to drive the compressor, whereas the rest of energy is utilized as useful work output.

The needs for energy production processes are becoming more and more complex as the demands of cost effective and environmentally friendly thermal energy devices are increasing to minimize the fuel consumption as well as to minimize the emission of harmful gases in order to avoid global warming. Gas turbines have this ability which makes them a valuable asset in the thermal power generation industry, as it not only ranges from a small scale of few kW's to large scale, MW's, for energy production but is also considered to be relatively more environmentally friendly when compared to the steam turbines.

- Advantages

  - One of the biggest advantages of the gas turbine is that they are simple in design and can be installed easily.
  - They have short start-up time and can be put in operation more quickly.
  - They are commonly used to meet the peak load demands etc.

- Disadvantages

  - Thermal efficiency deteriorates due to the hot weather condition, which is due to the decrease in the density of incoming air and this results in the decrease in the mass flow rate of working fluid (air).

According to Chaker et al. [12] a rise of 1°C causes an energy loss of about 0.54 ~ 0.9 %, which is a significant loss. Similarly, in another research by Bhargava et al. [13] concluded that the power output of gas turbines can drop as much as 15 to 20 % at an ambient atmospheric temperature of 35°C, which is a significant loss of energy.

1.3.2.1. Power Augmentation Techniques of Gas Turbines

The conventional approach to augment the power output of gas turbine system is to increase the combustion temperature. However, this leads to the use of high thermal materials and ultimately results in an overall increase in the cost of gas turbine systems. Therefore, it is indispensable to lower the incoming temperature of air in order to achieve higher power output from the gas turbine. One approach to overcome the loss of gas turbine power output during hot seasons (high demand periods) is to cool the inlet air. In fact, gas turbines are mass flow devices, i.e., higher the compressor mass flow is greater will be the power output capacity of the gas turbines will be and vice versa. In other words, the cooler the air is, the denser it is. Dense air provides higher mass flow rates and pressure ratios, which ultimately results in an increase in gas turbine power output. Thus, the basic aim of power augmentation is to make the compressor inlet air cooler by passing the warm air from a power augmentation system, as shown in Fig. 1.5. For that purpose different power augmentation techniques (by water) are proposed which can be mainly classified into two major categories as shown in Fig. 1.6.

Refrigeration Cooling Systems

In refrigeration cooling systems, the temperature of the inlet air is lowered down by the wet bulb temperature. This can be achieved by either an absorption or mechanical coils, as given schematically in Fig. 1.6 (a).

Evaporative Cooling Systems

Evaporative cooling systems are further categorized into two types, as shown in Fig. 1.6 (b).

1. Media Type Evaporative Cooling Systems

Figure 1.6 (b) – i shows the media type evaporative cooling system. In such systems, the air flows throw a wet honey-comb like structure which evaporates water from these convoluted surface, resulting in the cooling of the inlet air.

2. Fogging Systems

In fogging systems, fine droplets of pure water (i.e. demineralized water) is sprayed directly into the inlet plenum of the gas turbines from a rack of nozzles. Based on the position of the water ingestion position, the fogging system is mainly categorized as inlet fogging, Fig. 1.6 (b) – ii, and overspray fogging, as shown in Fig. 1.6 (b) – iii. The major difference in both the fogging system is the amount

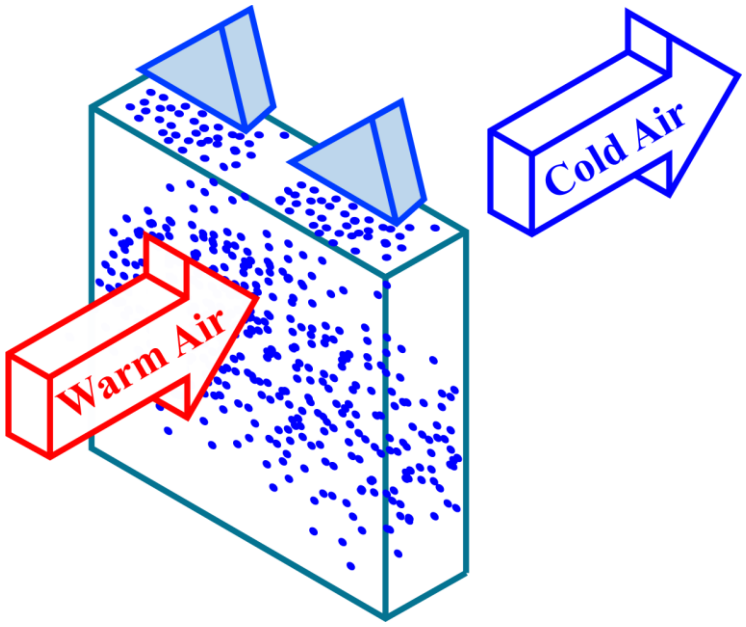

Figure 1.5 – Aim of power augmentation system

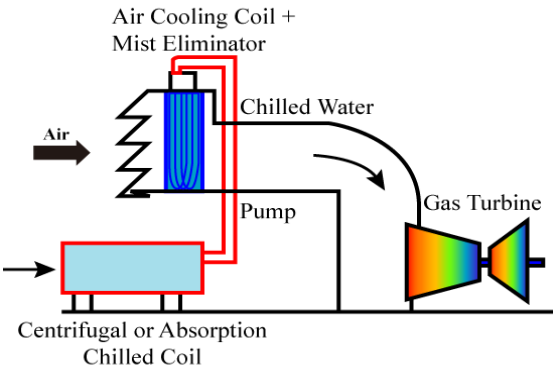

(a) Refrigeration Air Cooling (Inlet Air Chiller) [14]

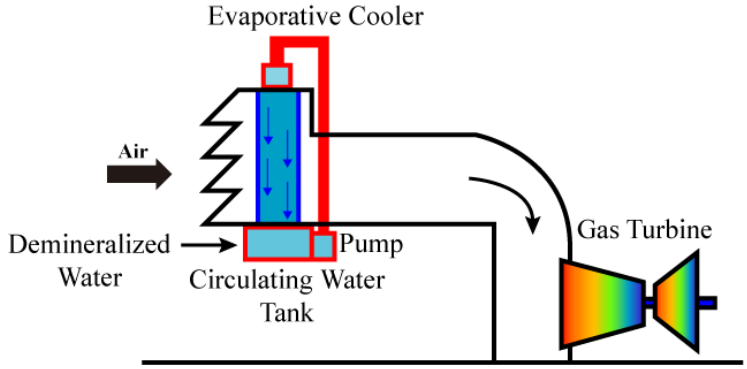

(i) Media-Type Evaporative Cooling [14]

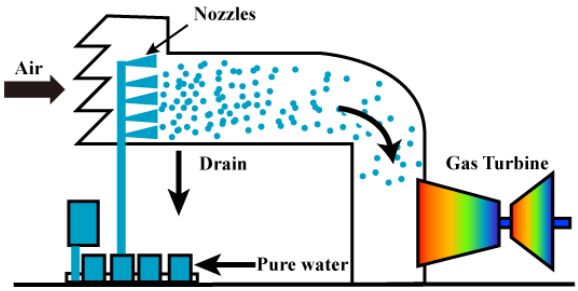

(ii) Inlet Fogging [14]

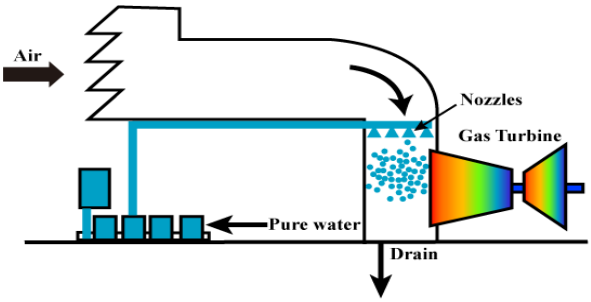

(iii) Over Fogging (Wet Compression)

(b) Evaporative Cooling

Figure 1.6 – Inlet Air Cooling Systems

of water evaporation. In inlet fogging, the fogging rack (i.e., array of nozzles) is mounted just after the filters, which evaporates as it reaches the compressor inlet, with little amount of water droplets. On the other hand, in over fogging due to closer position of nozzles to the compressor, a better control of the droplet size entering the compressor and minimize the sources of secondary (large) droplets can be achieve with ease. The water droplets along with the air reach the compressor part of the gas turbines. Due to the presence of the fine droplets in the air, it helps in increasing the density of the working fluid as well as cools down the inlet air into the gas turbine systems due to evaporation.

1.3.2.2. Best Technique

In order to choose the best available techniques from the above power augmentation techniques, several researches were done discussing the pros and cons of each technique, however, the most commonly and widely accepted is the fogging technique. According to Bhargava et al. [15] the overall cost of the fogging techniques can be as less than as five times compared to the other techniques. Similarly, according to Meher-Homji et al. [16] fogging can not only increase the thermal efficiency of the simple gas turbines systems but they can also be effectively used with the combined cycles (C/C) systems, which is not the case for the other inlet air cooling techniques. Table 1.1 compares the power augmentation techniques using different water ingestion techniques for gas turbines systems. Therefore, based on the overall best in efficiency and the relatively cheap among the commonly used power augmentation techniques, this thesis will be primarily focused from the fogging viewpoint mainly.

Table 1.1 – Comparison of Power Augmentation Techniques by Water for Gas Turbines [17]

	Fogging	Evaporative Cooling	Absorbers/Chilling
Output	Up to 20 %	Up to 15 %	Up to 20 %
Heat Rate	Up to -2.5 %	Up to -2 %	Up to -2 %
Maximum Humidity	100 %	< 85 %	>100 %
Installation	Nozzle Racks	Honey Comb	Compressor + Expansion
Medium	Demineralized Water	Potable Water	Freezing Absorber
Cost	$	$$	$$$

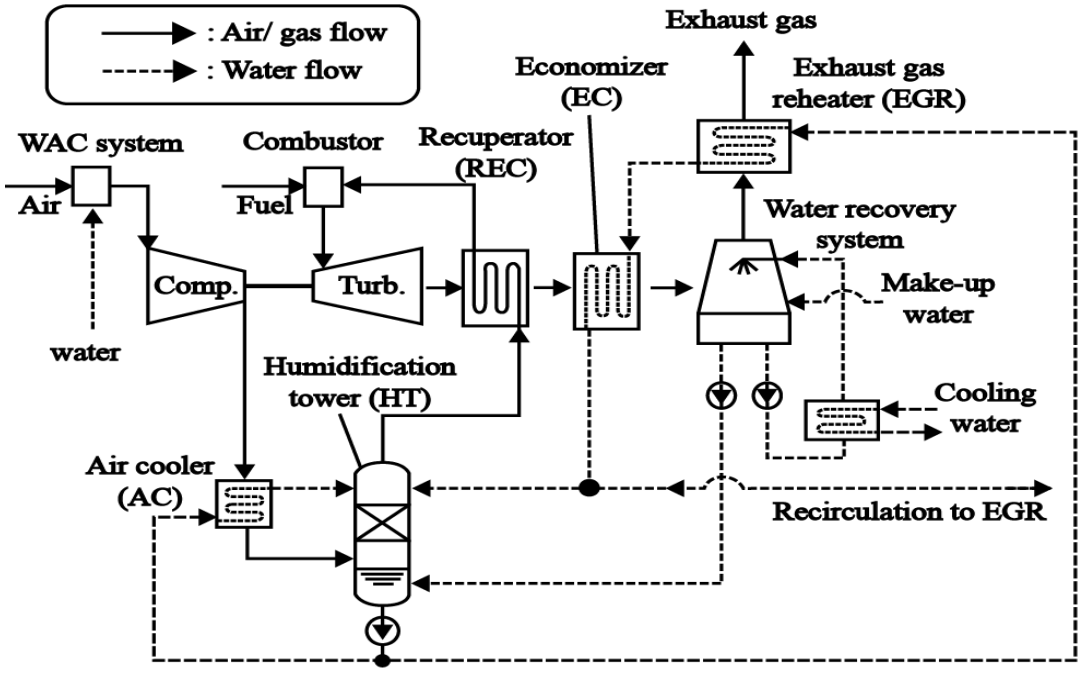

Figure 1.7 – Schematics of Advanced Humid Air Turbine (AHAT) System [19]

1.3.2.3. Available Systems on Fogging

Gotoh et al. [18] had discussed the benefits of water droplet ingestion systems by introducing a new gas turbine system, named Advanced Humid Air Turbine (AHAT). A detail schematics of AHAT system is given in Fig. 1.7. AHAT systems are expected to achieve higher efficiency without increasing the pressure or combustion temperature [18]. Despite due to their positive aspect, the physics of liquid film formation and droplet size distribution in the water ingestion systems have not been completely understood. Figure 1.8 compares the thermal efficiency of AHAT systems with commonly used gas turbines systems including combined cycle systems. It can be seen from Fig. 1.8 that the thermal efficiency of the AHAT system can be as much as equivalent to that of the Triple Pressure combined cycle units. Thus, AHAT systems are expected to be one of the major contributors in the near future for electric power generation. Moreover, from Fig. 1.8, the target output efficiency of AHAT systems is the best among all the existing medium-sized thermal power generation systems [19]. According to Hatamiya et al. [20], the efficiency of AHAT cycles is about 5% higher compared to that of the middle-sized combined cycles with no reheat, whereas, an increase of 10% efficiency is obtained when compared to the heat recovery steam generator (HRSG) with the same core engine [20]. AHAT systems are also economically cheap as the cost of installing AHAT plant is less than that of the combined cycle plants since the AHAT systems do not require any steam turbines and other high-pressure equipment, such as HRSG, etc.

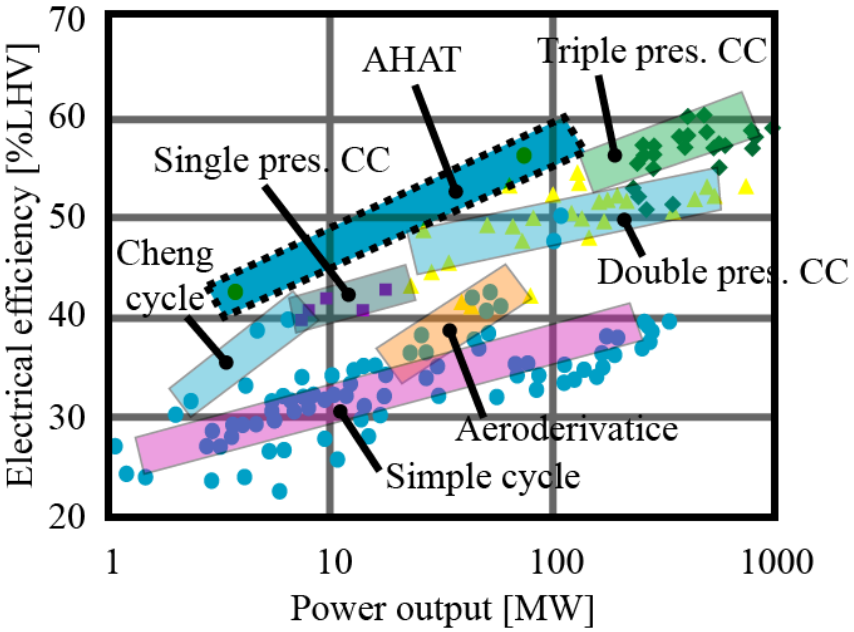

Figure 1.8 – Calculated thermal efficiency of AHAT and other gas turbine systems [19]

1.4. Liquid Presence in Turbine Systems

A brief phenomenon about the presence of liquid in the thermal power plants systems will be discussed in this section.

1.4.1. Steam Turbines

The low-pressure stage(s) of steam turbines rotor blades are the most critical element of the steam turbines as they are more likely to suffer from wear and tear by the impingement of condensed and coarse steam droplets, as shown schematically in Fig. 1.9. Steam droplets strike the low-pressure turbine blades, which results in the expansion of steam below the saturation line, resulting in the condensation of steam droplets. Thermodynamically it is always desirable to permit as much high degree of wetness as possible at the exhaust in order to get maximum work output from the steam but the pressure of water drops in the steam gives rise to certain losses which are highly undesirable. The initially condensed steam droplets are formed when it strikes the rotor blades, further condensation results in the growth of the droplets, as shown in Fig. 1.9 . These water droplets result in the reduction of thermodynamic efficiency of steam turbines due to the drag of water at relatively high speeds. Moreover, erosion of the rotor blades occurred due to impingement of high-speed coarse water droplets. The erosion phenomenon is highly undesirable in steam turbines as it has a very detrimental effect on the stage efficiency. It is already found that the formation of the water film on the stator blades gets deposited at the T.E. of the blade which results in coarse droplets formation, as shown in Fig. 1.9. These coarse droplets further undergo breakup due to the influence of aerodynamic forces. The breakup these steam droplets utilize the energy from the working fluid which results in the lowering of the working fluid speed and ultimately the overall efficiency of the steam turbine systems.

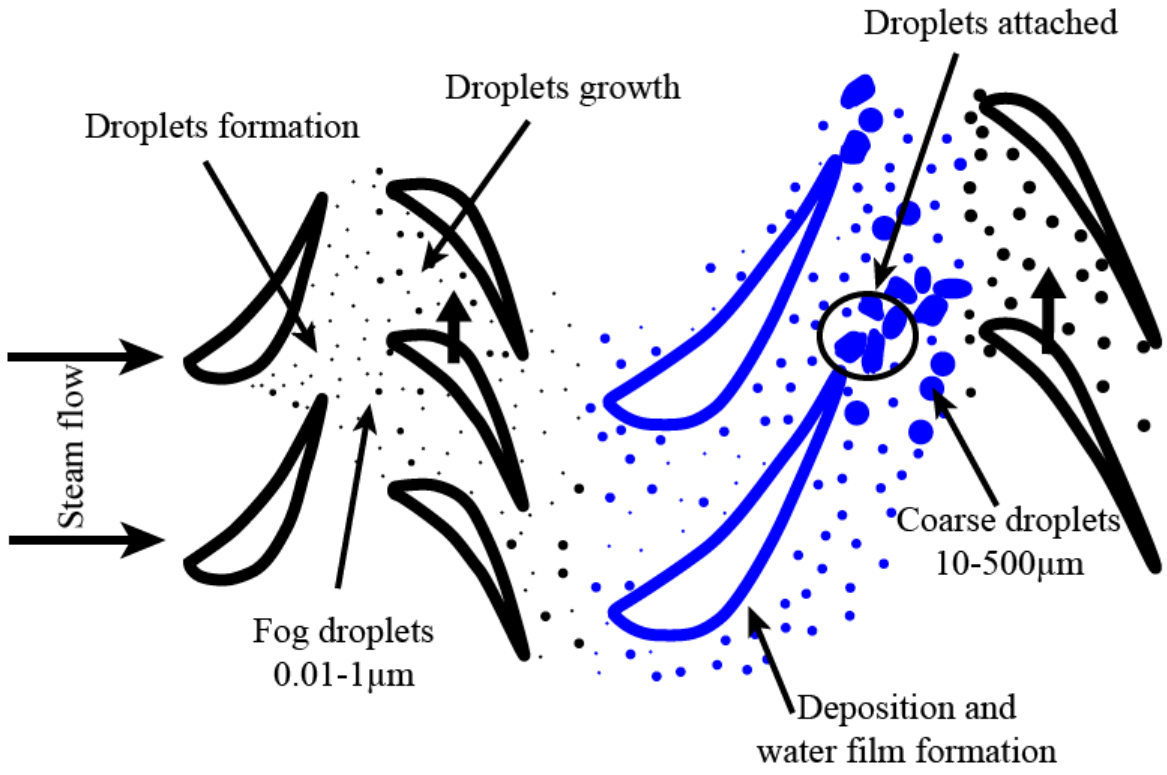

Figure 1.9 – Wetness formation in Steam Turbines [21]

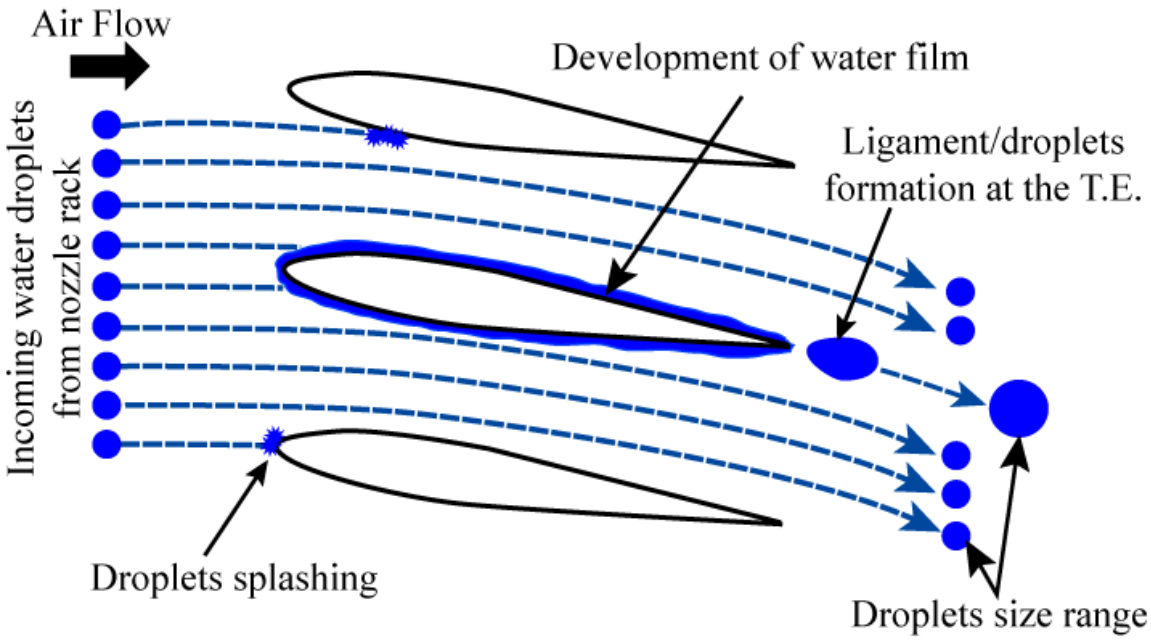

Figure 1.10– Typical Water Droplets Behaviour in a Compressor Cascade

1.4.2. Fogging of Gas Turbines

Fogging consists of an array of fog nozzles that are placed inside the inlet air duct of a gas turbine [23], as shown in Fig. 1.11. A high-pressure pumping system is used to deliver the demineralized water to the nozzle arrays. The nozzles are typically placed just downstream of the air filter elements to maximize the amount of time the fog droplets have to evaporate before entering the compressor section of the gas turbine [16]. The controllers of an inlet fogger ensure that the necessary amount of water is delivered to saturate the air as well as to utilize the minimum amount of demineralized water consumption [16].

Gas turbines are mainly designed for air as their working fluid. Therefore, the presence of any foreign particles can deteriorate their performance. Two phase phenomenon, especially air as a gaseous phase and water as a liquid phase is a highly complex process as it deals with many phenomena such as gas compression, droplets evaporation and droplet interactions (droplet-air, droplet-wall and droplet-droplet) etc. Figure 1.10 shows the schematics of droplet ingestion in a linear cascade of blades. Water droplets from the nozzle impinge on the Leading Edge (L.E.) of the compressor blades. Droplets impact on a surface is often accompanied by the breakup of larger droplets into smaller ones due to droplet deformation and splashing. The water in which these droplets are contained can either be ejected back into the airflow or moved as a thin film of water on the blade surface. This thin film of water continues to flow towards the Trailing Edge (T.E.) of the cascade blade due to the aerodynamic forces where they again recombine to form globules. These globules remain attached to the T.E. because of the influence of the surface tension of the liquid but grow in the direction of the airflow and along the T.E.. As the size of globules increases, the aerodynamic force acting to tear the droplet away from the T.E. also increases. And when the increasing aerodynamic

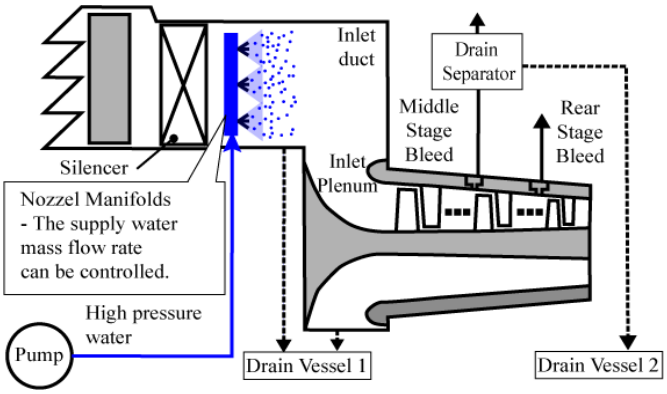

Figure 1.11 – Ingestion of Water droplets in Inlet Plenum of AHAT Gas Turbine Systems [23]

force exceeds the adhesive force of surface tension, which is holding the globules at the T.E., the globules will separate from the surface in the form of droplets and start flowing aft the T.E. region.

1.5. Possible Problems Due to the Presence of Water in Turbine Systems

Water presence is a major issue for both the steam and gas turbine systems. For the purpose of simplicity, a more general word "Wet Turbine System(s)" will be used in this thesis for the systems (Steam turbines and Gas turbines with fogging) which contain water droplets. From the brief discussion of the physical mechanism of water presence in wet turbine systems and our knowledge from previous research studies, following are the main adverse consequences which could occur due to the presence of water droplets in the wet turbine systems;

- Reduced efficiency
- Erosion of blades
- Damages to the blades

➢ Reduced Efficiency

Water droplets can easily disturb the main working fluid flow due to their relatively large density compared to the working fluid (i.e., air) as they can move slower and in a different direction due to their high momentum than that of the main flow, as shown in Fig. 1.12. From Fig. 1.12 (b), whenever the direction of flow is changed, water droplets get centrifuged because of their higher density than that of the main flow. Moreover, water droplets have to be accelerated by the main air flow, which results in the reduced velocity of the overall flow. As the droplets size increases more energy would be required from the main flow to accelerate them, which may ultimately lead to the reduced in the overall efficiency of the system. As a result, when these slow moving droplets enter the moving blades (Rotor), they will move more slowly than the blades themselves. Similarly, when these slowly moving droplets strikes the back side of rotor blades then due to such collision the rotor blades motion can be retarded, which can further lead to the overall decrease in the output of the systems.

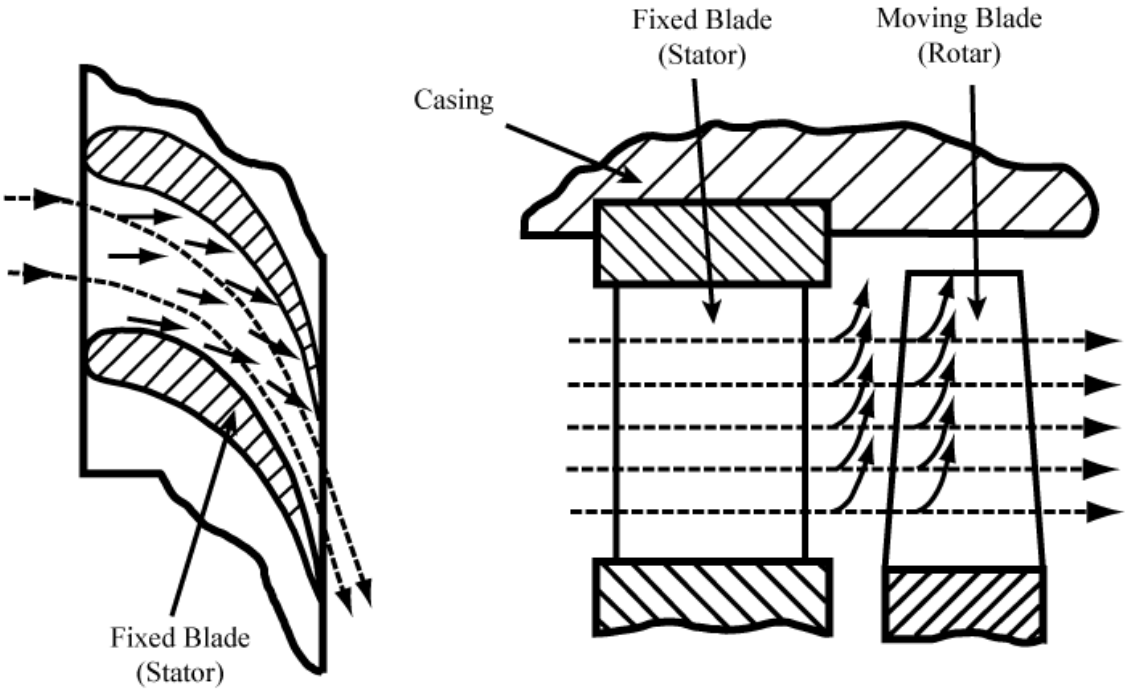

(a) Flow through Fixed Blades (b) Flow downstream of Fixed Blades

Figure 1.12 – Working Fluid and Water Trajectories [24]

Working Fluid Water Droplets

- Erosion of Blades

The most common cause of erosion in wet turbine systems is due to the collisions of water droplets onto the blade's surface. For example, in the case of steam turbines, the L.E. of the last stages of rotor blades close to their tip is the most typical site of erosion, due to the continuous bombardment of coarse droplets.

- Damages to the L.E. of the Blade

Striking of water droplets to the blade surface is also highly undesirable, especially the large droplets. Due to the continuous striking of water droplets on the blade surface for the longer time period will eventually lead to the formation of pits on (and near) the L.E. area of the blades. This will eventually lead to the undesirable flow over the blade's surface and such blades would ultimately need to be replaced for the save operation of the wet turbine systems.

1.6. Literature Review

1.6.1. Water Presence in Steam Turbines

Since late 19th century, substantial efforts have been made to improve the efficiency of steam turbine cycle. In this regard a lot of studies have been conducted to not only improve the design of the steam turbine blades and other components, materials etc. but also the most promising achievement was higher temperature and pressure of steam turbines. Extensive research has been conducted on various topics for the steam turbines, however, it is impossible to cover the outcomes of all these researches in this section. Blades of a steam turbine are the most critical components in power plants, which convert the energy possessed by the high temperature and high-pressure steam flowing down a pressure gradient into a rotary motion of the turbine shaft. If the blades of turbine get fail, the power plants would ultimately need to be shut down for breakup maintenance, which causes both long time systems failure and economic loss. Therefore, it is necessary to settle the failure analysis of turbine blades in order to increase the reliability and availability of turbine systems. Material losses from the L.E. is the result of commutative damage from the impact of water droplets. The existence of liquid phase in the Low Pressure (L.P.) steam turbines is responsible for well-known unfavourable phenomena. Energy losses, blades failures and erosion due to the corrosion effect in the phase transition zone consequently results in reduced efficiency and reliability of the systems [25]. Although well-established theoretical models of flow in dry stages of a steam turbine are available, comparatively little effort was spent on developing treatments for the two-phase stages [26, 27]. In general, the most serious problem caused by the wetness is the deviation of the system from thermodynamic equilibrium. This is due to the release of latent heat which affects the attainment of equilibrium in the neighbouring compressible vapour. Samoilovich et al. [28] had measured and predicted the turbine entry losses. They showed that the losses due to expansion through blade cascade reduce the efficiency and degree of reaction. Tatsumo et al. [29] use the optical fibre to measure the water droplet size in a steam turbine. They reported that average diameters were between 0.2 and 1 μm depending upon the degree of wetness (6–14%) and locations in the radial direction of the blade. Young [30] had conducted the comprehensive study on the condensation and evaporation of liquid droplets in a pure vapour at arbitrary Knudsen number. The physical model used was based on modified Langmuir analysis. He developed the sets of equations which govern the formation and evaporation of small liquid droplets in a pure vapour. However, more emphasis was given on the derivation of the energy equation as well as phenomenological coefficients relevant to mass transfer equation. He also demonstrated that the results of the analysis were in close agreement with the results obtained from other relevant analytical and numerical studies. The work provided give very useful information across the Knudsen layer in the continuum limit. However, the explicit formulation of the rate of droplet growth was not giving for both free molecular and continuum flow regimes. Experimental work in measuring the droplets size due to spontaneous nucleation was reported in [31, 32]. They have shown that the droplets radius increases with increasing droplet temperature up to the corresponding saturation temperature. In L.P. steam turbines, the erosion is becoming remarkable in all the stages due to the generation of liquid droplets, which impact on the blades. Figure 1.13, [33], shows the details of the two-phase phenomenon in the L.P turbines. The first transition line (a-a) denotes the saturation line, where under equilibrium assumption phase change occurs. Heterogeneous nucleation transition is denoted by line (b-b) which occurs due to contaminants

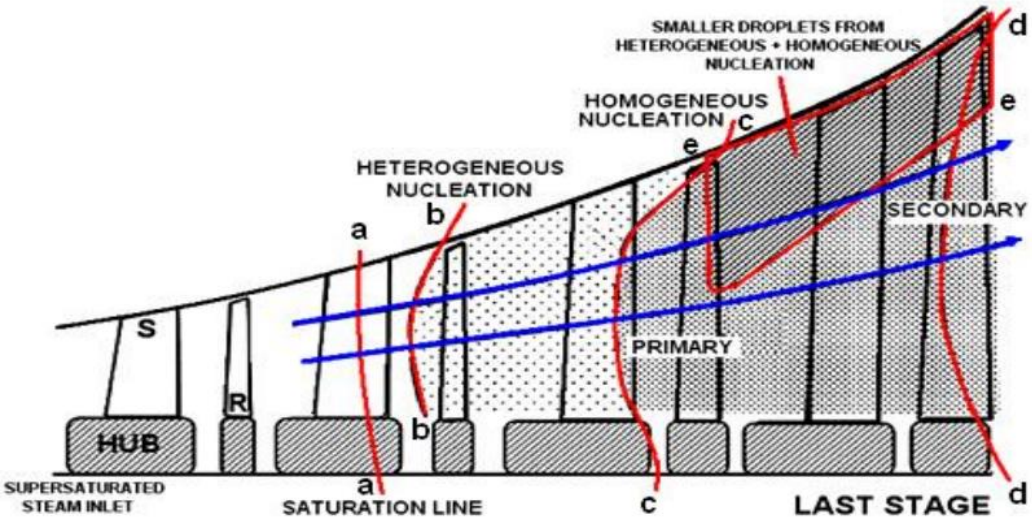

Figure 1.13 – Topology of Phase Change in Low-Pressure Steam Turbines [33]

in the flow and is generally insufficient to bring the flow in equilibrium conditions. Due to rapid expansion, super-cooling continues up to the line (c-c), which results in the generation of primary homogeneous nucleation. As flow continue to expand, significant super-cooling occur again leading to further secondary homogeneous nucleation as given along by line (d-d). Due to the centrifugal forces on the droplets, the droplets get confined at the shroud as given by region (e-e) in Fig. 1.13. According to Avallone et al. [34], the water droplets move relatively much slower than the surrounding steam velocity and results in unfavourable velocity when a strike at the rotor blades and could result in the breaking effects. Similarly, according to Michaelides [35], the continuous impact of water droplets would ultimately result in the formation of a liquid film on the wall surface, which would attenuate the forces due to the impact at subsequent times and this results in the long term wear on the surface. Renardy et al. [36] concluded that the impact of droplets causes very large deformations on the drop and creates radial jet during the early stages of impact, which finally induces the ejection of fluid at the sides of the flattened drop and ultimately lead to the formation of several smaller satellite droplets. A detailed description of the theory of erosion in steam turbines, related parameters and countermeasures can be found in [37–39]. To investigate the influence of different erosion parameters, a detailed experimental study is conducted at the Institute of Thermal Turbomachinery at the University of Stuttgart with the help of an erosion test rig. The details of this erosion rig can be found in [40, 41]. Some authors [42–44] had already found a strong influence of droplets size on erosion by an increase in the erosion rate with increasing droplet sizes. The influence of droplets size on the extent of erosion is used to explain the effective impact lengths which become smaller with smaller droplets [42] and by the impact pressure duration which increases with bigger droplets [45]. Moreover, Zhou et al. [46] numerically found that the amount of both water hammer pressure and the stress penetrated into the solid is independent of droplet size. On the other hand, the duration of water hammer pressure and the depth of stress penetration into the solids were found to be a linear function of droplet size. Corrosion-related failures of L.P. blades account for one-third of the total number of blade failures in the L.P. turbines, which are the main cause of forced outages of the steam turbine [46]. According to Mann et al. [47] corrosion fatigue along with pitting is considered to be the most common single factor. The formation of pits due to droplet erosion at a critical location on a turbine blade can act to aggravate cracking in two ways. Firstly, as a stress concentration causing the blade to experience high stresses (both static and cyclic) and secondly, as a stagnant corrosion cell where the environment at the base of the pit can change concentration as the corrosion proceeds [47].

1.6.2. Water Presence in Gas Turbines

Water droplets ingestion into the gas turbines is being studied over a long time. Numerous researchers [49, 50] had been conducted to understand the effects of two-phase phenomena for the aircraft gas turbines. These researchers had shown that the engine performance due to the presence of

water droplets at engine inlet can have an adverse effect on the engine performance. In particular, the surging of the engine and may suffer blow-out unsteadiness in the main burner. Different methods and techniques were devised to stop the presence of water in the engine, as at that time our knowledge about operating gas turbines was only limited with air as their only working fluid. However, with an advancement of high-pressure nozzles, the concept of water fogging has started to gain more interest in the power generation industry. Potential benefits of water ingestion were first reported in the 1940s [50]. According to Bianchi [50], water ingestion was used on older jet engines (with zero or low bypass ratios) to boost the take-off thrust when aircraft were operating on hot days or from high altitude airports.

Comparison of the different power augmentation technologies is conducted by Bianchi [51]. He reported that all technologies yield a percentage wise higher power boost than the corresponding change in heat rate in gas turbine applications. Potential benefits of water ingestion from the thermodynamic point of view is identified by many researchers ([52, 53]) etc. The experimental results presented by Utamura et al. [54] indicated that the water ingestion significantly increases the overall engine performance. Similarly, in another study by Utamura et al. [55] showed that the heat rate for the gas turbine cycle process decreases due to wet compression and the overall plant's thermal efficiency increases. White et al. [56] introduces a numerical method for the computation of the wet compression process in axial machines based on droplets evaporation model combined with simple polytropic compression calculations. He compared the actual work of compression with the one needed for the dry compression achieving the wet compression pressure ratio using the peak dry polytrophic efficiency. It was found that the actual work of wet compression is significantly smaller than the ideal polytropic work of wet compression, excluding aerodynamic losses. The difference ascends from 4% to 15% with the water mass flow increased from 1% to 10% of the air mass flow. Zheng et al. [57] presented a model to calculate the wet compression process and concluded that the water ingestion leads to overall increase in thermodynamic efficiency of gas turbines, provided that the droplet diameters should be small as they result in high evaporation rate. Similar, results shown by many other researchers ([58–60]) concluded that droplet evaporation strongly depends on the diameter of the injected droplets and it is the main driver for cooling efficiency within the flow, which results in reduced compressor work and higher efficiency. Utamura et al. [61] had shown that an overspray of 1% can result in an increase of power output and thermal efficiency of 10% and 3% respectively for a 115 MW GT (Hitachi Frame 9E). According to Bhargava et al. [62], the overspray level usually ranges between 0.5-1% of the mass flow rate of inlet air into the gas turbine but is machine specific and has suggested that water mass flow rate should not exceed 2%.

Eisfield et al. [63] did an investigation on the aerodynamic behaviour of a compressor aerofoil and concluded that the effects of water ingestion into a linear compressor cascade in terms of the loss coefficient are detrimental in the case of low blade loading and is beneficial in case of high blade loading. Park et al. [64] uses a numerical method based on Lagrangian particle tracking equations and confirmed that for the same inlet air velocity or mass flow rate in both dry and wet flow, the static pressure and Mach number distributions on the blade surface get significantly altered. They also argued that the shock wave moves towards the T.E. making the blade to operate in off-design conditions. This causes a change to the structural load and the vibration characteristics and consequently led to the material failure. It was reported at AGARD 1995 [65] that droplets size bigger than 70 μm are captured by the blades and therefore form a liquid film. On the other hand, the droplets size of 10 μm are affected by the aerodynamic forces and may pass through the blades row, as shown in Fig. 1.14.

Sun et al. [66] used a 3D model of an entire gas turbine to calculate the effects of water ingestion. They report that water ingestion leads to an increased mass flow and power output as well as a higher compressor efficiency. They also identify an improvement in the flow separation behaviour on the first stage of the compressor. Burn et al. [67] found that wet compression can result in a displacement of the operating point towards the surge line. Das et al. [68] concluded that the deposited droplet mass is higher at the L.E. near the tip and at the lowest rotor speed. They also reported that only very few droplets impinge on the L.E. of the rotor blade suction surface. However, their research focuses only on fine droplets of 30 μm. It is certain that larger droplets will impinge on the blade pressure surface even at high rotational speeds.

On the droplets impact at the blade surface, Rioboo et al. [69] considered a wide range of droplets velocities and diameters and suggest six different outcomes. The first outcome was "deposition" in

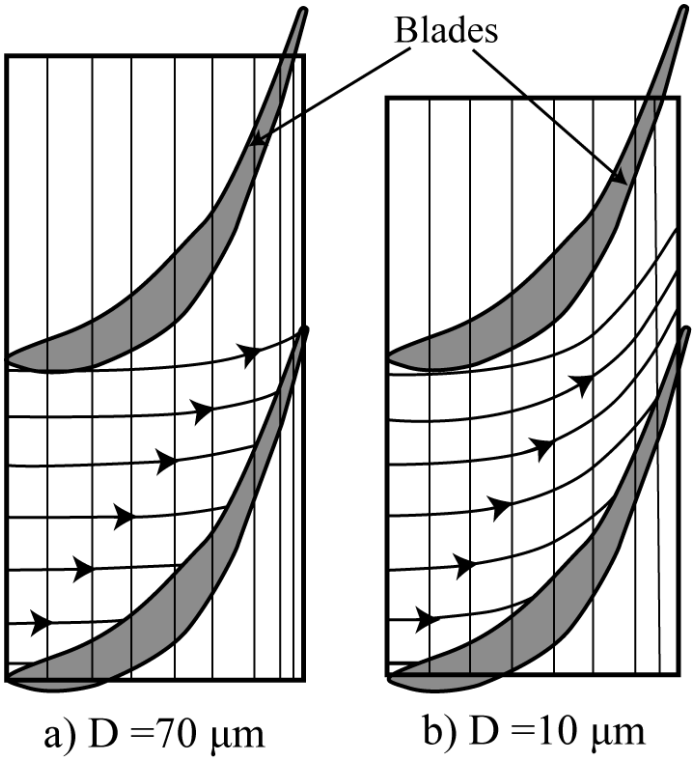

Figure 1.14 – Droplet Trajectories Estimation [65]

which the drops get deformed and stayed on the solid surface. The second was called "prompt splash" in which the droplets were ejected directly from the region between the surface and the liquid in the spreading phase of the lamella (the expanding liquid disk). The third is "corona splash" and takes place when a corona is formed during the spreading phase and eventually breakup into droplets. The fourth outcome was named "receding break-up" and occurred when the droplets were left on the surface during the receding phase of the impact. The fifth one was the "rebound" and is self-explanatory. The last one was the "partial rebound" where part of the drop attached to the surface while some part rebounds.

Bose et al. [70] investigated the influence of water ingestion on the blade clearance. They build a code (WINCLR), which provides a scheme for obtaining the performance and the blade clearance for axial-flow compressors working under given operating and water ingestion conditions. The authors concluded that the blade clearance is affected by the presence of water and the change in compressor's performance is substantial. They argue that the extent of changes in performance and clearance increases with an increase in the mass fraction of water entering the compressor. Their numerical results showed reported that the blade clearance at the 1st rotor blade reduces from 0.123 mm to 0.1 mm when water was ingested.

AGARD (1995) [65] describes that under rain conditions the compressor operates closer to the surge line. Heat and mass transfer between gaseous and liquid phases take place in the compressor but with a low rate, since residence time is small (fractions of sec). Water evaporates mainly in the combustor because of the higher temperature. The increased volume of water vapour occupies means that even smaller quantity of air enters into the combustor with constant fuel mass flow rate. Thus, in the final stages of the compressor, the air axial velocity increases and bearing in mind the rotor speed the incidence angle decreases (i.e. the known velocity triangle is modified). A reduced incidence angle results in a drop in compressor's efficiency and consequently deteriorates the mass flow by moving the operating point closer to the surge. It was highlighted that the above condition describes the aero-thermodynamic processes, which took place in the compressor-combustor components. It is thought that the mechanical effects are far more dominant because the water centrifugation precedes any other aero-thermodynamic process. Thus, the engine's rundown should be taken into consideration in any case.

In Fig. 1.15, Santa [71] demonstrated the movement of running line towards the surge line as the

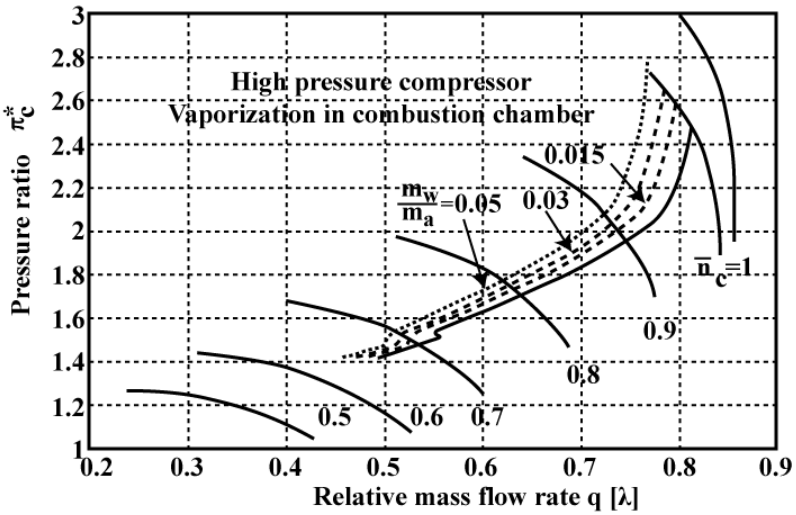

Figure 1.15 – High-Pressure Compressor Running Line Movement due to Water Ingestion [71]

water fraction increases. The author attempts to examine the water ingestion phenomenon and deals with its mathematical modelling. He focuses on the thermodynamic effects and assumes that evaporation occurs in the combustion chamber. Santa [71] argues that the operating point of the compressor moves towards the surge line, i.e. there is a reduction in surge margin, which is attributed due to evaporation, i.e., the increase of the air-water volume causes a reduction in air mass flow. It is believed that aerodynamic and mechanical effects should always be taken into consideration. Evaporation is the principal factor in cases of water ingestion or fog boosting to improve the cycle efficiency of industrial engines. On the other hand, rain ingestion involves large water droplets and the effect of evaporation is less important compared with the aerodynamic and mechanical effects.

1.7. Conclusions from the Literature Review

From the above literature review, for the development of modern and high-efficiency systems, wet turbines have led to an increase in deposition, erosion, corrosion problems etc. Close tolerances in the turbines, the use of high-strength materials and impure water all contribute to these conditions. The knowledge of liquid droplets size and its distribution is of extreme importance to avoid the failure of overall wet turbine system. Pitting, corrosion fatigue, and stress corrosion cracking problems can all occur in wet turbine systems. Therefore, a more fundamental study is needed to be conducted to understand the physical phenomenon of the presence of water droplets in detail.

1.8. Summary of Droplet Presence in Wet Turbine Systems

Figure 1.16 shows the detail flow chart of maximum possible physical interaction of droplets in wet turbine systems, as explain briefly below;

1.8.1. Droplet –Wall Interaction

Droplets in wet turbine systems can easily strike the blades. Upon interaction following four possible scenarios can occur as given in Fig. 1.16, which are;

1. Rebounding: Upon striking the blade a droplet can get reflected back into the main fluid stream. Depending upon the size and momentum of a droplet, a droplet may undergo a change in its momentum.
2. Splashing: A high-speed droplet upon striking a blade may disintegrate into further smaller droplets.
3. Deposition: When a relatively low-speed droplet strikes a blade, it may completely get deposited on a blade by spreading resulting in a formation of a thin liquid film at a blade surface.
4. Partial Deposition & Splashing: In this scenario, a droplet can undergo both deposition and splashing.

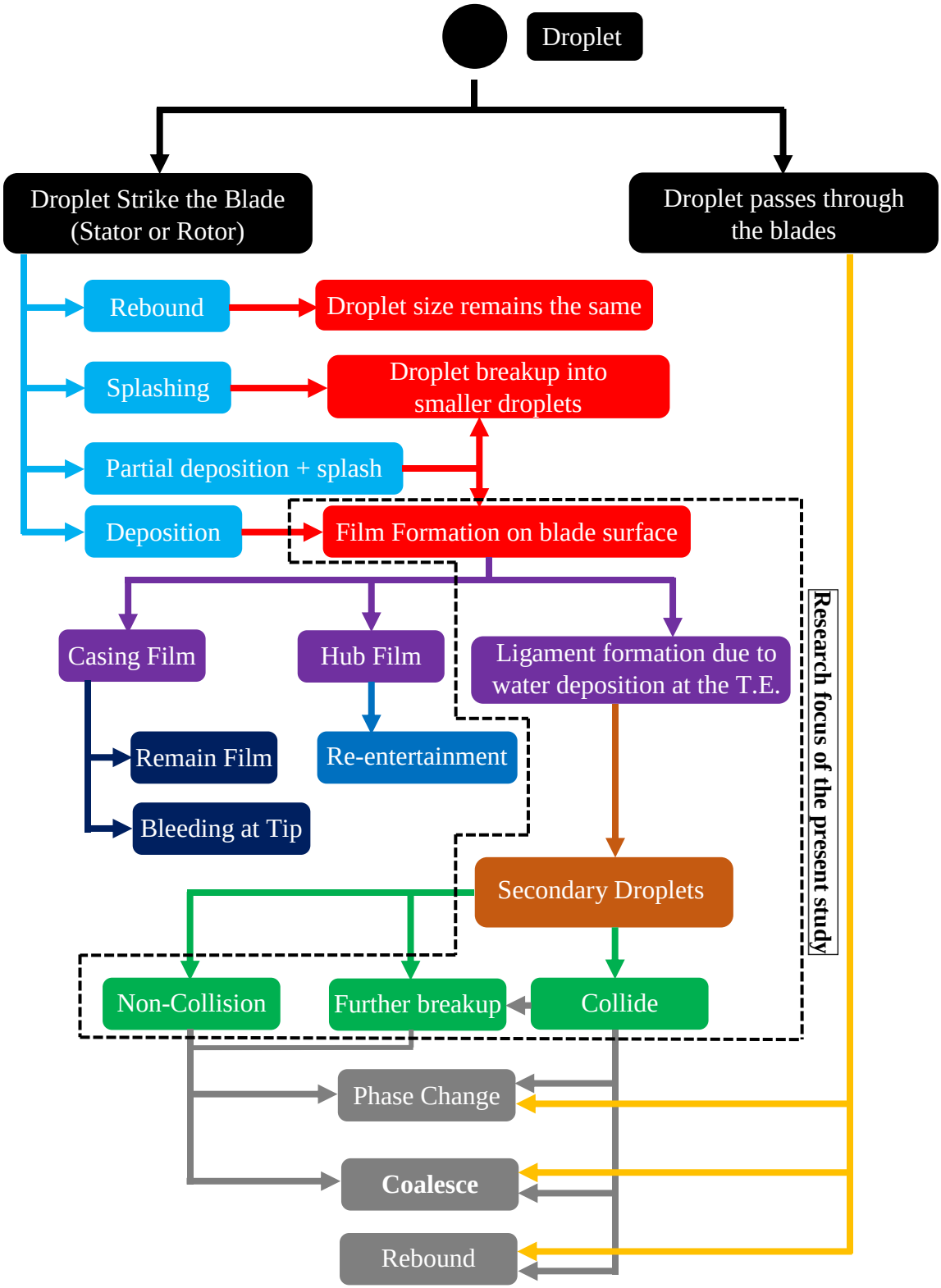

Figure 1.16 – Possible Scenario of droplet presence in a Wet System

In general, the partial deposition and splashing phenomena occurs in the wet turbine systems. The amount of water deposited and splashed usually depend on upon the incident angle between the aerofoil and the droplets.

1.8.2. Water Film Formation

The droplets which get deposited on the blade surface results in the formation of the liquid film, as shown in Fig. 1.16. The liquid film formed upon the blade surface will move axially along the blade surface due to the aerodynamic forces of the main flow field. However, due to the centrifugal effect, a portion of such film will move towards the tip region and casing also. The motion of film downstream towards the T.E. of a blade as a function of shear forces acted upon it due to the aerodynamic forces. Similarly, blade surface roughness can also significantly affects the liquid film motion. If the amount of droplets ingested are large enough then the film thickness will increase significantly, such that if it exceeds a critical limit a "virtual blade thickening" phenomena may occur. In such case, the flow aerodynamics and boundary layer stability will be significantly affected by the water film. If such film is formed on rotor blades then they might be operating at reduced speed due to the increased mass effects of the liquid film. A liquid film formed at tip section may ultimately result in the deterioration of flow in the tip region. Similarly, water film formed in the casing may lead to the mechanical malfunctioning of the system by bleeding into another mechanical component (such as gearbox, etc.).

1.8.3. Water deposition at T.E

The part of the film which ultimately reaches the T.E. of a blade can get deposited there and ultimately will get separated from the T.E, generating a wave-like structure (called ligament). The deposited film at the T.E. can be due to several factors, such as due to the surface tension property of the liquid, T.E. profile thickness, flow separation, aerodynamic effects etc. As the deposited film remain at the T.E. for a significantly long time leading to the erosion of blade.

1.8.4. Secondary droplets (ligament disintegration)

The ligament structure which is attached at the T.E. of a blade will interact with the surrounding flow field. The breakup of these ligaments can either be due to the dominant effects of the aerodynamic forces or the liquid's surface tension forces. Such interaction will ultimately lead to the disintegration of ligament into secondary droplets. These secondary droplets formed are usually greater in size compared to the droplets ingested into the wet turbine systems. The secondary droplets produced can further undergo disintegration, coalesce etc. Finally, these secondary droplets formed will strike the downstream blade and the same process will be repeated till the last stage of the wet turbine systems. These droplets usually undergo a phase change along with their passage in the humid environment of the wet turbine systems.

1.9. Scope of the Present Study

1.9.1. Motivation for the Present Research

Two phase phenomenon in turbine systems is a highly complex phenomenon, especially air as a gaseous phase and water as a liquid phase, due to the ability of water to get deform. Due to the deformation of liquid droplets, many phenomena are involved such as droplets evaporation, droplets interactions with each other as well as with the blades. Similarly, the droplets in the turbine systems can lead to the malfunctioning of the turbine systems by causing erosion due to the formation of coarse liquid droplets. In addition to the erosion, the non-uniform distribution of the liquid's droplets, especially the coarse droplets could results in the damaging of the L.E. of the turbine blades due to the relatively high momentum.

Unfortunately, the kinematics of liquid inside the wet turbine systems have not been completely understood. Moreover, according to the author knowledge very little experimental work has been done to understand the dynamics of liquid in the turbine systems.

1.9.2. Objectives of the Research Study

From the brief discussion, the presence of liquid droplets in the steam turbine have always been a problem. Moreover, since fogging in gas turbines is also gaining increasing importance for power augmentation one need to understand the characteristics of water presence in such systems also. Due to the presence of liquid in the steam as well as gas turbines this study will be primarily focused on a more fundamental study in order to understand the fundamental characteristics of liquid presence in the thermal systems, which should be applicable to both the steam and gas turbines. Therefore, the objective of this study is to perform fundamental experimental investigation on cascade blades to understand the;

1. Characteristics of liquid film formation on the cascade blade,
2. Characteristics of ligament and its breakup, and
3. Characteristics of droplets size distribution aft the T.E. region.

The research focus area is highlighted, as given by Fig. 1.16. For that purpose, geometrically simple cascade blade profile is used in the present study to understand the liquid phase characteristics under various operating conditions. The geometric profile is given in detail in section 3.3. Based on the experimental results, theoretical models are proposed to predict the characteristics of two-phase phenomena. It is expected that this fundamental experimental research will help in improving the design of turbine systems as well as contribute effectively in improving (or developing) the numerical codes for analysing the two-phase phenomenon in turbine systems.

1.10. Structure of the Thesis

The manuscript is divided mainly into the following three parts;

PART I – General introduction, objectives and fundamental study

- In the first part of the thesis, a detailed fundamental description of the two-phase physical phenomena and its effect are discussed. In Chapter 1 an introduction to the current energy resources and the available systems are discussed. The advantages and disadvantages of commonly used thermal systems (steam and gas turbines (including gas turbine combined cycles)) are made and possible limitation to these systems thermal efficiency limitations are also outlined briefly. A brief and separate literature review of two-phase phenomena in steam and gas turbine systems is made and the motivation and the scope of the present study is made to understand the fundamental phenomena of two-phase systems in the wet turbine systems. Chapter 2 deals with fundamental theoretical knowledge of the two-phase phenomena from the turbomachinery viewpoint, such as the interaction of droplets with the surrounding air flow environment and corresponding breakup type etc. as well as representative diameter representation and so on.

Part II – Experimental setup

- The second part (Chapter 3) is mainly focused on the development of an experimental facility, based on the objectives of this thesis. This section gives a detail explanation of various experimental hardware devices and their calibration method, as well as the purpose of using simple aerofoil geometry; namely – Elliptical profile. Finally, a detail theoretical background as well as the implementation of the Image Processing Algorithm is presented and discussed. This technique is used in the present study to experimentally measure the droplets size.

Part III – Experimental results

- The final part of the thesis is focused on the results and discussions. Chapter 4 is sub-divided into two main subsections;

  i. The first sub-section is completely devoted to the experimental investigation of the elliptical profile geometry, with a water ejection hole at the mid-span of the blade at 0 – degree angle of attack (AOA). The characteristics of liquid film formation and the corresponding droplets size distribution aft the T.E. of the cascade blade under different air momentum are discussed. A detailed investigation is made by taking shadowgraph images to visualize the liquid film structure as well as the formation of droplets and their breakup aft the T.E. of the blade.

Special attention is paid to the development of a theoretical model for predicting the primary coarse droplets formed, which get detached from the T.E. of the cascade blade, shedding frequency of accumulated water at the T.E., etc.

ii. In the second sub-section, the effect of angle of attack (3-, 5-, 7- and 10- degrees) on the characteristics of water film formation as well as the droplets size distribution are discussed in details for the elliptical profile blade.

- Conclusions are drawn and several recommendations for the potential further work are suggested in Chapter 5.

Additional Results

- Appendix A deals with the supplementary aerofoil geometry – named as flat profile blade geometry. This section is basically an extension to broaden the knowledge about how the water ejection hole size effects on the characteristics of liquid film and the droplets size distribution aft the T.E. of the blade to understand the effects of nozzles size in the real wet turbine systems.
- In Appendix B, a comparison of few characteristics of elliptical and flat blade profiles are considered. These includes the development of a theoretically model to understand the role of T.E. thickness, shedding angle distribution etc. Appendix C provides a brief introduction to the PIV method which is utilized in this thesis, whereas, Appendix D gives a comparison of experimental results with an in-house code, called CIP-LSM.

Chapter No. 2: Fundamental Theoretical Background

2.1. Two Phase Phenomena in Turbomachinery

Two phase phenomena is a highly complex phenomenon in turbomachines. Figure 2.1 summarizes and describe only the major important phenomena which one need to consider in turbomachines, assuming no phase change. From Fig. 2.1, it can be easily understood that the phenomenon is quite complex due to the interaction of different components of two phase not only with each other but their interaction with themselves also. For example, with the interaction of gaseous phase with the thin liquid film formation on the cascade blade will give rise to liquid waves, which can affect the boundary layer etc. On the other hand, the presence of liquid droplets will result in the breakup, deformation, coalescence etc. causing a reduction in the momentum of high-speed air. Therefore, for two-phase phenomena of wet turbines, one need to take into account all the relevant forces which can arise due to the interaction of gaseous, liquid and dispersed phase. Based on Fig. 2.1, a very fundamental study review will be made for the two-phase phenomena. It should be noted that in the present thesis phase change effects are not considered at all.

2.2. Basic Principle of Two-Phase Flow

Multi-phase flow implies the coexisting of at least two or more matters in motion. Two phase is one of the examples of multiphase flow. Most of the theoretical study of the two-phase phenomenon is based on a general flow, since the application of two-phase can be found in many industrial processes. In this section, the relevant theory which can be related to the two-phase theory to the droplets laden flow in turbomachinery will be discussed only. In the field of turbomachinery, two-phase flow is generally termed as gas-droplet flow or more occasionally, the gaseous phase is referred as a continuous phase whereas the droplets are referred as disperse phase. In turbomachines, unlike other two phase flow phenomenon, the major quantity of the liquid phase are in droplet form.

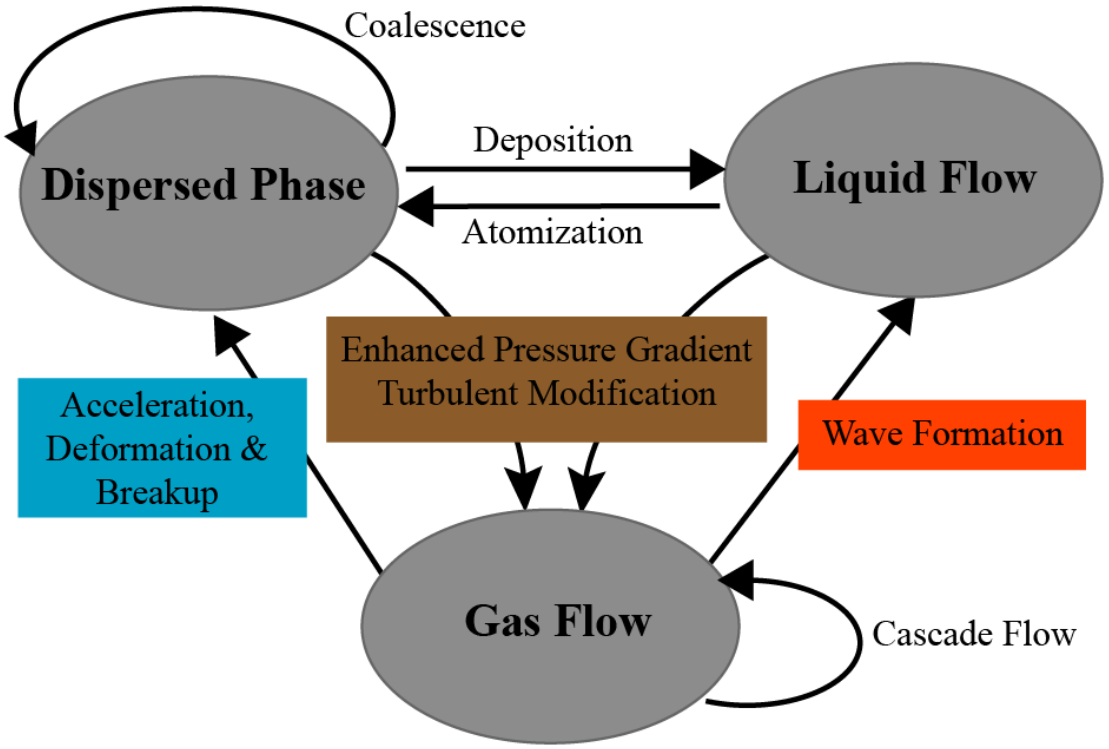

Figure 2.1 – General Interaction between Gas, Liquid and Dispersed Phase without phase change

2.2.1. Continuous Phase

Consider a flow velocity in a three-dimensional space (x, y, z) having velocity components (u, v, w), then the flow behaviour can be simplify described by the Navier-Stokes Eq.

Continuity Equation

$$\frac{D\rho}{Dt} + \rho\left(\frac{\partial u}{\partial x} + \frac{\partial v}{\partial y} + \frac{\partial w}{\partial z}\right) = 0 \tag{2.1}$$

Momentum Equations

x-direction:
$$\rho\frac{Du}{Dt} = \rho g_x + \frac{\partial}{\partial x}(\Pi_{xx}) + \frac{\partial}{\partial y}(\Pi_{xy}) + \frac{\partial}{\partial z}(\Pi_{xz}) \tag{2.2}$$

y-direction:
$$\rho\frac{Dv}{Dt} = \rho g_y + \frac{\partial}{\partial x}(\Pi_{yx}) + \frac{\partial}{\partial y}(\Pi_{yy}) + \frac{\partial}{\partial z}(\Pi_{yz}) \tag{2.3}$$

z-direction:
$$\rho\frac{Dw}{Dt} = \rho g_z + \frac{\partial}{\partial x}(\Pi_{xz}) + \frac{\partial}{\partial y}(\Pi_{yz}) + \frac{\partial}{\partial z}(\Pi_{zz}) \tag{2.4}$$

here, g is the acceleration due to the gravity, Π_{xx}, Π_{yy}, and Π_{zz} are the normal stress tensor, and Π_{xy}, Π_{yz}, and Π_{xz} are shear stress tensors, having normal in the x-, y-, and z- direction respectively.

It is possible to show that the stress tensor is symmetric, otherwise, any fluid element would suffer infinite angular acceleration, i.e.

$$\Pi_{xy} = \Pi_{yx}\ ;\ \Pi_{xz} = \Pi_{zx}\ ;\ \Pi_{yz} = \Pi_{zy} \tag{2.5}$$

The surface stresses [Π] on any element arise from a combination of pressure and viscous friction, as prescribed by the constitutive relations

$$\Pi_{xx} = -p + \lambda\,\nabla.\boldsymbol{U} + 2\mu\frac{\partial u}{\partial x}\ ;\ \Pi_{xy} = \mu\left(\frac{\partial u}{\partial y} + \frac{\partial v}{\partial x}\right) \tag{2.6}$$

$$\Pi_{yy} = -p + \lambda\,\nabla.\boldsymbol{U} + 2\mu\frac{\partial v}{\partial y}\ ;\ \Pi_{yz} = \mu\left(\frac{\partial v}{\partial z} + \frac{\partial w}{\partial y}\right) \tag{2.7}$$

$$\Pi_{zz} = -p + \lambda\,\nabla.\boldsymbol{U} + 2\mu\frac{\partial w}{\partial z}\ ;\ \Pi_{xz} = \mu\left(\frac{\partial u}{\partial z} + \frac{\partial w}{\partial x}\right) \tag{2.8}$$

For the flow to be incompressible,

$$\nabla.\boldsymbol{U} = 0 \tag{2.9}$$

Thus, the conservative relation can be reduced to,

$$\Pi_{ij} = -p\delta_{ij} + \mu\left(\frac{\partial u_i}{\partial x_j} + \frac{\partial u_j}{\partial x_i}\right) \tag{2.10}$$

here, Kronecker delta, such that $\delta_{ij} = 1$, if $i = j$ and $\delta_{ij} = 0$, if $i \neq j$

Thus, the incompressible Navier-Stokes Equation can be written as;

Continuity:
$$\frac{\partial u}{\partial x} + \frac{\partial v}{\partial y} + \frac{\partial w}{\partial z} = 0 \tag{2.11}$$

Momentum – x-direction:
$$\rho\frac{Du}{Dt} = \rho g_x - \frac{\partial p}{\partial x} + \mu\left(\frac{\partial^2 u}{\partial x^2} + \frac{\partial^2 u}{\partial y^2} + \frac{\partial^2 u}{\partial z^2}\right) \tag{2.12}$$

Momentum – y-direction:
$$\rho\frac{Dv}{Dt} = \rho g_y - \frac{\partial p}{\partial y} + \mu\left(\frac{\partial^2 v}{\partial x^2} + \frac{\partial^2 v}{\partial y^2} + \frac{\partial^2 v}{\partial z^2}\right) \tag{2.13}$$

Momentum – z-direction:
$$\rho \frac{Dw}{Dt} = \rho g_z - \frac{\partial p}{\partial z} + \mu \left(\frac{\partial^2 w}{\partial x^2} + \frac{\partial^2 w}{\partial y^2} + \frac{\partial^2 w}{\partial z^2} \right) \quad (2.14)$$

The turbulence velocity can be simply defined as the summation of average of velocity in the flow field and the fluctuation of the flow field about the mean flow velocity, i.e.

$$u = \bar{u}\,(x, y, z, t) + u'\,(x, y, z, t) \quad (2.15)$$

And similarly the velocity in the y- and z-direction can be given by Eq. (2.16) and (2.17) respectively.

$$v = \bar{v}\,(x, y, z, t) + v'\,(x, y, z, t) \quad (2.16)$$

$$w = \bar{w}\,(x, y, z, t) + w'\,(x, y, z, t) \quad (2.17)$$

Thus, the turbulence of the flow field can be determined as given by Eq. (2.18)

$$Tu = \frac{1}{U} \sqrt{\frac{1}{3} (\bar{u}'^2 + \bar{v}'^2 + w'^2)} \quad (2.18)$$

2.2.2. Dispersed Phase

Dispersed phase flow is a flow in which one phase, i.e., the dispersed phase, is not materially connected [76].

2.2.2.1. Droplets Behaviour

Due to the presence of droplets in cascade flow, it basically gives rise to three major phenomena

1. Droplet movement and forces acting on a droplet,
2. Droplet deformation and breakup, and
3. Phase change.

In the present study, the phase change phenomenon is not considered and therefore, would not be discussed in detail.

2.2.2.2. Droplets Movement and Acting Forces [76]

A droplet particle moving in a gaseous medium will experience several forces. In general, these forces can be divided into steady and unsteady forces, which are explained briefly as follow. A detailed study can be obtained from Crowe et al. [76].

(a) Steady Force

- Drag Force

The droplets in a cascade flow are subjected to the velocity gradient. Dispersed phase droplets in a two-phase flow will be subject to relative velocities as their inertia would lead to lower the acceleration. Thus, the time it takes for a droplet particle to respond to a change in fluid velocity can be estimated from the solution of simplified forms of the equation of particle motion, which can be given by Eq. (2.19)

$$m \frac{du_p}{dx} = \frac{1}{2} C_D \left(\frac{\pi d_p^2}{4} \right) \rho_c \left(u_c - u_p \right) |u_c - u_p| \quad (2.19)$$

here, u is the velocity, whereas, the subscript p and c represents the dispersed (i.e. droplets or particles) and the continuous (i.e., air) phase respectively. C_D is the coefficient of drag that is dependent on the shape and orientation to the flow as well as the flow parameters, such as Reynolds number (Re_p), which for the dispersed phase is given by

$$Re_p = \frac{\rho_c \, d_p \, |u_{rel}|}{\mu_c} \quad (2.20)$$

For a subcritical range of Reynolds Number, C_D can be approximated as follows

$$C_D = \begin{cases} \frac{24}{Re_p}\left(1 + 0.15\, Re_p^{2/3}\right) & for \quad Re_p < 1000 \\ 0.44 & for \quad 1000 < Re_p < 2\, x\, 10^5 \end{cases} \tag{2.21}$$

Introducing a drag factor, f_D given mathematically by Eq. (2.22)

$$f_D = \frac{C_D\, Re_p}{24} \tag{2.22}$$

Substituting Eq. (2.22) in Eq. (2.19), the equation of motion can be simplified as

$$\vec{F}_D = m\, \frac{du_p}{dx} = 3\, \pi\, f_D\, d_p^2\, \mu_c \left(\vec{u}_c - \vec{u}_p\right) \left|\vec{u}_c - \vec{u}_p\right| \tag{2.23}$$

Assuming low relative Reynolds Number of particles, i.e., $Re_p < 1$, then according to [75], $C_D \approx 24/Re_p$, thus the corresponding velocity (momentum) response time can be approximated as

$$\tau_p = \frac{\rho_p\, d_p^2}{18\, \mu_c} \tag{2.24}$$

Using the relaxation time, the non-dimensional Stokes Number (St) can be obtained from Eq. (2.25)

$$St = \frac{\tau_p}{\tau_f} \tag{2.25}$$

Here, τ_f is a characteristics time describing the flow. According to [75], this characteristics time is the ratio of chord length of the cascade blade (C) to the incident velocity of the main air flow (U)

$$\tau_f = \frac{C}{U} \tag{2.26}$$

Hence, the stokes number can be approximated as

$$St = \frac{\rho_p\, d_p^2\, U}{18\, \mu_c\, C} \tag{2.27}$$

Stokes number (St) describes the capability of a droplet particle to react to the changes in the velocity of free stream continuous flow. Such that if;

(i) $St \rightarrow 0$ ($\tau_p \approx 0$, since $d_p \ll 1$)

Droplet particles and fluid velocities are almost the same and the two phases are in thermodynamic equilibrium, thus, the droplet will easily adapt to the changes in the fluid velocity.

(ii) $St \rightarrow \infty$ ($\tau_p \gg 1$, since $d_p \gg 1$)

Droplet particles motion are almost independent of the fluid flow velocity and are not in thermal equilibrium. Thus, the droplet will be little affected by the de- or acceleration of the fluid flow.

- Force due to Pressure Gradient

The effect of local pressure gradient gives rise to a force on a droplet particle in the direction of the pressure gradient. Assuming that a constant pressure gradient act on droplet having volume (V_p), the pressure force can be given by

$$\vec{F}_P = \nabla p\, V_p \tag{2.28}$$

The pressure gradient has the same magnitude in the gaseous phase as the flow acceleration and can be expressed as

$$\frac{\partial P}{\partial x} \sim \rho_c \frac{Du_c}{Dt} \tag{2.29}$$

Therefore, the ratio of pressure force to the force needed to accelerate a droplet is

$$\frac{V_p \frac{dP}{dx}}{m_p \frac{du_p}{dt}} \sim \frac{\rho_c}{\rho_p} \frac{\frac{Du_c}{Dt}}{\frac{du_p}{dt}} \tag{2.30}$$

If the ratio of gaseous phase and dispersed phase are of the same order, then the ratio of pressure to the acceleration is equal to the density ratio of the corresponding phases (i.e. of an order 10^{-3})

$$\frac{V_p \frac{dP}{dx}}{m_p \frac{du_p}{dt}} \sim \frac{\rho_c}{\rho_p} \tag{2.31}$$

Therefore, pressure gradient force can be neglected in turbomachinery. Thus, in a steady state the total force acting on a droplet can be equivalent to the drag force (Eq. (2.19)), neglecting any buoyancy effect.

(b) Unsteady forces

The unsteady forces arise due to the acceleration of the relative velocity and can be mainly classified as

- Virtual mass effect (force required to accelerate the surrounding gaseous fluid particles)
- Basset force (force arises due to the lagging boundary layer development with changing relative velocity between the droplet and surrounding gaseous fluid)

- Virtual Mass Force

A deceleration or acceleration of a particle will affect the surrounding gaseous particles by the virtue of its mass and would result in Virtual Mass Force, whose correlation can be obtained as given in Eq. (2.32).

$$\vec{F}_{vm} = \frac{\rho_c u_p}{2} \frac{du_{rel}}{dt} \tag{2.32}$$

- Basset Force

The Basset force accounts for the temporal delay in the development of boundary layer, as the relative velocity changed with time. Due to this reason, it is usually termed as "history" term and is mathematically expressed as

$$\vec{F}_{Basset} = \frac{3}{2} d_p^2 \sqrt{\pi \rho_c \mu_c} \int_0^t \frac{\left(\frac{d\vec{u}_c}{dt} - \frac{d\vec{u}_p}{dt}\right)}{\sqrt{t - t'}} dt' \tag{2.33}$$

- Lift Forces

Lift forces on a droplet particle are mainly due to their rotation. The rotation can either be due to velocity gradient or due to any other sources, such as particle contact and rebound from the surface etc. In literature, the lift force is classified into two based on the lift mechanism on the droplets.

- Staffman Lift Force

This force is due to the pressure distribution developed on a particle due to rotation induced by a velocity gradient. Staffman formulated this force and found that the force magnitude can be expressed as

$$F_{staff} = 1.61 \mu_c d_p |u_{rel}| \sqrt{\frac{d_p^2}{\upsilon_c} \frac{du}{dy}} \tag{2.34}$$

➢ Magnus Force

If a droplet rotates then a difference of pressure above and below the particle can lead to the lift forces, called the Magnus Force, and can be approximated as

$$\vec{F}_{mag} = \frac{\pi}{8} |\vec{u}_c - \vec{u}_p| d_p^2 \rho_c c_{LR} \left[\frac{\vec{w}_{rel} |\vec{u}_c - \vec{u}_p|}{|\vec{w}_{rel}|} \right] \quad (2.35)$$

here, $\vec{w}_{rel}$ is the relative spin of a particle ($\vec{w}_p$) with respect to the surrounding fluid ($\vec{w}_c$) and C_{LR} is the lift coefficient, which is expressed mathematically as

$$C_{LR} = \frac{d_p |\vec{w}_p|}{|\vec{u}_c - \vec{u}_p|} \quad (2.36)$$

The combination of the above equations, i.e., drag force, the pressure force, virtual mass force, basset force and the body force (mass times the acceleration) is commonly known as Basset-Boussinesq-Oseen (BBO) Equation for a droplet in motion.

2.2.2.3. Droplet Deformation and Breakup

There are a large number of published reports on the droplet deformation and breakup. A list of commonly used non-dimensional groups which characterise the droplet breakup and fragmentation under different conditions is summarized in Table 2.1.

Table 2.1 – Non-Dimensional Number for Droplet Breakup Characterization

Non-Dimensional Group	Mathematical Representation	Physical Significance
Reynolds Number	$Re_p = \frac{\rho_c \lvert u_c - u_p \rvert d_p}{\mu_c} = \frac{\rho_c u_{rel} d_p}{\mu_c}$	$\frac{Inertia\ Force}{Viscous\ Force}$
Weber Number	$We = \frac{\rho_c u_{rel}^2 d_p}{\sigma}$	$\frac{Inertia\ Force}{Surface\ Tension}$
Ohnesorge Number	$Oh = \frac{\mu_c}{\sqrt{\rho_p d_p \sigma}}$	$\frac{Viscous\ Force}{Surface\ Tension}$
Laplace Number	$La = \frac{1}{Oh^2}$	$\frac{Surface\ Tension}{Viscous\ Forces}$
Bond Number	$Bo = \frac{\rho_p d_p^2}{\sigma} \frac{du_{rel}}{dt}$	$\frac{Gravity\ Force}{Surface\ Tension}$
Rabin Number	$Ra = \frac{We}{\sqrt{Re_p}}$	$\frac{Viscous\ Forces}{Surface\ Tension}$

- Classification of Droplet Deformation and Breakup Regimes

One does not necessarily need all of the above non-dimensional numbers to classify the breakup. For example, Bond Number is used only when the influence of gravity forces on the droplets cannot be neglected and similarly for the other non-dimensional numbers. However, in general, different regimes of droplets breakup are mainly classified based on the Weber number only since in most of the application the breakup occurs mainly in the presence of inertial forces which are opposed by the liquid's property of surface tension. When the Weber number (We) reaches a critical value (We_{cr}) the deformation of droplet start and when $We \geq We_{cr}$ the liquid droplet will break. Plich et al. [79] conducted a comprehensive analysis of the experimental data that were obtained by other researchers and used critical value of We_{cr} as to be 12. Detail schematics of different modes of droplets breakup are shown in Fig. 2.2.

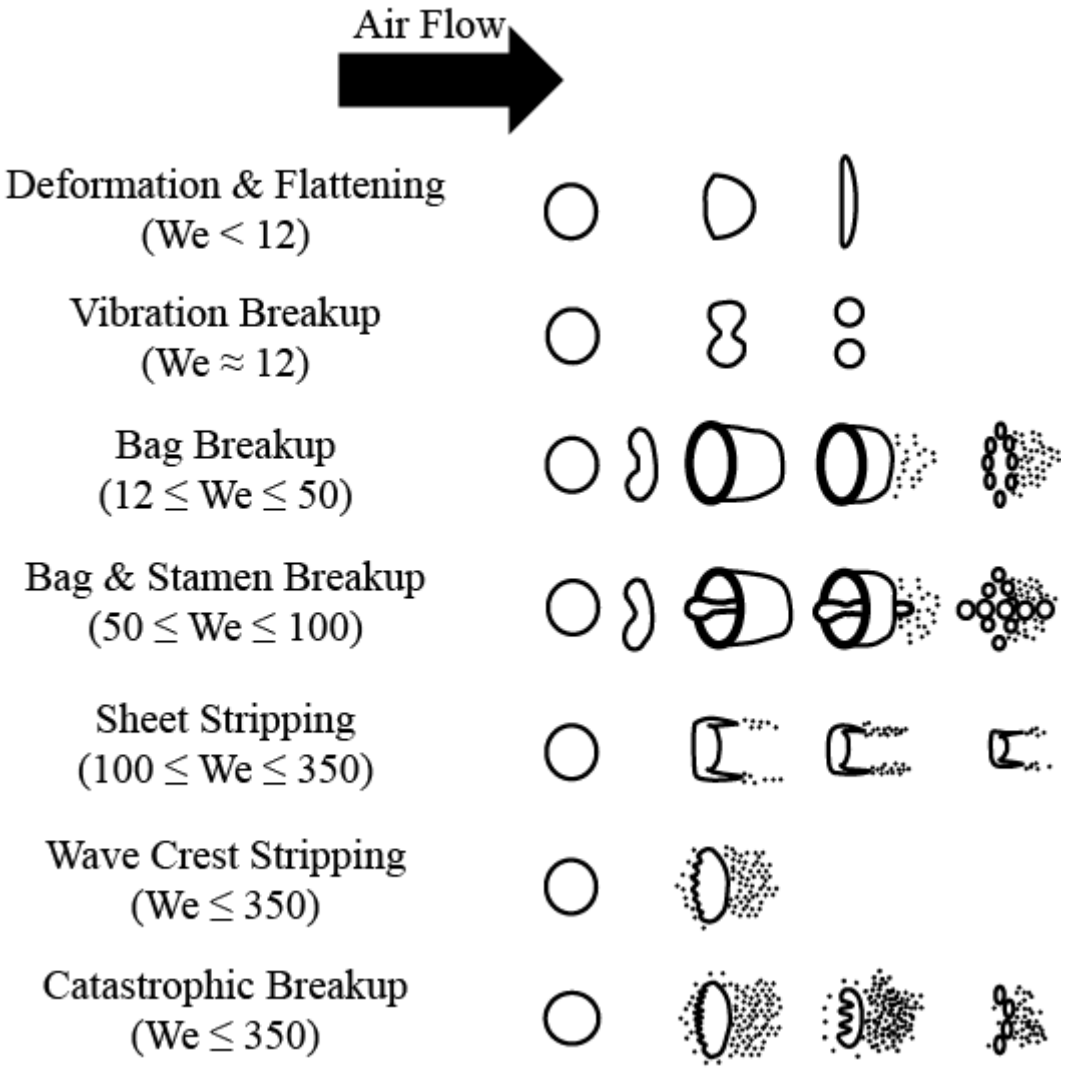

Figure 2.2 – Droplet Deformation and Breakup Regimes [76]

- Deformation & Flattening (First Stage of Breakup)

When the aerodynamic forces act on a droplet it causes the droplet to deform and flatten. If the We is less than the We_{cr} the droplet will retain its total mass (assuming no phase change occur due to evaporation). As in this case the liquid's surface tension is sufficient to overcome the external pressure forces, the droplet would not undergo any breakup. This is usually also called the first stage of droplet breakup and every droplet undergo deformation before breakup.

- Vibrational Breakup

When $We \approx 12$, the interaction between a droplet and surrounding gas increases, which causes a droplet to undergo oscillation deformation. The surrounding gaseous flow field interact with droplet in such a way as to increase the amplitude of oscillation of droplet, which ultimately leads to the breakup of droplet. In this breakup mode, the secondary droplets produced are nearly half in size and the number of droplets are comparatively very few compare to the other modes of breakup.

- Bag Breakup

When the Weber number is in the range ($12 \leq We \leq 50$), a droplet get flatten and is blown out into a hollow bag attached to a circular rim. On disintegration the bag produces numerous fine droplets, whereas rim contains large proportion of original drop (around 70% by mass [80]). Such type of breakup is also known as hat-type breakup.

- Bag and Stamen Breakup

When the Weber number is further increased in the range ($50 \leq We \leq 100$), the disintegration forces on droplet also increases. Like bag mode of breakup, in this case also fine droplets are formed from the bag whereas relatively large droplets are formed from the rim. The distinguish feature of this mode with the bag breakup is the formation of a column of liquid (stamen) in the direction of gaseous flow field and along the axis of droplets, which ultimately undergo breakup. As a result relatively large number of droplets are produced when compared to the bag breakup. This type of breakup is also called umbrella breakup.

- Sheet Stripping

When the Weber number is in the range ($100 \leq We \leq 350$), a completely different mode of breakup occurs compared to the above discussed cases. In this case the fine droplets continue to strip from the periphery of a droplet.

- Wave Crest Stripping

When the Weber number is further increased, it results in the formation of small wave like structure on the windward side of the droplets. The wave crest continues to erode as a droplet continues to move along a gaseous flow field.

- Catastrophic Breakup

At very high Weber number, a catastrophic breakup regime of droplet occur. According to Hwang and Reitz [78], as droplet accelerates in a very high surrounding gaseous field it develops Rayleigh-Taylor instability, due to which it breaks up into large-scale fragments. These fragments further disintegrate into ligaments and smaller droplets due to the formation of much shorter wavelengths (Kelvin-Helmholtz instability).

2.2.2.4. Breakup Time of Droplets

Plich et al. [79] estimated the breakup time of the above break regimes. Though the definition of initiation of breakup is arbitrary, however, in the case of the bag- and bag-stamen breakup the start of bag formation is chosen as start-up time. Similarly, for sheet stripping the first sign of sheet being drawn downstream of a droplet marks the initiation time, whereas, generation of mist in the windward direction of the drop can be chosen as the start-up time for a catastrophic breakup. The final time was chosen when the droplets get stable and undergo no further disintegration.

Plich et al. [79] had proposed a correlation between the total breakup time for low viscosity droplets ($Oh < 0.1$), which are given by

$$T = 6\,(We - 12)^{-1/4} \quad \text{for } 12 \leq We \leq 18 \tag{2.37}$$

$$T = 2.45\,(We - 12)^{1/4} \quad \text{for } 18 \leq We \leq 45 \tag{2.38}$$

$$T = 14.1\,(We - 12)^{1/4} \quad \text{for } 45 \leq We \leq 351 \tag{2.39}$$

$$T = 0.766\,(We - 12)^{1/4} \quad \text{for } 351 \leq We \leq 2670 \tag{2.40}$$

$$T = 5.5 \quad \text{for } We \geqq 2670 \tag{2.41}$$

2.2.3. Representative Diameter

In the field of atomization, it is often desirable to characterize a particular droplet distribution in terms of a single number, commonly termed as representative diameter. The polydisperse distribution is usually replaced by a monodisperse distribution. According to Lefebvre [80], the representative diameter can be represented by

$$D_{ab} = \left(\frac{\int_{D_o}^{D_m} D^a \left(\frac{DN}{dD}\right) dD}{\int_{D_o}^{D_m} D^b \left(\frac{DN}{dD}\right) dD} \right)^{\frac{1}{a-b}} \tag{2.42}$$

Eq. (2.42) may also be written in discrete form as,

$$D_{ab} = \left[\frac{\sum N_i \, D_i^a}{\sum N_i \, D_i^b} \right]^{\frac{1}{a-b}} \tag{2.43}$$

where, i denote the size range considered and N_i is the number of droplets in the range i.

There are many possible choices of representative diameter, the most commonly used diameters are summarized in Table 2.2, whereas Fig. 2.3 shows the corresponding graphical representation of the droplets distribution.

Table 2.2 – Representative Diameters and their Application [80]

Name	Symbol	Expression	Application
Arithmetic Mean	D_{10}	$\sum N_i \, D_i / \sum N_i$	average of all diameters
Surface Mean	D_{20}	$\left(\sum N_i \, D_i^2 / \sum N_i\right)^{1/2}$	surface area controlling
Volume Mean	D_{30}	$\left(\sum N_i \, D_i^3 / \sum N_i\right)^{1/3}$	volume area controlling
Sauter Mean Diameter (SMD)	D_{32}	$\sum N_i \, D_i^3 / \sum N_i D_i^2$	mass transfer, reaction
Mass Median Diameter (MMD)	D_{50}	$\left(\sum N_i \, D_i^5 / \sum N_i\right)^{1/5}$	median diameter of a spray system

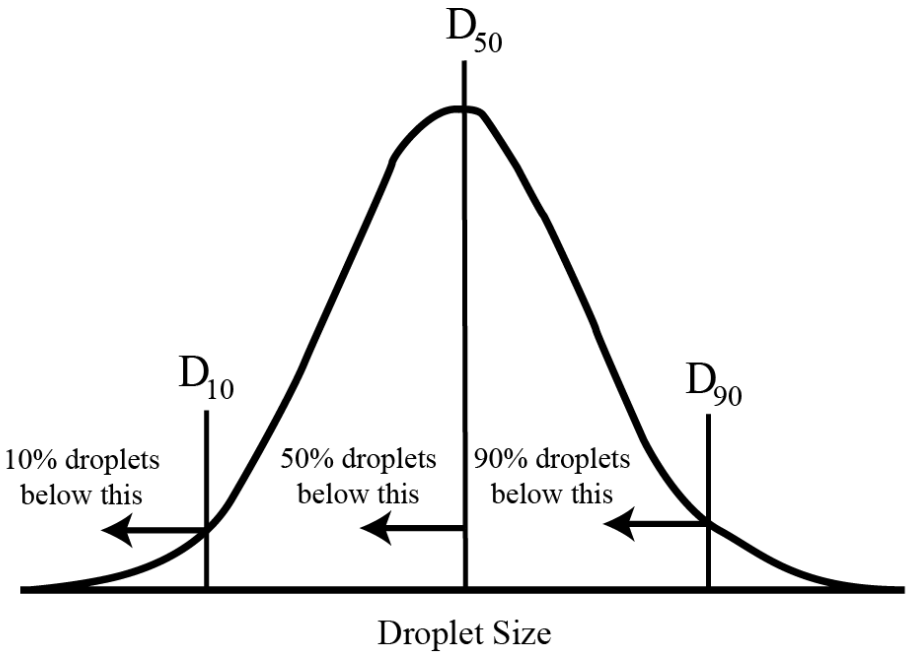

Figure 2.3 – Location of Various Representative diameters

2.2.4. Mathematical Distribution Function

A single representative diameter properly characterizes the entire range of spray parameters, many researchers have attempted to derive analytical expressions whose parameters can be obtained from a limited number of drop size measurement. According to Lefebvre [80], the main aim of such mathematical expression is to;

- Provide a satisfactory fit for drop size data.
- Allow extrapolation to drop size which is outside the range of measured values.
- Permit easy calculation of mean and representative diameters and other parameters of interest.
- Provide a means of consolidating large amounts of data.
- Understand some insight of basic mechanism involved in atomization.

Atomization is a highly complex phenomenon and there exist no single distribution that can represent all droplets size distribution. However, the most commonly used mathematical distribution are briefed as follow;

2.2.4.1. Normal Distribution

The normal distribution, also known as the Gaussian distribution, is usually expressed in terms of a number distribution function ($f\ (D)$) of a random number "x" is given by Eq. (2.44)

$$f\ (D) = \frac{1}{\sqrt{2\pi}} \exp\left[-\frac{x^2}{2}\right] \text{ for } -\infty < x < \infty \tag{2.44}$$

The linear transformation of $D = \overline{D} + x.\sigma$ in Eq. (2.44), with $-\infty < \overline{D} < \infty$, and $\sigma > 0$ will results in normal random variation with probability distribution function (pdf) ,which gives the number of particles of a given diameter ($\overline{D}$) is given by

$$f\ (D) = \frac{1}{\sigma\sqrt{2\pi}} \exp\left[-\frac{(D-\overline{D})^2}{2\,\sigma^2}\right] \text{ for } -\infty < D < \infty \tag{2.45}$$

The form of standard normal distribution is a well-known bell-shaped curve with a mean value of zero and a standard deviation of unity. Experimental data of droplet diameter in spray systems have already demonstrated an asymmetrical behaviour which makes the normal distribution unsuitable for characterizing the spray. However, successful attempts were made to use some derivatives of the normal distribution, the most commonly used one is log-normal along with root-normal and upper limit distributions which are also used in practice.

2.2.4.2. Log Normal Distribution

The log-normal distribution is obtained by applying the transformation to the standard normal distribution function. The transformation is given by

$$D = \frac{\ln x - \ln \overline{D}}{\ln \sigma} \tag{2.46}$$

Substituting Eq. (2.46) in Eq. (2.44) will leads to

$$f\ (D) = \frac{1}{D\ (\ln\sigma)\ \sqrt{2\pi}} \exp\left[-\frac{1}{2}\left(\frac{\ln\left(\frac{D}{\overline{D}}\right)}{\ln\sigma}\right)^2\right] \text{ for } 0 < D < \infty, \overline{D} > 0, \sigma > 0 \tag{2.47}$$

2.2.4.3. Rosin-Rammler Distribution

Rosin-Rammler is one the most commonly used the empirical expression for the droplet size distribution in sprays. In its cumulative form, it can be expressed as

$$F\ (x) = 1 - e^{-\left(\frac{D}{X}\right)^q} \tag{2.48}$$

where, $F\ (x)$ is the fraction of total volume for all the particles having a diameter less than D. The terms X and q are constants to be obtained from the experimental results. From Eq. (2.48), the Rosin-Rommler number distribution for spray can be given by

$$f\ (x) = \frac{d}{dx}\ F\ (x) = \frac{q}{X^{(q-3)}}\ x^{(q-4)}\ e^{-\left(\frac{D}{X}\right)^q} \tag{2.49}$$

In Eq. (2.48) and (2.49), the parameter q is a measure of dispersion for the droplets. Thus, the higher the value of q is, the distribution will be more uniform. If q is infinite then all droplets in a spray system will be of the same size.

2.2.4.4. Nukiyama-Tanasawa Distribution

Another empirical distribution that describes the actual distribution function is Nukiyam-Tanasawa, whose mathematical formulation is given by Eq. (2.50)

$$f\ (x) = a\ x^{p}\ e^{-bx^{q}} \tag{2.50}$$

where b, p and q are empirical constants. Like Rosin-Rommler, here q is also a measure of dispersion for the spray systems and a is a normalization parameter which is generally expressed as

$$a = \frac{q\ b^{(p+1)/q}}{\Gamma\left(\frac{3}{q}\right)} \tag{2.51}$$

In general, p is commonly taken as 2, thus the Nukiyama-Tanasawa distribution in its normalized number density can be re-written as

$$f\ (x) = \frac{q\ b^{3/q}}{\Gamma\left(\frac{3}{q}\right)}\ x^{2}\ e^{-bx^{q}} \tag{2.52}$$

Part –II Experimental Setup

Chapter No. 3: Experimental Facility & Flow Conditions

3.1. Experimental Facility

In order to have a deep understanding of the two-phase phenomenon involved in wet turbine systems, an open-type wind tunnel was manufactured from scratch with following requirements;

- Can operate at wide range of velocities,
- Ease of replacement of parts for the experimental setup,
- Ease of using different aerofoils shape,
- Ease of adjusting angle of attack (AOA) of the aerofoil,
- To have a better optical accessibility,
- To avoid secondary flows in order to have a uniform flow in the test facility, and
- Ease of modification to the test section as per required depending on the experimental objectives.

The outline of the main components of the test facility made at University of Tokyo Jet Propulsion Lab (UTJPL) is shown in Fig. 3.1. The air was supplied to the test section by using a centrifugal blower. Before air reached the test section, it passed through the settling chamber which removed turbulences from the air passage. A test blade was mounted in the test section at some fixed AOA and water was supplied to the test blade via a water tank. A droplet stopper and collector setup were placed at the end of the test section to drain off the collected water.

3.2. Shadowgraph Image Setup

Shadowgraph images were taken using the backlighting technique. A diffuser plate was placed between the high-speed camera and the light sources as shown in Fig. 3.1. By such experimental configuration, the light was uniformly scattered in all directions. Without a diffuser plate, a local brighter spot was seen in the shadowgraph images. This locally high light intensity significantly causes errors when using the image processing technique, as it leads to undesirable noise for measuring the droplets size distribution.

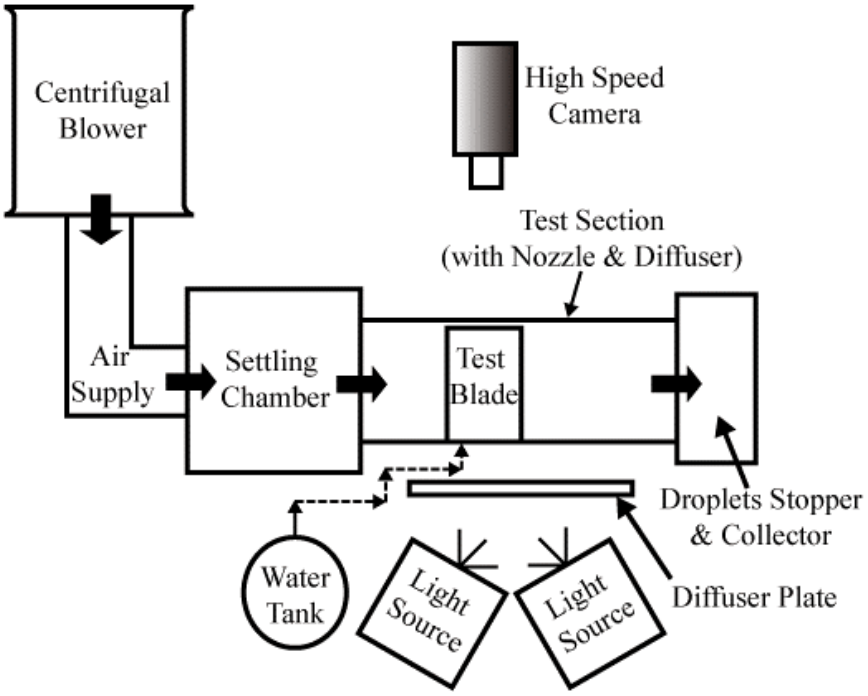

Figure 3.1 – Outline of the Experimental Setup

3.3. Main Experimental Equipment/Parts

3.3.1. Centrifugal Blower

In the current experimental setup, the wind tunnel was driven by a centrifugal blower, as shown in Fig. 3.2. The centrifugal blower was operated by a two-phase motor with an output power of 1.5kW when operated at a frequency of 50 Hz. Depending on an output frequency, the corresponding rotational speed was 2850 revolutions per minute. More details of the blower specifications are given in Table 3.1.

Figure 3.2 – Centrifugal Blower

Table 3.1 – Specifications of Centrifugal Blower
(Manufacturer: YODOGAWA DENKI SEISAKUSHO)

Specifications	**Value**	
Model	LA6TB	
Motor Output	1.5kW x 2P	
Power Supply	3φ x 200 V	
Frequency (Hz)	50	60
Current (A)	4.2	6.0
Revolution (rpm)	2850	3300
Static Pressure (kPa)	1.77	2.55
Air Capacity (m^3/min)	35	42
Weight (kg)	37.5	

3.3.2. Experimental Wind Tunnel

Experiments were performed in a conventional open – type wind tunnel shown schematically in Fig. 3.3 (isometric view), Fig. 3.4 (pictorial view) and Fig. 3.5 (side view). The air flowed from the centrifugal blower to the settling chamber (made from wood) of the wind tunnel via a connecting pipe having a diameter of 150 mm. Inside the settling chamber, a perforated metal plate was fixed which acted as a flow straightener. A nozzle duct was attached at the end of the settling chamber to accelerate the air flow. The nozzle was followed by the honeycomb section, which further straightened the airflow

and reduced the air turbulence. Finally, air reached the measuring section (or test section) having a length of 400mm. The cross section of the measurement section is 80x100 mm^2. The side walls of the measurement sections were manufactured from both the aluminium and transparent acrylic glass. The test section was followed by a diffuser, allowing the air to expand smoothly and more importantly to avoid any flow separation at the end of the test section. A stopper plate (perforated metal plate) was mounted to avoid the splashing and spreading of the droplets in the downstream region. The droplets upon striking the stopper plate lose their momentum and fell into a water bucket, placed just under the stopper plate, and was drained off. Depending upon the experimental objectives, the corresponding side walls material was used. In the case of a high-speed flow visualization using a high-speed camera, acrylic material side walls were used which provided good optical accessibility. Similarly, for measuring the velocity distribution inside the test section, aluminium side wall with a hole was used to provide better support to the pitot tube and hot-wire holder. Both the acrylic and aluminium side walls have a thickness of 15 mm. A single blade was used for a better understanding of the physics of ligament breakup and droplet distribution aft the T.E. region of the cascade blade. The used of a single blade also helped an ease of visualization of the thin liquid formed on the blade's surface.

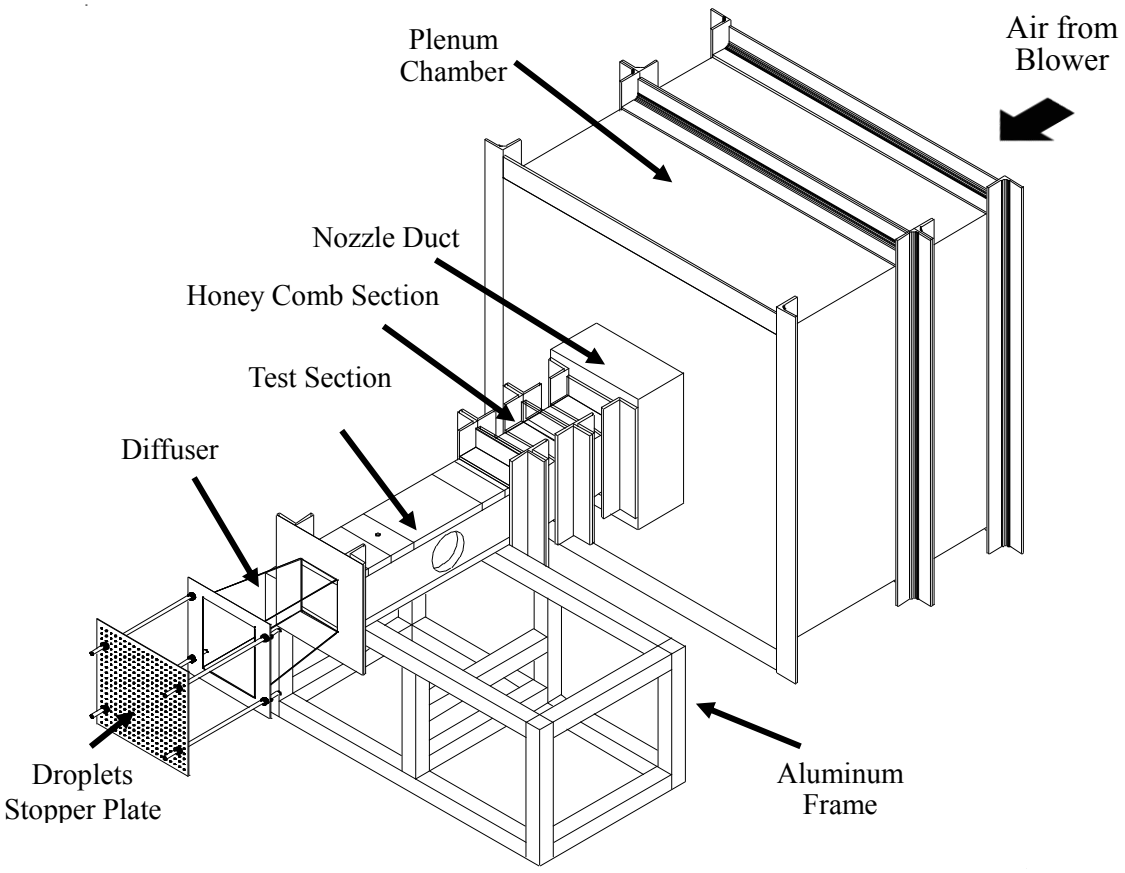

Figure 3.3 – Two Phase Experimental Wind Tunnel

Figure 3.4 – Test Facility (Pictorial View)

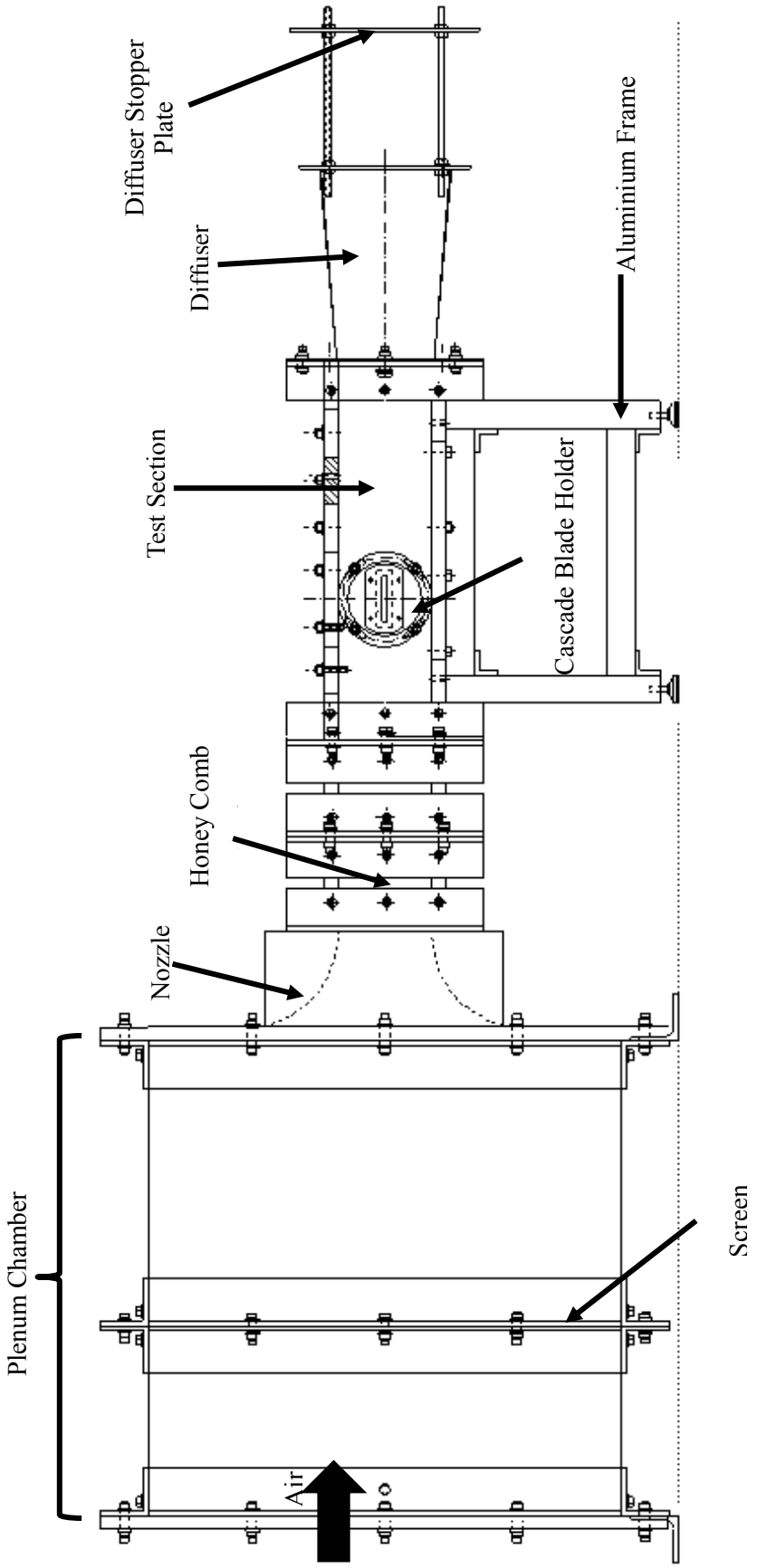

Figure 3.5 – Test Facility (Side View)

3.3.3. Water Supply Mechanism

Water was supplied to the test blade via a water column, having a diameter of 120 mm, as shown in Fig. 3.6. Figure 3.8 shows the schematics of the water supply mechanism used in the present study. The test blade and water column are connected via a connecting pipe, having a diameter of 6 mm, as shown

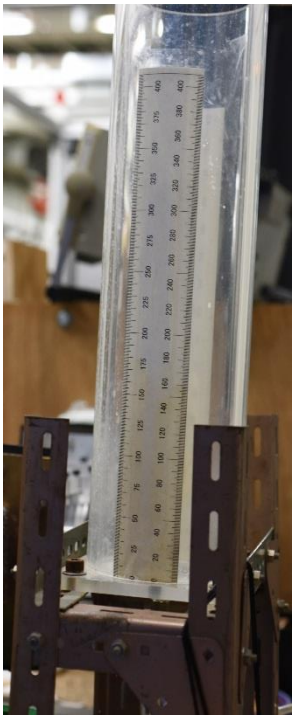

Figure 3.6 – Picture of Water Tank

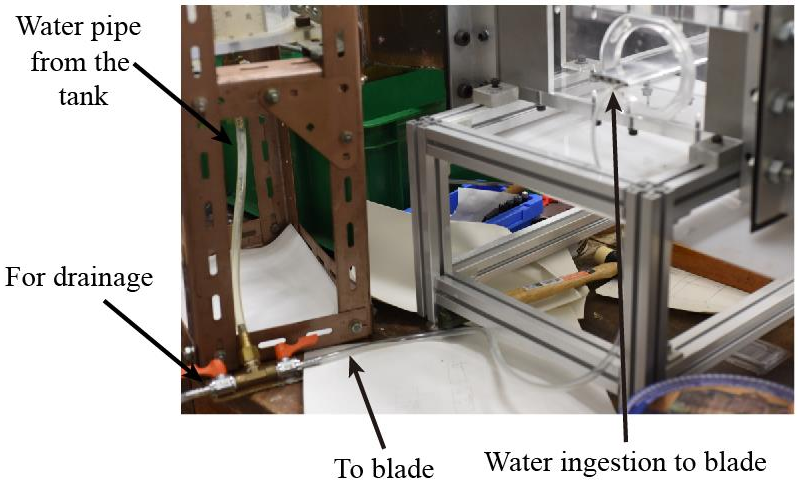

Figure 3.7 – Picture of water supply to blade

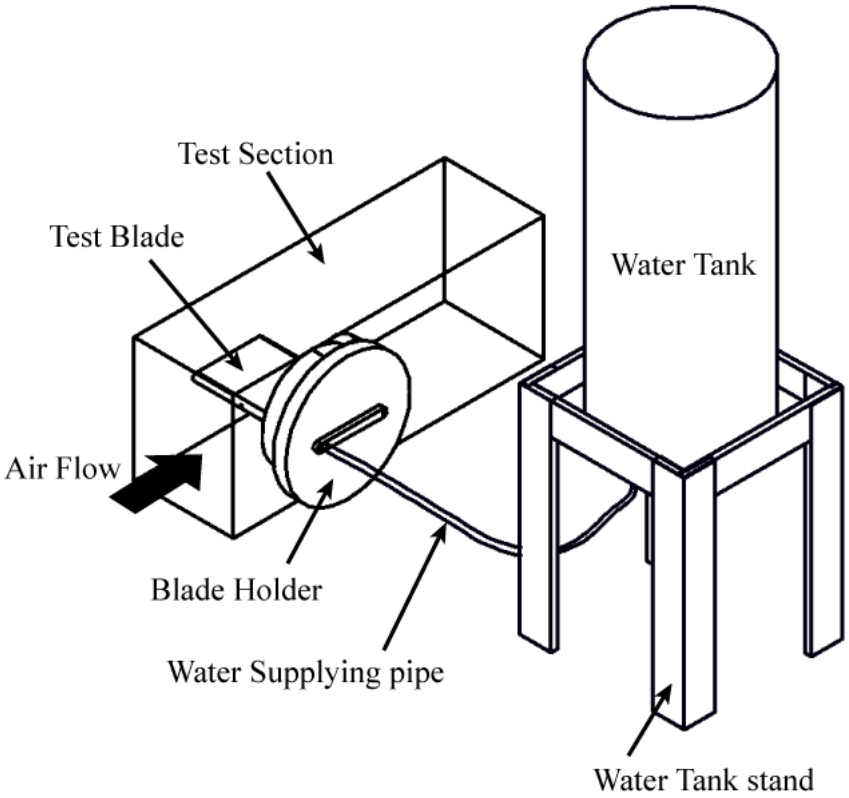

Figure 3.8 – Water Supply Mechanism

in Fig. 3.7. the mass flow rate of water to the test blade was controlled by adjusting the height of the water tank, whereas, a hand valve located at the bottom of the tank was used to control the supply of water. For emptying the tank, water supply mechanism was also equipped with a drainage pipe, as shown in Fig. 3.7.

3.3.4. Test Section

The wind tunnel used was 400 mm in length (x-direction) having a width (z-direction) and height (y-direction) of 80 mm and 100 mm respectively as shown in Fig. 3.9 and 3.10. This configuration allows a single blade to be fixed at a distance of 3 chord-length (150 mm) from the start position of the test section to the mid-chord position of the test blade (also the origin) as given by Fig. 3.10. The upper wall of the test section was made from several equally sized slabs with one slab twice in length, as shown schematically in Fig. 3.9. Among these slabs, only one slab contains a hole, which was used to insert the hot wire or pitot-tube in the test section. This simple design configuration allowed the

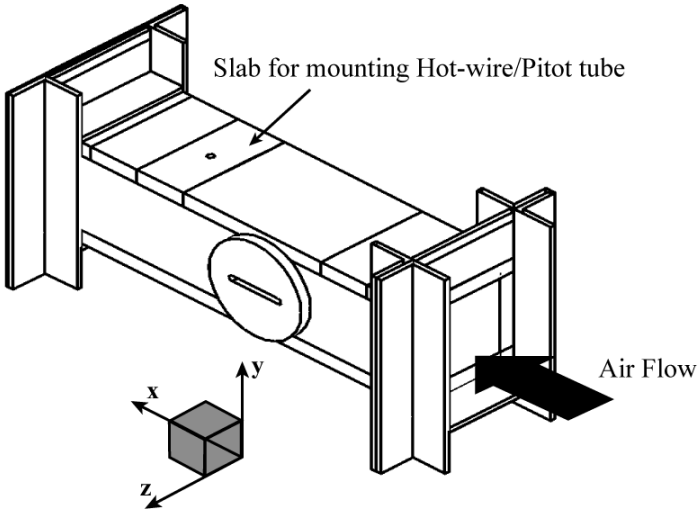

Figure 3.9 – Test Section and Coordinate System Definition

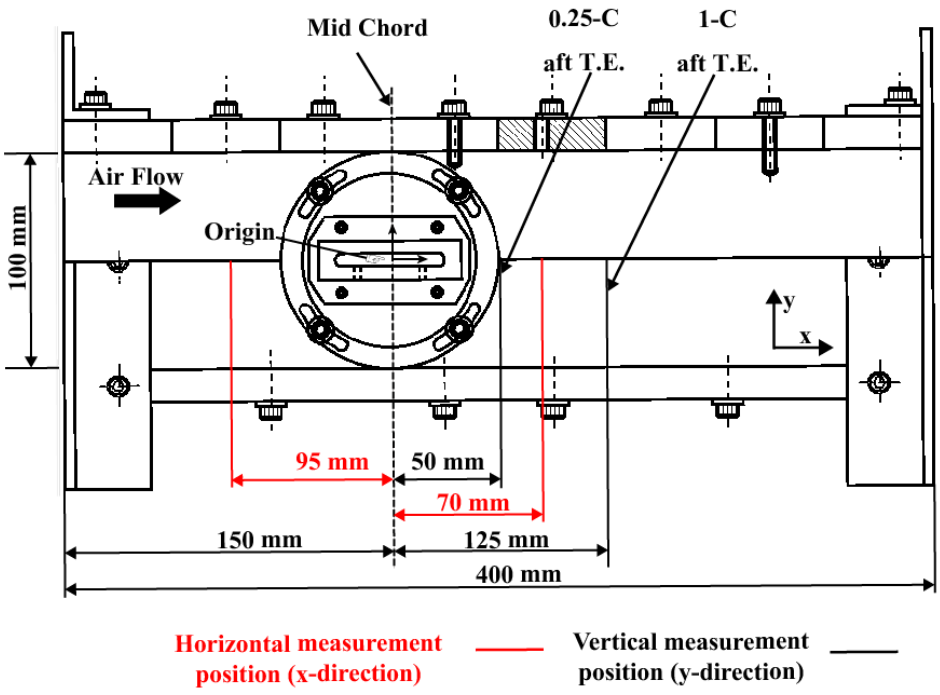

Figure 3.10 – Test Section and Velocity Measurement Position

Figure 3.11 – Elliptical Profile Blade Holder

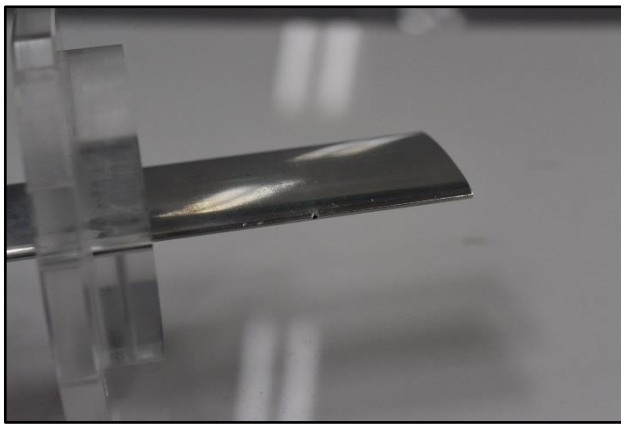

Figure 3.12 – Elliptical Profile Blade

(a) Digital (b) Analog

Figure 3.13 – Angle Measurement Devices

swapping of slabs and the air flow velocity, pressure and flow angles were calculated at various positions in the pitch-wise (y-) and width-wise (z-) direction of the test section. Figure 3.10 shows the detail measurement position used. Velocity distribution in the pitch-wise (y-) direction of the test sections were measured at the mid-chord (i.e., origin), 0.25-C and 1-C positions aft the T.E., whereas, the velocity distribution in the width-wise (z-) direction were measured upstream and downstream positions of the mid-chord position of the blade, as shown in Fig. 3.10.

3.3.5. Cascade Blade Holder

A removable round shape cascade blade holder which was designed based upon the geometric blade profile was used to mount the test blade inside the wind tunnel, as shown in Fig. 3.11. Due to the roundness in shape, the angle of attack of the test blade was also adjusted with ease. Similarly, angle gauge devices were used to set the blade at the required incidence angle, as given by Fig. 3.13.

3.3.6. Elliptical Profile Blade

In order to understand the two-phase phenomenon (i.e., liquid sheet formation and droplets distribution aft the blade), a geometrically simple cascade aerofoil was used as shown in Fig. 3.12. The Suction Side (S.S.) and Pressure Side (P.S.) of the blade possessed the elliptical profile configuration and was named as elliptical profile blade, as shown schematically by Fig. 3.14. Unlike the real turbo-machines, water was ejected via a 1 mm hole located at the mid-span of the L.E. of the blade to grasp the influence of the size and geometry of the nozzle in the real turbine systems. Figure 3.14 gives the detail configuration, whereas, Table 3.3 shows the specifications of the elliptical profile blade. The chord length of the blade corresponds to the major axis of the ellipse, whereas, the maximum thickness corresponds to the minor axis of the ellipse. The radius of curvature of the chord length (i.e., major axis) was 1.125 mm, which corresponds to the thickness of the T.E. as 2.25 mm. Due to elliptical profile the size of the blade gradually increases from the L.E. to the mid-chord position and then starts to decrease slowly in exactly the symmetrical way as it increases in the first half. The maximum thickness ratio of 15% was located at the mid-chord position, whereas, the thickness ratio of the T.E. was 4.5%. The blade used was made from the Aluminium material.

Table 3.2 – Elliptical Profile Blade Specification

Parameter	Value
Aerofoil Type	Elliptical
Material	Aluminium
Number of aerofoil in cascade	1
Chord Length (C)	50 mm
Span length (S)	80 mm
Maximum thickness	7.5 mm
Thickness ratio	15 %
Hole diameter (for injecting water)	3 mm
Hole diameter (Leading Edge)	1 mm
Trailing Edge Thickness	2.25 mm

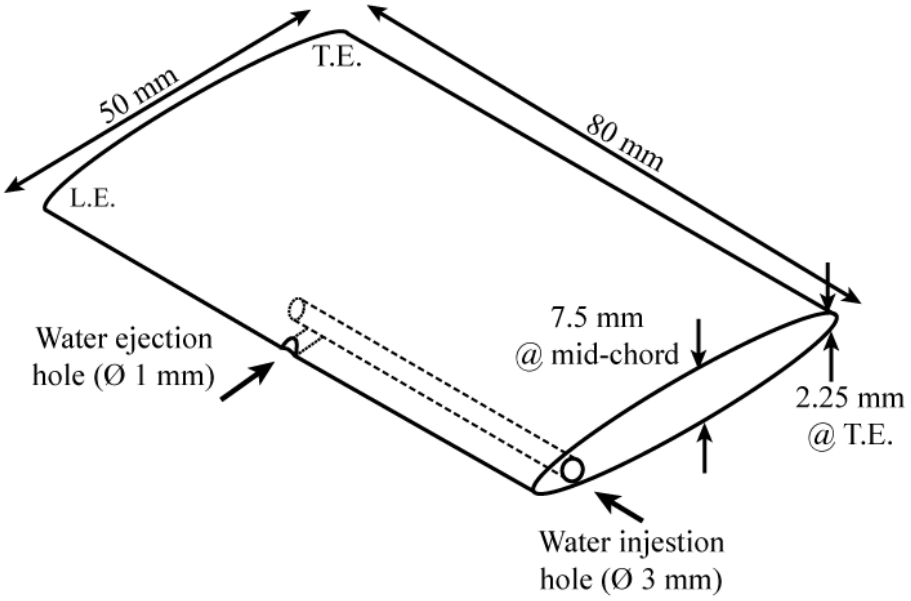

Figure 3.14 – Schematics of Elliptical Profile Blade

3.3.7. Water Ejection Method

To understand the fundamental two-phase phenomenon in turbine systems, water ingestion from a hole serves simplicity, better and detail understanding. By this method;

1. Phase change phenomenon of droplets (i.e., Evaporation) was avoided
2. The process got simplified due to negligible coalesces, the interaction of droplets etc.
3. The majority of coarse droplets formed in the wet turbine systems are mainly due to the accumulated water at the T.E. of the blades. Therefore, with this experimental setup, generation of coarse droplets from the T.E. as well as the effect of mass flow rate of the thin liquid film on the droplet formation could be understood.
4. The role of T.E. of the cascade blade upon the following characteristics became easy to understand
    a. Formation of liquid film,
    b. Water accumulation at the T.E. of the cascade blade,
    c. Water droplets size distribution aft the T.E. region of the cascade blade.
5. Lastly, the current setup gave an ease in visualizing the processes involved. If water droplets were injected via nozzles, it would have made the test section dense due to the generation of a large number of droplets, making it difficult to visualize and understand the above-mentioned characteristics.

In addition to the above mentioned reason, water ejection like that seems to be reasonable. In the real wet turbine systems, a water film is formed around the L.E. area of the blade. This water film is then converted into the rivulet (or water streak) like structure which travel down due to the aerodynamic forces. These, water streaks are then accumulated at the T.E. of the blade. Thus, in the present study, the water streak formed in the real machines can be easily assumed to that of the water ejection done in this study.

3.4. Experimental Equipment for Shadowgraph Images

The liquid film behaviour on the S.S. of the blade, accumulation of the water at the T.E. and the breakup of water ligaments from the T.E. of the blade were visualized by taking shadowgraph images using a high-speed camera (Photron FASTCAM APX-RS). The high-speed camera was equipped with the Micro-NIKKOR 105 mm lens with extension rings. Backlight illumination was achieved by using two high-intensity lights (Photron HVC-UL), each of which was 250W. The experimental equipment for the shadowgraph images is shown in Fig. 3.15.

(a) Photron HVC-UL (Backlights)

(b) Photron FASTCAM APX-RS (High-Speed Camera)

(c) Camera Lenses (105-, 85-, 60-mm)

(d) NIKON PK-11A/12/13 (Extension Rings)

Figure 3.15 – Experimental Apparatus for Shadowgraph Images

3.5. Experimental Flow Conditions

Four different air flow conditions were used to study the two-phase effects in a cascade wind tunnel. Though, the flow velocity is relatively very small compared to that of the real machines, however, the Reynolds number based on the chord length of the blade corresponds to that of the real machines (i.e. of an order of 10^5) [81], since fogging is more efficient for small to medium scale turbines. Table 3.3 summarizes the experimental flow conditions under which experiments are performed. The air flow velocity is divided into three groups. Throughout in this thesis, air velocity was termed as High Air Velocity Case (or High Air Momentum Case) and Low Air Velocity Case (or Low Air Momentum Case) corresponding to an air velocity of 40 (Case A) and 20 m/sec (Case D) respectively. Similarly, for an air velocity of 30 (Case B) and 25 m/sec (Case C) in combined were named as Medium (or Intermediate) Air Velocity, whereas in separate they are termed as High Medium (Intermediate) Air Velocity (30 m/sec) and Low Medium (Intermediate) Air Velocity (25 m/sec) respectively. Different mass flow rate of water are used for water ingestion from the nozzles. According to Mee [82] spraying 1% of the air mass flow as liquid water droplets can augment the power output by about 5%. Hatamiya et al. [83] utilized an ingestion water of 1% (by weight), whereas, Araki et al. [84] used 3.5% of water ingestion (by weight) to that of compressor inlet air respectively. Utamura et al. [61] had shown that an overspray of 1% can result in an increase of power output and thermal efficiency of 10% and 3% respectively for a 115 MW GT (Hitachi Frame 9E). According to Bhargava et al. [62], the overspray level usually ranges between 0.5-1% of the mass flow rate of gas turbine but is machine specific. He further suggested that water mass flow rate should not exceed 2%. Based on these studies, Fig. 3.16 compares the applicability range of the present experimental study to that of the gas turbine systems (small to medium size gas turbines).

Table 3.3 – Experimental Flow Conditions

Parameter		**Value**		
			Air Velocity (m/sec)	Reynolds Number (Re_a)
Case	High Air Velocity	$Case\ A$	40	$1.35\ x\ 10^5$
	Medium Air Velocity	$Case\ B$	30	$1.01\ x\ 10^5$
		$Case\ C$	25	$0.82\ x\ 10^5$
	Low Air Velocity	$Case\ D$	20	$0.67\ x\ 10^5$
Ambient Temperature (K)		298.5 (approx.)		
Water Temperature (K)		Room Temperature Water		
Dimensionless mass flow rate (MFR)		$2 \sim 32$		
Air Density (kg/m^3)		1.23		
Water Density (kg/m^3)		1000		

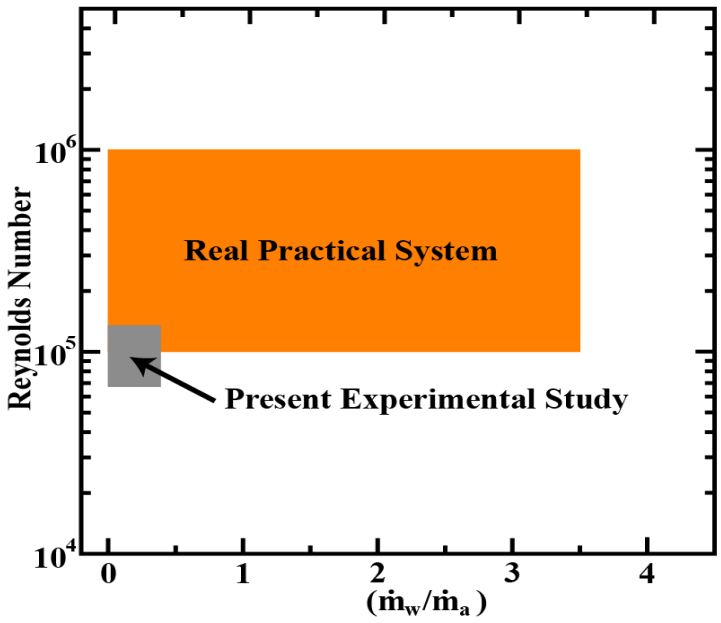

Figure 3.16 – Correspondence between the present experimental study and the real systems

3.6. Measurement Techniques

To acquire information about the characteristics of cascade wind tunnel, pressure and velocity quantities were measured by using pressure probe and hot-wire anemometry.

3.6.1. Pressure Probe

In the field of aeronautics, pressure probes are extensively used to measure the pressure as well as the velocity in a fluid stream. In this study, three hole pressure probe was used to investigate the pressure inside the cascade wind tunnel. The position of the holes and their geometry is shown in Fig. 3.17. Each of these probes had an outer diameter of 1 mm, whereas its inner diameter was 0.8 mm. The length and width of the stem were approximately 5.5 mm and 3 mm respectively. For the purpose of simplicity, the middle hole is named as P1, whereas the left and right are named P2 and P3 respectively, as shown in Fig. 3.19. The pressure at each hole depend on upon the incident angle of the probe with respect to the incoming air stream and is a combination of static and dynamic pressure. From the pressure measured at each hole, i.e., P1, P2 and P3, the local flow angle as well as the local velocity were obtained.

3.6.2. Calibration Procedure of Three Hole Pressure Probe

Three hole pressure probe was calibrated using the calibration wind tunnel at UTJPL. Calibration curve for 3-hole pitot tube was obtained by setting the calibration wind tunnel speed in the range of 20 to 50 m/sec. Static and total pressure were obtained in advance using a standard static pitot tube. Before calibrating the 3-hole pitot tube a mirror was fixed, whose reflection was used to measure the reference flow angle between the pressure tubes and the main air flow field. A water filled pipe was used to adjust the height of the light source with that of the Pitot tube mirror. The reflected ray of light from the mirror and the light source were aligned and the reference angle between the 3-hole pitot tube and the mirror was obtained. The pressure at each hole was measured and the correlation between the three holes was obtained by using the formula given by Eq. (3.1).

$$X = \frac{P_2 - P_3}{D_{PA}} \tag{3.1}$$

where,

$$D_{PA} = P_1 - \min(P_2, P_3) \tag{3.2}$$

The relation between the correlation factor, X, and the flow angle is shown in Fig. 3.18. The clockwise (CW) rotation of the pitot tube holder was considered as a positive angle. The Pitot tube was set at 0-degree, such that the value of the total pressure at the central probe (P1) was maximum, whereas, the values of P2 and P3 were almost the same. Coefficient of pressure for each pressure hole (P1, P2 and P3) was calculated to obtain corresponding values of C_{P1}, C_{P2} and C_{P3} as given by Eq. (3.3).

$$C_{Pi} = \frac{P_T - P_S}{\frac{1}{2}\rho V_S^2} \tag{3.3}$$

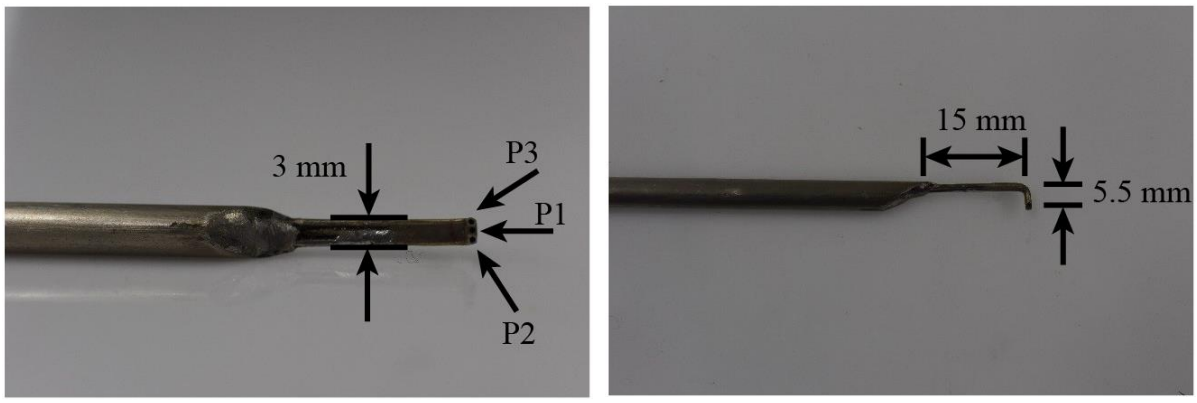

Figure 3.17 – Geometry and Position of Three Hole Pressure Tube

The whole process was repeated for every step angle (2 degrees) and the corresponding values of flow angle, velocity, static pressure (P_S) and total pressure (P_T) were obtained by the following process;

1. Pressure (P1, P2 and P3) was calculated at each step angle and the correlation, X, was obtained using Eq. (3.1).
2. The correlation factor, X, was plotted against the inflow angle as shown in Fig. 3.18.
3. The coefficient of pressure was calculated at the corresponding flow angle by using Eq. (3.3.)
4. The coefficient of pressure for each hole was measured at each step angle, and was plotted against the inflow angle, as shown in Fig. 3.19.
5. The flow velocity was calculated, using the Eq. (3.4) given below

$$V_S = \sqrt{\frac{2\Delta P_A}{\rho \Delta C_{PA}}} \tag{3.4}$$

here, $$\Delta C_{PA} = C_{P1} - \min(C_{P2}, C_{P3}) \tag{3.5}$$

6. The static pressure was calculated by using the formula

$$P_S = P_1 + \Delta P_A C_{PS} \tag{3.6}$$

here, $$C_{PS} = \frac{C_{P1}}{\Delta C_{PA}} \tag{3.7}$$

7. At last, the total pressure was obtained by the mathematical expression given by Eq. (3.8).

$$P_T = P_1 + \Delta_{PA} C_{PT} \tag{3.8}$$

here, $$C_{PT} = \frac{1 - C_{P2}}{\Delta C_{PA}} \tag{3.9}$$

Figure 3.18 and 3.19 were generated by varying the inflow angle from +30 degree to -30 degree, having a maximum value of C_{P1} at nearly 0-degree incident angle.

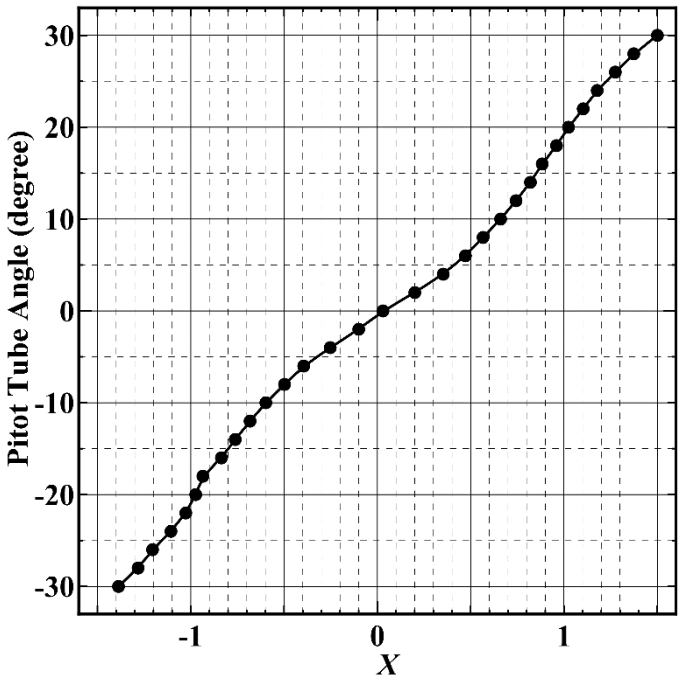

Figure 3.18 – X Vs Pitot Tube Angle (degree)

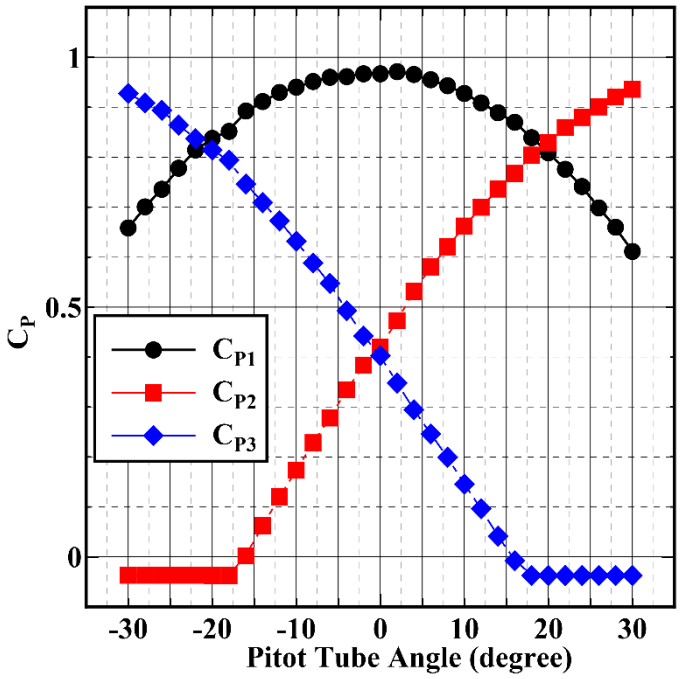

Figure 3.19 – Pitot Tube Angle (degree) Vs Pressure Coefficient (C_P)

3.7. Hot Wire

A hot-wire anemometer measures the high-frequency flow fluctuations by a small probe inserted into the flow. This makes them capable of measuring the turbulence in the flow field that cannot be measured by using pitot tubes. Hot-wire consist of an extremely thin tungsten material wire having a diameter of 5 μm and is spot-welded to needle-shaped prongs. Figure 3.20 shows the hot-wire measurement equipment used, whereas, Table 3.4 summarizes the specifications of the hardware. A single element probe hot-wire was used, which works on the basis of Constant Temperature Principle (also called Constant Temperature Anemometer (CTA)). CTA utilizes the wheat-stone bridge techniques to maintain the constant temperature of the wire and thus measure the incoming flow velocity.

Table 3.4 – Hot Wire Measurement Equipment

Specifications	Model
Hot Wire Probe	**0251R-T5** (KANOMAX)
Probe Support	**0103** (KANOMAX)
Lineariser	**HC-30** (SOKKEN)
Data Recorder	Unipulse **UL84**

(a) Linearizer (b) Hot-Wire Tube Holder (c) Data Logger

Figure 3.20 – Hot Wire Equipment

3.7.1. Principle of Hot Wire [85]

Hot-wire is usually placed in one arm of a Wheat-stone bridge opposite to a variable resistor, which defines the operating resistance and the operating temperature of hot-wire as shown in Fig. 3.21. In case the bridge is not balanced, no voltage difference exists across its diagonal. Any increase in the flow velocity results in the wire resistance to decrease. This leads to an increase in the probe's current, making the wire to heat up. This process kept on increasing the wire's resistance until the bridge was restored. Because of the high gain of the current regulating amplifier, a condition of bridge balance exists, which is independent of the incoming air flow velocity past on the wire.

Consider a wire that is immersed in a fluid flow, as shown in Fig. 3.21. Assume that the wire was heated up by an electrical current is in thermal equilibrium with its environment, then the electrical power input is equal to the power loss due to convective heat transfer is mathematically expressed as

$$I^2 R_w = hA_w(T_w - T_f) \tag{3.10}$$

where, I is the input current, R_w is the resistance of the wire, h is the heat transfer coefficient of the wire, A_w is the projected wire surface area, T_w is the temperature of the wire and T_f is the temperature of the fluid (air).

The heat transfer coefficient h is a function of fluid velocity, U, which can be given according to King's law

$$h = A + B.U^n \tag{3.11}$$

where, A, B and n are coefficients obtained from the calibration (n~0.5)

Similarly, wire resistance R_w is also a function of temperature and is given by Eq. (3.12)

$$R_w = R_{ref}[1+\propto (T_w - T_{ref})] \tag{3.12}$$

Combining, Eq. (3.10), (3.11) and (3.12) and solving for the fluid velocity, we can obtain

$$U = \left\{\frac{I^2 R_{ref}[1+\propto (T_w - T_{ref}}{A_w(T_w - T_f)} - A/B\right\}^{1/n} \tag{3.13}$$

As all the resistances in the bridge are constant, the squared output voltage directly represents the heat loss from the wire. Figure 3.22 shows the calibration curve for the single element hot-wire probe used in this research.

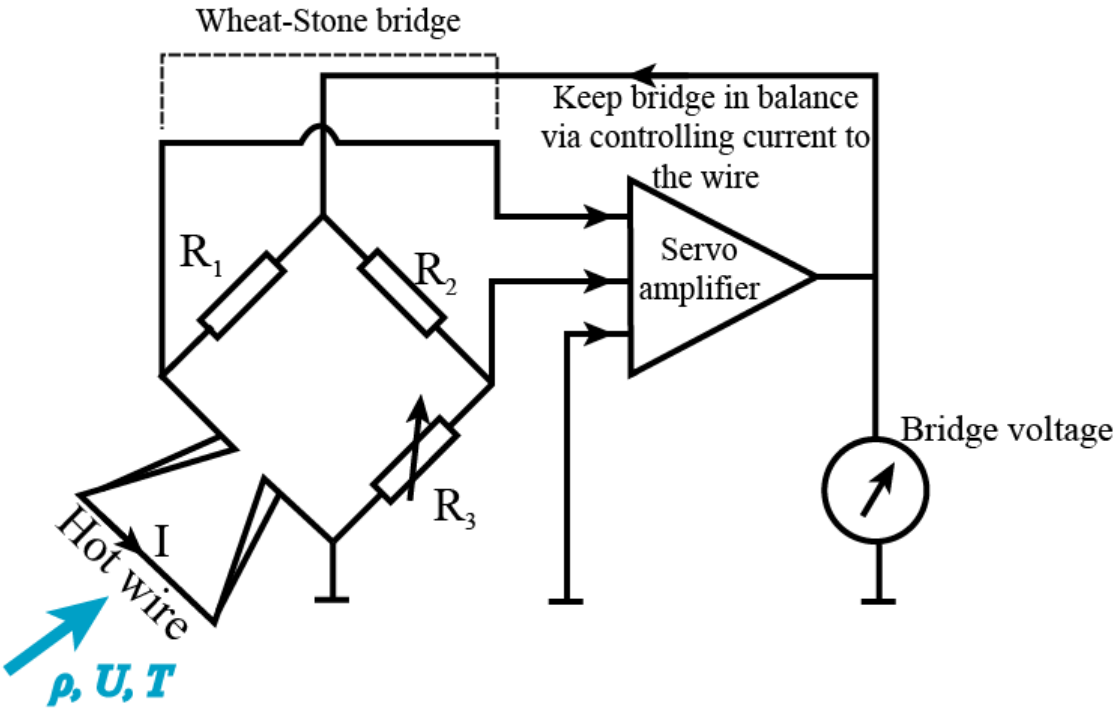

Figure 3.21 – Hot Wire Principle [86]

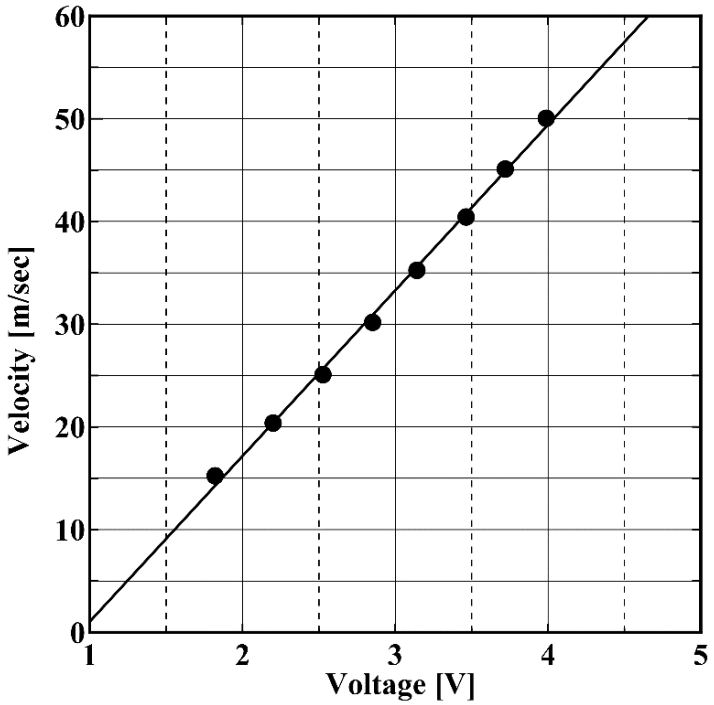

Figure 3.22 – Hot Wire Calibration

3.8. Image Processing Technique

Figure 3.23 shows a digital image A [M,N] described in a 2D discrete space derived from an analog image A (x,y) in a 2D continuous space through a sampling process, which is frequently referred as digitization. The 2D image A (x,y) is usually divided into N rows and M columns. The intersection of row and column is termed as a pixel. In a digital image, the values assigned to the integer coordinates [m,n] is schematically shown in Fig. 3.24.

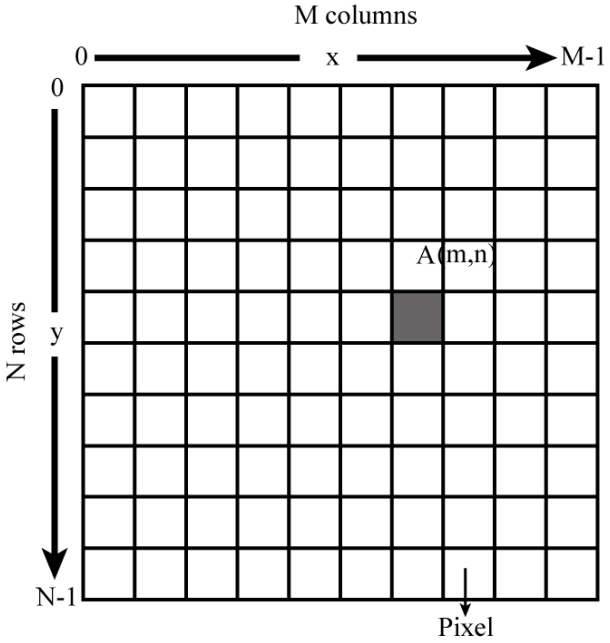

Figure 3.23 - Digital Image

where, m = {0, 1, 2, …, M-1} and n = {0, 1, 2, …, N-1}

A digital image is a function of many variables such as depth, colour and time etc. However, in the context of this study, only grayscale and binary images are considered. Each pixel of a grayscale image consists of different intensity scale, as given in Fig. 3.24. The intensity of the pixels is divided into 256 intensity scales, which changes gradually from a minimum intensity scale, 0, (white) to a maximum intensity scale, 255, (black), Fig. 3.24. On the other hand, a binary image is an image with two intensity levels only, i.e. 0 (white) and 255 (black). The black intensity level (255) is usually normalized and, in general, is expressed as 1 also, as shown in Fig. 3.25.

3.8.1. Image Segmentation

Figure 3.26 shows the shadowgraph image obtained by the experimental setup as given by Fig. 3.1. From Fig. 3.26, pixels possessing water (ligament as well as droplets) can be easily distinguished from its corresponding background based on its intensity. Image processing techniques can be applied to transform the grayscale image to a binary image. The liquid part is easy to distinguish from its background in a binary image and helps in measuring the different parameters with easiness.

The image segmentation techniques can be broadly classified into two techniques, namely;

1. Thresholding

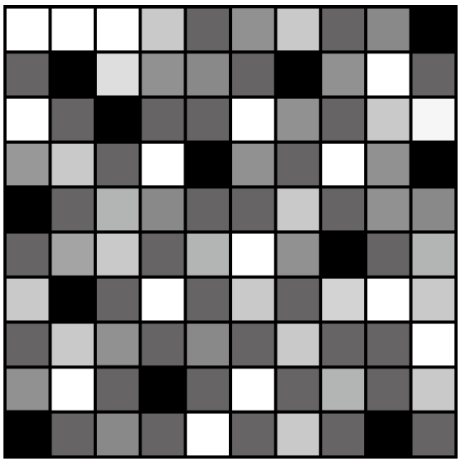

Figure 3.24 – Grey Scale

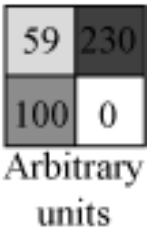

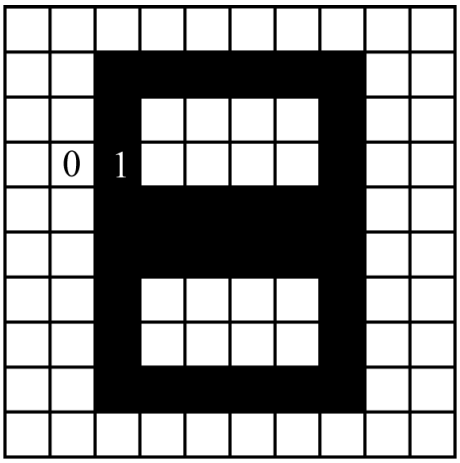

Figure 3.25 – Binary Image

2. Edge Filtering

In general, there is no universal rule for choosing the segmentation technique as it depends on the analysis object (i.e., a digital image).

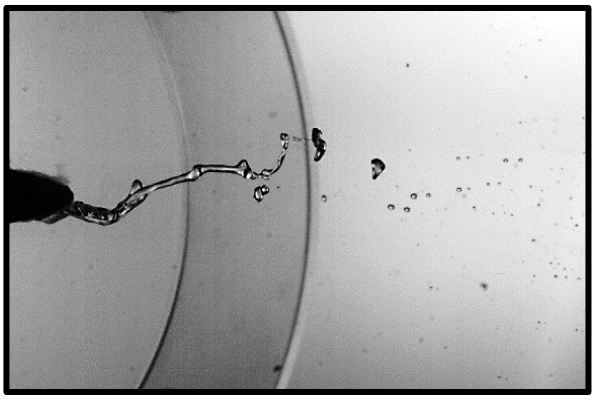

Figure 3.26 – Shadowgraph Image (water ligament/droplets have high intensity compared to the background)

(a) Thresholding

This technique is governed by a parameter, θ, usually called brightness threshold, which is used as a threshold value for a digital image A (m, n), as describe follow:

If $A\,[m,n] \geq \theta$ then $A\,[m,n] = object = 1$

Else $A\,[m,n] = background = 0$

In the above algorithm if the pixel value exceeds the threshold value, the object is assumed to be light (i.e., white) object, whereas, the pixels below the threshold value are assigned as a dark (i.e., black).

An alternate algorithm can also be chosen, by choosing the dark object on a light background as shown below

If $A\,[m,n] < \theta$ then $A\,[m,n] = object = 1$

Else $A\,[m,n] = background = 0$

Many thresholding techniques are available such as fixed threshold, Histogram-derived threshold, Iterative Self-Organizing Data Analysis Technique algorithm (ISODATA), Triangular algorithm, Background-symmetry algorithm etc. Due to the simplicity of Fixed Thresholding technique, this technique was used for generating binary video for visualization purpose only.

(b) Edge Finding

In an edge thresholding technique, those pixels which belong to the boundary of an object are to be chosen. In an Edge finding, the most commonly used techniques are the Gradient-based procedure and Zero-crossing based procedure. However, due to the simplicity of Gradient-based technique, this technique was used in the present study for measuring the droplets characteristics (area, diameter, circularity, etc.).

3.8.2. Binary Image Generation Procedure

3.8.2.1. Theoretical Background

The central challenge for the edge finding techniques was to find procedures that produce closed contours around the objects of interest. In the case of high signal to noise (SNR) objects, this can be achieved simply by calculating the gradient and then applying a suitable threshold. However, in reality, it is not applicable to most of the images.

(a) Smoothening Technique

A smoothing technique is applied in the present study. The smoothing operation was applied to reduce the noise and/or to prepare an image for further processing for segmentation. Following are the commonly used techniques and procedures used in the smoothening technique.

- Gaussian Filter

This is the most common smoothing kernel function. Due to the certain properties of the Gaussian (such as central limit theorem, minimum space bandwidth product) as well as several application areas such as edge finding and scale-space analysis and is commonly given by Eq. (3.14)

$$h(x,y) = g_{2D}(x,y) = \left(\frac{1}{\sqrt{2\pi\sigma}} e^{-\left(x^2/2\sigma^2\right)}\right) . \left(\frac{1}{\sqrt{2\pi\sigma}} e^{-\left(y^2/2\sigma^2\right)}\right) \quad (3.14)$$

or,

$$h(x,y) = g_{1D}(x) . g_{1D}(y)$$
$$h(x,y) = g_{1D}(x) . g_{1D}(y) \quad (3.15)$$

convolution using a finite number of samples (N_o) of the Gaussian as the convolution kernel. The localization error to detect edge increases with an increase of the Gaussian filter kernel size. The commonly chosen value of $N_o = [3\sigma]\ or\ [5\sigma]$

$$g_{1D}[n] = \begin{cases} \frac{1}{\sqrt{2\pi\sigma}} e^{-\left(x^2/2\sigma^2\right)} & |n| \le N_0 \\ 0 & |n| > N_0 \end{cases} \quad (3.16)$$

- Median Filter

A median filter is based upon moving a window over an image (as in a convolution) and computing the output as the median value of the brightness within the input window. If the window size is $J\ x\ K$, then we can order $J\ .\ K$ pixels in brightness value from the smallest to the largest.

- First Derivatives

An image is a function of two (or more) variables, therefore it is necessary to define the direction in which derivative is taken. Two-dimensional cases possessed two arbitrary directions (or more commonly horizontal direction and vertical direction). If a filter is applied in both directions represented by horizontal (matrix) and vertical derivative filter (matrix) as h_x and h_y respectively, then

$$[h_\theta] = cos\theta . [h_x] + sin\theta . [h_y] \quad (3.17)$$

➢ Gradient Filters

Knowing the derivatives in an arbitrary direction, the gradient of an image $\nabla A\ [m,n]$ is governed by the mathematical expression given by Eq. (3.18).

$$\nabla A = \frac{\partial A}{\partial x}\vec{\imath}_x + \frac{\partial A}{\partial y}\vec{\imath}_y = (h_x \otimes A)\vec{\imath}_x + (h_y \otimes A)\vec{\imath}_y \quad (3.18)$$

here, $\vec{\imath}_x$ and $\vec{\imath}_y$ are the unit vectors in x- and y- direction respectively.

Thus, the gradient magnitude and direction can be calculated by the expressions given in Eq. (3.19) and (3.20) respectively.

$$|\nabla A| = \sqrt{\left(\frac{\partial A}{\partial x}\right)^2 + \left(\frac{\partial A}{\partial y}\right)^2} = \sqrt{(h_x \otimes A)^2 + \left(h_y \otimes A\right)^2} \quad (3.19)$$

$$\psi(\nabla A) = arctan\left\{\frac{\frac{\partial A}{\partial x}}{\frac{\partial A}{\partial y}}\right\} = \arctan\left\{\frac{(h_x \otimes A)}{(h_y \otimes A)}\right\} \quad (3.20)$$

The values of h_x and h_y are usually based on the following commonly used standard methods

➢ Prewitt Gradient Filters

$$[h_x] = \frac{1}{3}\begin{bmatrix} 1 & 0 & -1 \\ 1 & 0 & -1 \\ 1 & 0 & -1 \end{bmatrix} = \frac{1}{3}\begin{bmatrix} 1 \\ 1 \\ 1 \end{bmatrix}\begin{bmatrix} 1 & 0 & -1 \end{bmatrix}$$

$$[h_y] = \frac{1}{3}\begin{bmatrix} 1 & 1 & 1 \\ 0 & 0 & 0 \\ -1 & -1 & -1 \end{bmatrix} = \frac{1}{3}\begin{bmatrix} 1 \\ 0 \\ -1 \end{bmatrix}\begin{bmatrix} 1 & 1 & 1 \end{bmatrix}$$

- Sobel Gradient Filters

$$[h_x] = \frac{1}{4}\begin{bmatrix} 1 & 0 & -1 \\ 2 & 0 & -2 \\ 1 & 0 & -1 \end{bmatrix} = \frac{1}{4}\begin{bmatrix} 1 \\ 2 \\ 1 \end{bmatrix}\begin{bmatrix} 1 & 0 & -1 \end{bmatrix}$$

$$[h_y] = \frac{1}{4}\begin{bmatrix} 1 & 2 & 1 \\ 0 & 0 & 0 \\ -1 & -2 & -1 \end{bmatrix} = \frac{1}{4}\begin{bmatrix} 1 \\ 0 \\ -1 \end{bmatrix}\begin{bmatrix} 1 & 2 & 1 \end{bmatrix}$$

3.8.2.2. Non - maximum Suppression (Edge Thinning/Detection)

Edge detection method was applied to convert the blurred edges in the image of the gradient magnitude to sharp edges. By doing this the local maxima in the gradient image were preserved, whereas, the non-gradient edges were removed from the image. Each pixel of gradient image followed the following algorithmic;

1. Corresponding to the neighbouring values, the gradient direction was rounded to the nearest 45-degree value,
2. The edge strength of the pixel was compared with the edge strength of the neighbouring pixels (both in the positive and negative directions). That is, if the gradient was in the east, then it was compared with the pixels located to the east and west.
3. If the pixel value became largest, then such value was used for edge strength, else it was suppressed.

Figure 3.27 shows the concept of edge detection method, in which the original image, Fig. 3.27 (a) was transformed by edge thinning to find the edges of an object, Fig. 3.27 (b).

3.8.2.3. Double thresholding

Lastly, double thresholding was done. Many of the edges obtained after edge thinning were true edges, however, there were still possibilities that few edges were generated due to some noise. The simplest way was to use some constant threshold value, such that if the value of edges was less than the defined threshold value then weak edge(s) were deleted while retaining the strong edges only.

(a) Original Image (b) Edge Detection

Figure 3.27 – Edge Detection

3.8.2.4. Procedure for Binary Image Generation

The binary images generated in the present study were based on Canny Edge Detection Algorithm. The complete procedure of the binary image generation is given as below:

1. Subtraction

At first, a two phase image containing water droplets, Fig. 3.28 (b), was subtracted from the dry (or single phase) image, Fig. 3.28 (a), i.e., which contain no water droplets, to obtain a subtracted image, as given by Fig. 3.28 (c).

2. Canny Edge Detection Algorithm

Canny Edge Algorithm was applied on the subtracted image, which consists of the following steps:

a. Smoothing: Blurring the image to remove the noise. (Median/Gaussian Filter).
b. Finding Gradients: The edges were marked where the gradients of the image had relatively large magnitudes. (First derivative).
c. Non-maximum Suppression: Only local maxima edges were marked. (Edge Thinning).
d. Double Thresholding: Potential edges were only chosen for thresholding.
e. Edge Tracking by Hysteresis: Finalize the edges, such that only strong edges were selected and weak edges were suppressed unless not connected to the strong edges. Figure 3.28 (d) was obtained after applying Canny Edge Method to the Fig. 3.28 (c).

3. Refinement

An additional criterion was made, such that if the area of an object is less than a certain value than those objects were deleted, as given in Fig. 3.28 (e). this refinement only helps in reducing the chances of error from the above-mentioned binary method

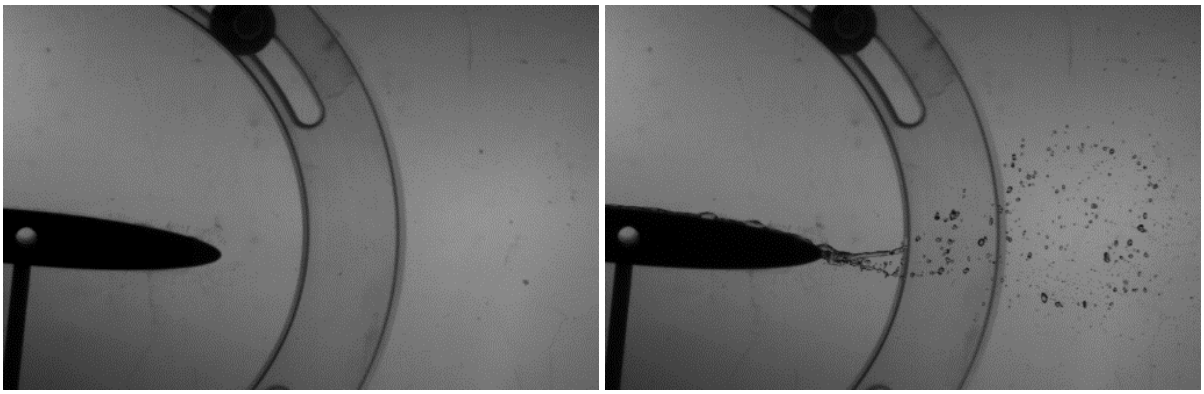

(a) Dry Image (b) Two-Phase Image

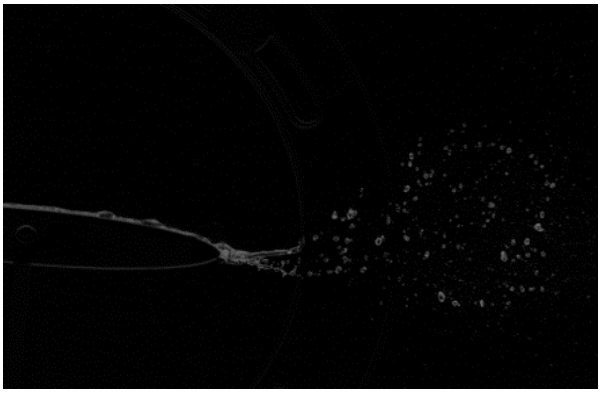

(c) Subtracted Image

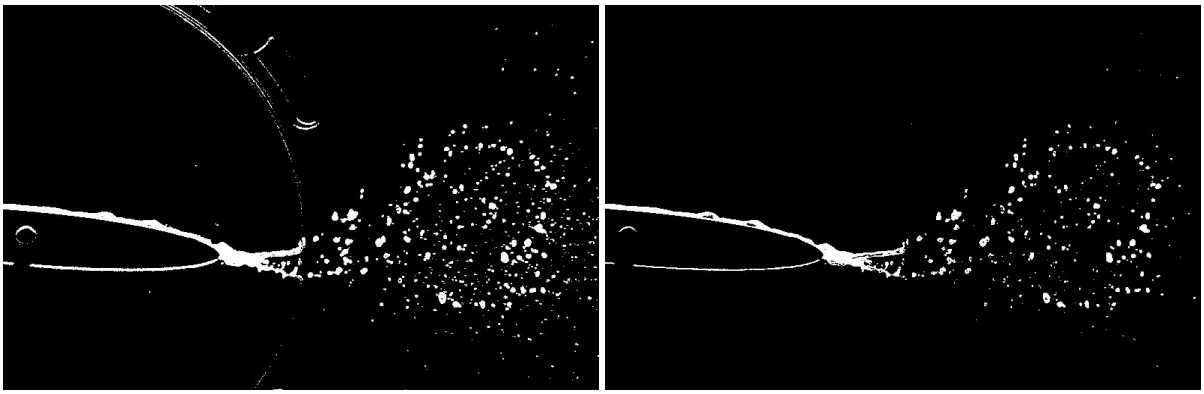

(d) Image obtained by Canny Edge Method (e) Refined Image

Figure 3.28 – Binary Image Generation

3.9. Data Processing Methods

3.9.1. Water Film Velocity Measurement Technique

One of the most fundamental parameters is the measurement of liquid film velocity. Unfortunately due to the non-availability of sensors the liquid film velocity was measured from the high-speed images. For that purpose, tracer particles were mixed in the water tank and were seeded along with the injected water to the cascade blade. As the size of the tracer particles is sufficiently small, it was assumed that these particles faithfully follows the flow dynamics. The motion of these seeding particles was then used to approximate the velocity of the thin liquid films. However, for a high degree of accuracy measurements, the author recommends the use of laser focus displacement (LFD) sensors.

3.9.2. Droplets Size Measurement Technique

Consider a binary image (matrix A) whose elements are represented by N rows and M columns, as given below

$$A = \begin{bmatrix} 0 & 1 & 1 & \cdots & 1 & 0 & 0 \\ & \vdots & & \ddots & & \vdots & \\ 1 & 1 & 0 & \cdots & 1 & 1 & 0 \end{bmatrix}$$

In the above arbitrary matrix, 0 and 1 correspond to the intensity levels of the binary image. The droplets characteristics were calculated from such matrices as explained below.

(a) Area:

The area of the droplet(s) can be calculated by the total numbers of "1" in the matrix.

(b) Equivalent Diameter:

Droplets were assumed to be almost spherical in nature and their diameter was considered to be equivalent to that of a circle

$$D_d = \sqrt{\frac{4\,A_d}{\pi}} \tag{3.21}$$

(c) Perimeter:

The perimeter of any bounded area (or droplet) was calculated by using a distance function in two-dimensional euclidean plane, expressed mathematically by Eq. (3.22)

$$\boldsymbol{P_{droplet} = \sqrt{(x_i - x_{i-1})^2 + (y_i - y_{i-1})^2}} \tag{3.22}$$

The distance was calculated between each adjoining pair of pixels around the boundary of the region and was summed up to obtain the perimeter of a bounded region.

(d) Circularity:

The most common shape factor is the circularity of a droplet, which is the function of area and perimeter, as given by Eq. (3.23).

$$C = \frac{\sqrt{4\pi A}}{P^2_{droplet}} \tag{3.23}$$

3.9.3. Droplets Size Measurement Positions

The measured frame rate of the high-speed camera was comparatively very large to that of the advection speed of droplets. For that reason, the recorded frame was divided into four sections at 0.25-, 0.5-, 0.75- and 1- chord length (C) downstream positions from the T.E, as shown schematically in Fig.

3.29. The size of each sub-frame was chosen to be 0.1-C in width and 1-C in height. The main purpose of doing such sub-framing was to avoid any repeatability of the droplets in an analysis frame.

Additionally, following sets of criteria were made for measuring the size of the droplets aft the T.E. region, which are;

- The typical frame rate of a high-speed camera was chosen as 1000 fps.
- The number of droplets counted at each position was at least 10,000. However, near the T.E., at 0.25-C, the droplets were generally always less than 10,000, which was mainly either the presence of ligament(s) or the formation of (newly) coarse droplets from the ligament and had not reached the breakup stage.
- Droplets were assumed to be spherical in nature and the diameter of the droplets size was approximated by using the Eq. (3.21)

here, D_d and A_d is the diameter and area of the droplets respectively.

Binary images were obtained as already explained in detail in Section 3.8 and the characteristics of each droplet, such as the area of the enclosed region, centre position, diameter and perimeter etc. were calculated as explained above.

In the field of atomization, a common way is to describe the probability and cumulative density functions of the droplets, which is mathematically represented by the following expressions

Probability Distribution Function (PDF)

$$PDF = \int_a^b f\,(x)dx \tag{3.24}$$

That is, PDF of variable X takes on a value in the interval [a, b] is the area under the density function from a to b.

And similarly, cumulative distribution function, is the integral of its probability density function $p\,(x)$, as given from Eq. (3.25)

$$CDF = \int_{-\infty}^{x} p\,(x)dx \tag{3.25}$$

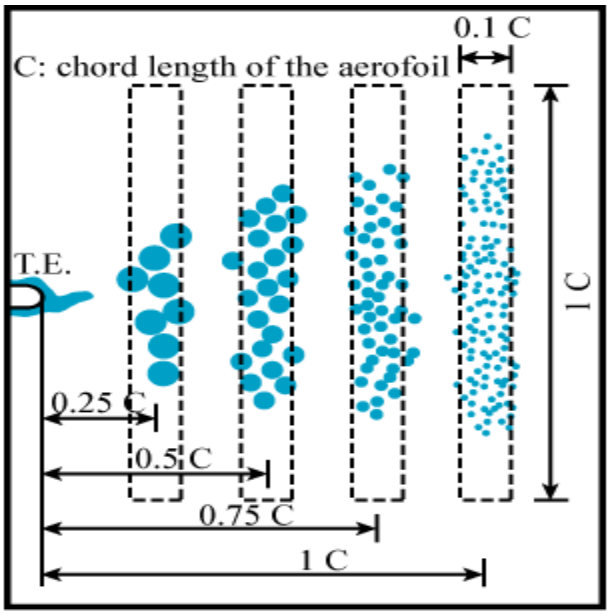

Figure 3.29 – Droplets Size Measurement Positions aft the T.E. of Aerofoil

3.9.4. Procedure for Calibration of Water Tank

Calibration of the water tank was performed by following the following procedure;

1. The test blade was inserted inside the wind tunnel at a particular angle of attack and the water connections between the water pipe and the test blade was made, as shown in Fig. 3.8.
2. At the bottom of the water tank, the hand valve was closed (to avoid the drainage of water) and the water tank was filled with water to a certain height.
3. Air was driven into the wind tunnel by switching on the centrifugal blower.
4. Once the centrifugal blower started to blow out air at its nominal operating speed, water was supplied to the test blade by opening the hand valve.
5. All the air bubbles were removed from the water connecting pipes.
6. The height of water tank was adjusted to an Optimal Height[1], (Fig. 3.30 (b)).
7. The height of water tank was measured at a regular step height (5 mm) and the corresponding time interval was recorded by using a stopwatch.
8. All the above process was repeated at least 3 to 5 times and a relationship between the mass flow rate against the water tank height was obtained, as shown in Fig. 3.31.
9. Empirical formula governing the relationship between the mass flow rate and the height of water tank was derived and was plotted, as shown in Fig. 3.31.

Once knowing the empirical relationship, the velocity and the mass flow rate of ejected water were also obtained.

In the present thesis, the mass flow rate of ejected water ($\dot{m}_W$) is expressed dimensionally by using the following relationship.

$$MFR = \frac{\dot{m}_W}{\mu_W \, C} \tag{3.27}$$

here, $\dot{m}_W$ and μ_W are the mass flow rate and viscosity of liquid, whereas, C is the chord length of the blade.

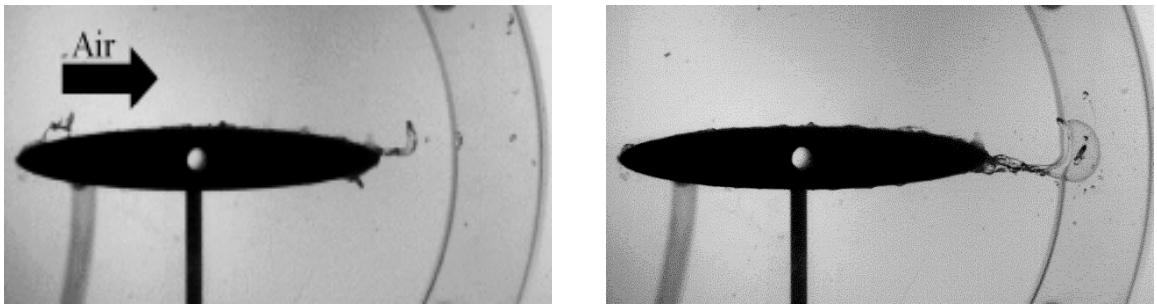

(a) Non-optimal Condition (large amount of water chunk being separated from the ejection hole)

(b) Optimal Condition

Figure 3.30 – Effect of optimal water height on the liquid film ejection

[1] **Optimal Height** is the height of water tank, such that above this height water ejection from the ejection hole results in the formation of water droplets either directly from the ejection hole or from the water film (Fig. 3.30 (a))

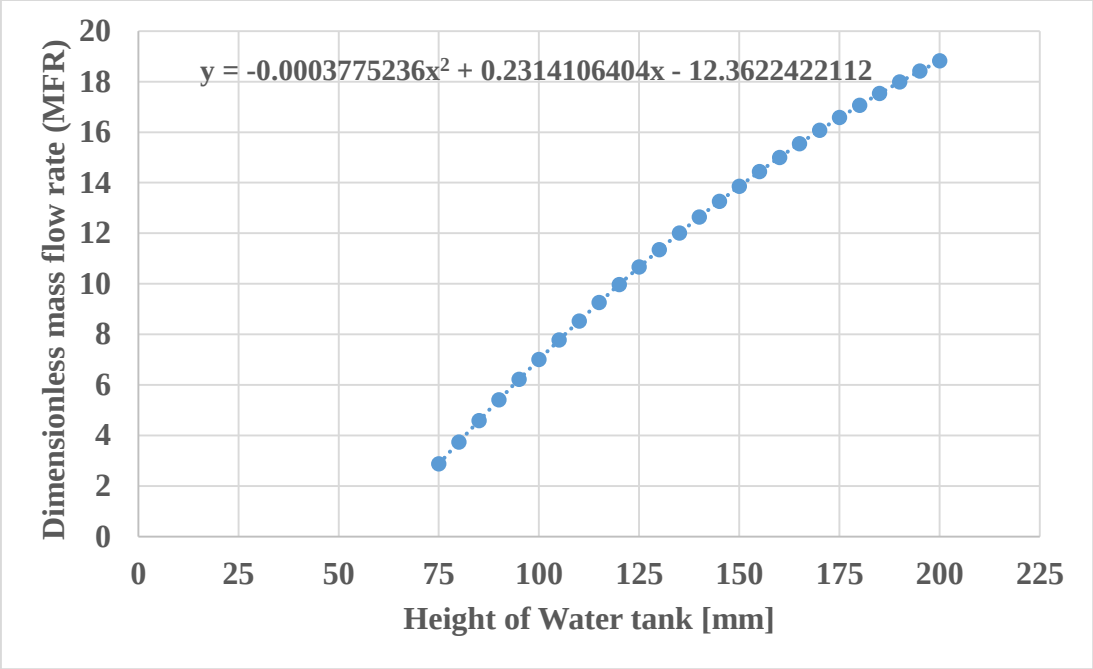

Figure 3.31 – Calibration Curve of water tank for Elliptical profile blade (Air velocity - 40 m/sec, AOA – 0-degree)

3.10. Conclusions

In this chapter, we have proposed the objectives for the manufacturing of the experimental facility and based on those objectives an experimental facility was designed. Specifications of the elliptical aerofoil were given in details with a hole for water ejection at the L.E. of the blade. Based on the Reynolds number and water ingestion flow rate (by weight), a comparison of the present experimental flow conditions with the gas turbine systems was also established. Moreover, a description of all the experimental equipment used in the present study was listed as well as the calibration procedures for three-hole pitot tube and hot-wire are given in detail. At the end of the chapter a detailed background as well as the procedure for obtaining the binary images from the shadowgraph images was explained.

PART –III Experimental Results

Chapter No. 4: Results & Discussions

Section 1.9 outlined the experimental objectives of the current research study, which are to understand the;

a. Characteristics of Liquid Film Formation,
b. Characteristics of Ligament, and
c. Characteristics of water droplets size distribution aft the T.E. region.

The operating parameters of two-phase phenomenon around the cascade blade are; air flow velocity, mass flow rate of the liquid and the chosen angle of attack. Focus points are the water film formation, the amount of water accumulation, the behaviour of accumulated water breakup and droplet disintegration due to aerodynamic forces, at and aft the T.E. of the blade.

This chapter is sub-divided into two main parts based on the experimental results performed at;

i. 0-degree AOA
ii. High degree AOA (3-, 5-, 7- and 10- degrees)

4.1. Fundamental Experimental Investigation

4.1.1. Velocity and Turbulence Measurement inside the Wind Tunnel

Figure 4.1 shows the pitch-wise velocity and turbulence intensity distribution measurements at the mid-chord position of the test wind tunnel (refer to Fig. 3.10) with the 3-hole pitot tube and the single element hot-wire. Here, filled marks (●) and hollow with the hole marks (⊙) represents the velocity distribution measured using a hot-wire and pitot tube respectively. In the case of hot-wire, velocity measurement was taken at every 2 mm. In the case of pitot tube near wall region (-0.5 to -0.3H and 0.5H to 0.3H) was measured at every 2 mm whereas the central half (-0.3H to 0.3H) was measured at every 5mm. From Fig. 4.1, the velocity distribution by the pitot-tube is perfectly symmetric, whereas in the case of hot-wire the velocity at the bottom half (0 to -0.5) gets slightly larger. Overall, both hot-wire and pitot tube measurement data shows very good agreement with each other's result. The hollow

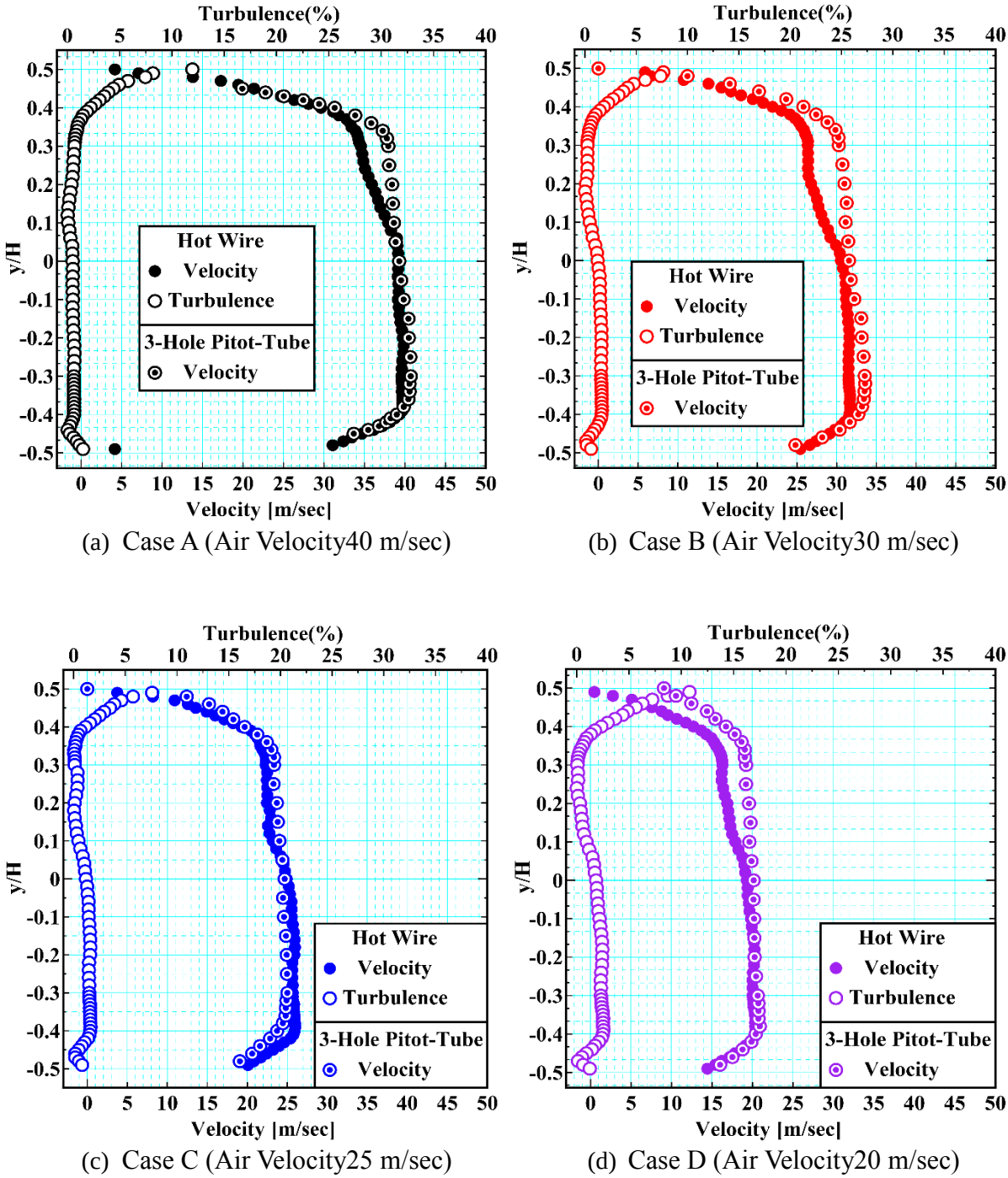

(a) Case A (Air Velocity40 m/sec) (b) Case B (Air Velocity30 m/sec)

(c) Case C (Air Velocity25 m/sec) (d) Case D (Air Velocity20 m/sec)

Figure 4.1 – Velocity Distribution in the pitch-wise direction at the origin

marks (○) in Fig. 4.1 represents the turbulence intensity data measured by hot-wire. From Fig. 4.1, the upper half of the wind tunnel (0 to 0.5) the turbulence intensity level was always less than 2% whereas in the lower half (0 to -0.5) it increases to as much as around 3%. This increase in the turbulence intensity was mainly caused by the blockage of air due to hot-wire holder which resulted in the local flow to increase slightly around hot-wire. As the present experimental setup allows hot-wire to be inserted from the top wall of the wind tunnel. Therefore, if the measurements of the lower half of the wind tunnel were done by inserting the hot-wire from the bottom walls of the test section, the velocity and turbulence results would have become more symmetrical, due to no (or little) blockage of air.

4.1.2. Characteristics of Airflow aft the T.E. Region (without water ingestion)

Preliminary experiments were performed to acquire the behaviour of velocity distribution aft the T.E. region of the elliptical profile blade. Figure 4.2 shows the velocity distribution aft the T.E. region of the elliptical blade using a single element hot-wire. The black, red, blue and violet colour lines correspond to Case A, Case B, Case C and Case D respectively. Similarly, the filled and unfilled symbols represent the velocity data measured at 0.25- and 1-C positions aft the T.E. As expected, due to the symmetric blade profile the wake profile was also symmetric with a large velocity deficit just behind the aerofoil, as shown in Fig. 4.2, A velocity deficit of around 25%, 20%, 18% and 15% occurred for the Case A, Case B, Case C and Case D respectively at 0.25-C position, which diminished gradually as the distance aft the T.E. increases.

Figure 4.3 shows the shedding frequency for the elliptical blade profile using a FFT analyser. According to Blevins [89], the variation in the Strouhal number is associated with the changes in the flow structure and for the Reynolds number range in the between $250 < Re < 2\times 10^5$ can be expressed mathematically by the empirical formula given by Eq. (4.1)

$$Sr = \frac{fL}{U} = 0.198\left(1 - \frac{19.7}{Re}\right) \tag{4.1}$$

Equation (4.1) utilizes the T.E. thickness as characteristics length (L). Table 4.1 compares the experimentally measured frequency data with the theoretical formula given by Eq. (4.1). For the same characteristics length the shedding frequency increases with an increase in air velocity and vice versa,

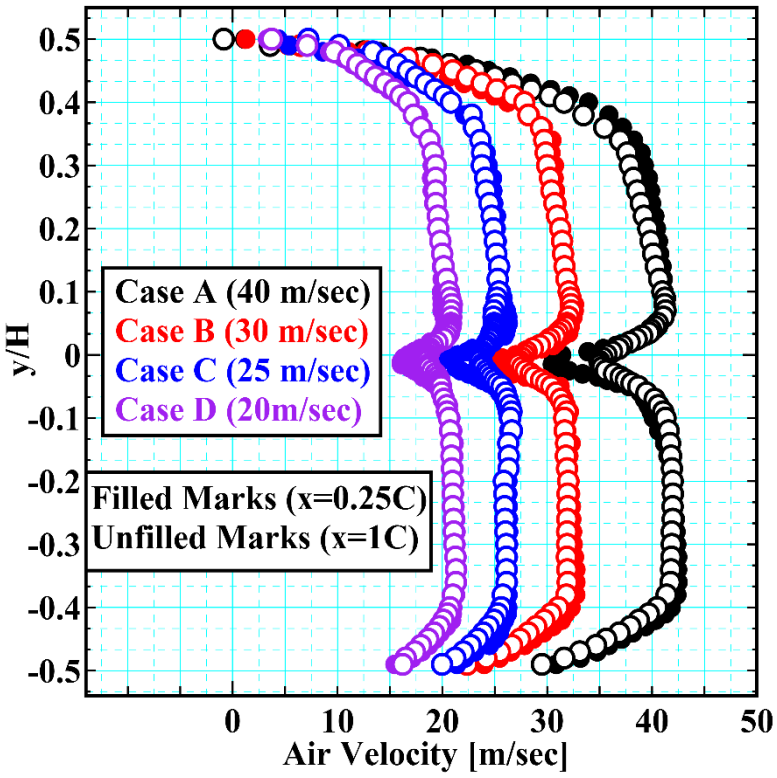

Figure 4.2 – Velocity Distribution aft the T.E. of Elliptical Profile Blade

as given in Table 4.1. It should be noted that Eq. (4.1) is a generalized equation for predicting the Strouhal frequency for circular cylinders. Due to different flow characteristics around a cylinder and flat blade, a discrepancy between the experimental and theoretical values was observed. But the important point to note here is that the order of strouhal frequency predicted is nearly the same order.

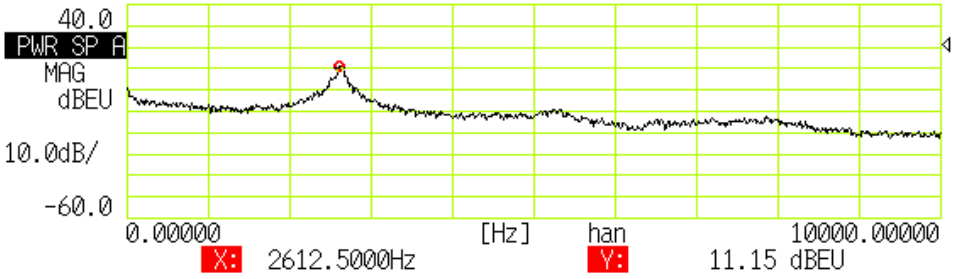

(a) Case A (Air Velocity 40 m/sec)

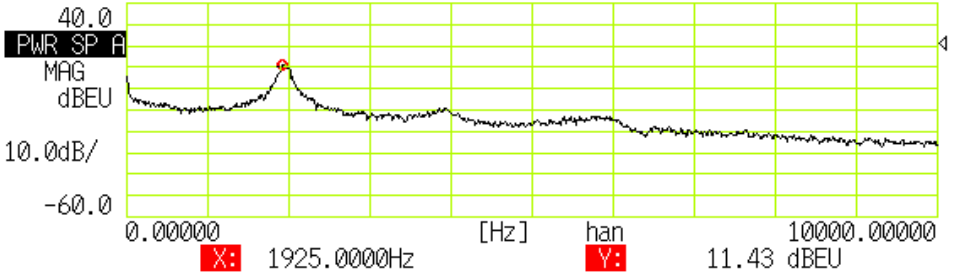

(b) Case B (Air Velocity 30 m/sec)

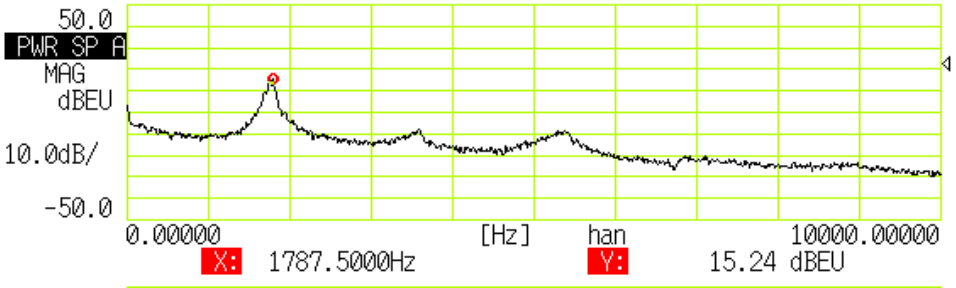

(c) Case C (Air Velocity 25 m/sec)

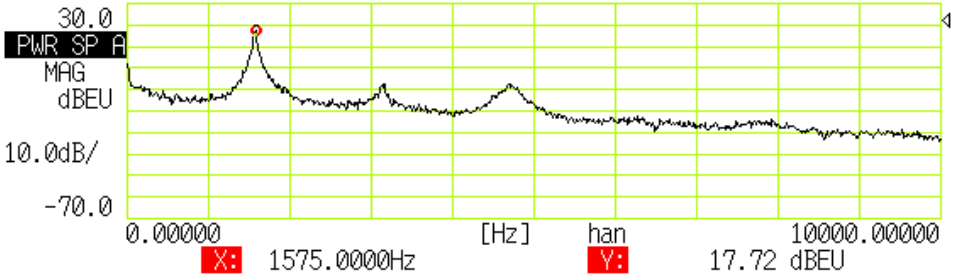

(d) Case D (Air Velocity 20 m/sec)

Figure 4.3 – Shedding Frequency Measured at 0.25-C from the tip of T.E.

Table 4.1 – Shedding Frequency (Elliptical Blade) – Unit (kHz)

Case	Experimental	Theoretical
Case A (Air Velocity 40 m/sec)	2.61	3.55
Case B (Air Velocity 30 m/sec)	1.93	2.66
Case C (Air Velocity 25 m/sec)	1.80	2.22
Case D (Air Velocity 20 m/sec)	1.60	1.77

4.1.3. Surface Oil Visualization of Test Blade

Surface oil visualization experiments were performed in order to obtain the basic flow pattern of air on the blade surface. For that purpose, a mixture of oil and titanium dioxide was painted as a thin uniformed layer on the surface of the blade (both suction side and pressure side). The blade was put inside the wind tunnel at the selected flow conditions for a predominant time length, which allowed the desired mean flow structure to establish the oil pattern on the blade surface. Figure 4.4 (a) and 4.4 (b) show the oil traces obtained on the suction side (S.S.) of blade surface for Case A and Case D respectively. For both cases, the flow remained attached for almost entire chord length of the blade as the oil was drawn out due to the sufficient surface shear along the flow directions. However, near the T.E. oil accumulation was due to the flow separation caused by the relatively large thickness of the blade at the mid-chord compared to the thickness of the T.E.. Also, due to the end wall effects very small corner stall region was also seen near the hub and tip side. Overall the flow remained attached and is seen to be two-dimensional in nature.

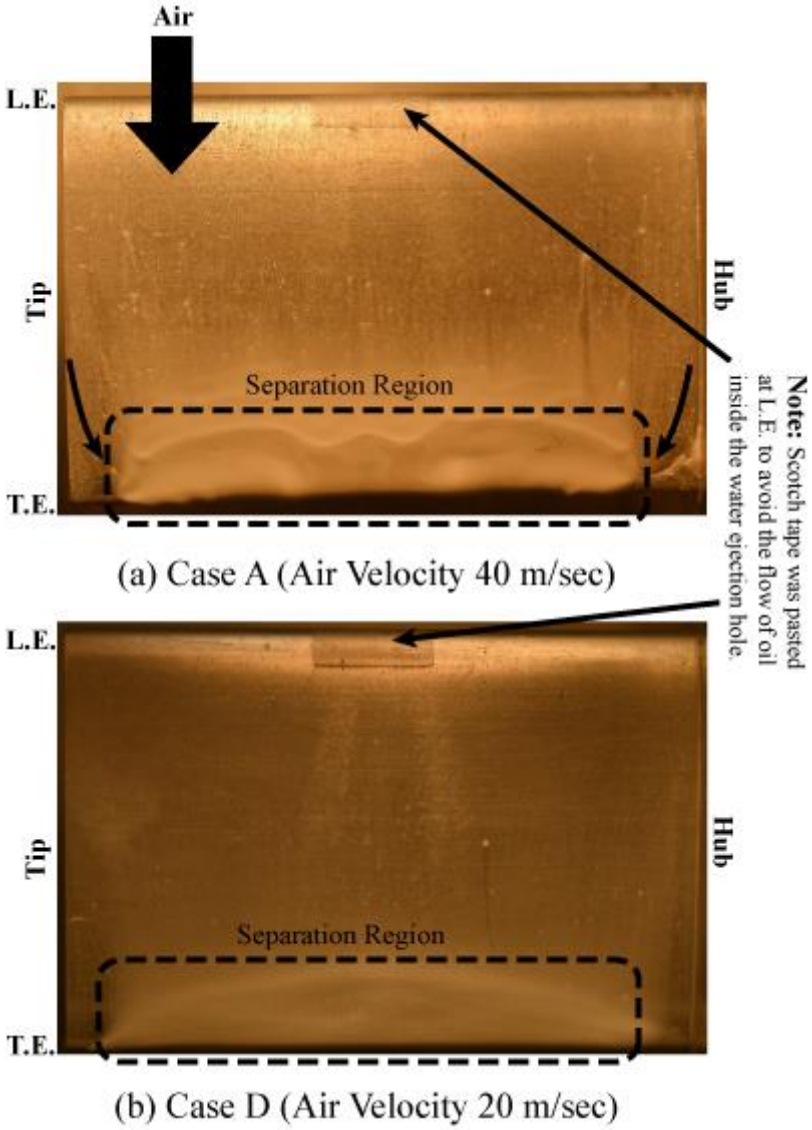

Figure 4.4 – Oil Flow Visualization of Elliptical Profile Blade @ 0-degree

I. Characteristics of two-phase phenomena around a Cascade Blade at 0 – degree AOA

4.2. Water Flow Visualization

Flow visualization was carried out using a high-speed camera to investigate the characteristics of water ingestion flow rate and air momentum. Regardless of air velocity and ingestion flow rate three basic phenomena were observed, as shown schematically in Fig. 4.5.

1. Water Film Formation.
2. Water Deposition at the T.E.
3. Breakup of ligament(s) from the T.E. and atomization aft the T.E.

4.2.1. Water Film Formation

Firstly, when the water was ejected from the hole, it formed a thin water film on the blade surface and was driven downstream due to the aerodynamic forces. It was observed that the film structure formed on the blade surface was mainly governed by the stresses exerted upon the film surface, i.e., characteristics of air velocity, as shown in Fig. 4.6, such that, at high air velocity (Fig. 4.6 (a)) an instability at air-liquid interface was observed. However, as the air velocity was reduced gradually the thin film became relatively smoothed (Fig. 4.6 (d)). The characteristics of the thin film will be explained in detail in Section 4.3.

4.2.2. Water Accumulation at the T.E.

Secondly, water film deposition was observed at the T.E. of the blade, as shown schematically in Fig. 4.5. Such that for high air momentum case (Case A – Fig. 4.6 (a)) water got deposited almost over the entire span length of the blade, whereas, as the air momentum was reduced to Case D (Fig. 4.6 (d)) a relatively small amount of water lump was attached at the T.E. This might be due to the relatively large velocity difference between the air and the film. From the visualization results the water deposition at the T.E. was due to the flow separation. From the comparison of the Fig. 4.6 (a) and 4.4 (a), the overall profile structure of the water accumulated and the oil accumulation was the same. Moreover, from Fig. 4.6 (a) the front edge of the water accumulation seems to correspond to the separation line of the oil flow visualization image, as shown in Fig. 4.4 (a).

4.2.3. Breakup of Ligament(s) from the T.E. & atomization aft the T.E.

Thirdly, Fig. 4.6 , and most importantly is the topology of droplet detachment from the T.E.. The profile of the T.E. greatly influenced the primary breakup phenomenon. Additionally, the breakup scheme also varied depending upon the air flow velocity. Air momentum clearly dominated the near-field breakup, as shown in Fig. 4.6. For low air momentum case (Case D) sufficient amount of liquid was accumulated at the T.E. and was stretched to strongly elongated ligament, which acted as a bridge between the water lumps at the T.E. and the bag breakup at the other end. However, on the other hand, for high air momentum case (Case A) droplets were seen to be stripping from the T.E. of the blade with occasional bag break up. From the shadowgraph images, it was observed that with an increased in the air momentum the ligament length decreased and vice versa. Thus, at low air momentum case, the surface tension of water dominates the breakup characteristics, whereas, at high air momentum case, the inertial forces of air dominate the breakup characteristics. The characteristic of atomization of droplets and breakup of ligament will be discussed in detail in Section 4.4 and 4.5 respectively.

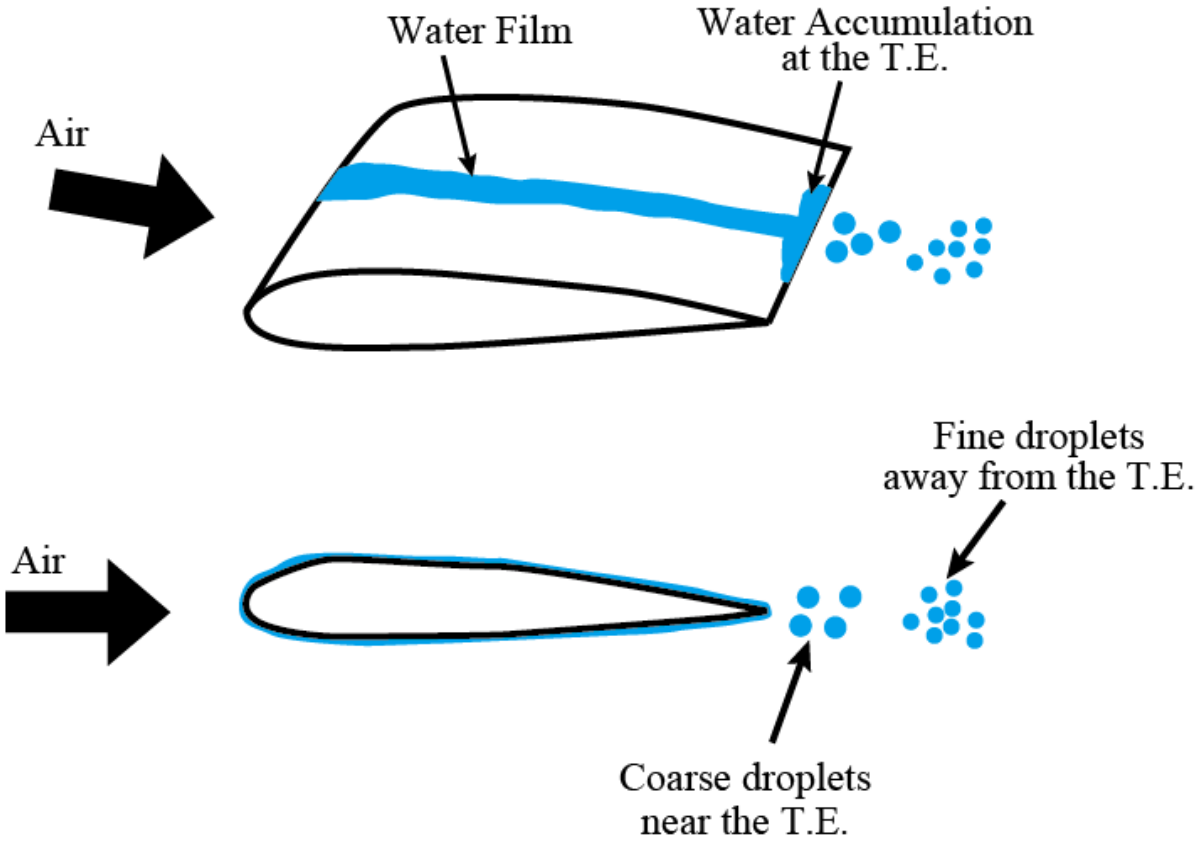

Figure 4.5 – Schematics of Water Film Flow

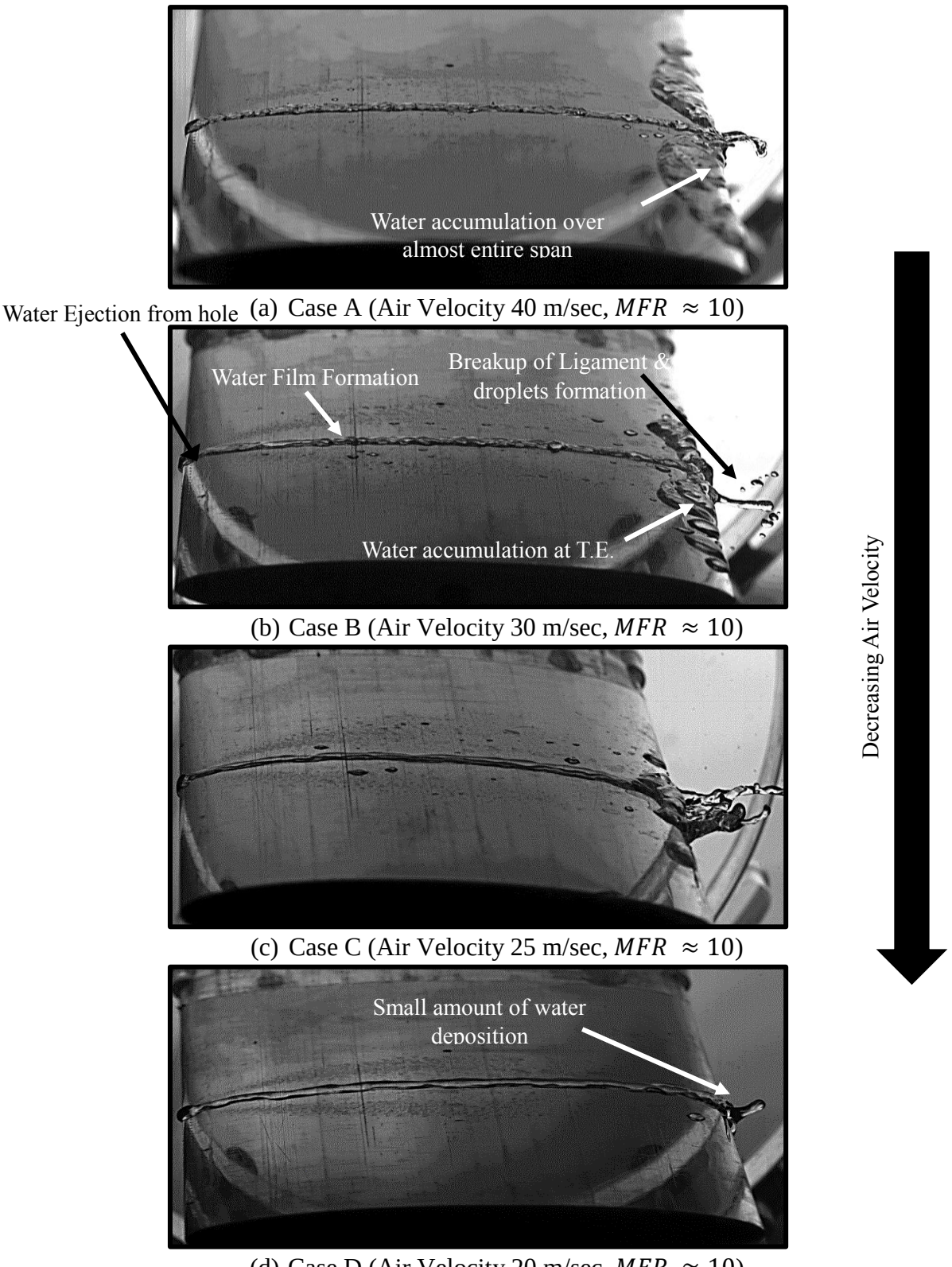

(a) Case A (Air Velocity 40 m/sec, $MFR \approx 10$)

(b) Case B (Air Velocity 30 m/sec, $MFR \approx 10$)

(c) Case C (Air Velocity 25 m/sec, $MFR \approx 10$)

(d) Case D (Air Velocity 20 m/sec, $MFR \approx 10$)

Figure 4.6 – Water Film Flow Visualization

4.3. Characteristics of Liquid Film

4.3.1. Liquid Film Visualization

From Fig. 4.6 shows the liquid film characteristics changes gradually due to the change in air velocity. Therefore, in order to further study the characteristics of liquid film formation on the blade surface, a more close view of liquid film formation on the blade surface was observed, as shown in Fig. 4.7 to 4.11. Based on the appearance of water film structure, they are classified into three major categories, which are;

1. Wavy Pattern
2. Mirror-Like Smooth Pattern
3. Intermediate Wavy Pattern (High and Low)

4.3.1.1. Wavy Pattern – Dominant Aerodynamic forces

For high air momentum case (Case A) a regular wave pattern was generated travelling downstream towards the T.E. of the blade as shown in Fig. 4.7. This wavy pattern appeared due to the transfer of energy from the gaseous phase to the liquid phase. In other words, the aerodynamic forces were strong enough than the corresponding liquid's surface tension forces and caused the wavy pattern at the air-liquid interface, Fig. 4.7. These waves were smaller in wavelength having large propagation speed. For relatively high liquid flow rate a visible wavy pattern was observed at the air-liquid interface (Fig. 4.7 (a)), however, when the liquid flow rate was reduced significantly, the air-liquid interface instability also get damped. But even at this very low liquid flow rate, small disturbances was seen which might be formed due to the formation of eddies in the air stream just above the thin liquid film, as shown in Fig. 4.7 (b).

4.3.1.2. Mirror-Like Smooth Pattern – Dominant Surface tension forces

For low air momentum case (Case D), a mirror (or crystal)-like smooth water film was formed on the suction side of the elliptical blade, as shown in Fig. 4.10. Such films moved very slowly compared to the wavy pattern, having smaller film width and much larger in thickness compared to the wavy pattern case. Their smooth structure was primarily governed by the liquid's surface tension forces which were capable of resisting any change in their film structure. Due to superior surface tension effects, the molecular bond is much stronger among the liquid particles resulting in thicker liquid films for this case. Moreover, their structure appearance didn't change with the change in the liquid flow rate.

4.3.1.3. Intermediate Wavy Pattern

At intermediate air velocity conditions, wave pattern exhibits characters between the above two discussed cases and are classified into intermediate high- and intermediate low- pattern, as illustrated in Fig. 4.8 and 4.9 respectively. The liquid film in this case moved faster than that of the low air momentum case with minute striations in the direction of air flow. For Intermediate High Wave Pattern, at relatively high liquid flow rate an instability wave pattern appeared on the liquid-air interface, Fig. 4.8 (a). However, as the flow rate of liquid was reduced minute striations appeared at the interface, Fig. 4.8 (b) just like Wavy pattern case, Fig. 4.7 (b). On the other hand, at a high liquid flow rate, small waves were seen to appear at the liquid-air interface for Intermediated Low Wave Pattern also, Fig. 4.9 (a), however, when the liquid flow rate was reduced the liquid film structure got smoothed, Fig. 4.9 (b), just like that of the smooth wave pattern.

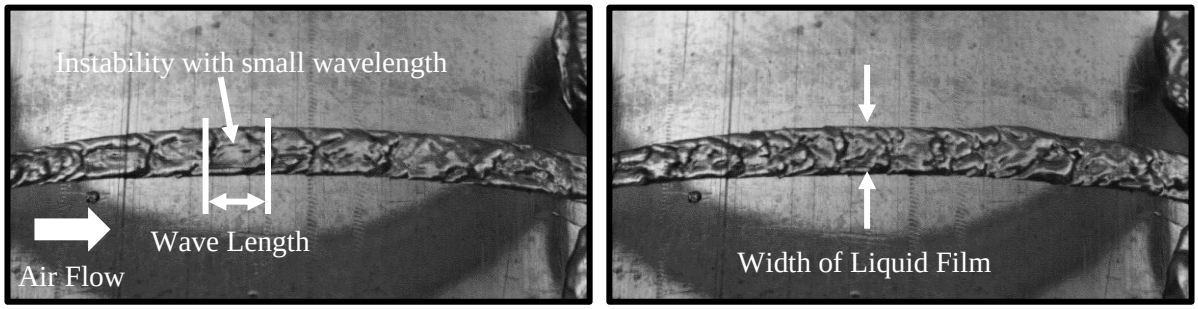

0.0 sec (a) High Water Ejection Flow Rate - $MFR \approx 13.5$ 0.1 sec

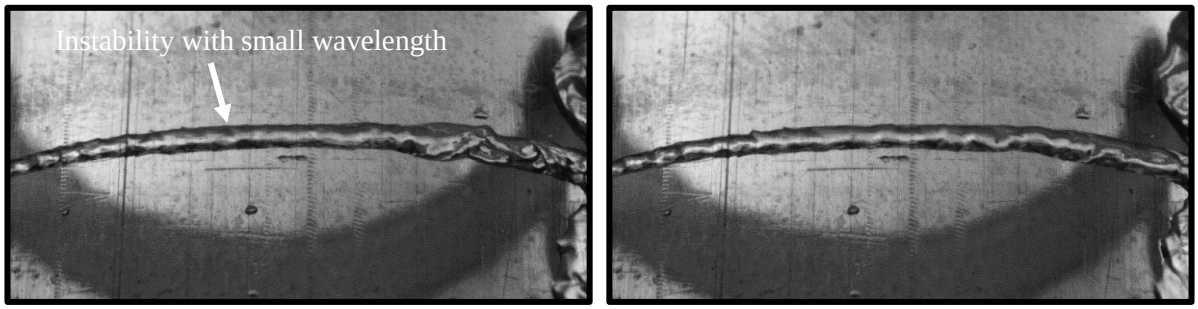

0.0 sec (b) Low Water Ejection Flow Rate - $MFR \approx 4.0$ 0.1 sec

Figure 4.7 – Wavy Pattern – Case A (Air Velocity 40 m/sec)

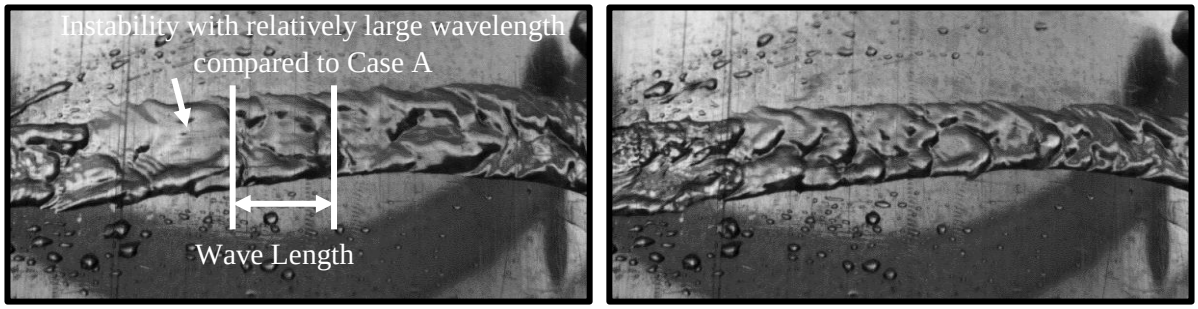

0.0 sec (a) High Water Ejection Flow Rate - $MFR \approx 14.5$ 0.1 sec

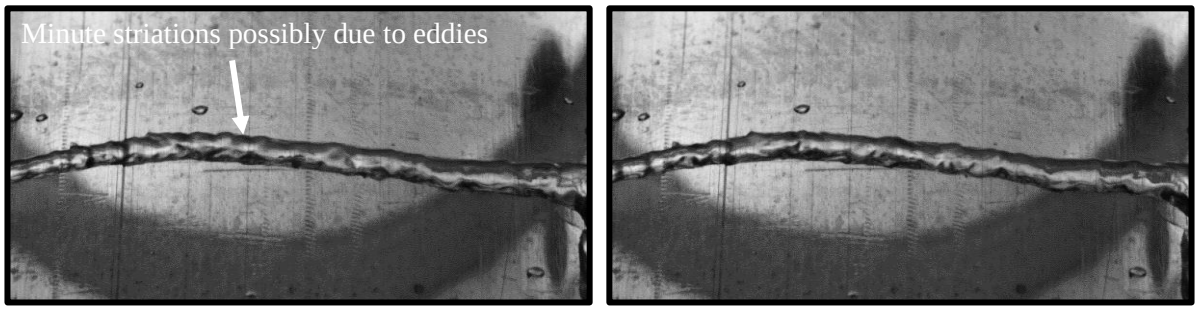

0.0 sec (b) Low Water Ejection Flow Rate - $MFR \approx 9.0$ 0.1 sec

Figure 4.8 – Intermediate High Wavy Pattern – Case B (Air Velocity 30 m/sec)

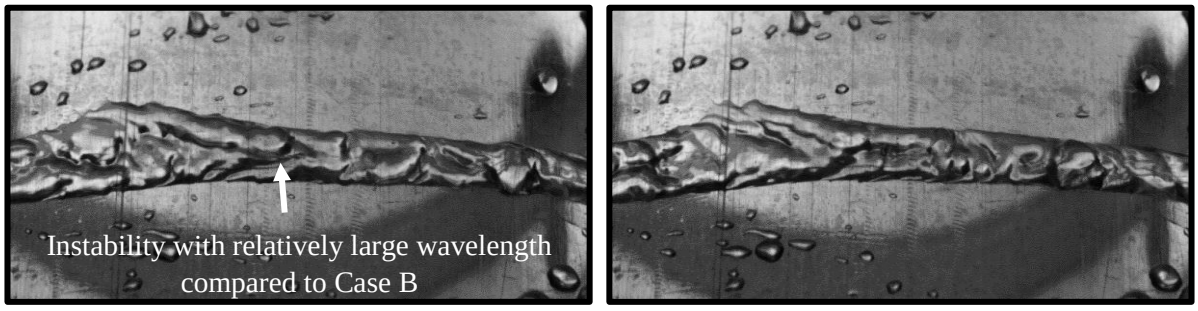

(a) High Water Ejection

0.0 sec Flow Rate - $MFR \approx 10.0$ 0.1 sec

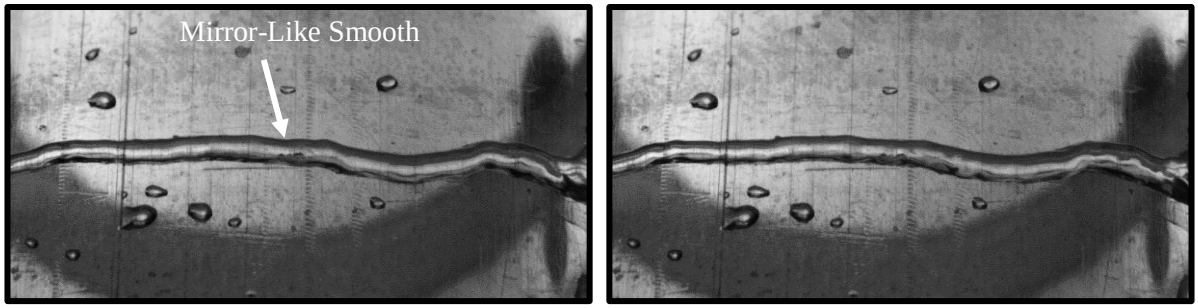

(b) Low Water Ejection

0.0 sec Flow Rate - $MFR \approx 4.5$ 0.1 sec

Figure 4.9 – Intermediate Low Wavy Pattern – Case C (Air Velocity 25 m/sec)

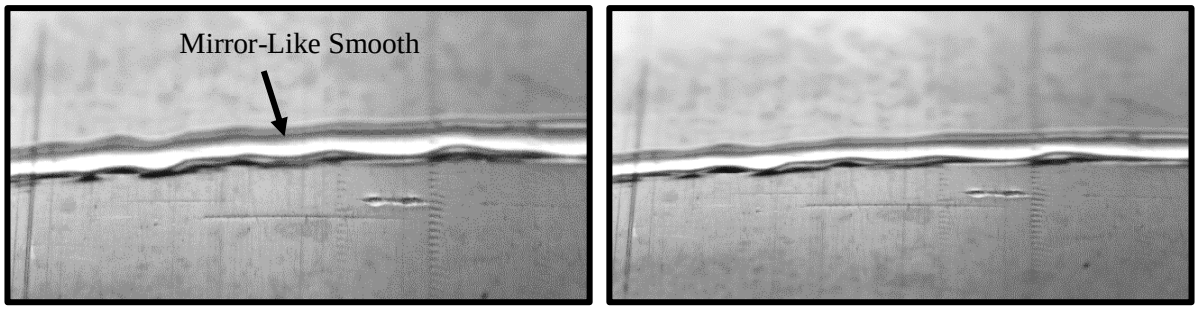

(a) High Water Ejection

0.0 sec Flow Rate - $MFR \approx 6.75$ 0.1 sec

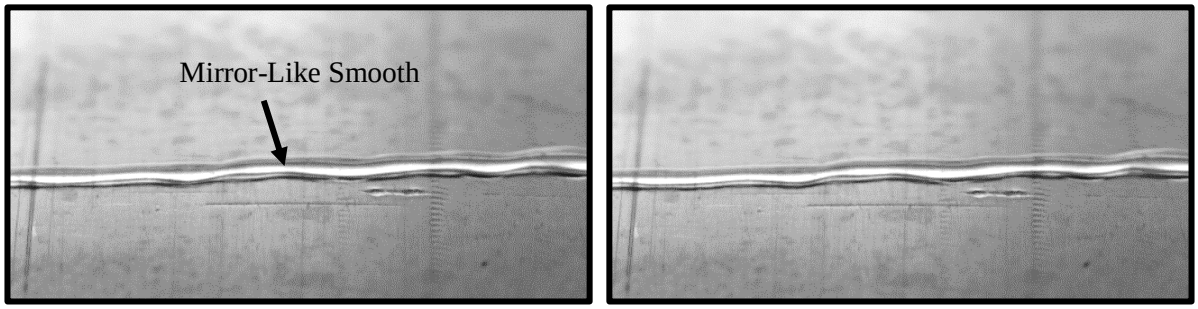

(b) Low Water Ejection

0.0 sec Flow Rate - $MFR \approx 2.25$ 0.1 sec

Figure 4.10 – Mirror-Like Smooth Wave Pattern – Case D (Air Velocity 20 m/sec)

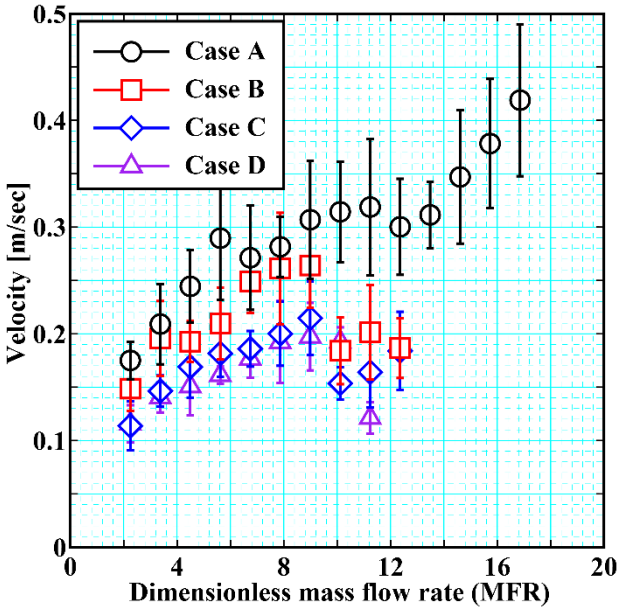

Figure 4.11 – Water Film Velocity

Based upon the above visualization results, aerodynamic forces are the dominant factor in defining the water film pattern for large air momentum, whereas, for low air momentum cases the surface tension of the liquid film governs the liquid film pattern structure.

In the present study, two most important characteristics of liquid film are studied, which are;

1. Thickness of Liquid Films, and
2. Instability Criteria of Liquid Films.

However, before analysing the above parameters, water film velocity is needed to be estimated as it is one of the most fundamental parameters which is always needed for the calculation of different parameters.

4.3.2. Water Film Velocity

Water film velocity was estimated from the tracer particles, as explained in Section 3.9. Figure 4.11 shows the average water film velocity with standard deviation approximated from the high-speed images near the mid-chord region. The liquid film velocity was accelerated with an increase in the aerodynamic forces. For example, for Case A the liquid film velocity was found to be maximum compared to the low air velocity (Case D). Moreover, the liquid film increases by increasing the mass flow rate (MFR) and vice versa. However, for a high degree of accuracy measurements, the author recommends the use of laser focus displacement (LFD) sensors.

4.3.3. Liquid Film Thickness

One of the most important characteristics is the thickness of thin liquid films. Unfortunately, the sensors available in the present study were not capable of measuring the thin liquid film, due to the smaller reference distance of sensor compared to the height of the wind tunnel used. For that purpose in the present study, the liquid film thickness is estimated theoretically by driving a model as explained below.

4.3.3.1. Theoretical Formulation of Liquid Film Thickness

It is assumed that the liquid film flow is similar to that of the Couette Flow, illustrated schematically by Fig. 4.12. Referring to Fig. 4.12, the Navier-Stokes equation can be written as follow;

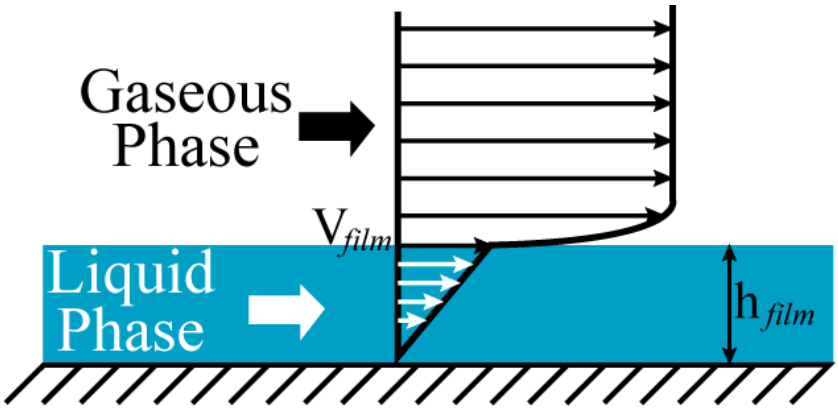

Figure 4.12 – Sketch of Couette Flow with Linear Velocity Profile

The Continuity Eq. for the thin film liquid can be given by Eq. (4.2).

$$\frac{\partial \rho}{\partial t} + \frac{\partial u}{\partial x} + \frac{\partial v}{\partial y} + \frac{\partial w}{\partial z} = 0 \tag{4.2}$$

Similarly the Momentum Eq. (in x-direction) can be expressed as follow

$$\frac{\partial}{\partial t}(\rho u) + u\,\frac{\partial u}{\partial x} + v\,\frac{\partial u}{\partial y} + w\,\frac{\partial u}{\partial z} = -\frac{1}{\rho}\frac{\partial p}{\partial x} + \upsilon\left(\frac{\partial^2 u}{\partial x^2} + \frac{\partial^2 u}{\partial y^2} + \frac{\partial^2 u}{\partial z^2}\right) \tag{4.3}$$

In Eq. (4.2) and (4.3), ρ is the density of the liquid film, u, v, w represents the flow velocity in x-, y- and z- direction respectively, p is pressure term and υ is dynamic viscosity.

It is further assumed that the flow is incompressible, steady in nature and there is no flow in the normal direction (z-direction). Based, on these assumptions, following deduction can be made in Eq. (4.2) and (4.3)

- Flow is infinite in the x-z plane

$$\frac{\partial u}{\partial x}\,;\,\frac{\partial w}{\partial z} = 0$$

- Steady State

$$\frac{\partial u}{\partial t} = 0$$

Thus, the Continuity Eq. (Eq. 4.2) can be simplified as follow;

$$\frac{\partial v}{\partial y} = 0\,;\, v = 0 \tag{4.4}$$

which states that υ is 0 at the boundaries and everywhere. Similarly, the momentum equation, Eq. (4.3) is re-written as

$$\frac{1}{\rho}\frac{\partial p}{\partial x} = \upsilon\,\frac{\partial^2 u}{\partial y^2} \tag{4.5}$$

$$u\,(y) = \frac{1}{2\mu}\frac{\partial p}{\partial x}\,y^2 + A\,y + B \tag{4.6}$$

From Fig. 4.12, the boundary conditions are

$$\vec{u}\,(y = 0) = (0, 0, 0)$$

$$\vec{u}\,(y = h_{film}) = (V_{film}, 0, 0)$$

Applying boundary conditions to Eq. (4.6) and after simplification

$$u\,(y) = \frac{1}{2\mu}\frac{\partial p}{\partial x}\,y\,(y-h) + \frac{V_{film}\,y}{h} \tag{4.7}$$

Assuming a linear profile, then $\partial p/\partial x \cong 0$, and Eq. (4.7) can be re-written as

$$u\,(y) = \frac{V_{film}\,y}{h} \tag{4.8}$$

which turn out that the velocity profile of the thin liquid film is linear.

The characteristic liquid film velocity at the free surface experiences shear stress due to the surrounding air is given by

$$\tau \approx \mu_{film}\frac{V_{film}}{h_{film}} \tag{4.9}$$

$$\frac{c_f\,\rho_a\,U_a^2}{2} \approx \mu_{film}\frac{V_{film}}{h_{film}} \tag{4.10}$$

where, c_f is the coefficient of air friction.

Thus, the liquid film velocity can be estimated by Eq. (4.11)

$$V_{film} = \frac{c_f\,\rho_a\,U_a^2}{2\,\mu_{film}}\,h_{film} \tag{4.11}$$

The volume flow rate of the liquid film can be written as

$$\dot{Q} = \int_A \vec{u}.\hat{n}\,dA = \int_0^{h_{film}}\int_0^{w_{film}} u\,(y)\,dz\,dy \tag{4.12}$$

here, w_{film} is width of the liquid film.

For a particular air flow velocity and the liquid flow rate, the width of the film remains almost constant. Similarly, the liquid film at the bottom plate is stationary, therefore, Eq. (4.12) can be re-written as

$$\dot{Q} = \frac{w_{film}\,h_{film}\,V_{film}}{2} \tag{4.13}$$

By substituting Eq. (4.11) into Eq. (4.13), the expression for the liquid film thickness can be estimated as given by Eq. (4.14)

$$h_{film} = 2\sqrt{\frac{\dot{Q}\mu_{film}}{c_f\,\rho_a w_{film} U_a^2}} \tag{4.14}$$

From Eq. (4.14), for the liquid film moving under the shear stresses, the thickness of liquid film decreases with an increase in air velocity and vice versa. Similarly, greater the viscosity of the liquid is, thicker is the liquid film and vice versa. From Eq. (4.14), it can also be concluded that the liquid film thickness with an increase in the flow rate of the injected water. In other words, the thickness of the liquid film is governed by the aerodynamic and the surface tension forces.

In the real machines additional forces on the liquid film due to the centrifugal forces causes the film to drive radially outward should also has to be taken into an account.

4.3.3.2. Film Thickness Results

Figure 4.13 shows the quantitative average water film thickness at the mid-chord of an elliptical blade, based on Eq. (4.14) at different air momentum cases, Section 4.3.2. Average film velocity (including standard deviation) was used to estimate the maximum and minimum deviation of film height.

The average water film width (w_{film}) was measured manually at the mid-chord of the blade from the high speed images by taking an average of about 100 frames. From Fig. 4.13, the height of liquid film decreases with an increase in air velocity and vice versa. The physical mechanism of change in film height due to aerodynamic forces is schematically illustrated in Fig. 4.15. At high air momentum the aerodynamic load on the liquid film is significantly larger compared to that of the low air momentum cases which causes the film height to decrease and vice versa Fig. 4.15 (b). It is due to this reason that at a high air velocity (Case A), Fig. 4.15 (b), liquid film became more wider and thinner. Low air speed (Case D) are dominated by the surface tension of the liquid resulting in a thicker liquid film, as shown schematically in Fig. 4.15 (a). For the fluids with large surface tension possesses stronger cohesive forces among the liquid molecules and results in thicker film. In other words, due to the weak adhesive forces it will have minimum width and vice versa. Figure 4.14 shows that the ratio of film height to its width remains nearly the same under the same aerodynamic load conditions. Such that for high air momentum cases the liquid film became much wider compared to its height and resulted in minimum height to width ratio (Case A), Fig. 4.14, and vice versa. This phenomenon can be understood based on the minimum energy principle. Under the same air flow conditions the aerodynamic forces experiences the same restoring forces from the liquid's surface tension. Liquid films, especially those driven by shear forces always have slightly greater width due to the additional external forces (i.e., aerodynamic forces) compared to the free air stream film. According to Lan et al. [90] at high liquid flow rate the liquid film deformed near the contact lines because of equivalent surface tension force, whereas, the central part results in flatter film thickness as shown schematically in Fig. 4.16 (b). This causes the water to eject towards the contact lines making the film to increase in the width and height wise direction, Fig. 4.16. As equilibrium was established, the expansion (i.e. in the width wise direction) energy and the equivalent surface tension balances each other and no further expansion of the film takes place. On the other hand, at low flow rate the amount of liquid ejected is small and the surface tension forces will avoid the expansion of the liquid film due to strong intermolecular forces, resulting in hat-column like structure, as shown in Fig. 4.16 (a). In the present study, the surface tension and aerodynamic forces remains the same due to which the height per unit width ratio also remained the same, as shown in Fig. 4.14.

4.3.4. Reynolds number of Liquid film

Figure 4.17 shows the corresponding Reynolds number of the liquid film based on the average velocity and height of liquid film. From Fig. 4.17 the order of Reynolds number of the thin liquid film is of order 10^2, which seems to be a reasonable range at the operating conditions.

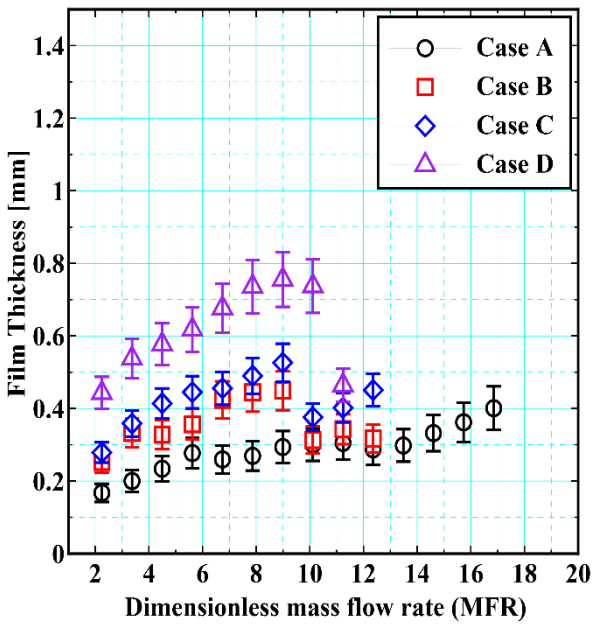

Figure 4.13 – Liquid Film Thickness @ Mid-Chord (Elliptical Blade)

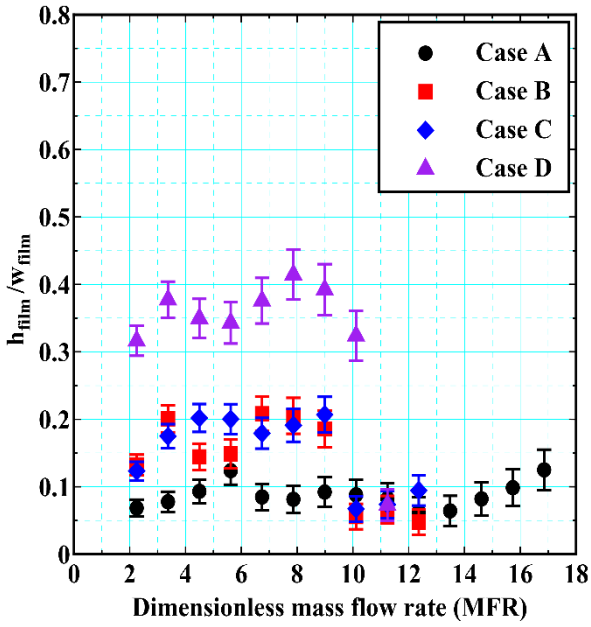

Figure 4.14 – Non-dimensional Film Thickness @ Mid-Chord (Elliptical Blade)

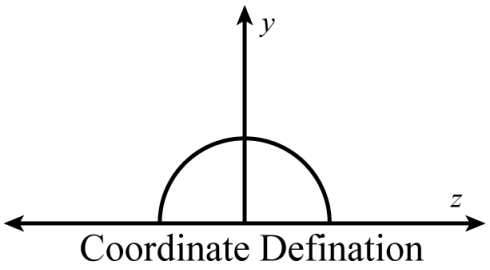

Note: Water (and air) flow in the x - direction, i.e., out of the page.

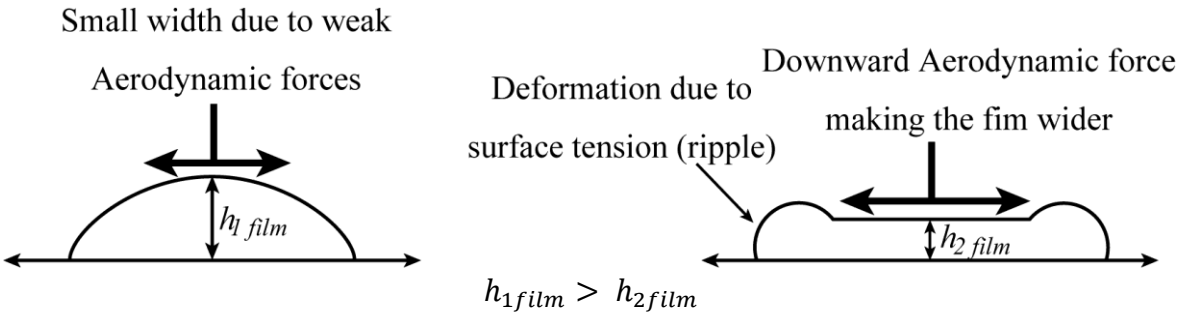

(a) Dominant surface tension effects (b) Dominant aerodynamic effects

Figure 4.15 – Effect of external (aerodynamic) forces on the liquid having same surface tension and flow rate

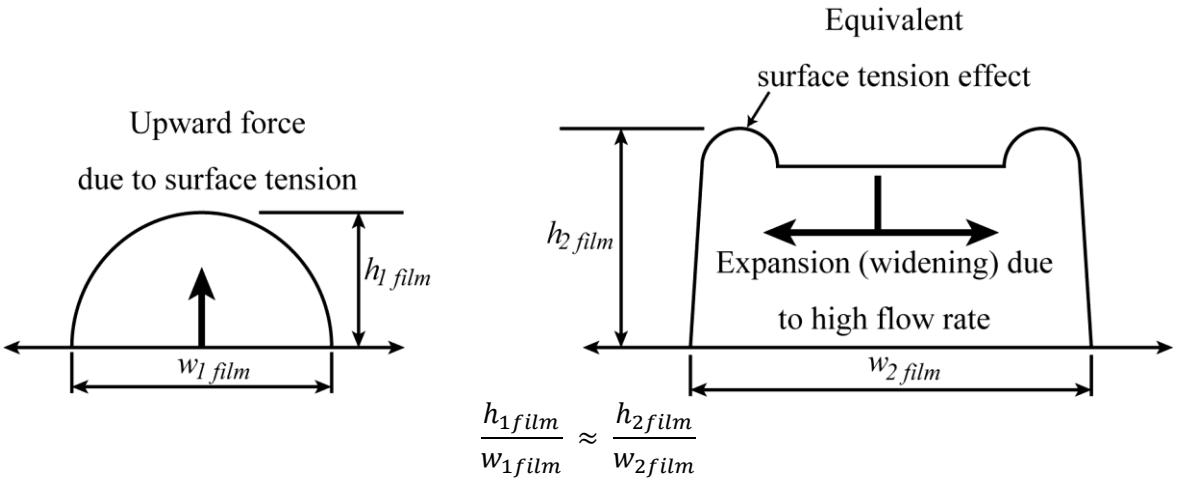

(a) Low Liquid Flow Rate (b) High Liquid Flow Rate

Figure 4.16 – Effect of flow rate of liquid under same aerodynamic and Surface Tesnion forces

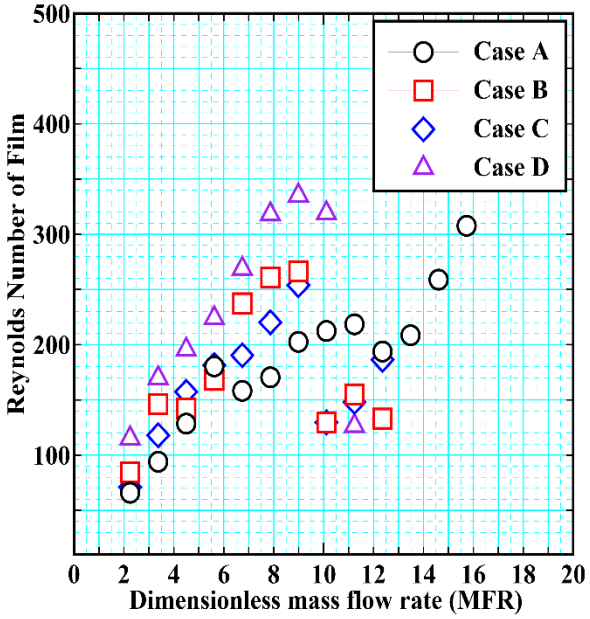

Figure 4.17 – Reynolds number of water film (based on average water film height)

4.3.5. Liquid Film Instability

Many researches have investigated the stability analysis of water film formation mostly on flat surfaces. Over time researchers have come to accept that there are multiple factors which affect the liquid film structure, such as, gaseous phase velocity, contact angle, film thickness, surface roughness, fluid properties of density, surface tension, wave disturbances, etc. According to author information, there is no single study which takes into account all these factors in a single study. Williams et al. [91] carried out extensive analytical research on the subject of droplet trajectories over a compressor blade and concluded that the inertia and friction forces affect more to the droplets motion, whereas, aerodynamic forces depends on water film or rivulet or discrete droplets on the blade surfaces. Similarly, Monnier et al. [92] predicted the breakup of the liquid film based on the minimal energy concept. However, for very thin liquid films, a simple and detailed analysis is suggested by Craik et al. [93]. In the present study, the author used Craik's criteria mainly because of being simple as well as his model utilizes detailed experimental study in nearly the same velocity range as being conducted in our study. For the purpose of simplicity, this will be called "Craik's Model" and is explained briefly below for the purpose of completeness.

4.3.5.1. Craik Model of Liquid Film Instability (Kelvin – Helmholtz criteria of thin liquid films) [93]

Craik's considered a unidirectional liquid film flowing in a horizontal direction, as shown schematically by Fig. 4.18, and whose dimensional velocity is mathematically expressed Eq. (4.15)

$$\bar{u}\,(y) = 1 + y \tag{4.15}$$

Craik further presumed a two-dimensional wave like perturbation on the liquid surface, which is represented by Eq. (4.16)

$$y = \eta\,(x\,,t) = \delta\, e^{i\,\alpha\,(x - c\,t)} \tag{4.16}$$

here, α is a real dimensionless wave number, which is given by Eq. (4.17) and c is the dimensionless wave velocity, which might be a complex.

$$\alpha = \frac{2\,\pi\,h_{film}}{\lambda} \tag{4.17}$$

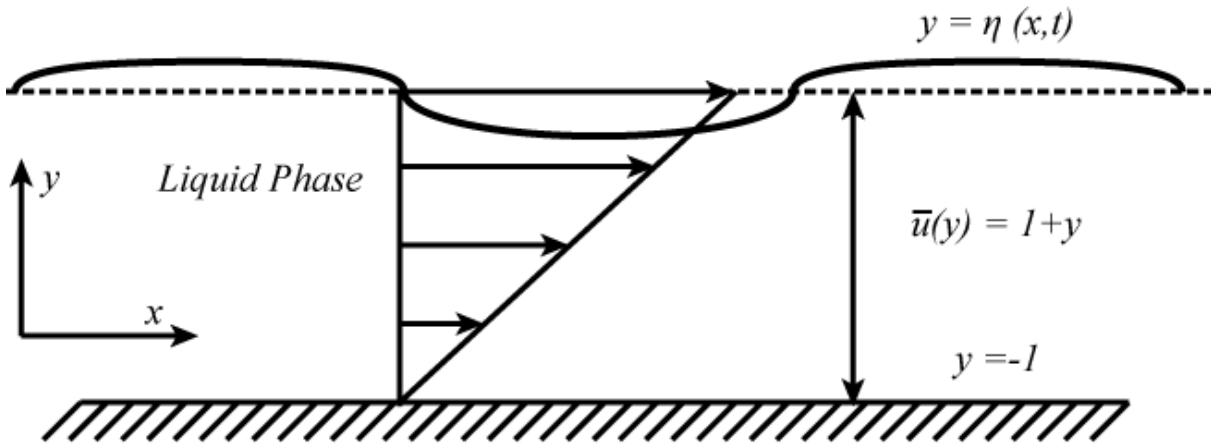

Figure 4.18 – Schematics of thin liquid film (Craik's Model)

By introducing the perturbation stream functions, Eq. (4.18), the perturbation velocity components are represented by Eq. (4.19)

$$\psi\,(x,y,t) = -\phi\,(y)\,\eta\,(x,t) \tag{4.18}$$

$$u = \psi_y = -\phi'\,\eta\,,\; v = -\psi_x = i\,\alpha\,\phi\,\eta \tag{4.19}$$

It should be noted that in Eq. (4.19), the differentiation is along the film height (i.e., in the y-direction). By substituting Eq. (4.15) and (4.19) in a Navier-Stokes equations, Craik obtained the Orr Sommerfield equation, Eq. (4.20), and the normal and tangential (shear) pressure terms are expressed mathematically by Eq. (4.21) and (4.22) respectively.

$$\phi^{iv} - 2\,\alpha^2\,\phi'' + \alpha^4\,\phi = i\,\alpha\,Re_{film}(1+y-c)(\phi'' - \alpha^2\,\phi) \tag{4.20}$$

$$p = \left[\,(1+y-c)\,\phi' - \phi \;\; - \left(i\,\alpha\,Re_{film}\right)^{-1}(\phi''' - \alpha^2\,\phi')\,\right]\eta\,(x,t) \tag{4.21}$$

$$\tau = Re_{film}{}^{-1}\left(u_y + u_x\right) = -Re_{film}{}^{-1}\left(\phi'' + \alpha^2\,\phi\;\right)\eta\,(x,t) \tag{4.22}$$

where, Re_{film} is the Reynolds no. of thin liquid film ($Re_{film} = \rho_l\,V_{film}\,h_{film}/\mu_l$).

The Orr Sommerfield Eq. is a fourth order equation which is solved by applying two boundary conditions at the wall, mathematically expressed by Eq. (4.23), and two boundary conditions at air-liquid interface, given mathematically by Eq. (4.24) below

$$\phi\,(-1) = \phi'\,(-1) = 0 \tag{4.23}$$

$$\sigma_{yy} = \Pi\,\eta\,(x,t)\,, \qquad \sigma_{xy} = \Sigma\,\eta\,(x,t) \tag{4.24}$$

In Eq. (4.24), ϕ_{yy} and ϕ_{xy} are the dimensionless normal and shear stresses at the air-liquid interface. Similarly, parameters Π and Σ are corresponding dimensional normal and shear pressure term at the air-liquid interface and can be complex. Moreover, according to Craik, linear kinematic condition at the air-liquid interface is expressed as follow

$$\phi\,(0) = 1 - c \tag{4.25}$$

Craik applied the condition of continuity for the shear stress term (i.e., $\tau = \sigma_{xy}$) at air-liquid interface and finally obtained Eq. (4.26)

$$(1-c)\phi' - \phi - \left(i\,\alpha\,Re_{film}\right)^{-1}(\phi''' - 3\,\alpha^2\,\phi') - (T\,\alpha^2 + G - \Pi)\,(1-c)^{-1}\,\phi = 0 \tag{4.26}$$

In Eq. (4.26), parameter T and G are defined as follow;

$$T^{-1} = \rho_l \, h_{film} \, V_{film}^2/\gamma \text{ (Inverse Weber Number of liquid Film)} \quad (4.27)$$

$$G^{-1} = V_{film}^2/g \, h_{film} \text{ (Inverse Froude Number)} \quad (4.28)$$

here, γ represent the coefficient of surface tension and g is acceleration due to gravity.

Substituting the above boundary conditions (Eq. (4.23) and (4.24)) in Orr Somerfield Eq., normal and shear pressure equations (Eq. (4.20), (4.21) and (4.22) respectively), Craik obtains the unknown constants were derived as follows,

$$\Pi = (\alpha/Re_{film} \, c_f) \, [I - \sqrt{3}s + i(2c_f - s)]$$

$$\Sigma = (2 \, \beta \, I/\sqrt{3}c_f) \, e^{\pi \, i/3} \alpha^3 (\alpha \, Re_{film})^{-4/3}$$

where,

$s = 0.6444 \Delta I$

$\Delta = (I/c_f) \, (\mu_a/\mu_{film})^{2/3} \, (\alpha \, Re_{film})^{-2/3} \, \alpha^2$

$2 \, \beta/\sqrt{3} \, = 1.372 \, (\upsilon_a/\upsilon_{film})^{2/3} \, (\rho_a/\rho_{film})^{1/3}$

$I = 2 \int_0^{H/2h_{film}} (2 \, y \, h_{film}/H)^{2/7} \, e^{-\alpha \, y} \, d(\alpha \, y)$

where, H is the height of the wind tunnel.

On substituting the power solutions for the perturbation stream function into boundary conditions, Craik obtained

$$T \, \alpha^2 + G - \, \Pi + \frac{3 \, i \, \Sigma}{2 \, \alpha} = (1 - c) \, \left\{ \frac{3}{i \, \alpha \, Re_{film}} + \frac{6}{5 \, (1 - c)} - \frac{7}{8} + \frac{27 \, \alpha^2}{i \, \alpha \, Re_{film}} \right\} \quad (4.29)$$

Upon separating the Eq. (4.29) into real and imaginary parts, the rate of amplification factor was derived given by Eq. (4.30)

$$\alpha \, c_i Re_{film} = \frac{(\alpha \, Re_{film})^2}{3} \left[\Pi_r + \frac{3 \, \Sigma_i}{2 \, \alpha} - T \, \alpha^2 - G \right] \quad (4.30)$$

According to the Eq. (4.30), the amplification growth rate is inversely proportional to the liquid's viscosity (given by Re_{film} term) and decreases with an increase in the liquid's viscosity. Another, important factor in Eq. (4.30) is given by the term in the parenthesis, which is called an Instability Criteria Term and is represented in the dimensionless and dimensional form as given in Eq. (4.31) and (4.32) respectively.

$$\left[\Pi_r + \frac{3 \, \Sigma_i}{2 \, \alpha} - T \, \alpha^2 - G \right] \quad (4.31)$$

$$\left[\mathrm{P}_r + \frac{3 \, \mathrm{T}_i}{2 \, \alpha} - \gamma \, k^2 - \rho \, g \right] \quad (4.32)$$

Thus, an instability occurs when the surface stresses is sufficient to overcome the restoring phenomena of flow inertia and surface tension, although, the normal pressure perturbation term (Π_r) is generally greater than the shear pressure perturbation term (Σi), the effect of variable shear stress cannot be neglected when α is small.

$$\left[\Pi_r + \frac{3\,\Sigma_i}{2\,\alpha} > T\,\alpha^2 + G\right]$$

$$\underbrace{\left[P_r + \frac{3\,T_i}{2\,\alpha}\right.}_{\text{Pressure Terms}} \underbrace{\left. > \gamma\,k^2 + \rho\,g\right]}_{\text{Restoring Terms}}$$

Pressure Terms
Causing Instability of liquid film

>

Restoring Terms
Causing Stability for liquid film
(applied due to Liquid's properties)

Instability Criteria

4.3.5.2. Physical Mechanism of Craik's Model

The physical phenomenon of Craik's Model can be understood by referring to Fig. 4.19. When air flows over a thin film, it generates instability on the surface of a liquid film, such that the normal stresses will apply a normal force to the liquid surface.

If a thin liquid film has enough restoring forces, which are due to the surface tension and inertia of the liquid film, it opposes the aerodynamic forces and results in a smooth liquid's surface, as shown in Fig. 4.19 (a).

(a) Restoring forces (liquid's surface tension and inertia) greater than External forces (aerodynamic forces)

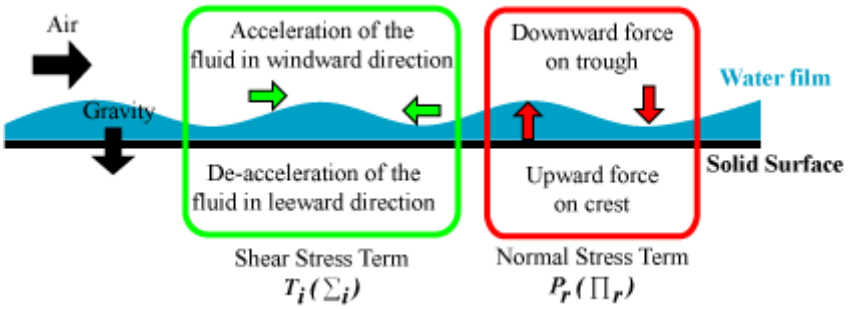

(b) Restoring forces (liquid's surface tension with favourable gravity force) lesser than External forces (aerodynamic forces) – S.S. of the blade

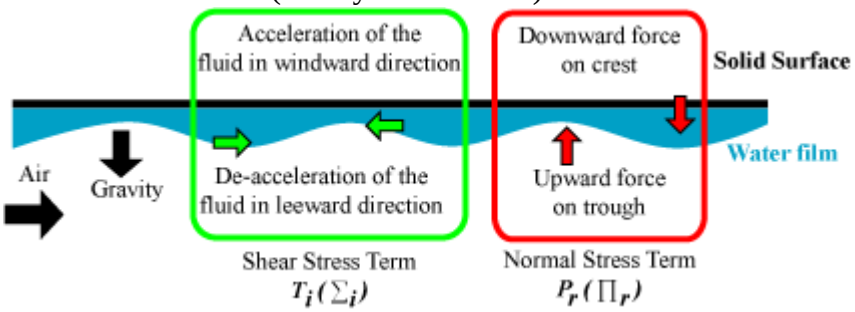

(c) Restoring forces (liquid's surface tension) lesser than External forces (aerodynamic forces) with un-favourable gravity force – P.S. of the blade

Figure 4.19 – Physical Mechanism of Craik's Model

On the other hand, if the aerodynamic forces exceed the liquid's restoring forces (surface tension and inertia), an instability pattern will appear on the surface of the liquid, as shown in Fig. 4.19 (b). Due to the aerodynamic force, a normal force is applied on the surface of the liquid resulting in the appearance of an instability pattern at the liquid's surface. The normal stress (P_r) applies an upward force on the crest and a downward force on the trough. This process results in displacing the liquid away from the troughs and towards the crests respectively. The shear stresses (T_i) due to the external forces accelerates the fluid in the windward direction (i.e., in the direction of external force) and deaccelerates the fluid in the leeward direction (i.e., in the direction opposite to the external force). This ultimately results in the acceleration of the liquid crest and de-acceleration of the liquid at its trough. According to Craik Model, the thinner the liquid's film thickness is the more unstable it will become and vice versa [93]. The role of gravity term is thought to be both acting as a stabilizing as well as an un-stabilizing factor. In case of the liquid is flowing on S.S. of the blade, , as shown in Fig. 4.19 (b), the gravity force along with the surface tension force will stabilize the liquid film by applying the downward force on the thin film to remain intact with the blade's surface. The analysis conducted by the Craik is primarily focused for the cases shown in Fig. 4.19 (b). However, for the case if the liquid is flowing on P.S. of the blade's surface, the gravity term are expected to destabilize the thin liquid film because of the unfavourable gravity effects, as shown in Fig. 4.19 (c), by applying a downward force, which causes the liquid film to move away from the blade's surface. However, the effect of gravity effect on the pressure is needed to be visualized.

One of the most important features of Craik's model is that though the shear pressure term is relatively smaller in value compared to the normal pressure. However, the importance of shear pressure cannot be neglected due to its significant dominance for thin liquid film cases. Thus, the shear stress term further contributes to make the overall process as irreversible. In this respect, Craik had also named such criteria as "Kelvin – Helmholtz" criteria for thin liquid films.

4.3.5.3. Instability Criteria Results

To utilize the Craik's model, the wavelength of the thin liquid film was measured manually from the high-speed images only at the S.S. of the blade, such as given by Fig. 4.7, and the dimensionless wave number was calculated by using Eq. (4.17). Table 4.2 below shows the values of dimensional wave number (α) based on the experimental results. Utilizing Eq. (4.27), the amplification factor is plotted, as shown in Fig. 4.20. The dots in Fig. 4.20 represents the experimental dimensionless wave number. In the present study, the stability of thin liquid film was conducted on the S.S. of the blade only. Based on Eq. (4.30), the restoring forces (inverse Weber number (T) and inverse Froude number (G)) terms are always less than zero and therefore, played an important role in the stabilizing of the thin liquid films. For Case A and Case B, the order of G was found to be of 10^1 whereas for Case C and Case D it is of the order 10^0. In other words, the Froude number is always less than one, i.e., making the nature of the flow pattern to be subcritical. The additional stabilizing forces are exerted due to the surface tension property of the water, i.e., the inverse Weber number term (T). This results in the thickening of the fluid film. However, for the Case A and Case B, the order of the normal and shear term due to the external forces was of 10^1 and 10^0 respectively. This means that the normal forces are the main cause of the liquid film destabilization, which is further enhanced by the shear term forces. Figure 4.20 shows that when the wave number exceeds the critical value of dimensionless wave number, the film becomes unstable due to less viscous dissipation than the energy input (i.e., aerodynamic force) to it. For large values of dimensionless wave number the waves would remain stable due to the dominance of liquid's surface tension. According to Craik [93], the energy takes place due to non-conservative forces (normal and shear pressure component), which became in phase with the wave slope and wave displacement respectively.

Table 4.2 – Dimensionless Wave Number

Dimensionless mass flow rate (MFR)	Dimensionless Wave Number	
7.86	0.68	-
10.11	0.9	0.55
12.36	1.01	-

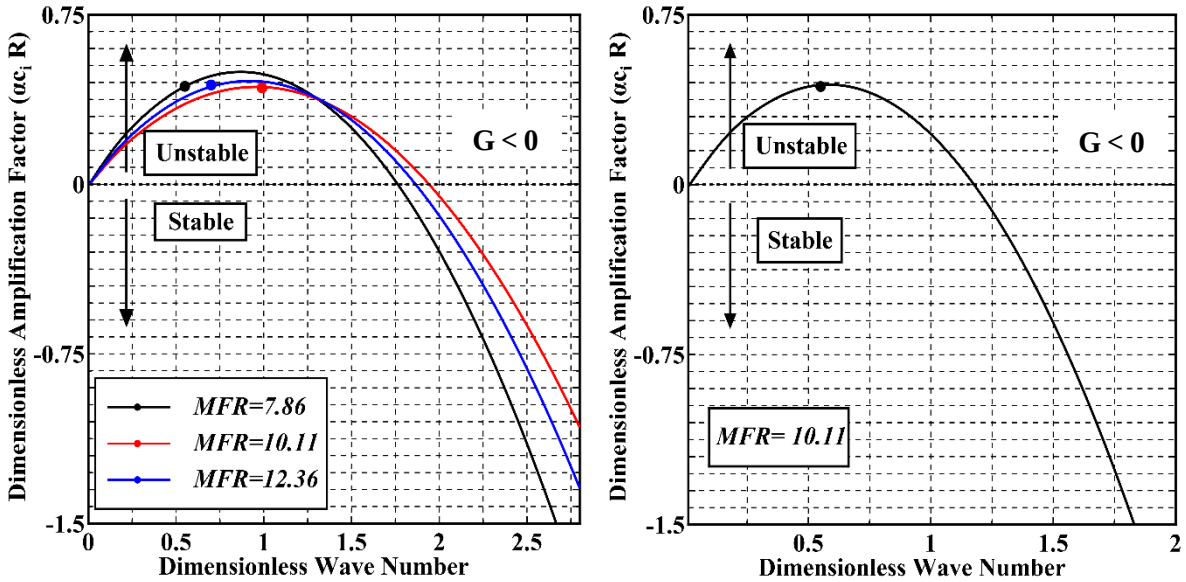

(a) Case A (Air Velocity 40 m/sec) (b) Case B (Air Velocity 30 m/sec)

Figure 4.20 – Water Film Stability Criteria

4.4. Characteristics of Droplets Size Distribution aft the T.E. Region

4.4.1. Importance of Droplets Size Distribution

The knowledge of knowing the droplet size distribution in wet turbine systems is considered highly important as it causes unavoidable damage to the wet turbine systems. Knowing the droplet helps in increasing the reliability, preventive maintenance and performances of the system for a long term availability of wet systems as;

1. Droplets shed can damage the blade profile by forming pits, especially the large droplets as they have relatively high momentum.
2. Droplets (especially the large droplets) are the main source of erosion in wet turbine systems.
3. Information about the droplets formation and breakup under the different operating condition is essential to avoid damages to other parts of the wet turbine systems also.
4. Role of mass flow rate of liquid in droplets size distribution.

4.4.2. Breakup Mechanism of Droplets aft the T.E. Region

From the extensive visualization of the high-speed images, it was found that the operating conditions strongly affects the growth and breakup of the liquid from the T.E. of the blade. The accumulation and disintegration of liquid into ligaments, primary droplets formation and subsequently into secondary droplets are primarily affected by three parameters, which are the surface tension of the liquid, thickness of the T.E. and the air velocity. The role of the thickness of T.E. is discussed in Appendix B. In this section main discussion is related to the velocity of air when the angle of attack was set at 0–degree. The effect of air velocity on the breakup mechanism is highly significant, as given by shadowgraphic images Fig. 4.21, 4.22, 4.23 and 4.24 for Case A, Case B, Case C and Case D respectively. The mechanism of droplets breakup at the T.E. is governed based on the Weber number of the T.E. (i.e., the thickness of the blade) of the aerofoil and momentum ratio as expressed mathematically by Eq. (4.33) and Eq. (4.34) respectively.

$$We_a = \frac{\rho_a U_a^2 t}{\sigma} \tag{4.33}$$

$$M = \frac{\rho_a U_a^2}{\rho_l U_l^2} \tag{4.34}$$

In Eq. (4.33) and Eq. (4.34), ρ, U, σ and t represents the density, velocity, surface tension of water and thickness of the T.E., whereas the subscript a and l stands for the air and liquid phase respectively.

In the following discussion, it should be noted that the momentum ratio was estimated by order estimation of ligament velocity at the T.E. (usually of order 10^{-1}, see Appendix C) from the high-speed images and should not be considered as a true (or final) value. Similarly, in all the cases the accumulated water oscillates up- and downwards due to the vortex being shed from the T.E of the blade.

4.4.3. Classification of Ligament Breakup

From the visualization of high-speed images the accumulated water at the T.E. of the blade was seen to breakup mainly due to the dominant effects of the following forces;

- Due to aerodynamic forces
- Due to surface tension forces

4.4.3.1. High Air Momentum (Case – A (Air Velocity 40 m/sec, $M \approx 192$, $We_a \approx 60$) – Breakup due to aerodynamic forces (Ref. Fig. 4.21)

From Fig. 4.21, for large momentum ratio and the Weber number cases possessed high wave speed, which plays a major role in the breakup of droplets from the T.E. [95]. Due to the large momentum of surface waves, Fig. 4.21 (h), when they reached the T.E. of the blade they break off directly, as shown in Fig. 4.21 (b), 4.21 (c), 4.21 (h), into droplets rather than accumulating at the T.E.. Due to the high momentum of these waves some of the momentum was also transferred to the already accumulated water at the T.E.. It was observed that the water usually accumulates towards the lower end of the T.E. (P.S.) possibly due to the higher density. When accumulated water reaches a critical amount, the vortex shed from the T.E. causes destabilization of accumulated water, leading to a larger chunk of accumulated water to shed into the T.E. region, as shown in Fig. 4.21 (d) and is called surface stripping in this thesis. The accumulated water moves upwards towards the S.S. and the vortex shed from the S.S. further enhances the stripping phenomenon by stripping a large number of droplets and started to move the accumulated water downwards. This process continues until enough amount of water in the form of droplets is shed off from the T.E.. Due to surface stripping, occasionally relatively big droplets were also formed in the near vicinity of the T.E. and soon underwent bag mode of a breakup, Fig. 4.21 (d). The cause of bag breakup near the vicinity of the T.E. is thought to be due to the low amplitude of oscillation of the ligament, due to the high aerodynamic forces (vortex shedding). When the surface waves did not possess high momentum then the water continue to accumulate at the tip of the T.E., leading to the bag mode of breakup directly from the T.E. of the blade as shown in Fig. 4.21 (c). In general, the coarse droplets formed in this case usually undergo mainly a vibrational mode of a breakup, as shown in Fig. 4.21 (g). The droplets formed in this case were comparatively smaller in size and flow along with the air path. It is generally accepted that the stripping of droplets due to aerodynamic forces is generally occurred due to the Kelvin – Helmholtz. In conclusion, the aerodynamic forces which lead to destabilization of wave crest result in very small ligament at the T.E. or direct stripping of droplets from the T.E. and most of the droplets breakup due to vibrational mode. From the flow visualization results, the secondary droplets formed in this case was minimum in size compared to the other cases.

4.4.3.2. Low Air Momentum (Case – D (Air Velocity 20 m/sec, $M \approx 48$, $We_a \approx 15$) – Breakup due to surface tension forces (Ref. Fig. 4.24)

Surface tension clearly dominated the near T.E. field breakup when the flow characteristics were reduced to $M \approx 48$ and $We_a \approx 15$, as shown in Fig. 4.24. In this case, the surface waves possessed low momentum and got accumulated at the T.E.. Even occasionally when the wave plunges, it usually did not break from the surface waves as the surface tension forces were dominant to cause any stripping. As the water continues to accumulate at the T.E. for long time, it results in large amount of water accumulation at the T.E., as shown in Fig. 4.24 (a). Like previous case, in this case too water usually accumulates on the lower end, which might be due to the gravity effect. Due to weak aerodynamic forces, the vortex sheds at the T.E. did not contribute towards the shedding of droplets, rather helped in elongating the thick ligament in the wind-ward direction. The ligament attached at the T.E. was observed to make radial excursions from the central axis of T.E., due to vortex shedding and when this ligament had a perpendicular contact with incoming air flow When accumulated water reaches critical

stage, the vortex shed resulted in the formation of large and multiple bags of the ligaments, as shown in Fig. 4.24 (b), whose length even exceeds 0.5-C. It was also observed that due to the weak aerodynamic forces and dominant effects of the liquid's surface tension, the amplitude of oscillation of the ligament was relatively large resulting in the droplets' breakup relatively far away from the T.E.. The bag formation was followed by the generation of large number of droplets (both fine and coarse) as shown in Fig. 4.24 (k). However, it was frequently observed that the droplets formed were usually coarse, due to strong surface tension forces. Due to relatively large droplets momentum, they usually don't flow along the flow path as that of Case A. It is important to mention here that the breakup of large droplets into smaller ones due to the effects of normal stresses is due to the Rayleigh – Taylor Instability.

4.4.3.3. Intermediate Air Momentum (Case – B (Air Velocity 30 m/sec, $M \approx 108$, $We_a \approx 34$) – Ref. Fig. 4.22) & (Case – C (Air Velocity 25 m/sec, $M \approx 75$, $We_a \approx 23.45$) – Ref. Fig. 4.23)

The intermediate air momentum cases showed characteristics which exhibit properties of both high air momentum (Case A) and low air momentum (Case D).

In the case of high intermediate air momentum case (Case – B, Fig. 4.22), occasional high-speed waves were seen, Fig. 4.22 (a), which resulted in the stripping of droplets from the T.E., Fig. 4.22 (c). However, due to the less air momentum compared to Case A, frequent ligaments were also seen to be formed at the T.E. whose length was relatively larger than that of Case A but much smaller than that of Case D, Fig. 4.22 (f). These ligaments oscillate up and down due to the vortex shedding and ultimately breakup either due to bag mode of a breakup, as shown in Fig. 4.22 (g), or due to vibrational breakup, Fig. 4.22 (i). In general, all coarse droplets formed underwent secondary breakup.

In case of low intermediate momentum Case (Case –C, Fig. 4.23), very rarely droplets were seen to be stripping due the surface waves, however and usually water got accumulated at the T.E.. This leads to the ligament formation whose length was longer than the Case B but shorter than that of the Case D. The thick ligament frequently breaks up due to the bag mode of breakup, as shown in Fig. 4.23 (k). The coarse droplets formed in this case frequently underwent bag mode of a breakup, Fig. 4.23 (g), with the occasional vibrational breakup.

In general, the droplets formed in the intermediate air velocity case follow a path somewhere between high- and low- air momentum case.

Table 4.3 summarizes the droplets breakup phenomena for the high to low momentum cases as shown in Fig. 4.21 to 4.24.

4.4.3.4. Summary of Droplets Formation Mechanism

In summary, the droplets size formed for high momentum ratio were always smaller than that of the low momentum cases, principally due to the high kinetic energy (K.E.) of surrounding air, Fig. 4.21, which resulted in the oscillation of ligament and stripping of droplets near the T.E.. For low momentum case, due to less K.E. of the surrounding air the surface tension forces kept the liquid to remain intact and resulted in the formation of thick ligaments, as shown in Fig. 4.24. In all the cases, the ligaments formed at the T.E. were stretched in the chord-wise direction due to incoming air and were oscillated in the pitch-wise direction due to the vortex shedding from the T.E., leading to the breakup of ligaments or droplets formation from the ligaments.

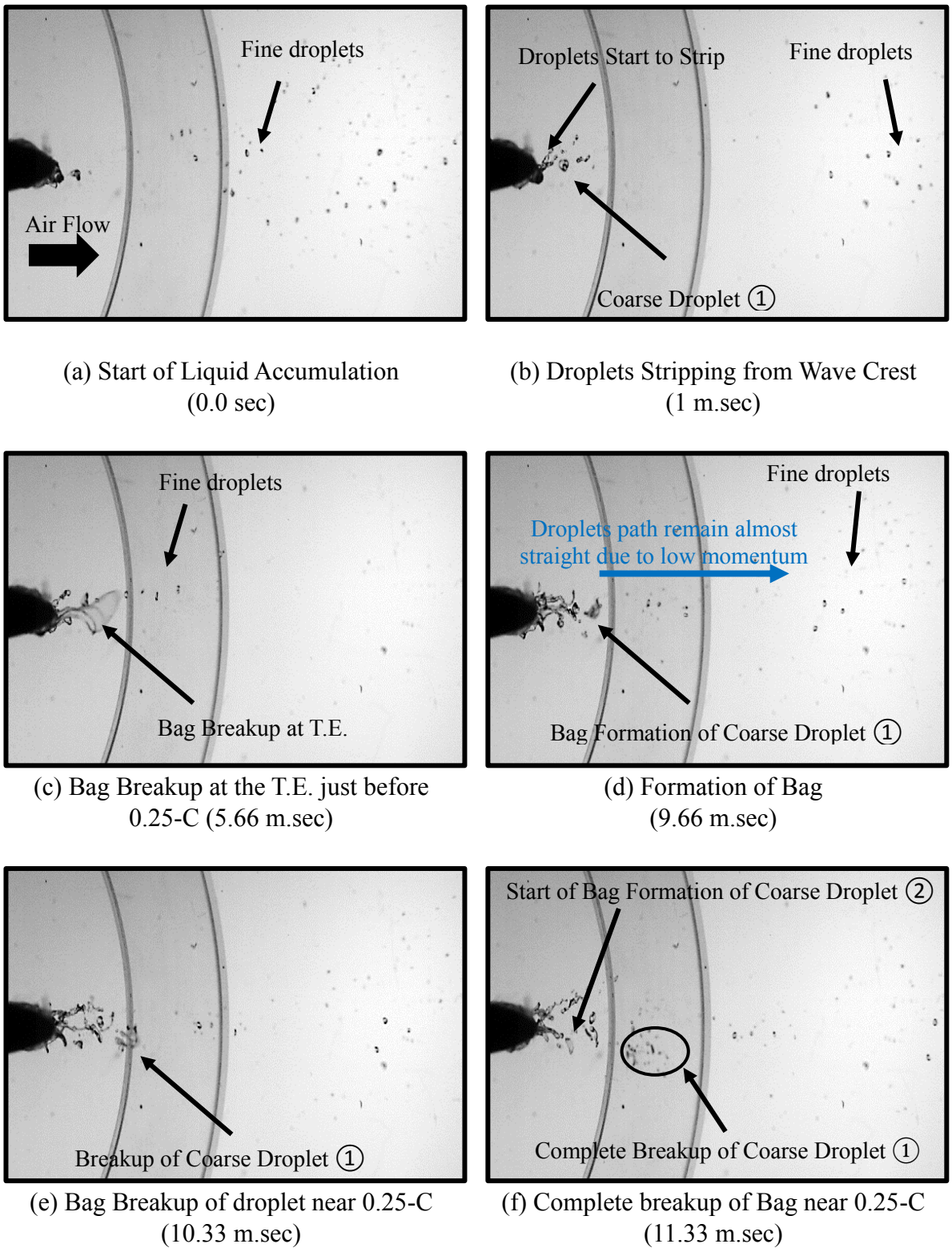

(a) Start of Liquid Accumulation (0.0 sec)

(b) Droplets Stripping from Wave Crest (1 m.sec)

(c) Bag Breakup at the T.E. just before 0.25-C (5.66 m.sec)

(d) Formation of Bag (9.66 m.sec)

(e) Bag Breakup of droplet near 0.25-C (10.33 m.sec)

(f) Complete breakup of Bag near 0.25-C (11.33 m.sec)

Figure 4.21 – Breakup and Atomization aft the T.E. – Case A (Velocity 40 m/sec), $MFR = 5.62$ ($M \approx 192, We_a \approx 60$) (1/2)

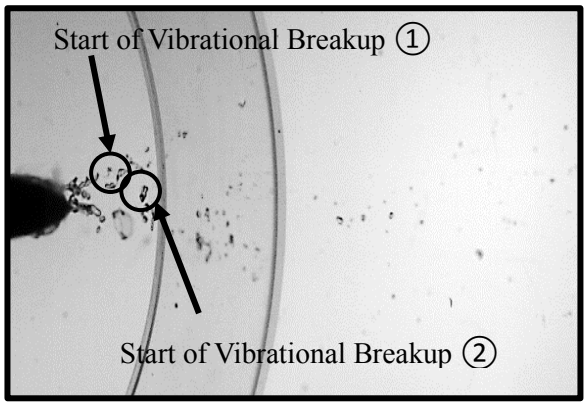

(g) Start of Vibrational Breakup (11.66 m.sec)

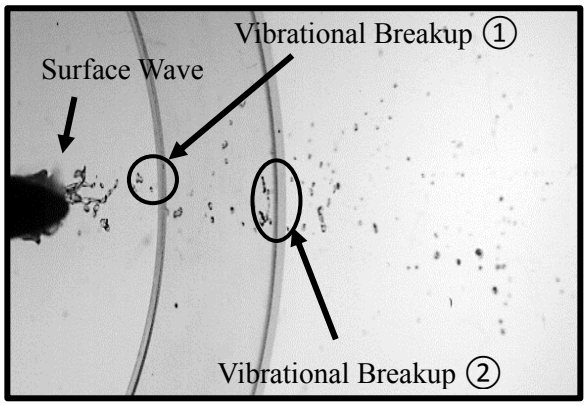

(h) Vibrational Breakup near 0.5-C (15 m.sec)

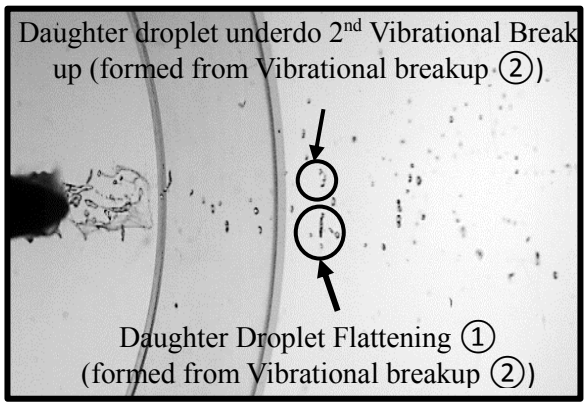

(i) Start of Vibrational Breakup (16 m.sec)

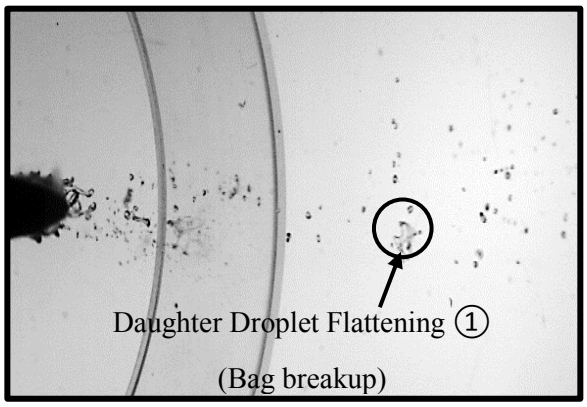

(j) Bag Breakup near 0.75C (17 m.sec)

Figure 4.21 – Breakup and Atomization aft the T.E. – Case A (Velocity 40 m/sec), $MFR = 5.62$ ($M \approx 192, We_a \approx 60$) (2/2)

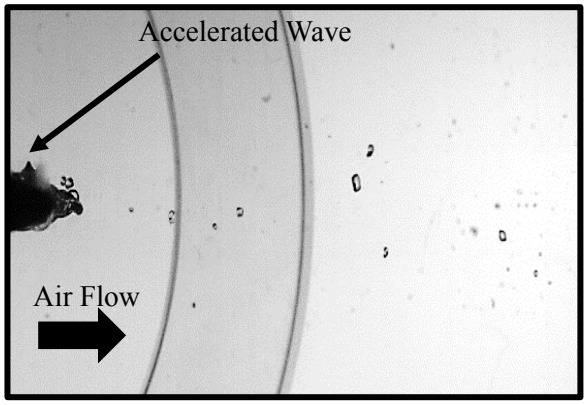

(a) Water accumulation (0.0 m.sec)

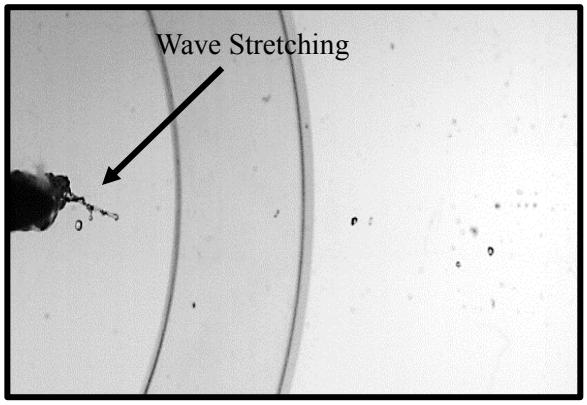

(b) Wave Stretching (4.66 m.sec)

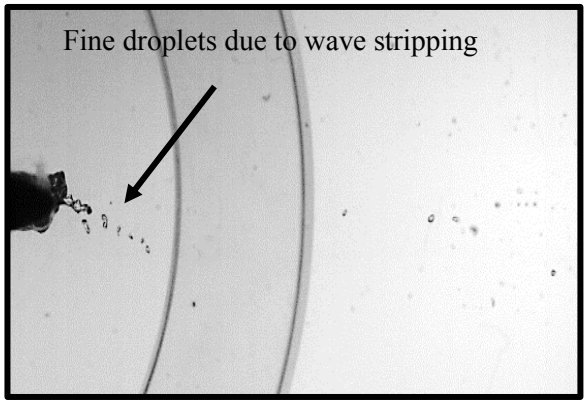

(c) Droplets generated from Wave Stretching (6 m.sec)

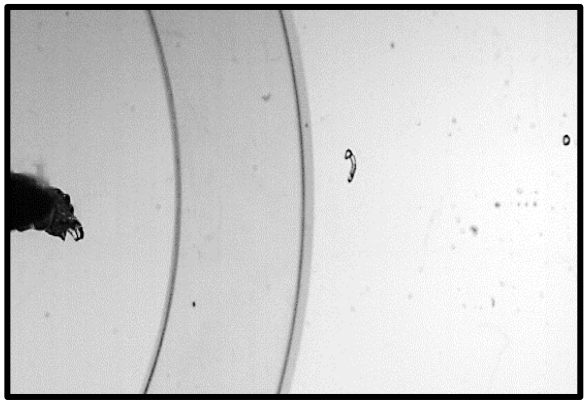

(d) More Liquid Start accumulating (19.66 m.sec)

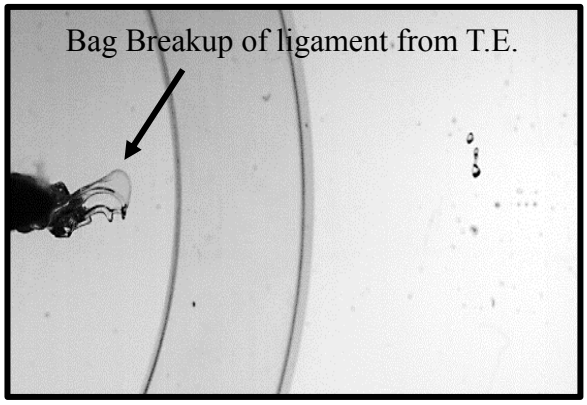

(e) Bag Breakup at the T.E. just before 0.25-C (21.66 m.sec)

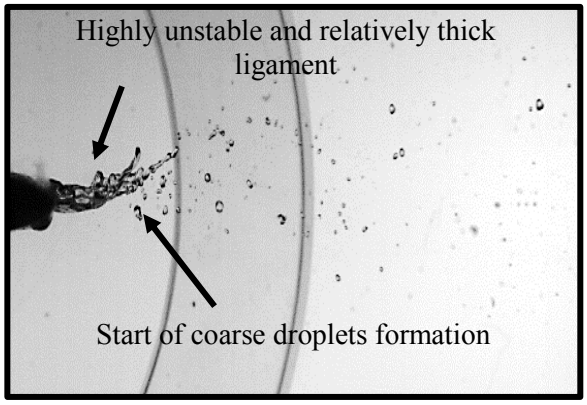

(f) Thick ligament elongation (29.33 m.sec)

Figure 4.22 – Breakup and Atomization aft the T.E. – Case B (Velocity 30 m/sec), $MFR = 11.23$ $(M \approx 108, We_a \approx 34)$ (1/2)

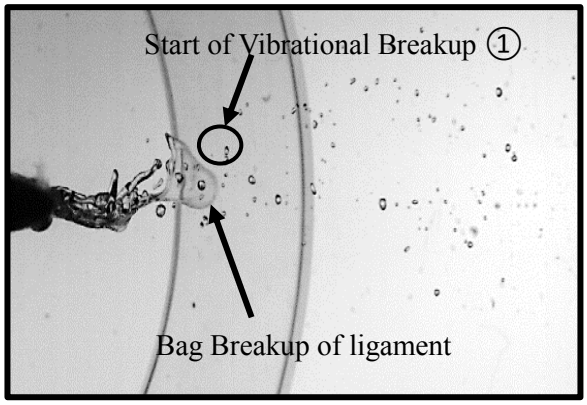

(g) Bag Breakup of ligament at 0.25-C (31 m.sec)

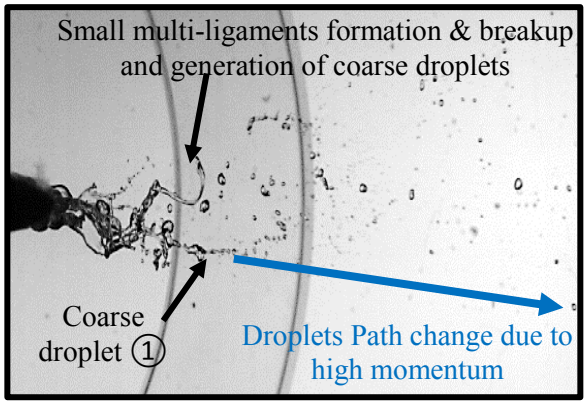

(h) Breakup of Ligaments into Small Ligament (33 m.sec)

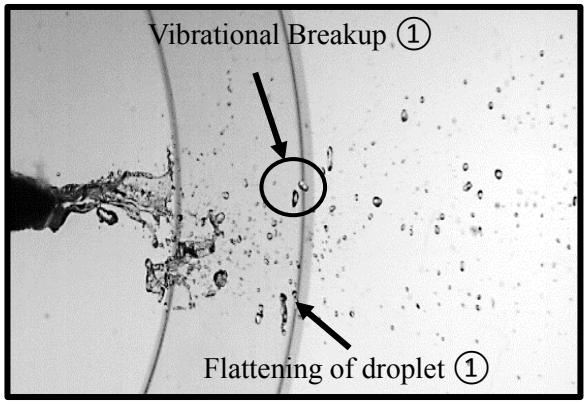

(i) Highly unstable ligament (35.66 m.sec)

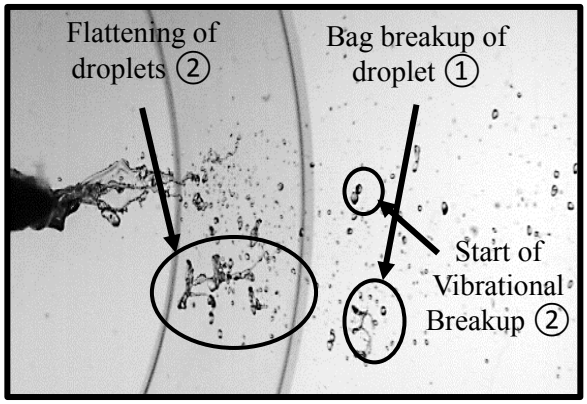

(j) Flattening of small ligaments (37 m.sec)

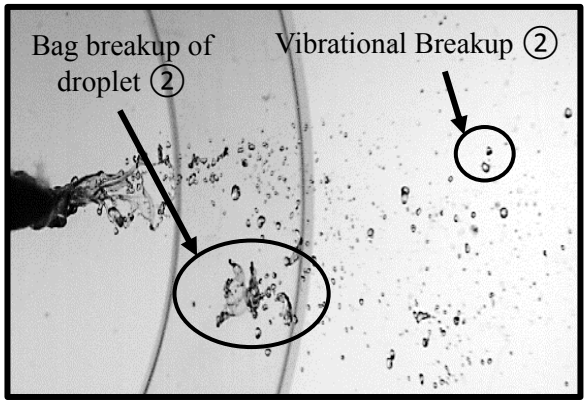

(k) Bag Breakup of ligament just before 0.5-C (38 m.sec)

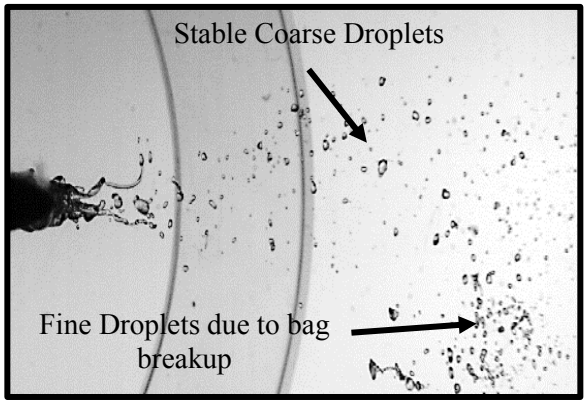

(l) Fine & Coarse Droplets (41.33 m.sec)

Figure 4.22 – Breakup and Atomization aft the T.E. – Case B (Velocity 30 m/sec), $MFR = 11.23$ $(M \approx 108, We_a \approx 34)$ (2/2)

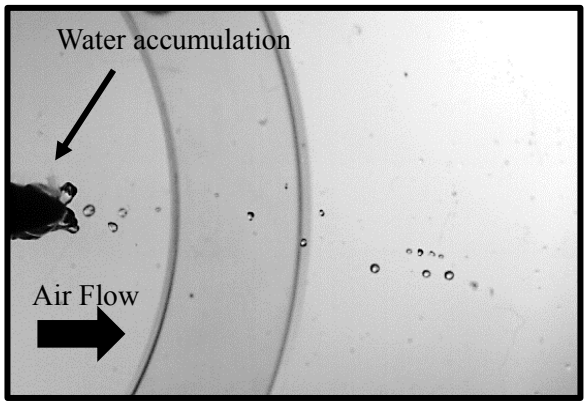

(a) Start of Water Accumulation (0.0 m.sec)

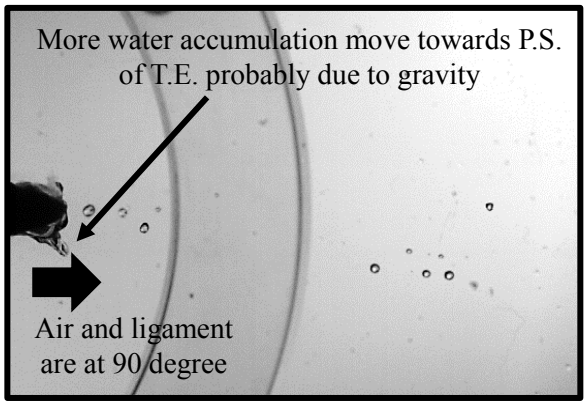

(b) More amount of water accumulation near the P.S. probably due to gravity effect (7 m.sec)

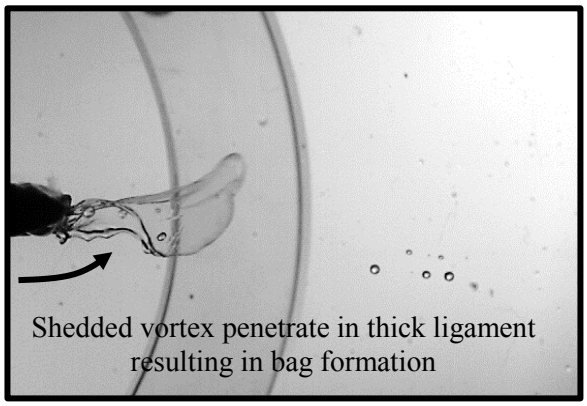

(c) Bag Formation from T.E. (length between 0.25- and 0.5-C) (10 m.sec)

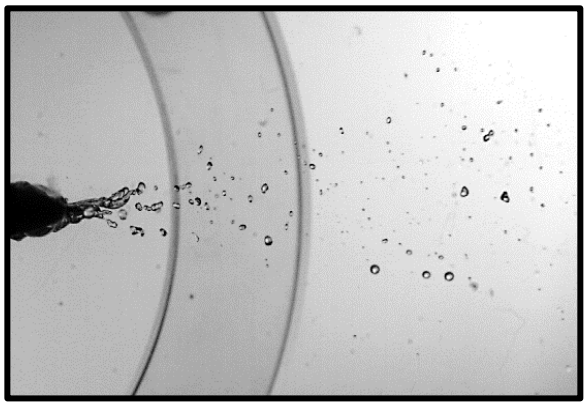

(d) Fine & Coarse droplets (16 m.sec)

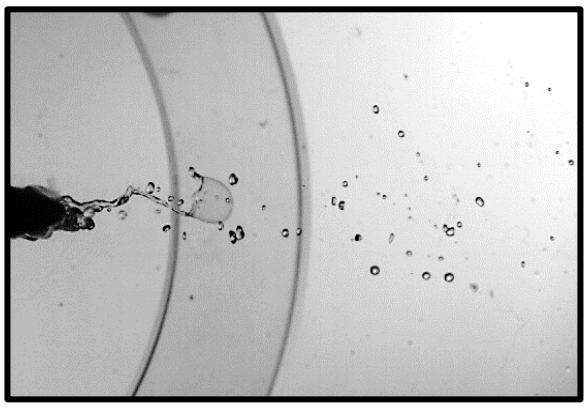

(e) Bag Breakup from ligament (length between 0.25- and 0.5-C) (20.66 m.sec)

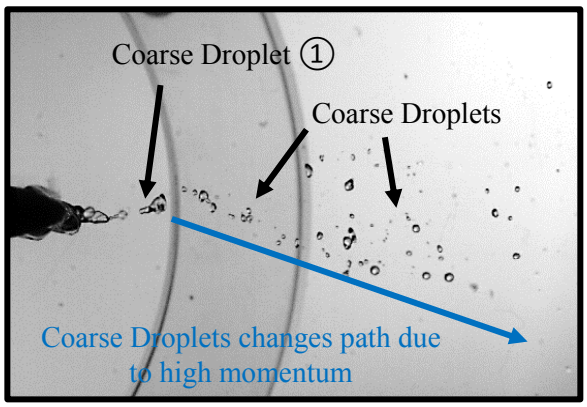

(f) Droplet formation from unstable ligament (24 m.sec)

Figure 4.23 – Breakup and Atomization aft the T.E. – Case C (Velocity 25 m/sec), $MFR = 10.0$ ($M \approx 75, We_a \approx 23.45$) (1/2)

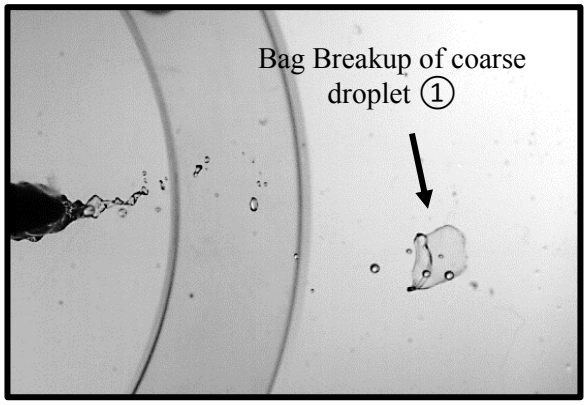

(g) Bag Breakup of coarse droplet near 0.75-C (36.33 m.sec)

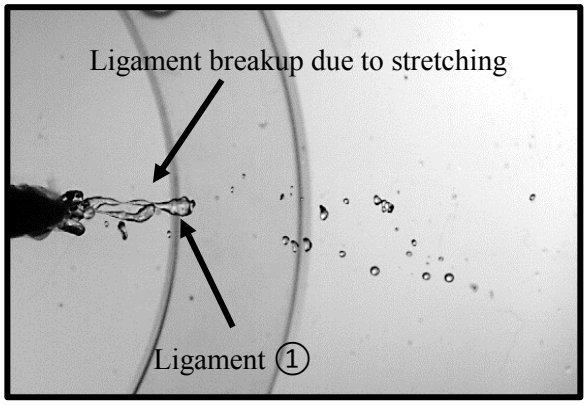

(h) Breakup of Ligaments due to stretching (100.33 m.sec)

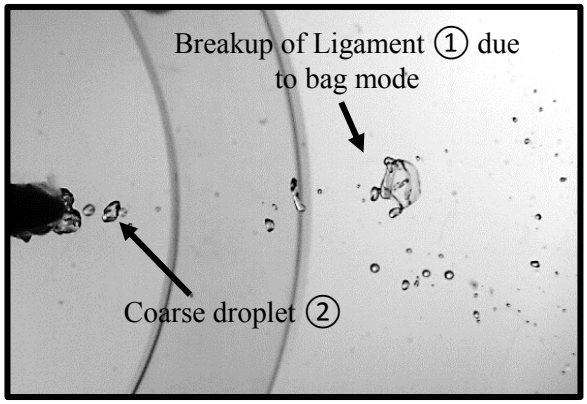

(i) Bag Breakup of droplet near 0.75-C (110 m.sec)

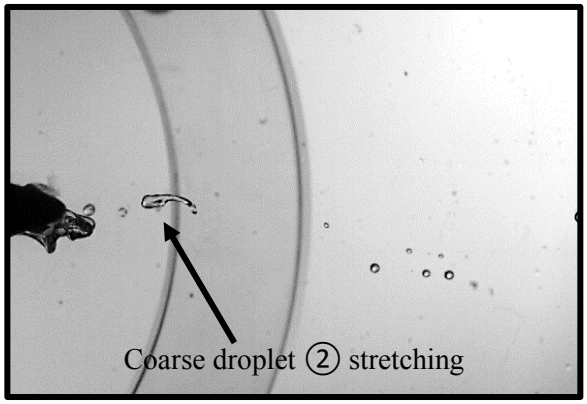

(j) Stretching of coarse droplet (119 m.sec)

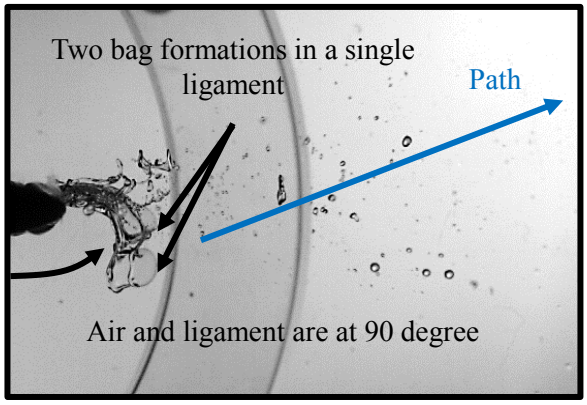

(k) Highly unstable ligament with 2 bag formations (126.33 m.sec)

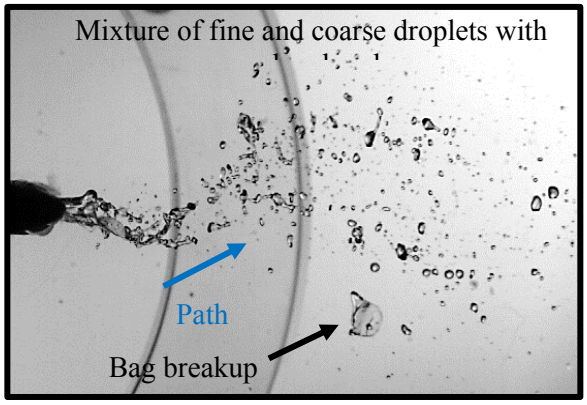

(l) Fine & Coarse Droplets with bag formation just before 0.75-C (132.66 m.sec)

Figure 4.23 – Breakup and Atomization aft the T.E. – Case C (Velocity 25 m/sec), $MFR = 10.0$ ($M \approx 75, We_a \approx 23.45$) (2/2)

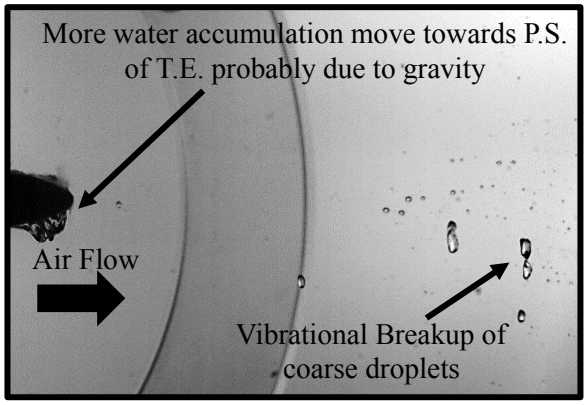

(a) Start of water accumulation with more water at P.S probably due to gravity effect (0.0 m.sec)

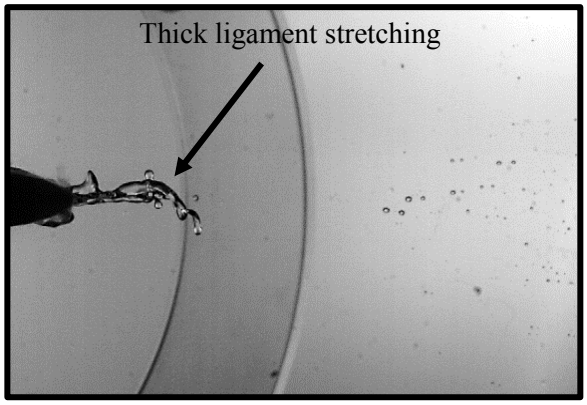

(b) Ligament Formation (15.33 m.sec)

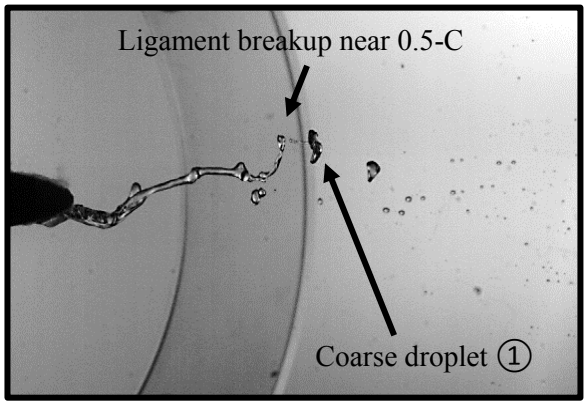

(c) Highly stretched ligament (length almost equal to 0.5-C (22.66 m.sec)

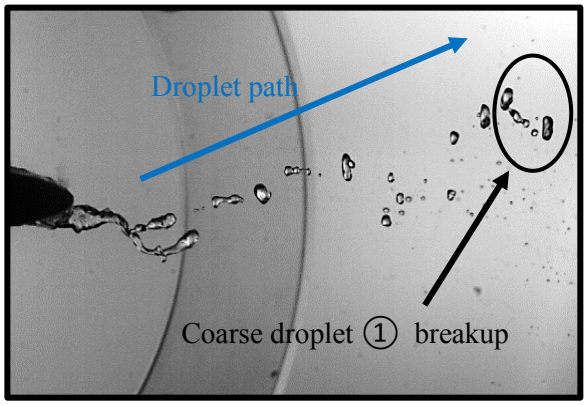

(d) Formation of Coarse droplets due to ligament breakup (28.33 m.sec)

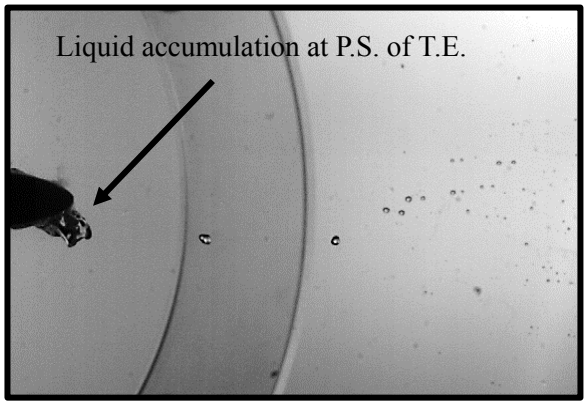

(e) More water accumulation at P.S. (165 m.sec)

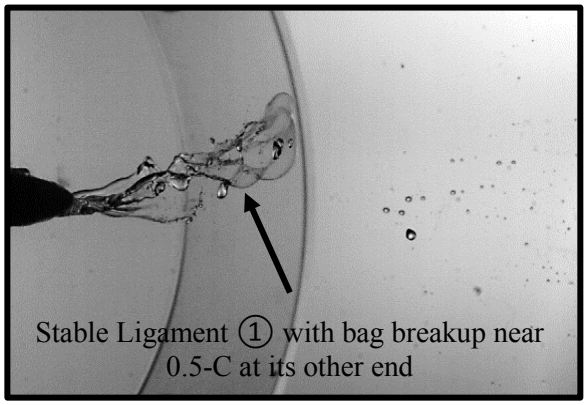

(f) Bag Formation with length almost equal to 0.5-C (175 m.sec)

Figure 4.24 – Breakup and Atomization aft the T.E. – Case D (Velocity 20 m/sec), $MFR = 10.0$ ($M \approx 48, We_a \approx 15$) (1/2)

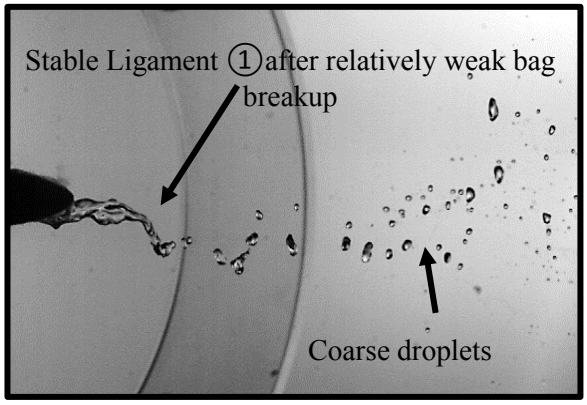

(g) Bag Breakup with still thick ligament remained (188 m.sec)

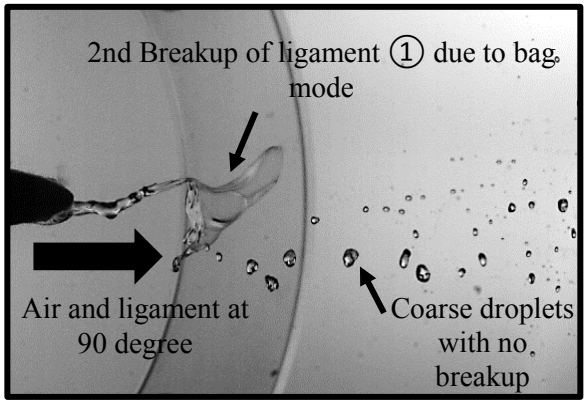

(h) Bag formation from thick ligament (190.33 m.sec)

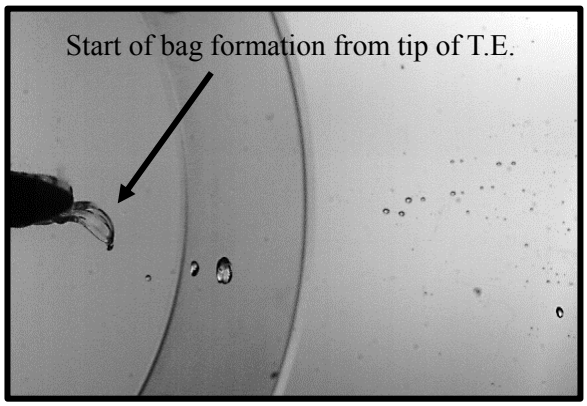

(i) Start of Bag Formation from the tip of T.E. (213.66 m.sec)

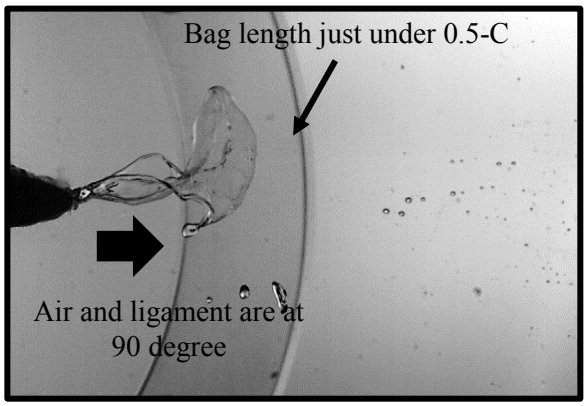

(j) Bag Formation (217 m.sec)

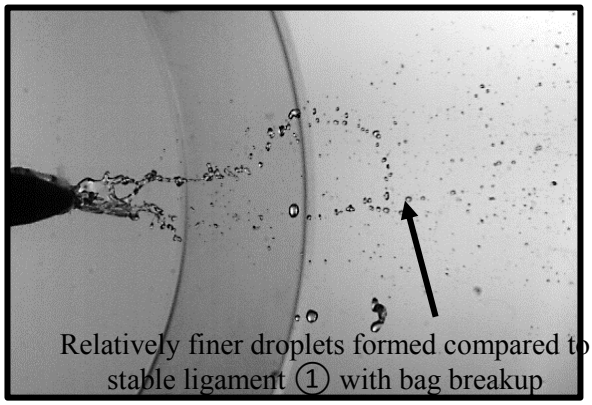

(k) Bag Breakup with maximum fine droplets (220.33 m.sec)

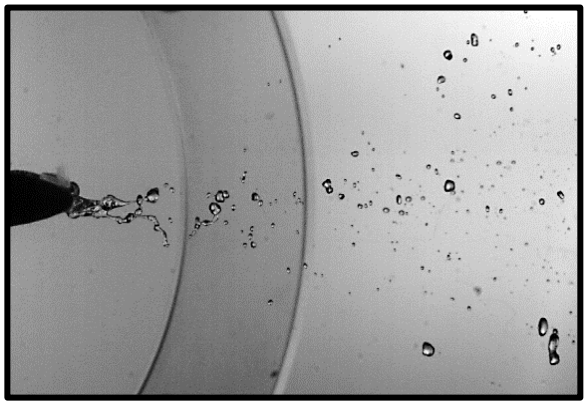

(l) Unstable ligament breakup with coarse droplets (224.66 m.sec)

Fig. 4.24 – Breakup and Atomization aft the T.E. – Case D (Velocity 20 m/sec), $MFR = 10.0$ ($M \approx 48, We_a \approx 15$) (2/2)

Table 4.3 – Summary of Droplets Breakup

Case	0 to 0.25-C	0.25-C to 0.5-C	0.5-C to 0.75-C	0.75-C to 1-C
Case A (Air Velocity 40 m/sec) $\boldsymbol{M \approx 192}$ $\boldsymbol{We_a \approx 60}$	• Wave stripping. • Coarse droplets (if formed) undergo bag breakup. • Occasional start of vibrational breakup. • Ligament length usually within this range. • Occasional bag breakup of ligament.	• Frequent vibrational breakup. • Occasional start of vibrational breakup.	• Occasional vibrational breakup.	• Rarely vibrational breakup.
Case B (Air Velocity 30 m/sec) $\boldsymbol{M \approx 108}$ $\boldsymbol{We_a \approx 34}$	• Occasional Wave stripping. • Ligament length usually within this range.	• Ligament length usually within this range. • Occasional bag & ligament breakup. • Occasional start of vibrational breakup. • Occasional bag breakup of ligament.	• Occasional vibrational breakup. • Occasional start of bag breakup. • Occasional bag breakup.	• Rarely vibrational breakup. • Rarely bag breakup.
Case C (Air Velocity 25 m/sec) $\boldsymbol{M \approx 75}$ $\boldsymbol{We_a \approx 23.45}$	• Rarely Wave stripping.	• Ligament length usually within this range. • Coarse droplets formation. • Occasional bag breakup of ligament.	• Occasional vibrational breakup. • Occasional start of bag breakup. • Occasional bag breakup. • Coarse droplets formation.	• Occasional vibrational breakup. • Occasional start of bag breakup. • Occasional bag breakup.
Case D (Air Velocity 20 m/sec) $\boldsymbol{M \approx 48}$ $\boldsymbol{We_a \approx 15}$	• Usually no breakup but frequently thick elongated ligament only.	• Ligament length usually within this range. • Coarse droplets formation. • Occasional bag breakup of ligament.	• Ligament length just under this range. • Coarse droplets formation. • Occasional start of vibrational breakup. • Occasional bag breakup of ligament.	• Occasional vibrational and rarely bag breakup.

4.4.4. Cumulative Volume & Number fraction distribution

Figure 4.25 below shows the droplets number fraction and cumulative distribution for different cases under the same ejection flow rate of the liquid. From Fig. 4.25, as the distance aft the T.E. region increases, the number of droplets generated also increases due to the breakup of droplets. For high momentum cases (Fig. 4.25 (a))the droplets formed at 0.25-C were nearly 6,000 in numbers which increased by almost 3 times to 18,000 as the distance aft T.E. increases to 1 C. However, for low momentum cases (Case D – Fig. 4.25 (d)), the number of droplets surge to nearly eightfold from approximately 1,000 to 7,500 as the distance increased from 0.25-C to 1-C. The increasing number of droplets resulted from the bag mode of the breakup of ligaments and droplets when exposed to the surrounding high aerodynamic forces. Though, from the experimental results, it was found that the number of droplets did not necessarily increase by above mention factor. Overall, however, it was found that the droplets fraction increased for low air momentum cases was always larger than that of the high air momentum cases, under the same condition of liquid flow rate. This was mainly due to a different mode of a breakup. High air momentum cases underwent frequently vibrational mode of a breakup, as

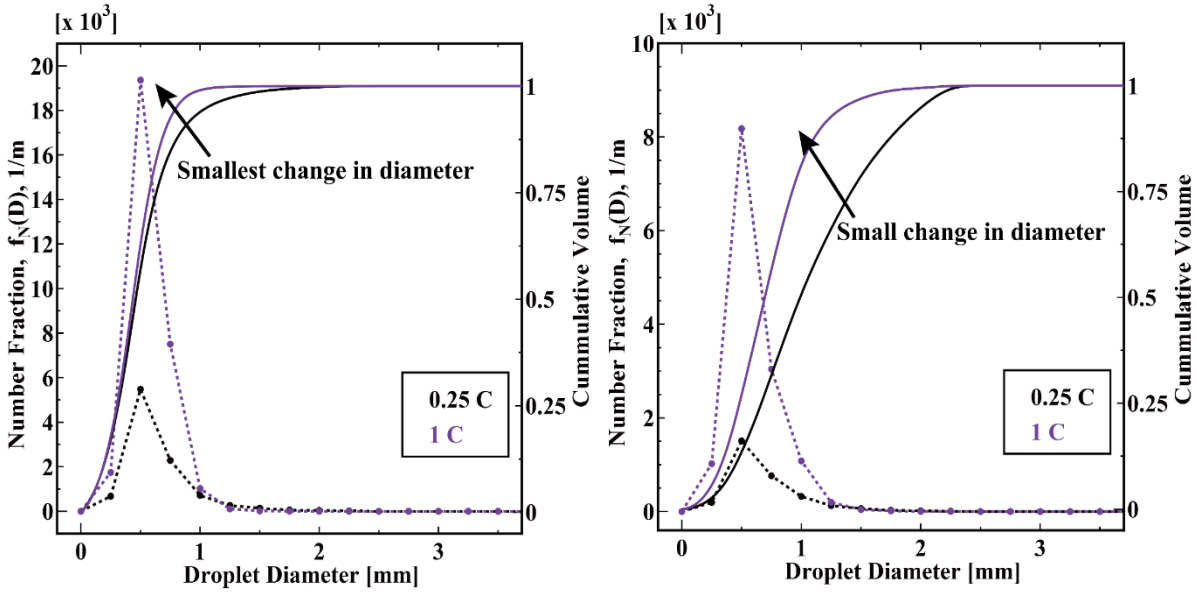

(a) Case A (Air Velocity 40 m/sec, ($M \approx 192, We_a \approx 60$))

(b) Case B (Air Velocity 30 m/sec, ($M \approx 108, We_a \approx 34$))

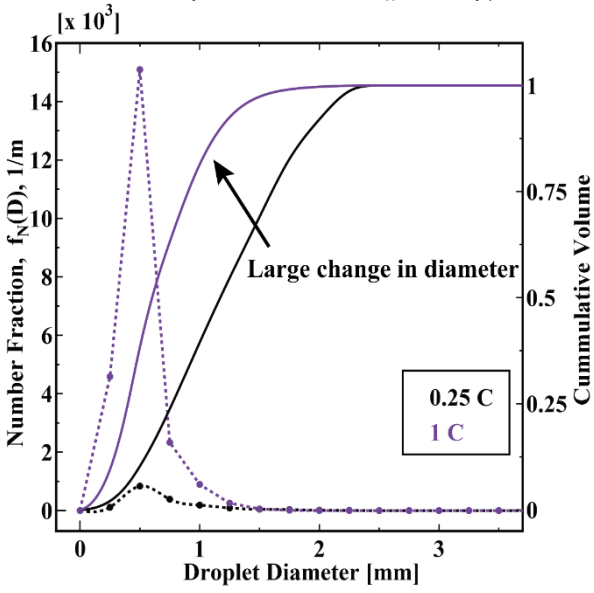

(c) Case C (Air Velocity 25 m/sec, ($M \approx 75, We_a \approx 23.45$))

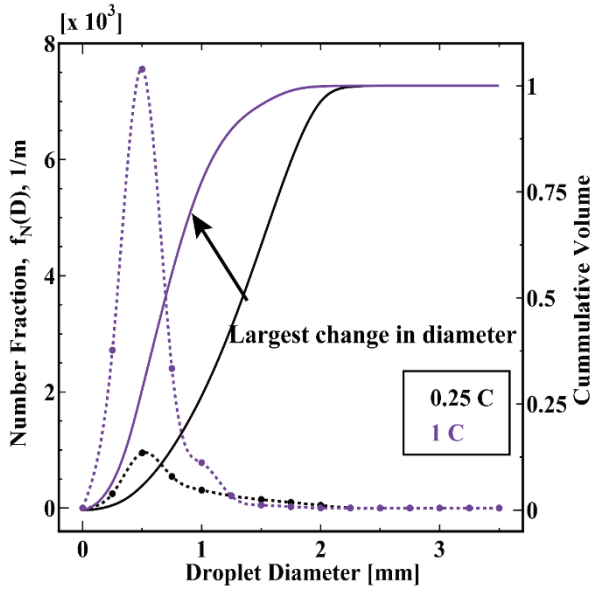

(d) Case D (Air Velocity 20 m/sec, ($M \approx 48, We_a \approx 15$))

Figure 4.25 – Droplets Size Frequency and Cumulative Volume Distribution @ $MFR \approx 9.0$

shown in Fig. 4.25 (a), resulting in overall smallest droplets size change. On the other hand, low air momentum cases (Case D – Fig. 4.25 (d)) underwent mainly bag breakup, which resulted in a drastic change in the droplets size as the distance aft the T.E. increases.

4.4.5. Droplets Size Distribution aft the T.E.

Figure 4.26 shows the atomization phenomenon aft the T.E. of the elliptical blade against the dimensionless flow rate (MFR). The droplet diameter was measured as explained in Section 3.9. The unfilled symbols, such as (o), and filled symbols, such as (●), represents the SMD (D32) and average (D10) droplets size distribution[2] aft the T.E. region, whereas, black, red, blue and violet colour indicates the droplets size distribution at 25 %, 50 %, 75 % and 100 % chord wise position from the tip of the T.E., as illustrated in Fig. 3.29. The dotted lines in Fig. 4.26 represents the average droplets size value, which is simply the average of the corresponding droplets size at different chord-wise positions aft the T.E. of the blade. From Fig. 4.26 (a – d), the change in the flow rate of liquid did not significantly affect the droplet size distribution aft the T.E. region. This is mainly because the droplet size distribution is primarily governed by the liquid's surface tension, T.E. profile and air momentum only. As the accumulated water at the T.E. was at rest, (nearly zero velocity) in comparison to the surrounding air flow field, the accumulated water experiences the identical aerodynamic forces under different MFR. In other words, the Weber number (Eq. 4.33) remains the same (i.e., the ratio between the aerodynamic and the surface tension effects remained unchanged) and so is the droplets size distribution. Once the ligaments/droplets were separated from the T.E. the droplets experiences the same slip velocity with the surrounding gaseous phase. It should be noted from Fig. 4.26 that the near the T.E., i.e., 0.25-C the droplets deviated more compared to the other positions due to the large deformation and the presence of ligaments as well. Figure 4.27, 4.28, 4.29 and 4.30 demonstrate the perimeter (see Section 3.9 for details) of droplets at 0.25-C and 1-C for selected liquid flow rate of liquid for Case A, Case B, Case C and Case D respectively. For high air momentum case (Case A), Fig. 4.27 (a) and 4.27 (b), sizeable change for the droplets perimeter was noticed as the distance aft the T.E. increases due to the superior effects of aerodynamic forces. An increase in the distance aft the T.E. tends the droplets to become more spherical due to the prevalent liquid's surface tension, which avoided further breaking up of droplets and retaining the droplet more spherical. For low air momentum case, Fig. 4.30 (a) and 4.30 (b), the droplets retain their circularity due to the dominance effect of liquid's surface tension. It was probably due to this reason droplets were deviated more near the T.E. for high air momentum cases, as shown in Fig. 4.26 (a).

Figure 4.31 and 4.32 summarizes the D10 and D32 droplets size distribution for the above-discussed cases. From Fig. 4.31 and 4.32, the droplets size for high air momentum cases are relatively much smaller near the T.E. compared to those of the low air momentum cases, which was mainly due to different droplet breakup mode near the T.E.. Quantitatively, at high momentum ratio (approx. 192) and Weber number ($We_a \approx 60$), the average droplet size (D10) measured at 0.25-C decreases to around 15% as the distance aft the T.E. increases to 1-C. Low momentum cases were seen to be dominated by the liquid's property of surface tension, resulting in the formation of thick and highly elongated ligaments. The droplets produced from the disintegration of these ligaments were relatively coarse. Quantitatively, at low momentum ratio (approx. 48) and Weber number ($We_a \approx 15$) the average droplets (D10) reduces by around 30% as the aft distance of the droplets increases from 0.25-C to 1-C. Overall, the gradient of droplets size change for low momentum is comparatively larger than that of the high momentum ratio, due to the bag mode of droplets breakup, as their distance aft the T.E. increases.

[2] **Note:** D10 and D32 droplets are defined in Table 2.2

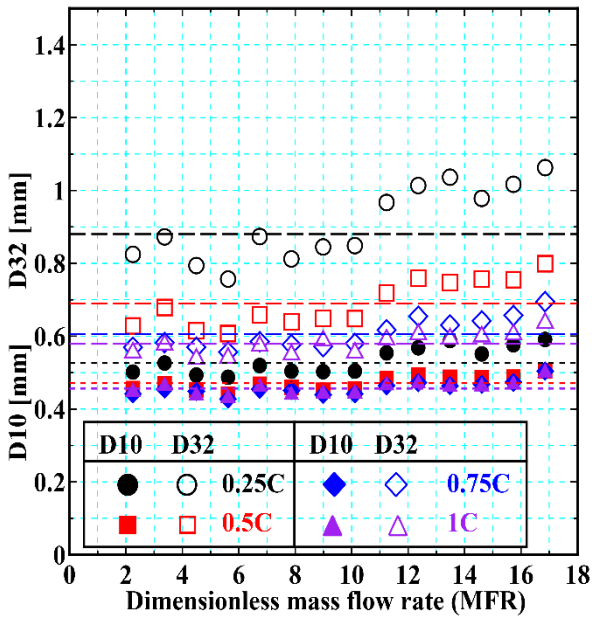

(a) Case A (Air Velocity 40 m/sec)
$(M \approx 192, We_a \approx 60)$

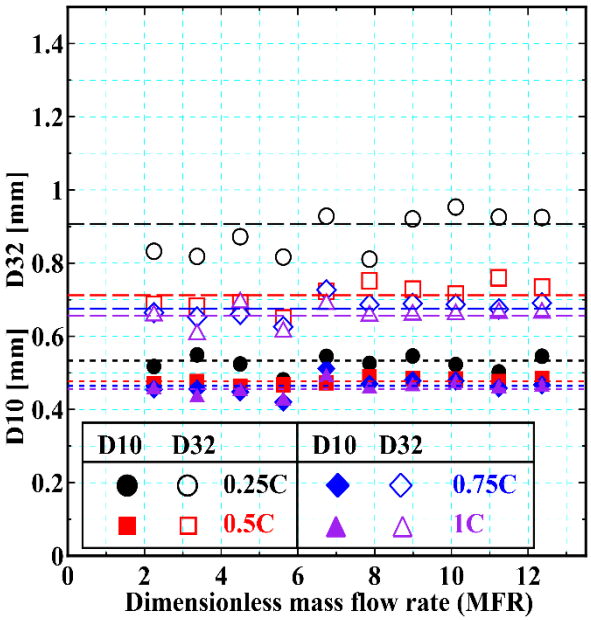

(b) Case B (Air Velocity 30 m/sec)
$(M \approx 108, We_a \approx 34)$

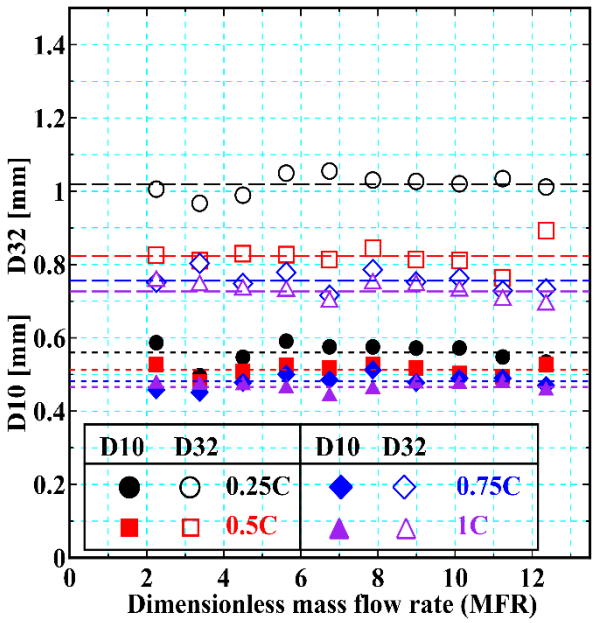

(c) Case C (Air Velocity 25 m/sec)
$(M \approx 75, We_a \approx 23.45)$

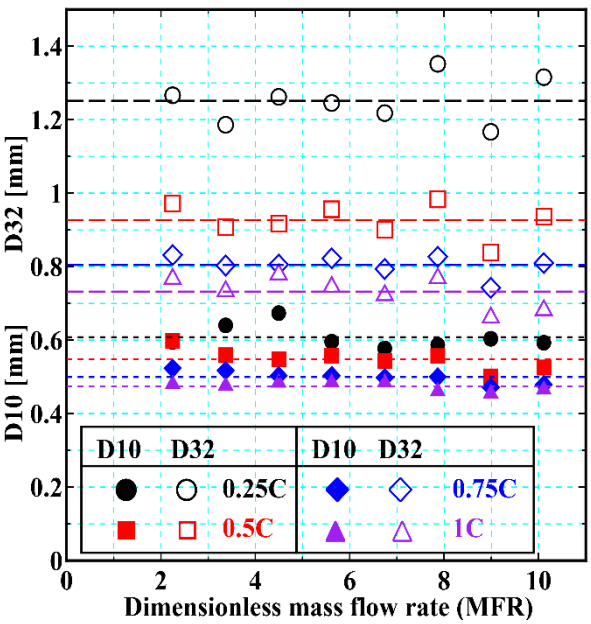

(d) Case D (Air Velocity 20 m/sec)
$(M \approx 48, We_a \approx 15)$

Figure 4.26 – Droplets Size Distribution aft the T.E. Region

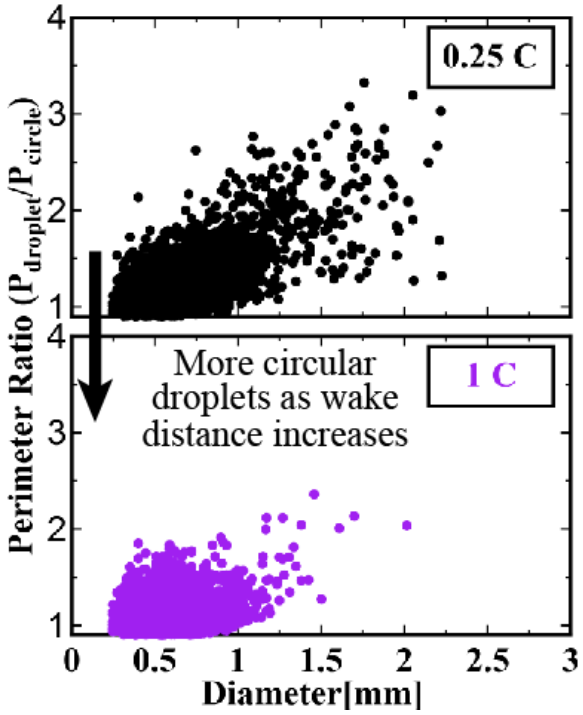

(a) $MFR \approx 4.45$

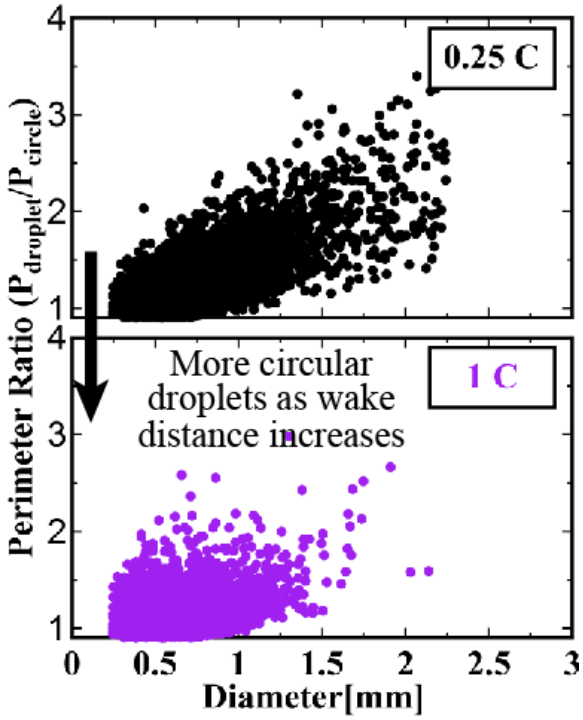

(b) $MFR \approx 11.2$

Figure 4.27 – Circularity of Droplets aft the T.E. Case A (Air Velocity 40 m/sec) ($M \approx 192, We_a \approx 60$)

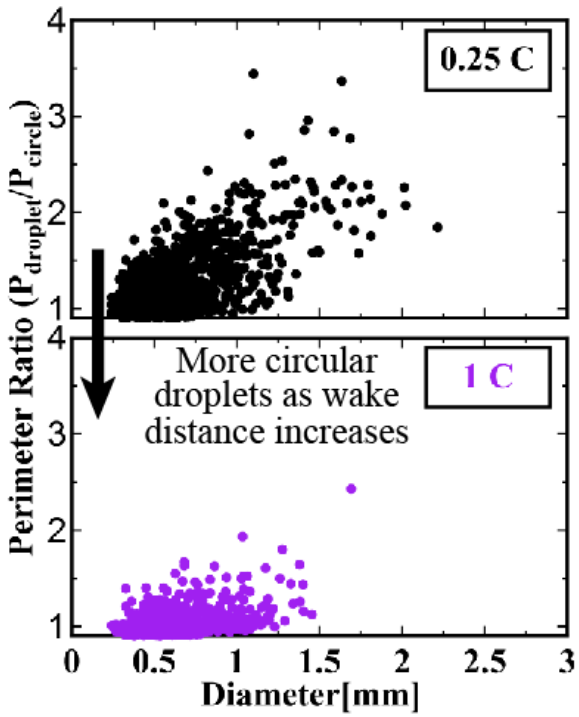

(a) $MFR \approx 4.45$

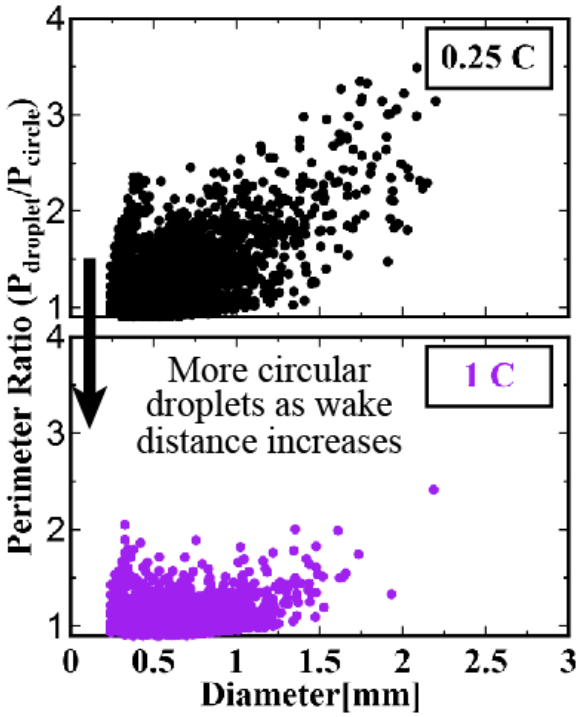

(b) $MFR \approx 11.2$

Figure 4.28 – Circularity of Droplets aft the T.E. Case B (Air Velocity 30 m/sec) ($M \approx 108, We_a \approx 34$)

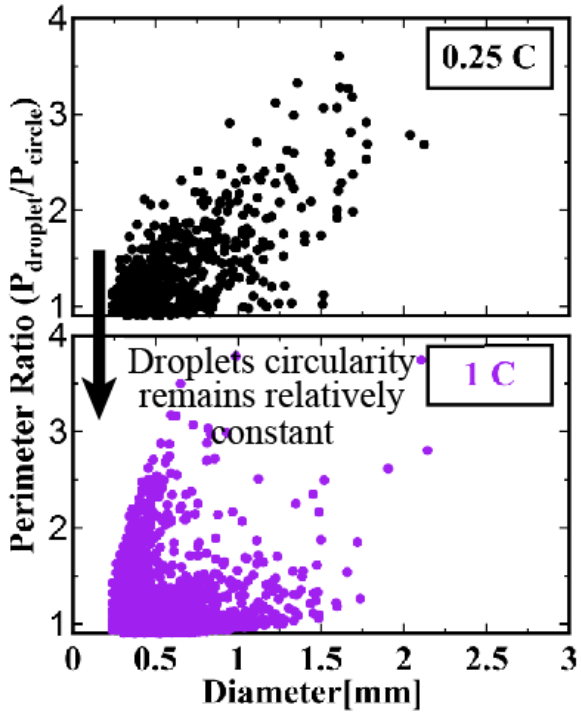

(a) $MFR \approx 2.25$

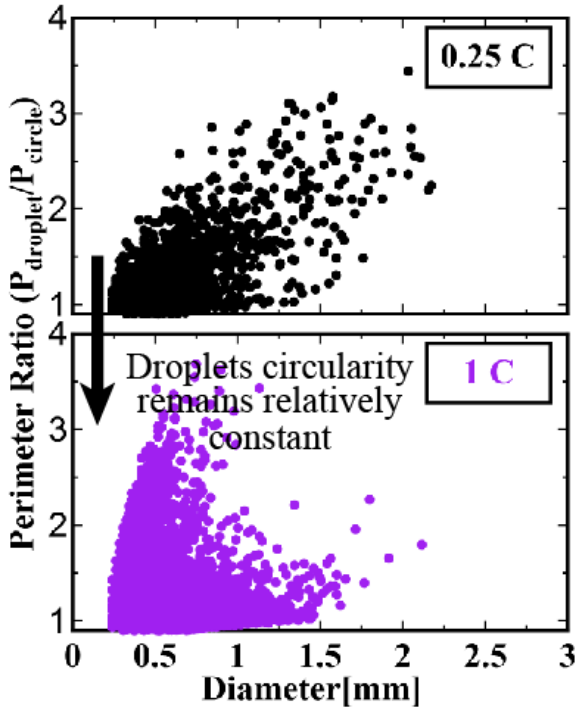

(b) $MFR \approx 9.0$

Figure 4.29 – Circularity of Droplets aft the T.E. Case C (Air Velocity 25 m/sec) ($M \approx 75, We_a \approx 23.45$)

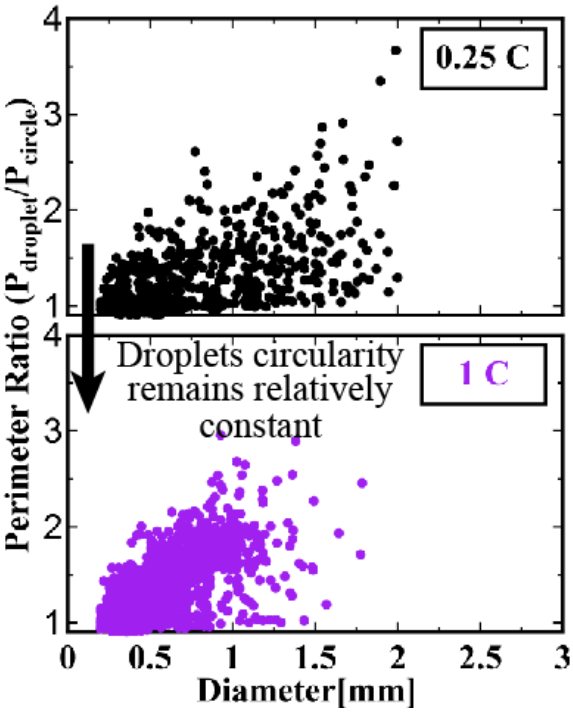

(a) $MFR \approx 2.25$

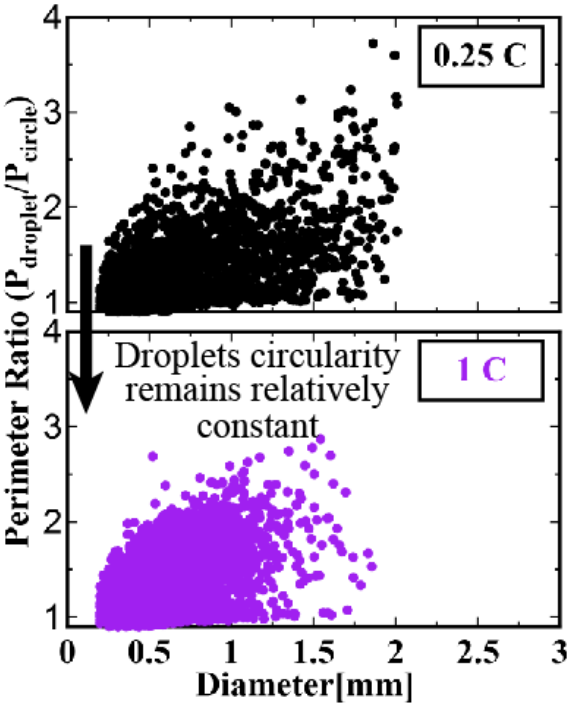

(b) $MFR \approx 9.0$

Figure 4.30 – Circularity of Droplets aft the T.E. Case D (Air Velocity 20 m/sec) ($M \approx 48, We_a \approx 15$)

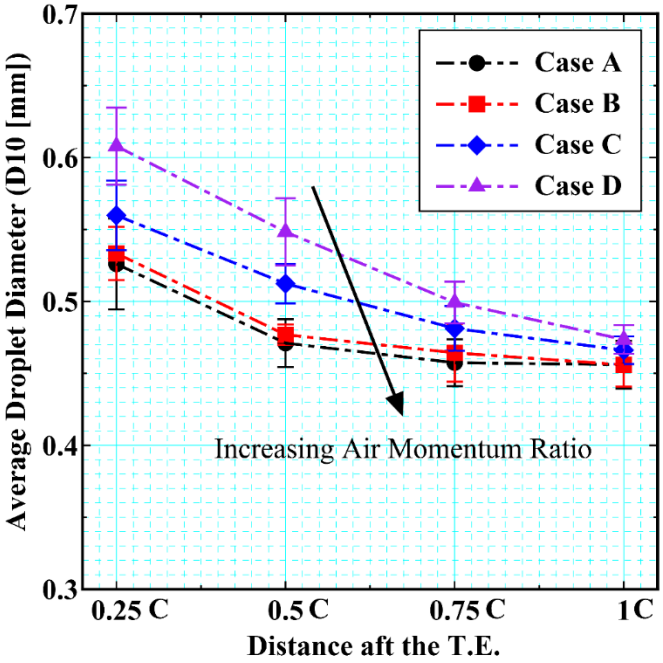

Figure 4.31 – Summary of Average Droplet Size (D10) Distribution aft the T.E.

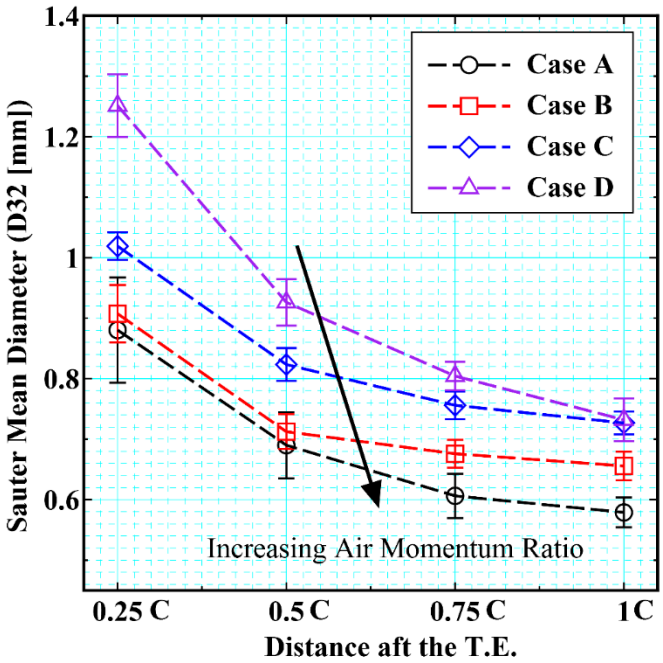

Figure 4.32 – Summary of Sauter Mean Diameter (D32) Distribution aft the T.E.

4.5. Characteristics of Water Accumulation at the T.E.

4.5.1. Qualitative Observation

The air stream which interacts with the liquid film produces small waves on the liquid film surface due to the local pressure difference as explained in Section 4.3 (Fig. 4.7 to 4.10). The amplitude of those waves was determined mainly by the T.E. thickness, air velocity and liquid film's surface tension, as shown in Fig. 4.21 to 4.24. At limiting conditions when sufficient amount of liquid is accumulated at the T.E., the incoming high-speed surface wave plunges the accumulated water to evolve into the ligaments and finally to the development of the droplets. Figure 4.33 (a) and 4.33 (c) shows the instantaneous images of the ligaments formation at high (Case A) and low (Case C) air momentum conditions respectively.

Figure 4.33 classify the near field based on the momentum ratio. From the comprehensive flow visualization of high-speed images, whatever the momentum ratio was selected, the ligaments were mainly formed at the mid-span of the blade only. Based on flow visualization the likely hood of droplet formation can be distinguished with the change in the value of momentum ratio.

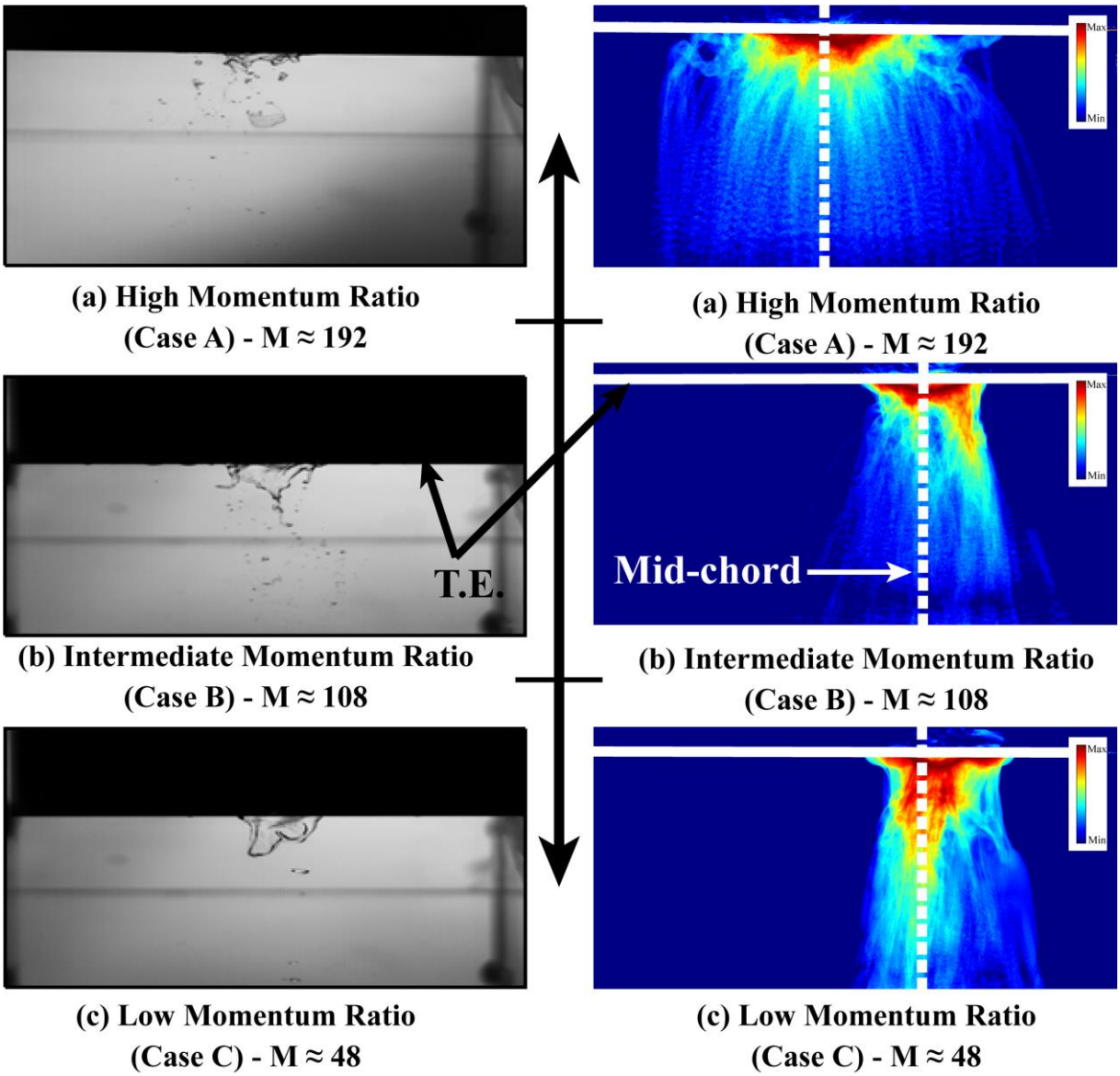

Figure 4.33 – Effect of Momentum Ratio in near T.E field breakup (instantaneous images)

Figure 4.34 – Threshold Intensity Distribution

4.5.1.1. High Momentum Ratio (Stripping of Droplets from the T.E.)

At high momentum ratio, the liquid accumulation was observed to form at relatively large span length. The ligaments length was significantly smaller in length and the breakup of ligaments due to the bag mode occurred occasionally very near (and mostly at) to the T.E.. Also, frequently droplets were observed to strip directly from the T.E., as shown in Fig. 4.21. Due to the dominant effects of aerodynamic forces, it was commonly observed that there were usually more than one ligaments which resulted in droplets fragmentation aft the T.E. region, as shown in Fig. 4.33 (a). This results in comparatively wider (in span-wise direction) droplet distribution region as given in Fig. 4.34 (a). Due to high momentum ratio, the near T.E. field droplets formed were also relatively smaller in size.

4.5.1.2. Low Momentum Ratio (Droplets formation mainly from deformed ligaments)

When the air momentum was reduced to that of Case D, the ligaments length became relatively large compared to that of the previous case, as shown in Fig. 4.24. In this case, the accumulated water evolved into a thick ligament and when it exceeds the critical value, the ligament sheet breakup due to the bag mode. Due to superior surface tension forces, only one dominant ligament was seen to be attached at the T.E., Fig. 4.33 (c). The ligament results in the bag formation and was followed by the generation of a large number of droplets aft the T.E. region in a relatively narrow (span-wise direction) droplet size distribution aft the T.E. region as shown in Fig. 4.34 (c). With the decrease in the momentum ratio, the near T.E. droplets formed were coarse and further underwent bag breakup as their distance aft the T.E. increases.

4.5.2. Theoretical Model Formulation for predicting two-phase characteristics

The in-depth knowledge of the characteristics of the liquid phase is profoundly important for the smooth functioning of the wet turbine system. In humid conditions, one of the most important factors is the prediction of droplet diameter which causes the erosion, reduced air momentum etc. According to the author knowledge, there exist no theoretical model which can estimate two phase characteristics in wet turbine systems. Therefore, a simple and convenient models are needed for a better understanding of the kinematics of two-phase phenomena in wet turbine systems.

It was concluded from the detailed analysis of the droplets characteristics that their size distribution aft the T.E. region is governed by the T.E. profile and air momentum, whereas it is independent of the liquid phase mass flow rate.

Continuous stresses are present at the air-liquid interface. For the disintegration of liquid ligaments at the T.E., the formation of waves is one of the recognized important factors which contributes to the breakup phenomena at the T.E.. For large values of momentum ratio, the interfacial water is accelerated by air velocity (already proposed by Craik et al. [93]). This results in the formation of the small boundary layer (δ), which can either be laminar or turbulent in nature over the surface of the liquid. Villermaux [94] had conducted detailed investigation about the coaxial jets and concluded that for coaxial jets Kelvin Helmholtz instability occurred if the following condition was satisfied

$$\delta \, (\rho_l \, / \, \rho_a)^{\,1/2} \; > \; \sigma \, \rho_l \, u_l^2 \tag{4.35}$$

that is,

$$We_\delta \, (\rho_l \, / \, \rho_a)^{\,1/2} \; > 1 \tag{4.36}$$

where, $We_\delta = \; \rho_l \, u_l^2 \, \delta \, / \, \sigma$, Weber Number based on the initial fast stream based on the boundary layer thickness.

Boukra et al. [95] showed a simplified diagrammatic representation for the co-current gas streams flowing over the liquid surface, as shown in Fig. 4.35. At first, shear instability controlled by gas vorticity thickness causes a Kelvin-Helmholtz instability (Fig. 4.35 (b)), which results in the generation of longitudinal wave having wavelength (λ_L) at the free surface of the film. Such destabilization mechanism is discussed in many studies, such as [94 - 96] and is also presented in Section 4.3. The crest of the liquid film further undergo transverse instability (λ_T). Marty et al. [97] concluded that the transverse instability is similar to Rayleigh-Taylor instability due to the aerial acceleration of waves.

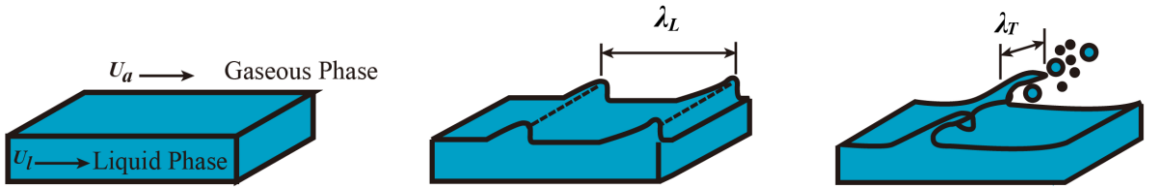

(a) Co-current Gaseous-Liquid Stream (b) Kelvin-Helmholtz Instability (c) Rayleigh-Taylor Instability

Figure 4.35 – Primary Breakup Mechanism [95]

According to Marmottant et al. [96] and Raynal et al. [98], the transverse perturbation results in an elongation of the crest waves leading to the formation of ligaments and finally into droplets.

4.5.2.1. Shedding Frequency

According to Villermaux [94], the wavelength (λ) of the shear layer developing between the light (air) medium and slower dense stream (water) is accelerated by the air to a velocity (U_c) larger than that of the liquid velocity (u_l). The shedding frequency measured downstream of the T.E. is the ratio of group velocity, (U_c) to the wavelength and is mathematically expressed as

$$f \approx \frac{U_c}{\lambda} \tag{4.37}$$

where,

$$U_c \approx \frac{\sqrt{\rho_l}\, u_l + \sqrt{\rho_a}\, U_a}{\sqrt{\rho_l} + \sqrt{\rho_a}} \tag{4.38}$$

Villermaux [94] further showed that for very large group phase velocity, the group velocity is re-modified as given by Eq. (4.39)

$$U_c \approx U_a \sqrt{\frac{\rho_a}{\rho_l}} \tag{4.39}$$

and, the wavelength of the shear layer developing at the air-liquid interface is proportional to the initial thickness of the velocity profile (δ) i.e., due to the boundary layer thickness

$$\lambda \approx \delta \sqrt{\frac{\rho_a}{\rho_l}} \tag{4.40}$$

Substituting Eq. (4.39) and (4.40) in Eq. (4.37) will results in the expression of shedding frequency of the ligaments, given by Eq. (4.41)

$$f \approx \frac{U_a}{\delta} \frac{\rho_a}{\rho_l} \tag{4.41}$$

Since in the present study, the maximum Reynolds number is $1.3\ x\ 10^5$, so for the purpose of simplicity it was assumed that the boundary layer developed was laminar in nature based on the Blasius analysis [74] i.e. ($Re < 5\ x\ 10^5$). Hence the boundary layer is approximated by Eq. (4.42).

$$\delta \approx \frac{4.91\ C}{\sqrt{Re}} \tag{4.42}$$

Substituting Eq. (4.42) into Eq. (4.41), then the theoretical model for the shedding frequency of the ligament from the T.E. of aerofoil can be approximated as

$$f = const. \frac{U_a \sqrt{Re}}{4.91\ C} \left(\frac{\rho_a}{\rho_l}\right) \tag{4.43}$$

where, U_a is the gaseous phase velocity, C is the chord length of the blade, Re represents the Reynolds number based on the chord length of aerofoil, ρ_a and ρ_l represents density of gaseous and liquid phase respectively.

From Eq. (4.43) shedding frequency is directly proportion to gaseous phase velocity and density, both having an order of 1.5 and is inversely proportion to the density of the liquid phase. In other words, the shedding frequency increases with an increase in the aerodynamic forces whereas it decreases if the liquid used is denser in nature and vice versa.

4.5.2.2. Ligament Wavelength (Span-wise Direction)

According to Varga et. al. [99], the primary destabilization of ligament draws waves out of the liquid due to R-T instabilities, Fig. 4.35 (c). This occurs when the high-speed gas is perpendicular to the liquid segment resulting in accelerative destabilization and eventually leads to the formation of droplets. By careful observation of shadowgraph images, the various stages of the droplets development from the T.E. are summarized as shown in Fig. 4.36. At first, liquid started to accumulate at the T.E., Fig. 4.36 (a). With increasing time, the amount of liquid accumulation increases, resulting in the formation of ligaments, Fig. 4.36 (b). When the aerodynamic forces overtake a limiting value of surface tension, the ligament breaks up from the T.E. of the blade, Fig. 4.36 (c). This leads to the formation of a finite ligament wavelength, as shown in Fig. 4.36 (e), the edges of which results in the generation of coarse droplets, as shown in Fig. 4.36 (e). In addition to the coarse droplets, Fig. 4.36 (e), relatively fine droplets are also formed.. Based on the different stages of droplets generation, a simple theoretical model is proposed, given schematically by Fig. 4.37.

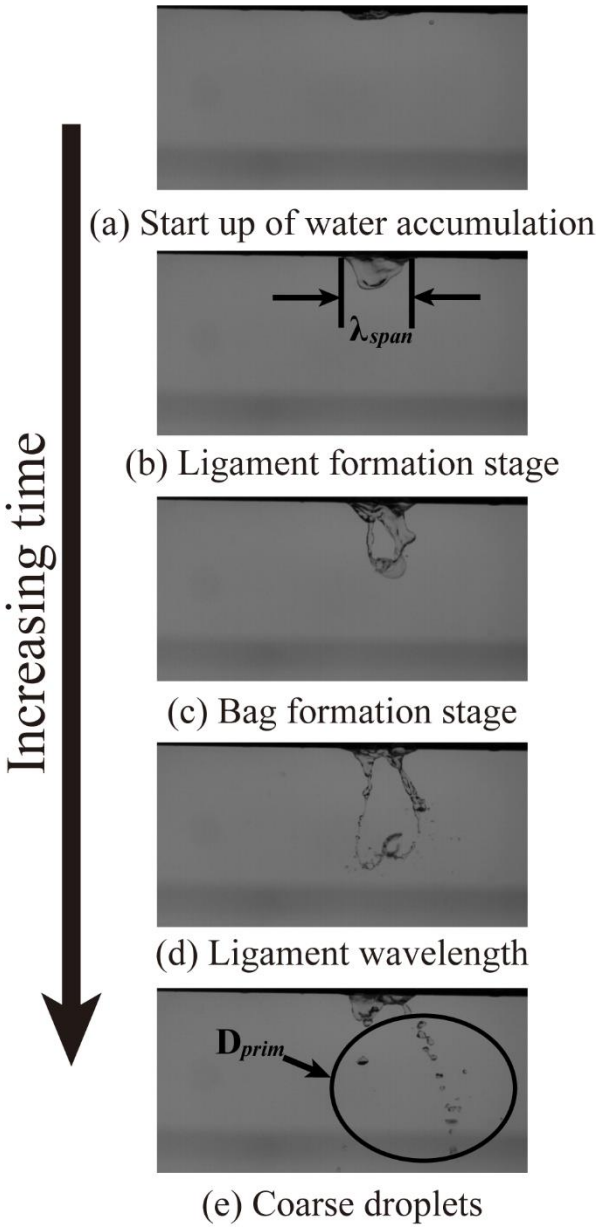

Figure 4.36 – Breakup of ligaments at the T.E.

In the proposed model it was assumed that the amount of water accumulated at the T.E. of the cascade blade was equivalent to that of the cylinder attached in the span-wise direction, as represented schematically in Fig. 4.37. The mass of this attached water is expressed mathematically by Eq. (4.44)

$$m_{span} = \rho_l V_l \approx \rho_l \frac{\pi}{4} D_{span}^2 \lambda_{span} \tag{4.44}$$

where,

D_{span} is the diameter of the cylinder attached at the T.E. of the cascade blade in the span wise direction.

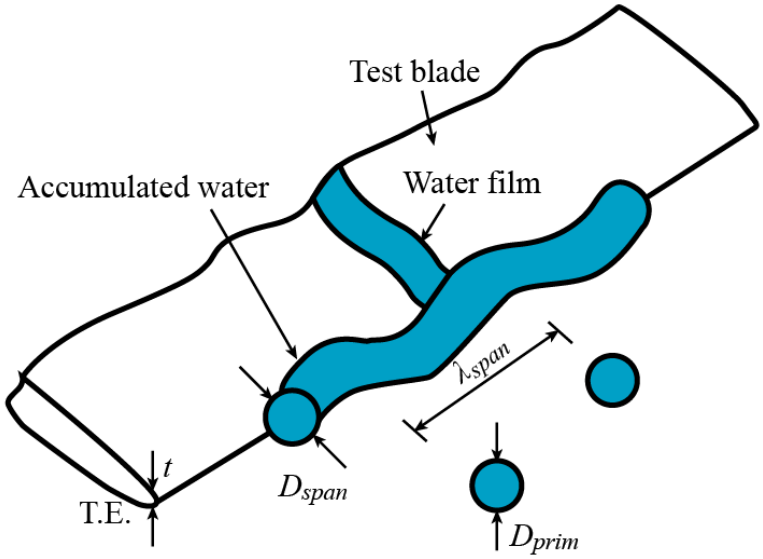

Figure 4.37 – Theoretical Model Sketch for droplets formation from the accumulated water at T.E.

λ_{span} is the wavelength of the cylinder from which the droplets are produced in the span wise direction.

By the law of conservation of mass, the amount of water ejected from the inlet hole (located at the L.E.) equals to that of the amount of water accumulated at the T.E., i.e.

$$m_{span} \approx m_{in} \tag{4.45}$$

$$\rho_l \frac{\pi}{4} D_{span}^2 \lambda_{span} \approx \frac{\dot{m}_{in}}{f} \tag{4.46}$$

According to Rayleigh (Lefebvre [80]), the diameter of the water attached at the T.E. is approximated as,

$$\lambda_{span} \approx 4.51\, D_{span} \tag{4.47}$$

Substituting Eq. (4.47) in Eq. (4.46), and making use of the expression for frequency, Eq. (4.43), the theoretical expression of the wavelength of the ligament at the T.E. of the cascade was obtained as expressed in Eq. (4.48)

$$\lambda_{span} \approx \sqrt[3]{\frac{400\, C}{\pi\, \rho_a} \left(\frac{\dot{m}_l}{U_a}\right) Re^{-\frac{1}{2}}} \tag{4.48}$$

From Eq. (4.48), the wavelength of the ligament(s) attached at the T.E. is inversely proportional to the square root of the gaseous phase velocity. Thus, with an incrementing the aerodynamic forces, the ligament length will decrease and vice versa. Similarly, the ligament length increases with an increase in the (mass) flow rate of the liquid.

4.5.2.3. Primary Droplets Formation

One of the most important parameters in the wet turbine systems is to predict the size of the droplets. Figure 4.37 shows the schematic sketch of the droplets formed from the T.E.. It is important to mention here that in the present analysis only coarse droplets formed are considered.

It was further assumed that the droplets formed were spherical in nature and the mass of the primary droplets formed is expressed to be equivalent to that of a circle

$$m_{prim} = \rho_l V_l = \rho_l \left(\frac{4}{3} \pi \left[\frac{D_{prim}}{2}\right]^3\right) \approx \frac{2}{3} \rho_l A_{prim} D_{prim} \tag{4.49}$$

For the ligament (attached at the T.E.) to atomize completely without any external forces (i.e., aerodynamic forces), the energy required can be approximated by

$$E_{lig} \approx \sigma A \approx \sigma \Delta A \approx \sigma \left[4 A_{prim} - A_{span}\right] \tag{4.50}$$

here,

$$A_{span} = \frac{m_{span}}{\rho_l \lambda_{lig}} \quad \text{and} \quad A_{prim} = \frac{3}{2} \frac{m_{prim}}{\rho_l D_{prim}} \tag{4.51}$$

Substituting Eq. (4.51) into Eq. (4.50)

$$E_{lig} \approx \frac{m_l \sigma}{\rho_l} \left[\frac{4}{D_{prim}} - \frac{1}{\lambda_{span}}\right] \tag{4.52}$$

The limiting value of Eq. (4.52) is given by the term in the parenthesis. That is,

$$\left[\frac{4}{D_{prim}} - \frac{1}{4.51\, D_{span}}\right] = 0 \tag{4.53}$$

If in Eq. (4.53), it is assumed that the primary droplet is related to the thickness of the T.E. (t) by some arbitrary constant value, i.e.,

$$D_{prim} \approx const.\, t \tag{4.54}$$

Then by substituting Eq. (4.54) in Eq. (4.53), Eq. (4.55) is obtained

$$D_{span} \geq 18\, const.\, t \tag{4.55}$$

Equation (4.55) gives a theoretical approximation about the maximum diameter size of the accumulated water attached at the T.E., if the thickness of the accumulated water transcends the above criterion (given by Eq. (4.55)), then the atomization of the droplets happens without an aid of any external forces (i.e. aerodynamic forces).

Similarly, the energy required from the gaseous phase to atomize the droplets from the T.E. is approximated by the K.E. of air

$$E_a = \frac{1}{2}\, m_a\, U_a^2 \tag{4.56}$$

Based on the energy conservation principle, it can be approximated that

$$E_{lig} = k.\, E_a \tag{4.57}$$

where, k is the proportionality constant whose value is found from the experiment

Substituting Eq. (4.52) and Eq. (4.56) in Eq. (4.57), and replacing the mass (m) with the mass flow rate term $(\dot{m})$

$$\frac{\dot{m}_l \sigma}{\rho_l} \left[\frac{6}{D_{prim}} - \frac{1}{\lambda_{span}}\right] = k. \left[\frac{1}{2}\, \dot{m}_a\, U_a^2\right] \tag{4.58}$$

Furthermore, the mass flow rate of air, which atomizes the droplets is given as,

$$\dot{m}_a = \rho\, \delta\, U_a \tag{4.59}$$

Substituting Eq. (4.42), (4.48) and (4.59) in Eq. (4.58), and after simplification, an expression for the primary droplet formation aft the T.E. is established

$$D_{prim} \approx \frac{6}{\left[\frac{k.A_f}{2} + \frac{1}{\lambda_{span}}\right]} \tag{4.60}$$

Here, factor A_f is given by,

$$A_f = \frac{4.91\,\rho_l}{\sigma} . \left(\frac{400}{\pi}\right)^{\frac{1}{3}} . (\dot{m}_l)^{-\frac{2}{3}} . (C)^{\frac{4}{3}} . (\rho_a)^{\frac{2}{3}} . (U_a)^{\frac{8}{3}} . (Re)^{-\frac{2}{3}}$$

From Eq. (4.60), the primary droplets formed is inversely proportional to the aerodynamic forces, whereas, larger surface tension forces results in coarse droplets formation and vice versa.

4.5.3. Comparison of Theoretical Expressions and Experimental Results

4.5.3.1. Shedding Frequency

Figure 4.38 shows the experimentally measured frequency from the high-speed images for each air velocity case under different liquid mass flow rate (MFR) conditions. In Fig. 4.38, the marks symbolizes the experimentally and the solid line represents the mean of the experimental data. From Fig. 4.38, the shedding frequency remains almost constant for a particular air momentum under varying liquid mass flow rate (MFR), due to nearly the stationary state of the accumulated water at the T.E. in contrast to the surrounding air velocity. Therefore, whatever the liquid mass flow rate is the shedding frequency remained the same. Figure 4.39 compares the theoretically measured frequency (Eq. (4.43)) with the experimentally measured results. In Eq. (4.43) a constant value of 2 was chosen. From Fig. 4.39, the experimental measured values shows a good agreement with the theoretically obtained formula. From Eq. 4.43, the shedding frequency increases linearly with an increase in air velocity and vice versa, as shown in Fig. 4.39. However, more experimental data is needed to be compared with theoretical expression to obtain a better validity, since the shedding frequency was measured manually from the high speed images.

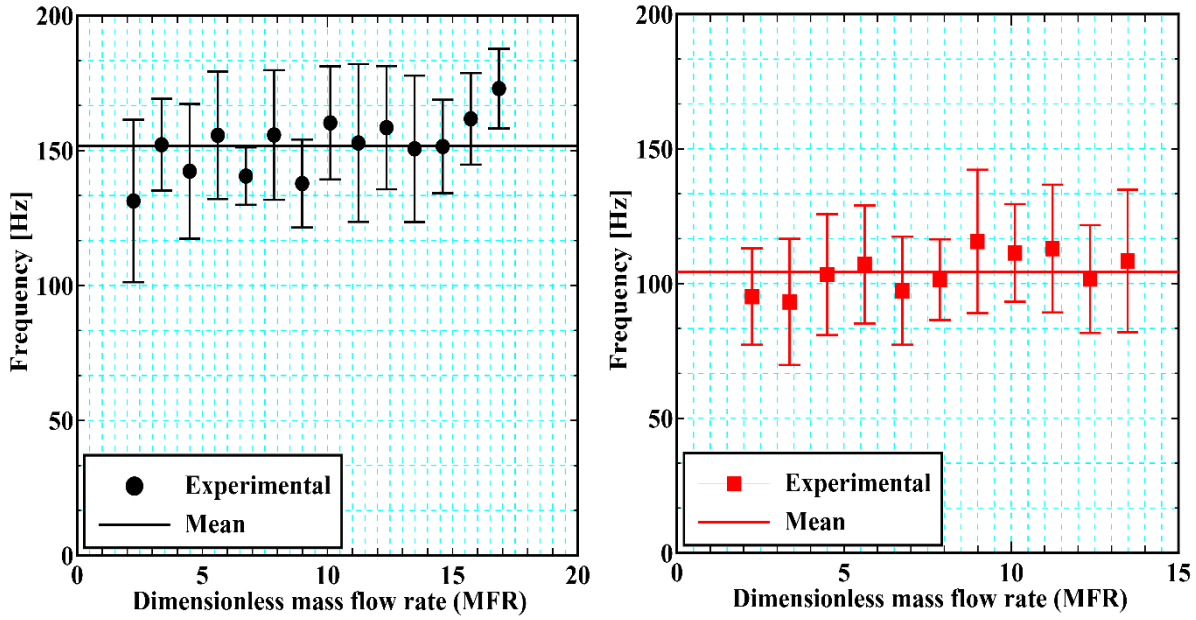

(a) Case A (Air Velocity 40 m/sec) $(M \approx 192, We_a \approx 60)$

(b) Case B (Air Velocity 30 m/sec) $(M \approx 108, We_a \approx 34)$

(c) Case C (Air Velocity 25 m/sec) $(M \approx 75, We_a \approx 23.45)$

(d) Case D (Air Velocity 20 m/sec) $(M \approx 48, We_a \approx 15)$

Figure 4.38 – Experimentally measured shedding frequency

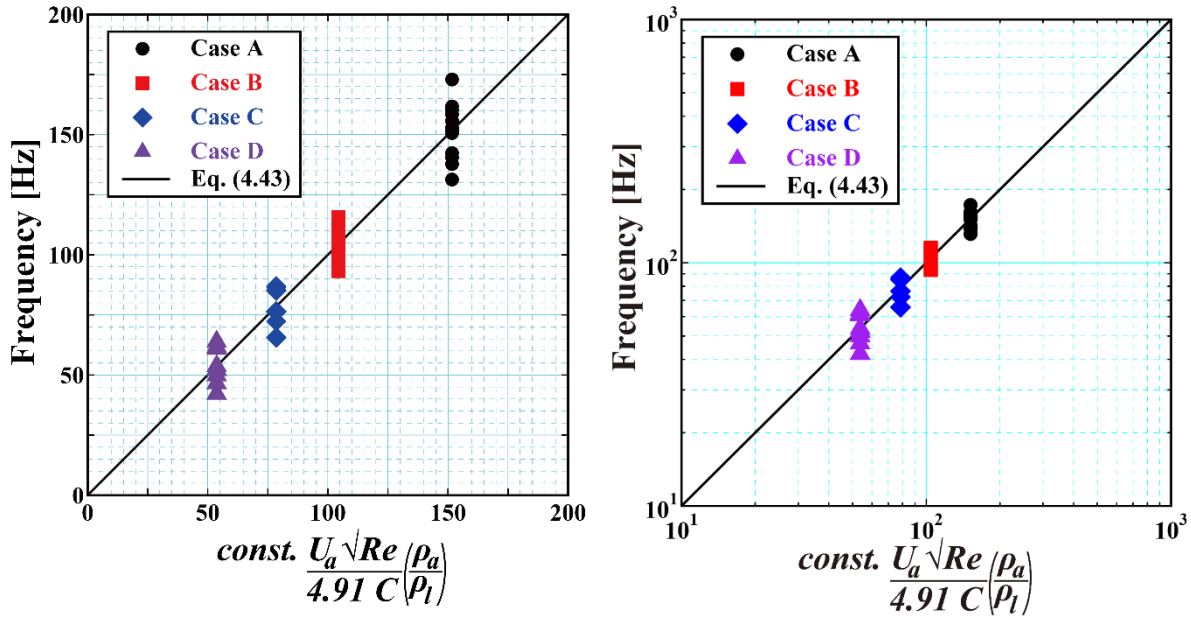

(a) Normal Scale (b) Log Scale

Figure 4.39 – Comparison of Experimental Frequency Vs Theoretically predicted (Eq. 4.43) [units – Hz]

4.5.3.2. Ligament Wavelength

Figure 4.40 (a – d) shows the experimentally measured wavelength for Case A to Case D under different liquid flow rate (MFR) conditions. Like shedding frequency, the values of wavelength were also measured manually from the high speed images. Figure 4.40 (a – d) shows slightly large discrepancy of experimental results with the theoretically predicted wavelength, Eq. (4.48). Especially the Case A, is largely underestimated by the theoretical expression (Eq. (4.48)) as shown in Fig. 4.40 (a) and need further detail investigation. However, the predicted formula for the wavelength shows a decent agreement with the experimental data. Figure 4.41 summarizes the experimental results of Fig. 4.40, and shows a reasonable consistency with to that of the theoretical derived function.

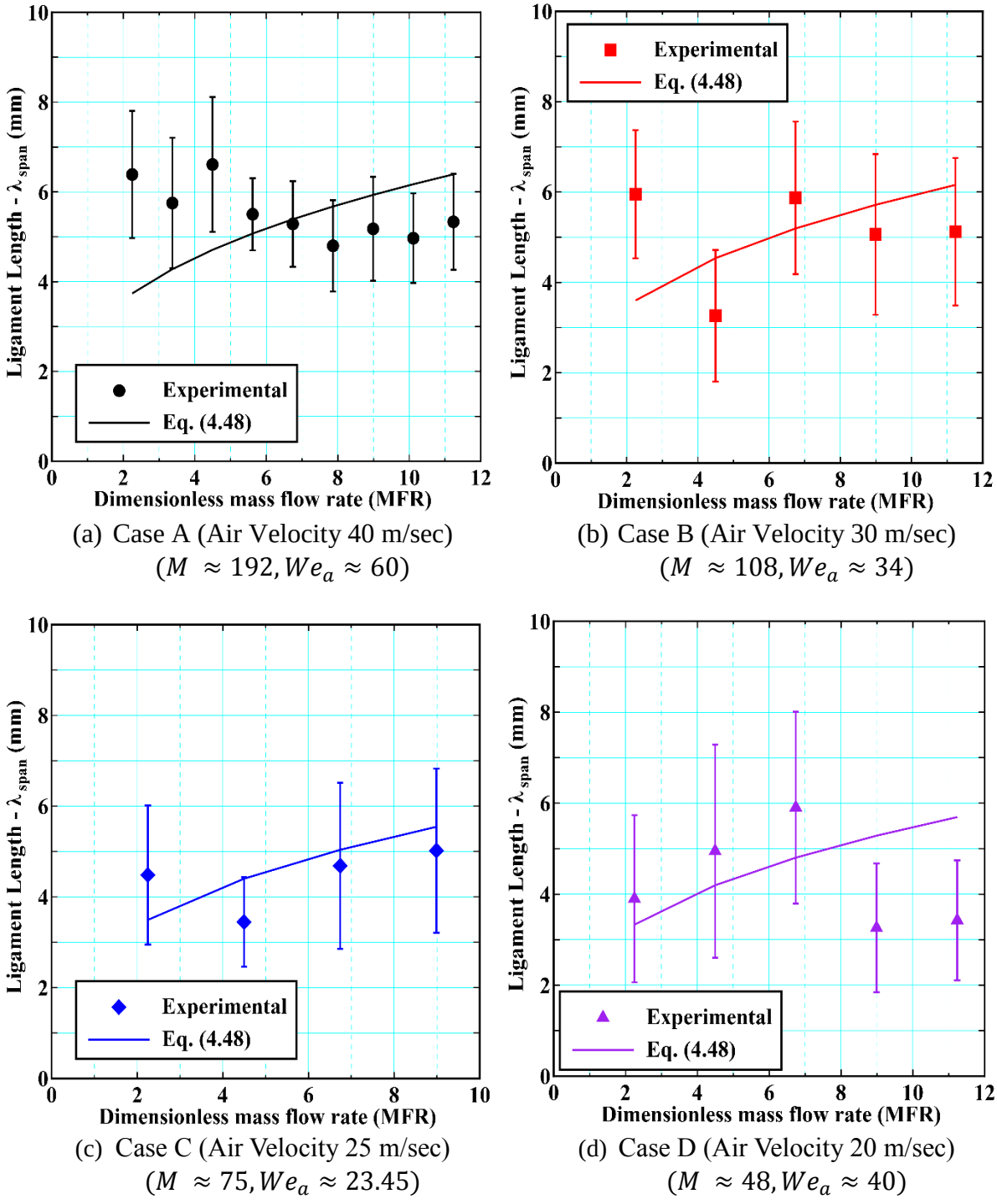

(a) Case A (Air Velocity 40 m/sec) ($M \approx 192, We_a \approx 60$)

(b) Case B (Air Velocity 30 m/sec) ($M \approx 108, We_a \approx 34$)

(c) Case C (Air Velocity 25 m/sec) ($M \approx 75, We_a \approx 23.45$)

(d) Case D (Air Velocity 20 m/sec) ($M \approx 48, We_a \approx 40$)

Figure 4.40 – Span Wise Wavelength – Experimental Vs Theoretical Prediction (Eq. 4.48)

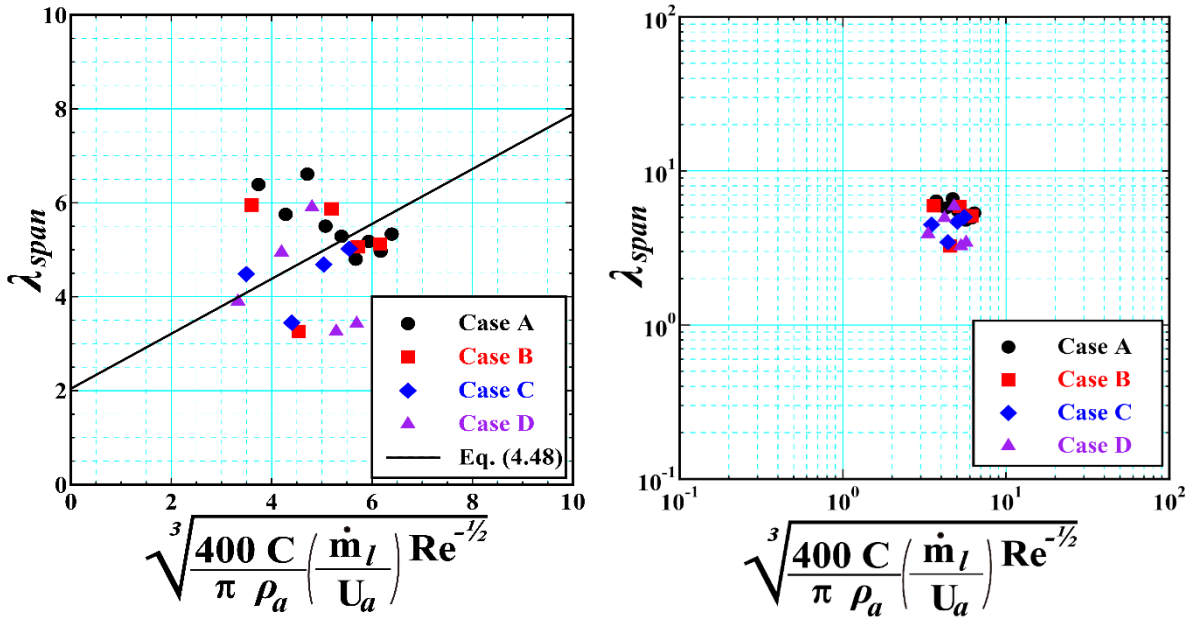

(a) Normal Scale (b) Log Scale

Figure 4.41 – Wavelength – Experimental Vs Theoretical Prediction [units – mm]

4.5.3.3. Droplet Diameter

Lastly, Fig. 4.42 (a – d) shows the experimentally measured droplets for high air velocity case (Case A) to low air velocity case (Case D) against different values of liquid flow rate (MFR). As expected the droplets size remains nearly the same whatever the liquid flow rate was used for the same air momentum. The dotted line in Fig. 4.42 represents the average of droplet obtained in the present study. Figure 4.43 represents the graphical relationship between the experimental results and the theoretical diameter (Eq. (4.60)). One can obtain the term "*k*" in Eq. (4.60) by several ways, however, in the present thesis it was estimated by the least sum of square standard deviation method. The presented theoretical model gives highly reliable results with the experiments performed. Though, it is seen from Fig. 4.43 that as the air velocity reduces from Case A to Case D, the droplets deviate from the theoretically predicted line. This deviation might be caused due to the underestimation of the *k* term. Another reason for such deviation is thought to be the consideration of coarse droplets only in the present experimental data, whereas in actual case small droplets were also present which were completely ignored in the present study. One more reason for such discrepancy is apparently due to the neglecting of the phase change phenomenon. Figure 4.44 summarizes all the cases of Fig. 4.43 in combined. A maximum deviation of around 20% is occurred in the present study. It should be noted that the 20% deviation maybe specific to the present case only.

The theory presented in this section is expected to hold equally for the real turbine systems because the theory is derived primarily based on the mass and energy conservation principles. Though, in the real machines one has to consider additional effects on the liquid film, due to the centrifugal force. In the derivation of this theory, laminar boundary thickness was assumed, given by Eq. (4.42). However, in real systems the Reynolds number is expected to be higher than the experiments conducted in this study. Therefore, if the boundary condition term is replaced by the turbulent boundary term (i.e., $\delta \approx 0.37C/Re^{1/5}$) then the corresponding frequency, wavelength and primary diameter equations can be re-derived in an exactly the same manner.

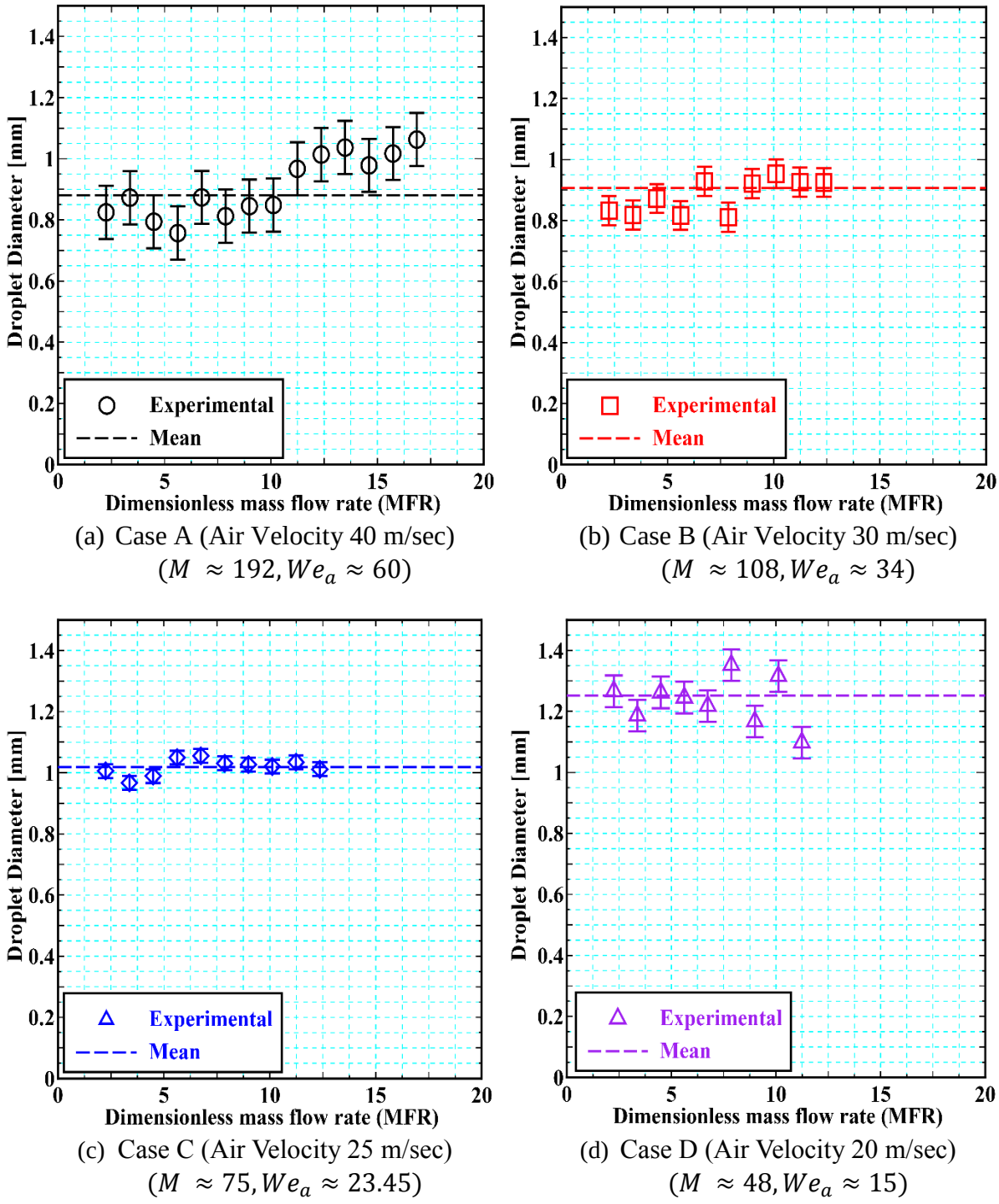

(a) Case A (Air Velocity 40 m/sec) ($M \approx 192, We_a \approx 60$)

(b) Case B (Air Velocity 30 m/sec) ($M \approx 108, We_a \approx 34$)

(c) Case C (Air Velocity 25 m/sec) ($M \approx 75, We_a \approx 23.45$)

(d) Case D (Air Velocity 20 m/sec) ($M \approx 48, We_a \approx 15$)

Figure 4.42 – Droplet diameter near the T.E.

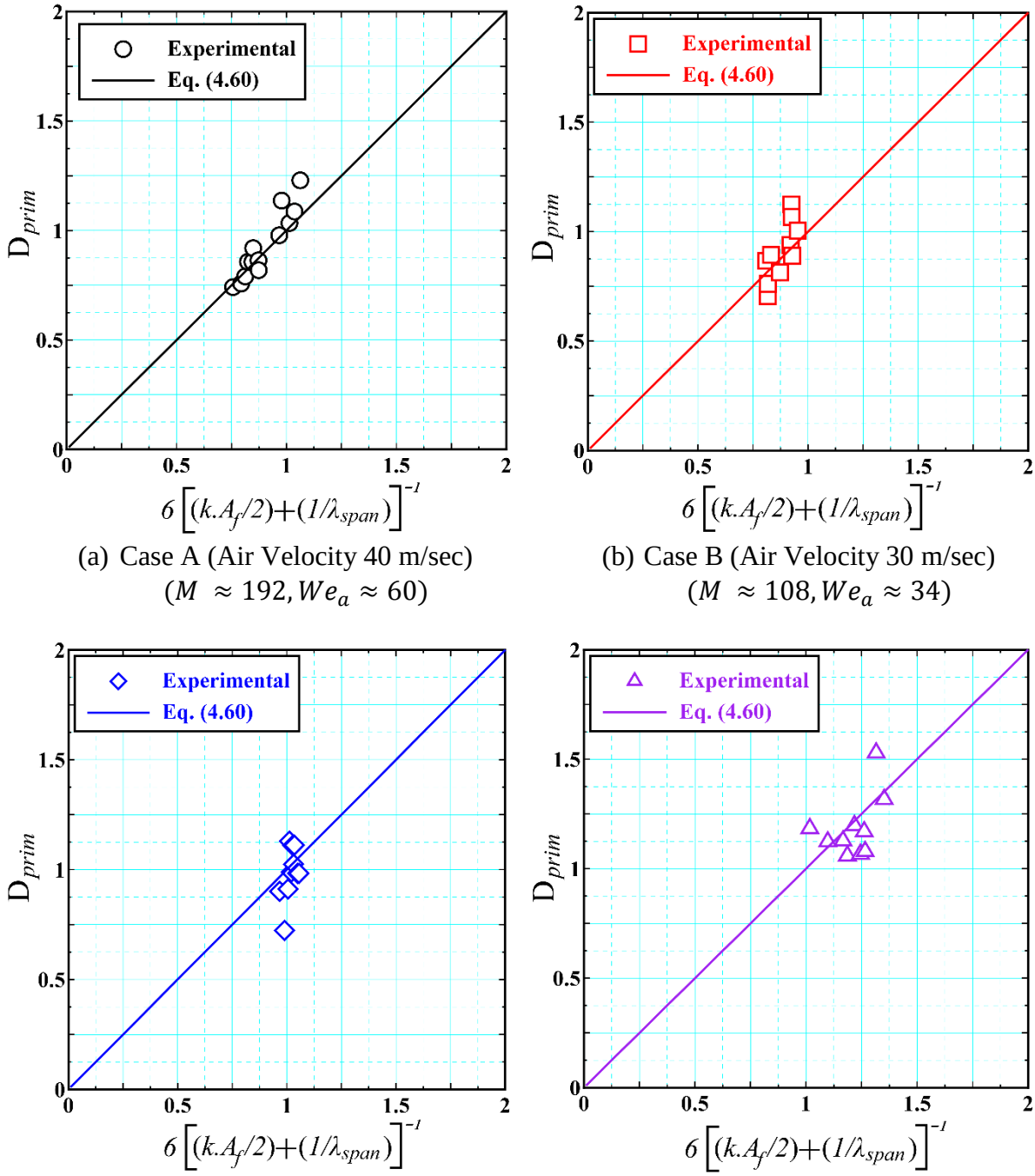

(a) Case A (Air Velocity 40 m/sec) $(M \approx 192, We_a \approx 60)$

(b) Case B (Air Velocity 30 m/sec) $(M \approx 108, We_a \approx 34)$

(c) Case C (Air Velocity 25 m/sec) $(M \approx 75, We_a \approx 23.45)$

(d) Case D (Air Velocity 20 m/sec) $(M \approx 48, We_a \approx 15)$

Figure 4.43 – Theoretical Prediction of droplet diameter – (Eq. 4.60) [units – mm]

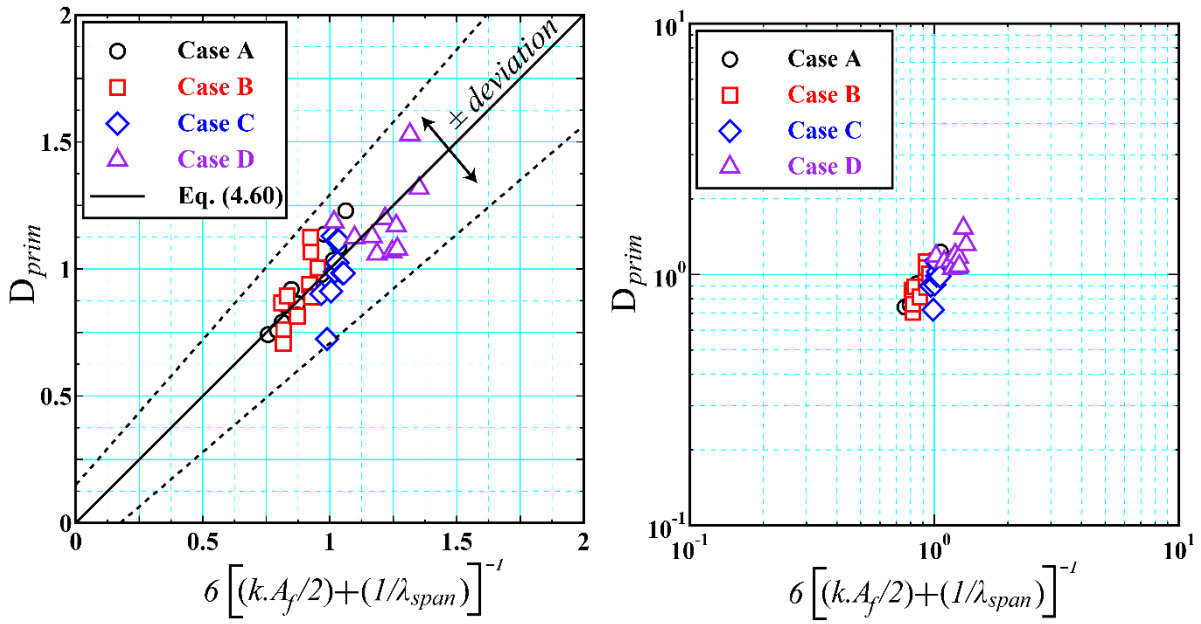

(a) Normal Scale (b) Log Scale

Figure 4.44 – Droplet Diameter – Experimental Vs Theoretical Prediction

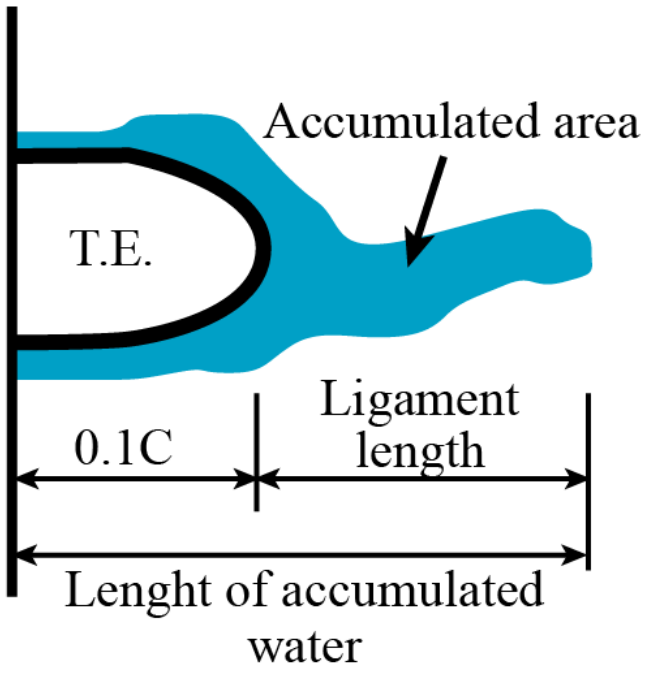

Figure 4.45 – Definition of Water Accumulated at the T.E.

4.5.4. Other properties

Another important parameter to consider is the amount of accumulated water at the T.E. of the blade. The presence of water accumulation at the flow separation region results in the acceleration of the blade erosion. Especially, the water accumulation at the T.E. of the stator blade causes the generation of large droplets which splashes onto the rotor blade. This might lead to the removal of substantial loss of mass of the rotor blade. Also the accumulation of water possesses the ability to the block the flow and generating additional losses in a humid environment of wet turbine systems.

Figure 4.45 shows the schematics representation of water accumulation at the T.E. of the cascade blade. The ligament length is defined as the horizontal length of the water accumulated from the tip of the T.E. of the cascade blade. Similarly, overall water accumulated area at the T.E. of the blade is defined as the area of ligament length plus the area of water accumulation 0.1-C upstream of the T.E. as shown schematically in Fig. 4.45. The main reason for including a 0.1-C upstream region can be easily explained by referring to the high-speed images given in Section 4.4, such as Fig. 4.24 (a) and 4.24 (c). As water is always accumulated at the T.E., there are many occasions when the tip of the accumulated water was even before the tip of the T.E., as shown in Fig. 4.24 (a). An inclusion of small region before the tip of T.E., where water is always present and accumulated, due to flow separation, is thought to be necessary for reliable quantitate analysis.

An algorithm to measure the accumulated water at the T.E. was developed using MATLAB. The binary images were obtained as explained above in Section 3.8. However, the image obtained by the above process contains a large number of droplets in the analysis window, as shown in Fig. 4.46 (b), which may affect the post processing results. Therefore, the amount of liquid which is not attached to the T.E. is needed to be removed from the analysis window and was achieved by the indexing of water droplets. In this method, the amount of water which was present at the same index as that of the coordinates of the T.E. was chosen only, whereas, the other indexes containing water were deleted from the analysis window, as shown in Fig. 4.46 (c). Additionally, it was observed that the area of the accumulated water was always much larger than that of the droplets, and further criterion was imposed such that if the chosen accumulated water must also be greater in the area compared to the other droplets present in the analysis window. This helped in reducing the chances of errors and the water accumulated at the T.E. was selected with ease. Figure 4.47 (a) and 4.47 (b) shows the time history of the area and length of the accumulated water at the T.E. From Fig. 4.47 (a) and 4.47 (b), spikes are seen at random time steps, which indicates an increase in the amount of accumulated water and ligament length respectively. It should be noted from Fig. 4.47 (b) that when accumulated water reached a maximum value (maximum peak value of spike) the breakup of ligament took place soon after it by a decrease in the value of ligament length. In the present study, this maximum length of ligament just before the breakup was taken as ligament length (L_{lig}), i.e., local peak value, as shown in Fig. 4.47 (b), and is explained in Section 4.5.4.1., whereas, the amount of water accumulated (A_{accum}) is taken as an average of the whole time step.

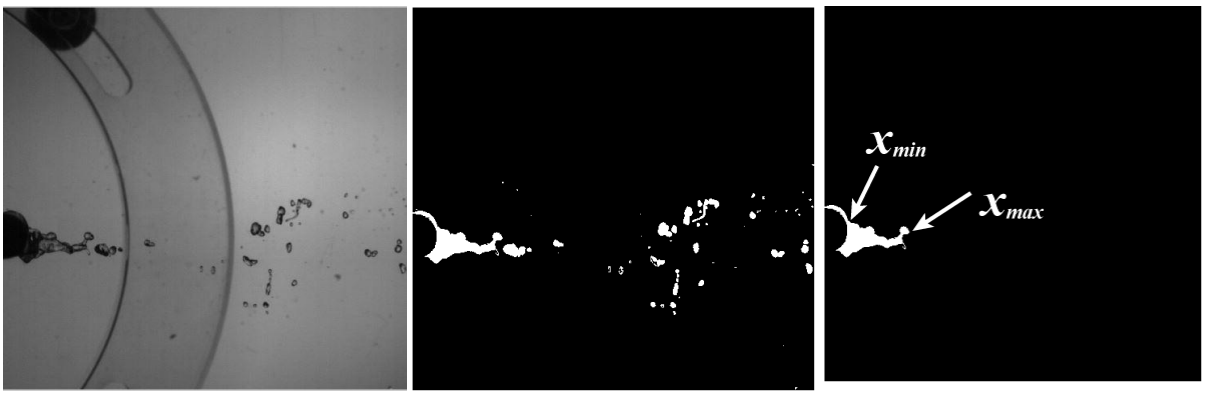

(a) Original Image (b) Binary Image (c) Modified Binary Image

Figure 4.46 – Image Processing for the measurement of T.E. properties

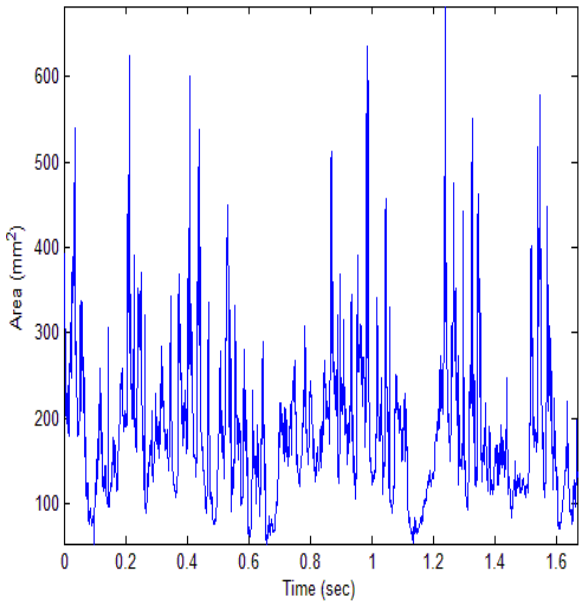

(a) Water Accumulated area

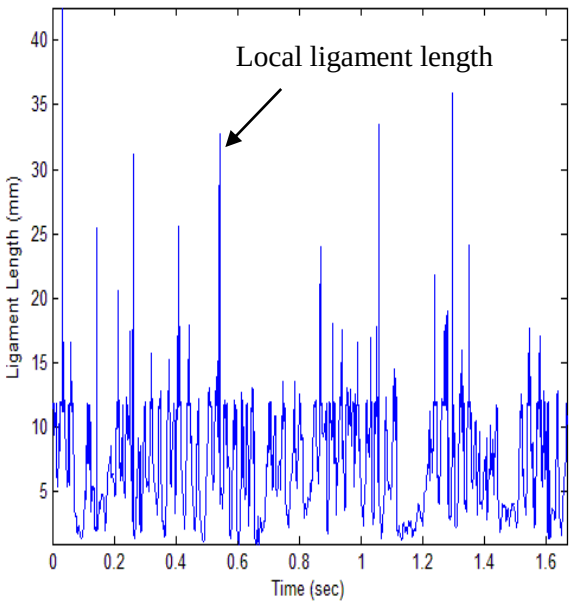

(b) Instantaneous Ligament Length (ΔX)

Figure 4.47 – Time History of Water attached to the T.E.

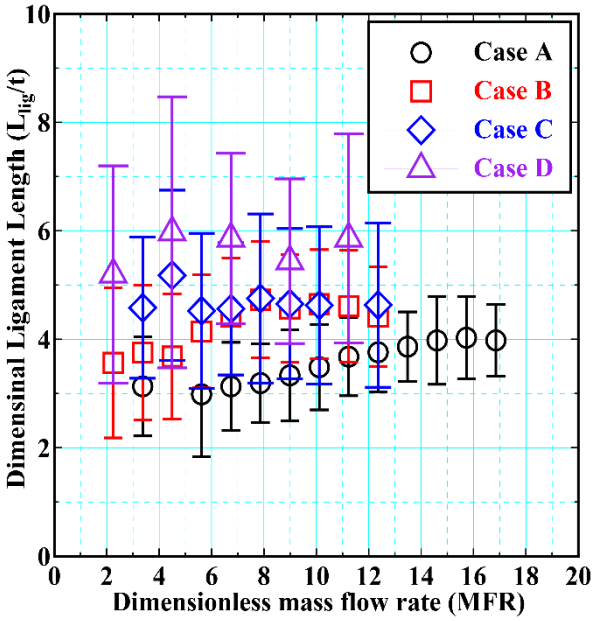

Figure 4.48 – Dimensional ligament length

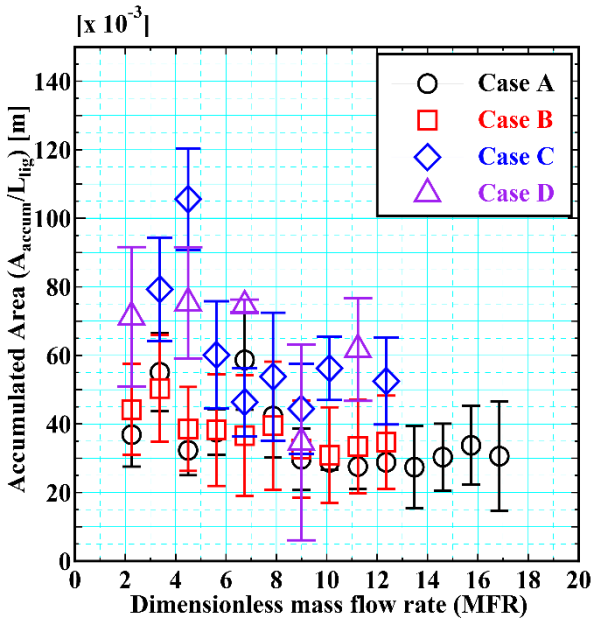

Figure 4.49 – Normalized water accumulation per unit length

4.5.4.1. Ligament Length

Ligament length was calculated by processing nearly 10,000 high-speed frames, as shown in Fig. 4.46. This was done by identification of the coordinates of the tip of T.E. edge of the cascade blade (X_{min}) and the farthest edge of the ligament (X_{max}). The farthest end of the ligament (X_{max}) was identified effectively due to the jump of a binary value from 0 to 1 (i.e., white to black). The chord-wise positions of these two critical points was recorded as X_{min} and X_{max}, and the instantaneous ligament length was calculated for each frame, as given by Eq. (4.61)

$$L_i = \Delta X = X_{max_{(local)}} - X_{min} \tag{4.61}$$

As it can be seen from Fig. 4.47 (b), the instantaneous ligament length (ΔX) gradually increases with time followed by a sharp increase and then a sharp decrease. This transition point of sharp decrease provides an approximate value of the maximum ligament length (or simply ligament length). At this point the local maximum ligament length was recorded separately as L_{max}, and the mean ligament length was calculated by using the mathematical expression given by Eq. (4.62)

$$L_{lig} = (L)_{mean} = \frac{1}{i}\sum_{i=1}^{N}(L_{max}) \tag{4.62}$$

where "i" is the number of binary images in which local maximum ligament values were recorded, such as Fig. 4.46 (c).

Figure 4.48 shows the average dimensionless ligament length formed aft the T.E. of the cascade blade. It is evident from the Fig. 4.48 that the ligament length is highly dependent upon the air velocity and the amount of liquid flow rate. When the air momentum is increased from Case D (20 m/sec) to Case A (40 m/sec), the ligament length reduced nearly 1.5-2 times. The reduction in the ligament length was due to an increase in the kinetic energy aft the T.E. of the blade, resulting from high aerodynamic forces. In other words, at high air velocity cases (Case A) the turbulence intensity of air was strong enough to break up the ligament at a relatively faster rate while keeping it relatively smaller in length. Similarly, Fig. 4.48 also shows the dependence of ligament length on the liquid flow rate of water, as the flow rate of water increases the corresponding ligament length also increased and vice versa. This effect is more visible at relatively high air velocity cases (Case A). From Fig. 4.48, at low-velocity cases (Case D) the ligament length did not change much, possibly due to the fact that the turbulence intensity of air was not strong and the liquid's surface tension helped in destabilizing the ligament and its breakup. Also, due to the presence of water at the T.E., the K.E. of the surrounding air diminish locally, as the water is nearly thousand times heavier than the air. The ligament length was also measured from the grey scale images using a Java based image processing software, ImageJ. The measured images by both in-house code and ImageJ gave almost the same result having a minute difference of approximately 10% on average.

4.5.4.2. Water accumulation at the T.E.

The amount of water accumulated at the T.E. increases due to a decrease in the air momentum and vice versa, as shown in Fig. 4.49. The main reason for this was also due to the fact that an increase in the aerodynamic forces leads to the reduction of accumulated area and vice versa as already explained above.

4.5.4.3. Droplets Distribution Angle

The disintegration of droplets from the T.E. of the blade is not merely the breakup of ligament and droplets formation but also the discharge of these disintegrated droplets into the surrounding gaseous medium. Depending on the air momentum the droplets formed from the stator blade can spread in either a wide angle or narrow angle, as illustrated in Fig. 4.50. A wider droplets distribution region not only affect the surrounding air momentum but also causes damages to the incoming rotor blades by the bombardment of droplets over a large area of the rotor blades, Fig. 4.50.

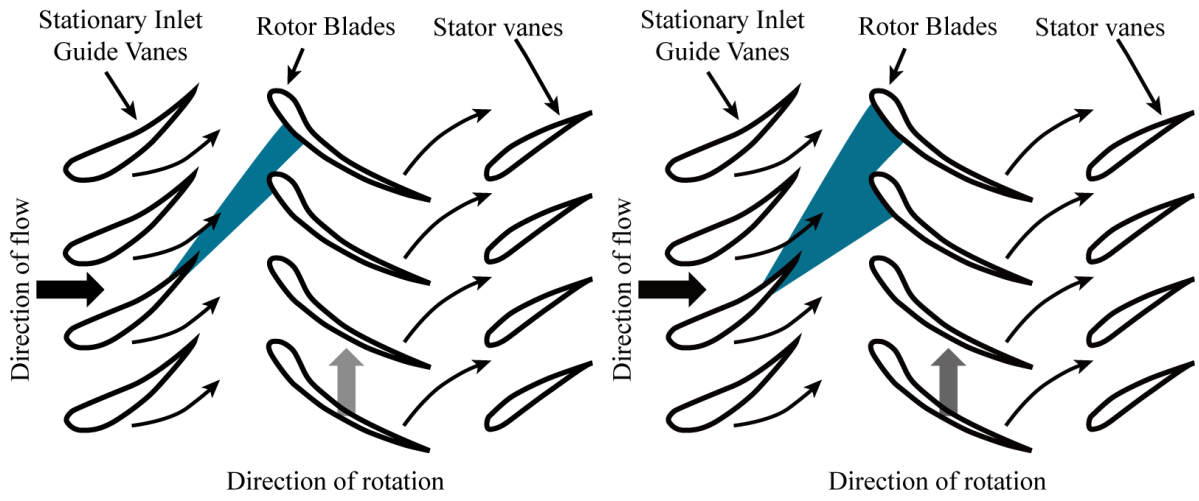

(a) High Air Momentum (b) Low Air Momentum

Figure 4.50 – Schematics of droplets shedding under different air momentum

To estimate the droplets distribution angle aft the T.E. region of the cascade blade, intensity images were generated by adding 1000 grey scale images. These images were then converted to their corresponding RBG image, Fig. 4.51 (a), and are further modified by reducing the threshold intensity level to the 70% of the original image, Fig. 4.51 (a), to obtain the corresponding modified image, Fig. 4.51 (b). From Fig. 4.51 (b), near the T.E. a red region was observed, which represents the high water accumulation region whereas, away from the T.E. blue region corresponds to low (water) intensity region. The blue region in Fig. 4.51 (b) was separated from the surrounding black region (containing no water) due to different threshold intensity levels, making it simpler to approximate the droplets distribution angle. Though, in fact, there is a major difficulty in defining the distribution angle as the droplets boundary became slightly curved as the distance aft the T.E. increases, however, to overcome this the droplets distribution angle was defined by the two straight threshold lines (white lines), as shown in Fig. 4.51 (b). The angle suspended between the two thresholds lines was then used to approximate the droplets shedding angle, as shown in Fig. 4.51 (b). Figure 4.52 shows the effect of air momentum on the droplets angle distribution aft the T.E., such that as the flow velocity was reduced the corresponding distribution angle increases and vice versa.

$$\theta \propto \frac{1}{U_a} \tag{4.63}$$

The increase in the distribution angle was mainly due to change in the mode of a breakup. Since at high air momentum (Case A) the droplets mainly undergo breakup due to vibrational breakup, which results in the generation of smaller droplets size. These droplets continued to follow the main air stream and result in small distribution angle, as given by Fig. 4.52 (a). However, for low air momentum (Case D) the ligament attached as well as the droplets underwent bag mode of a breakup. This causes the coarse droplets formation possessing high momentum and the higher droplets distribution angle, as shown in Fig. 4.52 (d). Figure 4.53 represents the quantitative measurement of distribution angle aft the T.E. of the cascade blade at different flow velocity. The droplets distribution angle increases with an increase in the air momentum and vice versa, and is effective with the change in the flow rate of the liquid as the droplets size remains the same at a particular position aft the T.E..

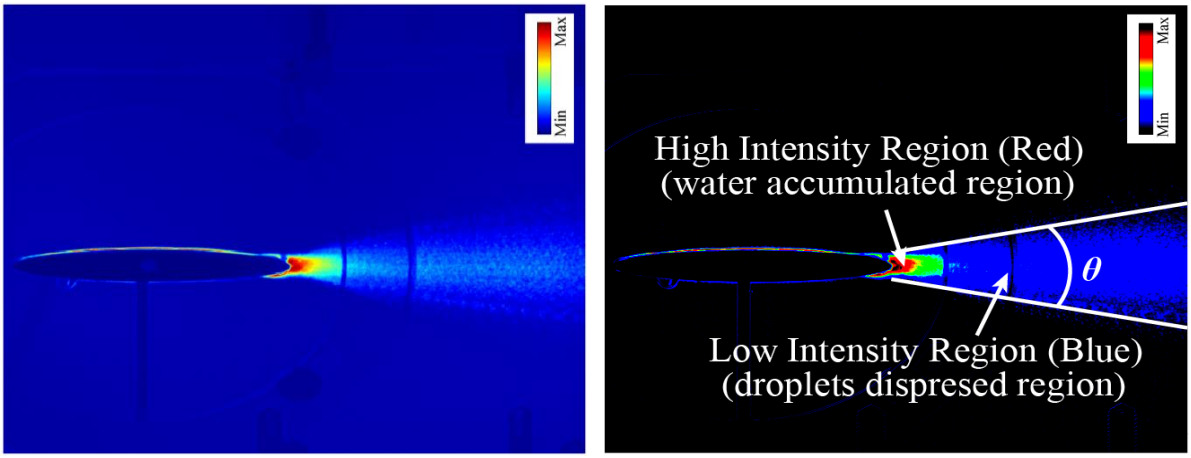

(a) Original Image (b) Threshold Intensity Image

Figure 4.51 – Image Intensity

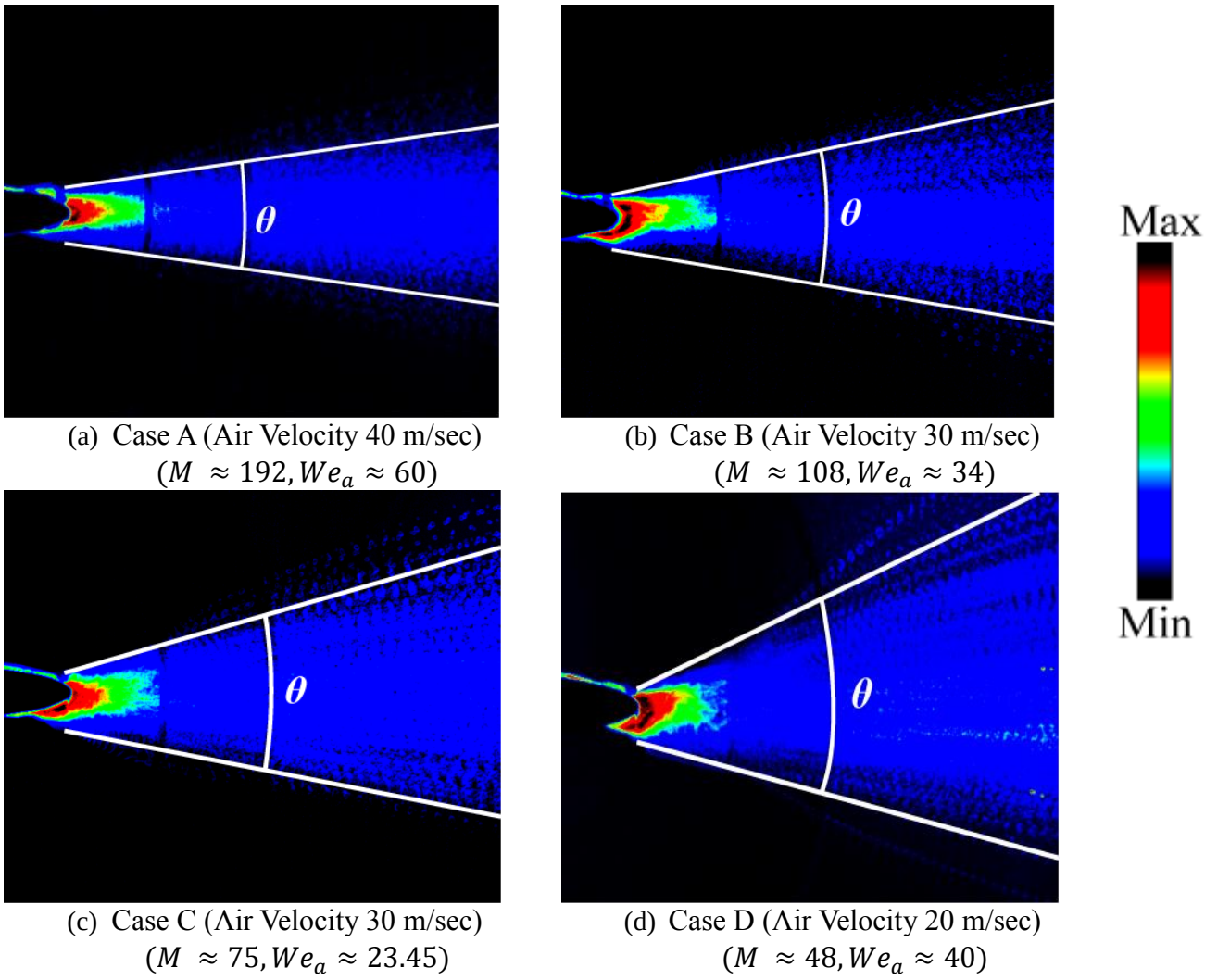

(a) Case A (Air Velocity 40 m/sec) ($M \approx 192, We_a \approx 60$)

(b) Case B (Air Velocity 30 m/sec) ($M \approx 108, We_a \approx 34$)

(c) Case C (Air Velocity 30 m/sec) ($M \approx 75, We_a \approx 23.45$)

(d) Case D (Air Velocity 20 m/sec) ($M \approx 48, We_a \approx 40$)

Figure 4.52 – Droplets Intensity and distribution angle

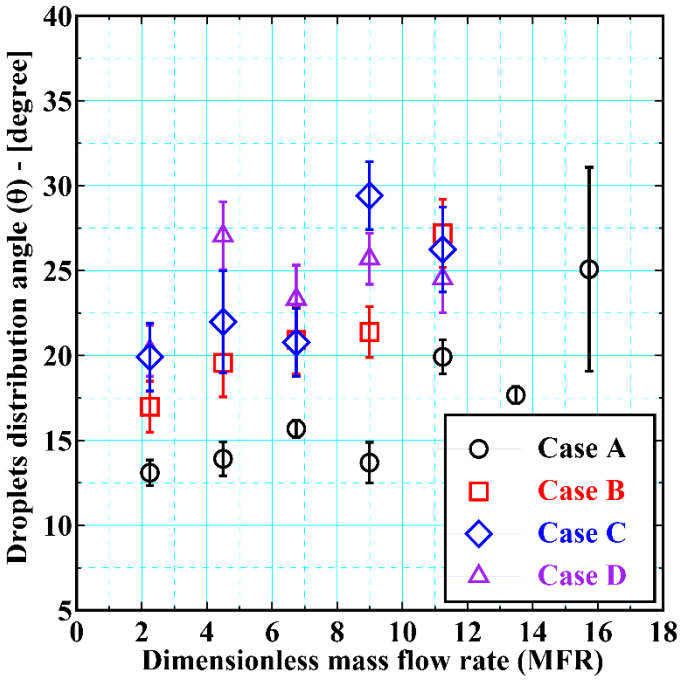

Figure 4.53 – Droplets Distribution Angle (Elliptical Blade)

II. Characteristics of two-phase phenomena around a Cascade Blade at Higher AOA

4.6. Fundamental Phenomena at High AOA

4.6.1. Effect of Incident Angle of Attack

Figure 4.54 shows the effect of angle of attack on the air flow physics around a blade. At low angle of attack, the flow remains attached to both the upper and lower surfaces. However, as the angle of attack increases separation point starts to move forward towards the L.E., which results in the airflow to detach from the upper surface earlier. As the angle of attack is increased beyond a certain limit stalls phenomenon occurred resulting in a largely separated flow region to expand upon the upper surface. This results in the large surface drag and reduced lift. In other words, fluid particles flowing along the upper surface of the wing experience a change in pressure, moving from the ambient pressure in front of the wing to a lower pressure over the surface of the wing and then back to the ambient pressure behind the wing. The region where fluid must flow from low to high pressure (adverse pressure gradient) is responsible for flow separation. If the pressure gradient is too high, the pressure forces overcome the fluid's inertial forces, causing the flow to depart from the wing contour.

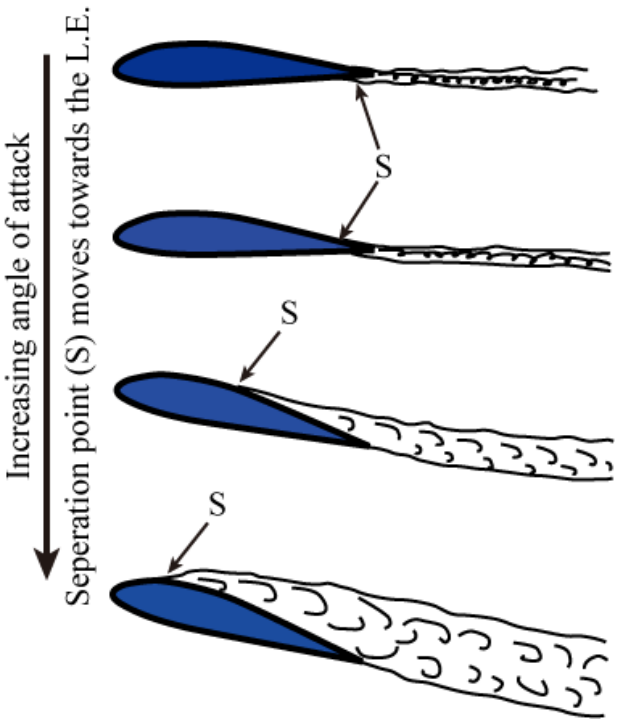

Figure 4.54 – Effect of Flow Angle on Air flow around a wing

4.6.2. Experimental Velocity Distribution aft the T.E.

Figure 4.55 below shows the velocity distribution data measured aft the T.E. of the elliptical blade for different AOA cases, by using a single probe hot-wire. Filled and unfilled labels represent the velocity measurements at 0.25- and 1-C position from the tip of the T.E.. From Fig. 4.55, aft the T.E. of the blade a wake region develops due to the boundary layer developing on the suction and pressure side of the cascade blade.

For each velocity case (Case A to Case D) the velocity deficit aft the T.E. increases as the AOA of the blade was increased. Further downstream (1-C) the velocity deficit was slowly recovered, which was accompanied by a decrease in the thickness of the wake. Moreover, from the comparison of Fig. 4.55 (a) and Fig. 4.55 (d) a significant velocity deficit was noted even at a 1-C distance from the T.E. For example, for Case A at 1-C, the minimum local velocity for 10-degree case (Fig. 4.55 (d)) was measured to be around 8% lower than that of the minimum local velocity for 3-degree case (Fig. 4.55 (a)).

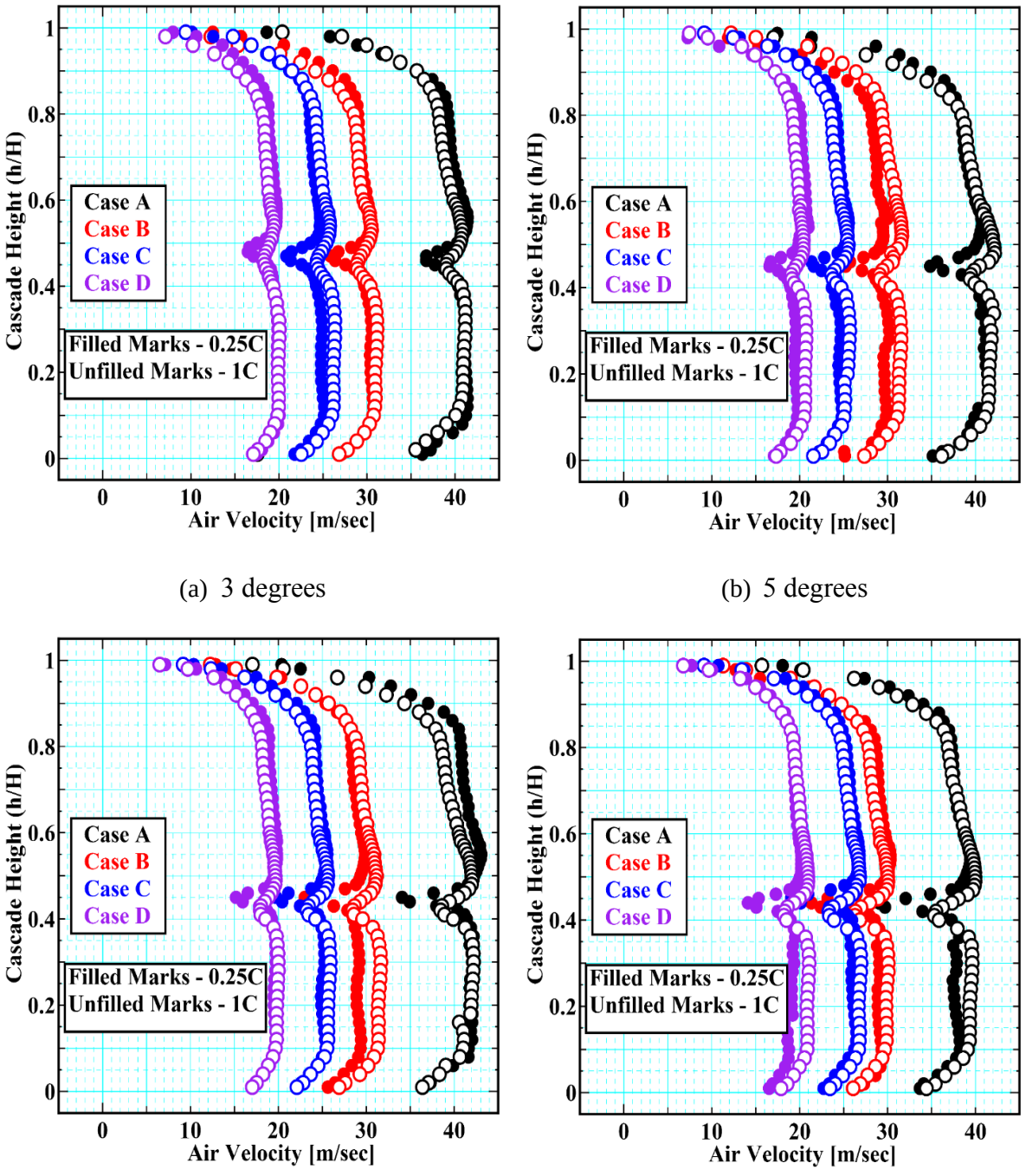

(a) 3 degrees

(b) 5 degrees

(c) 7 degrees

(d) 10 degrees

Figure 4.55 – Velocity Distribution aft the T.E. Region

4.7. Characteristics of Liquid Film (High AOA)

4.7.1. Water Film Visualization (High AOA)

When AOA was increased then irrespective of the air velocity and the level of increase in AOA, the water film was seen to form only on the upper surface of the blade with no water flowing on the lower surface.

4.7.1.1. High Momentum Case (Case A, Air Velocity 40 m/sec, M ≈ 192) – Dominant Aerodynamic Forces

Figure 4.56 and Fig. 4.57 shows the effect of angle of attack for high air momentum (Case A) at low angle (3-) and high (10- degree) angle of attack respectively. As the AOA was increased then due to the flow separation made the film structure to widen, such that, the film width at 10 degree was almost 4 times wider than the film width at the 3 degree AOA. The wave pattern showed complex structure primarily due to the large flow separation. For Case A at 10-degree whatever the injected liquid flow rate was used, few droplets were seen to form from the ingestion hole directly, whereas, a large amount of injected liquid deformed to form a liquid film. This might be caused due to the stalling of the flow at this particular condition. Comparing Fig. 4.57 with 4.58, an increase in AOA causes a large amount of water to accumulate at the T.E., which was also due to the flow separation. For high AOA, it was observed that many small wavelet appeared at the mid of the film, making the film relatively thinner in thickness, whereas, the edges were relatively thicker probably due to the equivalent surface tension effects, as shown in Fig. 4.57. Overall, the liquid film formed in this case moved with high velocity and were thinner.

4.7.1.2. Low Momentum Case (Case D, Air Velocity 20 m/sec, M ≈ 48) – Dominant Surface Tension Forces

Figure 4.62 and 4.63 demonstrate the water film pattern for the low air momentum (Case D) at an AOA of 3- and 10-degree respectively. From Fig. 4.62, a slight increase in AOA results in the small wave patterns started to appear in the liquid film, which did not occur at all when the AOA was kept at 0-degree. Though, the liquid's property of surface tension still appeared to be more prevalent than the aerodynamic forces. At high AOA (10-degree), Fig. 4.63, though wavelets were seen to appear on the film structure, which was primarily due to the separation caused at such AOA. Even at these high AOA the wave structure was much smoother compared to that of high air momentum case. Like high-velocity case (Case A), in this case also became wider having the width almost 4 times in comparison to the 3-degree case. However, due to superior surface tension effects, the molecular bond is much stronger among the liquid particles resulting in thicker liquid films for this case.

Intermediate air momentum, Fig. 4.58 to Fig. 4.61, shows transitional phenomena to that of Fig. 4.56 and 4.63.

Figure 4.64 shows the schematics of the water film formation on the blade's surface and the corresponding droplets size distribution aft the T.E. of the blade at high AOA.

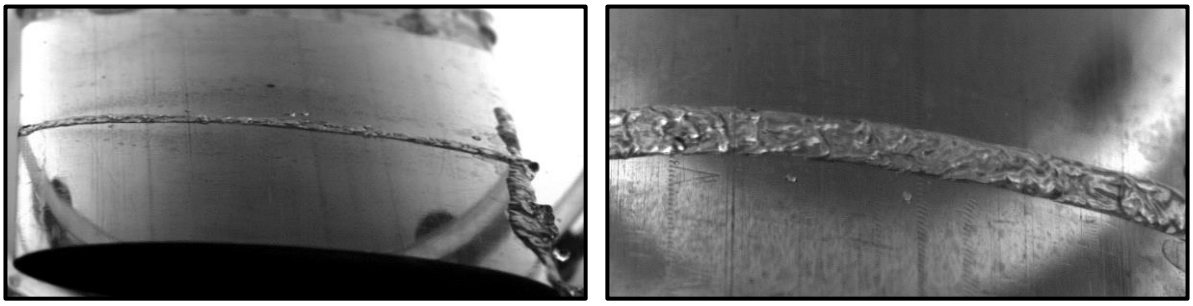

(a) Low Water Ejection Flow Rate – $MFR \approx 6.75$

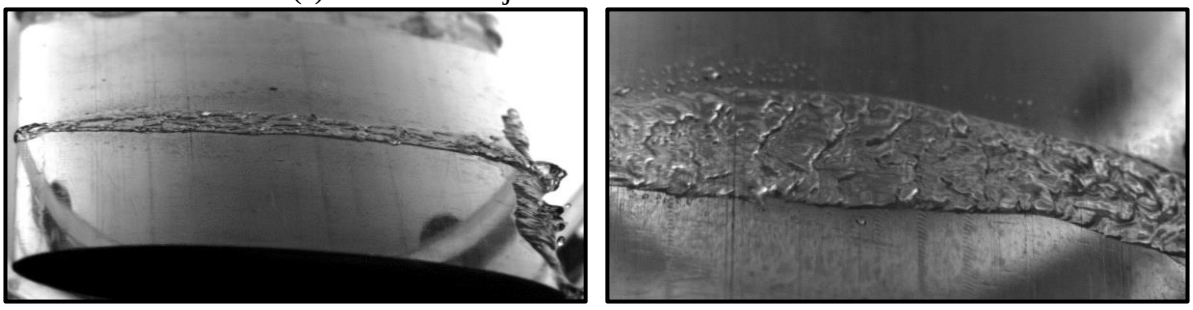

(b) High Water Ejection Flow Rate – $MFR \approx 16.85$

Far View Close View

Figure 4.56 – Water film structure at low angle of attack (3-degrees) (Case A – Air Velocity 40 m/sec)

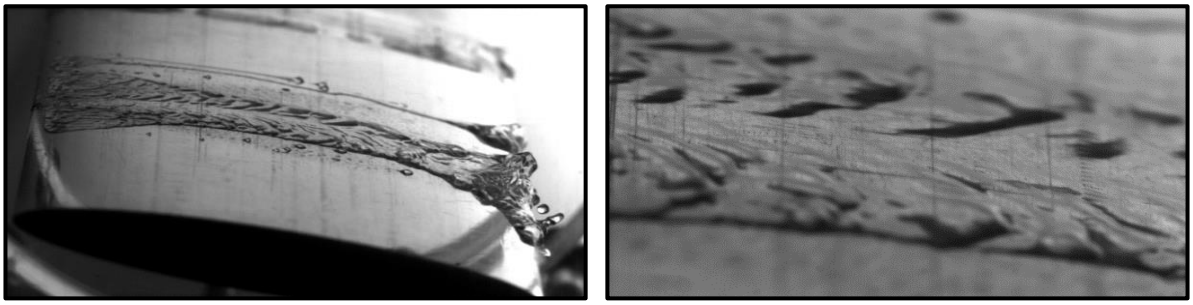

(a) Low Water Ejection Flow Rate – $MFR \approx 6.75$

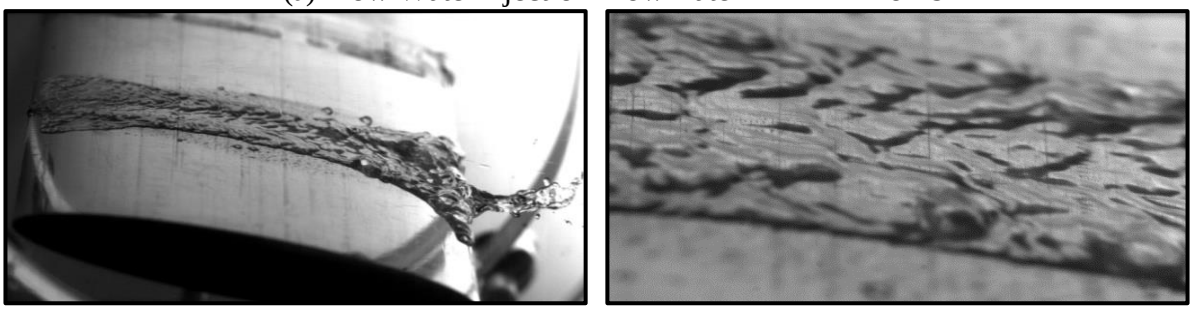

(b) Low Water Ejection Flow Rate – $MFR \approx 21.35$

Far View Close View

Figure 4.57 – Water film structure at high angle of attack (10-degrees) (Case A – Air Velocity 40 m/sec)

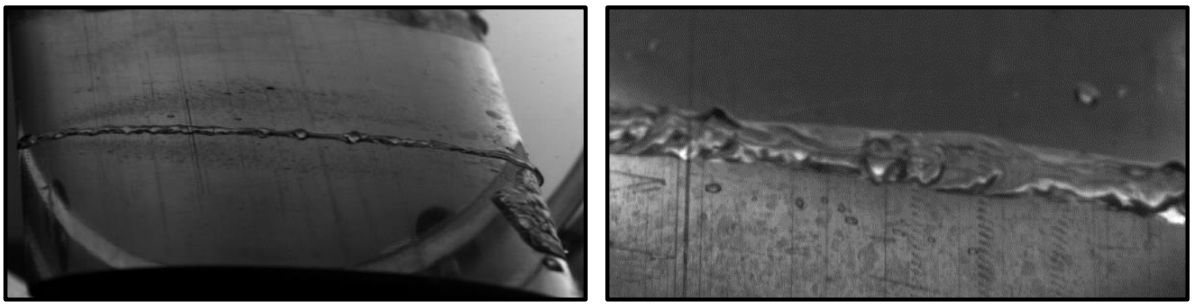

(a) Low Water Ejection Flow Rate – $MFR \approx 5.6$

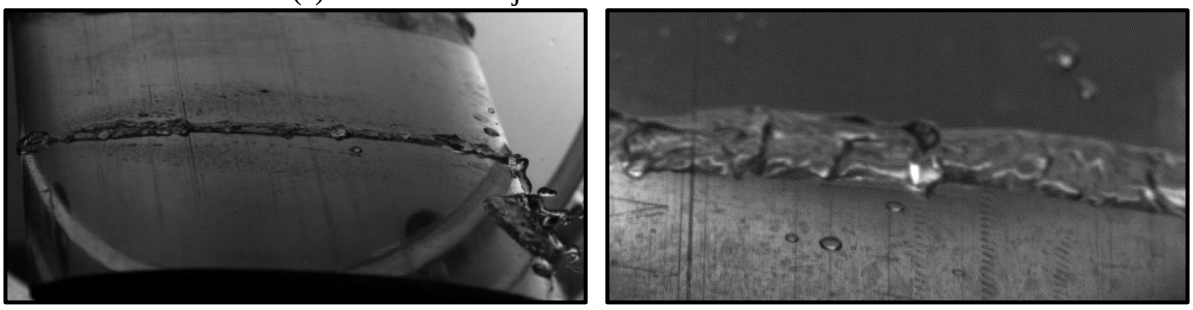

(b) Low Water Ejection Flow Rate – $MFR \approx 13.5$

Far View Close View

Figure 4.58 – Water film structure at low angle of attack (3-degrees) (Case B – Air Velocity 30 m/sec)

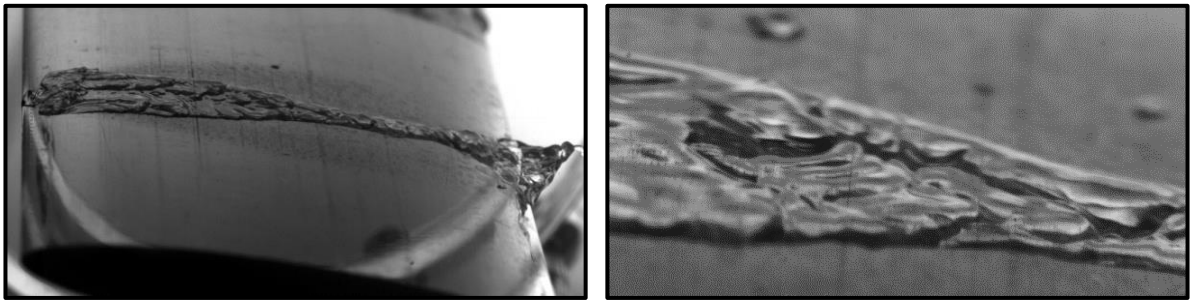

(a) Low Water Ejection Flow Rate – $MFR \approx 6.75$

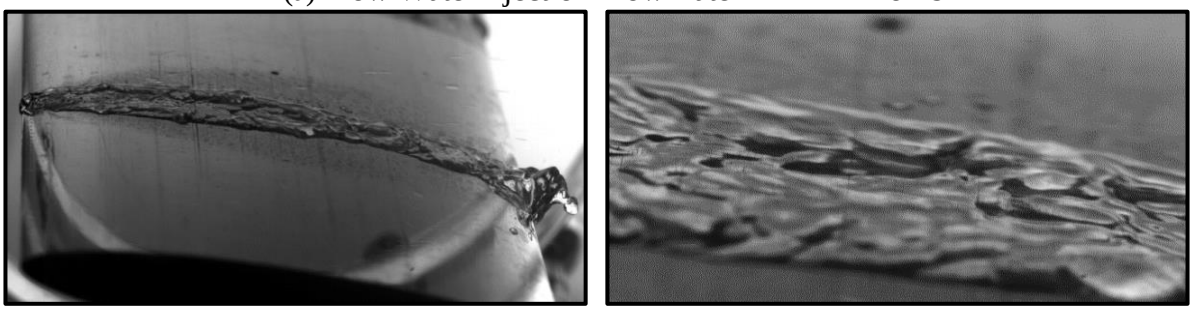

(b) Low Water Ejection Flow Rate – $MFR \approx 20$

Far View Close View

Figure 4.59 – Water film structure at high angle of attack (10-degrees) (Case B – Air Velocity 30 m/sec)

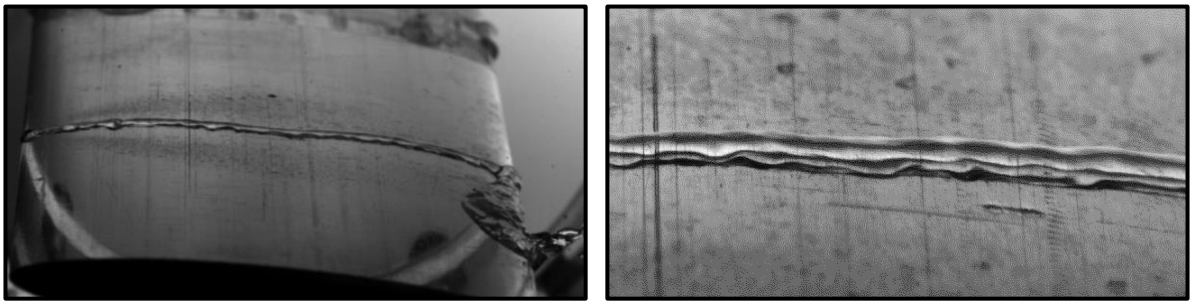

(a) Low Water Ejection Flow Rate – $MFR \approx 4.5$

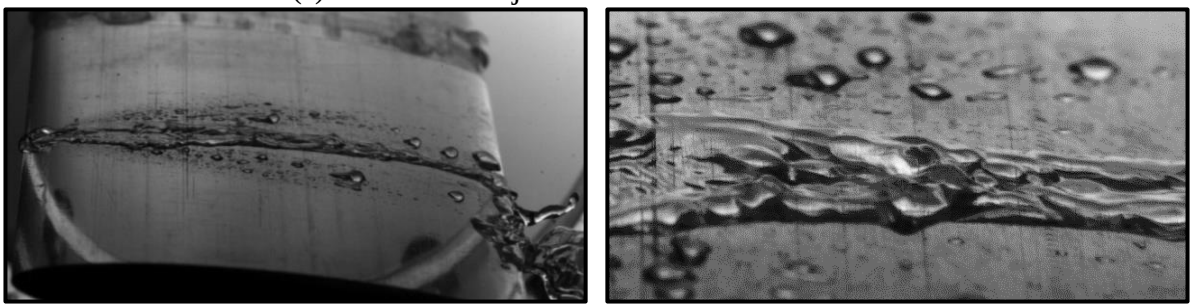

(b) Low Water Ejection Flow Rate – $MFR \approx 13.5$

Far View Close View

Figure 4.60 – Water film structure at low angle of attack (3-degrees) (Case C – Air Velocity 25 m/sec)

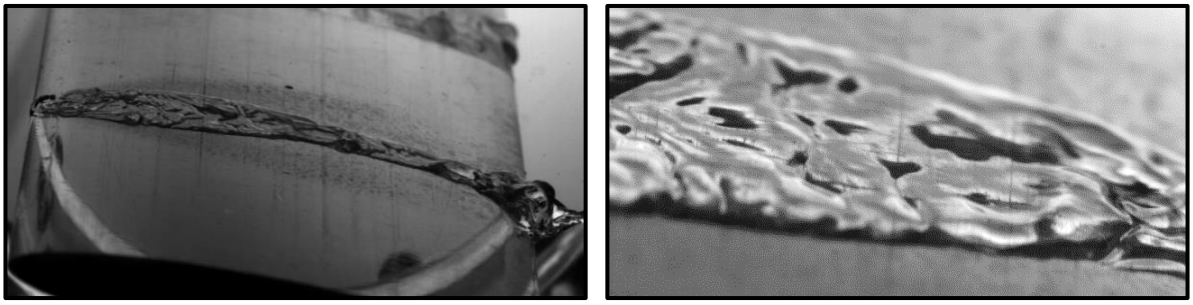

(a) Low Water Ejection Flow Rate – $MFR \approx 6.75$

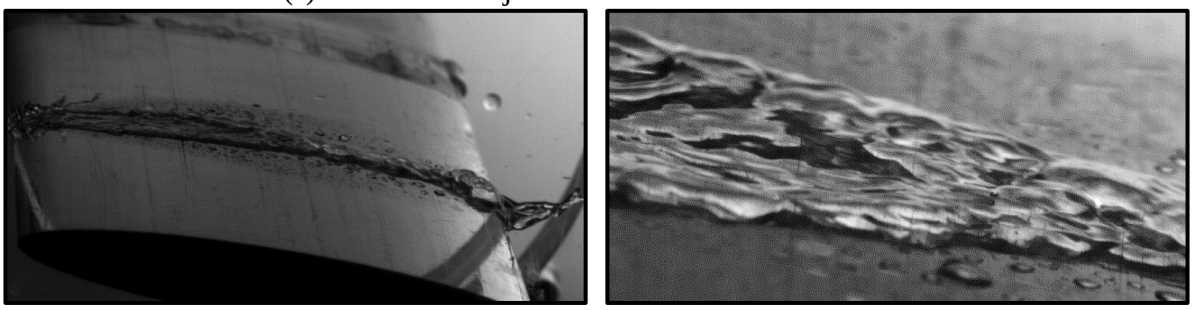

(b) Low Water Ejection Flow Rate – $MFR \approx 21.35$

Far View Close View

Figure 4.61 – Water film structure at high angle of attack (10-degrees) (Case C – Air Velocity 25 m/sec)

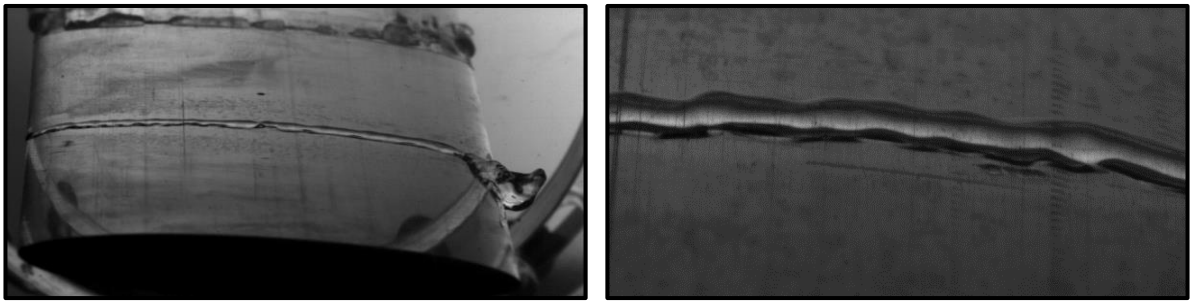

(a) Low Water Ejection Flow Rate – $MFR \approx 4.5$

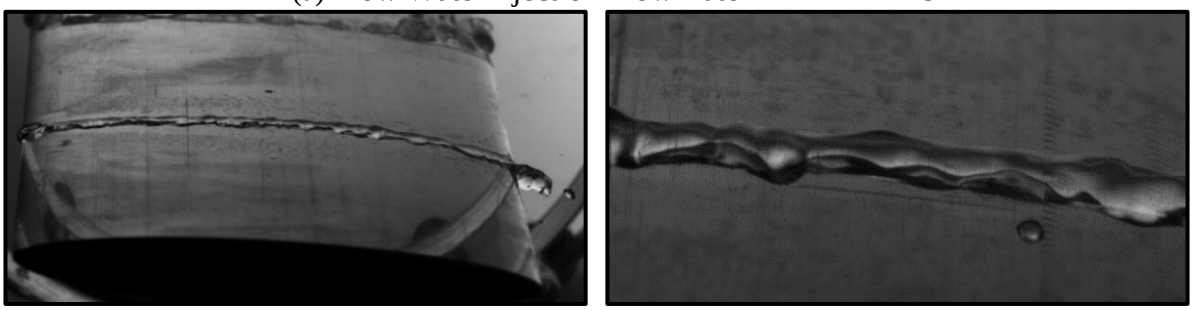

(b) Low Water Ejection Flow Rate – $MFR \approx 11.2$

Far View Close View

Figure 4.62 – Water film structure at low angle of attack (3-degrees) (Case D – Velocity 20 m/sec)

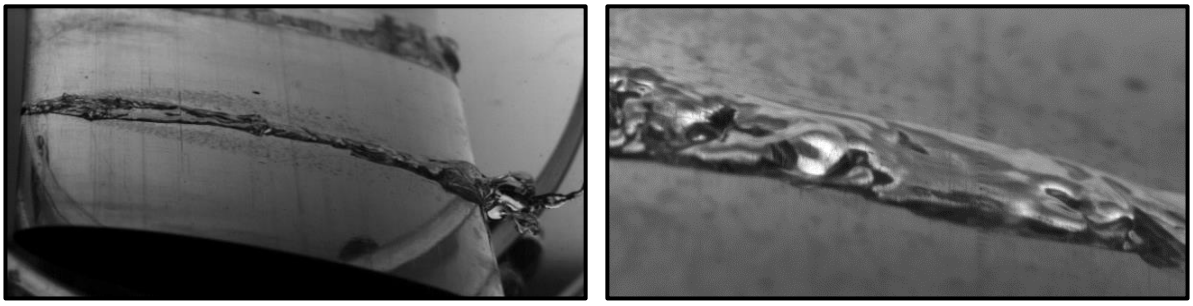

(a) Low Water Ejection Flow Rate – $MFR \approx 4.5$

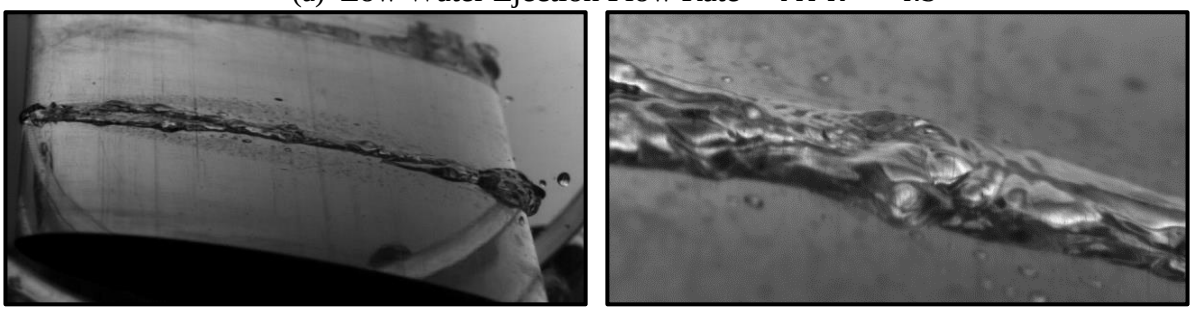

(b) Low Water Ejection Flow Rate – $MFR \approx 13.5$

Far View Close View

Figure 4.63 – Water film structure at high angle of attack (10-degrees) (Case D – Air Velocity 20 m/sec)

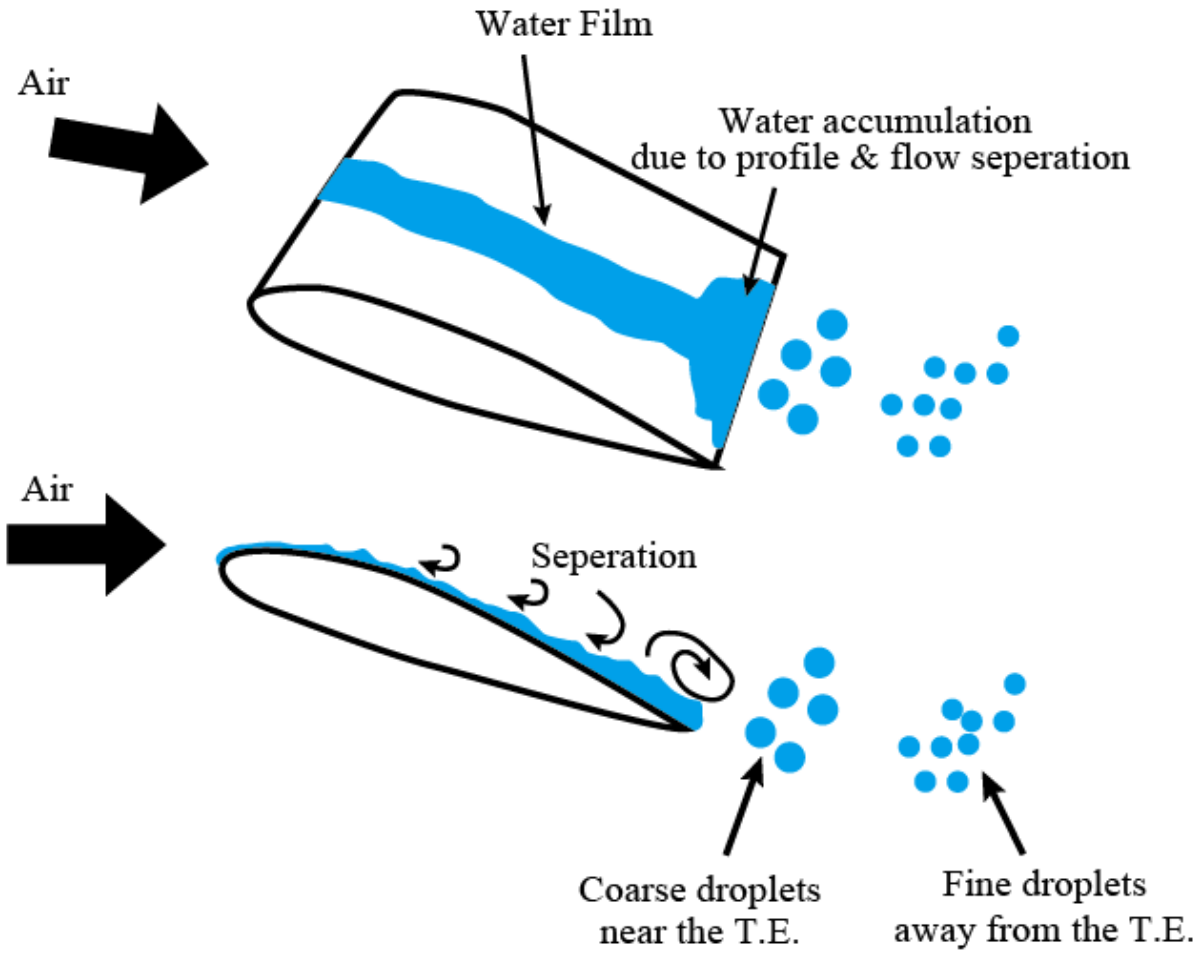

Figure 4.64 – Schematics of water film formation and droplets size distribution at High Angle of Attack

4.7.2. Water film Velocity at High AOA

For higher AOA, the water film thickness was quantitatively measured in an exactly the similar way as that of the 0-degree incident case, Section 4.3. Figure 4.65 shows the film velocity measurement at the mid-chord position at different AOA of the blade. It was recognized from Fig. 4.65 that the film velocity decreases with incrementing AOA, which was attributed due to the flow separation on the S.S. of the blade, which is shown schematically in Fig. 4.54.

4.7.3. Liquid Film Thickness

Figure 4.66 (a – d) shows the water film height for 3-, 5-, 7-, and 10- degree for Case A to Case D. As expected, for a particular AOA, the water film height increases with an increase in flow rate whereas it decreases with an increase in air momentum and vice versa. The surge in film height was due to the flow separation from the blade's surface, resulting in lowering the air velocity over blade surface and leading to the weakening of aerodynamic forces. Similarly, Fig. 4.67 shows the Reynolds number of the film based on the film thickness calculated at the mid-chord of the blade, which is of order 2 and seems to be reasonable under the given flow conditions. The Reynolds number is maximum for Case D due to the greater film thickness compared to the other cases. Figure 4.68 illustrate the water film height to width ratio at an AOA of 3-, 5-, 7- and 10-degrees respectively. The ratio of film height to width remains nearly the same at a particular angle and air flow conditions due to the similar effects of aerodynamic forces and surface tension forces as been explained in Section 4.3 and schematically represented by Fig. 4.15 and 4.16.

Figure 4.69 compares the water film thickness at various air momentum conditions used in the present study. In all the four cases the water film height was recognized to maximize at 3-degree. This is thought to be chiefly due to the effect of aerofoil shape generating optimal flow conditions at this angle. From Fig. 4.69, as the AOA increases the corresponding film height decreases due to flow separation. The maximum height was quantitatively observed for low air momentum conditions (Case D) whereas high air momentum conditions (Case A) tends to the minimum height.

Figure 4.70 summarizes the water film height to width ratio for Case A, Case B, Case C and Case D. Like film height, the film height to width ratio also get maximize at 3-degree for all the air velocity cases and afterwards starts to decline with an increment in the AOA. Table 4.4 summarizes the film height to width ratio, indicating the maximum value recorded for the Case D at 3-degree whereas Case A at 7-degree shows the corresponding minimum value.

Table 4.4 – Average water film height to width ratio

Angle of Attack (degree)	Case A (Air Velocity 40 m/sec)	Case B (Air Velocity 30 m/sec)	Case C (Air Velocity 25 m/sec)	Case D (Air Velocity 20 m/sec)
0	0.073 ± 0.005	0.12 ± 0.008	0.13 ± 0.004	0.22 ± 0.033
3	0.071 ± 0.004	0.13 ± 0.007	0.16 ± 0.01	**0.33** ± 0.009
5	0.023 ± 0.004	0.066 ± 0.006	0.09 ± 0.006	0.19 ± 0.008
7	**0.016** ± 0.007	0.026 ± 0.013	0.026 ± 0.008	0.18 ± 0.01
10	-	0.03 ± 0.009	0.026 ± 0.009	0.095 ± 0.014

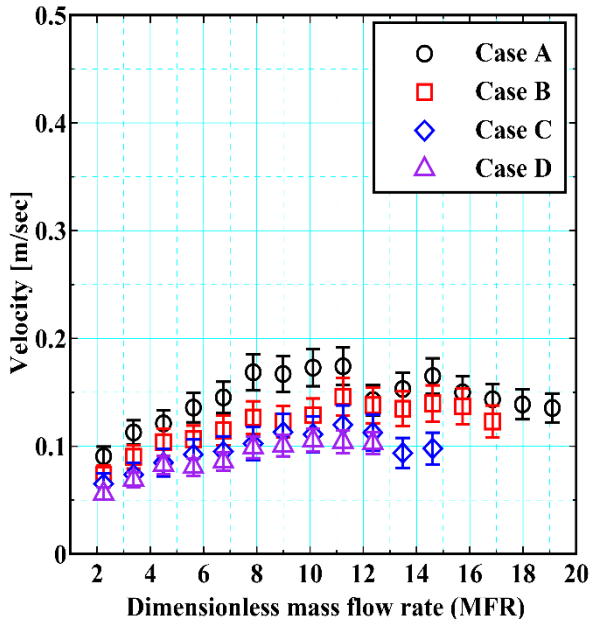

(a) 3 degree

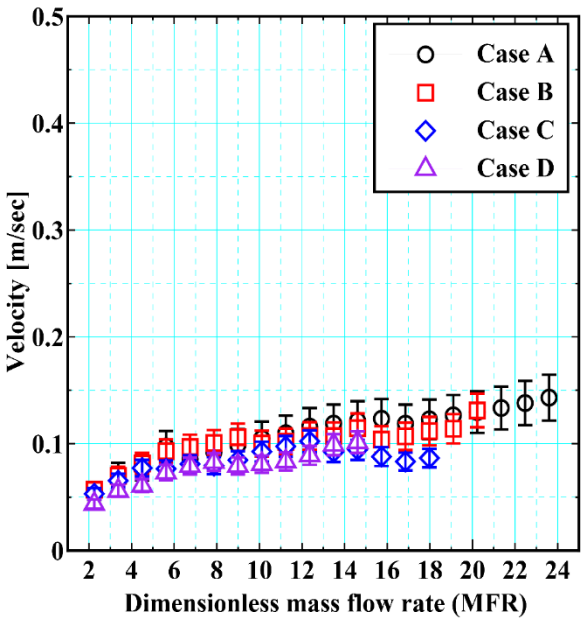

(b) 5 degree

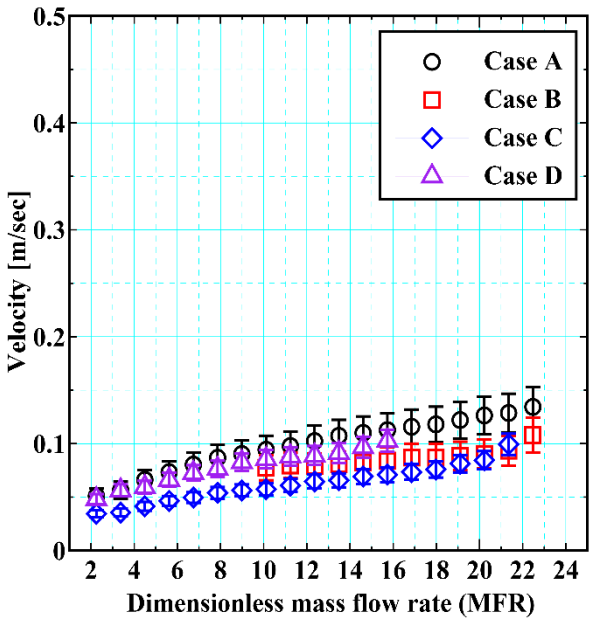

(c) 7 degree

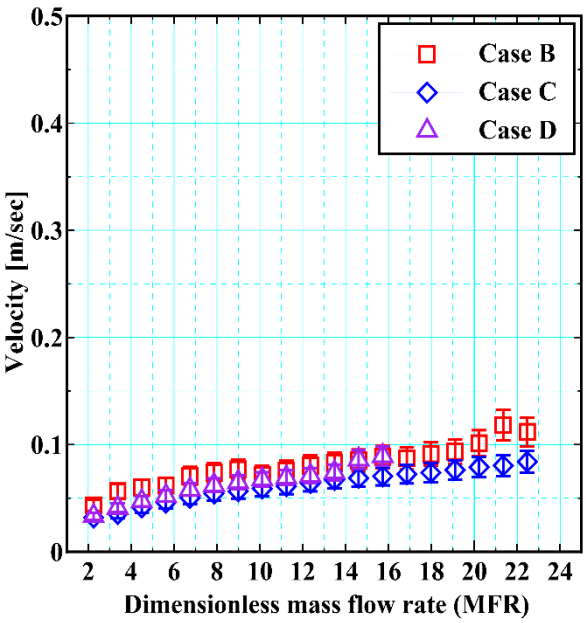

(d) 10 degree

Figure 4.65 – Liquid film velocity @ Mid-Chord (Elliptical Blade)

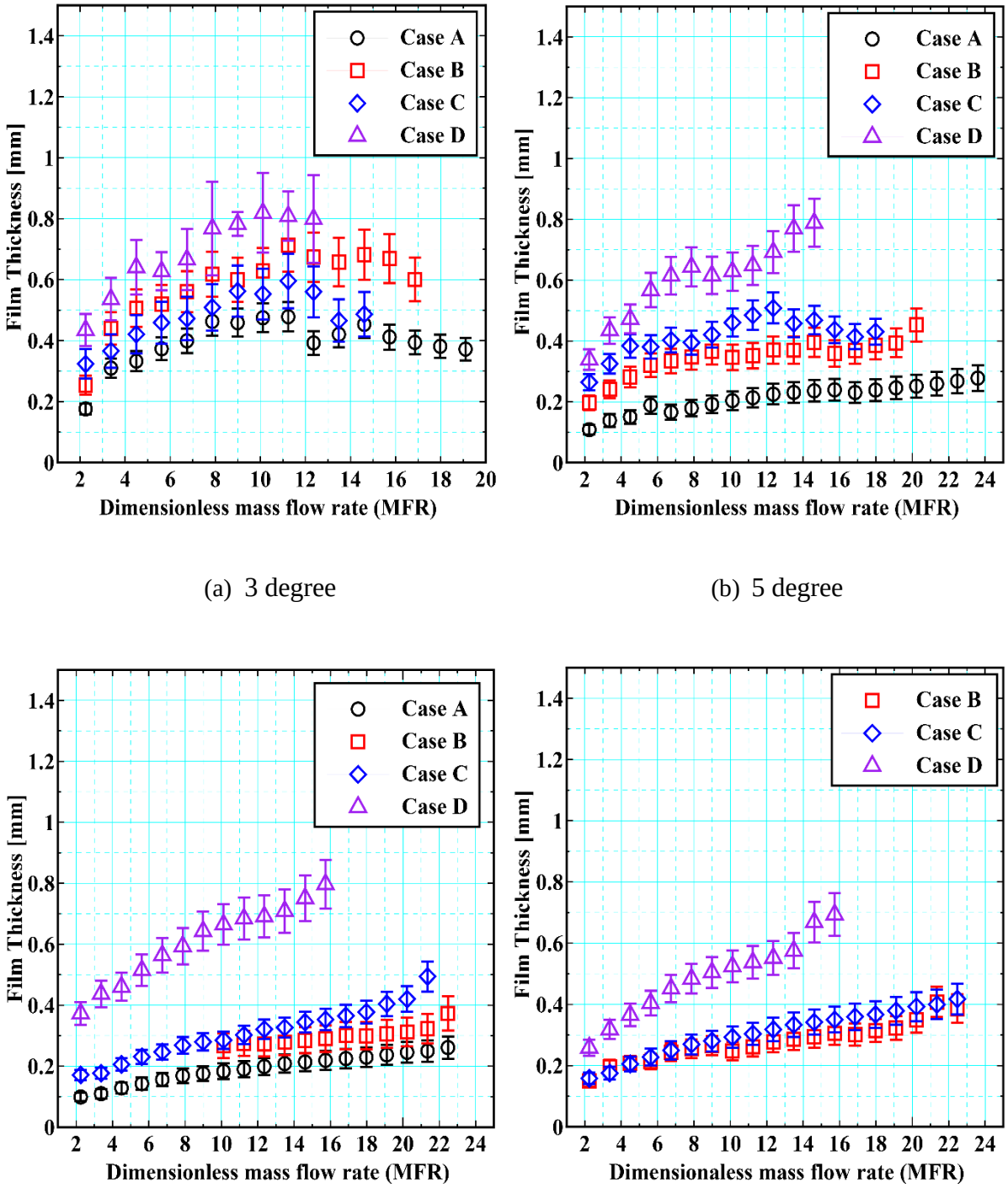

(a) 3 degree

(b) 5 degree

(c) 7 degree

(d) 10 degree

Figure 4.66 – Liquid Film Thickness @ Mid-Chord (Elliptical Blade)

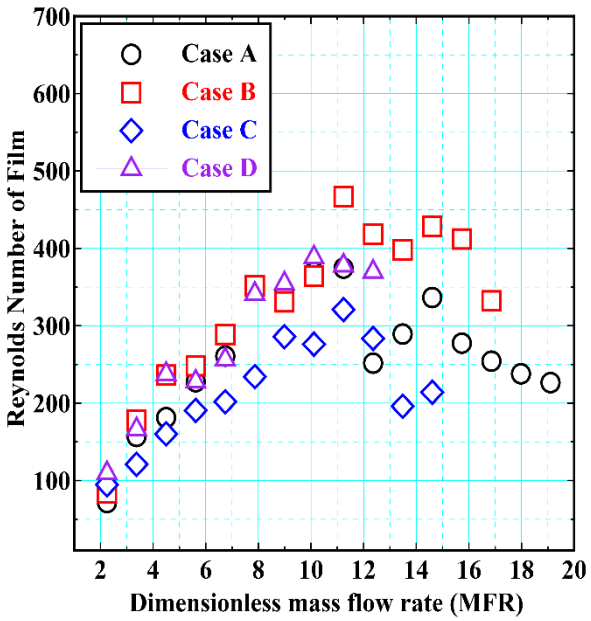

(a) 3 degree

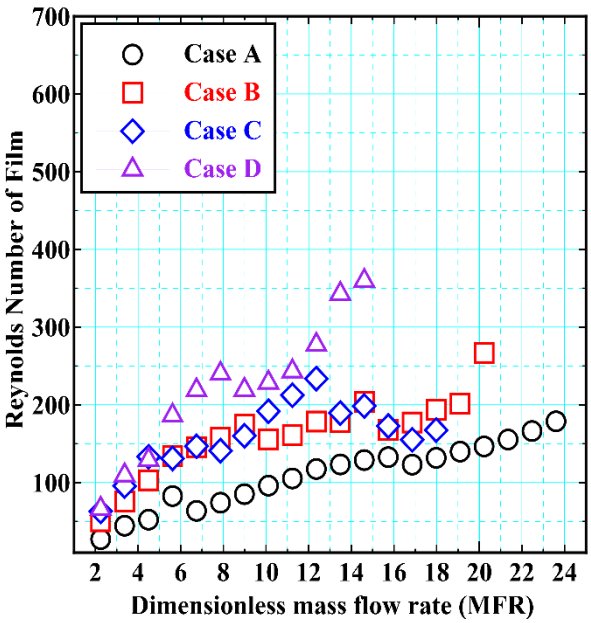

(b) 5 degree

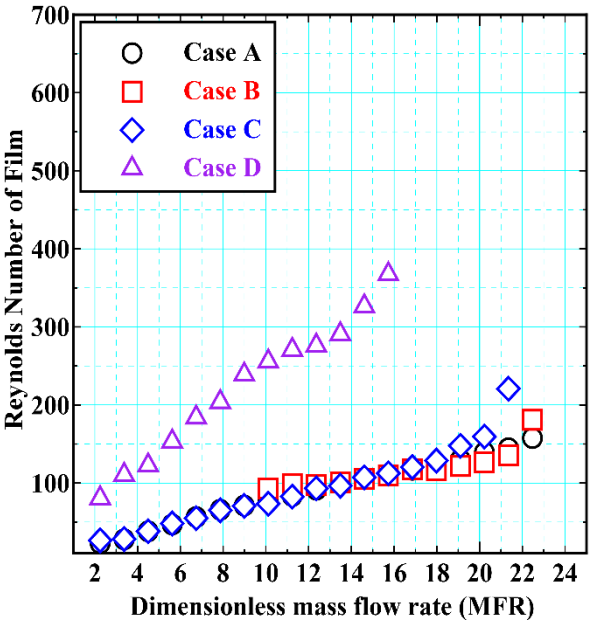

(c) 7 degree

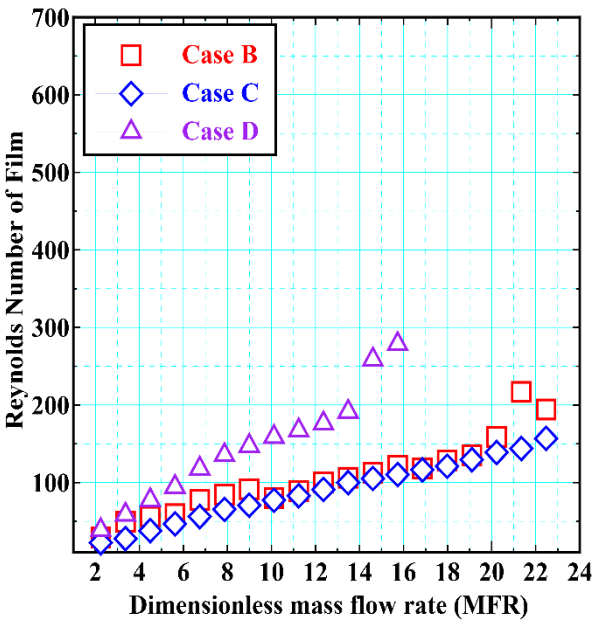

(d) 10 degree

Figure 4.67 – Reynolds number of film (based on film thickness @ mid-chord)

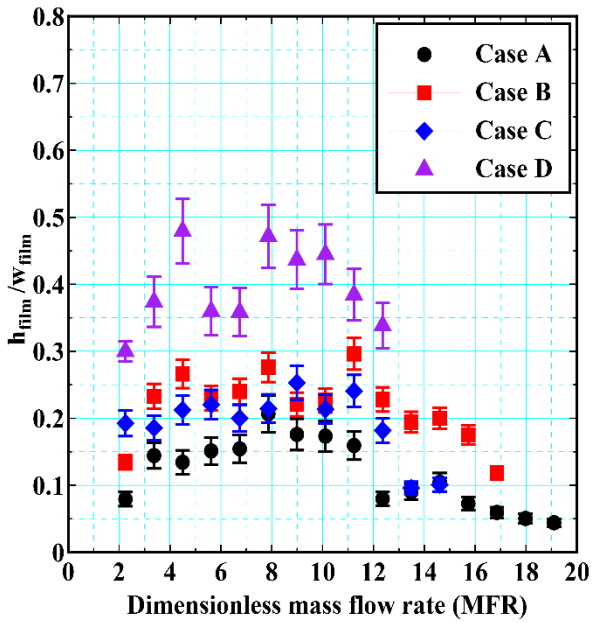

(a) 3 degree

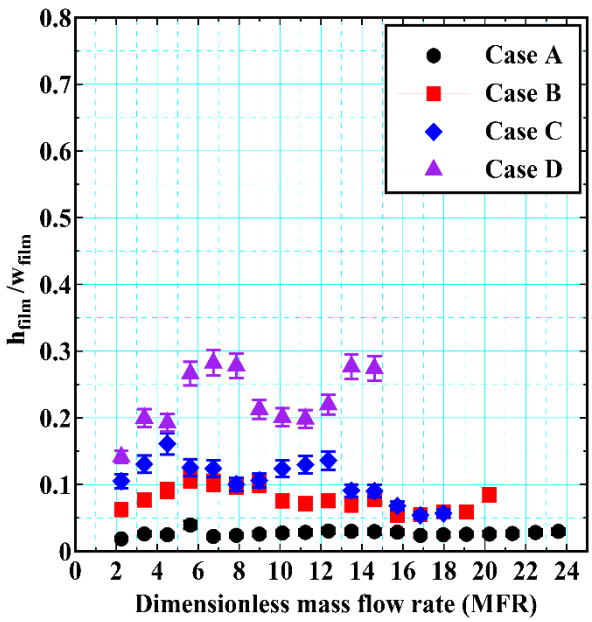

(b) 5 degree

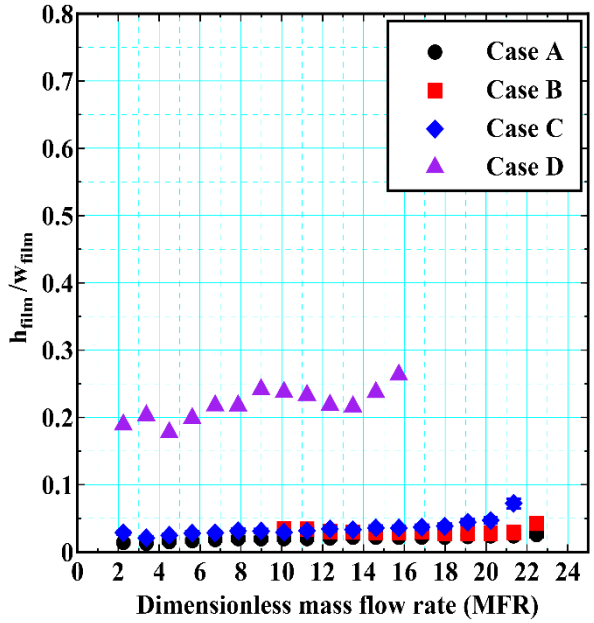

(c) 7 degree

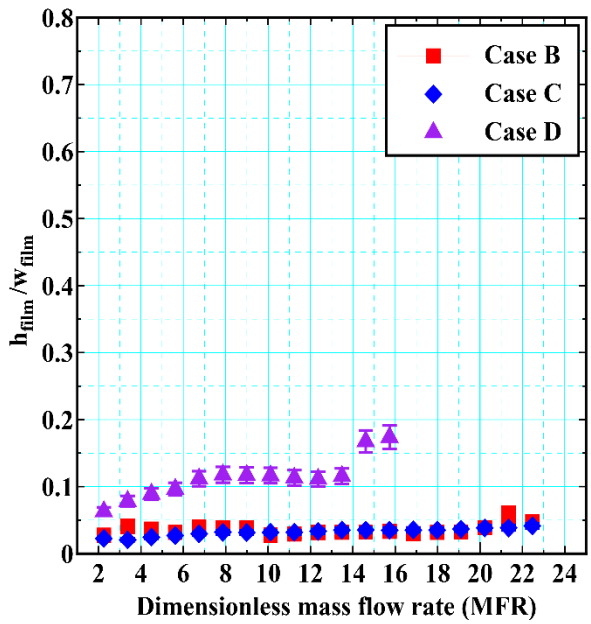

(d) 10 degree

Figure 4.68 – Dimensional Film Thickness @ Mid-Chord (Elliptical Blade)

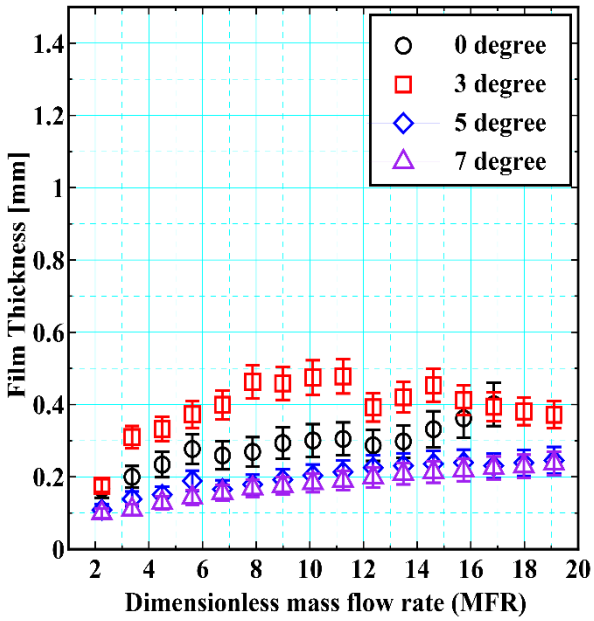

(a) Case A (Air Velocity – 40 m/sec) – $M \approx 192$

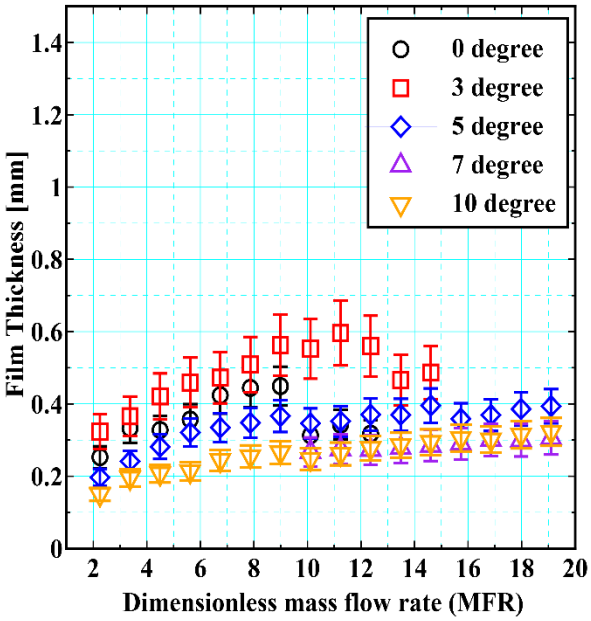

(b) Case B (Air Velocity – 30 m/sec) – $M \approx 108$

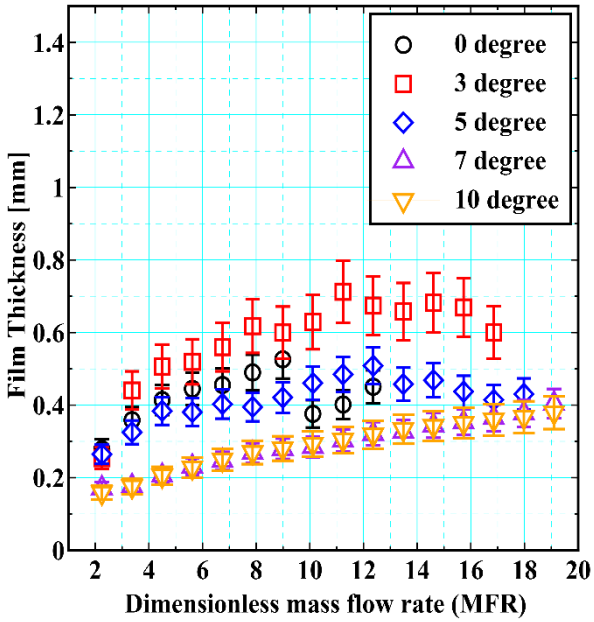

(c) Case C (Air Velocity – 25 m/sec) – $M \approx 75$

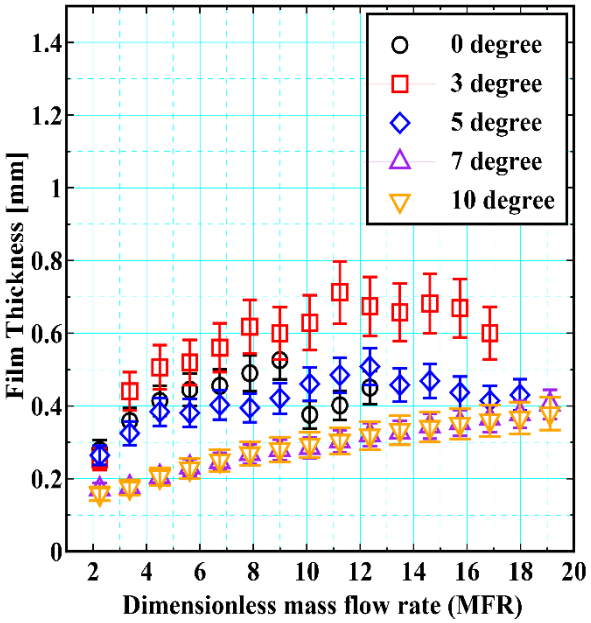

(d) Case D (Air Velocity – 20 m/sec) – $M \approx 48$

Figure 4.69 – Comparison of Film Height under same Air Velocity

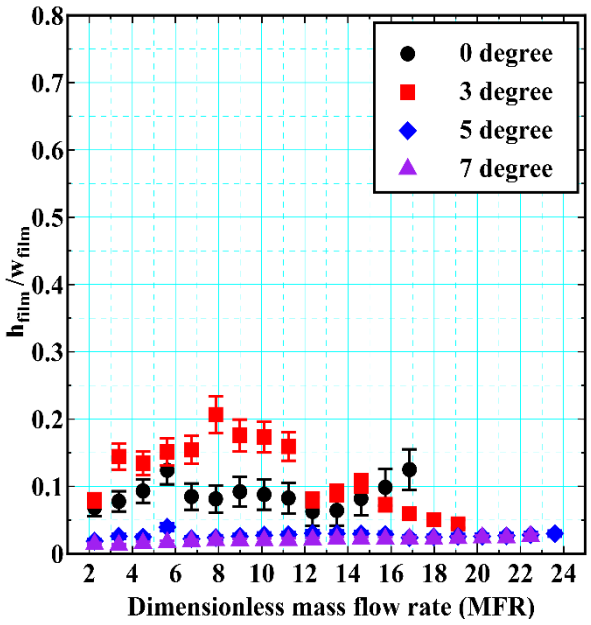

(a) Case A (Air Velocity – 40 m/sec) – $M \approx 192$

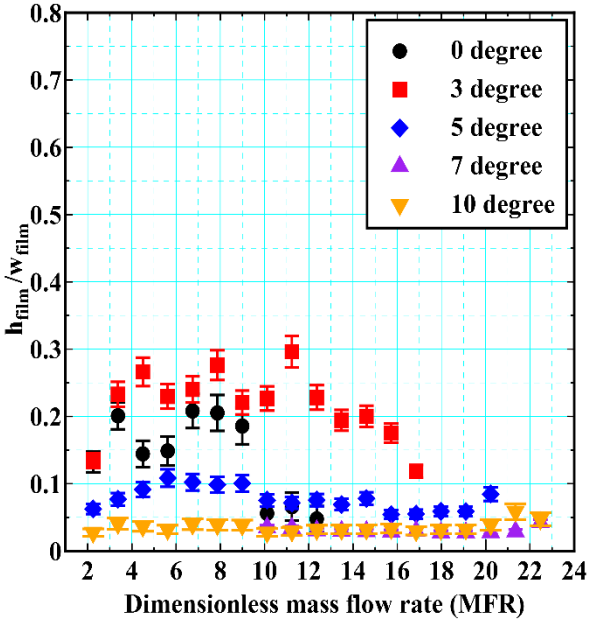

(b) Case B (Air Velocity – 30 m/sec) – $M \approx 108$

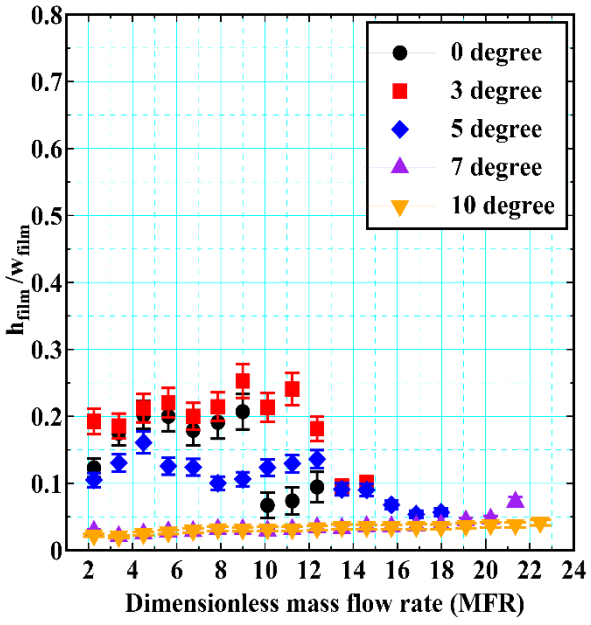

(c) Case C (Air Velocity – 25 m/sec) – $M \approx 75$

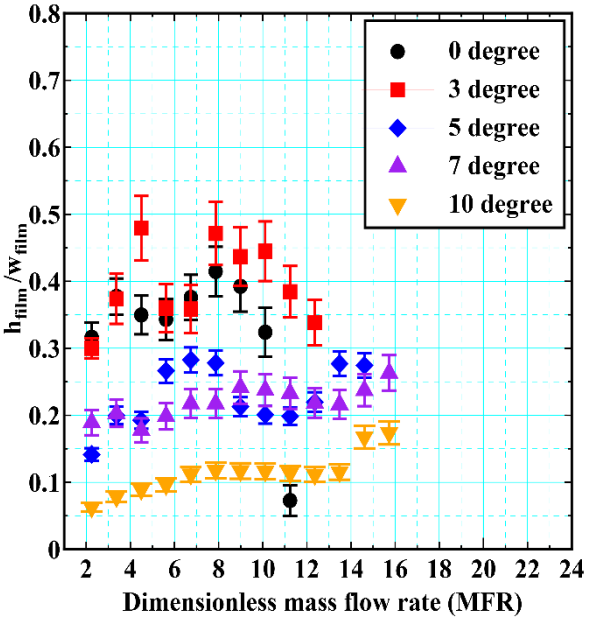

(d) Case D (Air Velocity – 20 m/sec) – $M \approx 48$

Figure 4.70 – Comparison of Film Height to Width ratio

4.8. Characteristics of Droplets Size Distribution aft the T.E. Region (High Angle of Attack)

The flow properties aft the T.E. changes due to the change in the AOA of the blade, consequently transforming the droplets size distribution. From the detailed visualization, it was observed that it took relatively large time for the droplets to shed from the T.E. of the blade, which was caused primarily due to the large flow separation with incrementing AOA, either low or high momentum ratio. Additionally, whatever the momentum ratio is a slight increase in the ligament length and amount of water accumulation was also observed as well as the number of droplets breakup due to the bag mode of breakup also increases.

4.8.1. Flow Visualization

4.8.1.1. High Momentum Case (Case A, Air Velocity 40 m/sec, M ≈ 192) – Dominant Aerodynamic Forces

Figure 4.71 and 4.73 represents the water accumulation and droplets breakup phenomena for the high momentum case at an angle of 3- and 10-degrees respectively. It was observed that the droplets formed became larger in size as the AOA was slightly increase from lower value, Fig. 4.71 (h), to higher value, Fig. 4.73 (l). From the detailed flow visualization, it was observed that due to the flow separation the shedding frequency of the droplets shedding also reduced significantly when compared to the 0-degree case. This results in massive amount of water accumulation at the T.E. of the blade due to the increased effects of flow seperation, as shown in Fig. 4.71 (k) and Fig. 4.73 (j) for an AOA of 3- and 10-degree respectively. When the water reaches its critical amount, the vortex shed from the T.E. (mostly from the P.S.) destabilizes the accumulated water and results in the stripping of large number of droplets from the ligament as well as the bag breakup of the ligaments. Though, the aerodynamic forces were strong enough to strip the droplets from the ligaments, however, an increase in the droplets fragmentation events due to the bag mode of breakup was also observed. The

4.8.1.2. Low Momentum Case (Case D, Air Velocity 20 m/sec, M ≈ 48) – Dominant Surface tension Forces

Figure 4.72 and 4.74 represents the water accumulation and droplets breakup phenomena at low air momentum (Case D) for 3- and 10-degree respectively. A considerably reduction in the droplets shedding frequency was observed, which is primarily due to the dominant effects of the liquid's surface tension property and the flow separation in combined. Due to these combined effects, large amount of water was also observed to be accumulated at the T.E.. At lower AOA (Fig. 4.72) the disintegration of ligament due to the bag breakup from almost at the tip of the T.E., as shown in Fig. 4.72 (b). However, when the AOA was increased to 10-degree the point of ligament formation further moved upward on the upper surface (S.S.) of the blade, Fig. 4.74 (b), such that even the ligament breakup (due to the bag mode) with its base remained attached at the upper surface of the blade, as shown in Fig. 4.74 (c). Due to stronger surface tension forces combined with low air velocity (due to flow separation), the droplets formed in this case were relatively bigger at each position compared to the 0-degree case. Also with the increasing AOA, the ligament length exceed to as much as nearly 0.75-C (for 10 – degree case), resulting in the formation of primary droplets further away from the T.E..

Like 0 – degree case, the droplets formed for the medium air momentum cases at higher AOA showed an intermediate behaviour of the above two cases.

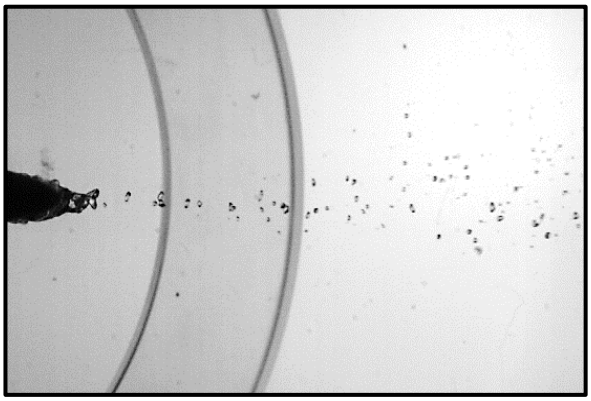

(a) Start of Water Accumulation (0.0 m.sec)

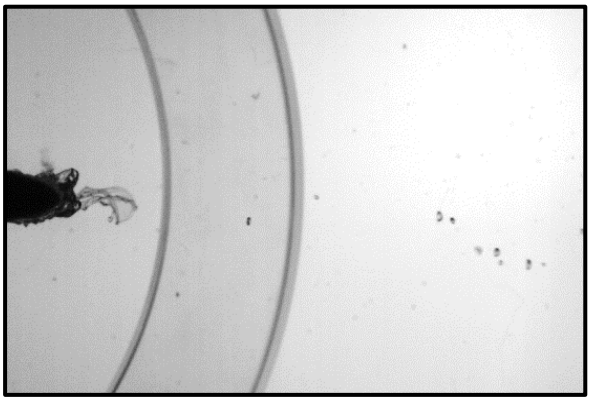

(b) Bag Formation from the tip of T.E. (4.66 m.sec)

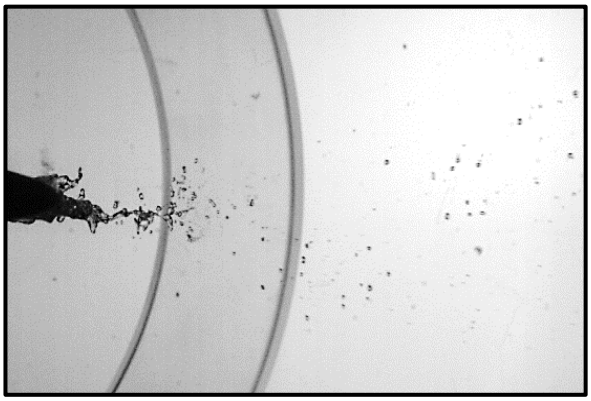

(c) Stripping of Droplets from the Ligament (10.33 m.sec)

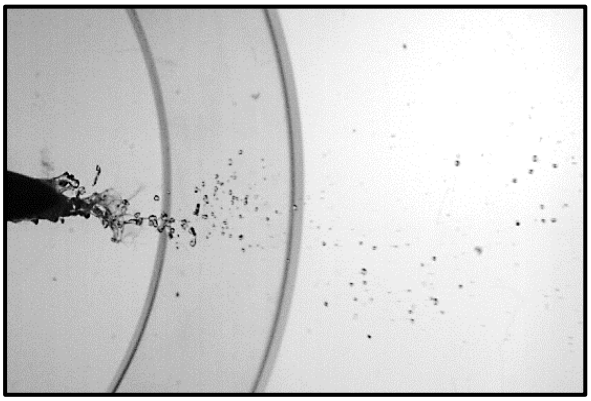

(d) Stripping of Droplets from Surface Wave (11 m.sec)

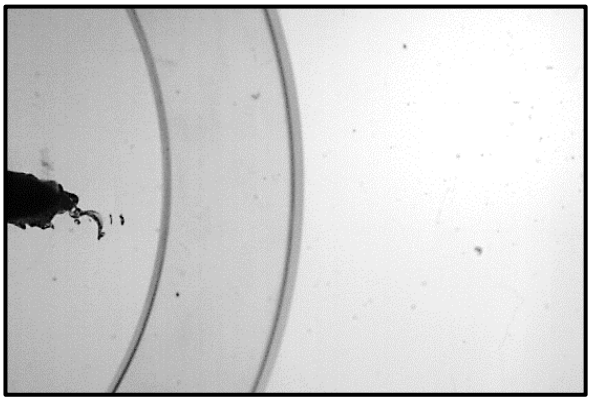

(e) Bag Formation due to Vortex shedding (28 m.sec)

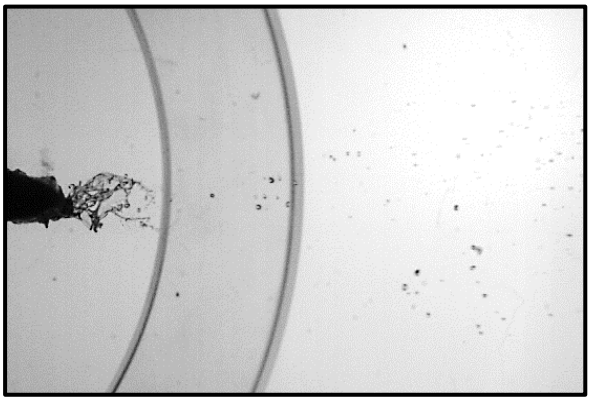

(f) Accumulated Water moves upward due to vortex (32.33 m.sec)

Figure 4.71 – Breakup and Atomization aft the T.E. – 3 degrees - Case A (Velocity 40 m/sec) – ($M \approx 192,\ We_a \approx 60, MFR = 16.85$) (1/2)

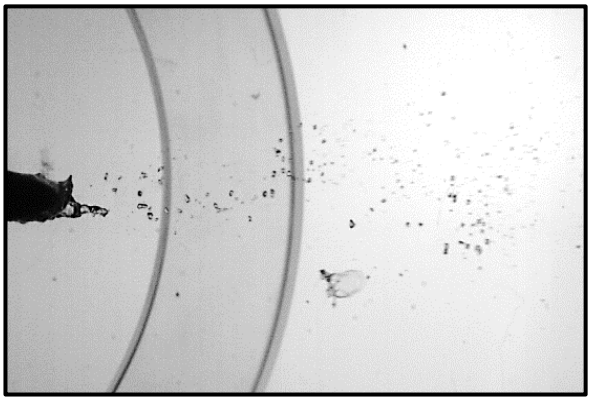

(g) Bag Breakup of coarse droplet just after 0.5-C (31 m.sec)

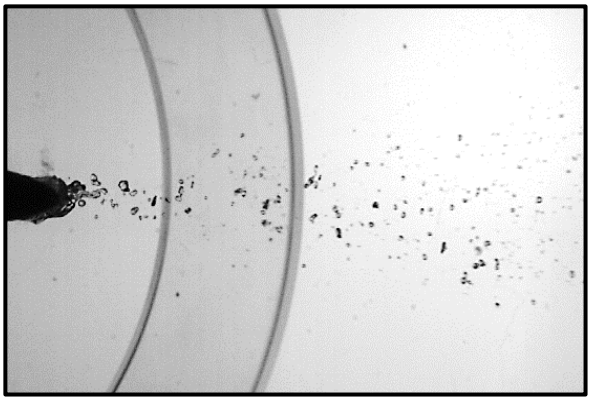

(h) Karman Vortex Street of Droplets (88 m.sec)

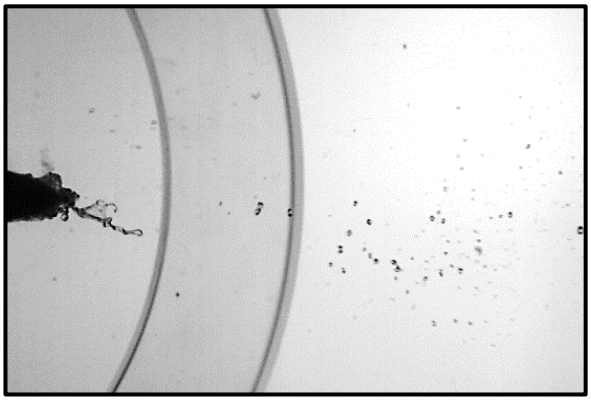

(i) Stretching of Ligament & Accumulation of water at T.E. (94.33 m.sec)

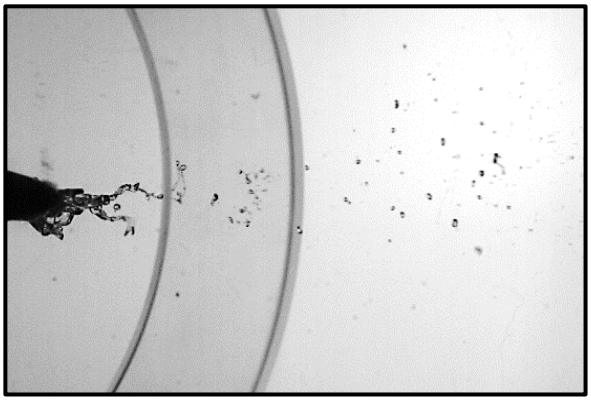

(j) Start of disintegration of large amount of water accumulated (126 m.sec)

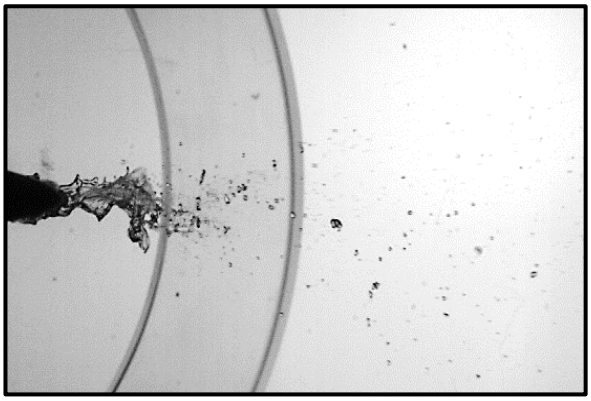

(i) Disintegration of water from T.E. (131 m.sec)

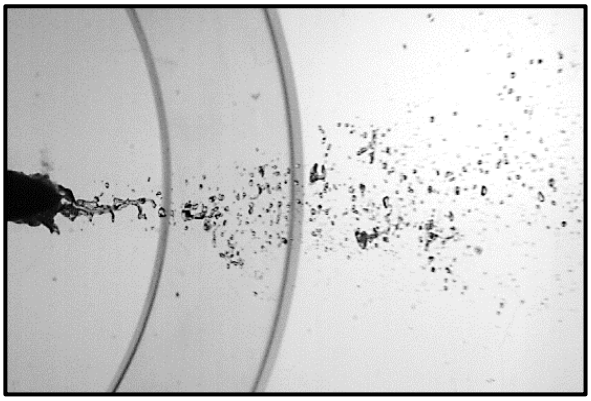

(l) Fine & Coarse Droplets Formation (135.66 m.sec)

Figure 4.71 – Breakup and Atomization aft the T.E. – 3-degrees - Case A (Velocity 40 m/sec) – ($M \approx 192,\ We_a \approx 60, MFR = 16.85$) (2/2)

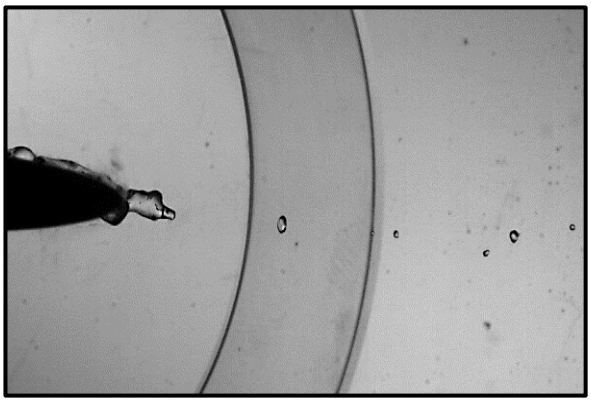

(a) Start of Water Accumulation (0.0 m.sec)

(b) Start of Bag Formation from the ligament (13 m.sec)

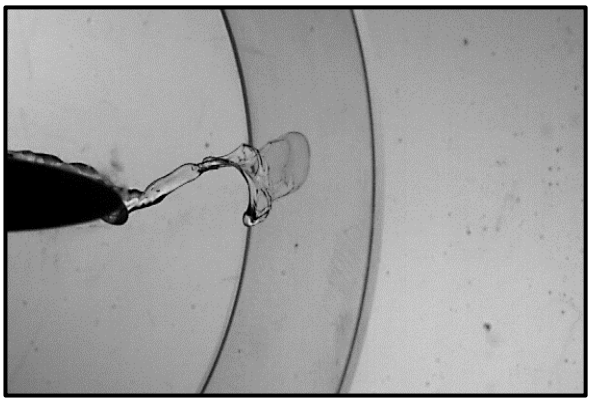

(c) Bag formation & elongation of ligament due to vortex (15.33 m.sec)

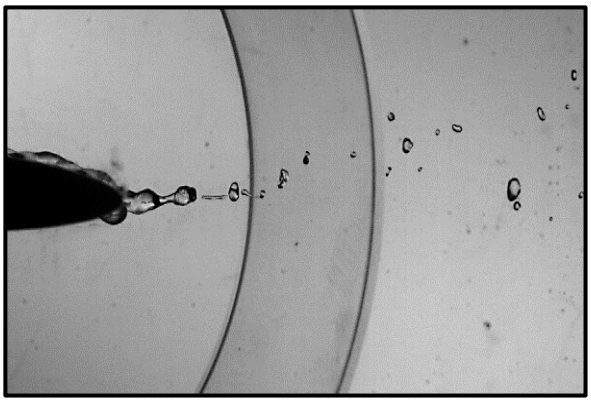

(d) Destabilization of thick ligament & coarse droplets formation (24.66 m.sec)

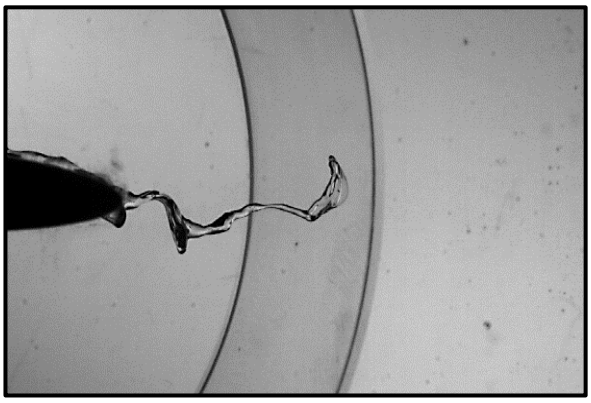

(e) Elongated ligament with destabilization due to vortex (73 m.sec)

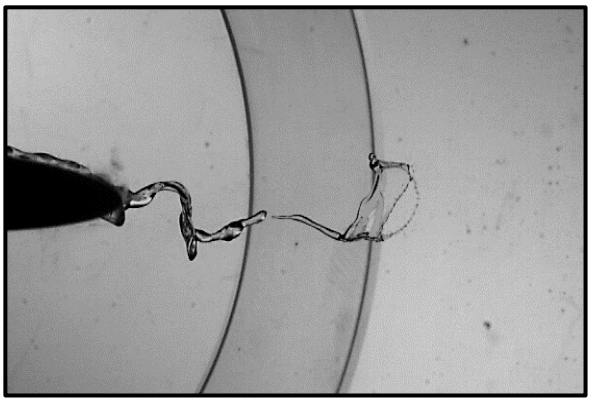

(f) Bag Formation due to vortex (74.33 m.sec)

Figure 4.72 – Breakup and Atomization aft the T.E. – 3-degrees - Case D (Velocity 20 m/sec) – ($M \approx 48, We_a \approx 15, MFR = 11.24$) (1/2)

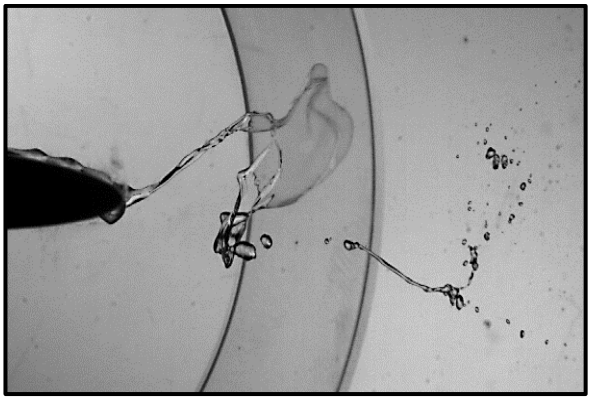

(g) Bag Breakup of ligament just under 0.5-C (77.33 m.sec)

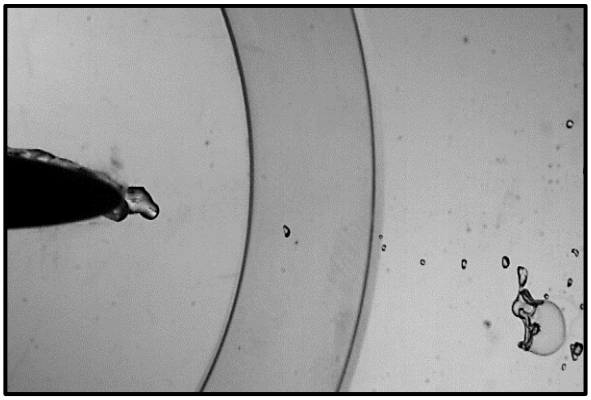

(h) Breakup of coarse droplets near 1-C (90 m.sec)

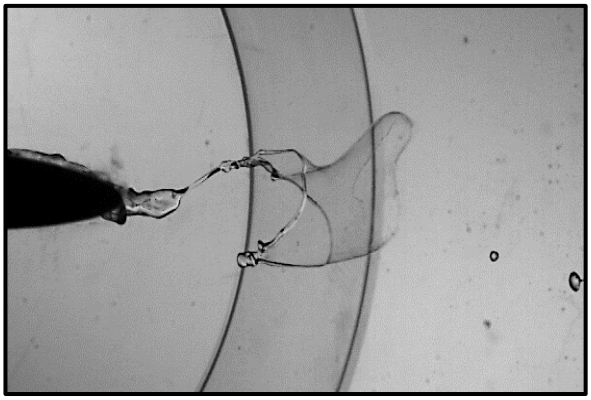

(i) Bag formation of ligament slightly greater than 0.5-C (122.33 m.sec)

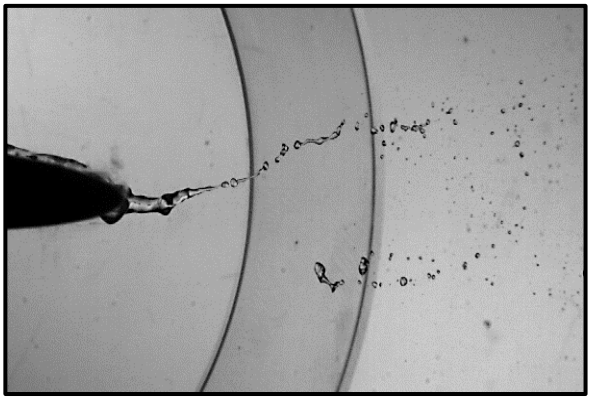

(j) Fine & coarse droplets (125.33 m.sec)

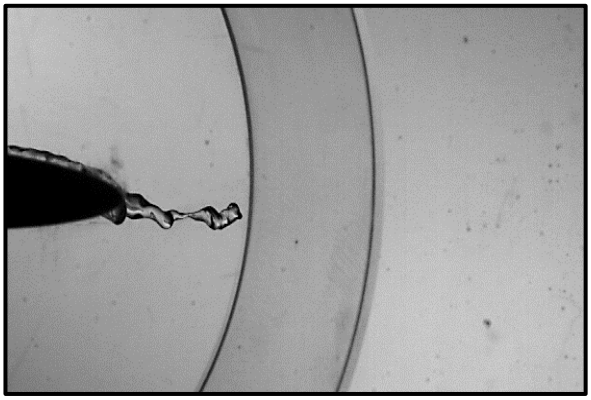

(k) Breakup of coarse droplets from the tip of ligament (151.66 m.sec)

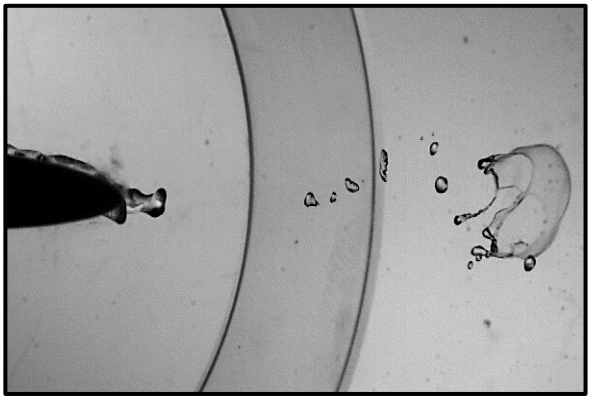

(l) Bag breakup of coarse droplets (169.33 m.sec)

Figure 4.72 – Breakup and Atomization aft the T.E. – 3-degrees - Case D (Velocity 20 m/sec)– ($M \approx 48, We_a \approx 15, MFR = 11.24$) (2/2)

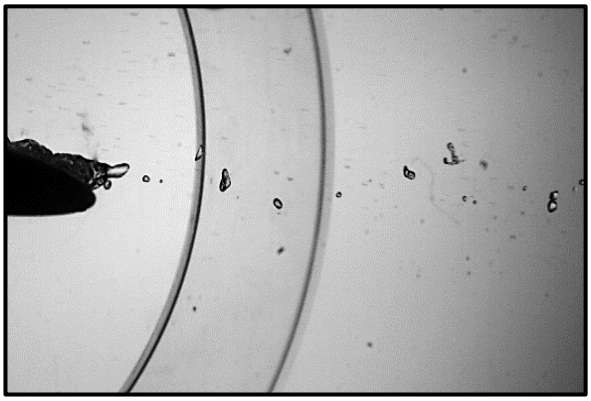

(a) Start of Water Accumulation (0.0 m.sec)

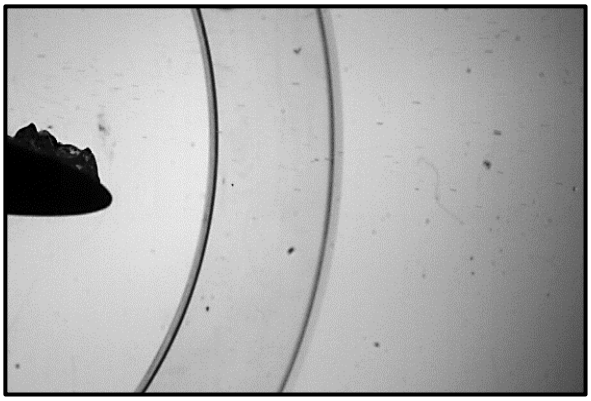

(b) Accumulation of large amount of water (18.66 m.sec)

(c) Ligament Formation (35.33 m.sec)

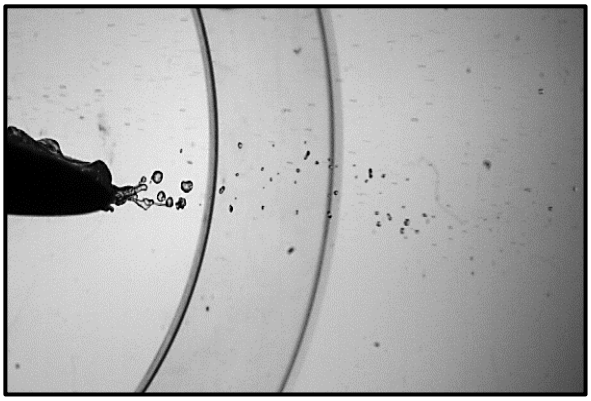

(d) Stripping of coarse droplets from T.E. due to vortex (42 m.sec)

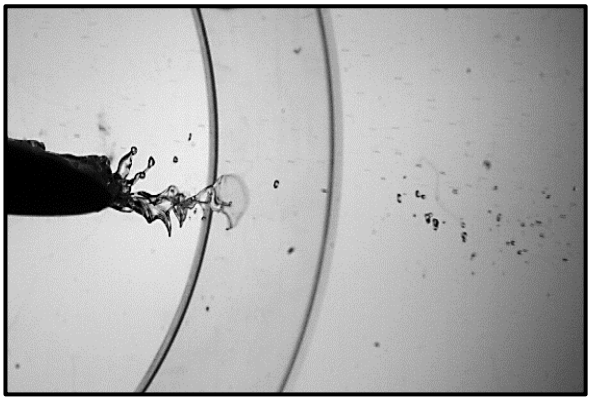

(e) Bag Breakup due to vortex (66.33 m.sec)

(f) Disintegration of accumulated water at T.E. due to vortex shedding (68 m.sec)

Figure 4.73 – Breakup and Atomization aft the T.E. – 10-degrees - Case A (Velocity 40 m/sec) – ($M \approx 192, We_a \approx 60, MFR = 20$) (1/2)

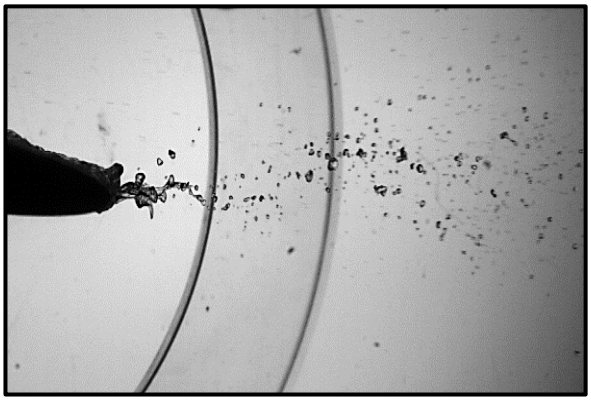

(g) Karman Vortex Street of droplets (71.66 m.sec)

(h) Stripping of droplets from T.E. (75.66 m.sec)

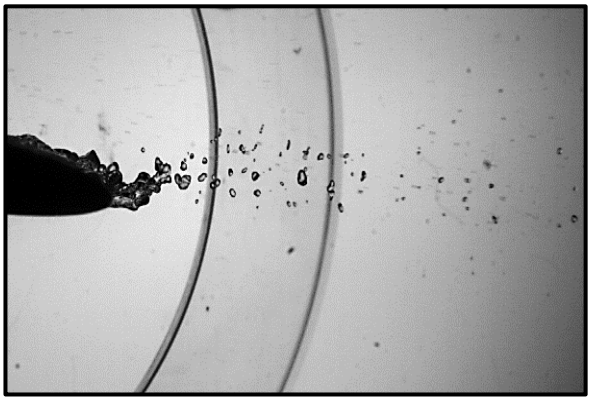

(i) Coarse droplets (99.33 m.sec)

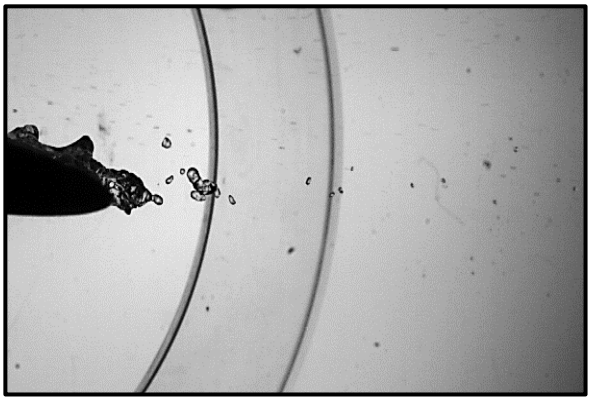

(j) High speed surface wave accumulation at T.E. (155.66 m.sec)

(k) Disintegration of large chunk of accumulated water (176.33 m.sec)

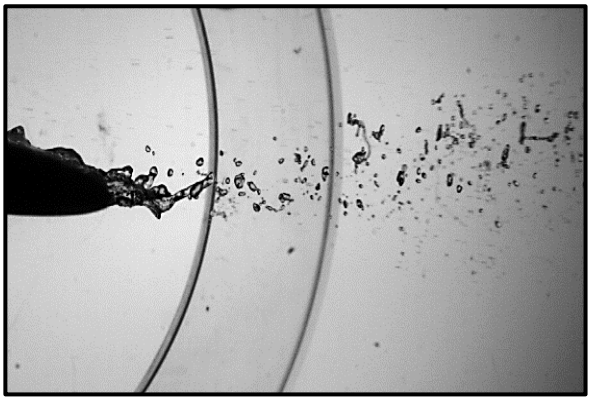

(l) Fine & Coarse Droplets in Karman Vortex Street (176.66 m.sec)

Figure 4.73 – Breakup and Atomization aft the T.E. – 10-degrees - Case A (Velocity 40 m/sec) – ($M \approx 192, We_a \approx 60, MFR = 20$) (2/2)

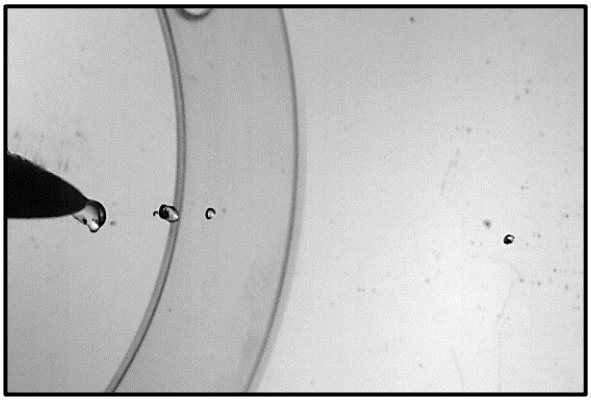

(a) Start of Water Accumulation at T.E. (0.0 m.sec)

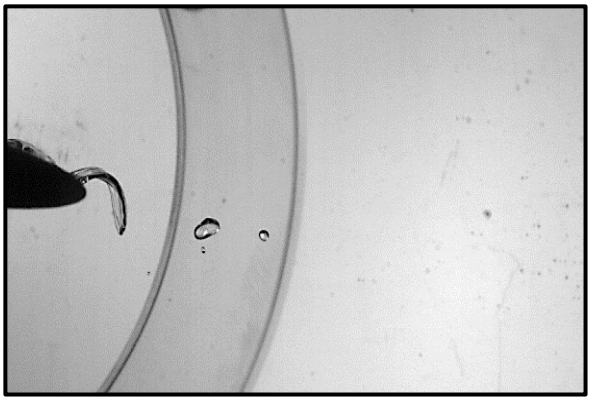

(b) Start of bag formation with tip at S.S. (6.66 m.sec)

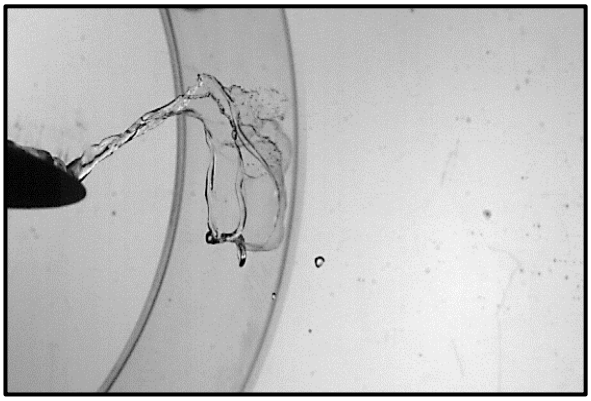

(c) Bag breakup with tip of ligament at S.S. (11.33 m.sec)

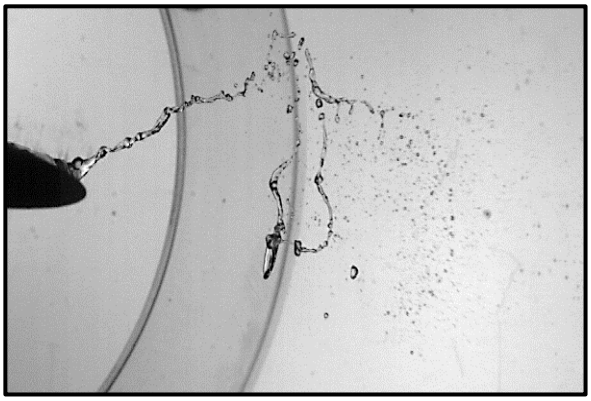

(d) Coarse & fine droplets formation due to bag breakup (13.33 m.sec)

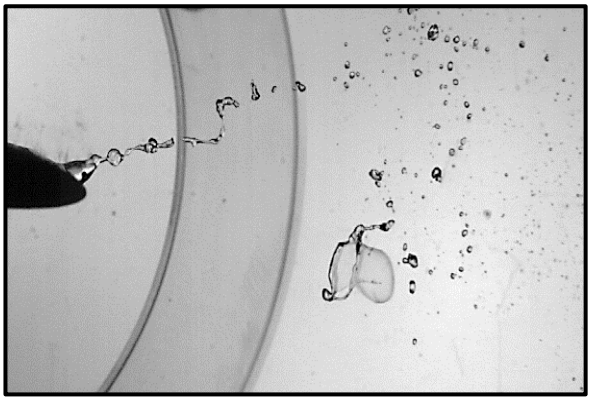

(e) Bag Breakup of coarse droplets (16 m.sec)

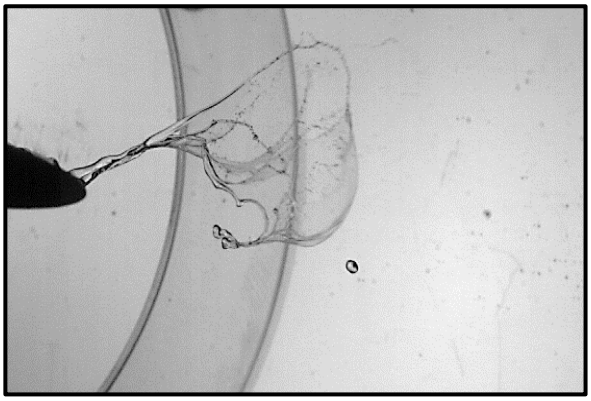

(f) Bag formation beyond 0.5-C (40 m.sec)

Figure 4.74 – Breakup and Atomization aft the T.E. – 10-degrees - Case D (Velocity 20 m/sec) – ($M \approx 48, We_a \approx 15, MFR = 13.5$) (1/2)

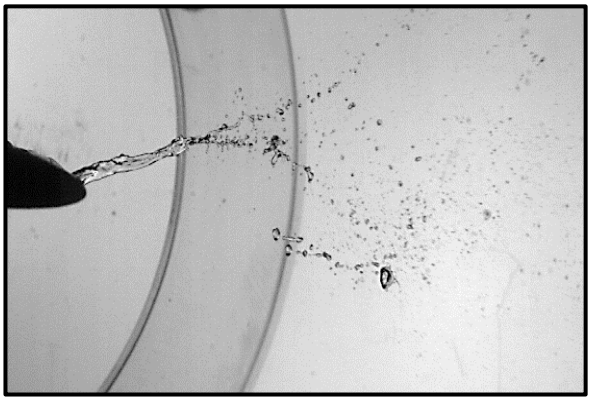

(g) Bag Breakup of ligament (41.66 m.sec)

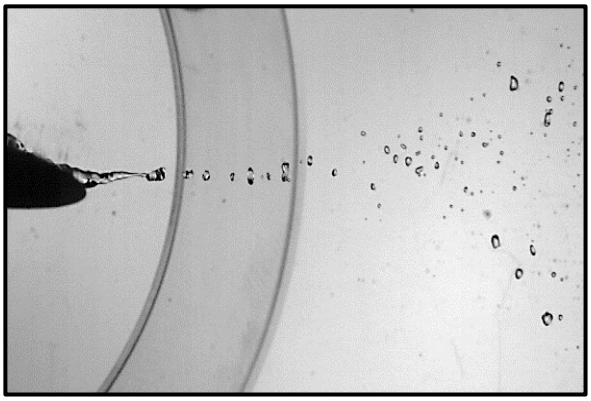

(h) Coarse droplets aft the T.E. (47 m.sec)

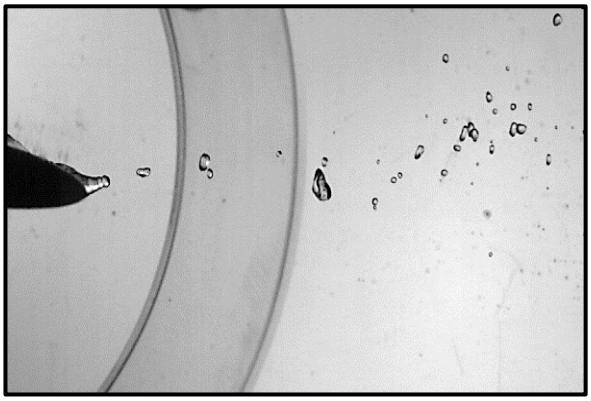

(i) Coarse droplets aft the T.E. (117.66 m.sec)

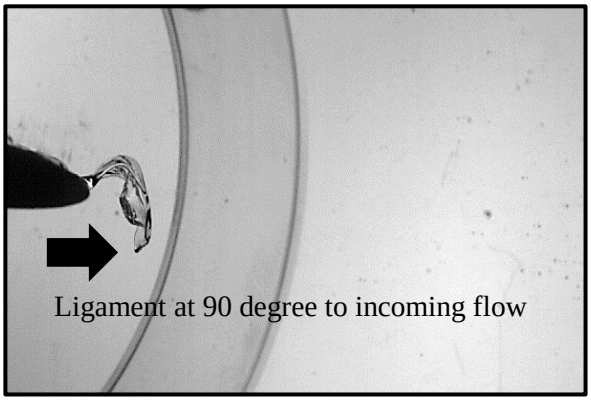

(j) Start of bag formation (164.33 m.sec)

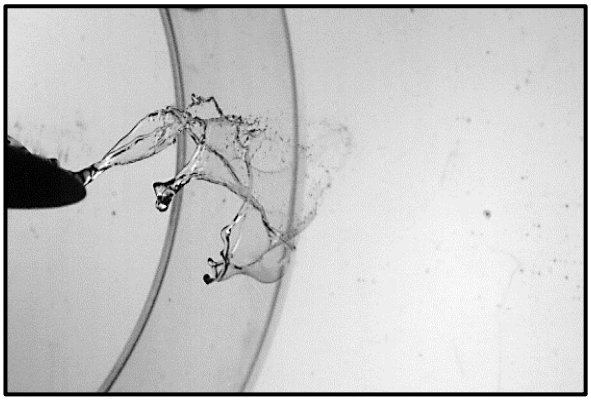

(k) Multiple Bag Breakup of ligament from T.E. (167.33 m.sec)

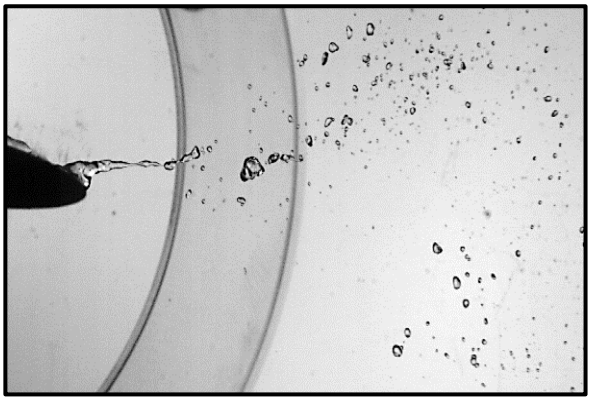

(l) Fine & Coarse Droplets (172.33 m.sec)

Figure 4.74 – Breakup and Atomization aft the T.E. – 3-degrees - Case D (Velocity 20 m/sec) – ($M \approx 48, We_a \approx 15, MFR = 13.5$) (2/2)

4.8.2. Droplets Size Distribution

The droplets size distribution aft the T.E. of the blade was conducted in a similar way as that of 0-degree AOA case. Droplets size were measured at 0.25-, 0.5-, 0.75- and 1-C downstream of the T.E. as shown in Fig. 3.29 and the same criteria were applied as already explained in Section 3.9. Except the number of droplets counted was relatively few in numbers (around 7000 – 10,000 on average) as it took a long time for the ligaments to form and breakup because of flow separation. Figure 4.75, 4.78, 4.81 and 4.84 shows the experimentally measured D10 and D32 droplets size for an AOA of 3-, 5-, 7-, and 10-degree respectively. Similarly, Fig. 4.76, 4.79, 4.82 and 4.85 shows the summarize results for D10 size distribution and Fig. 4.77, 4.80, 4.85 and 4.86 show the summarize results for D32 size distribution at 3-, 5-, 7-, and 10-degree respectively. Like the 0-degree case, the droplets size distribution exhibits a similar pattern at higher AOA, i.e., the droplets were greater in size near the T.E., which decreases as the distance aft the T.E. increased. Also, the droplets size distribution for a particular air momentum and AOA remained the same due to the uniform slip velocity between the droplets and air particles. The summarized D10 (Fig. 4.76, 4.79, 4.82 and 4.85 at 3-, 5-, 7-, and 10 degree respectively) and D32 (Fig. 4.77, 4.80, 4.85 and 4.86 at 3-, 5-, 7-, and 10-degree respectively) droplets distribution formed near the T.E., i.e. at 0.25-C is large compared to the other positions. Furthermore, from summarized D10 and D32 droplets size distribution, the primary droplets formed near the T.E. (0.25-C) in Case of high air momentum (Case A) are smaller than that of low air momentum cases (Case D), which were governed by the aerodynamic forces. Though, with an increase in the AOA, the breakup due to bag mode increases on account of reduced air velocity effects behind the T.E.. Like 0-degree case, the droplets formed near the T.E., at 0.25-C, for high AOA cases (Fig. 4.75, 4.78, 4.81 and 4.84) showed more deviation compared to the other positions aft the T.E. region, which was due to the presence of relatively longer ligaments as well as the high non-circularity of these droplets.

Table 4.5 and Table 4.6 represents the summarized change in the D10 and D32 droplets size distribution with-respect-to the near T.E. field droplets, i.e., at 0.25-C, and with-respect-to the 0-degree angle case. In both the tables, the negative "–" sign corresponds to a decrease, whereas, the positive "+" sign corresponds to an increase in the droplets size. Figure 4.87 and 4.88 summarizes and compares the corresponding D10 and D32 droplets size distribution at each measured position for all the air momentum. From Fig. 4.87 and 4.88, the droplets size increases with an increase in the AOA due to an increase in the velocity deficit aft the T.E. region of the blade. This resulted in the weakening of aerodynamic forces, making the breakup phenomenon to be governed by the surface tension forces, which retained the droplets size to remain large. At each position the D10 and D32 droplets for high air momentum cases (Case A) was always smaller than that of the low momentum cases (Case D), due to prevailing high aerodynamic forces and vice versa. From Table 4.5, in the case of high air momentum (Case A), the near T.E. D10 (0.25-C) droplets size distribution continues to increase to nearly 10% as the AOA is increased from 0 to 10 degree respectively. This is mainly due to an increase in the bag mode of droplets breakup, whereas, for low air momentum speed (Case D), the D10 soared to about 25 % and was greatly affected by the AOA. A similar trend was observed for low momentum case at further downstream position (1-C), whereas, for high momentum case the corresponding droplets size change was not significant as given in Table 4.5 and Table 4.6 respectively.

Figure 4.89 and 4.90 compares the D10 and D32 droplets size distribution for different AOA for a fixed air momentum case. Due to the lessening in aerodynamic forces, the near T.E. droplets size increases. From Table 4.6 and Fig. 4.87, in the case of high air momentum cases (Case A) the gradient of droplet size change remained essentially the same as the distance aft the T.E. region increased, Fig. 4.87 (a), by the virtue of the vibrational mode of a breakup. Though, with increasing AOA the occurrence due to bag mode of breakup got increased but overall the gradient of droplets size change remained the same. The droplet size change (D10) for 0-degree at 1-C (with-respect-to 0.25-C) decreased marginally (about 16%) whereas for 10-degree case the droplets size change at 1-C)with respect to 0.25-C) reduces marginally to nearly 10%. This small change in the droplets size change is primarily due to the vibrational mode of droplets breakup due to large aerodynamic forces. However, when the air momentum was increased slightly (Case B and Case C), the gradient of droplet decrease was significant near the T.E. as shown in Fig. 4.87 (b) and 4.90 (c). From the quantitative analysis view, for Case B as the AOA increases from 0 to 10 degree, the gradient of D10 droplet size distribution at 1-C (with respect to 0.25-C) decreases by approximately 13% and 35% for 0 – and 10 – degree respectively, Fig. 4.87 (b) (Table 4.5). For Case C the corresponding tendency was from 17% and 38%

approximately for 0 – and 10 – degree cases, as shown in Fig. 4.87 (c) – Table 4.5. For low momentum case (Case D) a slight shift of droplet gradient was observed, as shown in Fig. 4.87 (d). At lower AOA (0 to 5 degree) the maximum decrease in D10 droplets was observed near the T.E. region (between 0.25- and 0.5-C). Whereas, for medium AOA range the maximum decrease in droplets size was found to be between 0.5- and 0.75-C. Quantitatively this change was around 20% in this region, as given in Table 4.5. At higher AOA (10-degree) the gradient further shift downstream (0.75- to 1-C), as shown in Fig. 4.87 (d), indicating the breakup of droplets occurred further downstream due to enlarging ligament length. A similar trend was seen for D32 droplets size distribution, as shown in Fig. 4.90. The gradient of droplet size change at low AOA (i.e., 0 – degree) was about 25 % at 0.5-C and 40% at 1-C, Table 4.6. As the AOA was increased to 10 – degree the droplets size change remained almost identical, as shown in Fig. 4.90 (a) (Case A). On the other hand, for low air momentum (Case D), Fig. 4.90 (d), the gradient of droplets size reduces marginally near the T.E. (0.25-C) with increasing in the AOA (0 – 5 degrees). Further increase in AOA makes the gradient of droplets size change to shift towards the downstream region (from the T.E) caused by the corresponding velocity deficit at higher AOA. Quantitatively, at 0.25-C the droplets size change was just above 25% at 0 – degree, which reduces to 7% and 5% as the AOA was increased to 7 – and 10 – degrees.

Table 4.5 and Table 4.6 also compare the droplets size distribution with respect to the 0 –degree AOA. The average droplets size (D10) at an AOA of 10 – degree (when compared to the average droplets at 0 – degree) at 0.25-C and 1-C increases to around 10% and 15% respectively for high momentum ratio case (192). However, when the momentum ratio was reduced to 48, the average droplets size (D10) for 10 – degree AOA case (when compared to 0 –degree AOA case) increases to around 35% and 40% for the droplet measured position at 0.25-C and 1-C respectively. A similar trend when different percentage of droplets size increase was observed for the sauter mean diameter (D32). This is primarily due to the reduced velocity effects as the AOA is increased. For high momentum cases, the number of droplets breakup due to bag mode increases as shown in, Fig. 4.73, however, in this case the aerodynamic forces are still dominant when compared to the low momentum cases, in which the droplets breakup is primarily dominant by the surface tension forces, as shown in Fig. 4.74. In case of a high momentum ratio (Case A – $M \approx 192$) at 0– and 10–degree, the quantitative value of the gradient of D10 droplets size change from 0.25 – C to 0.5 – C position was found to be almost the same, i.e., -12% and -9% respectively. As the distance aft the T.E. increases, the D10 droplets gradient from 0.75 – C to 1 – C position was also found to be the same, which was -2% and -1.5% respectively, as shown in Fig. 4.89. However, at low momentum ratio (Case D – $M \approx 48$) the phenomenon was found to be completely different. Quantitatively the gradient of D10 droplet size change from 0.25 – C to 0.5 – C position was found to be almost the same at 0– and 10–degree case , which were -10% and -7% respectively. However, away from the T.E., i.e., from 0.75 – C to 1 – C position, the D10 droplets gradient for low AOA (i.e., 0 – degree) reduces to -5% whereas for high AOA (i.e., 10 – degree) still significant change of 10% was measured, as shown in Fig. 4.89. Thus, for low momentum as the AOA was increased the gradient of droplets size change moves away from the T.E. whereas for high momentum ratio it remains nearly the same. A similar trend of gradient of droplets size change was also observed for the D32 droplets size, as shown in Fig. 4.90.

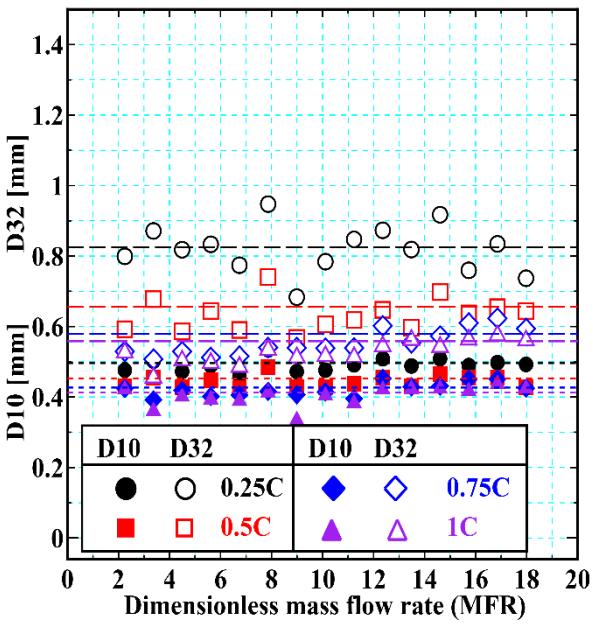

(a) Case A (Air Velocity – 40 m/sec)
($M \approx 192, We_a \approx 60$)

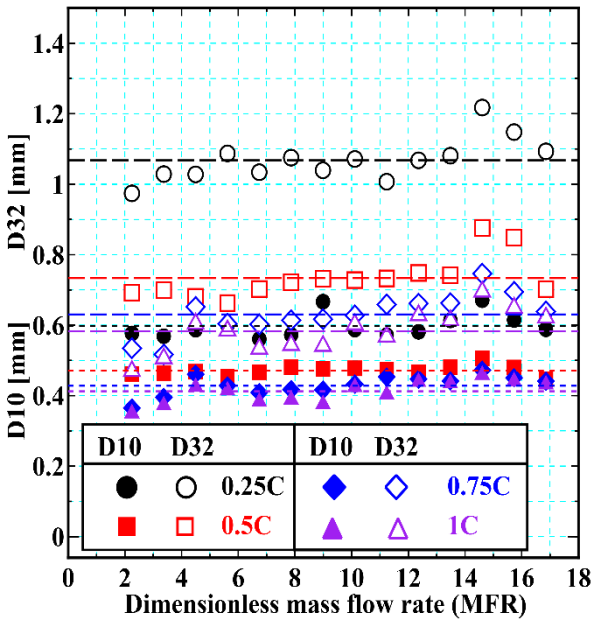

(b) Case B (Air Velocity – 30 m/sec)
($M \approx 108, We_a \approx 34$)

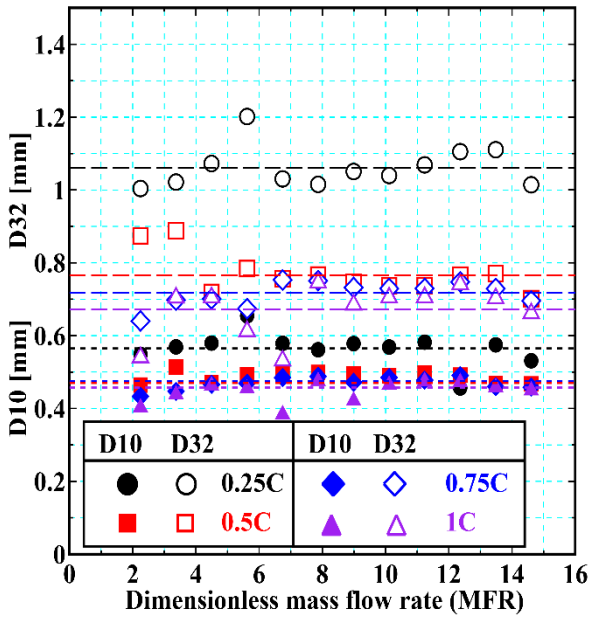

(c) Case C (Air Velocity – 25 m/sec)
($M \approx 75, We_a \approx 23.45$)

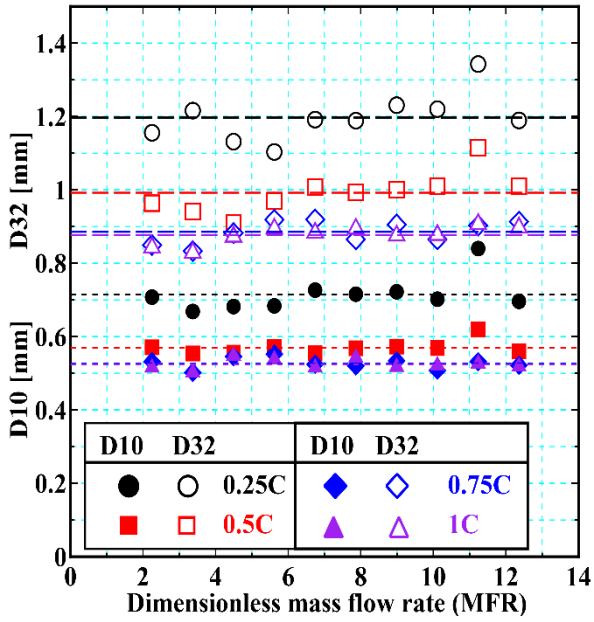

(d) Case D (Air Velocity – 20 m/sec)
($M \approx 48, We_a \approx 15$)

Figure 4.75 – Droplet Size Distribution aft the T.E. Region (AOA – 3-degrees)

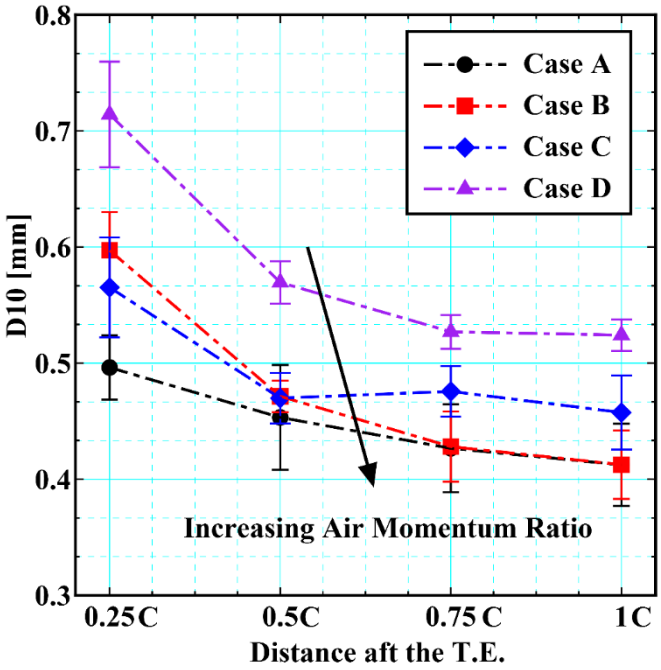

Figure 4.76 – Summary of Average Droplet Size (D10) distribution aft the T.E. – (AOA – 3-degrees)

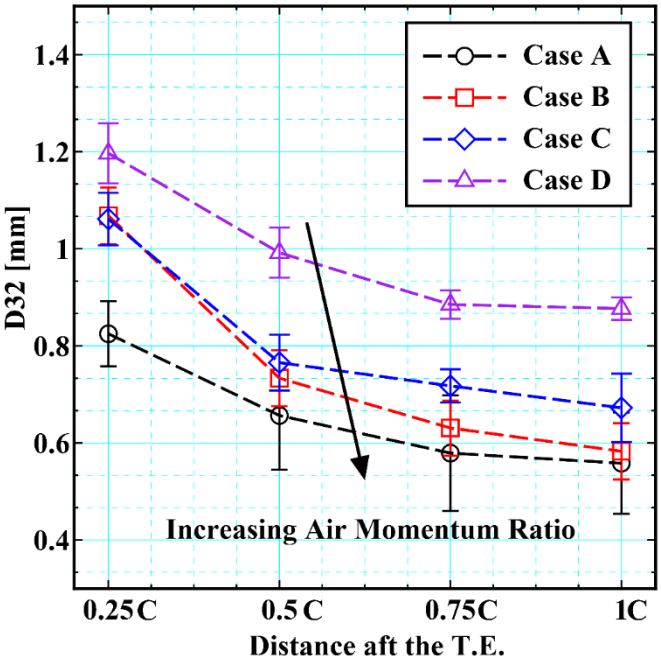

Figure 4.77 – Summary of Sauter Mean Diameter (D32) distribution aft the T.E. – (AOA – 3-degrees)

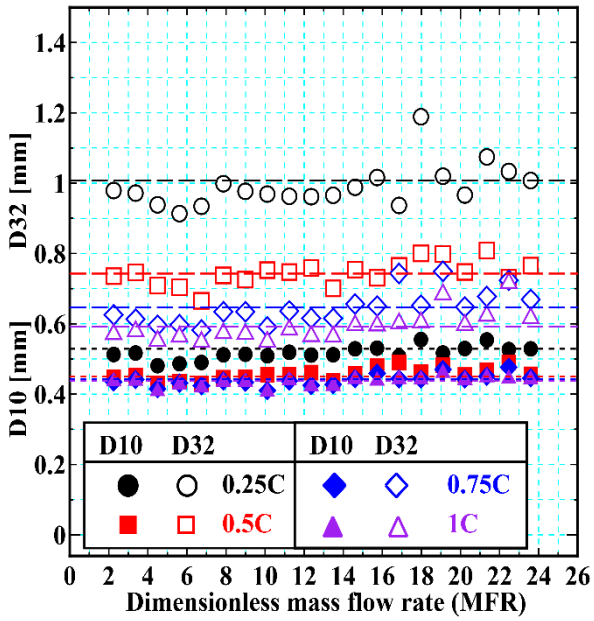

(a) Case A (Air Velocity – 40 m/sec)
($M \approx 192, We_a \approx 60$)

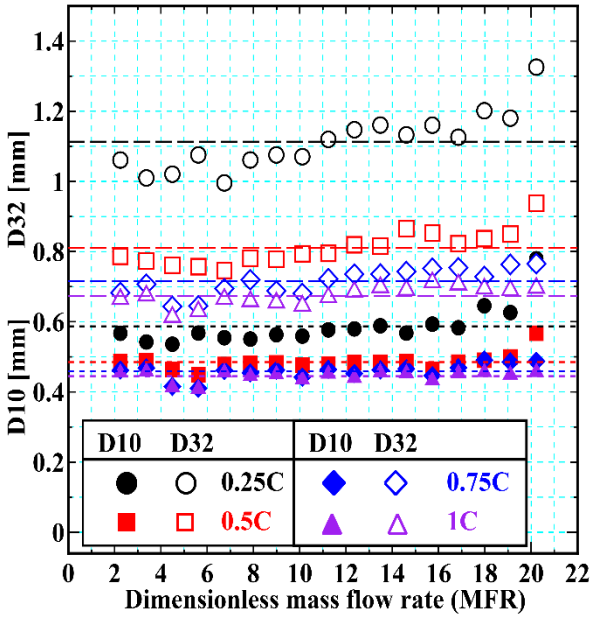

(b) Case B (Air Velocity – 30 m/sec)
($M \approx 108, We_a \approx 34$)

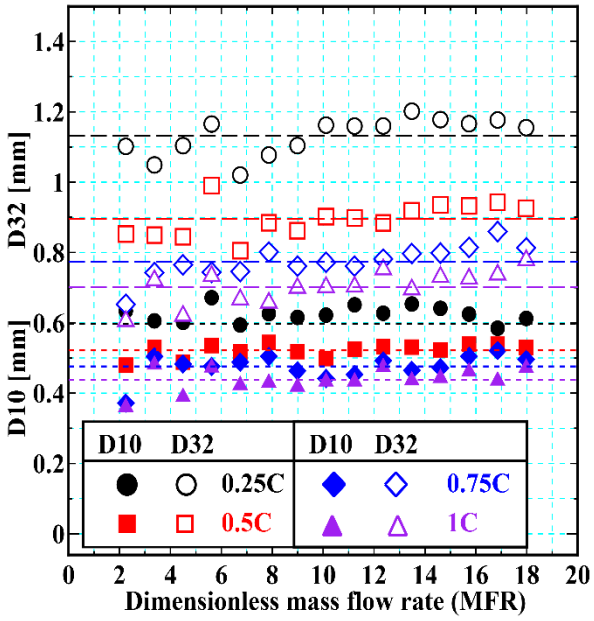

(c) Case C (Air Velocity – 25 m/sec)
($M \approx 75, We_a \approx 23.45$)

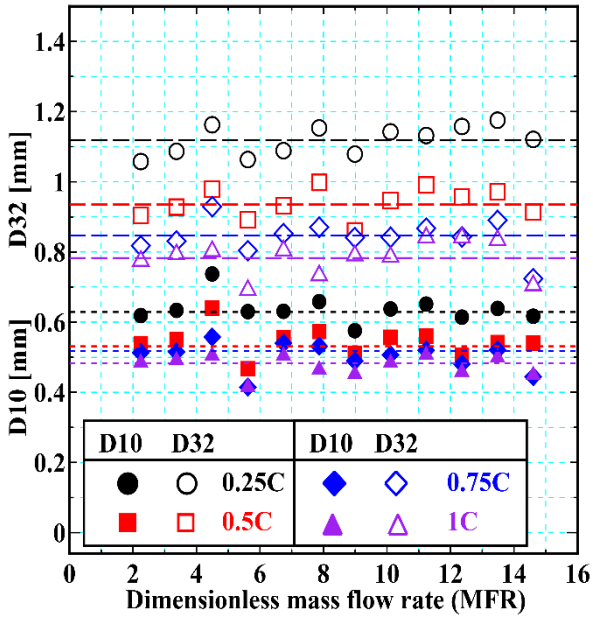

(d) Case D (Air Velocity – 20 m/sec)
($M \approx 48, We_a \approx 15$)

Figure 4.78 – Droplet Size Distribution aft the T.E. Region (AOA – 5-degrees)

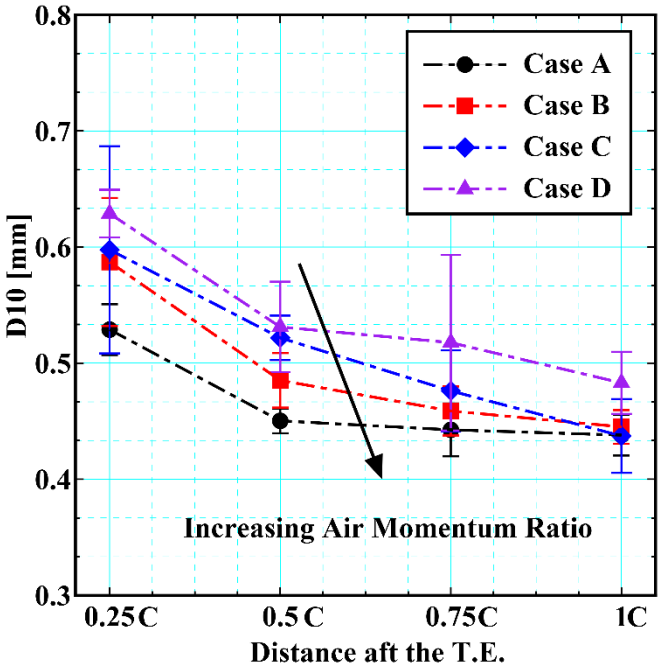

Figure 4.79 – Summary of Average Droplet Size (D10) distribution aft the T.E. – (AOA – 5-degrees)

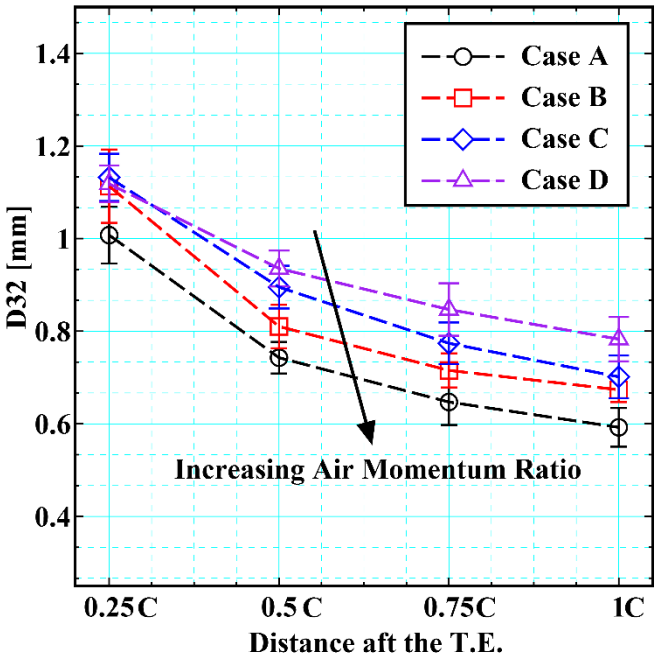

Figure 4.80 – Summary of Sauter Mean Diameter (D32) distribution aft the T.E. – (AOA – 5-degrees)

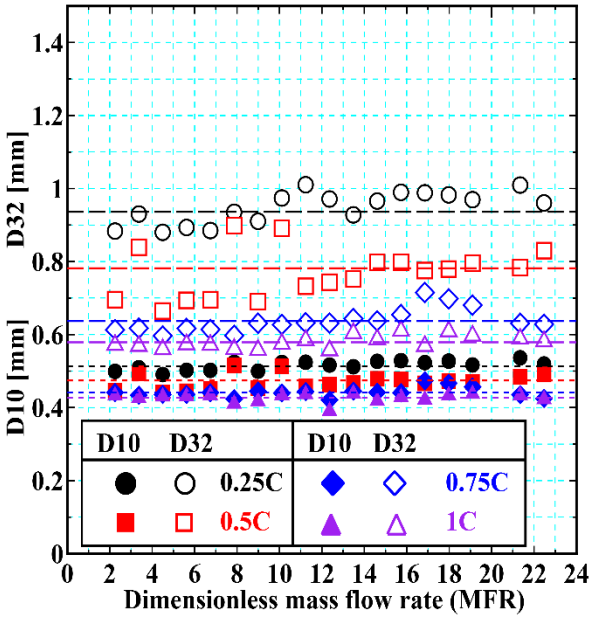

(a) Case A (Air Velocity – 40 m/sec)
($M \approx 192, We_a \approx 60$)

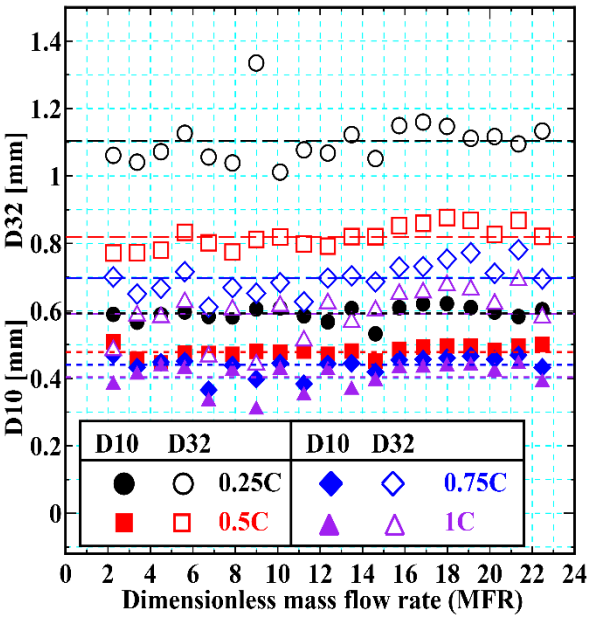

(b) Case B (Air Velocity – 30 m/sec)
($M \approx 108, We_a \approx 34$)

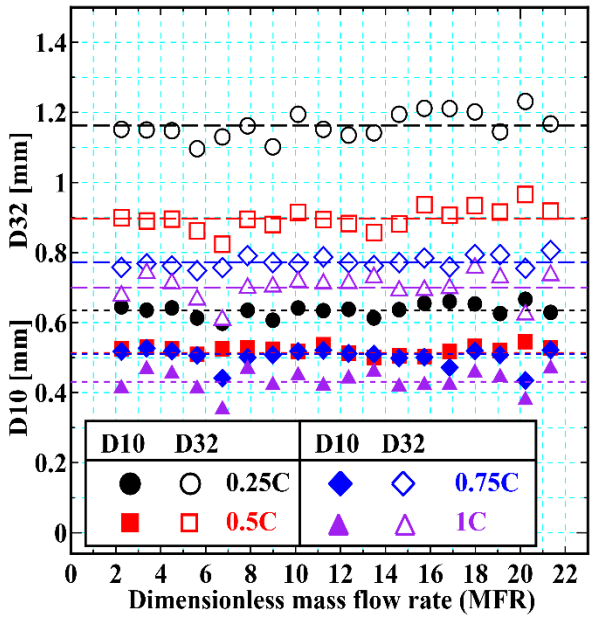

(c) Case C (Air Velocity – 25 m/sec)
($M \approx 75, We_a \approx 23.45$)

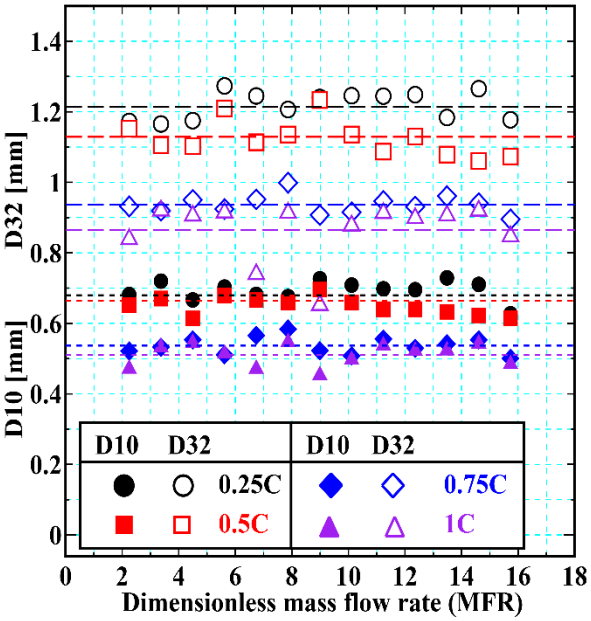

(d) Case D (Air Velocity – 20 m/sec)
($M \approx 48, We_a \approx 40$)

Figure 4.81 – Droplet Size Distribution aft the T.E. Region (AOA – 7-degrees)

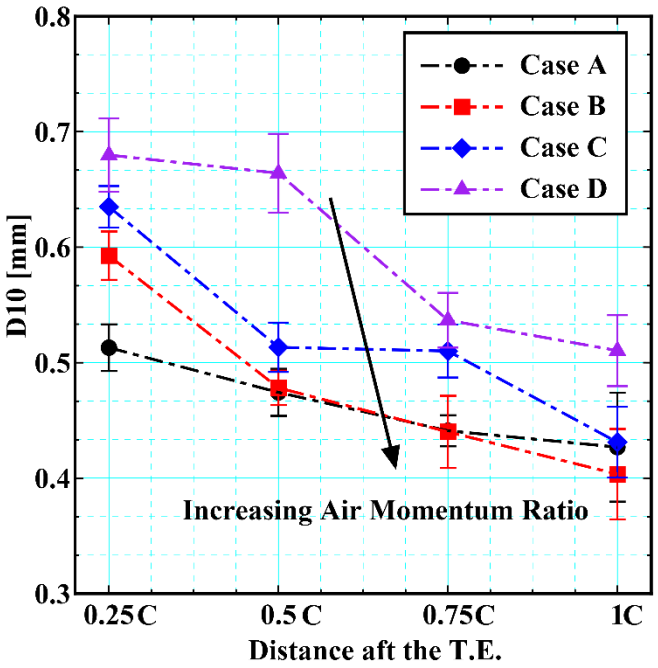

Figure 4.82 – Summary of Average Droplet Size (D10) distribution aft the T.E. – (AOA – 7-degrees)

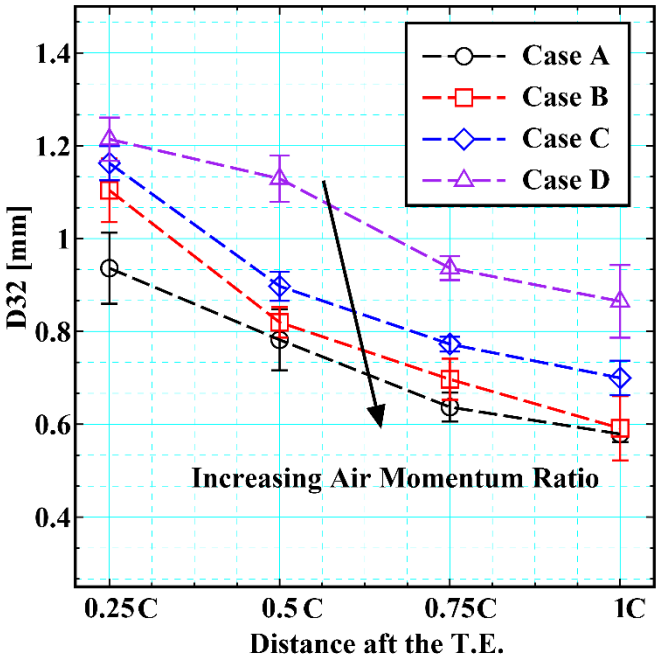

Figure 4.83 – Summary of Sauter Mean Diameter (D32) distribution aft the T.E. – (AOA – 7-degrees)

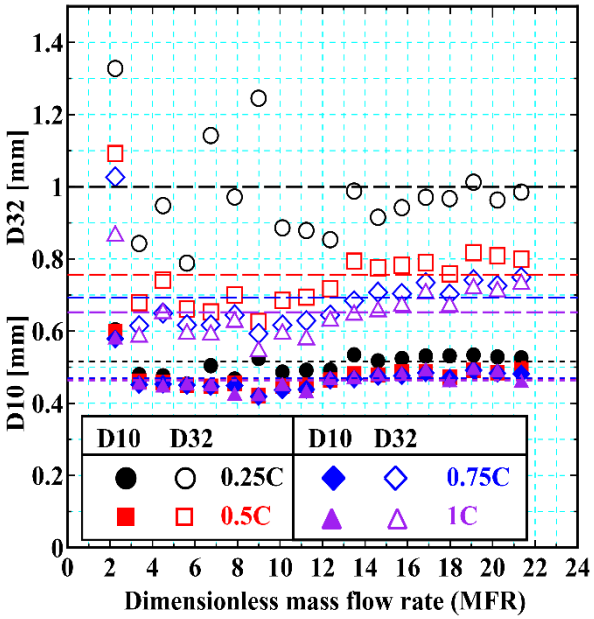

(a) Case A (Air Velocity – 40 m/sec)
($M \approx 192, We_a \approx 60$)

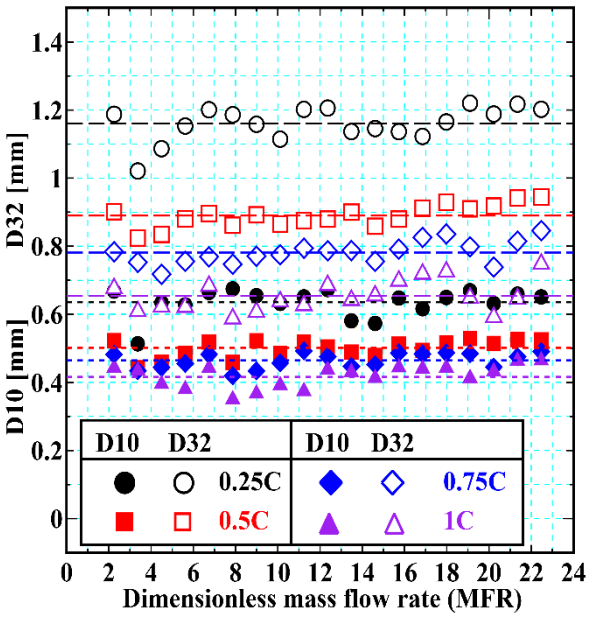

(b) Case B (Air Velocity – 30 m/sec)
($M \approx 108, We_a \approx 34$)

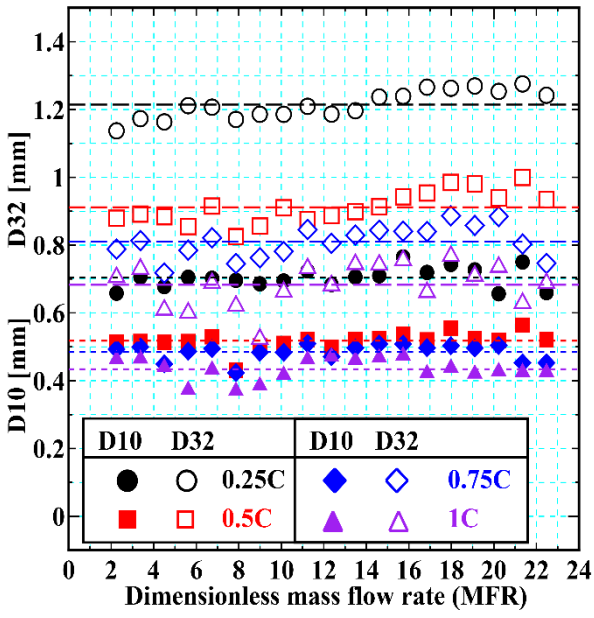

(c) Case C (Air Velocity – 25 m/sec)
($M \approx 75, We_a \approx 23.45$)

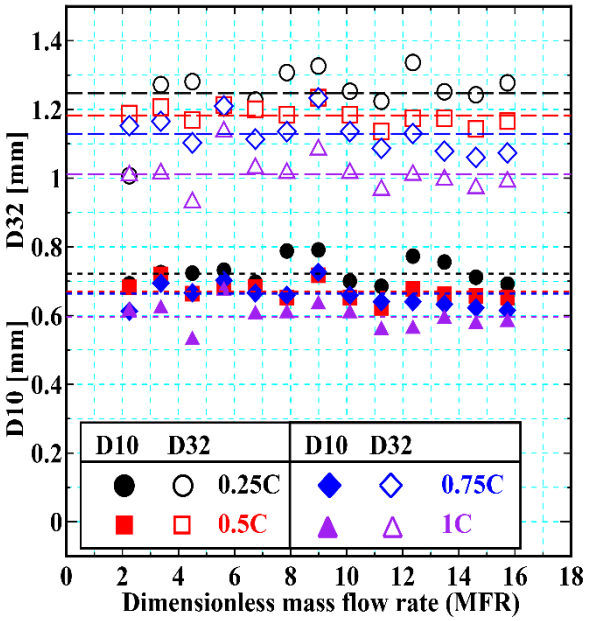

(d) Case D (Air Velocity – 20 m/sec)
($M \approx 48, We_a \approx 15$)

Figure 4.84 – Droplet Size Distribution aft the T.E. Region (AOA – 10-degrees)

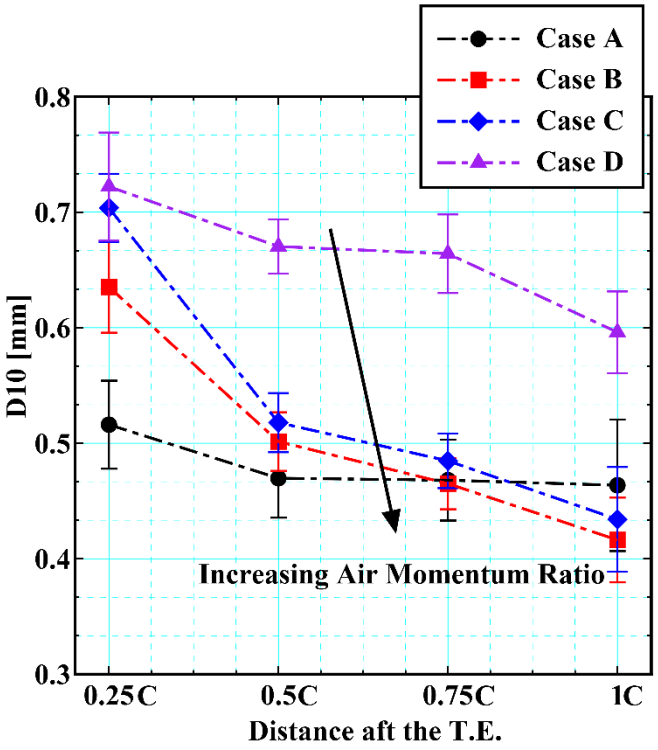

Figure 4.85 – Summary of Average Droplet Size (D10) distribution aft the T.E. – (AOA – 10-degrees)

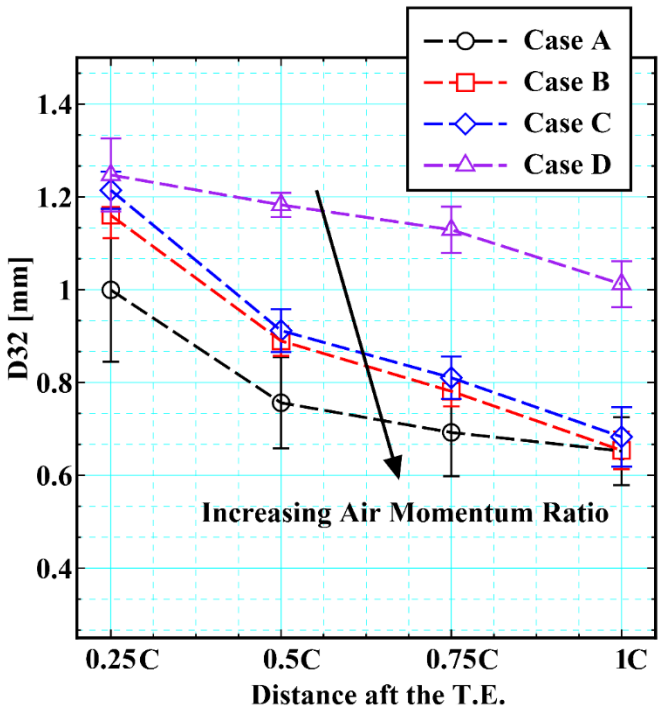

Figure 4.86 – Summary of Average Droplet Size (D32) distribution aft the T.E. – (AOA – 10-degrees)

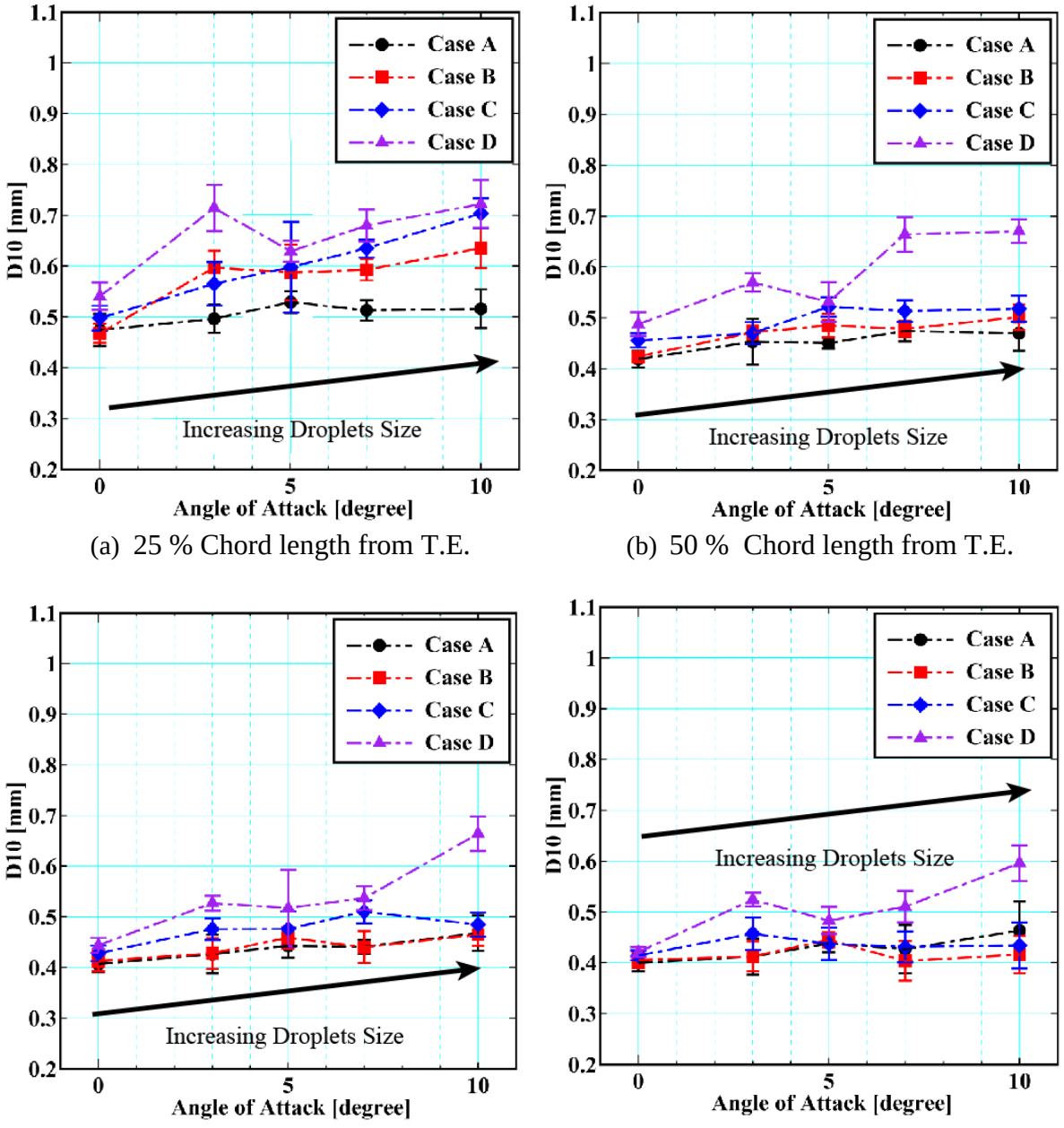

(a) 25 % Chord length from T.E.

(b) 50 % Chord length from T.E.

(c) 75 % Chord length from T.E.

(d) 100 % Chord length from T.E.

Figure 4.87 – Comparison of Average Droplets (D10) Size Distribution aft the T.E. at each position for various AOA

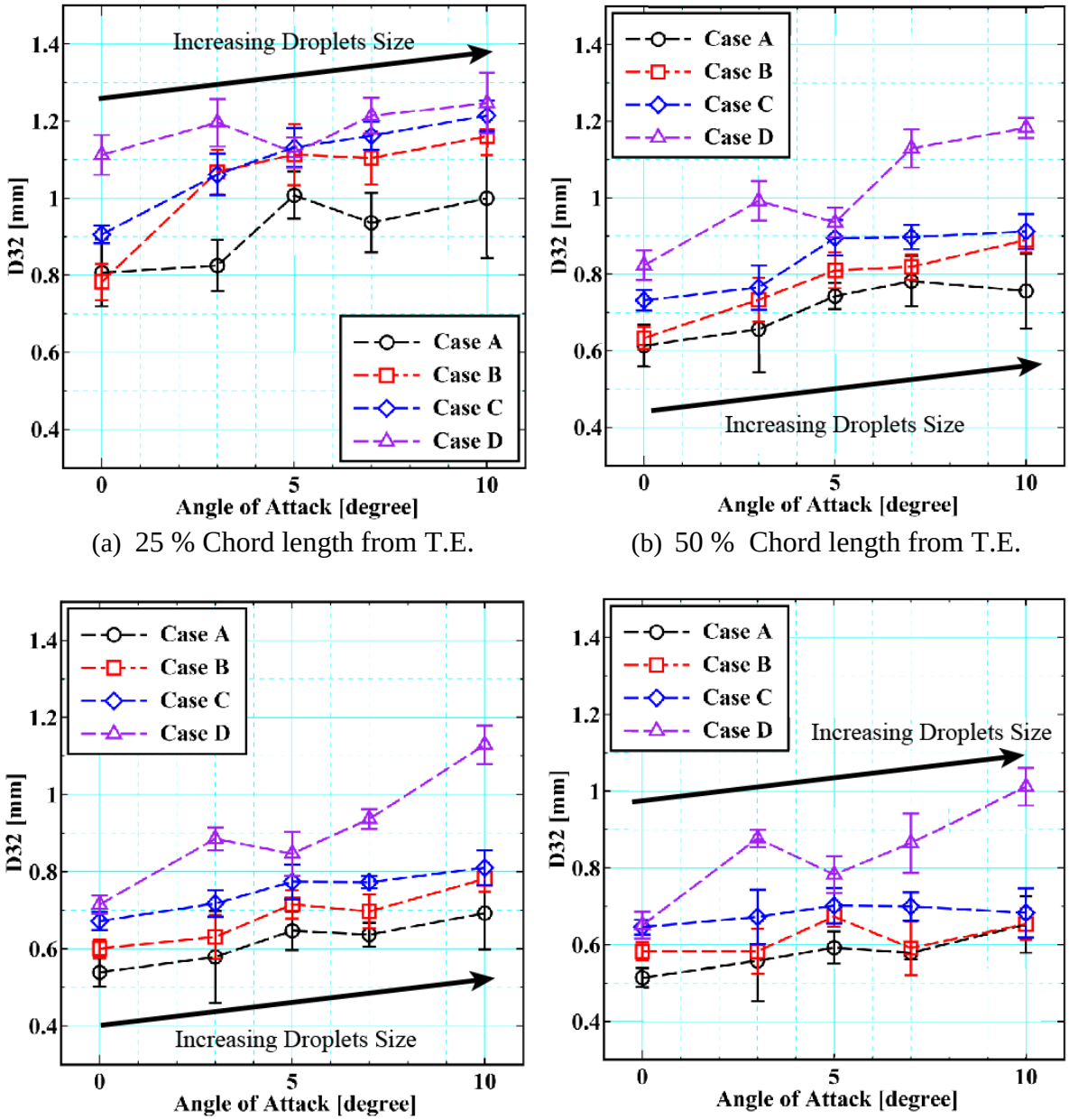

(a) 25 % Chord length from T.E.

(b) 50 % Chord length from T.E.

(c) 75 % Chord length from T.E.

(d) 100 % Chord length from T.E.

Figure 4.88 – Comparison of Sauter Mean Droplets (SMD) Size Distribution aft the T.E. at each position for various AOA

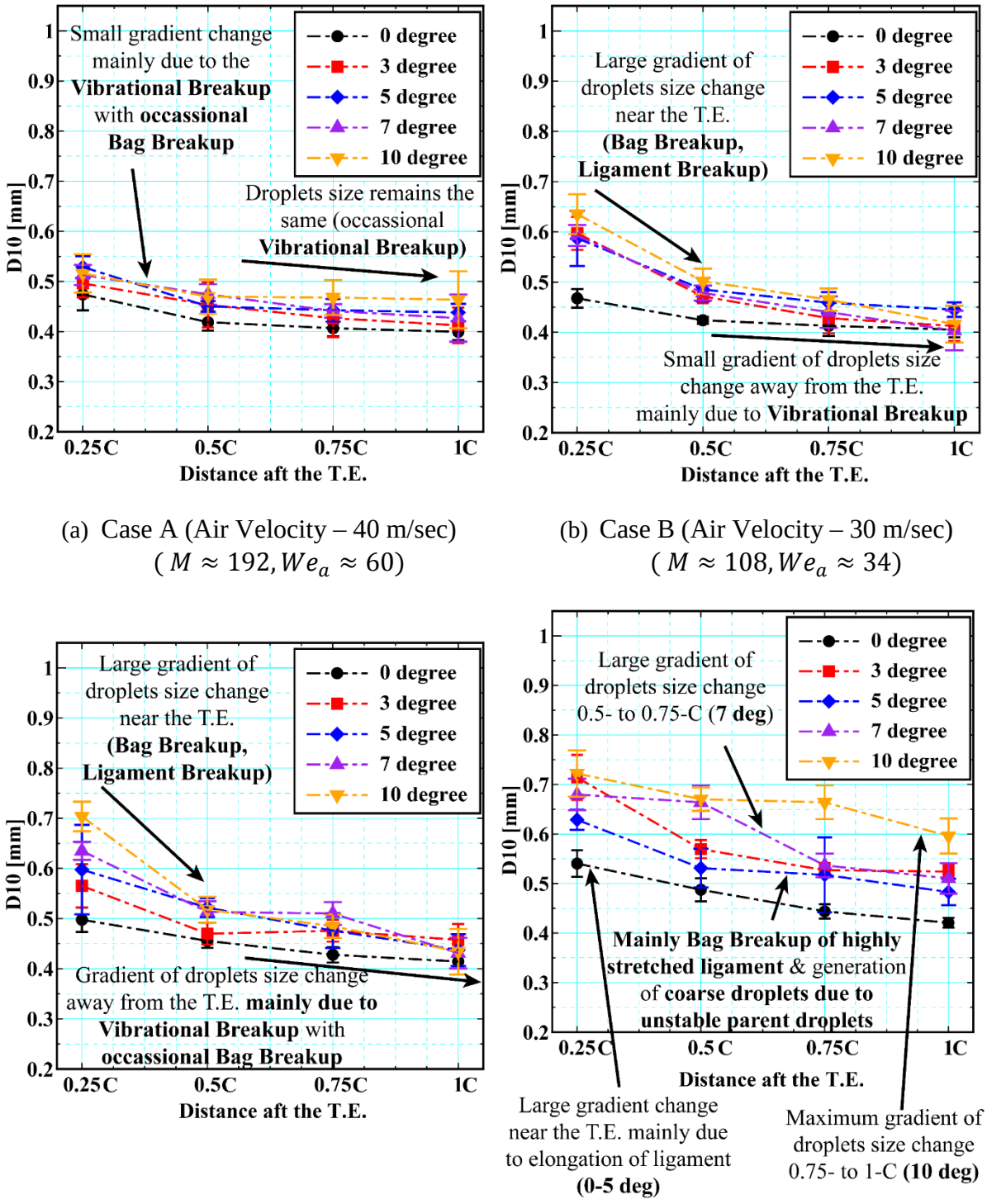

(a) Case A (Air Velocity – 40 m/sec) ($M \approx 192, We_a \approx 60$)

(b) Case B (Air Velocity – 30 m/sec) ($M \approx 108, We_a \approx 34$)

(c) Case C (Air Velocity – 25 m/sec) ($M \approx 75, We_a \approx 23.45$)

(d) Case D (Air Velocity – 20 m/sec) ($M \approx 48, We_a \approx 15$)

Figure 4.89 – Effect of AOA on D10 droplets size distribution aft the T.E.

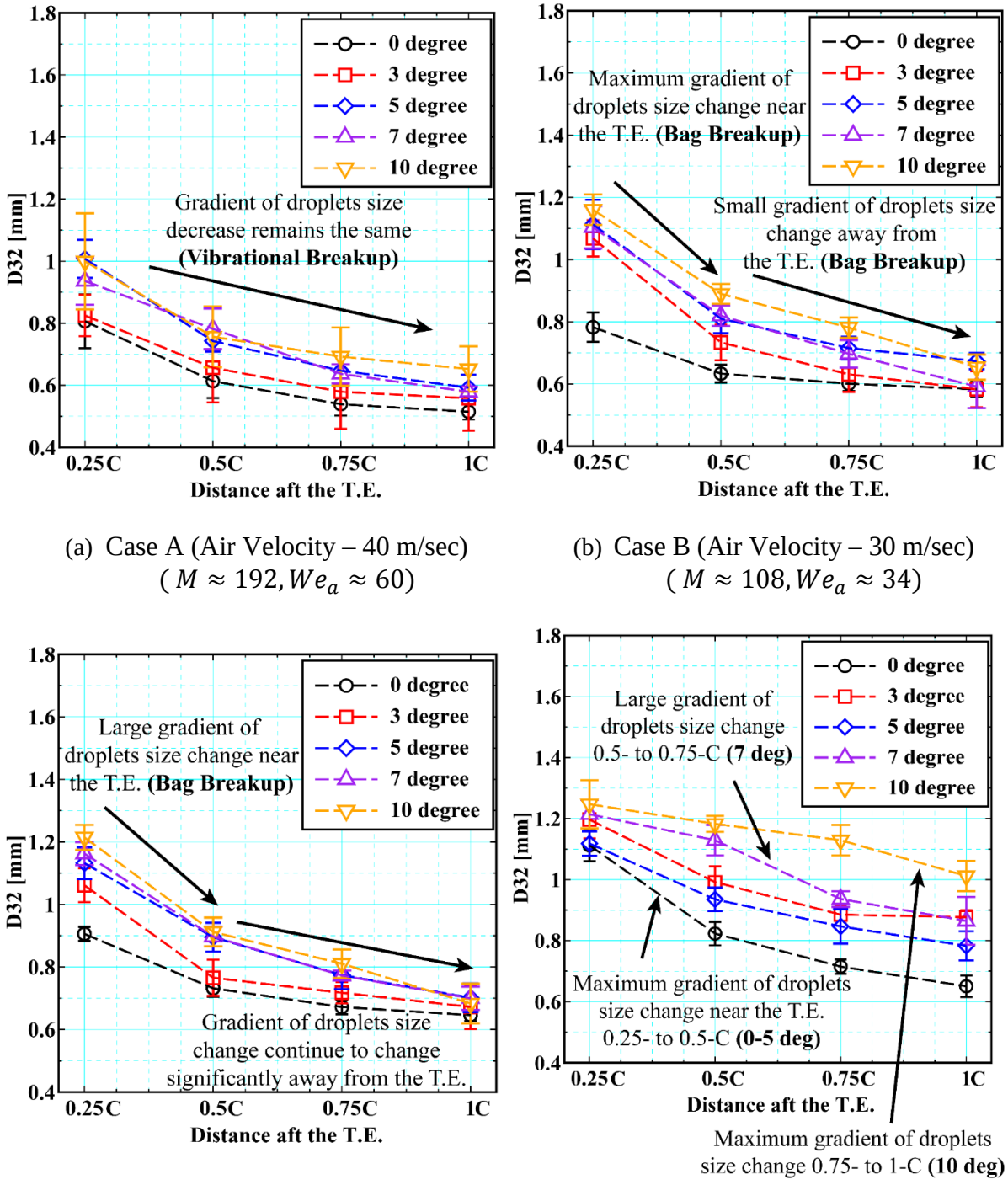

(a) Case A (Air Velocity – 40 m/sec) ($M \approx 192, We_a \approx 60$)

(b) Case B (Air Velocity – 30 m/sec) ($M \approx 108, We_a \approx 34$)

(c) Case C (Air Velocity – 25 m/sec) ($M \approx 75, We_a \approx 23.45$)

(d) Case D (Air Velocity – 20 m/sec) ($M \approx 48, We_a \approx 15$)

Figure 4.90 – Effect of AOA on D32 droplets size distribution aft the T.E.

Table 4.5 – Comparison of Average Droplets (D10) Size at Various Angle of Attack

Angle of Attack (degree)	**Case**	**Percentage Change (with ref. to 0.25-C)**				**Percentage Change (with ref. to 0-degree)**			
		0.25-C	**0.5-C**	**0.75-C**	**1-C**	**0.25-C**	**0.5-C**	**0.75-C**	**1-C**
0	Case A (Air Velocity 40 m/sec), $M \approx 192, We_a \approx 60$	-	-12	-14	-16	-	-	-	-
3		-	-9	-14	-17	+5	+8	+5	+3
5		-	-15	-16	-17	+12	+8	+9	+10
7		-	-8	-14	-17	+8	+13	+9	+7
10		-	-9	-10	-11	+9	+12	+15	+16
0	Case B (Air Velocity 30 m/sec) $M \approx 108, We_a \approx 34$	-	-9	-12	-13	-	-	-	-
3		-	-21	-28	-31	+27	+11	+4	+2
5		-	-17	-22	-24	+25	+14	+11	+10
7		-	-19	-26	-32	+26	+13	+7	0.0
10		-	-21	-27	-35	+33	+18	+13	+3
0	Case C (Air Velocity 25 m/sec) $M \approx 75, We_a \approx 23.45$	-	-9	-14	-17	-	-	-	-
3		-	-17	-16	-20	+14	+3	+11	+10
5		-	-13	-20	-27	+20	+15	+11	+6
7		-	-19	-20	-32	+28	+13	+19	+4
10		-	-26	-31	-38	+41	+14	+13	+5
0	Case D (Air Velocity 20 m/sec) $M \approx 48, We_a \approx 15$	-	-10	-18	-22	-	-	-	-
3		-	-20	-26	-27	+32	+17	+19	+25
5		-	-16	-18	-23	+16	+9	+17	+15
7		-	-2	-21	-25	+26	+36	+21	+21
10		-	-7	-8	-17	+34	+37	+50	+42

Table 4.6 – Comparison of Sauter Mean Droplets (D32) Size at Various Angle of Attack

Angle of Attack (degree)	**Case**	**Percentage Change (with ref. to 0.25-C)**				**Percentage Change (with ref. to 0-degree)**			
		0.25-C	**0.5-C**	**0.75-C**	**1-C**	**0.25-C**	**0.5-C**	**0.75-C**	**1-C**
0	Case A (Air Velocity 40 m/sec), $M \approx 192, We_a \approx 60$	-	-24	-33	-37	-	-	-	-
3		-	-20	-30	-32	+2	+7	+7	+8
5		-	-26	-36	-41	+25	+21	+20	+15
7		-	-16	-32	-38	+16	+27	+18	+13
10		-	-24	-31	-35	+24	+23	+28	+27
0	Case B (Air Velocity 30 m/sec) $M \approx 108, We_a \approx 34$	-	-19	-23	-26	-	-	-	-
3		-	-31	-41	-46	+36	+16	+5	0.0
5		-	-27	-36	-40	+42	+28	+19	+15
7		-	-26	-37	-47	+41	+29	+16	+1
10		-	-23	-33	-44	+48	+40	+30	+12
0	Case C (Air Velocity 25 m/sec) $M \approx 75, We_a \approx 23.45$	-	-19	-26	-30	-	-	-	-
3		-	-28	-32	-37	+17	+5	+7	+4
5		-	-21	-32	-38	+25	+22	+15	+9
7		-	-23	-34	-40	+28	+23	+15	+8
10		-	-25	-33	-44	+34	+25	+21	+5
0	Case D (Air Velocity 20 m/sec) $M \approx 48, We_a \approx 15$	-	-26	-36	-42	-	-	-	-
3		-	-17	-26	-27	+8	+20	+24	+35
5		-	-16	-24	-30	+1	+14	+18	+20
7		-	-7	-23	-29	+9	+37	+31	+33
10		-	-5	-9	-19	+12	+44	+58	+56

4.8.3. Ligament Length, Accumulated Water & Droplets Shedding Angle at the T.E.

Figure 4.91 and 4.92 shows the effect of angle of attack on the amount of water accumulated per unit ligament length and the ligament length per unit T.E. thickness respectively. As already discussed and showed that the water got accumulated at the flow separation region, for high AOA due to increase in the flow separation past an aerofoil. The larger amount of accumulated water is usually undesirable, since it causes an increase in the virtual weight (added mass) of the blade and could result in the reduced rotational speed of the blades, leading to the overall decrease in the efficiency of the system. Additionally, it may accelerate the phenomena of erosion due to the presence of a large amount of water in contact with the blades surface for a longer time. Though, at a high angle of attack, due to the velocity deficit the ligament length increased as well as oscillated up and down due to the vortex shed from the T.E..

Figure 4.93 compares the droplets distribution angle aft the T.E. of the blade for different AOA cases. Figure 4.93 was obtained in a similar way as Fig. 4.51. From Fig. 4.93, an increase in shedding angle was seen when the air flow velocity was reduced and the AOA was increased and vice versa.

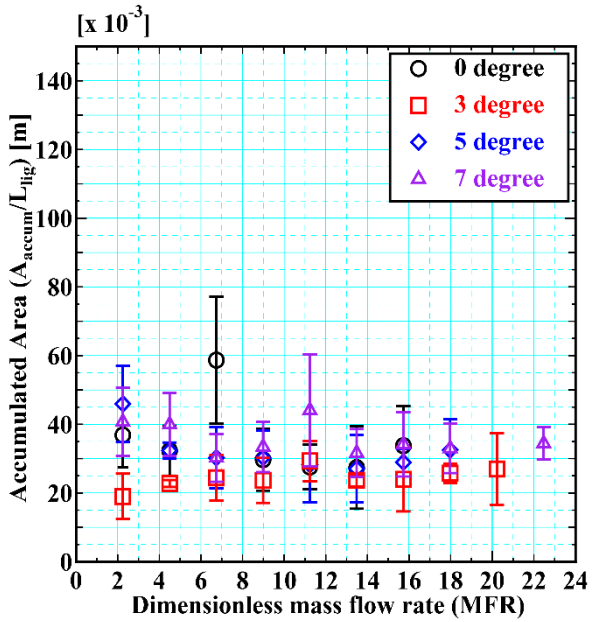

(a) Case A (Air Velocity – 40 m/sec)
($M \approx 192, We_a \approx 60$)

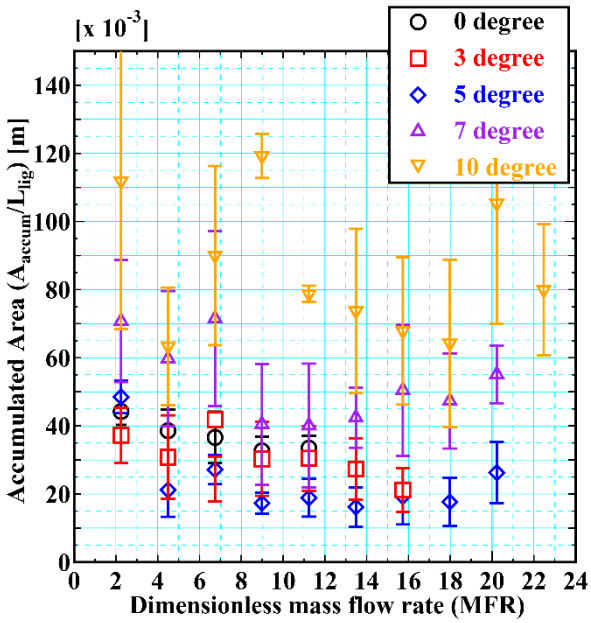

(b) Case B (Air Velocity – 30 m/sec)
($M \approx 108, We_a \approx 34$)

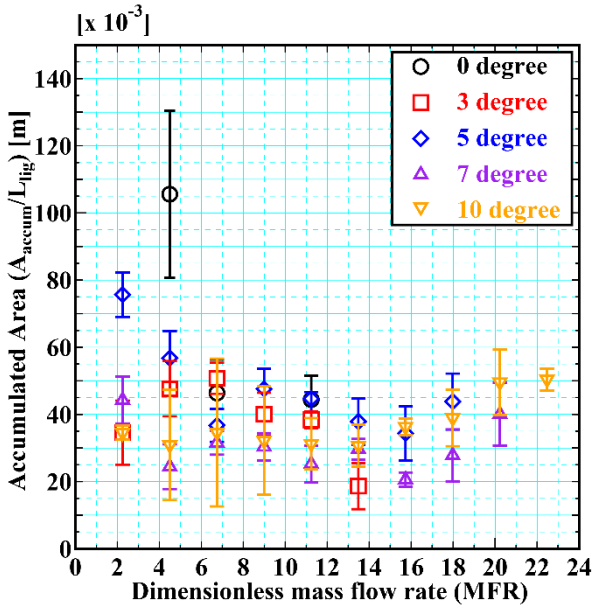

(c) Case C (Air Velocity – 25 m/sec)
($M \approx 75, We_a \approx 23.45$)

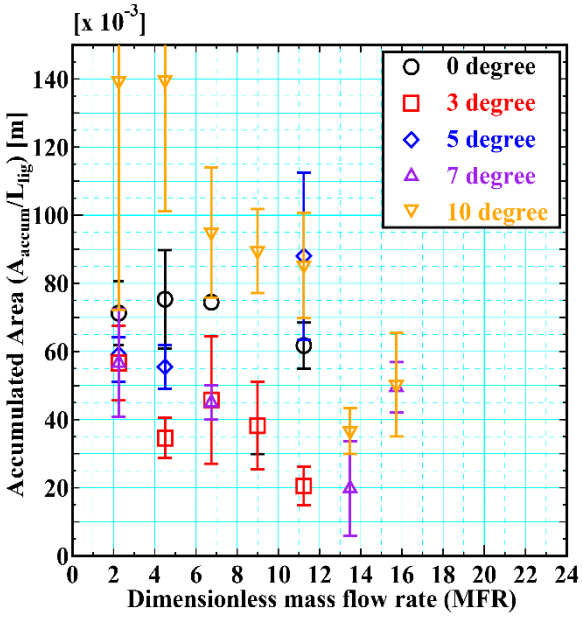

(d) Case D (Air Velocity – 20 m/sec)
($M \approx 48, We_a \approx 15$)

Figure 4.91 – Amount of Water Accumulation at the T.E. for different incidence angle

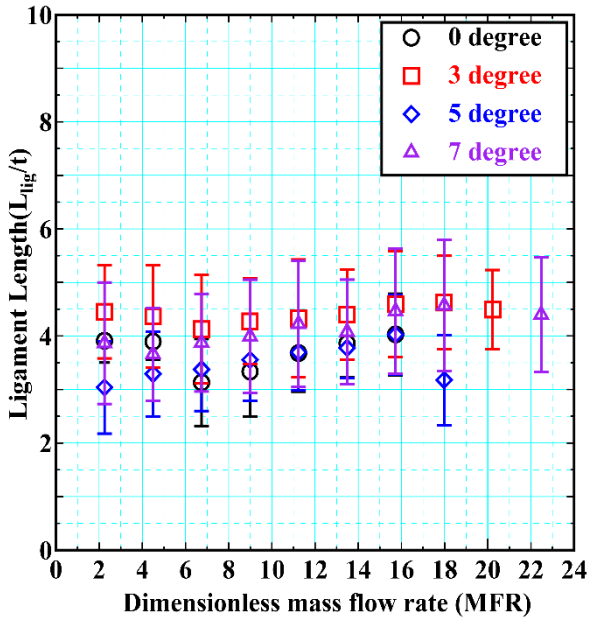

(a) Case A (Air Velocity – 40 m/sec)
($M \approx 192, We_a \approx 60$)

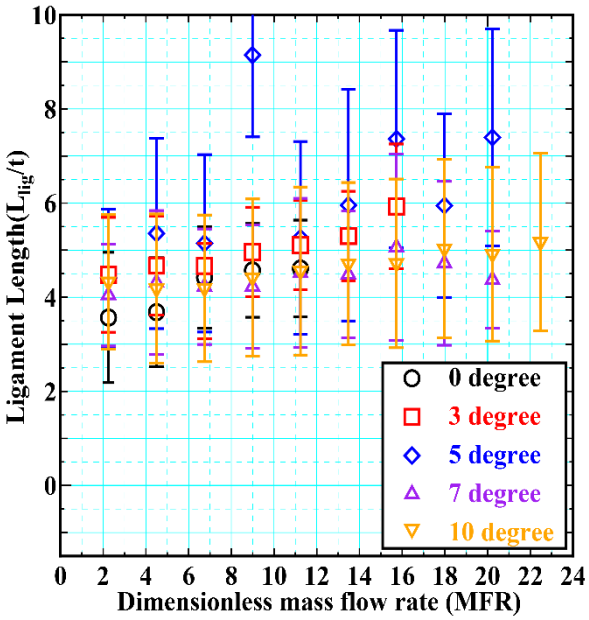

(b) Case B (Air Velocity – 30 m/sec)
($M \approx 108, We_a \approx 34$)

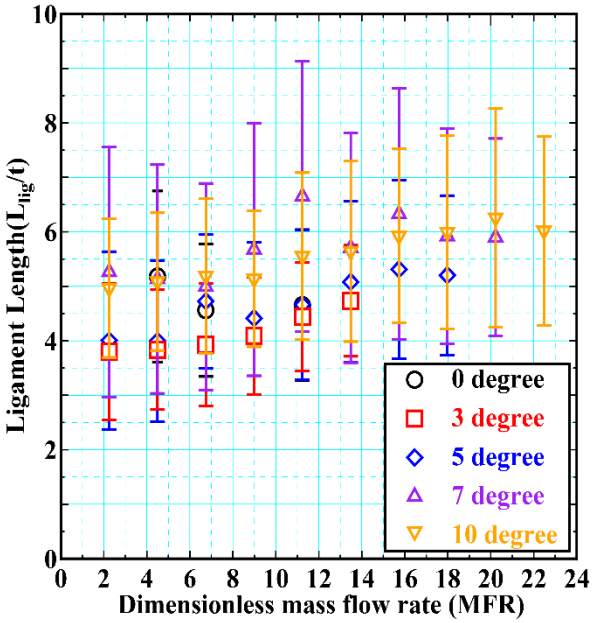

(c) Case C (Air Velocity – 25 m/sec)
($M \approx 75, We_a \approx 23.45$)

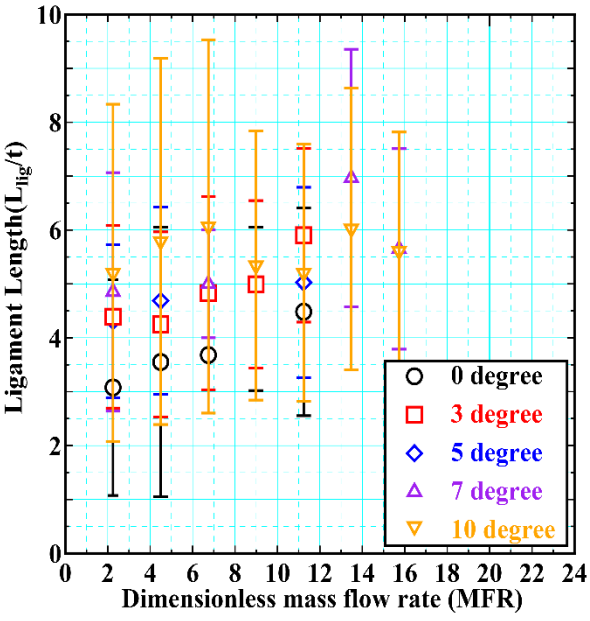

(d) Case D (Air Velocity – 20 m/sec)
($M \approx 48, We_a \approx 15$)

Figure 4.92 – Ligament Length Formation for different incident angle

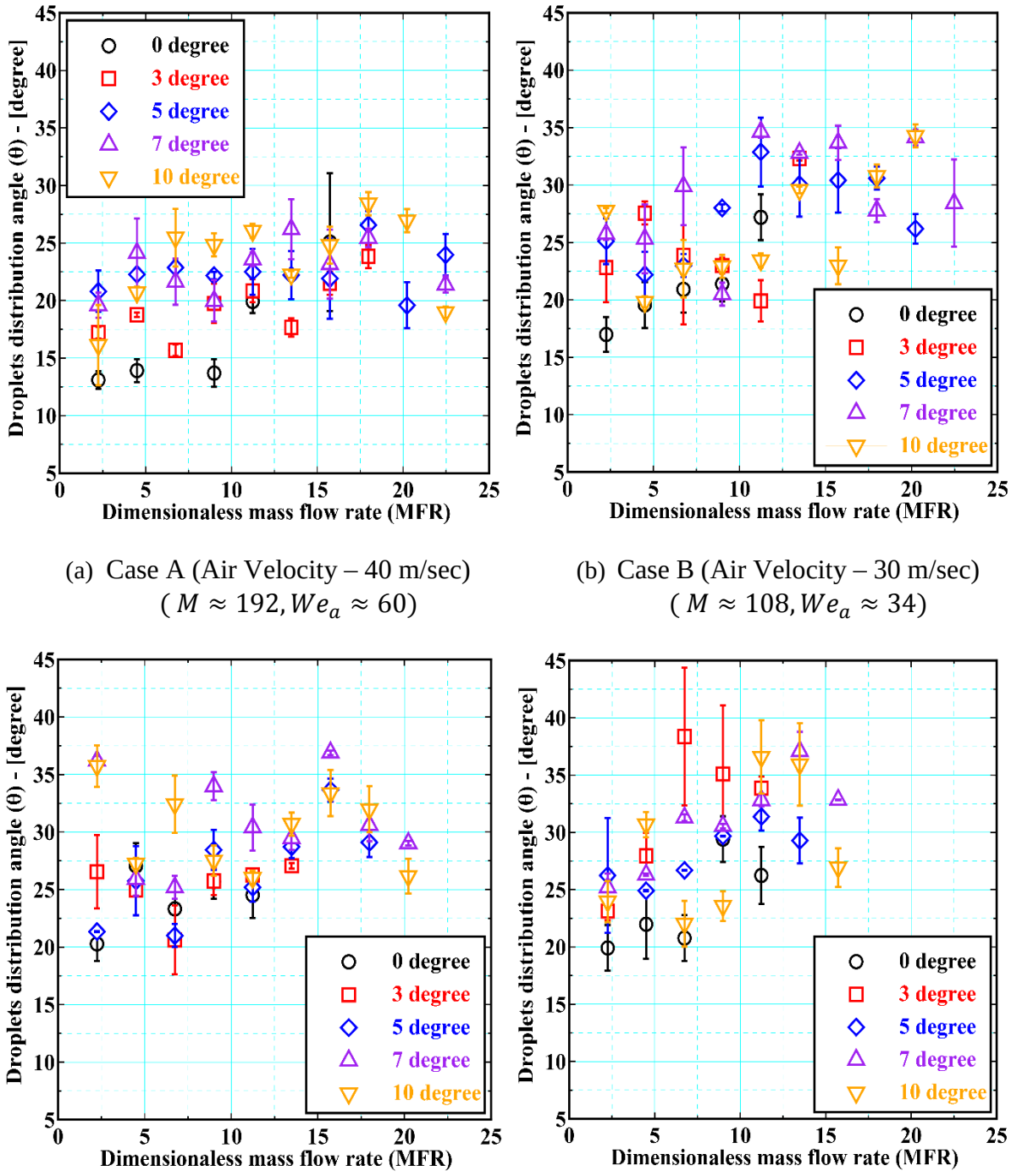

(a) Case A (Air Velocity – 40 m/sec) ($M \approx 192, We_a \approx 60$)

(b) Case B (Air Velocity – 30 m/sec) ($M \approx 108, We_a \approx 34$)

(c) Case C (Air Velocity – 25 m/sec) ($M \approx 75, We_a \approx 23.45$)

(d) Case D (Air Velocity – 20 m/sec) ($M \approx 48, We_a \approx 15$)

Figure 4.93 – Effect of Angle of Attack on droplets distribution angle

4.9. Conclusions of effect of incident AOA on two-phase phenomena around a Cascade Blade

This chapter deals with a detailed experimental investigation of the characteristics of liquid film, water accumulation and the droplets size distribution aft the T.E. of the Elliptical profile blade at 0- and high-AOA. For both the cases, fundamental experimental regarding velocity distribution aft the T.E. of the blade profile were performed, showing the maximum velocity deficit aft the T.E. for high air velocity and high AOA.

Firstly, the complex configuration of thin liquid films was visualized. Based on extensive visualization, the thin liquid film was categorized into three categories; wavy-, intermediate- and smooth (or mirror-like) pattern. Visualization results showed that the ingested water formed a thin film on the blade surface, such that as the mass flow rate of water was increased, the film got wider and thicker and vice versa. The thin film of water was driven downstream by aerodynamic forces and deposited at the T.E. of the blade, due to the influence of the surface tension of the liquid. Unfortunately, the sensors in the present study available were not capable of measuring thin liquid film thickness, and the water film thickness expression was modelled theoretically by assuming Couette flow and Linear velocity profile. Due to air-liquid interaction, water film instability was also seen at the air-liquid interface and was understood based on the Craik's model. By utilizing Craik's model, the role of normal stress component was found to be a principle factor in destabilizing thin film structure, whereas, the role of tangential stress component was found to further destabilize the thin liquid films. The liquid film thickness to width ratio was found to dependent on aerofoil configuration.

At the T.E. of the blade, the thin film deposited in the form of globules. As the aerodynamic force exceeded the adhesive force of surface tension, the globule got separated from the T.E.. For high air momentum case, the droplets were seen to be stripping either from the T.E. directly or due to the bag mode breakup. On the other hand, for low air momentum case, relatively large ligaments were observed between the T.E. and bag breakup mode. The droplet distribution aft the T.E. was found to be independent of the ingestion mass flow rate of water, due to the identical slip velocity between the droplets and the surrounding air at a particular position.

Theoretical models were proposed to predict the shedding frequency of droplets, ligament length and primary coarse droplets formation based on the energy and mass conservation principles. These proposed theoretical models showed good agreement with the experimentally measured results. Lastly, experiments were performed at high AOA, and it was concluded that the liquid film thickness and the droplets size distribution were incremented with and an increase in the AOA.

Chapter No. 5: CONCLUSIONS & PROSPECTS OF FUTURE RESEARCH

5.1. General Conclusions

This study was motivated by the importance of liquid presence in the wet turbine systems (fogging of gas turbines and steam turbines). In the context of this study fundamental experimental study was conducted aiming for a better understanding of the kinematics of liquid presence in the wet turbine systems. The objectives of this study are categorized into the following three categories, which are to understand the characteristics of;

- Liquid film formation on the blade's surface,
- Water accumulation, ligament and its breakup from the T.E. of the blade, and
- Droplets size distribution aft the T.E. of the blade.

In order to achieve these objectives, geometrically simple profile blade was used, which is named as elliptical profile blade. To further get a deeper understanding of the above-mentioned objectives, water ingestion holes(s) were made at the L.E. of the blade profile to grasp the influences of the size and geometry of striking droplets in the real wet turbine systems. Further simplifications were made by using a single blade. The main parameters of this thesis are the mass flow rate of water ingestion, the angle of attack of the blade, water ingestion hole geometry, the air flow momentum, thickness of the T.E. of the blade and the surface tension of the liquid. Optical technique (shadowgraph) was used to understand the dynamics of the liquid in cascade flow and following main conclusions are drawn;

Results showed that the liquid film formed on the blade surface was a function of air flow velocity (which apply aerodynamic forces), mass flow rate of ingested water and the surface tension property of the liquid. It was observed that the aerodynamic forces and the liquid's surface tension play a major role in defining the thickness as well as the pattern of thin liquid films. When the liquid's surface tension forces exceed the aerodynamic forces (due to air) a mirror-like smooth and thicker liquid film structure appear on the blade's surface. On the other hand, if aerodynamic forces exceed the liquid's surface tension forces, wavy film pattern due to K-H type instability appeared on the wave surface. Liquid film thickness was modelled by assuming the Couette flow and linear velocity assumption, such that greater the air flow velocity and mass flow rate of the liquid is, thicker is the liquid film formed on the blade's surface and vice versa. Craik's Instability criteria for thin films was applied for the instability pattern on the wave surface. It was concluded that the amplification growth rate is inversely proportional to the liquid's viscosity. Additionally, based on Craik's model it was shown that the normal pressure force applied on the air-liquid surface played a dominant role by displacing the liquid towards the crests and away from the troughs. However, the role of shear pressure force in destabilizing liquid films cannot be neglected, since it enhanced the destabilization phenomena by accelerating the liquid films in the windward direction at the crests and de-accelerating the liquid film at troughs in the leeward direction. Thus, the thinner the liquid film the more unstable it would become and vice versa.

Surrounding air accelerates the liquid film towards the T.E. of the blade. Due to airflow separation at the T.E., it leads to the local concentration of water at the T.E. The extent of this effect was mainly determined by the blade's geometry, the angle of attack and the surrounding air flow velocity. Theoretical models were derived to calculate the droplets shedding frequency, span-wise length of the ligament attached at the T.E. and the primary coarse droplets formation from the T.E.. It was assumed that the liquid accumulation at the T.E. is torn by high-speed gas shearing, followed by Varga mechanism by accelerating the crests of the waves by high-speed shearing air and ultimately leading to the R-T instability, which evolves into the elongated ligaments. Experimental results had shown that high-frequency Strouhal number was caused by small-scale instabilities due to the separation of viscous shear layer whereas for low-frequency Strouhal number was attributed to the large scale instability of the ligament in the wake. It was under high air momentum in which the stripping of droplets was seen from the T.E. or very near to the T.E. region mainly due to the aerodynamic destabilization of the crest waves; it had also be shown that the theoretical expression of the shedding frequency of droplets breakup increases with the aerodynamic forces and decreases for denser fluid. The accumulated water for high momentum air results in the smaller ligament length and droplets size distribution formation (due to the vibrational mode of droplets breakup). However, for low air velocity a large amount of ligament remained attached at the T.E due to the dominant effect of liquid's surface tension, with a low frequency of breakup. This ultimately resulted in an increase in liquid's ligament length and was observed to oscillate up and down excursions at the T.E. of the blade. When this ligament segment get

exposed to the incoming air flow, which was almost perpendicular to the exposed ligament, it penetrates into the ligament segment resulting in the formation of the elongated bag and ultimately leads to the disintegration of the water segment due to the bag mode of a breakup. From the visualization results, due to different breakup mode of the ligament from the T.E. the droplets distribution angle aft the T.E. was found to be inversely proportional to the air velocity. It was also derived theoretically and proven experimentally that if the Weber number of blades based on their T.E. thickness were the same, then the one with greater atomization edge thickness (i.e. T.E.) results in more coarse droplets formation and vice versa. In the context of the derivation of this models, it was also theoretically proven that the primary coarse droplets formed aft the T.E. was also directly proportional to the liquid property of surface tension and was inversely proportional to the square of the air velocity.

An image processing code was developed based on the canny edge method which transforms the grey scale images to the corresponding binary images. These binary images obtained were used to measure the droplets size distribution aft the T.E. of the blade at 25%, 50%, 75% and 100% chord length of the blade. From the experimental results, it was found that the role of mass flow rate of water was only limited to the number of droplets produced, however, the droplet diameter at a particular position aft the T.E. of the blade remained the same due to the same slip velocity between the droplets and the surrounding air. Overall low air velocity cases resulted in coarse droplets size distribution since the surface tension property of the liquid was strong to resist the breakup due to the aerodynamic forces. For high air velocity cases, the droplets produced were smaller in size, compared to the low air velocity cases, due to the dominant aerodynamic forces resulting in the stripping of droplets from the surface waves, formed at the T.E.. Moreover, in case of high air momentum the gradient of droplets size changed marginally as its distance aft the T.E. increases primarily due to the vibrational mode of droplet break-up, whereas, for low air momentum the gradient of droplets size change largely as the distance aft the T.E. of the blade was increased, due to the bag mode of breakup. It was also concluded that the shape of ingestion hole didn't affect the droplet size distribution aft the T.E. region. With an increase in the angle of attack, the droplets size distribution remains the same at a particular position for a particular momentum ratio. However, greater the AOA was, coarser droplets were formed due to the reduce velocity effect in the aft the T.E. region.

Summing up, from all the experimental results conducted, following conclusions were drawn;

Characteristics of Water Film Formation:

- The liquid film thickness is a governed by the blade configuration, mass flow rate, surface tension and the air velocity only.
- It is almost independent of the size of the ingestion hole geometry.
- An increase in air velocity, a decrease in the mass flow rate and surface tension causes the film thickness to decrease and vice versa.
- Large aerodynamic forces causes the thin liquid film to destabilize whereas the large liquid's surface tension forces leads to stable film structure.
- Liquid film thickness increases with an increase in AOA.
- The liquid film thickness to width ratio remains unchanged for a particular air flow conditions due to the similar properties of liquid's surface tension and the aerodynamic forces, based on the minimum energy principle.
- The liquid film thickness to width ratio is maximum for low air momentum cases due to the dominant effects of surface tension and is minimum for high momentum cases due to the dominance of aerodynamic forces.

Characteristics of Water accumulation and the ligament formation

- Droplets shedding increases with an increase in the air momentum and decrease for high-density liquid and vice versa.
- Primary droplets formed aft the T.E. region is a function of the T.E. profile and the air momentum only, and is independent of the mass flow rate and the geometry of the ingestion hole.
- For the same T.E. profile, the primary droplet size decreases with an increase in the air momentum and vice versa.

- For identical Weber number (based on the T.E. thickness) the droplets formed from the thicker T.E. is larger than that formed from the thinner T.E. profile.
- Ligament size increases for low air momentum cases and vice versa. Similarly, it increases as the angle of attack of the blade is increased.
- The primary droplets size form due to the breakup of the ligaments is inversely proportional to the square of the air velocity.
- Primary droplets formed are larger in size for liquids having higher surface tension as well as low surrounding air velocity and vice versa.

Characteristics of Droplets Size Distribution aft the T.E. of the blade

- Droplets size distribution is governed by T.E. profile, liquid's surface tension and air momentum only.
- The droplet size distribution aft the T.E. region remains the same irrespective of the mass flow rate as the slip velocity between the droplets and the surrounding air remains identical.
- Droplet size decreases as its distance aft the T.E. increases.
- For high momentum ratio and weber number the droplets size distribution is at narrow area whereas for low momentum ratio and the weber number the droplets size distribution is at the relatively wider region.
- At high momentum ratio and weber number, droplets primarily undergo vibrational breakup (due to dominant aerodynamic forces) and for low momentum ratio and weber number droplets breakup mainly due to bag mode of breakup (due to dominant liquid's surface tension forces).
- Droplets size increases with an increase in AOA.

5.2. Future Aspects

Fundamental experimental study and theoretical models derived in this study had helped to identify a deep inside into the fundamental phenomena of the characteristics of the liquid behaviour for a cascade blade. Though, several findings were made in this study, however, further fundamental experimental researches are still needed to be performed to understand the two-phase phenomena in wet turbine systems in a better way.

Following are the few suggestions from the author which are recommended for the further research study in the future.

5.2.1. Numerical Study (CFD)

One of the most important and highly recommended future work areas is the meaningful comparison of the current experimental study with that of the numerical models. The two-phase models known to the author are not yet able to account for the important influences, such as accurately capturing the characteristics of thin liquid film onto the blade surface, detachment and distribution of the droplets from the T.E.. Therefore, the visualized and measured data of this study is expected to be a good source for the verification of numerical simulation results.

5.2.2. Characteristics of Liquid Film

The data for the liquid film presented was based on several assumptions (such as Couette flow, linear velocity profile). In the present study, the quality of liquid film structure visualization was good and is expected to further help in evaluating (or improving) the current models, such as the interaction of the boundary layer with the thin liquid film surface, etc. Based on the present study, it is highly expected that such investigation could be further extended to thin film formation in the rotating environment by taking into account additional forces, such as corrillis and centrifugal forces.

Though, in the present study the effect of surface roughness on the thin film formation was ignored, however, a meaningful and detail study is still needed in this area and its effect on other parameters, such as the amount of accumulated water at the T.E., frequency of shedding, erosion rate etc. According to author knowledge, measurements with Laser Induced Fluorescence systems can provide a much more accurate and reliable measurement values for the liquid film thickness and the velocity compared to the measurements made for the thin liquid film velocity in this study.

To author knowledge, no reliable model exists which predicts the nature of the thin liquid film in a more reliable way. It is highly recommended by the author for the development of a model which takes into account multiple factors to understand the nature of the thin liquid film. According to author experience if any model takes into account of the following factors, then the exact nature of thin liquid film can be understood in a much better way. These factors are gas phase velocity, contact angle, the thickness of the liquid film, the surface roughness of the solid surface, wave disturbances, fluid properties of density, surface tension, etc. Such study can help in better understanding the interaction of water film layer and its influences on the losses.

5.2.3. Phase Change

Phase change phenomena especially evaporation were not considered in the present study, as it is beyond the scope of the present study. Also, the current experimental setup was not capable of doing such study. Chaker et al. had already investigated that the relative humidity has no significant effects on the droplets size distribution, which is also the case in the present study. However, for the better and detail understanding of the droplets size distribution, this phenomenon must also have to be taken into account.

5.2.4. Improvement in Test Facility

At present, the current experimental is capable of mounting a single blade. In the future few modifications are recommended to be made in the current experimental setup to be capable of performing experiments with at the minimum three cascade blades (or much better if seven). This helps to get a deep inside about the interaction (such as coalesce, bounce etc.) of the droplets shed from the T.E. of the blade and results in a much better understanding of the effects of droplets size distribution. Finally, it helps in the effect of characteristics of the liquid film formation on a cascade of blades such as, film structure, thickness etc.

References

1. U.S. EIA International Energy Statistics. (2010)
2. "Key World Energy Statistics 2012". International Energy Agency. (2012)
3. https://en.wikipedia.org/wiki/Nuclear_power#cite_note-oecd_pdf-6 (Accessed date: 31st October, 2015)
4. The World Wind Energy Association, 2014, 2014 Half-year Report. WWEA
5. World watch Institute, 2012, "Use and Capacity of Global Hydropower Increases",(January 2012)
6. Javed, B., 2011, "Control of Wave Energy Farm", Master Dissertation, Imperial College London
7. International Energy Outlook 2013 DOE/EIA-0484 (2013)
8. http://www.hydrogenambassadors.com/background/images/world-energy-cons-region.pdf (Accessed date: 31st October, 2015)
9. Starzmann, J., Casey, M. V., and Mayer, J. F., 2012, "Water Droplet Flow Paths and Droplet Deposition in Low Pressure Steam Turbines", High Performance Computing in Science and Engineering '12, Springer
10. https://en.wikipedia.org/wiki/Thermal_power_station (Accessed Date: 21st November, 2015)
11. U.S. EIA "Annual Energy Outlook 2014 with projections to 2040", DOE/EIA-0383, 2014, April 2014
12. Chaker, M., A., Meher-Homji, Cyrus, B., and Mee, Thomas, 2004, "Inlet Fogging of Gas Turbine Engines-Part I: Fog Droplet Thermodynamics, Heat Transfer and Practical Considerations" ASME J. of Engg. for Gas Turb. & Power
13. Bhargava, R., K., Meher-Homji, C., B., Chaker, M., A., Bianchi, M., Melino, F., Peretto, A., and Ingistov, S., 2005, "Gas Turbine Fogging Technology: A State-of-the-Art Review—Part I: Inlet Evaporative Fogging— Analytical and Experimental Aspects", ASME Turbo Expo 2006, Paper No. GT2005-68336
14. Komuro, T., Ito, E., Sonoda, T., Tomita, Y., Hidaka, K., and Shibutani, S., 2010, "Power Output Augmentation of Gas Turbine Combined Cycle by Inlet-Air Cooling System of Chiller Type under High Ambient Air Temperature", Mitsubishi Heavy Industries Technical Review Vol. 47 No. 4, December 2010
15. Bhargava, and Meher-Homji, C., B., 2002, "Parametric Analysis of Existing Gas Turbines with Inlet Evaporative and Overspray Fogging", ASME Turbo Expo 2002, Amsterdam, The Netherlands
16. Meher-Homji, C. B., B. and Mee III, T., R., 1999, "Gas Turbine Power Augmentation by Fogging of Inlet Air", In: Proceedings of the 28th Turbomachinery Symposium. Houston, Texas, USA, 1999, pp. 93–113
17. http://www.energyfog.com/whyfogging.html (Accessed Date: 31st October, 2015)
18. Gotoh, J., Sato, K., Araki, H., and Marushima, S., 2011, "Efficient and Flexible AHAT Gas Turbine System" Hitachi Review, vol. 60, No. 7
19. Araki, H., Koganezawa, T., Myouren, C., Higuchi, S., Takahashi, T., and Eta, T., 2012, "Experimental and Analytical Study on the Operation Characteristics of the AHAT System", Journal of Engineering for Gas Turbines and Power, MAY 2012, Vol. 134 / 051701-1

20. Hatamiya, S., Araki, H., Katagiri, Y. and Marushima, S., 2007, "An Experimental and Analytical Study on the advanced Humid Air Turbine System", International Conference on Power Engineering-2007, October 23-27, 2007, pp. 290-296, Hangzhou, China
21. Starzmann, J., Casey, M. V., and Mayer, J. F., 2012, "Water Droplet Flow Paths and Droplet Deposition in Low Pressure Steam Turbines", High Performance Computing in Science and Engineering '12, Springer
22. Phillips, J., N., and Levine, P., "Boosting gas turbine power…" Engineering Practice, Fern Engineering Inc.
23. Yagi, M., Araki, H., Tagawa, H., Koganezawa, T., Myoren, C., and Takeda, T., 2013, "Progress of the 40 MW-Class Advanced Humid Air Turbine Tests", Journal of Engineering for Gas Turbines and Power, Vol. 135 (11), 112002
24. https://canteach.candu.org/Content%20Library/20042401.pdf (Accessed Date: 21st November, 2015)
25. Moore, M.J., and Sieverding, C.H., 1976, "Two Phase Steam Flow in Turbines and Separators", McGraw Hill
26. Weir, C.D, 1985, "An analytical approach to the estimation of the performance of steam turbine cycles off-design", Proc. Instn. Mech. Engrs. 199(A1) (1985) 33–43
27. Samoilovich, G.S. and Troyanovskii, B.M., 1982, "Variable and Transient Operation Mode in Steam Turbines". Erergoizdat, Vol. 29, 496 pp
28. Samoilovich, G.S., Afonin, M.V., Barrientos, K.A. and Romanov, K., 1984, "Theoretical and experimental determination of entry losses in turbine stage", Thermal Engineering 31(2), 105–109.
29. Tatsumo, K. and Nagao, O.S., 1986, "Water droplet size measurements in an experimental steam turbine using an optical fibre droplet sizer", J. Heat Transfer, 108, 939–945
30. Young, J.B., 1991, "The condensation and evaporation of liquid droplets in a pure vapour at arbitrary Knudsen number", Int. J. Heat Mass Transfer 34(7), 1649–1661.
31. Gyarmathy, G. and Lesch, F., 1970, "Fog droplet observations in laval nozzles in an experimental turbine', Proc. Instn. Mech. Eng. 184(3G) (III), 29–36.
32. Walters, P.T., 1973, "Optical measurement of water droplets in wet steam flows", In: Heat and Fluid Flow in Steam and Gas Turbine Plant, Conf. Publ. No. 3. Institute of Mechanical Engineers, Vol. 187, p. 216
33. Martinez, Rueda, M.,C., F., 2011, "Theoretical and Numerical Analysis of Erosion in Steam Turbine Blades", Doctoral Thesis, Instituto Politecnico Nacional
34. Avallone, Eugene, A., Baumeister III Theodore, 1996, "Mark's Standard Handbool for Mechanical Engineers", McGraw Hill, 10th Edition
35. Michaelides, E.,E., 2006, "Particles, Bubbles and Drops, Their Motion, Heat and Mass Transfer", World Scientific Publishing
36. Renardy, Y., Popinet, S., Duchemin, L., Renardy, M., Zaleski, S., Josserand, C., Drumright-Clarke, M., A., Richrad, D., Clanet, C., Quere, D., 2003, "Pyramidal and Toroidal Water Drops Impact on a Sold Surface", Journal of Fluid Mechanics, Vol. 484, pp 69-83
37. Gerber, A., G., Sigg, R., Völker, L., Casey, M., V., and Sürken, N., 2007, "Predictions of nonequilibrium phase transition in a model low pressure steam turbine", IMechE Journal of Power and Energy, Part A 221, 825–835.

38. Young, J., B., and Yau, K., K., 1988, “The inertial deposition of fog droplets on steam turbine blades”, Journal of Turbomachinery 110, 155–162,
39. Lesser, M., B., Field, J., E., 1983, “The impact of compressible liquids”, Annual Review of Fluid Mechanics 15, 97–122.
40. Ahmad, M., Sigg, R., Casey, M., and Sürken, N., 2009, “Steam turbine blade erosion assessment using specimens with blade-like profile”, Proceedings of the 8th European Turbomachinery Conference Graz, Austria, pp. 1125–1136.
41. Ahmad, M., Casey, M., and Sürken, N., 2009, “Experimental assessment of droplet impact erosion resistance of steam turbine blade materials”, Wear 267 (9–10), 1605–1618.
42. Pouchot, W., D., 1970, “Hydrodynamic model of correlation of metal removal rates from repetitive drop impact”, ASTM STP 474, 383–408.
43. ASTM G73-98, Standard Practice for Liquid Impingement Erosion Testing, 2005, pp. 1–19.
44. Shuji Hattori, 2010, “Effects of Impact Velocity and Droplet Size on Liquid Impingement Erosion”, Proceedings of the International Symposium on the Ageing Management and Maintenance of Nuclear Power Plants, pp. 58–71.
45. Bowden, F., P., and Field, J., E., 1964, “The brittle fracture of solids by liquid impact, by solid impact, and by shocks, Proceedings of the Royal Society of London 282 (1390), 331–352, Nov. 24.
46. Zhou et al., “Analysis of water drop erosion on turbine blades based on a nonlinear liquid–solid impact model”, International Journal of Impact.
47. Mann, B., S., and Vivek Arya, 2003, “HVOF coating and surface treatment for enhancing droplet erosion resistance of steam turbine blades”, Wear, 254, 652–667
48. MacGregor, C.A. and Bremer, R.J., 1973, "An Analytical Investigation of Water Ingestion in the B-1 Inlet," Rockwell International, NA-73-181, June 1973
49. Papadaes, B.S. and Taylor, D.W., 1976, "A Review of Sea Loiter Aircraft Technology," AIAA Paper No. 76-876, September 1976
50. Meher-Homji, C., B., and Mee III, T., R., “Gas Turbine Power Augmentation by Fogging of Inlet Air”, Proceedings of the 28th Turbomachinery Symposium
51. Bianchi, M., Branchini, L., De Pascale, A., Melino, F., Peretto, A., Bhargava, R., K., and Chaker, M. A., 2010, “Gas turbine power augmentation technologies: A systematic comparative evaluation approach,” ASME Turbo Expo 2010, GT2010-22948
52. Eisfeld, T., and Joos, F., 2012, “On the thermodynamic modelling of two-phase flow compression with dispersed water droplets in air” ISROMAC 14, Paper-227, Honolulu, US
53. Horlock, J. H., 2001, “Compressor performance with water injection”, ASME Paper No. GT 2003-38517
54. Utamura M.,Takehara, I., Horii, N., and Kuwahara, T., 1997, “A new gas turbine cycle for economical power boosting”, ASME Paper No. 97-AA-142
55. Utamura, M., Takehara, I., and Karasawa, H., 1998, “MAT, A Novel, Open Cycle Gas Turbine for Power Augmentation”, Energy Conversion Management 39, No. 16-18, pp. 1631–1642
56. White, A. J., and Meacock, A. J., 2004, “An Evaluation of the Effects of Water Injection on Compressor Performance”, Journal of Engineering for Gas Turbines and Power 126, pp. 748–754

57. Zheng, Q., 2002, “Thermodynamic analyses of wet compression process in the compressor of gas turbine,” Proceedings of ASME Turbo Expo 2002, GT2002-30590
58. Horlock, J., H., 2001, “Compressor performance with water injection,” Proceedings of ASME Turbo Expo 2001, 2001-GT-0343
59. Bhargava, R., K., Meher-Homji, C., B., Chaker, M., A., Bianchi, M., Melino, F., Peretto, A., and Ingistov, S., 2007, “Gas turbine fogging technology: A state-of-the-art review: Part II: Overspray fogging-analytical and experimental aspects,” Journal of Engineering for Gas Turbines and Power
60. Zheng, Q., Li, M., and Sun, Y., 2003, “Thermodynamic performance of wet compression and regenerative gas turbine,” Proceedings of ASME Turbo Expo 2003: Power for Land, Sea and Air, GT2003-38517
61. Utamura, M., Kuwahara, T., Murata, H., and Horii, N., 1999, “Effects of Intensive Evaporative Cooling on Performance Characteristics of Land-Based Gas Turbine,” Joint Power Generation Conference, PWR-Vol. 34.
62. Bhargava, R., K., Meher-Homji, C., B., Chaker, M., A., Bianchi, M., Melino, F., Peretto, A., and Ingistov, S., 2005, “Gas Turbine Fogging Technology: A State-of-the-Art Review—Part II: Overspray Fogging—Analytical and Experimental Aspects”, ASME Turbo Expo 2006, Paper No. GT2005-68336
63. Eisfeld and Joos, 2010, “Experimental investigation of the aerodynamic performance of a linear axial compressor cascade with water droplet loading,” ASME Turbo Expo 2010, GT2010-22831
64. Park K. and Chang K., 2000, “Computation of Gas-Liquid Droplet Cascade Flows Using Multigrid Adaptive Unstructured Grid”, Journal of Propulsion and Power, 16 (6), p. 1002-1010.
65. AGARD Advisory Report No 332 (1995). “Recommended Practices for the Assessment of the Effects of Atmospheric Water Ingestion on the Performance and Operability of Gas Turbine Engines”, Neuilly-sur-Seine, France.
66. Sun, L., Zheng, Q., Luo, M., Li, Y., Wang, J., and Bhargava, R., 2012, “Numerical through flow simulation of a gas turbine engine with wet compression,” Proceedings of ASME Turbo Expo 2012, GT2012-68846
67. Brun, K., Kurz, R., and Simmons, H., 2006, “Aerodynamic instability and life limiting effects of inlet and inter stage water injection into gas turbines”, Journal of Engineering for Gas Turbines and Power, vol. 128, pp. 617–625
68. Das K., Hamed A., and Basu D., 2006, “Droplet trajectories and collection on fan rotor at off-design conditions”, Proceedings of ASME Turbo Expo 2006 Power for Land, Sea and Air, Barcelona, Spain, GT-2006-91214
69. Rioboo R., Tropea C. and Marengo M., 2001, “Outcomes from a drop impact on solid surfaces”, Journal of atomization and sprays, 11, p. 155-165
70. Bose T. K. and Murthy S. N. B., 1994, “Blade Clearance Estimation in a Generic Compressor with Air-Water Mixture Operation”, 30th AIAA, ASME, SAE, and ASEE Joint Propulsion Conference, Indianapolis, IN, AIAA 94-2693, p. 30-40
71. Santa I., 2000, “The effect of water ingestion on the operation of the gas turbine engine”, 22nd International Congress of Aeronautical Sciences, Harrogate, United Kingdom
72. Dixon, S., L., “Fluid Mechanics and Thermodynamics of Turbomachinery”, 5th Edition, Elsevier Butterworth-Heinemann

73. Cumpsty, N., A., "Compressor Aerodynamics", Longman
74. Schlichting, "Boundary Layer Theory", 7th Edition, McGraw Hill Book Company
75. Kleinstreuer, C., "Two Phase Flow Theory and Application", Taylor and Francis
76. Crowe, C., Sommerfield, M., Tsuji, Y. "Multiphase Flows with Droplets and Particles", CRC Press
77. http://hmf.enseeiht.fr/travaux/bei/beiep/content/2012-g16/droplets-distribution (Accessed Date: 2nd December, 2015)
78. Hwang, S.S., Liu, Z., and Reitz, R.D., 1996, "Breakup mechanisms and drag coefficients of high-speed vaporizing liquid drops", Atomization and Sprays, 6, 353-376.
79. Pilch, M. and Erdman, C., 1987, "Use of break-up time data and velocity history data to predict the maximum size of stable fragments for acceleration-induced break-up of a liquid drop", International Journal of Multiphase Flow, 13, pp:741-757
80. Lefebvre, A., H., 1989, "Atomization and Sprays", *Taylor & Francis*
81. Ryzhov, O., S., 2006, "Transition length in turbine/compressor blade flows", Proceedings of Royal Society A (2006) 462, 2281–2298
82. http://www.meefog.com/wp-content/uploads/ar-gt-inlet-fogging-doing-it-right.pdf (Accessed date; 4th February, 2016)
83. Hatamiya, S., Araki, H., Katagiri, Y., and Marushima, S., 2007, "An Experimental and Analytical Study on the Advanced Humid Air Turbine System", Proceedings of the International Conference on Power Engineering 2007, pp 290-296
84. Araki, H., Koganezawa, T., Myouren, C., Higuchi, S., Takahashi, T., and Eta, T., 2011, "Experimental and Analytical Study on the Operation Characteristics of the AHAT System", Journal of Engineering for Gas Turbines and Power, May 2012, Vol. 134 / 051701-1
85. Finn, E. "How to Measure Turbulence with hot-wire anemometers – A Practical Guide", DANTEC Dynamics
86. http://tx.technion.ac.il/~jetlab/11thSymposium/Principle%20And%20Practice%20Of%20Hotwire%20Constant%20Temperature%20Anemometry%20In%20Turbomachinery%20Applications.pdf (Accessed Date: 25th November, 2015)
87. Young, I., T., Gerbrands, J., J., and Vilet, L., J., "Fundamentals of Image Processing", Delft University of Technology http://homepages.inf.ed.ac.uk/rbf/CVonline/LOCAL_COPIES/TUDELFT/FIP2_3.pdf
88. http://www.cse.iitd.ernet.in/~pkalra/csl783/canny.pdf
89. Blevins R. D., 1990, Flow Induced Vibrations, 2nd Edition, Van Nostrand Reinhold Company
90. Lan, H., Wegener, J., L., Armaly, B., F., and Drallmeier, J. A., 2013, "Developing Laminar Gravity Driven Thin Liquid Film Flow Down an Inclined Plane", Journal of Fluid Engineering, Vol. 132, 081301-1
91. Williams, J. and Young, J., B., 2006, "Movement of de-posited water on turbomachinery rotor blade surfaces", ASME Turbo Expo, GT 2006-90792
92. Monnier, H., Mhiri, N and Falk, L., 2010, "Falling liquid film stability in microgas / liquid absorption", Chemical Engineering and Processing, Vol. 49, Issue 9, pp. 953-957
93. Craik, A., D., 1966, "Wind-generated Waves in Thin Films", Journal of Fluid Mech., vol. 26, part 2

94. Villermaux. E., 1998, “Mixing and Spray Formation in Coaxial Jets”, Journal of Propulsion & Power, Vol 14,No. 5 September-October 1998
95. Boukra, M., Catellier, A., Ducasse, E., Gajan, P., Lalo, M., Thomas, N. and Strzelecki, A., 2009, “Use of Fraday Instability to enhance fuel pulverisation in air-blast atomizer”, Combustion for Aerospace Propulsion, Comptes Rendus Mecanique
96. Marmottant, P., and Villermaux, E., 2004, “On Spray Formation”, Journal of Fluid Mechanics, Vol. 498,73
97. Marty, S., Matas, J.,-P., and Cartellier, A., 2013, “Study of liquid-gas mixing layer: Shear Instability and size of produced drops”, Combustion, flow and spray dynamics for aerospace propulsion, Comptes Rendus Mecanique
98. Raynal, L., Villermaux, E., Lasheras, J., and Hopfinger, E., J., 1997, “Primary Instability in liquid gas shear layers, 11th Symposium on Turbulent Shear Flows, Vol. 3, pp: 27.1-27.5
99. Varga, C. M. ; Lasheras, J. C. ; Hopfinger, E. J., 2003, “Atomization of a small-diameter liquid jet by a high-speed gas stream”, Proceedings of ICLASS 2003
100. Willert, C. E. and Gharib, M., 1991, “Digital particle image velocimetry”, Experiments in Fluids, 10, 181–193.
101. Raffel, M., Willert, M., and Kompenhans, J., 1998, “Particle Image Velocimetry, A Practical Guide”, Springer-Verlag Berlin, Heidelberg
102. Westerweel, J., 1997, “Fundamentals of digital particle image velocimetry”, Meas. Science Technology, 8, 1379-1392
103. http://www.dantecdynamics.com/measurement-principles-of-piv
104. Soria, J., 1996, “An investigation of the near wake of a circular cylinder using a video-based digital cross-correlation particle image velocimetry technique”, Experimental Thermal and Fluid Science, 12, 221-233
105. Westerweel J., Dabiri D., and Gharib M., 1997, “The effect of a discrete window offset on the accuracy of cross-correlation analysis of digital PIV recordings”, Experiments in Fluids, 23, 20-28
106. Westerweel, J. & Scarano, F., 2005, “Universal outlier detection for PIV data”, Experiments in Fluids 39, 1096–1100.
107. Himeno, T., Sugimori, D., Uzawa, S., Watanabe, T., and Nonaka, S., 2010, “Heat Exchange and Pressure Drop Enhanced by Violent Sloshing”, 46th AIAA/ASME/SAE/ASEE Joint Propulsion Conference & Exhibit, AIAA 2010-6979
108. Himeno, T., Umemura, Y., Watanabe , T., and Aoki, H., 2008, “Preliminary Investigation on Heat Exchange Enhanced by Sloshing”, 44th AIAA/ASME/SAE/ASEE Joint Propulsion Conference & Exhibit, AIAA 2008-4550
109. Inoue, C., Watanabe, T., Himeno, T., and Uzawa S., 2013, “Impinging Atomization Enhanced by Microjet Injection - effect, mechanism and optimization -”, 49th AIAA/ASME/SAE/ASEE Joint Propulsion Conference, AIAA 2013-3705
110. Himeno, T., Watanabe, T., Nonaka, S., Naruo, Y., and Inatani, Y., 2004, “Numerical Analysis of Sloshing and Wave Breaking in a Small Vessel by CIP-LSM”, JSME International Journal, Series B, Vol. 47, No. 4, 2004.

Appendix A: Flat Blade

In chapter 4, the blade profile was kept constant and the effects of different parameters were studied by changing the AOA and keeping the size of ingestion hole geometry same. In this section, additional experiments were performed with different water ingestion hole to grasp the effects of ingestion hole size on the real wet turbine systems on the characteristics of

- Liquid film and
- Droplets size distribution.

For that purpose a geometrically simple profile geometry was used, named as a flat profile blade, as shown in Fig. A.1, due to the flat Suction Side (S.S.) and Pressure Side (P.S.), with round L.E. and T.E.. Water was ejected via different size holes located at different positions at the L.E. of the blade, schematically shown in Fig. A.2. Table A.1 represents the specification of the blade, which is made from the brass. The chord length and the span length of the blade are 50 mm and 80 mm in length respectively. Compared to the elliptical profile blade, the flat profile blade has slightly less thickness ratio, i.e., 12%. However, its edges (L.E. and T.E.) are thicker than that of the elliptical profile blade, which is 6 mm and having a thickness ratio of 12% also. In the case of the flat blade, the thickness reached the maximum just near the L.E. (at 0.12-C) and remains constant from 0.12- to 0.88-C. Figure A.3 shows the location and geometry of the four types of holes made on the L.E.. Table A.2 gives the detail of the ingestion holes shapes and size. The S.H geometry was located at the mid-span of the blade whereas, M.H and L.H geometries were present at 0.1-S from the mid-span, Fig. A.3. The slit geometry was present at 0.1-S from the L.H, i.e., 0.2-S from the mid-chord.

Table A.2 – Water Ejection Holes at L.E. Specifications

Name	Size
Small Hole (S.H.)	Ø 1 mm
Medium Hole (M.H.)	Ø 1.2 mm
Large Hole (L.H.)	Ø 1.5 mm
Slit	1 mm x 3 mm

Table A.1 – Flat Profile Blade Specification

Parameter	Value
Aerofoil Type	Flat (with round edges)
Material	Brass
Number of aerofoil in cascade	1
Chord Length (C)	50 mm
Span length (S)	80 mm
Maximum thickness	6 mm
Thickness ratio	12 %
Hole diameter (for injecting water)	5 mm
Trailing Edge Thickness	6 mm

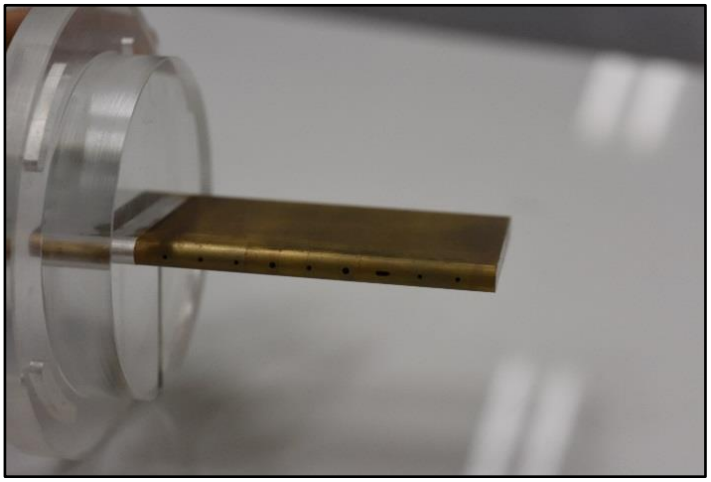

Figure A.1 – Flat Profile Blade

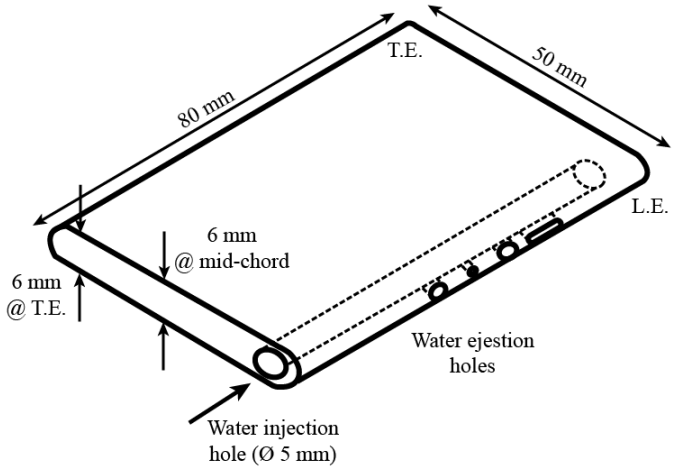

Figure A.2 – Schematics of Flat Profile Blade

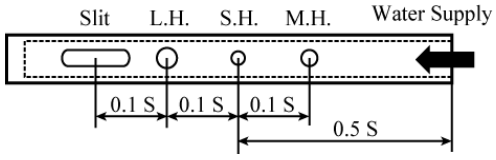

Figure A.3 – Position of Ejection Holes at the L.E

A.1. Fundamental Investigation

A.1.1. Characteristics of Airflow aft the T.E. Region (without water ingestion)

Preliminary experiments were performed to acquire the fundamental velocity distribution aft the T.E. region of the Flat Profile blade. Figure A.4 shows the velocity distribution aft the T.E. region of the flat profile blade using a single probe hot-wire. Here, black, red, blue and violet colour lines correspond to Case A, Case B, Case C and Case D respectively. Whereas the filled and unfilled labels represent the velocity distribution measured at 0.25- and 1-C positions from the T.E. Velocity distribution away from the blade profile (-0.5 to -0.1-C and 0.1-C to 0.5-C) was measured at every of 2 mm in pitch-wise direction, whereas, in the near wake region (0.1-C to -0.1-C) measured at each 1 mm. From Fig. A.4, the wake profile is almost symmetric, due to the symmetric profile of blade, with a large velocity deficit just behind the aerofoil. A velocity deficit of around 67%, 70%, 71% and 75% occurred for the Case A, Case B, Case C and Case D respectively at 0.25-C position, which diminishes gradually to 82%, 86%, 81% and 86% for Case A, Case B, Case C and Case D respectively, as the distance aft the T.E. increases.

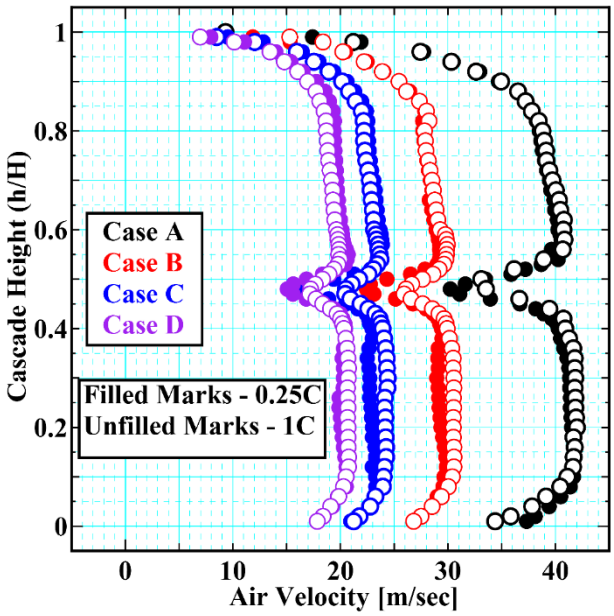

Figure A.4 – Velocity Distribution aft the T.E. of Flat Profile Blade

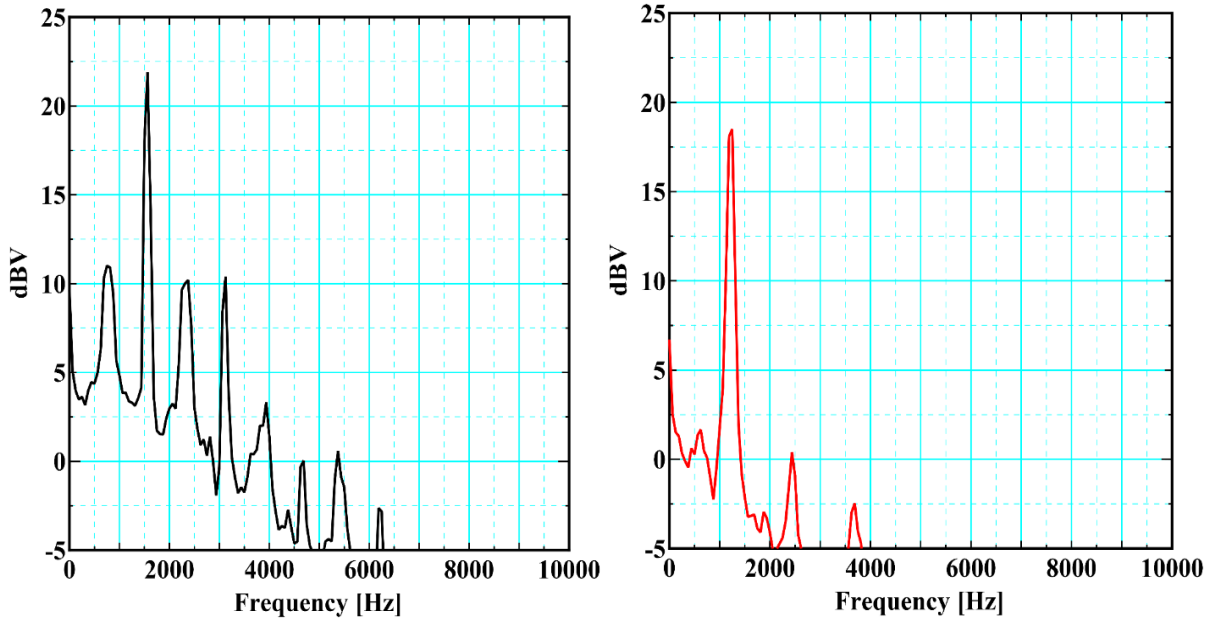

(a) Case A (Air Velocity – 40 m/sec) (b) Case B (Air Velocity – 30 m/sec)

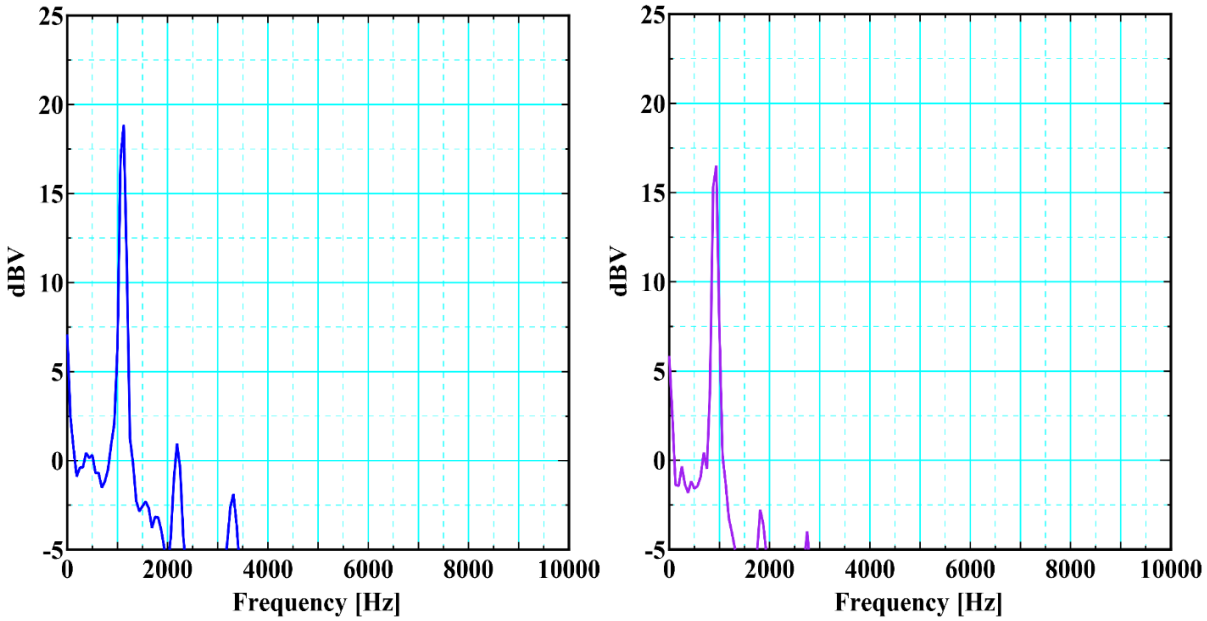

(c) Case C (Air Velocity – 25 m/sec) (d) Case D (Air Velocity – 20 m/sec)

Figure A.5 – Shedding Frequency (measured at 0.25-C from tip of T.E.)

Table A.3 – Shedding Frequency - Unit (kHz)

Case	Experimental	Theoretical
Case A (Air Velocity 40 m/sec)	1.55	1.33
Case B (Air Velocity 30 m/sec)	1.25	1.0
Case C (Air Velocity 25 m/sec)	1.11	0.83
Case D (Air Velocity 20 m/sec)	0.925	0.66

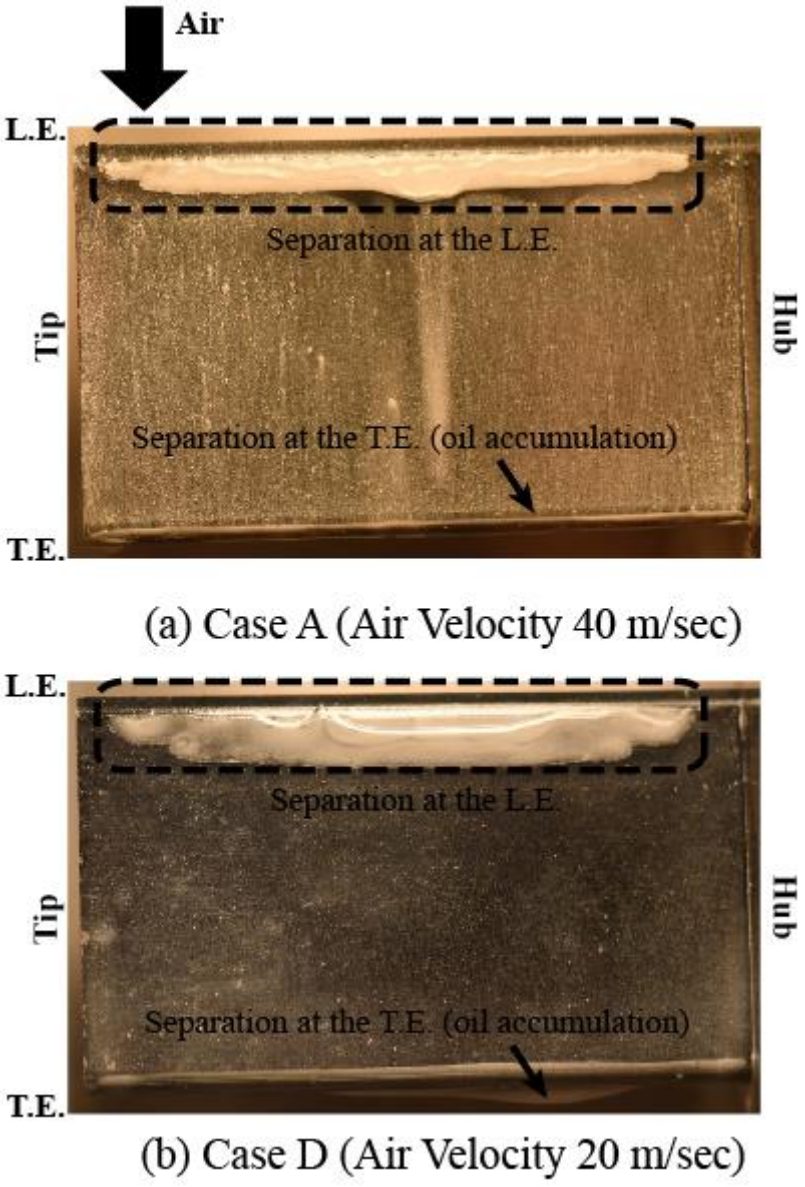

Figure A.6 – Oil Flow Visualization of Flat Profile Blade

Similarly, Fig. A.5 shows the shedding frequency in case of a Flat blade profile. In this case too the shedding frequency was measured at 0.25-C from the tip of the T.E.. Experimental results of shedding frequency was measured using a FFT analyser, whereas the theoretical values of shedding frequency were calculated using Eq. (4.1). As expected, the order of shedding frequency measured was of the order as that of the theoretical formula as given in Table A.3.

A.1.2. Surface Oil Visualization of Test Blade

The surface oil flow visualization of Flat profile blade was also conducted by preparing a mixture of oil and titanium dioxide. This mixture was painted as a thin layer on the blade profile and the blade was put inside the wind tunnel at the selected flow conditions. Figure A.6 (a) and A.6 (b) shows the oil traces on the suction side of the blade for Case A and Case D respectively at 0-degree AOA. A flow separation took place just near at the L.E. of the blade. Moreover, at the T.E. of the blade, a thin line of oil also get accumulated due to the profile separation caused by the flow separation. Overall the flow remained attached and was almost two dimensional in nature.

A.2. Liquid Film Visualization

Like an elliptical profile blade, in this case also, three basic phenomena of water were observed as shown in Fig. A.7, irrespective of the air flow velocity and the ejection flow rate of water, which are;

1. Thin water film formation on the blade surface.
2. Water accumulation at the T.E..
3. Breakup of ligaments and droplets aft the T.E. region of the blade.

A.2.1. Liquid Film Formation

Firstly, when the water was ejected from the hole at the L.E. it formed a thin liquid on the blade surface, as shown in Fig. A.7. Near the L.E. of the blade a small amount of water got accumulated due to the profile separation, which resulted in the local increase in the film thickness. Due to this flow separation, a thin liquid film also gets widened. The widening of this thin liquid film depends on the air momentum, such that at relatively high air momentum (Case A), Fig. A.7 – (i) – (a), the width of the liquid film get widened abruptly at once whereas at low air momentum this thin liquid film gets widened marginally, Fig. A.7 – (i) – (d). Similarly, this thin liquid film flows towards the T.E. of the blade due to the aerodynamic forces exerted by the surrounding airfield. Under the similar flow air conditions, the width of the thin film when ejected from the S.H (1-mm) geometry was smaller in width than that of the other geometries and was maximum for Slit geometry. This was mainly due to the difference in the width of water ejection hole geometry. However, it will be discussed later in Section A.3.2 that the thickness of the thin liquid film remains the same, whatever, the ingestion hole geometry was used. In the case of a flat profile blade, Fig. A.7, at relatively large air momentum (Case A) an instability pattern is seen on the blade surface, whatever the water ejection hole was used. This film pattern gets smooth with no instability at low air momentum (Case D) as shown in Fig. A.7.

Due to relatively large thickness of the flat profile blade, occasionally water film was seen to be formed only on one side of the blade (either at the suction side or pressure side), especially for S.H hole (1-mm) which was mainly due to relatively small ejection hole size compared to that of the thickness of the blade.

A.2.2. Water Accumulation at the T.E.

Secondly, the thin liquid film upon reaching the T.E. started to accumulate mainly due to the profile separation, as shown in Fig. A.7. The surface tension of the liquid kept the liquid to remain attached which resulted in an increase in the amount of accelerated water. For high momentum ratio (Case A), irrespective of the type of ejection hole geometry used. Similarly, when the air momentum was reduced the corresponding liquid accumulation per unit span length decreases and was the minimum for Case D as shown in Fig. A.7.

A.2.3. Breakup of Ligaments and droplets formation aft the T.E. region

Finally, from Fig. A.7, the accumulated water started to grow in the windward direction due to the destabilization caused by the aerodynamic forces. When the aerodynamic forces exceed the critical value, shedding of ligament(s) and droplet(s) took place from the T.E.. In the case of a large droplet(s) or ligament(s) shed, fragmentation of further underwent breakup until they reached the stable size. Since at high air momentum (Case A) the aerodynamic forces were strong enough the corresponding water droplets formed were smaller in size. On the other hand, for low air momentum case (Case D)

the corresponding droplets were larger in size due to the weak aerodynamic forces. From the visualization videos, droplets formed just behind the T.E. (i.e. in the wake region) were usually smaller in size due to high turbulent energy compared to those formed outside the wake region.

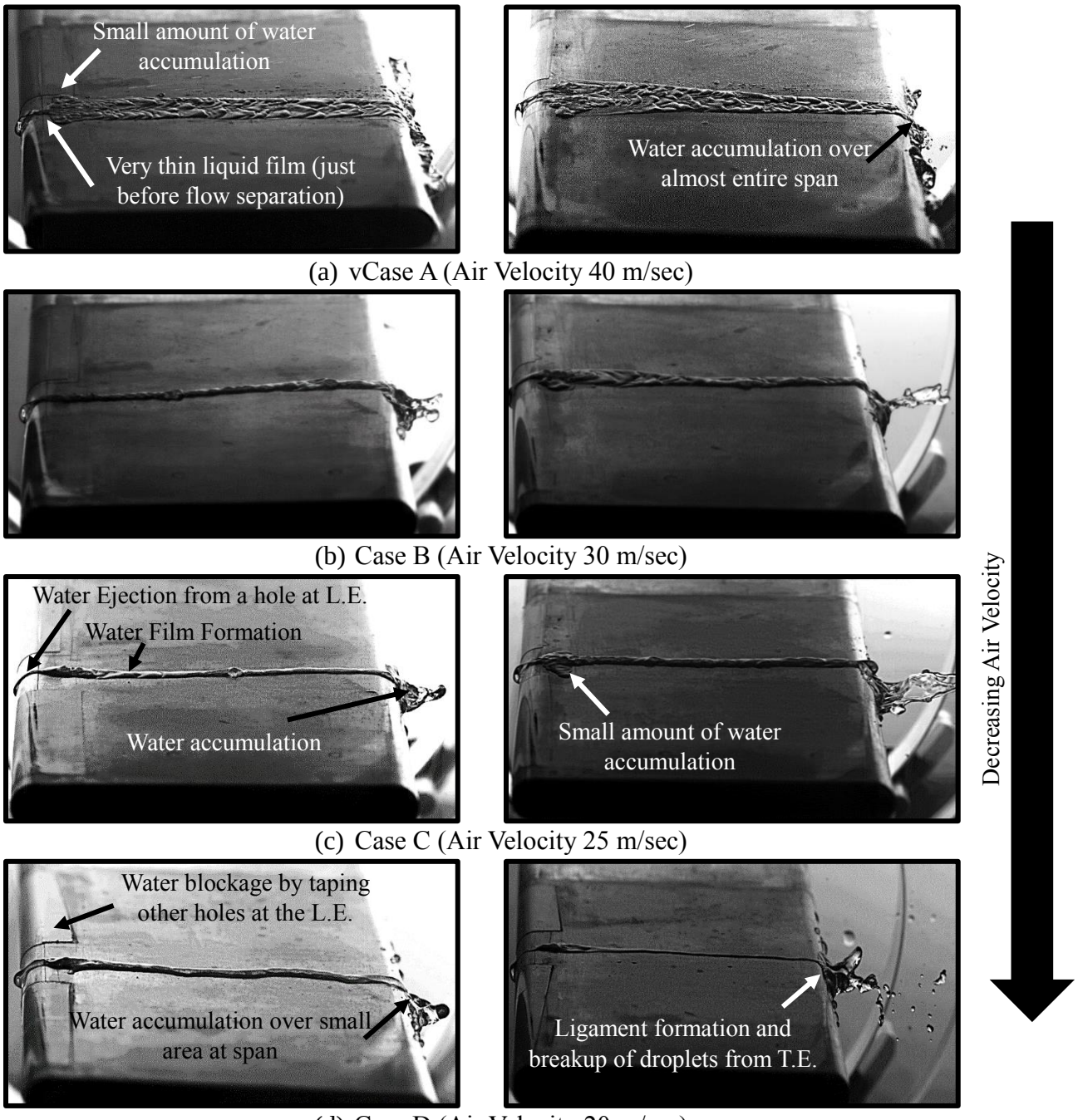

(a) vCase A (Air Velocity 40 m/sec)

(b) Case B (Air Velocity 30 m/sec)

(c) Case C (Air Velocity 25 m/sec)

(d) Case D (Air Velocity 20 m/sec)

(i) Dia. 1 mm (ii) Dia. 1.2 mm

Figure A.7 – Water Film Flow Visualization (1/2)

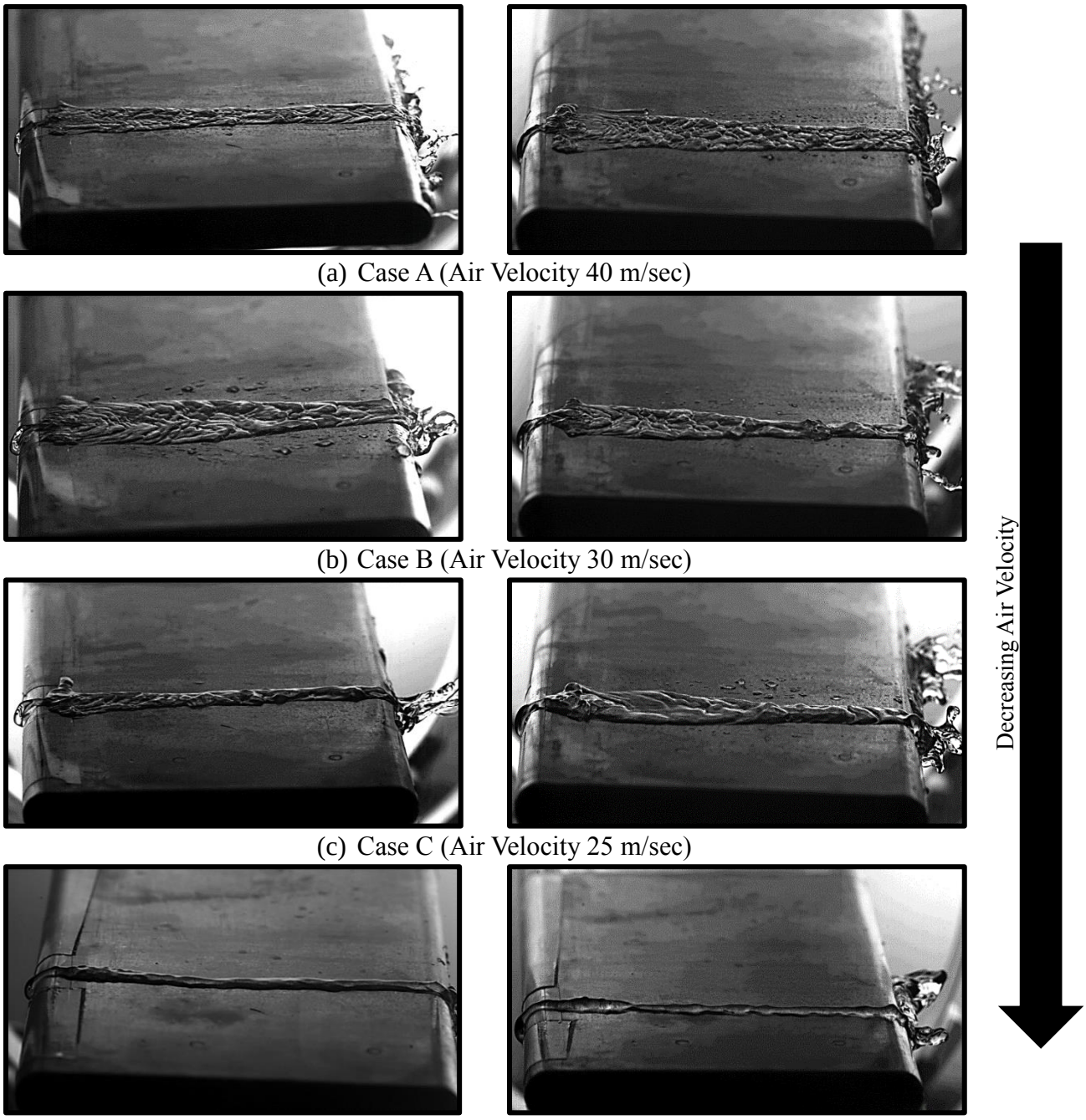

(a) Case A (Air Velocity 40 m/sec)

(b) Case B (Air Velocity 30 m/sec)

(c) Case C (Air Velocity 25 m/sec)

(d) Case D (Air Velocity 20 m/sec)

(iii) Dia. 1.5 mm (iv) Slit

Figure A.7 – Water Film Flow Visualization (2/2)

A.3. Effect of ingestion hole diameter on the characteristics of Liquid Film

A.3.1. Liquid Film Visualization

The liquid film pattern in the case of Flat blade profile also show some resemblance to that of the previously discussed elliptical profile case, and is therefore categorized into the same three categories, i.e.,

1. Wavy Pattern
2. Smooth (Mirror-Like) Pattern
3. Intermediate Wavy Pattern (High and Low)

A.3.1.1. Wavy Pattern

Figure A.8 (a) – (i), – (ii), – (iii) and – (iv) shows the wavy film structure formed from the S.H., M.H., L.H. and Slit ejection hole geometries at high air momentum (Case A). From the flow visualization results, whatever the hole geometry pattern used, the wave structure formed on the suction side of the blade was almost identical due to the similar effects of the aerodynamic forces. The wave structure showed more complex structure, compared to the elliptical profile blade under the same air momentum conditions (Fig. 4.7 to 4.10), which was thought to be due to the flow near at the L.E. of the flat blade (which did not happen for the elliptical profile due to relatively smooth profile). The flow separation at the L.E. resulted in an abrupt widening of the thin film, resulting in a large surface area exposed to the free stream air (possessing high aerodynamic forces), and resulted in a more complex wavy pattern. These waves had relatively high wave velocity and were smaller in wavelength. Due to widened width, the film thickness in this case was the smallest.

A.3.1.2. Smooth (Mirror-Like) Pattern

For the air momentum case (Case D), the water film pattern got the mirror-like smooth structure, as shown in Fig. A.8 (d) – (i), – (ii), – (iii) and – (iv) for S.H., M.H., L.H. and Slit hole geometries respectively. From the high-speed images visualization, it was observed that the smoothness of the water film structure was almost independent of the ingestion hole geometries and was governed by the surface tension forces and the surrounding aerodynamic forces. Similarly, the smoothness of the thin liquid film was not affected by the liquid mass flow rate. The liquid film moved much slower than that of the wavy film pattern with rarely visible long wavelength to appear on the wave surface but overall the wave pattern remained the smooth.

A.3.1.3. Intermediate Wavy Pattern:

Like an elliptical profile blade, in this case also, the intermediate wave pattern was sub-categorized into High- and Low- Intermediate Wavy Pattern due to the appearance of instability on the interface which had shown similar characteristics as already above two discussed cases.

At high intermediate wavy pattern, the wavy film structure appeared at the interface at a relatively high liquid flow rate, which appeared similar to the wavy pattern, as shown in Fig. A.8 (b) – (i), – (ii), – (iii) and – (iv) for S.H., M.H., L.H. and Slit hole geometries respectively. However, as the liquid flow amount was reduced the strength of the wave pattern also get reduced significantly, but still appeared visible waves. For the low intermediate wavy pattern, the wave pattern appeared at relatively high liquid flow rate but as this flow rate was reduced the wave structure also got smoothed as almost similar to that of the mirror-like pattern, as shown in Fig. A.8 (c) – (i), – (ii), – (iii) and – (iv) for S.H., M.H., L.H. and Slit hole geometries respectively. The intermediate wave pattern had high propagation speed than that of the smooth wave structure but was shown than that of the wavy pattern. Moreover, these wave patterns were smaller in height than that of mirror-like wave structure but thicker in size to that of the wavy pattern.

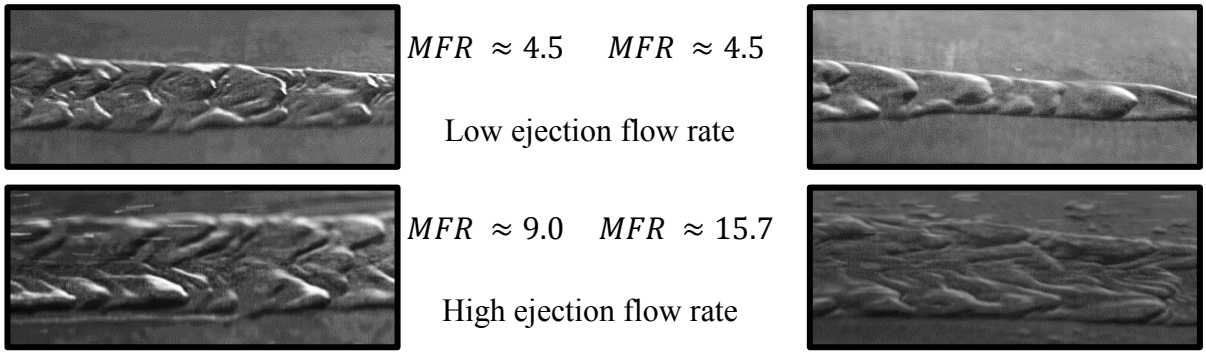

(a) Wavy Pattern - Case A (Air Velocity 40 m/sec)

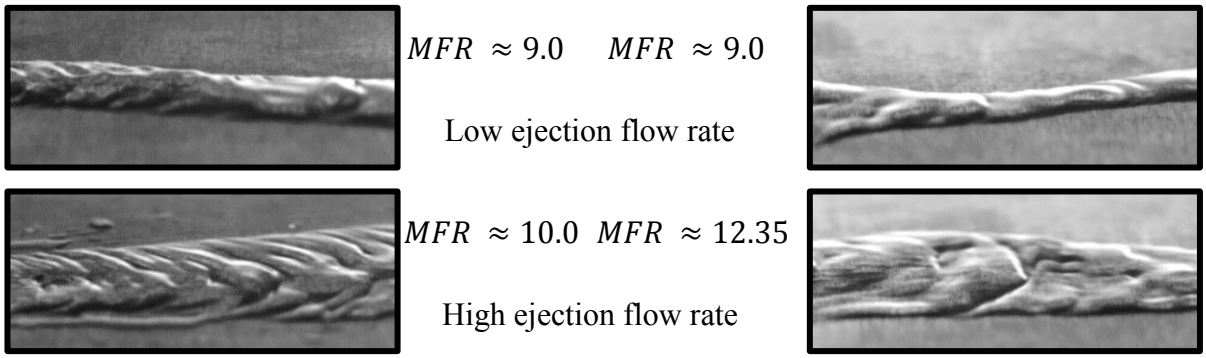

(b) (High) Intermediate Wave Pattern - Case B (Air Velocity 30 m/sec)

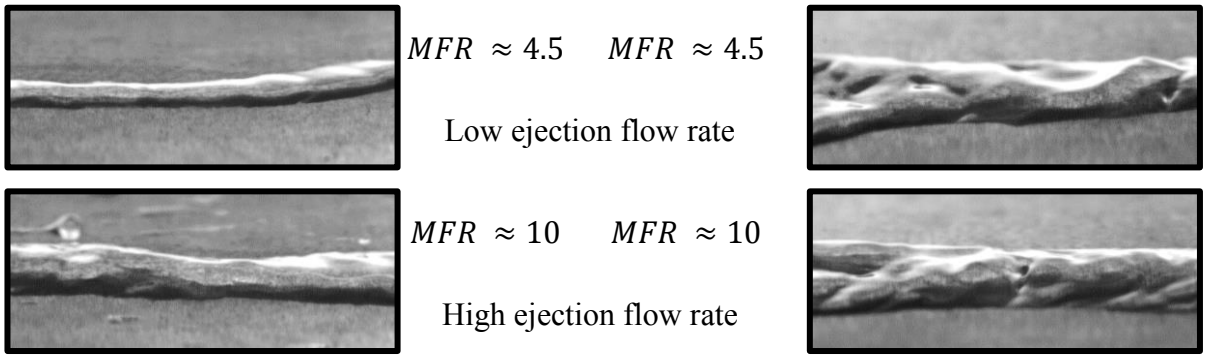

(c) (Low) Intermediate Wave Pattern - Case C (Air Velocity 25 m/sec)

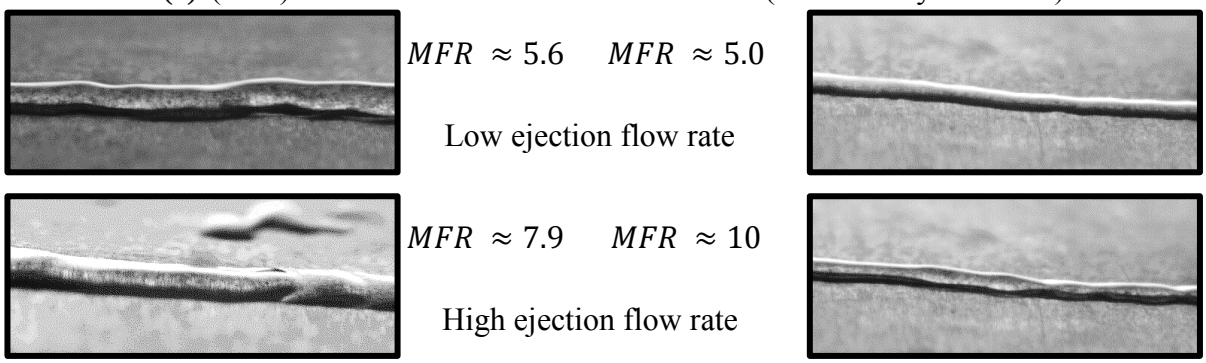

(d) Mirror like Smooth wave Pattern - Case D (Air Velocity 20 m/sec)

(i) Dia. 1.0 mm (ii) Dia. 1.2 mm

Figure A.8 – Water Film Flow Visualization at Mid-chord (1/2)

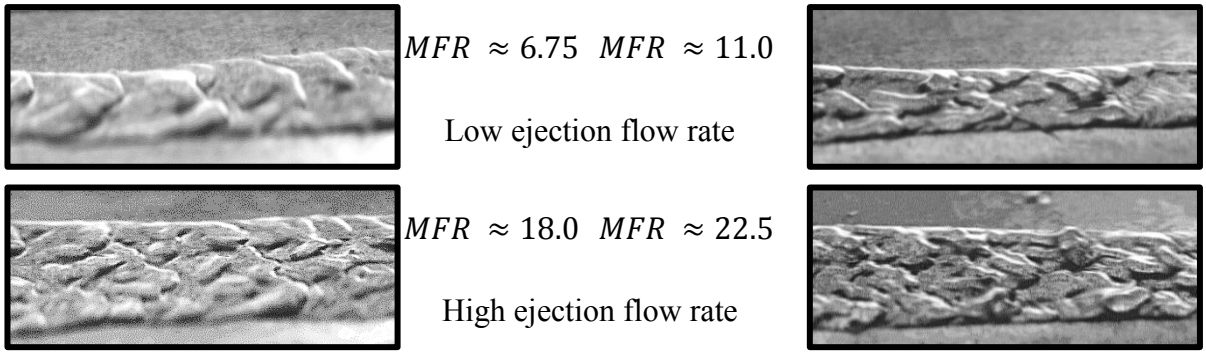

(a) Wavy Pattern - Case A (Air Velocity 40 m/sec)

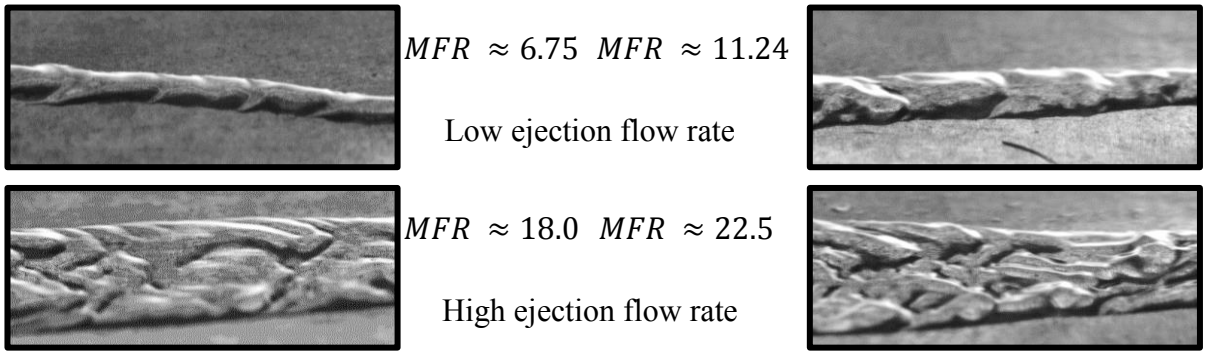

(b) (High) Intermediate Wave Pattern - Case B (Air Velocity 30 m/sec)

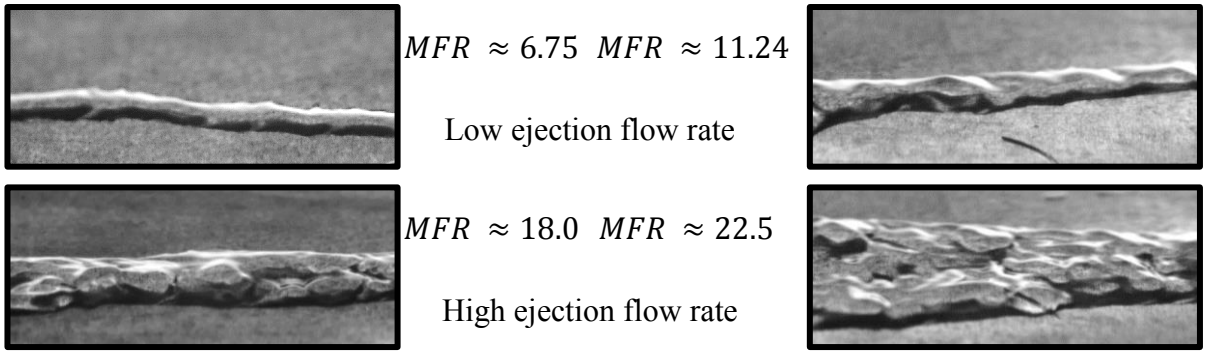

(c) (Low) Intermediate Wave Pattern - Case C (Air Velocity 25 m/sec)

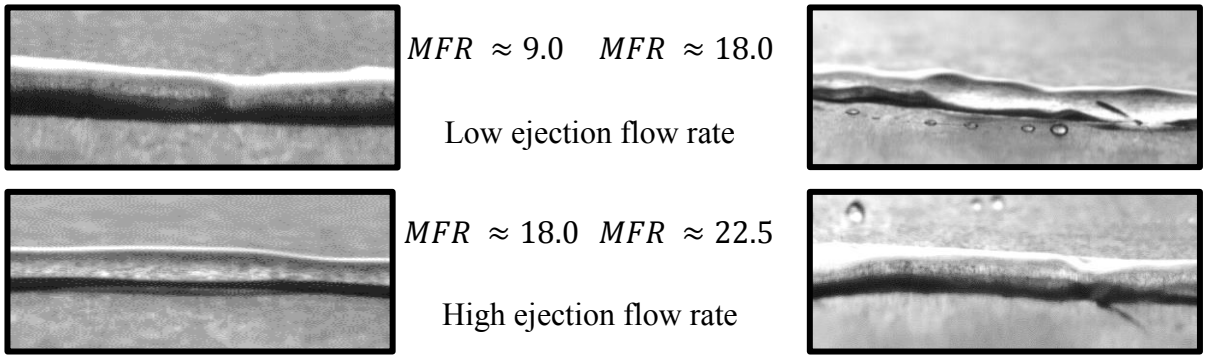

(d) Mirror like Smooth wave Pattern - Case D (Air Velocity 20 m/sec)

(iii) Dia. 1.5 mm (iv) Slit

Figure A.8 – Water Film Flow Visualization at Mid-chord (2/2)

In this case too the following two important characteristics of liquid film were studied

1. Thickness of liquid films.
2. Instability criteria of liquid films.

A.3.2. Liquid Film Velocity and Thickness

The velocity of the thin liquid film was measured in exactly the same way as that for the elliptical blade, see Section 4.3 for details. From Fig. A.9 shows that whatever the ingestion hole size used the liquid flow velocity remained almost the identical. This is mainly because the liquid film experiences the same aerodynamic forces and independent of the ingestion hole size. The liquid film flow was considered to be given by similar to that of the Couette flow and linear velocity profile for the water film is assumed, as shown in Fig. 4.12. Based on this assumption the thickness of the thin liquid film was calculated theoretically by using the mathematical expression given by Eq. (4.14).

Figure A.10 shows the water film thickness at the mid-chord of the flat blade profile. The water film width was experimentally measured at the mid-chord of the blade, whereas the velocity of the thin film was also experimentally measured by measuring the distance tracker particles moved in two consecutive frames. From the experimental results, Fig. A.10 and Eq. (4.14) the liquid film thickness was dependent only on the liquid and gaseous state properties and was completely independent of the ingestion hole geometry. Monnier et al. [92] consider the stretching of the liquid film by using the minimum energy concept. Based on the minimum energy principle, the shape and motion of the liquid film become stable under the conditions at which the total energy gained by the liquid from the air become minimum. As the total energy gained by the liquid is governed of liquid's surface tension property only and not the shape of the ingestion hole profile, therefore, whatever the size of the ingestion hole was used, the minimum energy makes the liquid film stable by changing the width of the film. This results in the height of the liquid film to change accordingly. Though, in Fig. A.10 small discrepancies of experimental data are observed, which might be due to the fact that the aerodynamic forces might be marginally different due to the different ingestion holes positions. However, the measurement of liquid film thickness via laser sensors is highly recommended to validate the applicability of the theoretical expression given by Eq. (4.14).

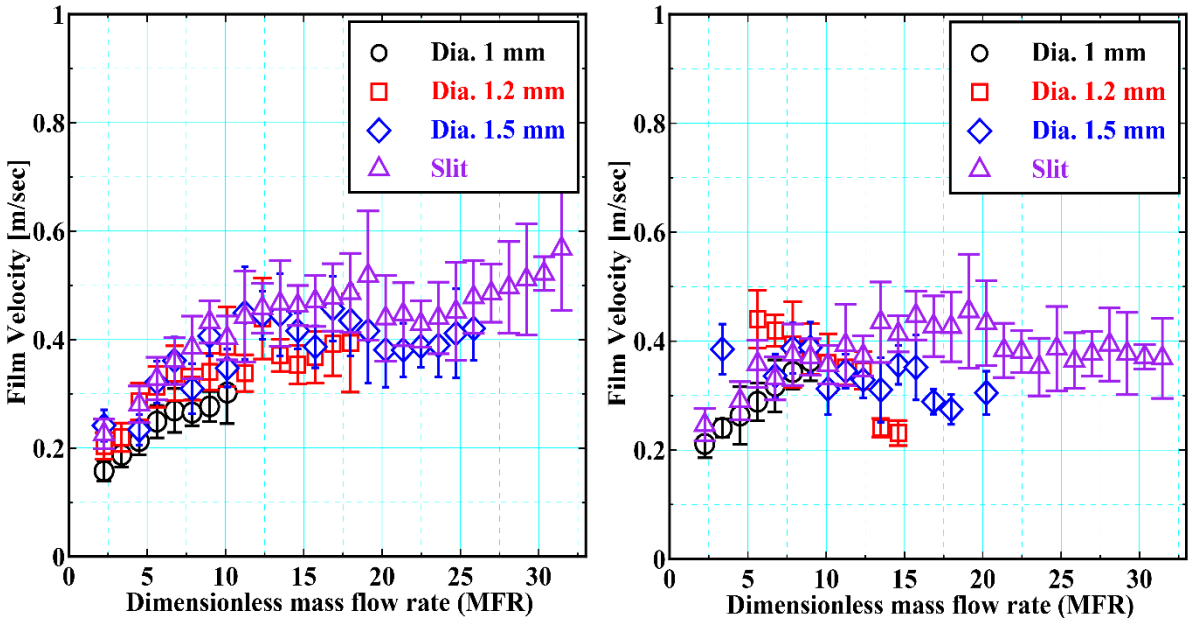

(a) Case A (Air Velocity 40 m/sec)

(b) Case B (Air Velocity 30 m/sec)

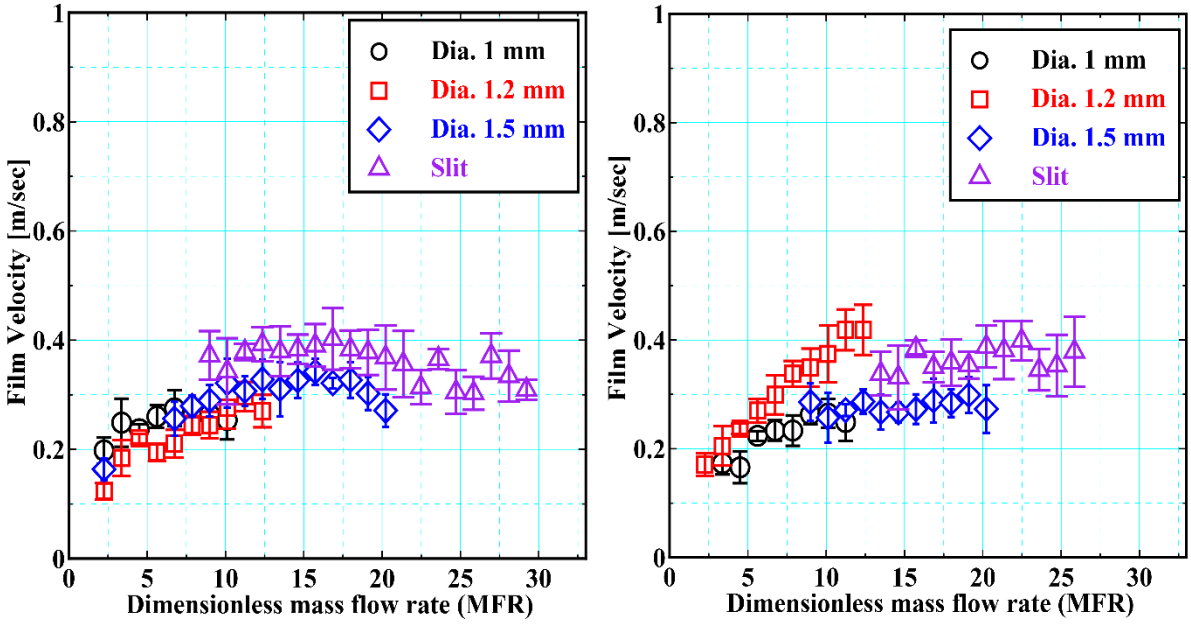

(c) Case C (Air Velocity 25 m/sec)

(d) Case D (Air Velocity 20 m/sec)

Figure A.9 – Liquid Film Velocity @ Mid-chord (Flat Blade)

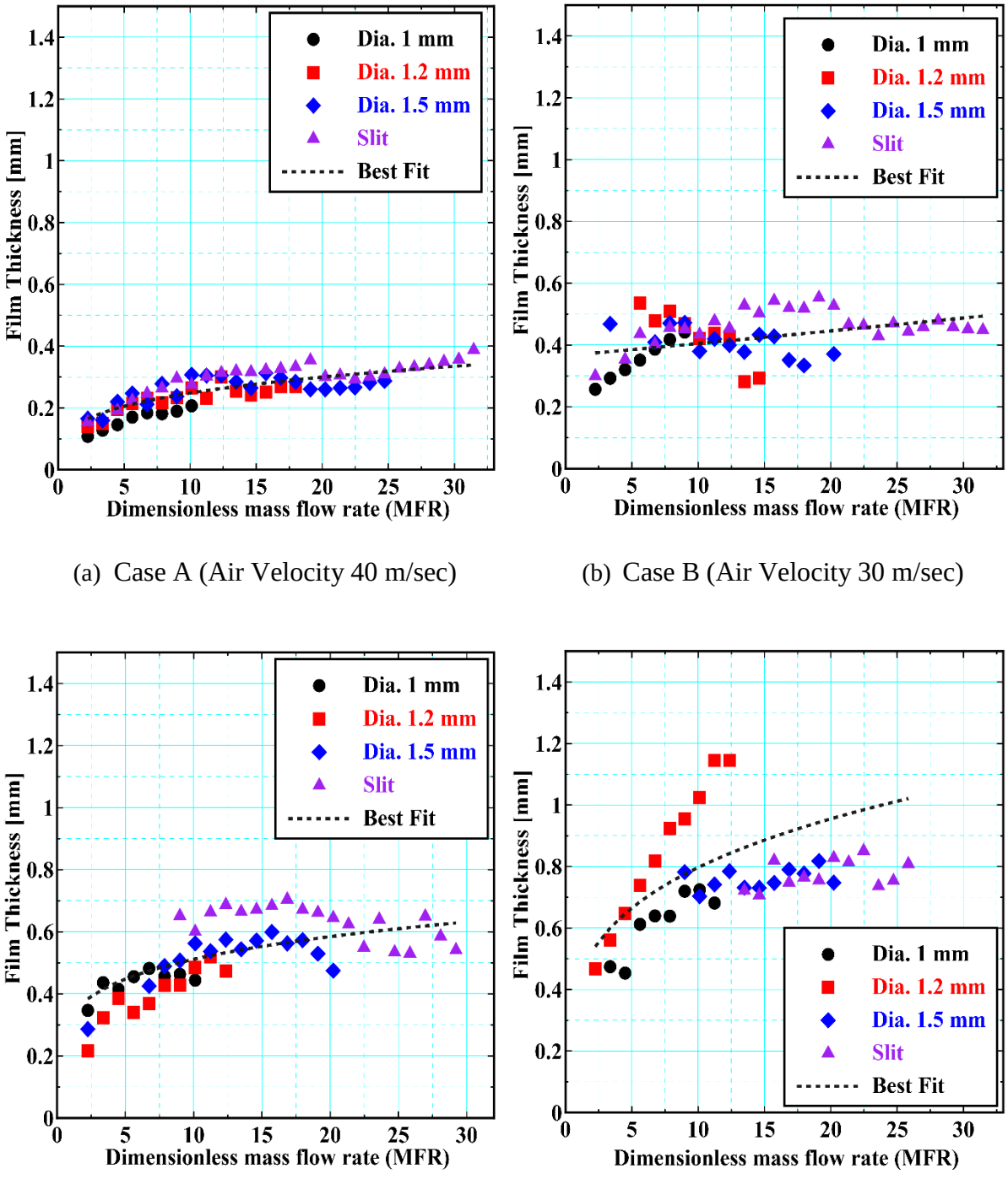

(a) Case A (Air Velocity 40 m/sec)

(b) Case B (Air Velocity 30 m/sec)

(c) Case C (Air Velocity 25 m/sec)

(d) Case D (Air Velocity 20 m/sec)

Figure A.10 – Liquid Film Thickness @ Mid-chord (Flat Blade)

A.3.3. Water Film Instability (Craik's Model of thin Film Instability)

Craik's model of instability was applied to investigate the instability criteria of thin liquid films as given in detail in Section 4.3. Based on Craik's model of thin film instability, it was explained physically and expressed mathematically that an instability on the thin liquid films occurs when the surface stresses (due to the aerodynamic forces) is sufficient to overcome the restoring phenomenon of inertia and surface tension.

As already explained in detail in Section 4.3 that in general the surface stresses is dominated by the normal pressure perturbation term (Π_r), which causes an upward force on the crest and downward force on the trough. Additionally, in thin films the effect of shear pressure perturbation (Σ_i) also get dominant as it accelerate and de-accelerate the fluid in the windward and leeward direction respectively. Thus, if both factors overcome the liquid surface tension and inertia effect then an instability pattern appears on the air-liquid interface.

Figure A.11 shows the instability pattern obtained based on the Craik criteria whereas Table A.4 gives the experimentally measured wavelength of the liquid films under different geometries. The dimensional wavelength was approximated identical values of liquid rate and under the same air momentum cases. Thus, as the wave number exceeded the minimum level of α an instability pattern appeared on the interface due to the viscous dissipation. However, for larger value of α the liquid surface tension get dominant and vice versa. From Table A.4, the values of wavelength are nearly the same for the different ingestion hole types for the identical conditions of liquid flow rate and the air momentum. Moreover, it should be noted that for high momentum case (Case A), the dimensional wavelength is smaller than the Case B, corresponding to that fact that at high momentum more energy transfer took place. This is also given from Fig. A.11, which shows that at the same value of dimensional wave number, the corresponding value of dimensionless amplification factor is greater and vice versa.

Table A.4 – Dimensionless Wave Number

Dimensionless Mass Flow Rate (MFR)	6.75	10.0
Ejection Hole Size	Dimensionless Wave Number	
	Case A	Case B
Diameter 1-mm	0.37	0.59
Diameter 1.2-mm	0.57	0.61
Diameter 1.5-mm	0.36	0.67
Slit	0.45	0.61

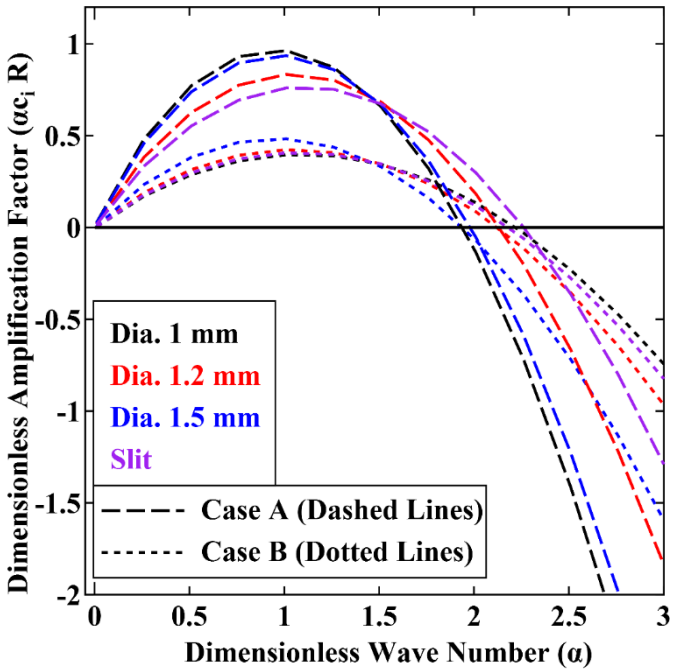

Figure A.11 – Water Film Stability Criteria (Flat Blade)

A.4. Effect of Ingestion hole diameter on droplet size distributions aft the T.E. of Cascade Blade

For fogging in gas turbines different type of nozzles are used for water ejection. A lot of general experimental material were presented in the past, which explained in details the effect of droplets size distribution for different nozzle types geometries. However, so far according to author's knowledge, no in-depth knowledge is obtained about the effect of different nozzle geometries and their effects on the droplets size distribution aft the T.E. of the cascade blade. Additionally, no or perhaps very few experimental study were conducted which consider the effect of droplets breakup from the T.E. of the cascade blade due to the different nozzle types. Therefore, this study is expected to provide a detailed insight of the fundamental phenomena involved by utilizing different ingestion hole types.

A.4.1. Droplets breakup Mechanism aft the T.E. Region

The droplet breakup phenomenon can be easily understood based on the Weber number of T.E. profile thickness and the momentum ratio as given in Eq. (4.33) and (4.34) respectively. Here, the order of momentum ratio was also roughly approximated (about 10^{-1} to 10^{-2} but 10^{-1} was chosen, see Appendix C). From the extensive visualization results, it was also found that in general the ligament formation and the droplets shedding phenomenon were the same whichever ingestion hole geometry was used. However, for the purpose of completeness in this thesis, a pictorial detail visualization phenomenon are given for the S.H. geometry case only, Fig. A.12 to A.15. It should be noted that the detailed visualization were performed for all the ejection geometries also.

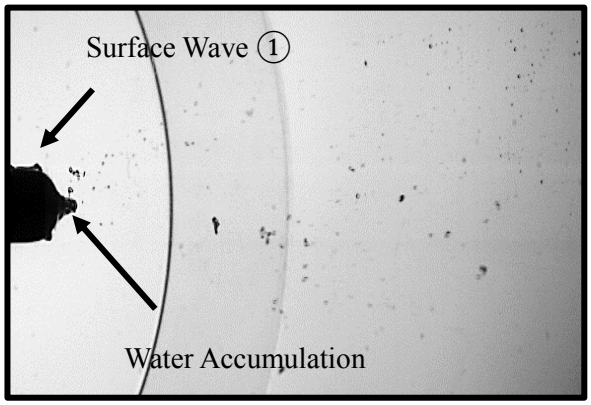

(a) Start of Liquid Accumulation (0.0 sec)

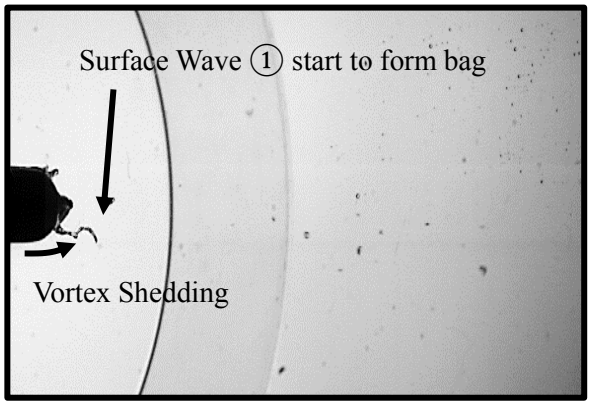

(b) Surface Wave start to form bag (5.66 m.sec)

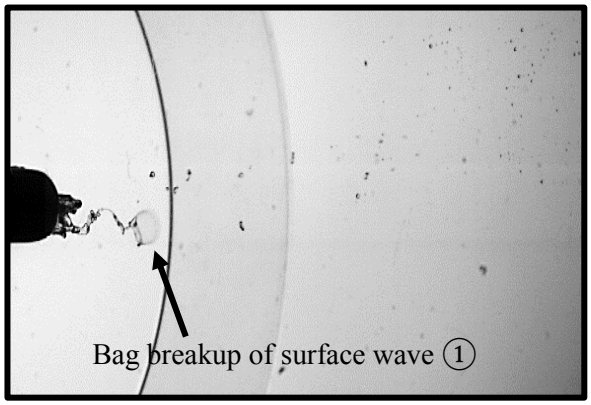

(c) Bag Breakup of surface wave 0.25-C (10.33 m.sec)

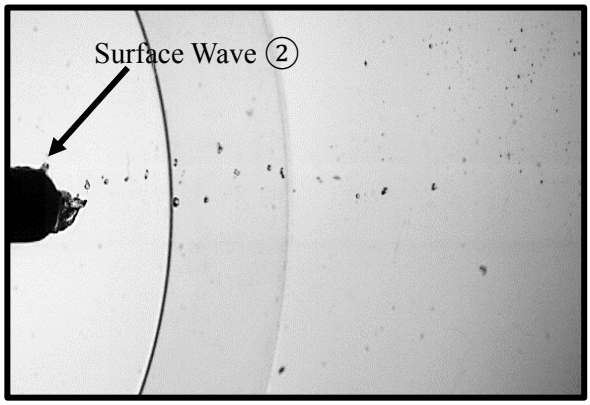

(d) Another incoming surface wave (17 m.sec)

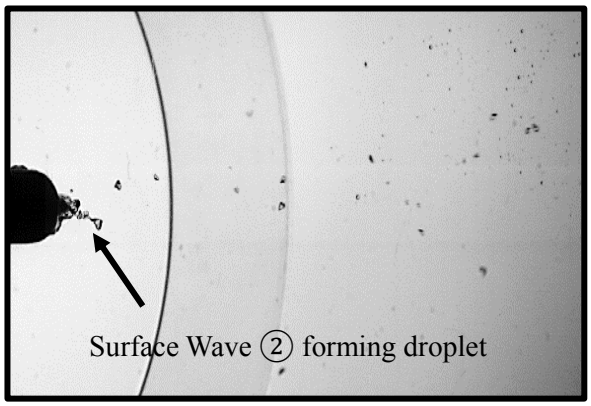

(e) Stripping of droplet from the surface wave accumulated at T.E. (20 m.sec)

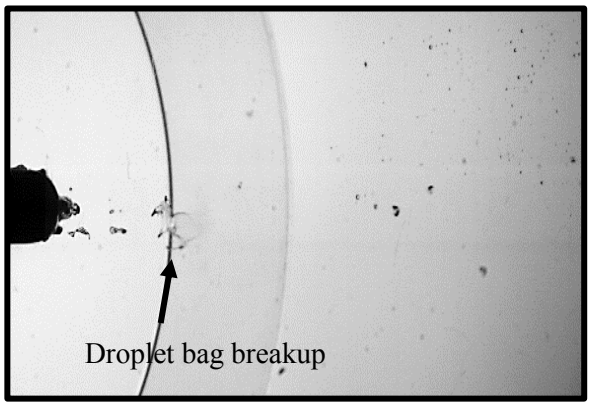

(f) Bag breakup of surface wave near 0.25-C (22 m.sec)

Figure A.12 – Breakup and Atomization aft the T.E. – Case A (Velocity 40 m/sec), $MFR = 11.24$ ($M \approx 192, We_a \approx 160$) (1/2)

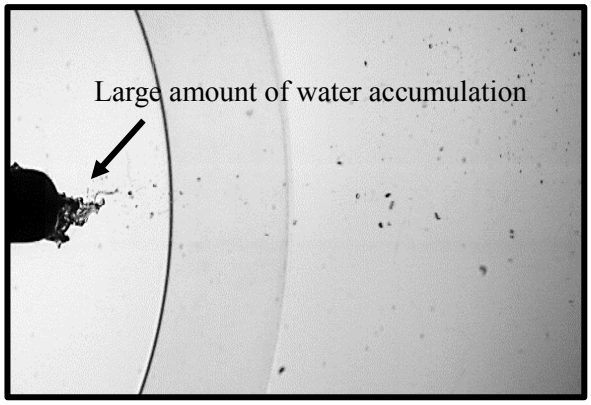

(g) Large amount of water accumulation at T.E. (140.33 sec)

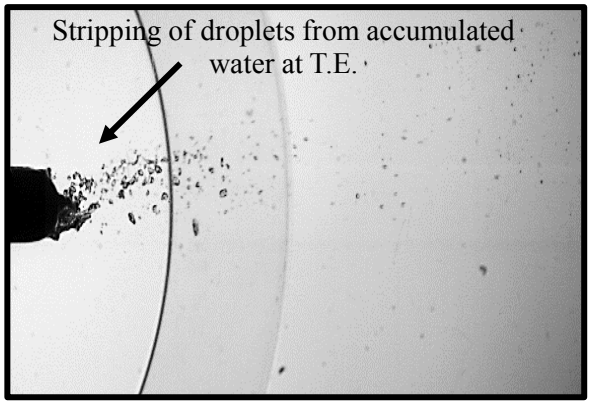

(h) Droplets Stripping from accumulated water at T.E. (145.66 m.sec)

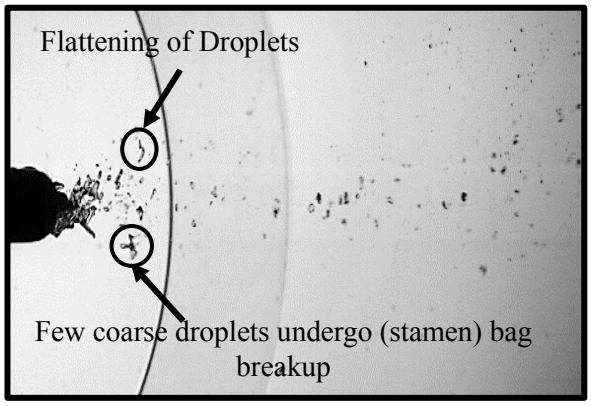

(i) Breakup of coarse droplets due to bag mode near 0.25-C (150.66 m.sec)

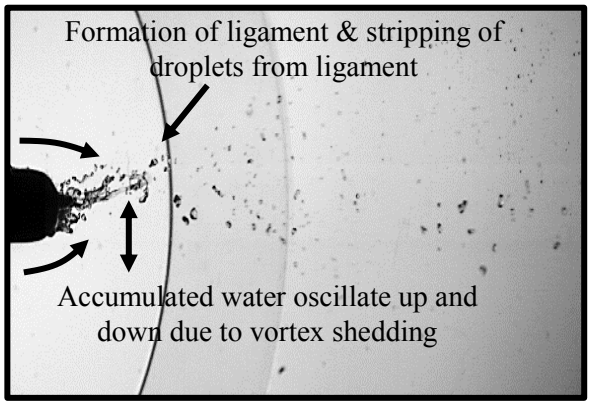

(j) Oscillation of accumulated water due to vortex shedding (152.66 m.sec)

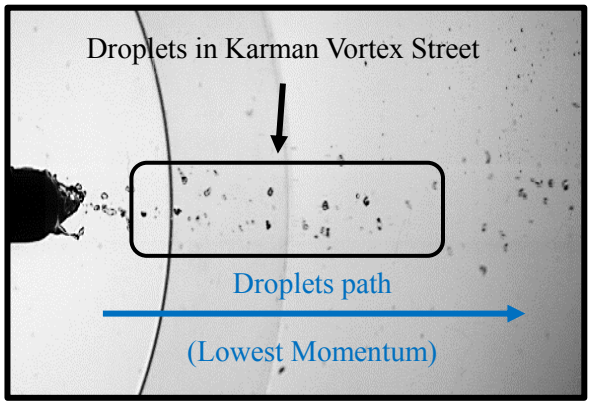

(k) Karman Vortex Street of droplets (192 m.sec)

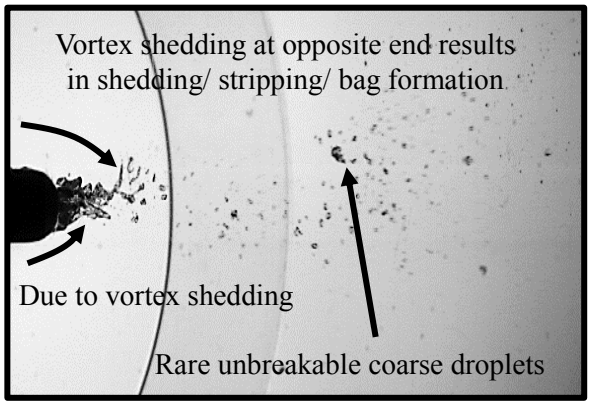

(l) Vortex Shedding changing the path of droplets (195.33 m.sec)

Figure A.12 – Breakup and Atomization aft the T.E. – Case A (Velocity 40 m/sec), $MFR = 11.24$ ($M \approx 192, We_a \approx 160$) (2/2)

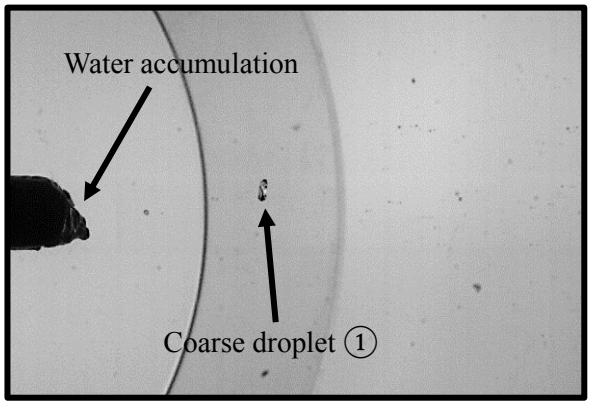

(a) Start of Liquid Accumulation (0.0 sec)

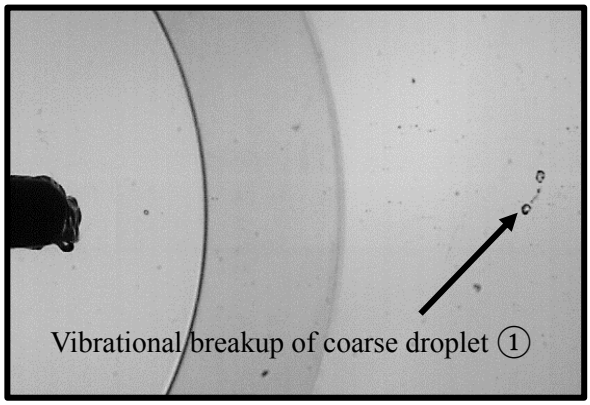

(b) Vibrational breakup of droplet (6 m.sec)

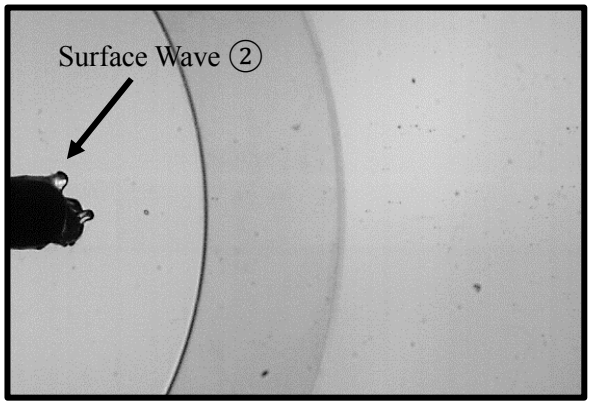

(c) Bag Breakup at the T.E. just before 0.25-C (5.66 m.sec)

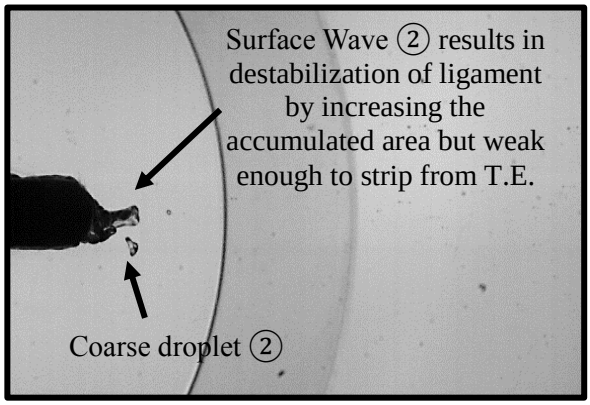

(d) Accumulated water amount increases due to surface wave at T.E. (25.66 m.sec)

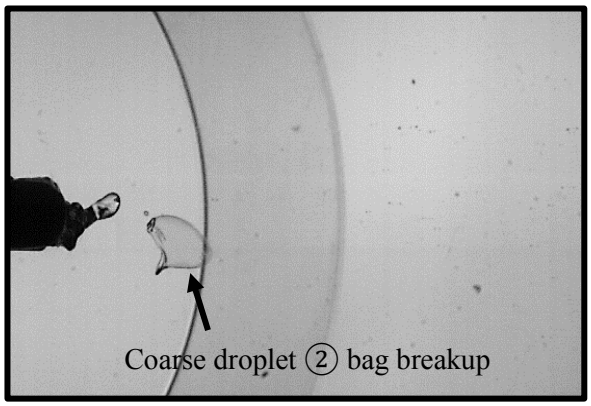

(e) Bag Breakup of droplet near 0.25-C (28.33 m.sec)

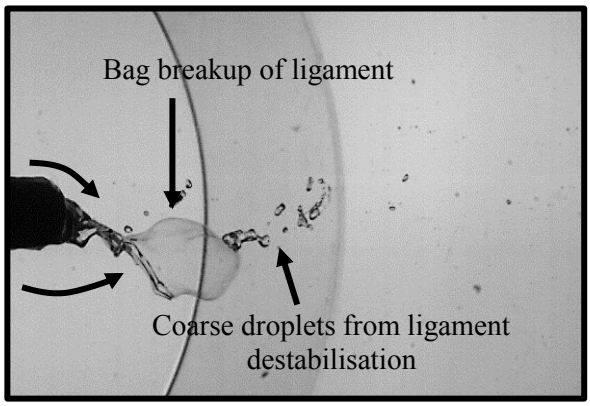

(f) Bag formation of ligament (just greater than 0.25-C) (47 m.sec)

Figure A.13 – Breakup and Atomization aft the T.E. – Case B (Velocity 30 m/sec), $MFR = 11.24$ ($M \approx 108, We_a \approx 90$) (1/2)

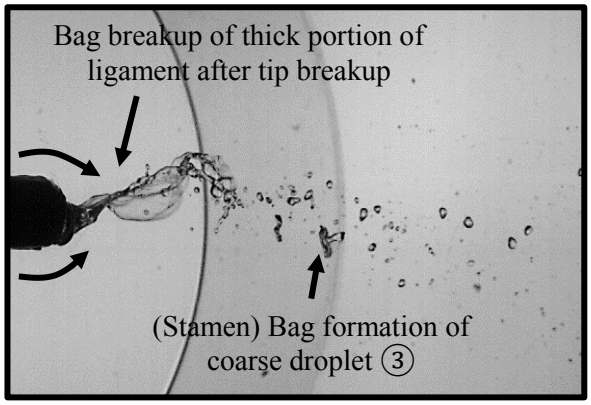

(g) Bag formation of ligament and Vortex shedding oscillating a ligament (133.3 m.sec)

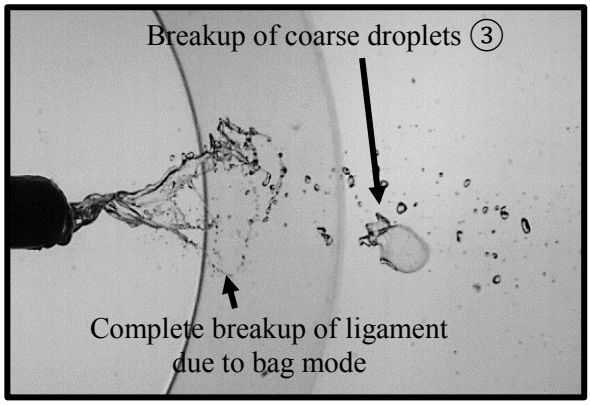

(h) Bag breakup of ligament (just after 0.25-C) & coarse droplets (144 m.sec)

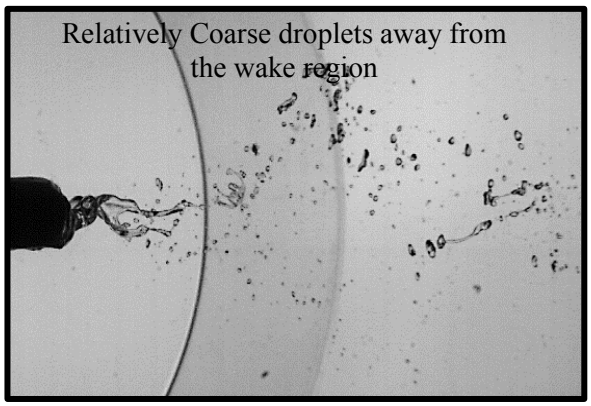

(i) Coarse droplets aft the T.E. region (145.66 m.sec)

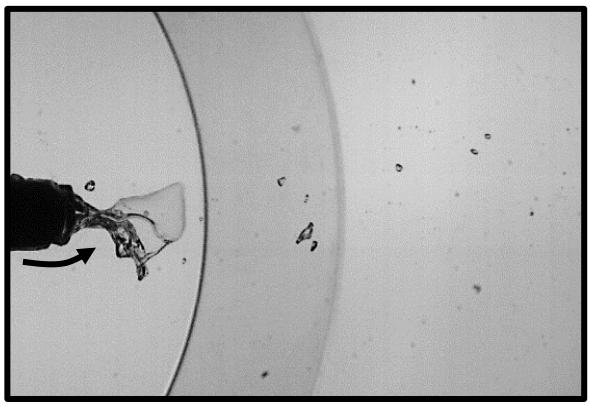

(j) Formation of Bag due to vortex (239.66 m.sec)

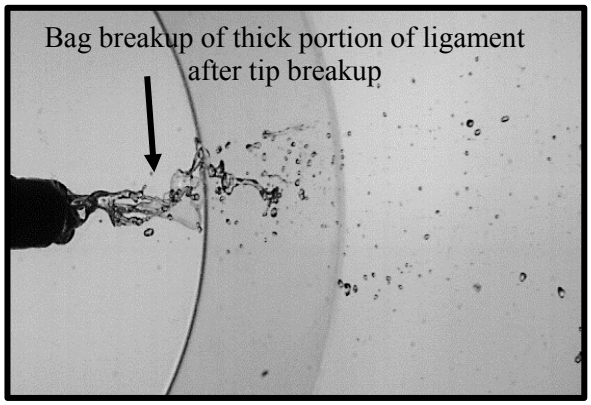

(k) Bag Breakup from ligament tip with more bag formation in ligament due to counter vortex (241 m.sec)

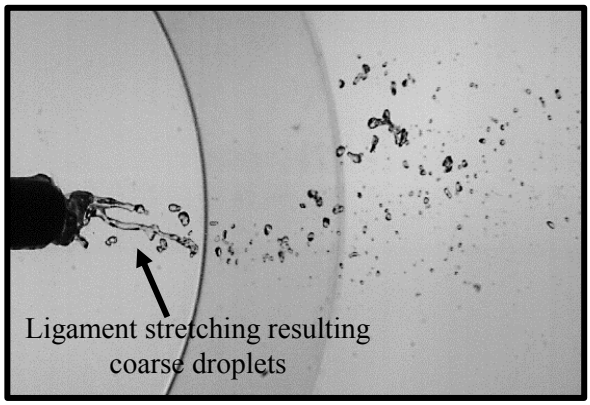

(l) Ligament stretching resulted in coarse droplets formation (244.33 m.sec)

Figure A.13 – Breakup and Atomization aft the T.E. – Case B (Velocity 30 m/sec), $MFR = 11.24$ ($M \approx 108, We_a \approx 90$) (2/2)

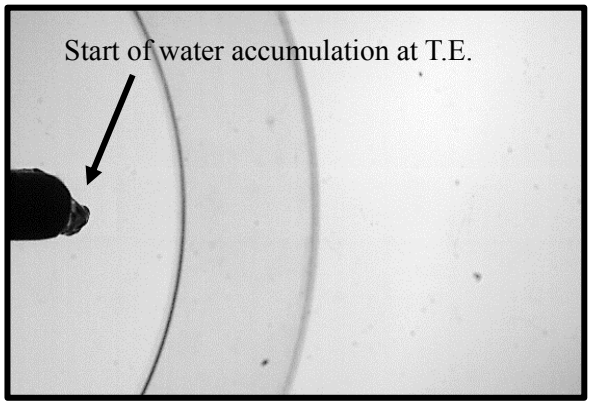

(a) Start of Liquid Accumulation (0.0 sec)

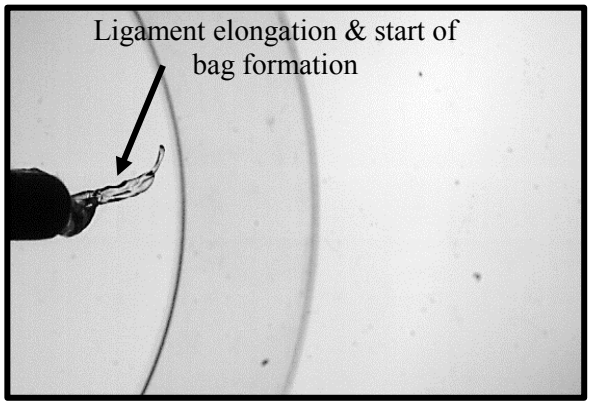

(b) Thick ligament start to form bag (22 m.sec)

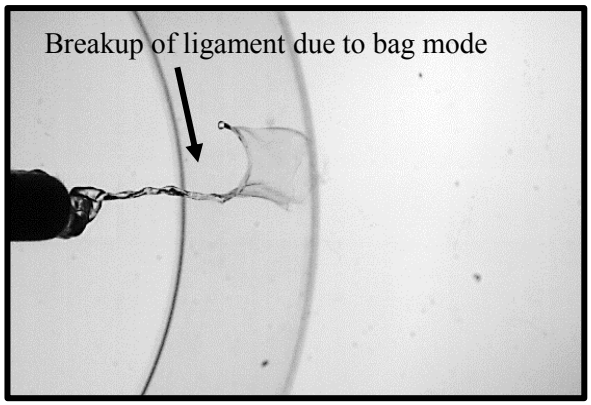

(c) Bag Breakup from the tip of ligament at 0.5-C (24.66 m.sec)

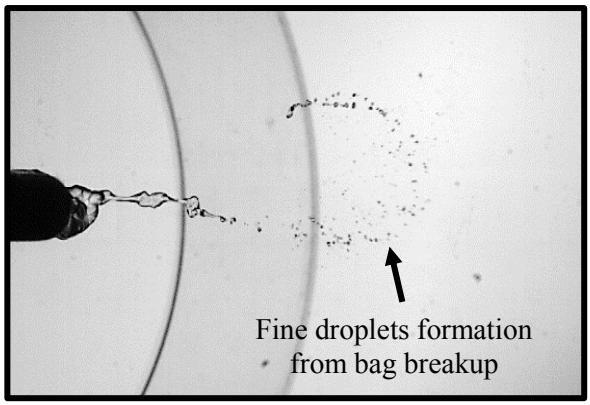

(d) Formation of fine droplets from bag breakup (26.33 m.sec)

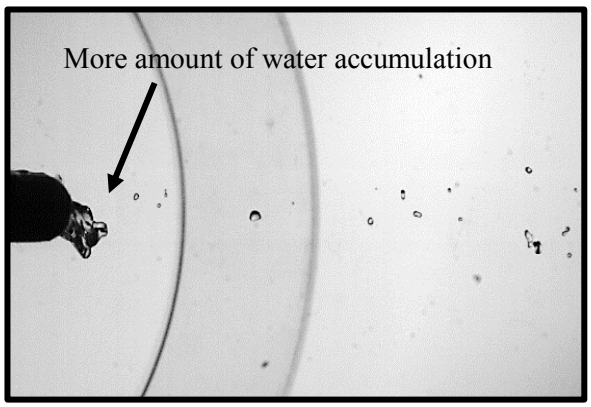

(e) Large lump of water accumulated at T.E. (114.33 m.sec)

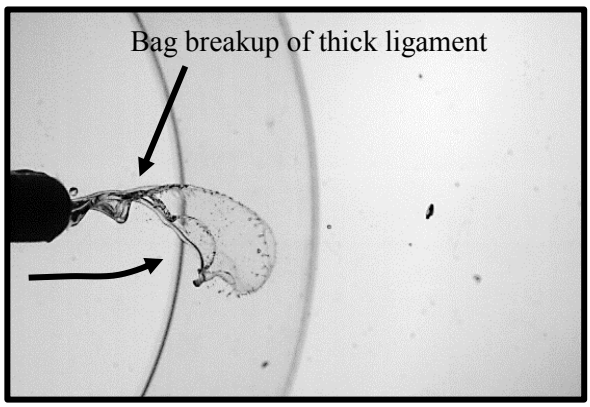

(f) Bag breakup of ligament between 0.25- and 0.5-C (120 m.sec)

Figure A.14 – Breakup and Atomization aft the T.E. – Case C (Velocity 25 m/sec), $MFR = 11.24$ ($M \approx 75, We_a \approx 62.5$) (1/2)

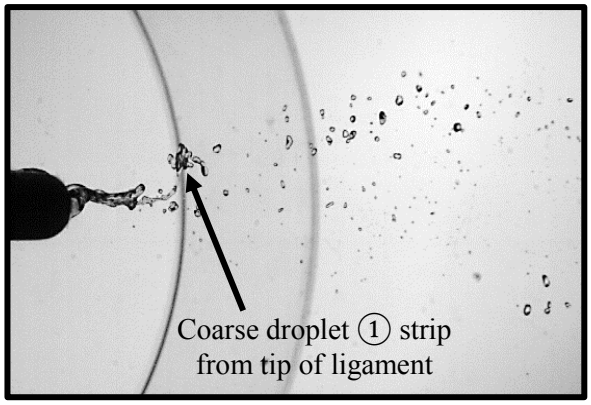

(g) Coarse droplet stripped from unstable thick ligament (125.66 sec)

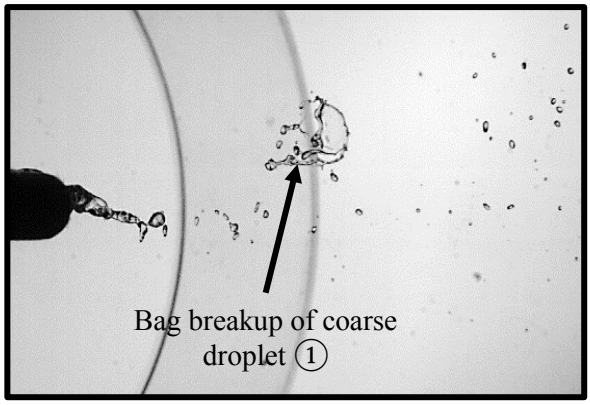

(h) Bag breakup of coarse droplet (129.66 m.sec)

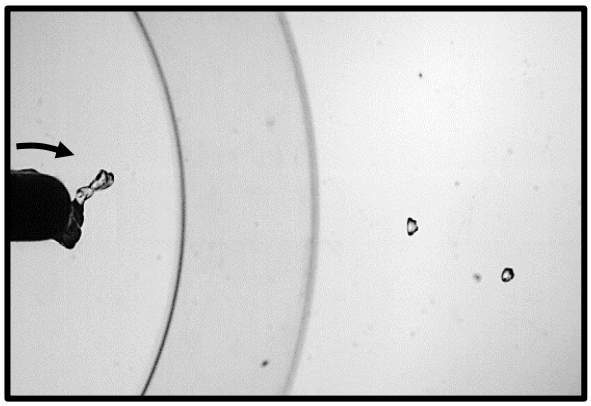

(i) Stripping of droplet from the edge of accumulated water due to vortex (881.66 m.sec)

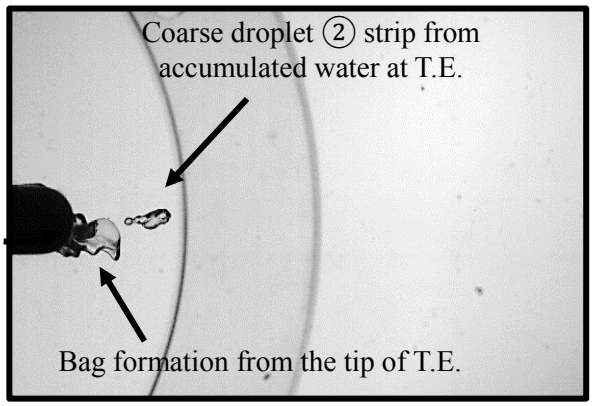

(j) Formation of Bag at the T.E. (888 m.sec)

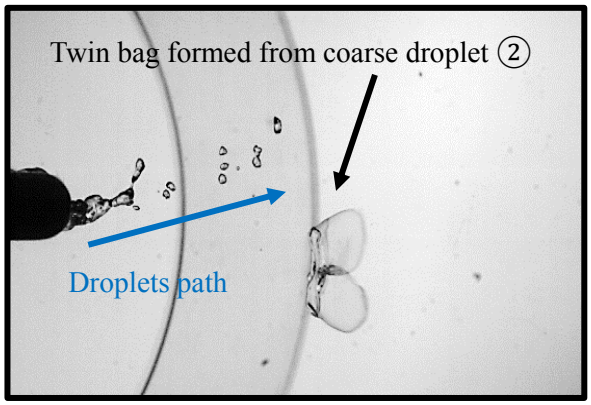

(k) Twin bag breakup from stripped droplet (897.66 m.sec)

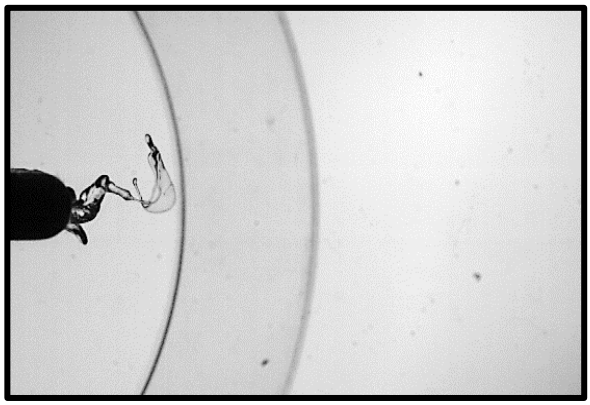

(l) Bag Formation (928 m.sec)

Figure A.14 – Breakup and Atomization aft the T.E. – Case C (Velocity 25 m/sec), $MFR = 11.24$ ($M \approx 75, We_a \approx 62.5$) (2/2)

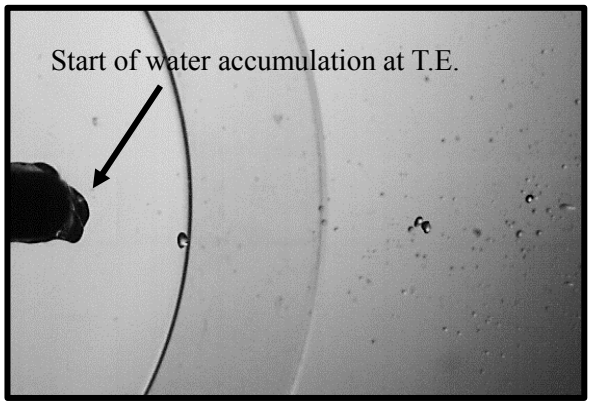

(a) Start of Liquid Accumulation (0.0 sec)

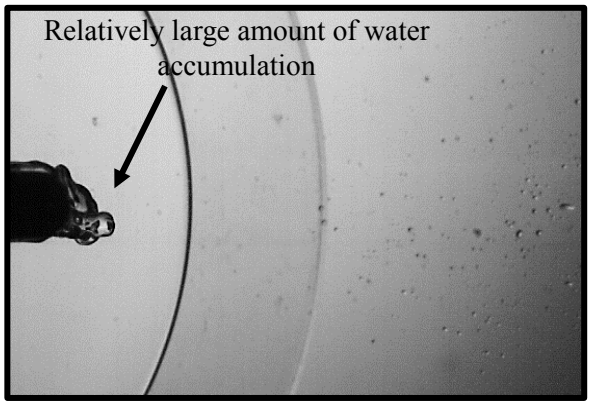

(b) Large amount of water accumulated at T.E. (39.66 m.sec)

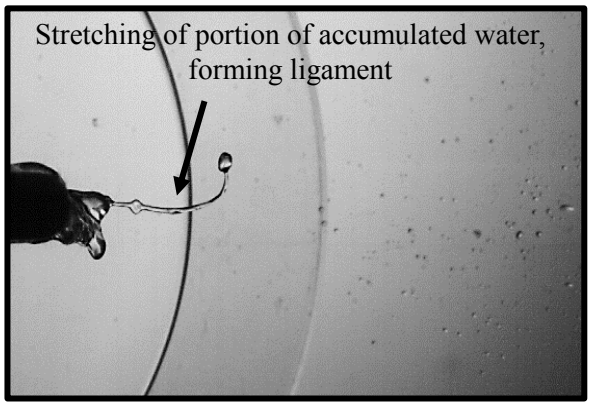

(c) Stretching of portion of ligament beyond 0.25-C (67 m.sec)

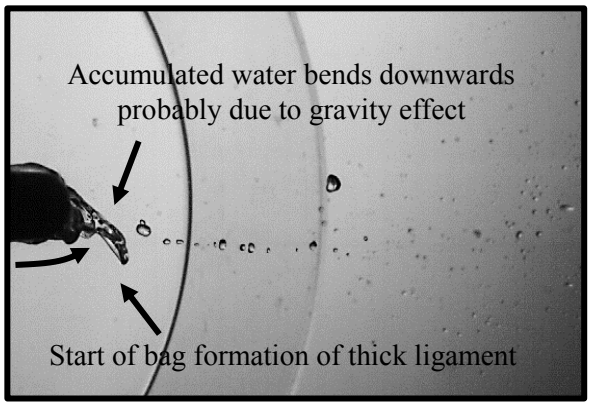

(d) Start of Bag formation from thick ligament (71.66 m.sec)

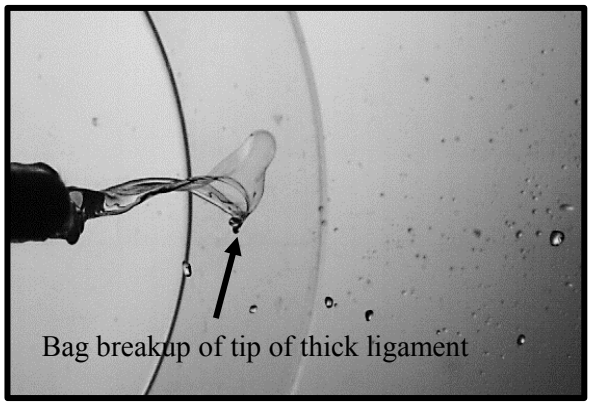

(e) Bag Breakup of ligament between 0.25- and 0.5-C (79 m.sec)

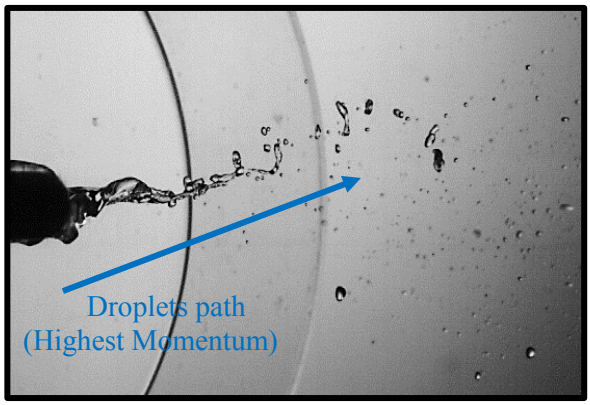

(f) Coarse droplet (High Momentum) (86 m.sec)

Figure A.15 – Breakup and Atomization aft the T.E. – Case D (Velocity 20 m/sec), $MFR = 18$ ($M \approx 48, We_a \approx 40$) (1/2)

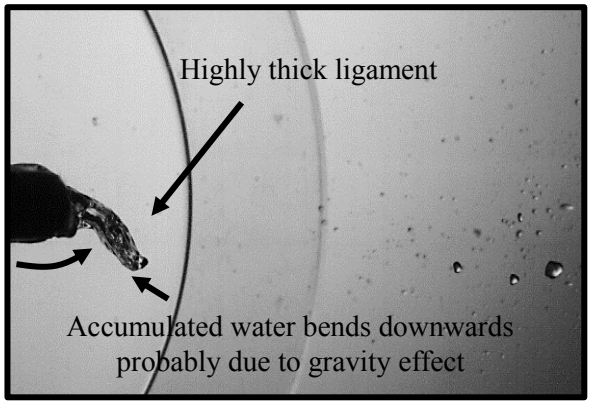

(g) Highly stable thick ligament at T.E. (104.33 sec)

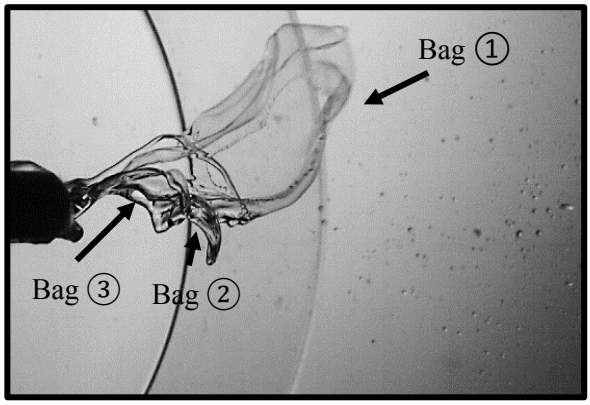

(h) Large Bag formation whose length exceeds 0.5-C (110.66 m.sec)

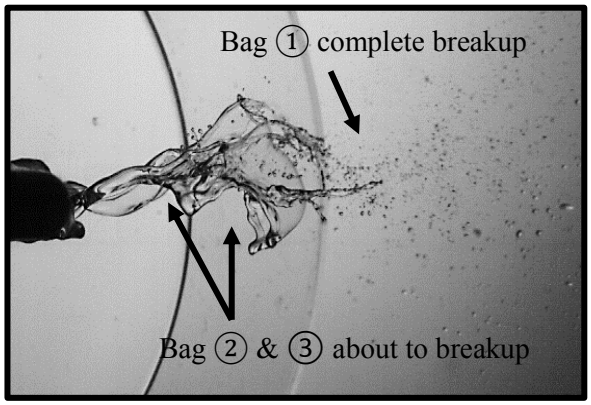

(i) Multiple bag formation in thick ligament (112.66 m.sec)

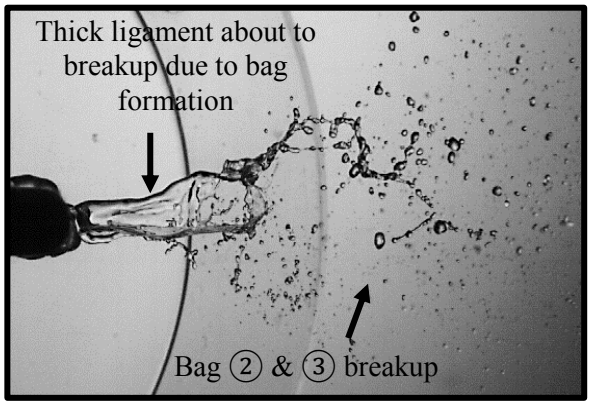

(j) Breakup of thick ligament with still sufficient amount of water accumulated at T.E. (117 m.sec)

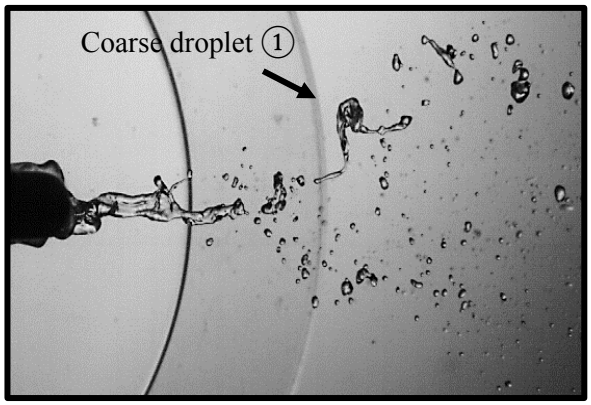

(k) Highly coarse droplets (or ligament like structure) aft the T.E. region (122.33 m.sec)

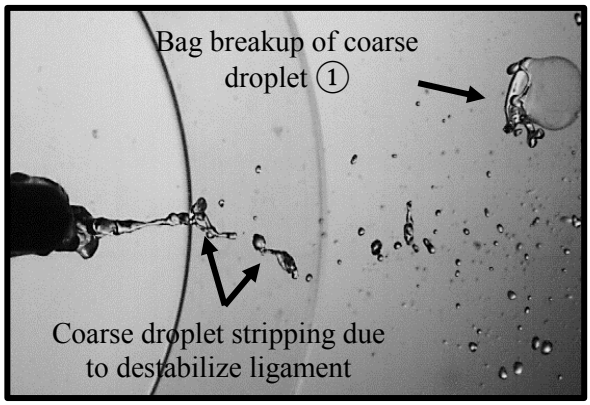

(l) Breakup of coarse droplet between 0.75- and 1-C (127.66 m.sec)

Figure A.15 – Breakup and Atomization aft the T.E. – Case D (Velocity 20 m/sec), $MFR = 5.62$ ($M \approx 48, We_a \approx 40$) (2/2)

A.4.1.1. High Air Momentum (Case A (Air Velocity 40 m/sec), $M \approx 192, \mathrm{We}_a \approx 160$ – Fig. A.12) – Breakup due to Aerodynamic forces

At relatively high air momentum ($M \approx 192$) and weber number ($\mathrm{We}_a \approx 160$) the role of surface waves formed on the blade surface played a major role in the breakup of droplets from the T.E.. Following are three main breakup cases that were observed due to these surface waves when accumulate at the T.E..

(a) Breakup due to Bag mode of Breakup

For high propagation speed the surface waves reached the T.E. of the blade, leading to the formation of a small ligament (Fig. A.12 (b)) on its own and stripped from the T.E. of the blade due to the bag breakup (Fig. A.12 (c)). Since only single wave resulted in the fragmentation of the ligament, the number of droplets produced were also few in numbers.

(b) Stripping of the droplets directly from the waves

Another frequently observed phenomena was the formation of small ligaments from the high-speed waves. However, due to the relatively large momentum of the surface wave, coarse droplets shed from the tip of the ligaments as shown in Fig. A.12 (e). The droplets shed were usually unstable and soon underwent breakup either due to the bag mode or the vibrational mode of a breakup. Figure A.12 (f) shows a case in which relatively coarse droplets undergo bag mode of a breakup. In few cases, the droplets formed were stable enough and did not undergo any breakup.

(c) Destabilization of the accumulated water at T.E.

Another commonly seen phenomenon was the accumulation of water at the T.E.. When accumulated water reached a certain amount (Fig. A.12 (g)), the vortex shed from the T.E. of the blade destabilized of the accumulated water. This results in the chunk of a large number of droplets to shed from the T.E.. It was generally observed that due to the relatively large density of the liquid, water starts to accumulate towards the pressure side of the blade (probably due to gravity effect) and droplets shedding mostly starts from the P.S. of the T.E. of the blade. The accumulated water moves upward, i.e., towards the suction side. The vortex shed from the opposite side (suction side) further enhanced this phenomenon by fragmentation of a large amount of droplets from the accumulated water and also started to move the accumulated water downwards. This process kept on continuing until enough amount of water in the form of droplets was shed aft the T.E. region.

The droplets formed were smaller in size due to the vibrational mode of a breakup. the droplets generated possessed low momentum and followed the air path. Occasionally it was also observed that the droplets were travelling in the Karman Vortex Street structure, as shown in Fig. A.12 (k).

A.4.1.2. Low Air Momentum (Case – D (Air Velocity 20 m/sec), $\mathrm{M} \approx 48, \mathrm{We}_a \approx 40$ – Fig. A.15) – Breakup due to Surface Tension forces

For low momentum ratio, $M \approx 48$ and $We_a \approx 40$, a completely different breakup phenomenon occurred, as shown in Fig. A.15. Due to the dominance of surface tension forces, the water accumulates at the T.E. remains attached for long time resulting in the large amount of water accumulation. The accumulated water was always seen to be oscillating upwards and downwards due to the vortex shedding from the T.E.. Due to relatively weak aerodynamic forces, the vortex shed did not contribute to the fragmentation of droplets from the accumulated water at T.E., instead elongated the accumulated water in the wind-ward direction, as shown in Fig. A.15 (d), the accumulated water bends downwards due to gravity effect, such as shown in Fig. A.15 (g). When the accumulated water reached its critical amount the vortex shed (mostly from the pressure side) resulted in the formation large bag or even multiple bags of ligaments whose length even exceeded beyond 0.5-C, as given in Fig. A.15 (h). Since the droplets formed in this were mainly larger in size, the droplets had relatively high momentum compared to the high momentum case and generally did not follow the air path.

A.4.1.3. Intermediate Air Momentum (Case – B (Air Velocity 30 m/sec), $M \approx 108, We_a \approx 90$ (Fig. A.13) & Case – C (Air Velocity 25 m/sec), $M \approx 75, We_a \approx 62.5$ (Fig. A.14)

The Intermediate Air momentum shows an intermediate droplets size breakup and distribution aft the T.E. region when compared to High- and Low-Air Momentum cases. In this case, the amount of water accumulated at the T.E. was relatively larger compared to Case A, due to relatively weak aerodynamic forces, and smaller when compared to the Case D.

For Case B (Air Velocity 30 m/sec,$We_a \approx 90$), surface waves accumulates at the T.E. usually did not possess high momentum to strip directly from the T.E.. However, they do destabilized the water accumulation at the T.E., and usually results in the stripping of coarse droplets from the T.E as shown in Fig. A.13 (d). The coarse droplets formed further breaks up either due to vibrational or bag mode of breakup, Fig. A.13 (e). However, due to vortex shedding the ligament oscillate to and froth at the T.E. and a results in the bag mode of breakup of ligament, as shown in Fig. A.13 (g) to A.13 (i). Due to oscillation, at one cycle the bag breakup occurred by one vortex (from pressure side) whereas at other cycle it occurred from the opposite vortex (suction side) and vice versa.

For Case C ($M \approx 75$, $We_a \approx 62.5$), it took relatively long time for the water to accumulate at the T.E. compared to High Air Momentum (Case A) and comparatively short time when compared to Low Air Momentum (Case D). Once the sufficient amount of water accumulates it started to form bag with relatively longer ligaments length compared to, as shown in Fig. A.14 (c) and Fig. A.14 (f). In this case stripping of droplets due to surface tension form the ligament was observed, as given by Fig. A.14 (g). The coarse droplets which resulted from such breakup often underwent bag breakup, as shown in Fig. A.10 (h). Occasional stripping of coarse droplets directly from the T.E. was also observed which ultimately breakup mainly after the bag breakup, Fig. A.14 (k). Figure A.14 (k) shows a completely unique type of bag breakup was observed. The coarse droplet shed from the T.E. formed a twin bag, Fig. A.14 (k), such that the two bags were of the same size and were also perfectly symmetric. According to author's knowledge, such twin bag breakup had never been observed before and probably such breakup is observed for the very first time. From the extensive experimental visualization such mode of breakup was observed only once.

A.4.2. Droplets Size Distribution aft the T.E. Region

The droplets size distribution aft the T.E. of the blade was conducted in an exactly the similar way as that of the Elliptical profile blade, i.e., droplets size distribution was measured at 0.25-, 0.5-, 0.75- and 1-C downstream from the tip of the T.E., as shown in Fig. 3.29. The size of measurement window was chosen to be of 0.1-C in width having a height of 1-C. The droplet criteria were set as given in detail in Section 3.9 having an average number of droplets to be around 10,000.

Figure A.16, A.17, A.18 and A.19 shows the Average (D10) and Sauter Mean Droplets (D32) size distribution aft the T.E. of the blade for Case A, Case B, Case C and Case D respectively. In all these figures (Fig. A.16 to A.19), filled symbols, such as (●), represent D10 droplets whereas unfilled symbols, such as (o) represents D32 droplets size distribution. The dotted and dashed lines represent the average D32 and D10 droplets size distribution respectively. The black, blue, red and violet represent the corresponding droplets size at 0.25-, 0.5-, 0.75- and 1-C respectively. As expected the droplets size distribution remained the same at a particular position whatever the ingestion flow rate of liquid was, for each ejection hole geometry under identical air flow momentum conditions. This is primarily because the droplets size is governed by the T.E. thickness and surrounding air momentum. As the velocity of accumulated water at the T.E. is considered to be nearly zero, the accumulated water experiences uniform aerodynamic forces under different liquid mass flow rate. This ultimately results in the identical slip velocity between the droplets and the surrounding air, generating identical droplets size at each position aft the T.E.. Like elliptical profile, in flat profile also the deviation of droplets was large near the T.E. (at 0.25-C), which was mainly due to the presence of ligaments as well as highly deformed droplets near the T.E., such as shown in Fig. A.16 (d), A.17 (b), A.17 (c), A.17 (d), A.18 (b), A.18 (c) and A.18 (d) in particular. The slit position which is positioned near the test section wall (Fig. A.3), causing the droplets to easily get deposited at the side wall, resulting in a large deviation of droplets size, as shown in Fig. A.16 (d) and A.17 (d).

Figure A.20 and A.21 show the summarized D10 and D32 droplets size distribution respectively for Case A, Case B, Case C and Case D. From Fig. A.20 and A.21, the droplets size remained the same if the air momentum conditions and the T.E. profile configuration were kept identical, whereas, the effects of ingestion hole geometries had no significant effect on droplets size distribution due to the similar slip velocity between the droplets and the surrounding air.

For Case A (Fig. A.20 (a) and A.21 (a)), a small gradient of droplets size change was seen near the T.E. which was mainly due to the vibrational mode of droplets near the T.E. with occasional bag mode of a breakup. However, as the distance aft the T.E. increases the droplet size remained unchanged with almost no or rarely vibrational mode of a breakup. In other words for Case A the droplets almost stabilize after travelling a distance of 1-C aft the T.E.. For Case B (Fig. A.20 (b) and A.21 (b)), the gradient of droplet size change was large near the T.E. only, which reduced significantly as the distance aft the T.E. increases due to the dominance of vibrational mode of droplets breakup with occasional bag breakup. When the air velocity was further reduced to Case C, (Fig. A.20 (c) and A.21 (c)), the gradient of droplets size change near the T.E. was large due to the bag mode of a breakup. As the distance aft the T.E. region increased a significant change in the droplets size was still observed, which was mainly due to the bag mode of the breakup of large droplets. The gradient of droplets size change downstream of the T.E. was significantly large for Case C compared to Case B. from the shadowgraph images, the droplets for Case B started to show occasional vibrational breakup near the 1-C position and it is expected that slightly further downstream (i.e., aft 1-C) the droplets might have reached their stable conditions, however, this was not verified experimentally. For Case C the stable droplets were expected to be further downstream compared to the Case B, due to occasional bag breakup near the 1-C position. Finally, for the low air momentum case (Case D), two types of the detachment were observed from the tip of T.E., as shown in Fig. A.20 (d) and A.21 (d). One was the direct breakup of ligament due to the bag mode of breakup and second was the generation of the coarse droplets from the ligaments. In the case of occasional coarse droplets detached from the ligament, it was observed that these coarse droplets were mostly unstable and the surface tension forces which was holding these droplets were not strong enough for long duration and therefore the size of these droplets results in abrupt fragmentation of the droplets due to the bag mode. This resulted in a large gradient change of droplets size change. Briefly, from Fig. A.20 and A.21, an increase in air momentum resulted in smaller primary droplets and a decrease in air velocity resulted in coarse primary droplets. From high air momentum ratio due to large K.E. of air, droplets underwent vibration breakup whereas for low air momentum ratio the droplets size reduced abruptly due to the bag mode of a breakup. Table A.5 summarizes the droplet breakup phenomena at various positions aft the T.E. of the flat blade.

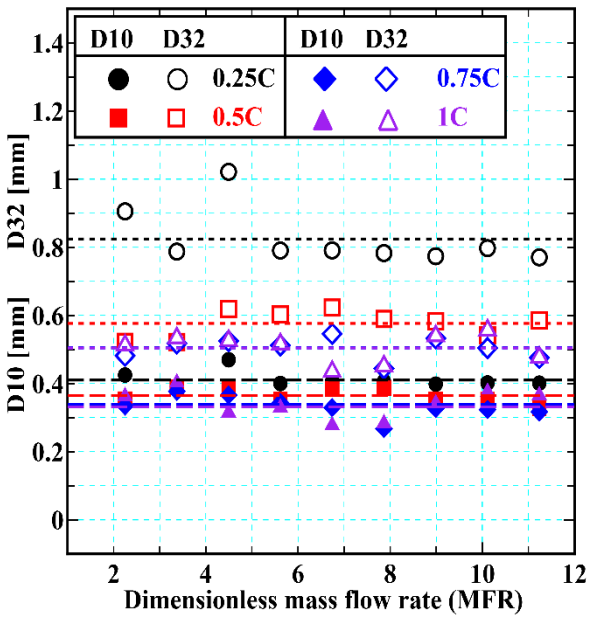

(a) Diameter 1 mm

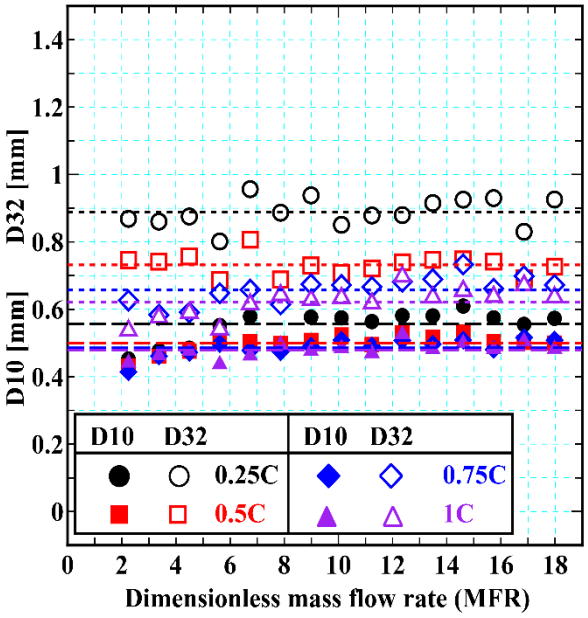

(b) Diameter 1.2 mm

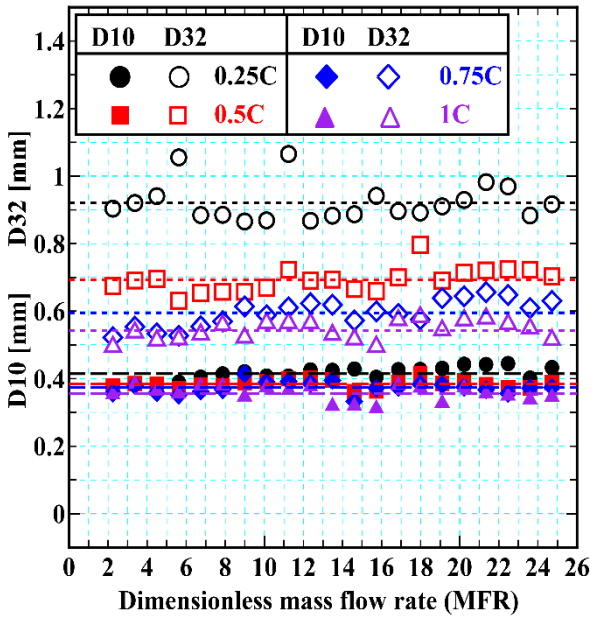

(c) Diameter 1.5 mm

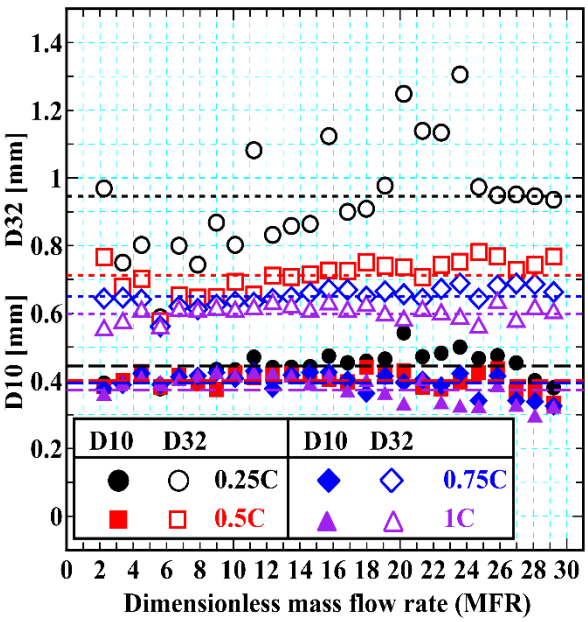

(d) Slit

Figure A.16 – Droplets Size Distribution aft the T.E. Region- Case A (Velocity 40 m/sec) – ($M \approx 192, We_a \approx 160$)

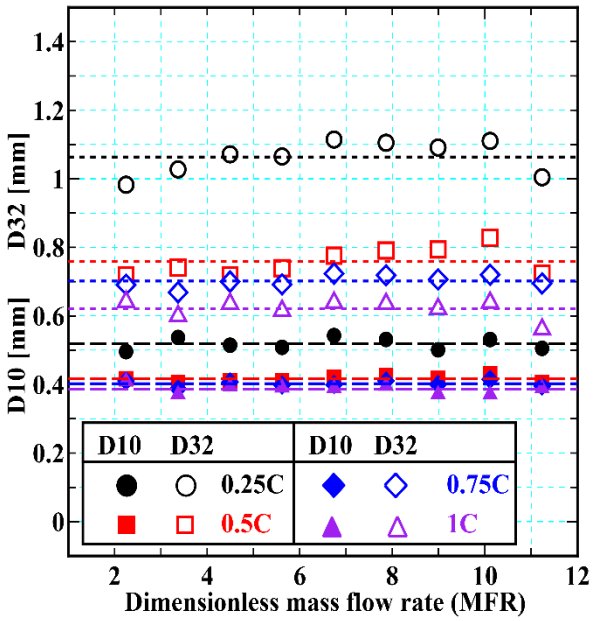

(a) Diameter 1 mm

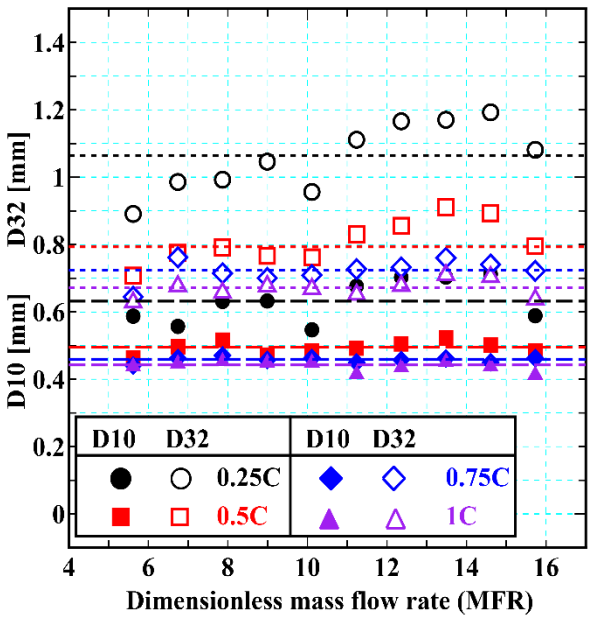

(b) Diameter 1.2 mm

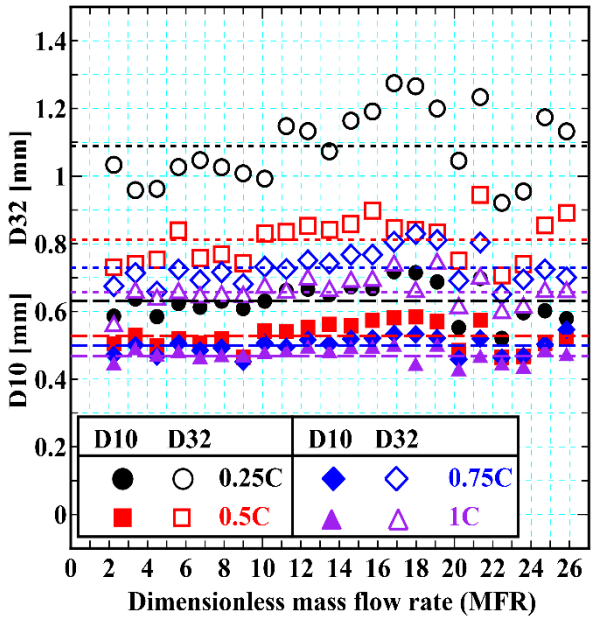

(c) Diameter 1.5 mm

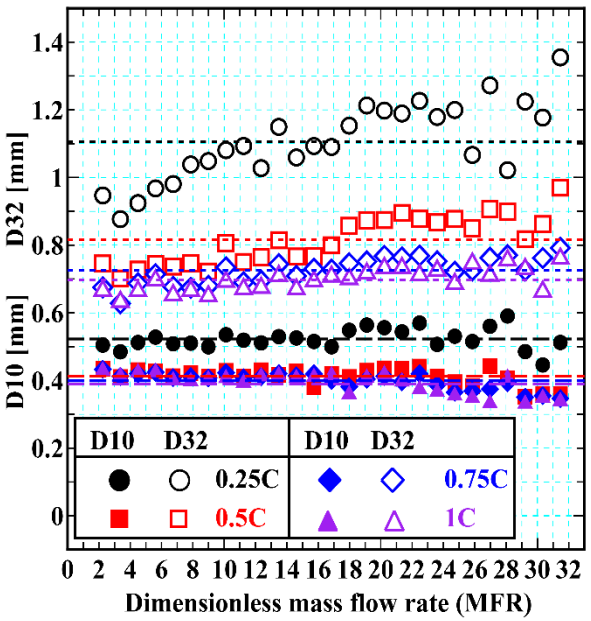

(d) Slit

Figure A.17 – Droplets Size Distribution aft the T.E. Region- Case B (Velocity 30 m/sec) – ($M \approx 108, We_a \approx 90$)

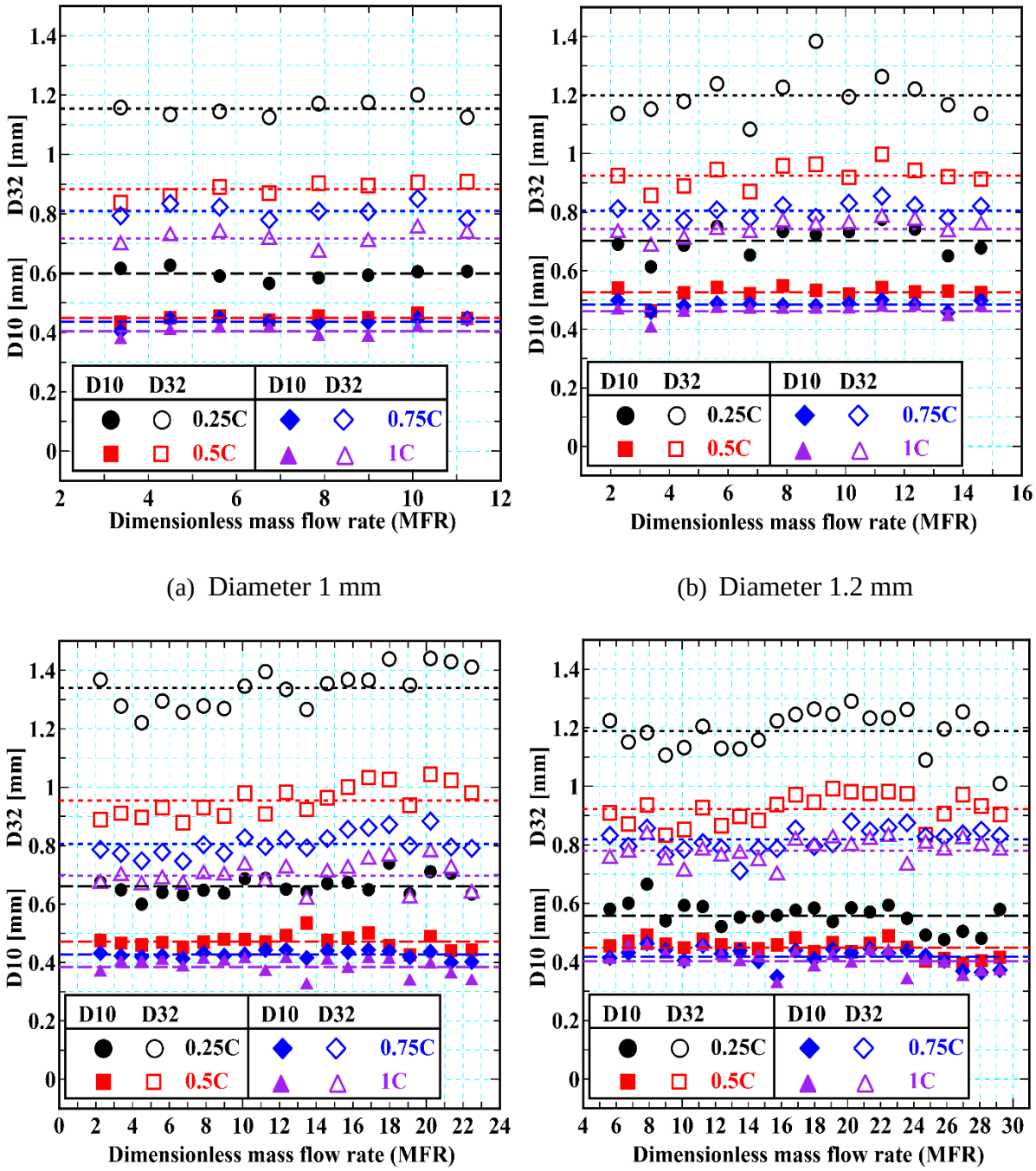

(a) Diameter 1 mm

(b) Diameter 1.2 mm

(c) Diameter 1.5 mm

(d) Slit

Figure A.18 – Droplets Size Distribution aft the T.E. Region- Case C (Velocity 25 m/sec) – ($M \approx 75, We_a \approx 62.5$)

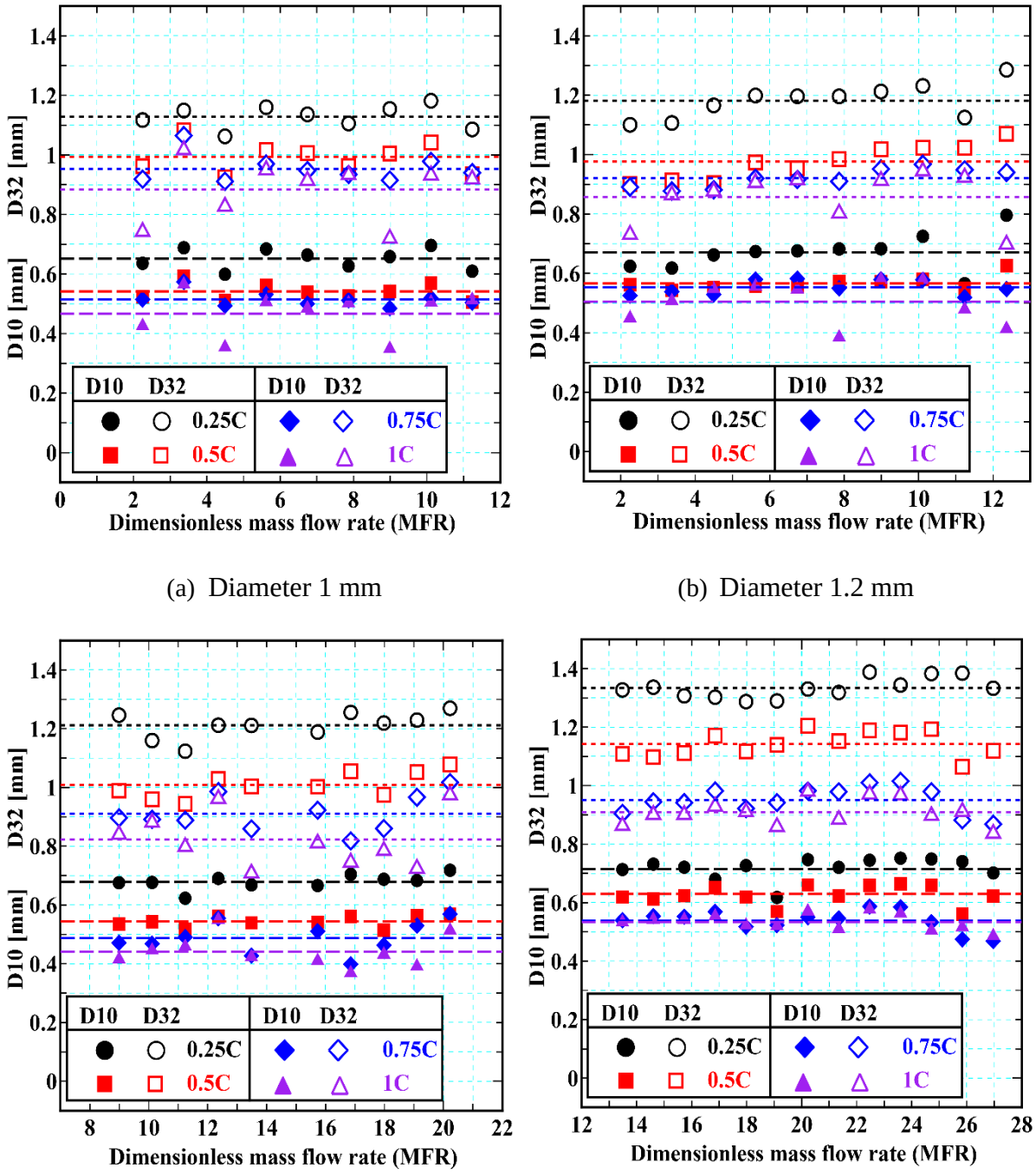

(a) Diameter 1 mm

(b) Diameter 1.2 mm

(c) Diameter 1.5 mm

(d) Slit

Figure A.19 – Droplets Size Distribution aft the T.E. Region- Case D (Velocity20 m/sec) – ($M \approx 48, We_a \approx 40$)

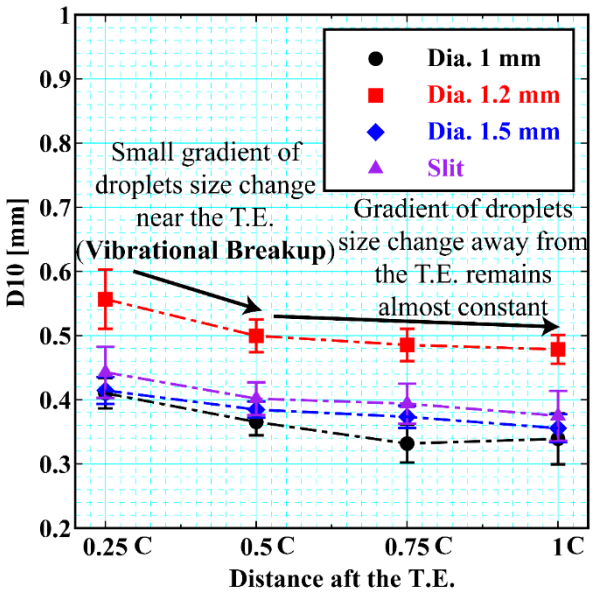

(a) Case A (Velocity 40 m/sec) – ($M \approx 192, We_a \approx 160$)

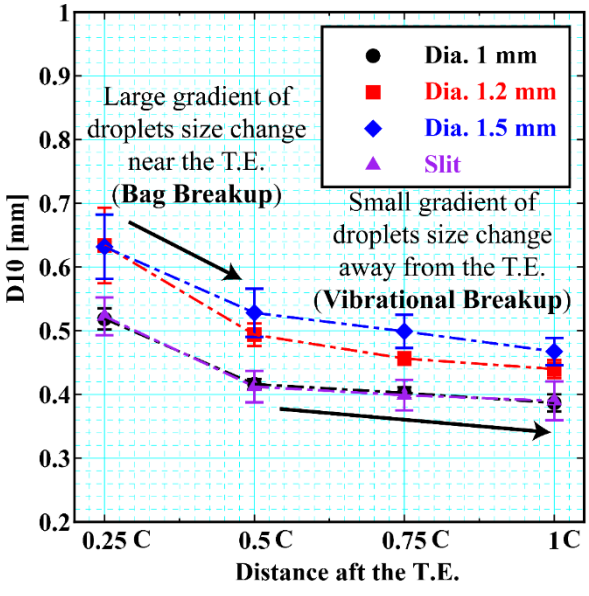

(b) Case B (Velocity 30 m/sec) – ($M \approx 108, We_a \approx 90$)

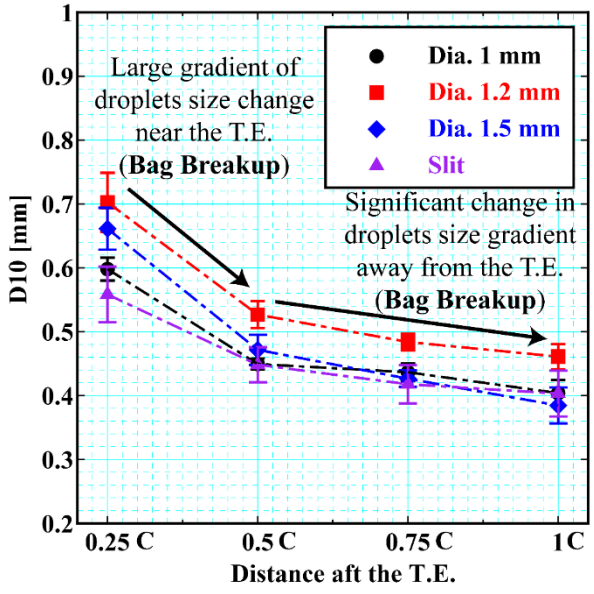

(c) Case C (Velocity 25 m/sec) – ($M \approx 75, We_a \approx 62.5$)

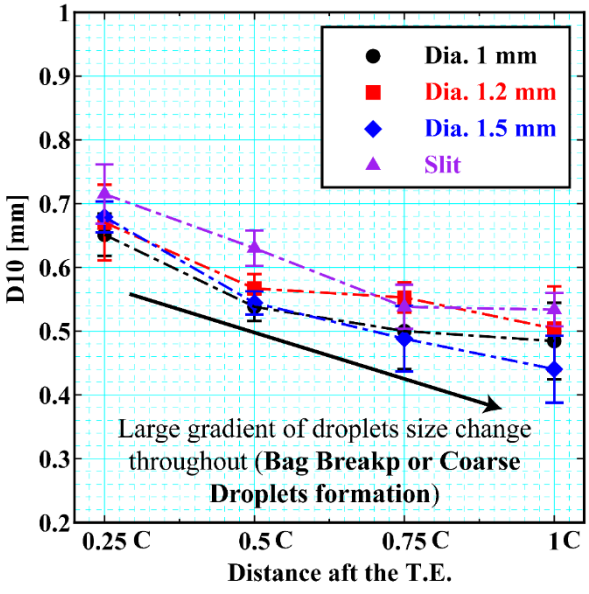

(d) Case D (Velocity 20 m/sec) – ($M \approx 48, We_a \approx 40$)

Figure A.20 – Summary of D10 droplets size Distribution

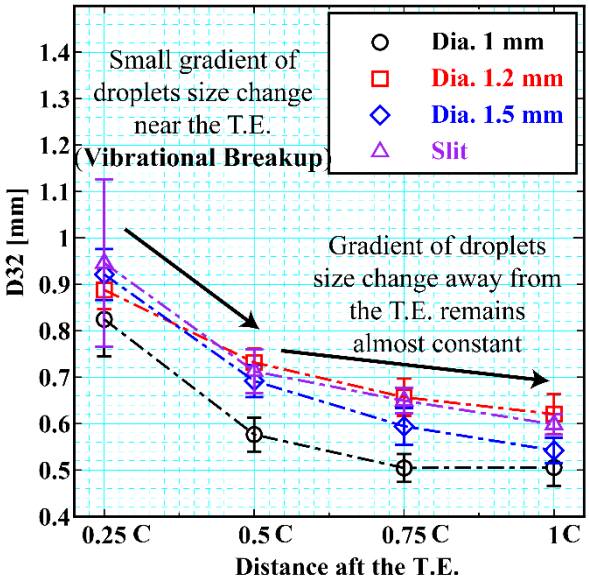

(a) Case A (Velocity 40 m/sec) – ($M \approx 192, We_a \approx 160$)

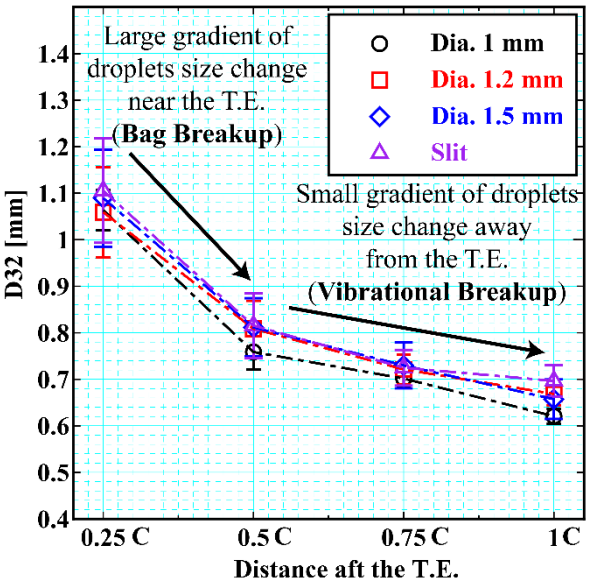

(b) Case B (Velocity 30 m/sec) – ($M \approx 108, We_a \approx 90$)

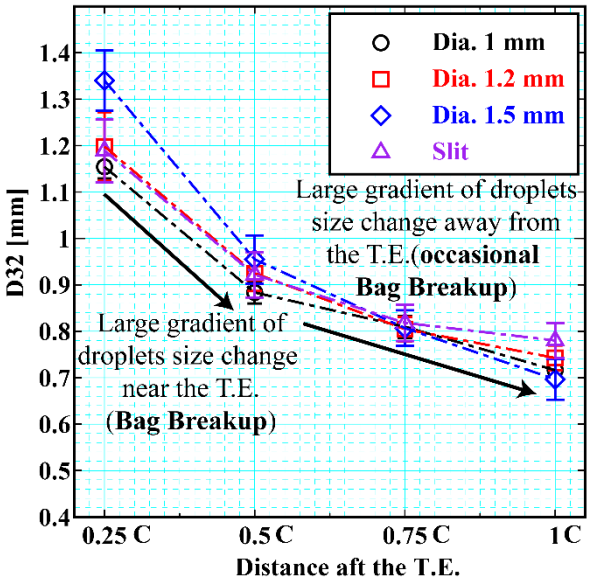

(c) Case C (Velocity 25 m/sec) – ($M \approx 75, We_a \approx 62.5$)

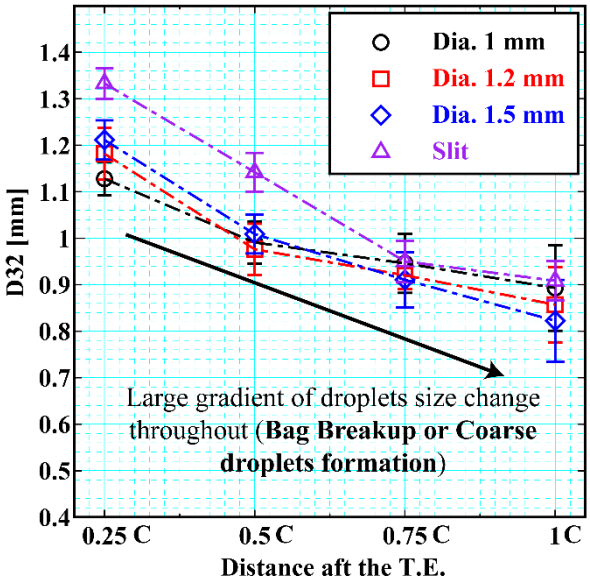

(d) Case D (Velocity 20 m/sec) – ($M \approx 48, We_a \approx 40$)

Figure A.21 – Summary of D32droplets size Distribution

Table A.5 – Summary of Droplets Breakup

Case	0 to 0.25-C	0.25-C to 0.5-C	0.5-C to 0.75-C	0.75-C to 1-C
Case A (Air Velocity 40 m/sec) $M \approx 192$ $We_a \approx 160$	• Oscillation of accumulated water. • Wave stripping. • Coarse droplets (if formed) undergo bag breakup. • Occasional start of a vibrational breakup. • Ligament length usually within this range. • Occasional bag breakup of the ligament. • A chunk of a large number of droplets breakup due to vortices.	• Frequent vibrational breakup. • Occasional start of a vibrational breakup.	• Occasional vibrational breakup.	• Rare vibrational breakup.
		Karman Vortex Street of droplets		
Case B (Air Velocity 30 m/sec) $M \approx 108$ $We_a \approx 90$	• Oscillation of accumulated water. • Occasional stripping of coarse droplets. • Rare bag breakup of droplets. • Multiple bag formations from the thick ligament.	• Ligament length usually within this range (near 0.25-C). • Occasional bag and ligament breakup of the ligament.	• Occasional vibrational breakup. • Occasional bag breakup.	• Rare vibrational breakup. • Occasional bag breakup.
Case C (Air Velocity 25 m/sec) $M \approx 75$ $We_a \approx 62.5$	• Oscillation of accumulated water. • Multiple bag formations from the thick ligament. • Stripping of coarse droplets from thick ligament.	• Ligament length usually within this range (near 0.5-C). • Occasional bag and ligament breakup of the ligament.	• Rare vibrational breakup. • Occasional bag breakup.	• Rare vibrational breakup. • Rarely bag breakup.
Case D (Air Velocity 20 m/sec) $M \approx 48$ $We_a \approx 40$	• Oscillation of accumulated water. • Multiple bag formations from the thick ligament.	• Ligament length occasionally within this range (around 0.5-C). • Multiple bags formed from thick ligament usually break in this range mainly due to bag breakup. • Coarse droplets formation.	• Ligament length occasionally within this range (around 0.5-C). • Coarse droplets formation. • Rare bag breakup.	• Rare Bag breakup • Rare vibrational breakup.

A.5. Characteristics of Ligaments

A.5.1. Prediction of Primary Droplets Formation

The droplet diameters were calculated based on the theoretical model given in detail in Section 4.5. The theoretical diameter was calculated by using the Eq. (4.60). Figure A.22 (a – d) shows the experimentally measured droplets using an image processing code for Case A to Case D. The droplets size measured remained unchanged for identical momentum ratio at different liquid mass flow rate conditions. As explained earlier that in the case of the slit ingestion hole few droplets get attached to the side walls. It should be noted that the wavelength (λ_{span}), see – Fig. 4.37, was calculated theoretically using the Eq. (4.48) but was not verified for the flat profile blade. However, the theoretical expression for droplets size prediction (Eq. (4.60)) gives a good approximation of droplets size. As Eq. (4.60) is derived based on mass and energy conservation principles, the theoretical formula is independent of the profile and thickness of the T.E.. Figure A.23 shows the comparison of the theoretical model with the experimental data for each momentum case. It should be noted that the experimental results in Fig. A.23 includes all the ejection holes, i.e., S.H., M.H., L.H. and Slit. From the comparison of theoretical and experimental data, an approximate maximum difference found from all the cases was just under 25%. But on average the difference between the theoretical and experimental value in most of the cases was nearly 10%. Figure A.24 represents the experimental data of Fig. A.22 into a single figure. As expected, overall, Eq. (4.60) shows a good correlation with the experimental data.

A.5.2. Water accumulation and Ligament length at the T.E.

Figure A.25 shows the threshold intensity images aft the T.E. of the flat blade. From Fig. A.25, the droplets distribution remains almost identical due to the same slip velocity for a particular momentum ratio. It is important to mention here that the number of droplets generated for the S.H. geometry was less compared to the slit geometry under the same liquid's flow rate condition, due to the less amount of water ejected per unit area. It was also due to this reason that the amount of water accumulation at the T.E. for S.H. geometry was the least and that for the Slit was maximum, as shown in Fig. A.25. Figure A.26 shows the corresponding ligament length attached from the tip of the T.E. for all the ejection hole geometries used in the present study, as explained in Section 4.5. From Fig. A.27, the length of ligament remained almost the same and was independent of the size of ingestion hole geometry, due to the similar amount of aerodynamic forces being experienced by droplets.

A.5.3. Droplets Shedding Angle

Figure A.28 shows the experimentally measured droplets shedding angle in the pitch wise direction, which was measured from the images shown schematically in Fig. A.25. For high air momentum ratio (Case A) the average droplets distribution angle was nearly 10 degrees which became more than twice (about 25 degree) for the low air momentum ratio (Case D), due to an increase in the bag mode of droplets breakup. From Fig. A.28, it was concluded that the shedding angle was also independent of the size or type of the ingestion hole geometry and remained almost the same since the droplets size distribution remained the same, due to the same phenomenon for a particular profile of T.E. at the same momentum ratio. Figure A.28 shows that the shedding angle deviates for different ingestion hole geometry, such deviation might be due to slightly different aerodynamic forces caused by the different position of ingestion holes. It is expected that if the ingestion holes positions were located at the same position, the droplets distribution aft the T.E. would also be independent of the ingestion holes size.

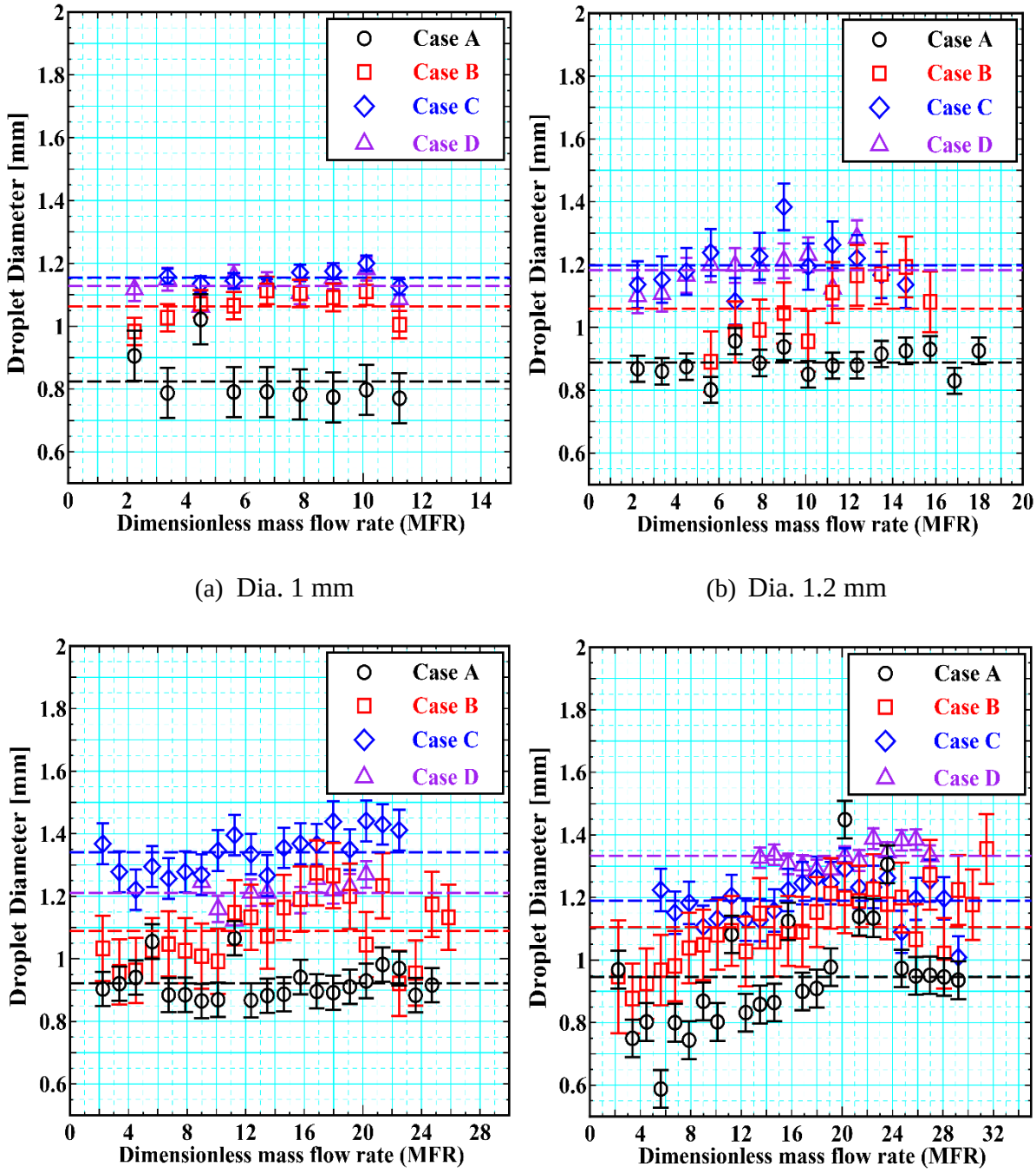

(a) Dia. 1 mm

(b) Dia. 1.2 mm

(c) Dia. 1.5 mm

(d) Slit

Figure A.22 – Primary droplets diameter measurement near the T.E.

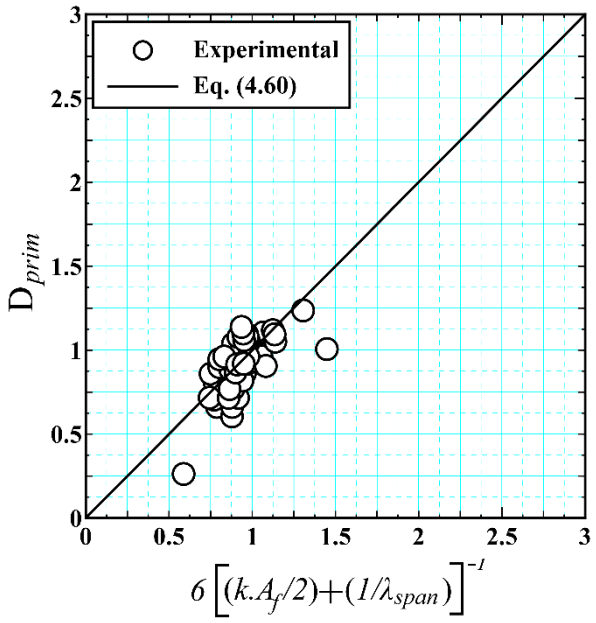

(a) Case A (Velocity 40 m/sec) – ($M \approx 192, We_a \approx 160$)

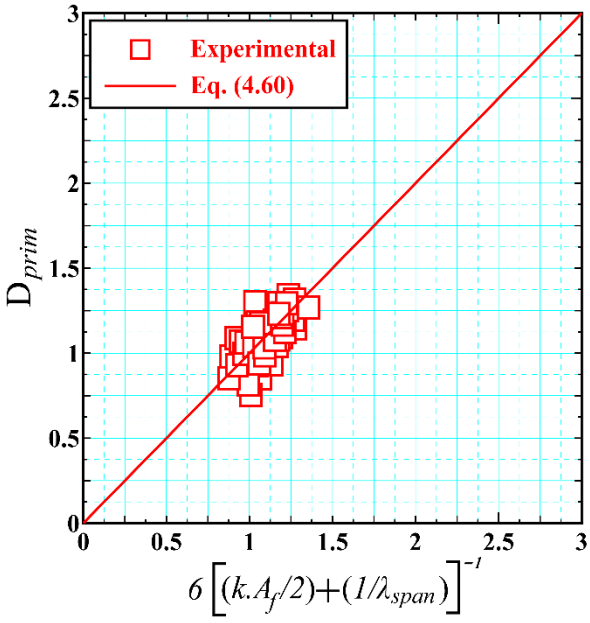

(b) Case B (Velocity 30 m/sec) – ($M \approx 108, We_a \approx 90$)

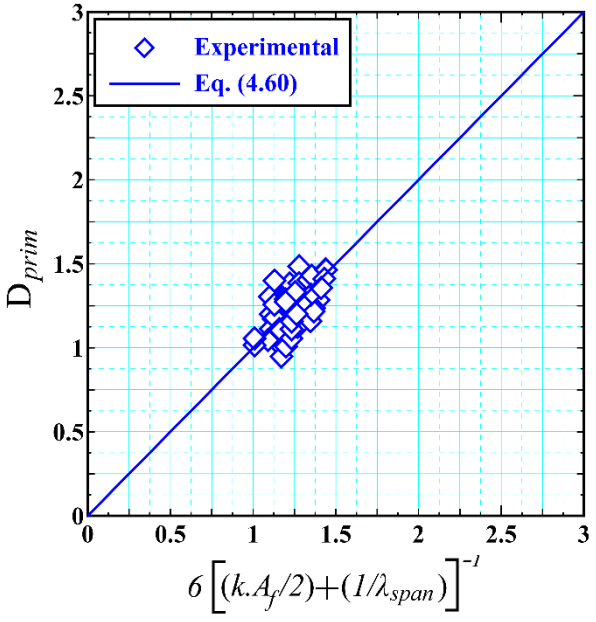

(c) Case C (Velocity 25 m/sec) – ($M \approx 75, We_a \approx 62.5$)

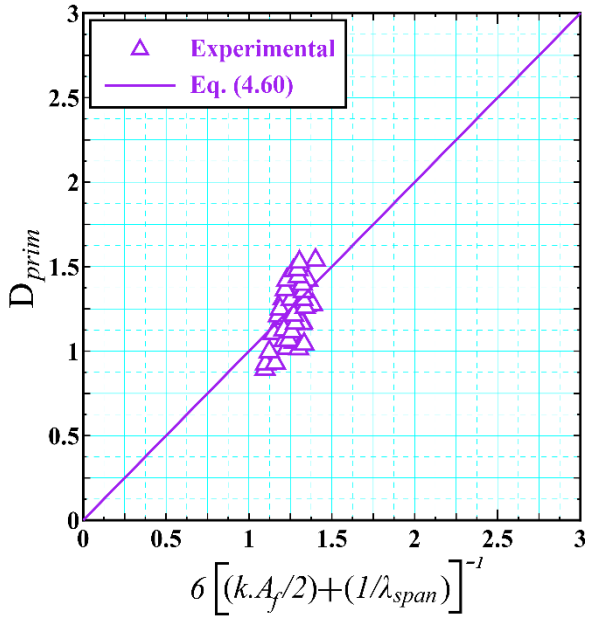

(d) Case D (Velocity 20 m/sec) – ($M \approx 48, We_a \approx 40$)

Figure A.23 – Droplet Diameter Experimental Vs Theoretical Prediction (Flat Blade) – [units – mm]

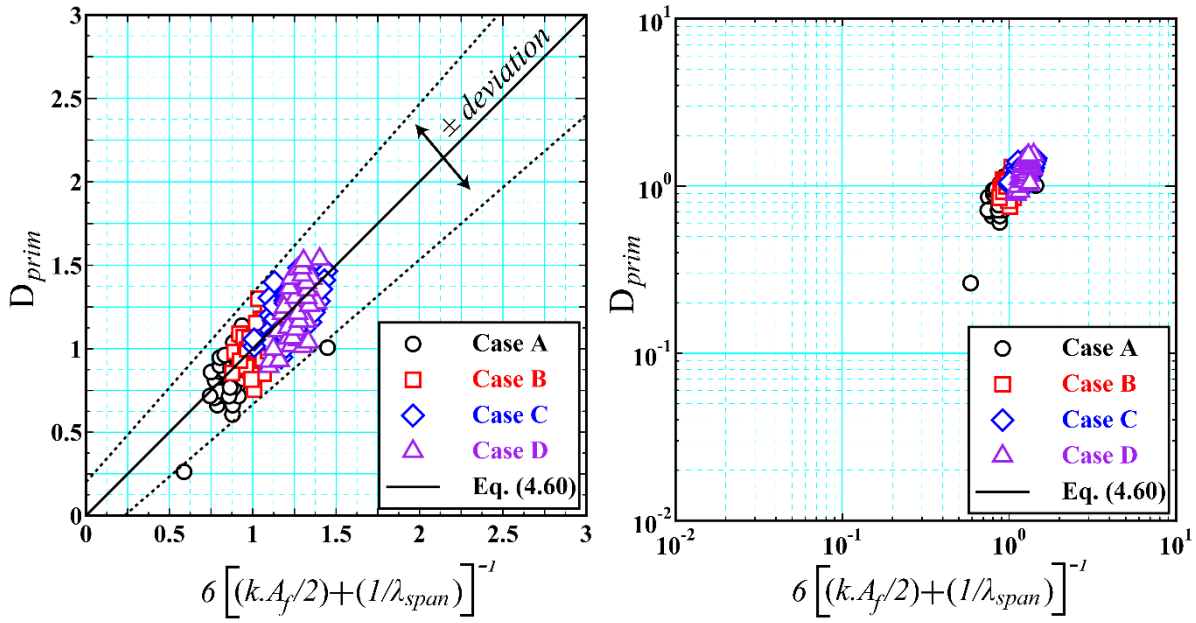

(a) Normal Scale (b) Log Scale

Figure A.24 – Summary of comparison of Experimental & Theoretical Prediction (Flat Blade) – [units – mm]

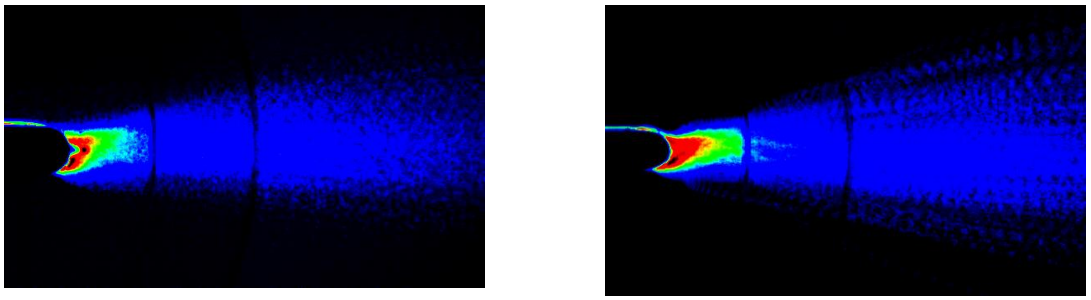

Dia. 1-mm

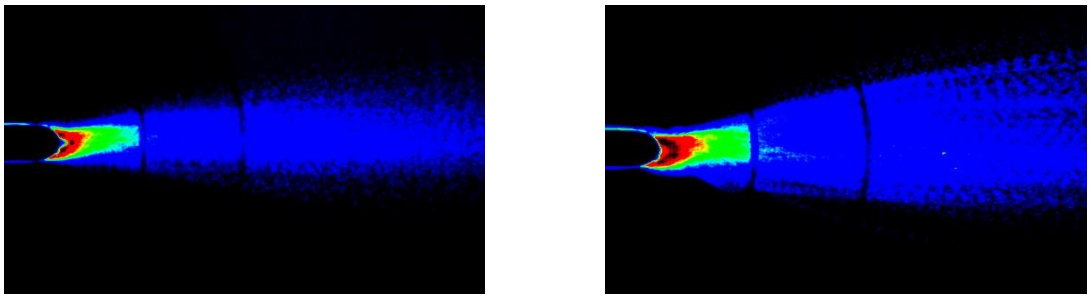

Dia. 1.2-mm

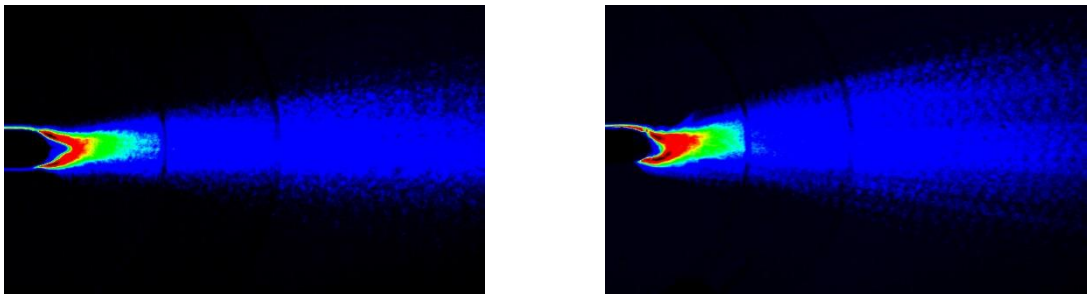

Dia. 1.5-mm

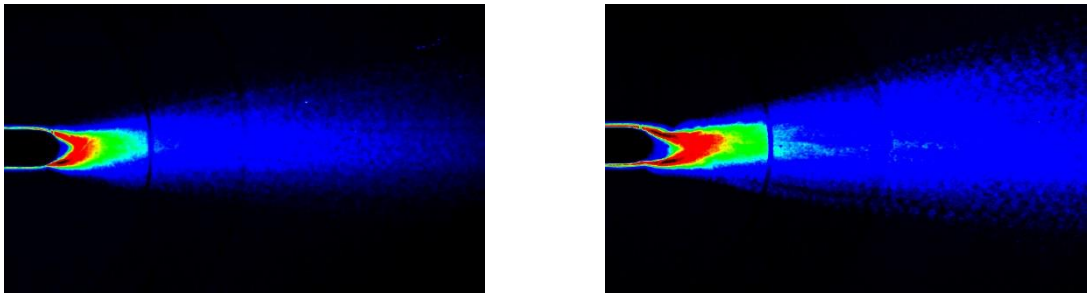

Slit

(a) Case A (Velocity 40 m/sec) – ($M \approx 192, We_a \approx 160$)

(b) Case B (Velocity 30 m/sec) – ($M \approx 108, We_a \approx 90$)

Figure A.25 – Droplets Distribution angle for different ejection hole geometries (1/2)

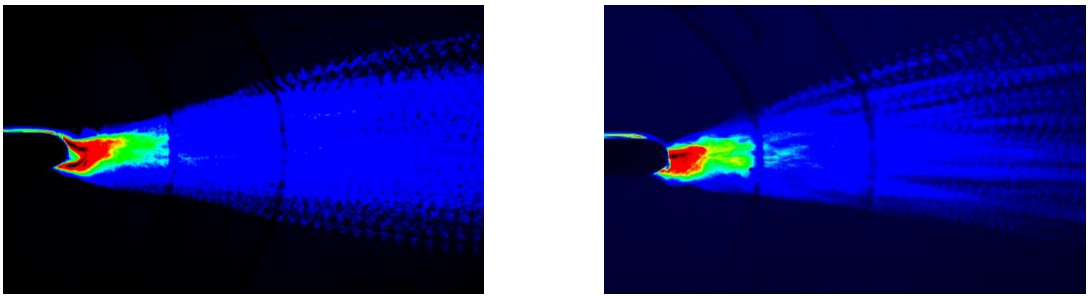

Dia. 1-mm

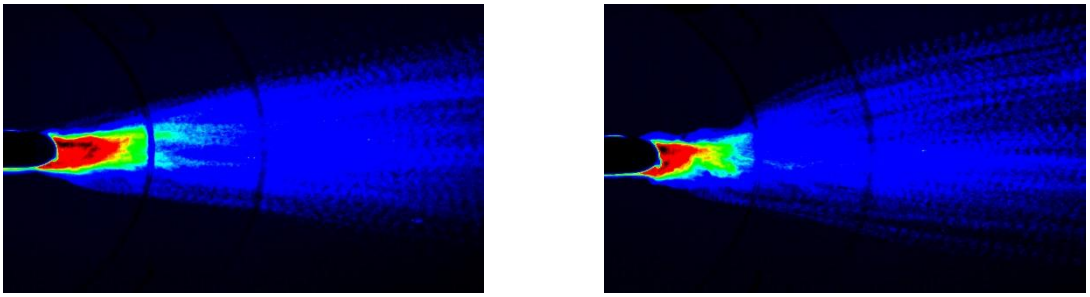

Dia. 1.2-mm

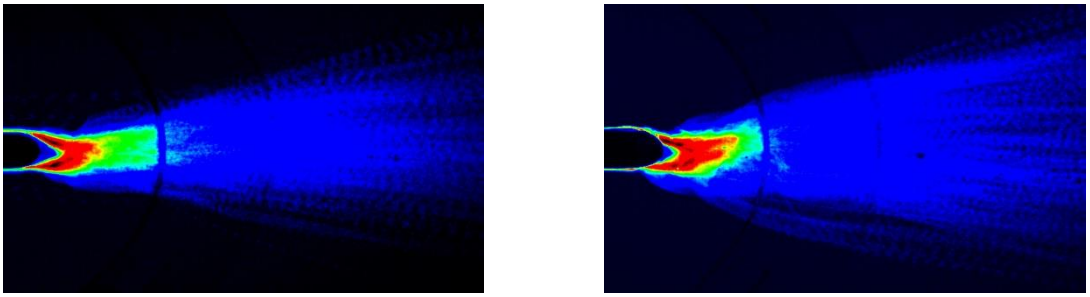

Dia. 1.5-mm

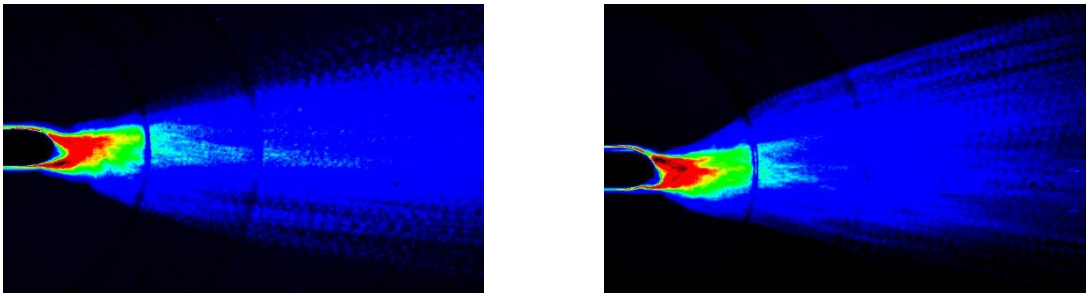

Slit

(c) Case C (Velocity 25 m/sec) – ($M \approx 75, We_a \approx 62.5$)

(d) Case D (Velocity 20 m/sec) – ($M \approx 48, We_a \approx 40$)

Figure A.25 – Droplets Distribution angle for different ejection hole geometries (2/2)

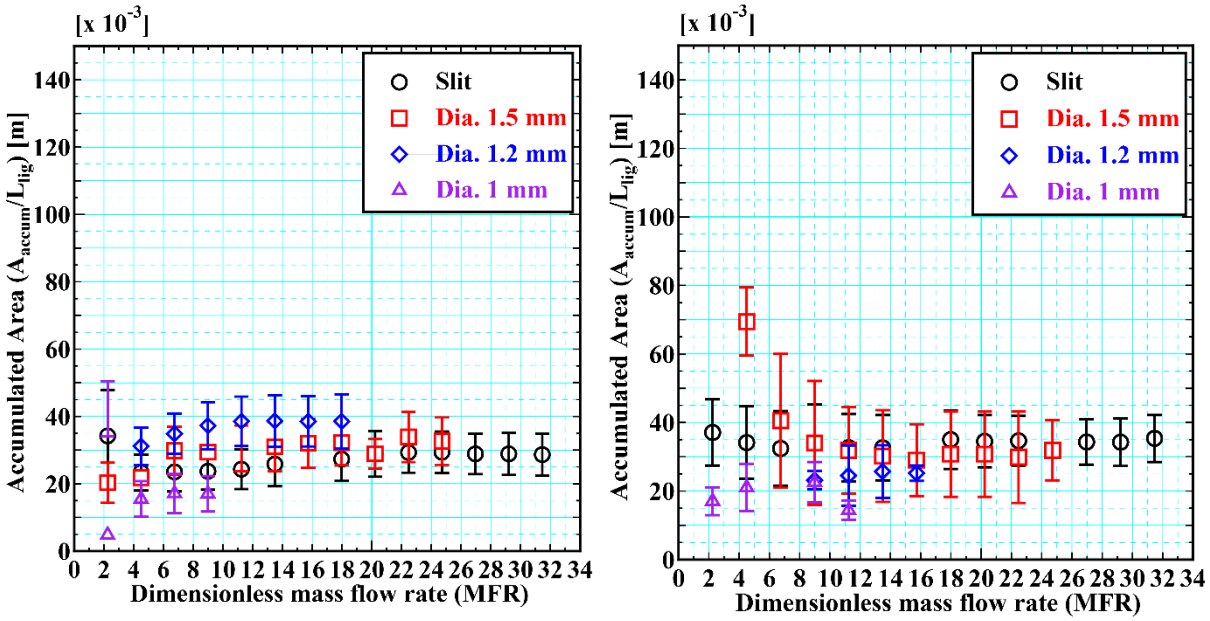

(a) Case A (Velocity 40 m/sec) – ($M \approx 192, We_a \approx 160$)

(b) Case B (Velocity 30 m/sec) – ($M \approx 108, We_a \approx 90$)

(c) Case C (Velocity 25 m/sec) – ($M \approx 75, We_a \approx 62.5$)

(d) Case D (Velocity 20 m/sec) – ($M \approx 48, We_a \approx 40$)

Figure A.26– Water Accumulation for Different Ejection holes

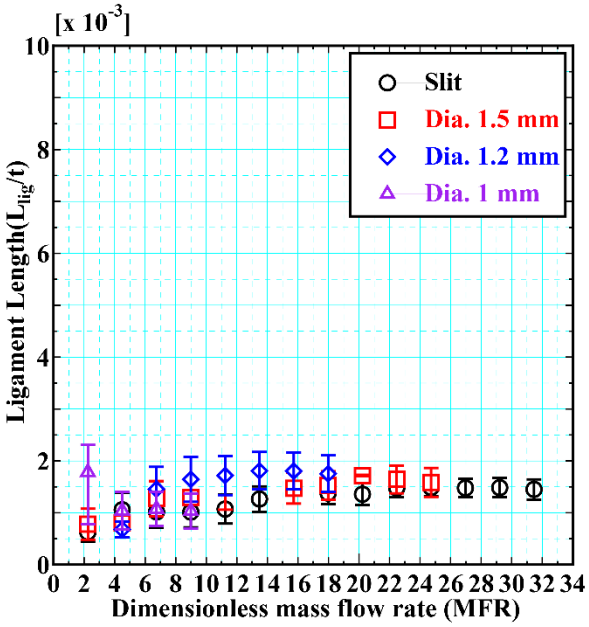

(a) Case A (Velocity 40 m/sec) – ($M \approx 192, We_a \approx 160$)

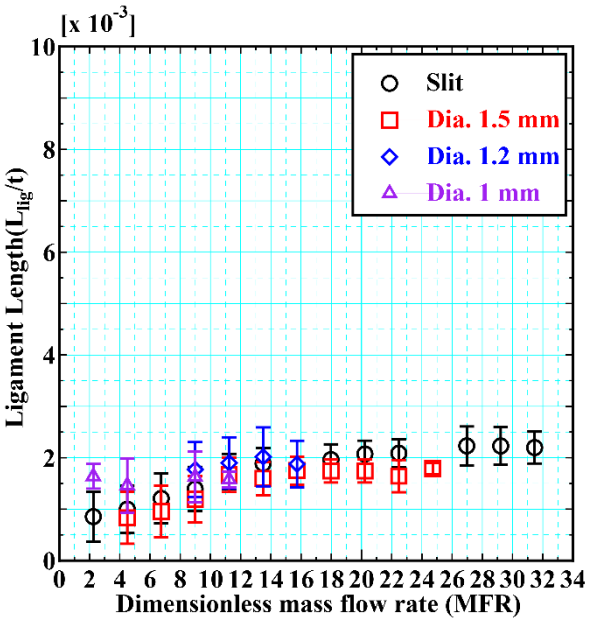

(b) Case B (Velocity 30 m/sec) – ($M \approx 108, We_a \approx 90$)

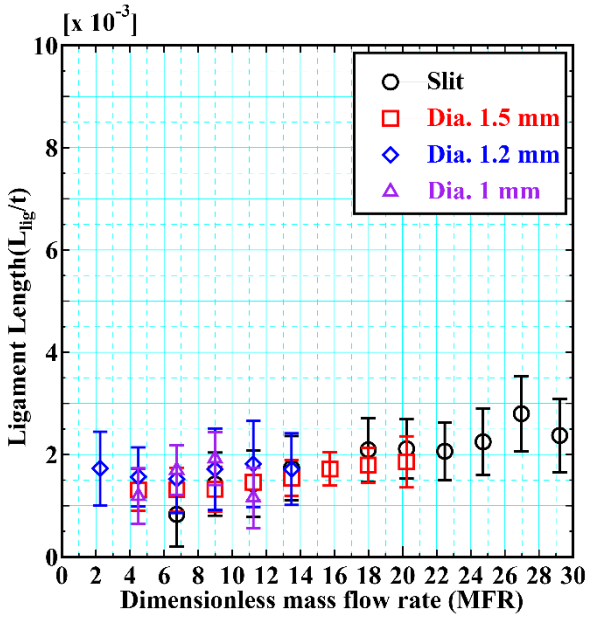

(c) Case C (Velocity 25 m/sec) – ($M \approx 75, We_a \approx 62.5$)

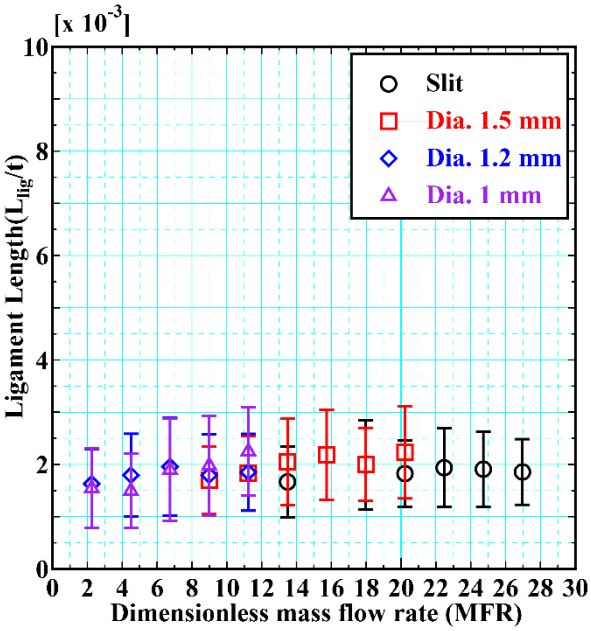

(d) Case D (Velocity 20 m/sec) – ($M \approx 48, We_a \approx 40$)

Figure A.27 – Ligament Length Formation for Different Ejection Hole Diameters

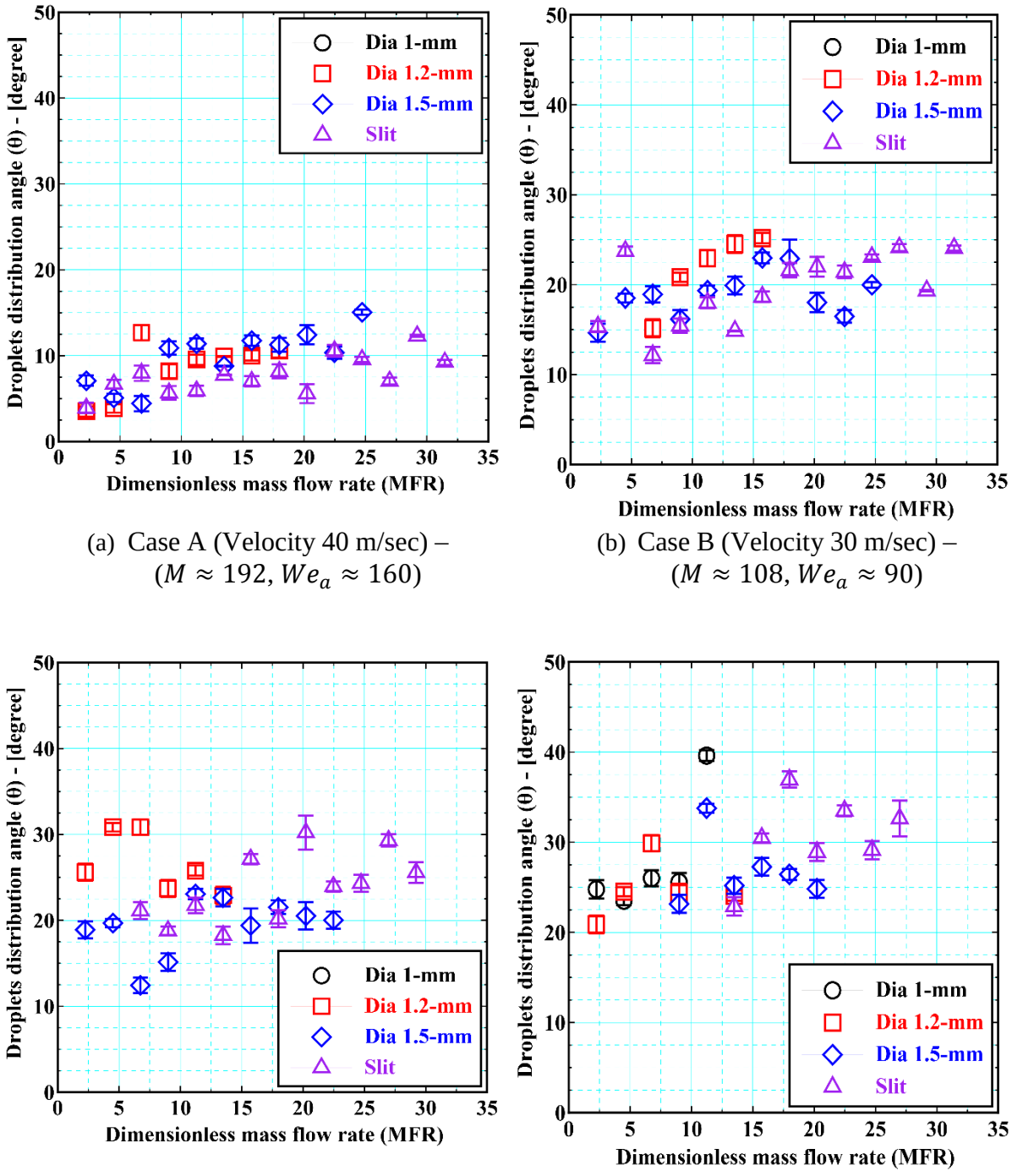

(a) Case A (Velocity 40 m/sec) – ($M \approx 192, We_a \approx 160$)

(b) Case B (Velocity 30 m/sec) – ($M \approx 108, We_a \approx 90$)

(c) Case C (Velocity 25 m/sec) – ($M \approx 75, We_a \approx 62.5$)

(d) Case D (Velocity 20 m/sec) – ($M \approx 48, We_a \approx 40$)

Figure A.28 – Droplets Distribution angle for different ejection hole geometries

A.6. Conclusions of effect of ingestion hole diameter on droplets size distribution aft the T.E. of Cascade Blade

This section outline a detailed experimental study on the effect of ingestion hole size on the characteristics of liquid film formation and droplets size distribution aft the T.E. of flat blade profile. The liquid film thickness remained unchanged for the different ingestion hole geometries, mainly due to the minimum energy principle, i.e., the aerodynamic forces experienced by the liquid remained the same (due to the same surface tension of liquid used). Similarly, the droplets size distribution aft the T.E. of the blade were found to remain the same at a particular position keeping the air momentum to be kept constant and were found to be completely independent of the ingestion hole geometry and the mass flow rate of water. Lastly, experiments highlighting primary breakup encountered aft the T.E. of the blade were compared with the theoretically proposed model and were found to show an overall good agreement.

Appendix B: Effects of T.E. thickness on droplets size distribution aft the T.E.

B.1. Effect of T.E. size on droplets size distribution

It is mentioned previously that one of the most important parameters which define the characteristics of ligament and droplets size distribution is the profile thickness of the T.E.. Though, in the present study the profile geometry of the two blades are completely different which results in different flow velocity distribution aft the T.E. of the blade. However, making a highly conservative assumption that both blades configuration are equivalent in profile but only have different T.E. thickness. By this assumption, the effect of T.E. thickness on the characteristics of ligament and droplets size distribution aft the T.E. region can be easily compared by using a non-dimensional parameter. Such assumption is considered to be appropriate as the liquid film usually accumulates at the T.E. and starts to form droplets (or ligaments) from over there.

Table B.1 categorizes the Weber number based on the thickness of the blades and is mathematically given by Eq. (B.1)

$$We_a = \frac{\rho_a U_a^2 t}{\sigma} \tag{B.1}$$

Table B.1 – Weber Number based on the blade profile thickness (density – air)

Parameter		Blade Profile	
	Air Velocity (m/sec)	Flat	Elliptical
T.E. thickness [mm]		6	2.25
Weber no. based on T.E. thickness (We_a) (approx.)	40	160	60
	30	90	34
	25	62.5	23.45
	20	40	15

According to law of conservation of mass (see Fig. 4.37)

$$m_{span} \approx m_{prim} \tag{B.2}$$

$$\frac{\pi}{4} D_{span}^2 \lambda_{span} \approx \frac{\pi}{6} D_{prim}^3 \tag{B.3}$$

According to Lefebvre [80]

$$D_{span} \approx \frac{\lambda_{span}}{4.51} \tag{B.4}$$

$$\lambda_{span} \approx 13.6\, D_{prim} \tag{B.5}$$

For the ligament to atomize without an aid of any external forces, the energy can be approximated by

$$E_{span} \approx \sigma A \approx \sigma \Delta A \approx \sigma \left(4A_{prim} - A_{span}\right) \tag{B.6}$$

$$E_{span} \approx \frac{m_l \sigma}{\rho_l} \left[\frac{4}{D_{prim}} - \frac{4}{\lambda_{span}}\right] \tag{B.7}$$

Substituting Eq. (B.5) in Eq. (B.7)

$$E_{span} \approx \frac{m_l \sigma}{\rho_l} \left[\frac{3.7}{D_{prim}}\right] \tag{B.8}$$

Similarly, the energy required from the gaseous phase to atomize the droplets from the T.E. of the cascade blade can be approximated by the K.E. of air

$$E_a = \frac{1}{2}\, m_a\, U_a^2 \tag{B.9}$$

Thus, based on the energy conservation principle, it can be approximated that

$$E_{span} = k.E_a \tag{B.10}$$

here, k is the proportionality constant whose value can be obtained from the experiment.

$$\frac{m_l\, \sigma}{\rho_l}\left[\frac{3.7}{D_{prim}}\right] = \frac{1}{2}\, m_a\, U_a^2 \tag{B.11}$$

By re-arranging the Eq. (B.11)

$$D_{prim} \approx \frac{7.4}{k}\,\frac{m_l}{m_a}\,\frac{\sigma}{p_l\, U_a^2} \tag{B.12}$$

$$\frac{D_{prim}}{t} \approx \frac{7.4}{k\,(ALR)\,We_t} \tag{B.13}$$

where,

$$ALR = \frac{m_a}{m_l} \tag{B.14}$$

$$We_t = \frac{\rho_l\, U_a^2\, t}{\sigma} \tag{B.15}$$

Based on Eq. (B.13) if the weber number, based on the thickness of the T.E., remains the same then the thicker the blade is greater will be the size of the primary droplets produced and vice versa. The Weber number at the T.E. was obtained based on the air velocity only and not on the basis of velocity difference of the droplet and the surrounding airflow as accumulated water is at rest, and is given by Eq. (B.15). Figure B.1 compares the experimental results of droplets size distribution at 0.25-C obtained for the elliptical and flat (1 mm) profiles blade respectively, and were compared to the weber number of the T.E., as given by Eq. (B.15). As predicted, the primary droplets produced from the thicker T.E. (i.e., Flat Blade) are greater in size compared to the thinner T.E. profile (i.e., Elliptical Blade), which agrees with the theoretically derived Eq. (B.13).

Table B.2 – Weber Number based on the blade profile thickness (density – water)

Parameter		Blade Profile	
	Air Velocity (m/sec)	Flat	Elliptical
T.E. thickness [mm]		6	12.5
Weber no. based on T.E. thickness (We_t) x 10^3 (approx.)	40	33	60
	30	52	20
	25	75	28
	20	133	50

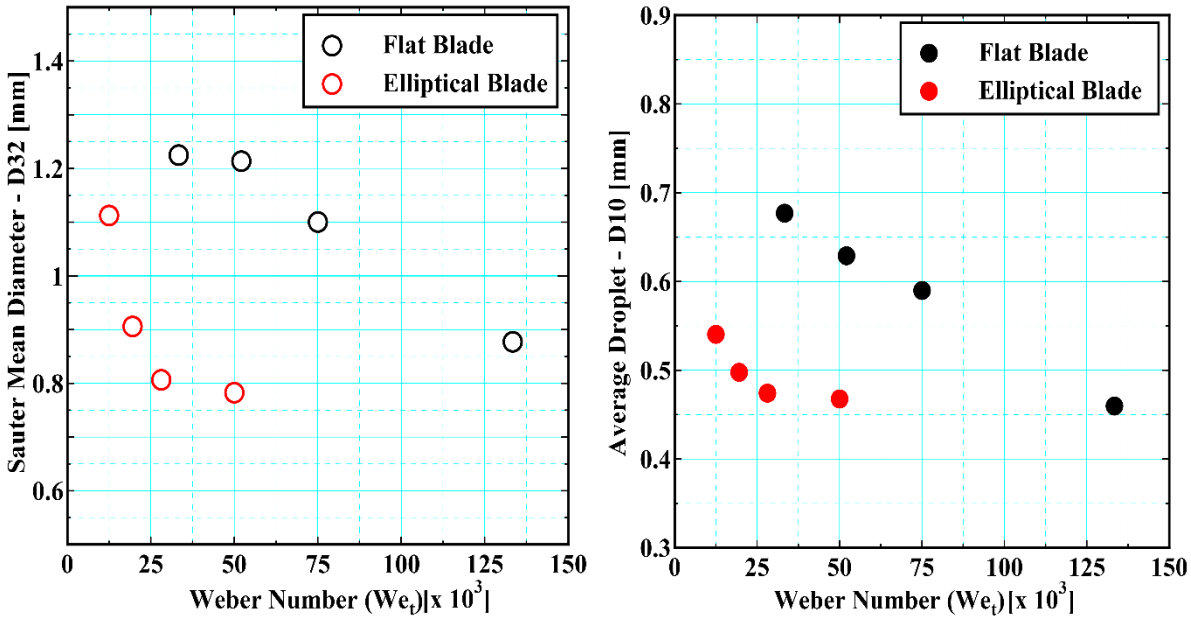

(a) Sauter Mean Diameter – D32 (b) Average Mean Diameter – D10

Figure B.1 – Primary Droplets Size Comparison aft the T.E.

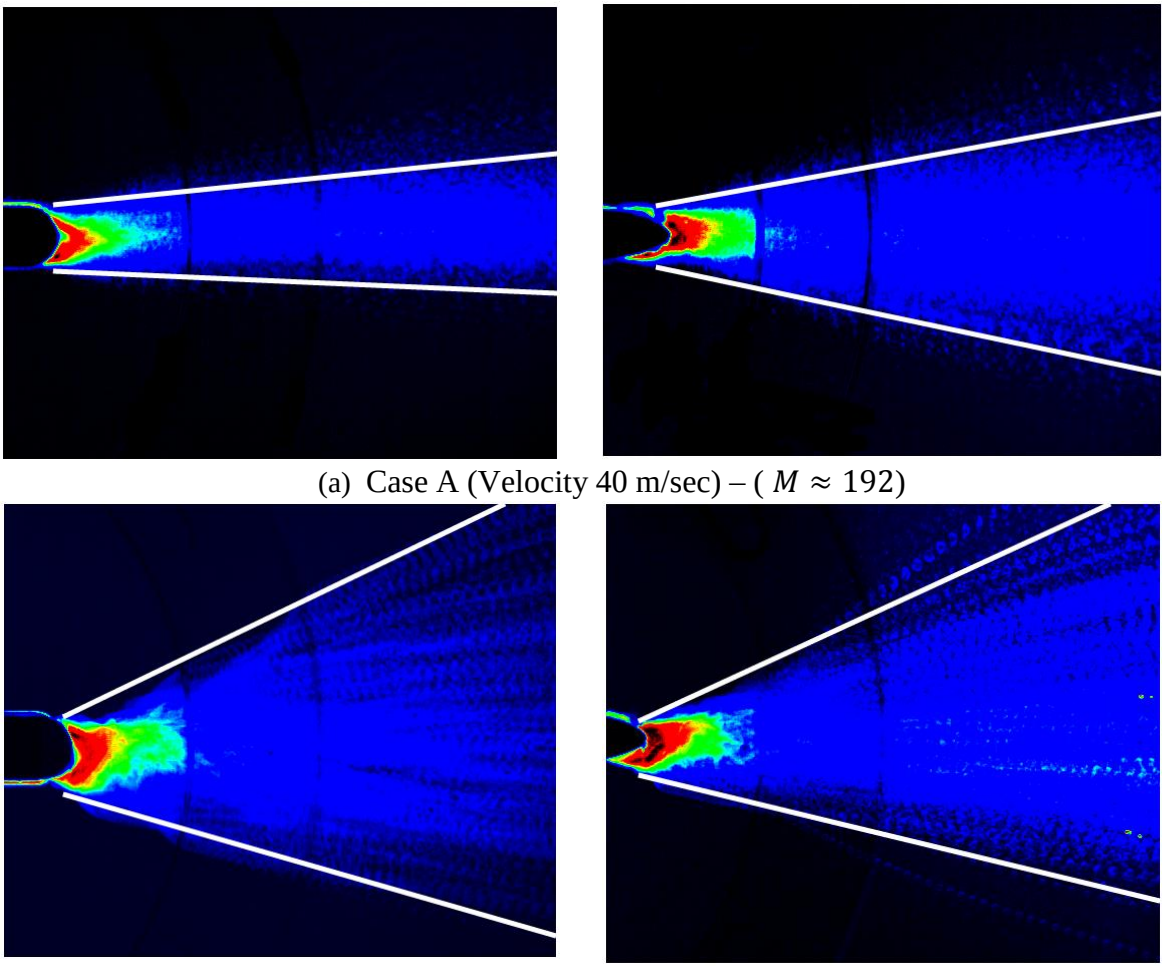

(a) Case A (Velocity 40 m/sec) – ($M \approx 192$)

(b) Case D (Velocity 20 m/sec) – ($M \approx 48$)

i. Flat Blade ii. Elliptical Blade

Figure B.2 – Effect of T.E. on droplets shedding

B.2. Droplets Shedding Angle

Figure B.2 shows the effect of air velocity on the droplets distribution angle. At relatively high air momentum, the droplets distribution angle for the flat blade, Fig. B.2 (i – a), is relatively smaller compared to that of the Elliptical blade, Fig. B.2 (ii – a). For low air momentum ratio, the droplets shedding angle for the flat blade was larger than that of the elliptical blade. In order to understand this phenomenon, the Stokes number of the droplets were calculated as shown in Fig. B.3 using Eq. (2.31). From Fig. B.3 (a), at high air momentum the Stokes number of the droplets for the Flat blade is marginally less than that of the elliptical blade resulting the droplets to continue to flow along with the main air flow. As the Stokes number for the elliptical blade (Fig. B.3 (a)) is marginally larger, than the corresponding droplets distribution angle formed was also slightly larger, as shown in Fig. B.2 (ii – a). However, when the air velocity was reduced, the corresponding distribution angle for the flat blade became larger than that of the Elliptical blade, as shown in Fig. B.2 (b). Comparing this with Fig. B.3 (d), the corresponding Stokes number of the flat blade was found to be greater than that of the Elliptical and therefore, resulted in the formation of relatively coarse droplets which did not follow the air path due to the high momentum of droplets and thus resulted in larger shedding angle, as shown in Fig. B.2.

B.3. Ligament Length & Accumulated Area

Figure B.4 and B.5 shows the comparison of the water accumulated area at the T.E. and the ligament length for the flat and elliptical blade profiles. Though overall the accumulated water and ligament length were larger for the elliptical blade profile, due to large profile separation near the T.E.. As the water accumulation and the ligament length depends on the air flow around the T.E.. From the quantitative results it was expected that the elliptical profile blade is under high liquid stresses compared than that of the Flat blade, as the former had accumulated a large amount of water per unit ligament length and vice versa. Also by comparing Fig. B.2 (i) and B.2 (ii), the near T.E. field region (red region) shows a large amount of water accumulated for the elliptical profile than that of the flat blade profile mainly due to the different T.E. profiles and causing more water to be trapped for the elliptical blade.

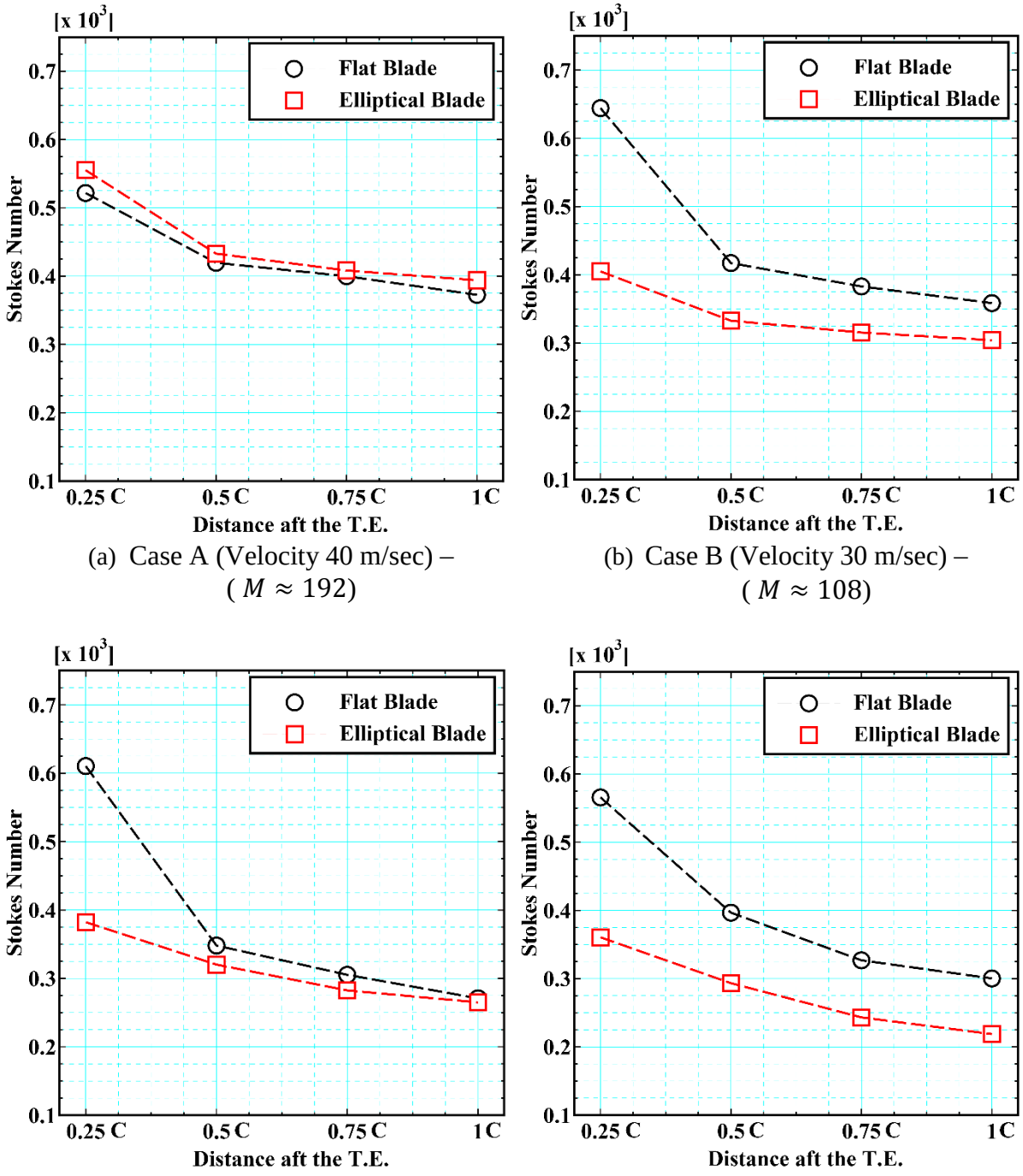

(a) Case A (Velocity 40 m/sec) – ($M \approx 192$)

(b) Case B (Velocity 30 m/sec) – ($M \approx 108$)

(c) Case C (Velocity 25 m/sec) – ($M \approx 75$)

(d) Case D (Velocity 20 m/sec) – ($M \approx 40$)

Figure B.3 – Comparison of Stokes Number

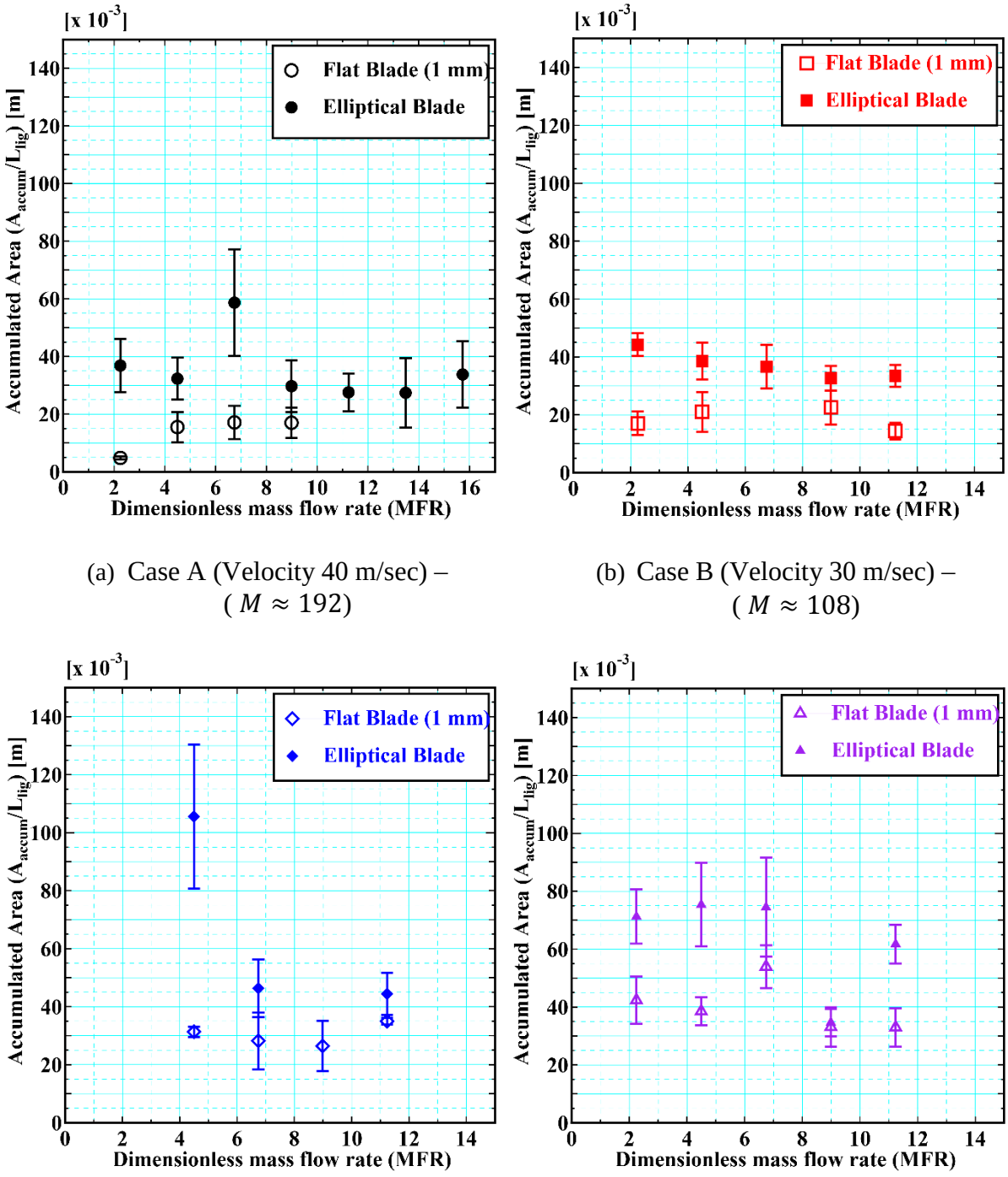

(a) Case A (Velocity 40 m/sec) – ($M \approx 192$)

(b) Case B (Velocity 30 m/sec) – ($M \approx 108$)

(c) Case C (Velocity 25 m/sec) – ($M \approx 75$)

(d) Case D (Velocity 20 m/sec) – ($M \approx 40$)

Figure B.4 – Comparison of Water Accumulation at the T.E.

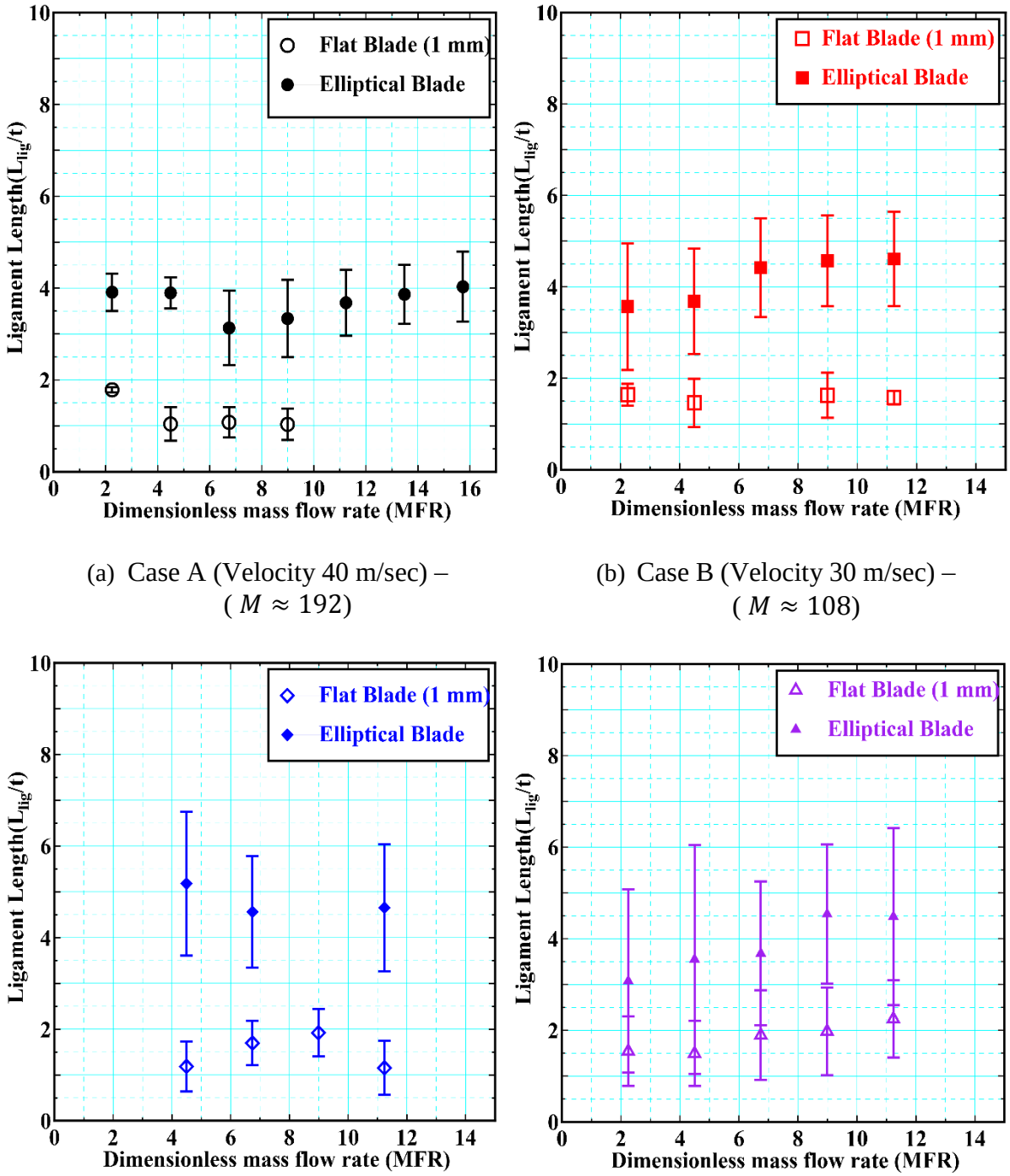

(a) Case A (Velocity 40 m/sec) – ($M \approx 192$)

(b) Case B (Velocity 30 m/sec) – ($M \approx 108$)

(c) Case C (Velocity 25 m/sec) – ($M \approx 75$)

(d) Case D (Velocity 20 m/sec) – ($M \approx 40$)

Figure B.5 – Comparison of Ligament Length at the T.E.

B.4. Conclusions of effects of T.E. size on droplets size distribution

In this section, a comparison of droplets size formation aft the T.E. of the elliptical and flat profile blades were discussed. For the purpose of comparison and simplicity, it was assumed that the profile geometry did not have any major role in droplets size distribution aft the T.E. of the blade. Based on this assumption, a theoretical model was proposed to compare the role of the thickness of the T.E. on the primary droplets formation aft the T.E. of the blade. According to the theoretical model if the Weber number of the two profiles are kept constant then greater the thickness of the T.E. profile is, the greater is the primary droplets formed and vice versa. Moreover, it was found that the amount of the water accumulation at the T.E. of the elliptical profile blade was larger compared to the flat blade profile, which was mainly due to the different air flow separation characteristics of the two aerofoils.

Appendix C: Particle Image Velocimetry (PIV)

In this section a PIV technique for estimating the velocity is discussed. Different researches had been conducted for the implementation and optimization of the PIV [100-103].

Though in the PIV setup, a double pulse laser and a double shutter camera are synchronized to record two particle images within the very short time duration. However, unlike, in this study the binary images were used to estimate the order of velocity.

A detail mathematical principle of PIV can be found in many texts, such as in [101], but in brief two images (A and B) are captured at time t_0 and $t_0 + \Delta t$. The particle velocities was derived by the distance (x) travelled by the particle(s) in time (Δt) from image A to B. Once the images are successfully recorded, the next step is to divide these images into small interrogation windows. These interrogated images are cross correlated to obtain the most probable particle displacement in the interrogation areas. Mathematically, this cross correlation is given by

$$R\,(m,n) = \sum_{j=1}^{M}\sum_{i=1}^{N} A(i,j).B(i-m,j-n) \tag{C.1}$$

where A and B are the corresponding interrogation areas from image A and image B. This procedure is outlined in Fig. C.1.

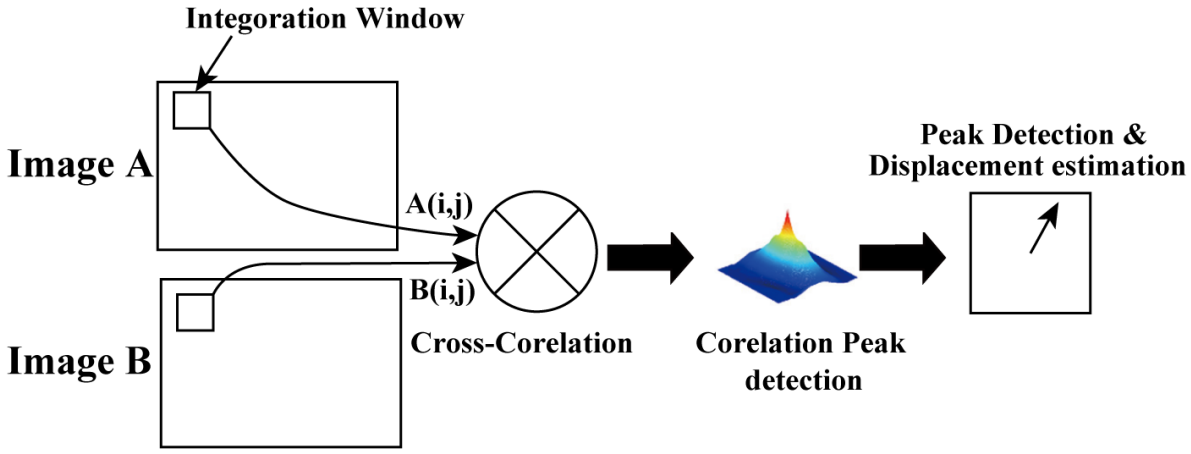

Figure C.1 – Cross-correlation procedure using FFT

Different approaches are used to solve the above equation, however, the most classical and widely used approach is to compute the correlation matrix in the frequency domain, called Discrete Fourier Transformation. The DFT is calculated using a fast Fourier transform. More details of solving the cross correlation can be found in [104]. In order to obtain reliable results post processing was done by using a universal outlier detection method [106] that automatically adapts to local flow situations. Figure C.2 (b) shows the mean velocity distribution aft the T.E. of the blade by averaging 100 images. Similarly, Fig. C.3 (a) and C.3 (b) show the corresponding local velocity measurement for Case A and Case D in the pitch wise direction at about 0.1-C from the T.E. of the blade. In both the cases the order of velocity is approximately the same, probably due to the fact that the accumulated water at the T.E. starts accelerating from almost at rest (i.e. 0 velocity).

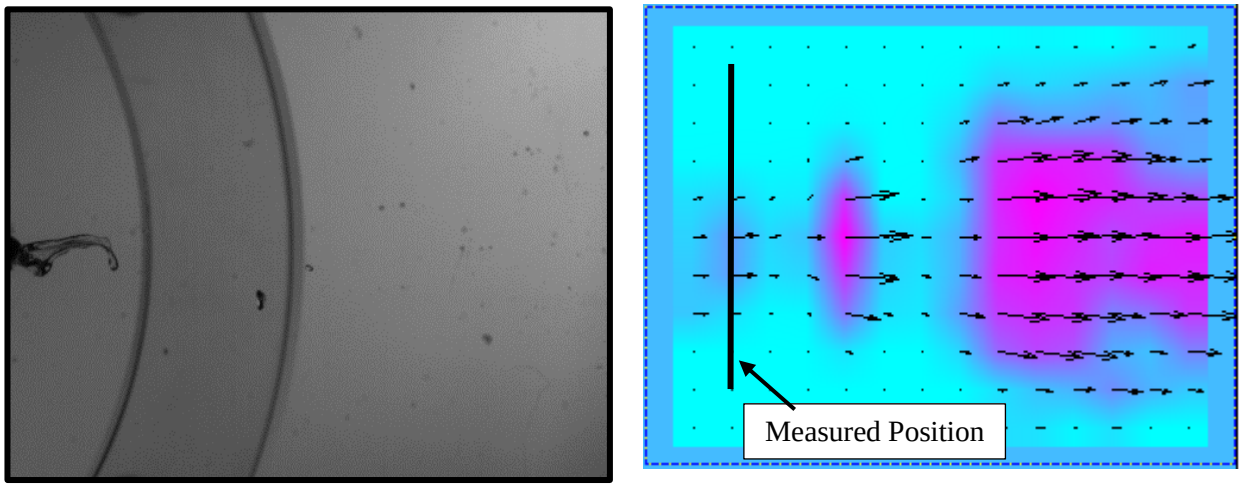

(a) Original Image (instantaneous image)

(b) Velocity Distribution (mean of 100 images)

Figure C.2 – Procedure for obtaining PIV Image

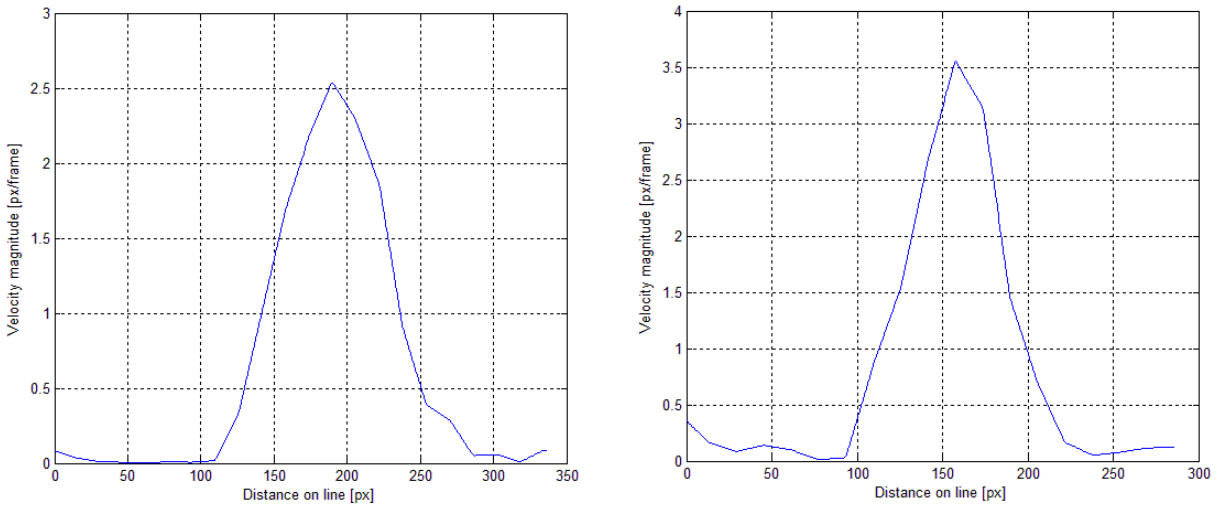

(a) Case A (Air Velocity 40 m/sec)

(b) Case D (Air Velocity 20 m/sec)

Figure C.3 – Velocity aft the T.E. of the blade (measured at about 0.1-C position)

Appendix D: CIP-LSM (Cubic Interpolated Pseudo-particle with Level Set Method)

An in-house numerical simulation named as CIPLSM was used to simulate the two-phase phenomena. The details of this code can be found in [107 – 110]. The governing equations are solved with TCUP (temperature based Combined Unified Procedure), which derived from original CIP-CUP (CIP Combined Unified Procedure). The CIP-CUP is a kind of fractional step methods including pressure based Poisson solver. Figure D.1 shows the algorithm of CIP-CUP schematically, where the

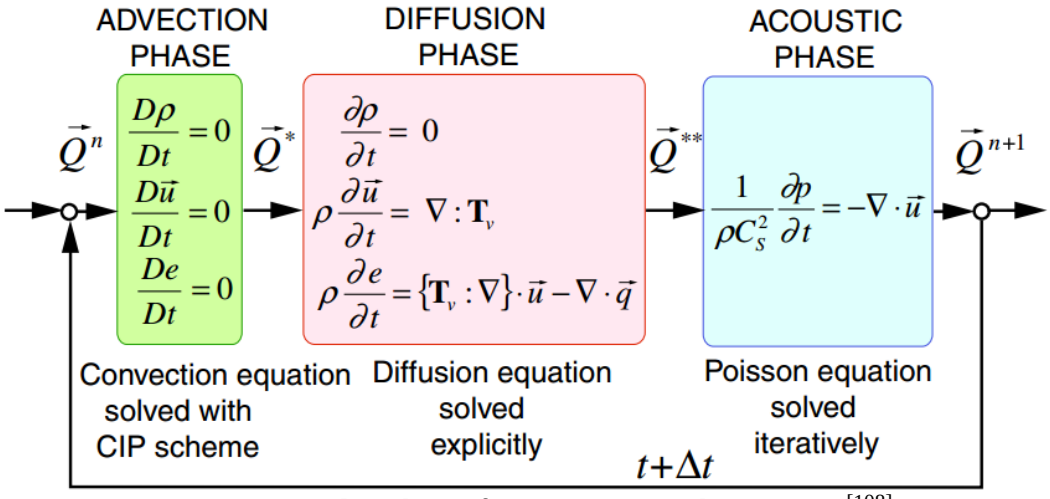

Figure D.1 – Flowchart of CIP-CUP at each time step [108]

Table D.1 – Algorithm of TCUP scheme [108]

Variant	$\vec{Q}=(\vec{u},p,T)^T$
Advection Phase	$\vec{Q}^n \rightarrow \vec{Q}^*$
$\vec{Q}$	$\frac{\partial\vec{Q}}{\partial t}+U_c^n\frac{\partial\vec{Q}}{\partial\xi}+V_c^n\frac{\partial\vec{Q}}{\partial\eta}+W_c^n\frac{\partial\vec{Q}}{\partial\zeta}=\vec{0}$
	Solved with CIP scheme
Diffusion Phase	$\vec{Q}^*$ to $\vec{Q}^{**}$
$\vec{u}$	$\int_\Omega \rho^*\frac{\vec{u}^{**}-\vec{u}^*}{\Delta t}\,dV=\int_\Omega \nabla:\boldsymbol{T}_v^*\,dV=\int_\Omega \boldsymbol{T}_v^*:d\vec{S}$
T	$\frac{T^{**}-T^*}{\Delta t}=\frac{\gamma^*}{(\rho C_p)^*}Q_{DIF}$
p	$\frac{p^{**}-p^*}{\Delta t}=\frac{\gamma^*-1}{(1+\rho C_p\mu_j)^*}Q_{DIF}$
	Solved explicitly
Acoustic Phase	$\vec{Q}^{**}$ to $\vec{Q}^{n+1}$
p	$\int_\Omega \frac{1}{(\rho C_s^2)^{**}}\frac{p^{n+1}-p^{**}}{\Delta t}\,dV=-\int_{\partial\Omega}\left(\vec{u}^{**}-\frac{\nabla p^{n+1}}{\rho^{**}}\Delta t\right).d\vec{S}$
	Solved with iterative method (BiCG-STAB)
$\vec{u}$	$\frac{\vec{u}^{n+1}-\vec{u}^{**}}{\Delta t}=-\frac{\nabla p^{n+1}}{\rho^{**}}$
T	$T^{n+1}-T^{**}=\frac{(1+\rho C_p\mu_j)^{**}}{(\rho C_p)^{**}}(p^{n+1}-p^{**})$
	Solved explicitly

change of flow field in a computational time step Δt is divided into advection phase, diffusion phase and acoustic phase, whereas, Table D.1 gives the algorithm of the TCUP scheme.

Surface Capturing

In order to track the liquid surface at a certain point in the flow field, the level set function (ϕ) is introduced with a signed distance from the liquid-surface distance.

Near the liquid surface	$\lvert\nabla\phi\rvert = 1$	(D1)
On the liquid surface where $H_s = 0$	$\phi = 0$	(D2)

Furthermore, the Heaviside function values were defined with a constant value of 0.5 and -0.5 for the liquid and gaseous phase respectively. And hence the interface was defined as 0, as given follow

$$\begin{aligned} \boldsymbol{H_s} = +0.5 \quad if \quad \phi > 0 \ (liquid\ phase) \\ \boldsymbol{H_s} = 0 \quad if \quad \phi = 0 \ (interface) \\ \boldsymbol{H_s} = -0.5 \quad if \quad \phi > 0 \ (gaseous\ phase) \end{aligned} \tag{D3}$$

Numerical Results

Numerical Grid

Figure D.2 shows the 3D computational grid used in the present study for the Elliptical profile blade. A single zone was made with an O-type grid around the blade. The total number of grid cells generated in the computational domain was 400,000, with 300 cells in the axial, 100 cells in the pitch and 20 cells in the span-wise direction. The minimum grid spacing near the blade's surface was set to 5.8 x 10^{-6} [m]. Figure D.3 illustrate a more close up view of the numerical grid near the T.E.. In this analysis, the objective was not to calculate the droplets diameter and their distribution but to grasp the general breakup of liquid ligaments from the T.E.. Hence, the grid resolution is not enough to capture the tiny droplets produced aft the T.E. region.

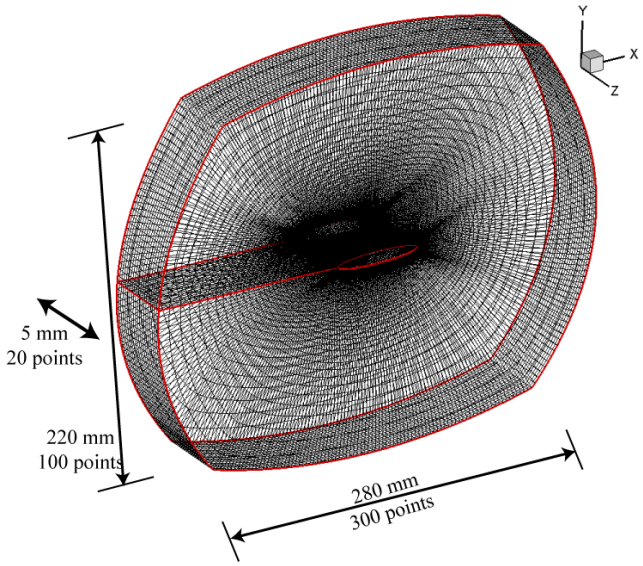

Figure D.2 – Numerical Grid Shape

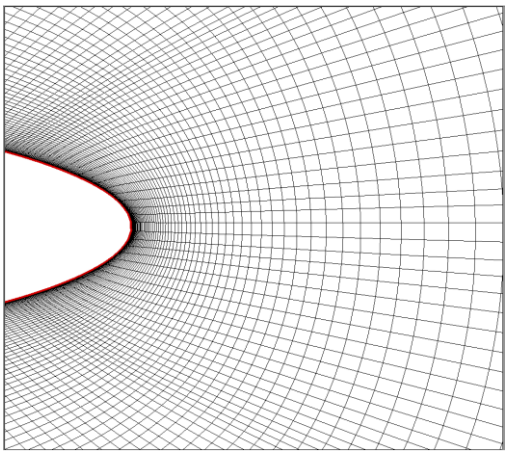

Figure D.3 – Numerical Grid near the T.E.

Table D.2 – CFD Grids Points

Chord-wise (axial direction)	300
Pitch-wise	100
Span-wise	20
Total	400,000

Boundary Condition

For the three-dimensional analysis, span-wise isothermal, uniform air velocity condition was applied at the inlet boundary conditions. The blade hub and wall surfaces were treated as an adiabatic, slip wall conditions, whereas a no-slip boundary condition was applied on the blade's surface (south). At the outflow boundary, static pressure was fixed and other physical quantities were extrapolated. Similarly, east and west boundary conditions were set as periodic. All the flow calculations were simulated at a 0-degree angle of attack.

Table D.3 – Boundary Conditions

Inlet conditions	U and T fixed, P extrapolated
Outlet conditions	P fixed, U and T extrapolated
Wall condition	No – slip wall condition
Other boundaries (front and back)	Slip – wall condition

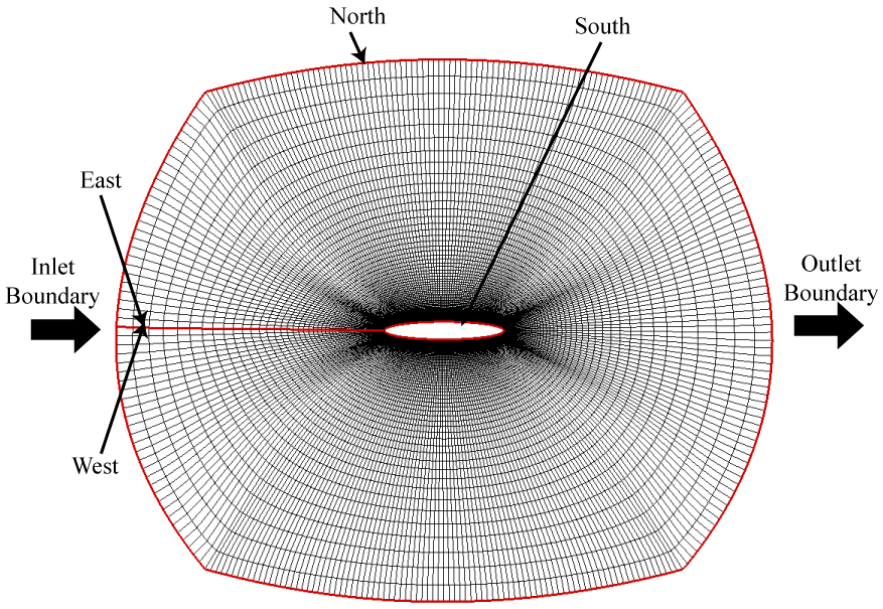

Figure D.4 – Boundary conditions

Single Phase Results

Single phase calculations were done using the CIP-LSM code for Case A (air velocity 40 m/sec) and Case D (air velocity 20 m/sec). Figure D.5 (a) and D.5 (b) shows the Mach number distribution for Case A and Case D respectively. Karman Vortex Street can be seen detaching aft the T.E. of the blade. Similarly, Fig. D.6 (a) and D.6 (b) shows the corresponding Cp distribution at the mid-span of the Elliptical blade. The C_p distribution remains symmetric on both the suction and pressure side of the blade, due to the symmetric nature of the blade. The pressure coefficient had a large suction peak near the L.E. and remained almost uniform over the chord length wise direction. However, near the T.E. due to flow separation, it gives rise to adverse pressure gradient (Fig. D.6) and thus leads to the vortex shedding as shown in D.5.

Two Phase Results

An attempt was made to numerically investigate the water film formation on the blade's surface. Analysis conditions corresponded to the experimental conditions, with water ingestion from the L.E., as shown in Fig. D.7, having an ingestion mass flow rate of liquid set at 6. Two cases were numerically investigated, Case A (Air velocity 40 m/sec) and Case D (Air velocity 20 m/sec).

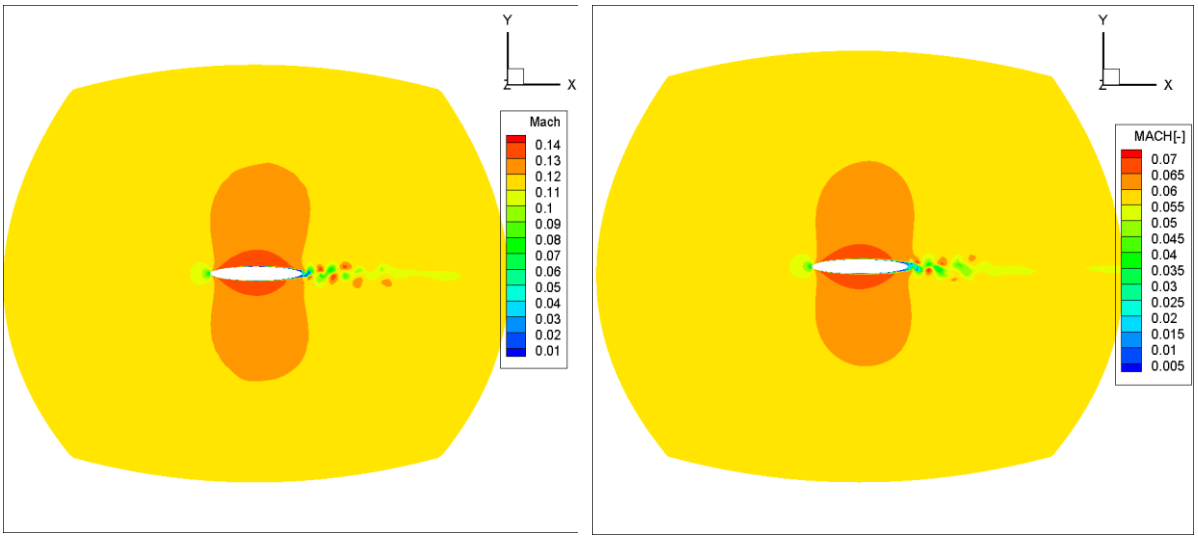

(a) Case A (Air Velocity 40 m/sec) (b) Case D (Air Velocity 20 m/sec)

Figure D.5 – Mach Number contour

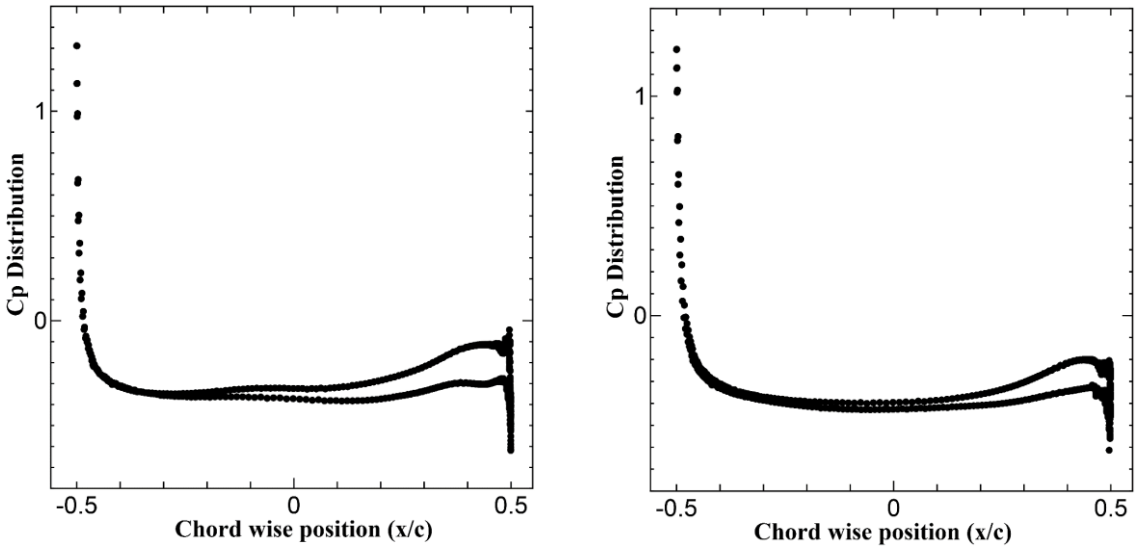

(a) Case A (Air Velocity 40 m/sec) (b) Case D (Air Velocity 20 m/sec)

Figure D.6 – Coefficient of pressure distribution (@ Mid-span)

Water Film Formation

Figure D.8 (a) and D.8 (b) show the water film formation on the S.S. of blade surface for Case A and Case D respectively. For Case A some unsteadiness was obtained on the blade's surface (Fig. D.8 (a)) but the wave structure did not correspond to the wave structure observed from the shadowgraph images for the Case A, which might be due to less number of grid points to capture film thickness. Similarly, for Case D, a smooth water film structure was observed on the blade's suction side, as shown in Fig. D.8 (b), giving a fair appearance with the shadowgraph images

Water Presence at and aft the T.E.

The water film structure accumulated at the T.E. of the cascade blade is shown in Fig. D.9 and D.10 for Case A and Case D respectively. The numerical simulation shows some (visualized) correspondence with that of the experimental results. Due to the coarse grid structure, it was unable to capture the droplets formation away from the T.E. of the blade. However, the near the T.E. water accumulation shows relatively good correspondence to that of the experimentally visualized results as shown in Fig. D.9 and D.10. The experimental and numerical time step were compared by using a non-dimensional time step given by

$$t^* = \frac{t\,U}{C}$$

where, t^*, t, U and C are the non-dimensional time step, time, air velocity and chord length respectively.

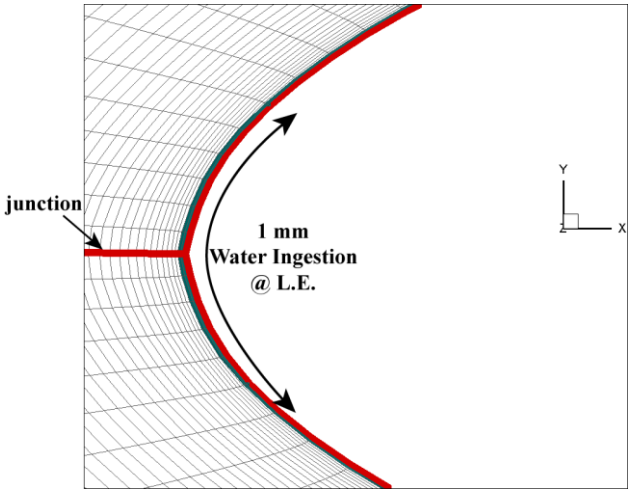

(a) Water ingestion at the L.E. (Side View – Case A)

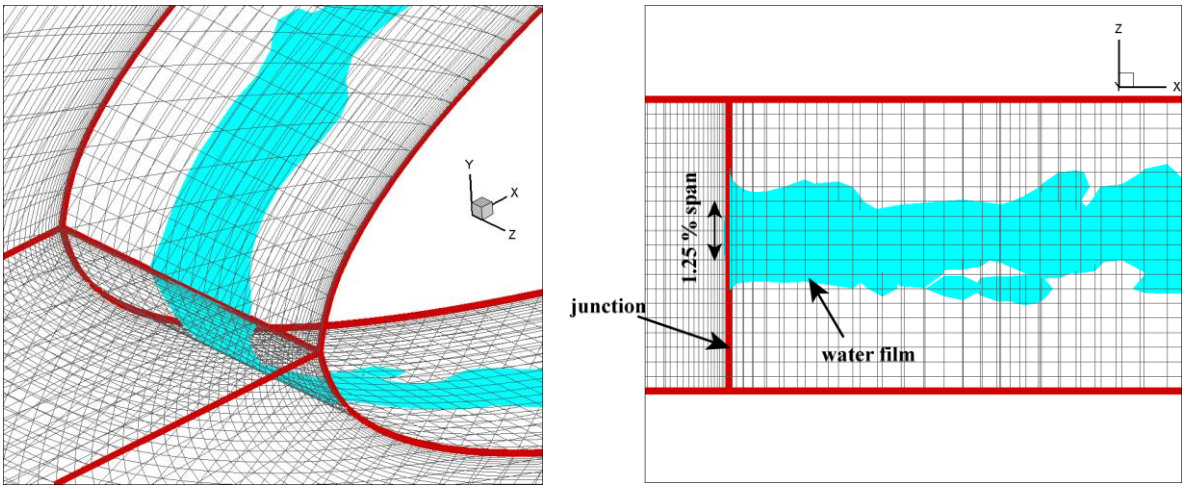

(b) Isometric View (c) Side View

Figure D.7 – Water film formation on the blade's surface

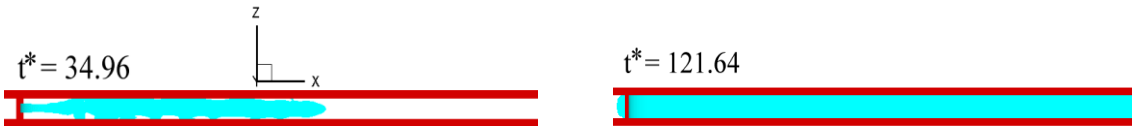

(a) Case A (Air Velocity 40 m/sec) (b) Case B (Air Velocity 20 m/sec)

Figure D.8 – Water Film Structure

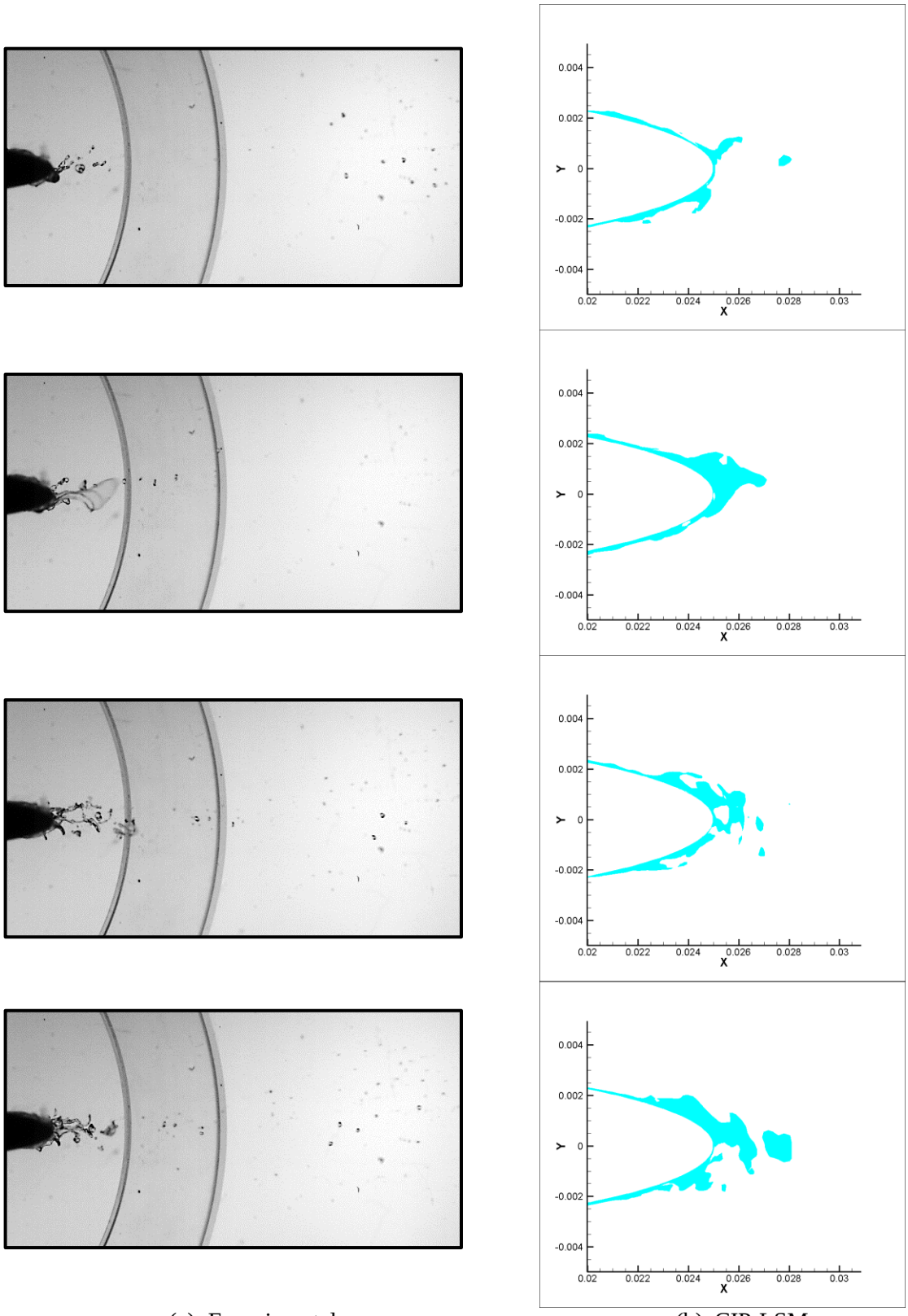

(a) Experimental (b) CIP-LSM

Figure D.9 – Comparison of experimental and numerical simulation (Case A - Air Velocity 40 m/sec) (1/2)

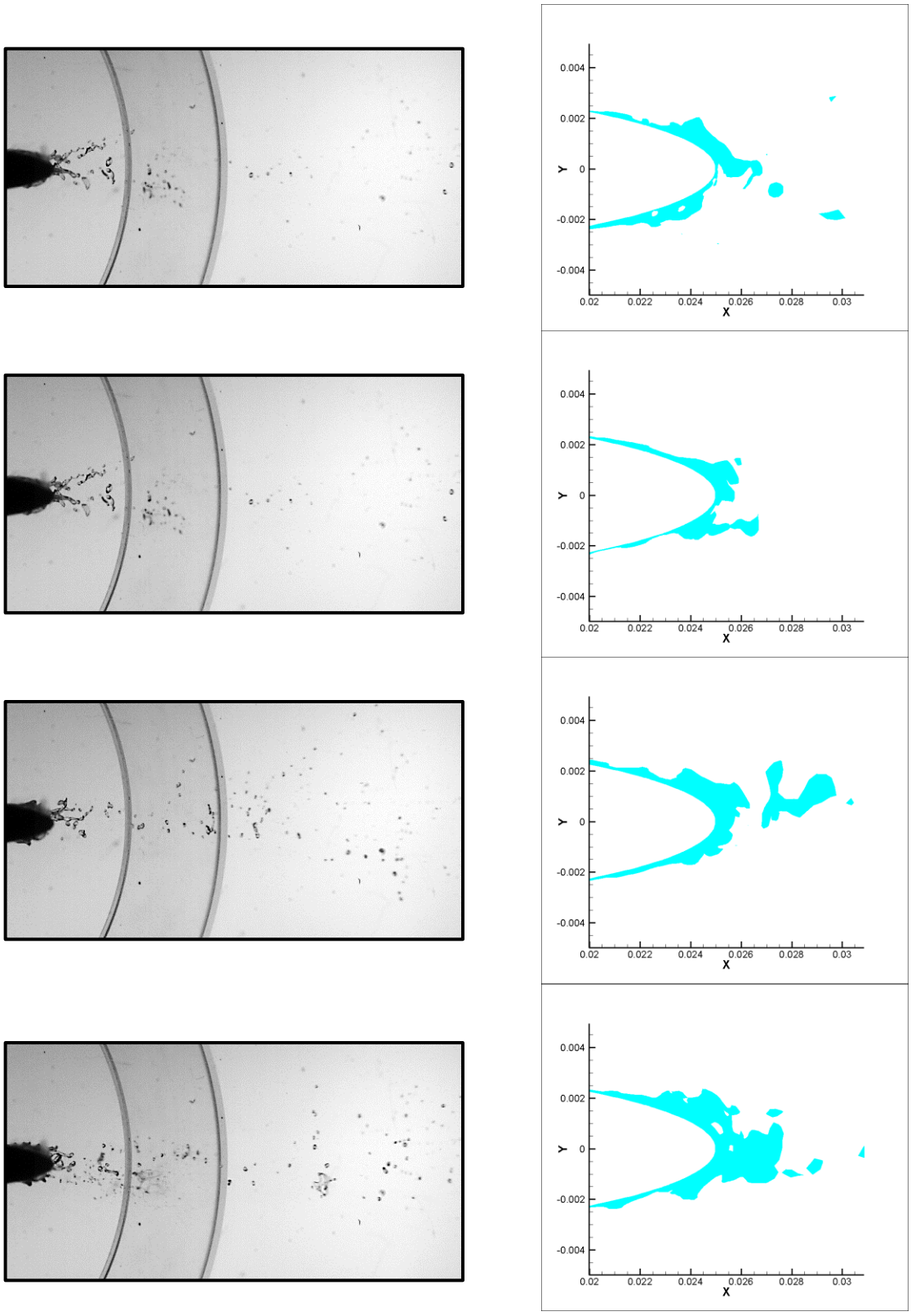

(a) Experimental (b) CIP-LSM

Figure D.9 – Comparison of experimental and numerical simulation (Case A - Air Velocity 40 m/sec) (2/2)

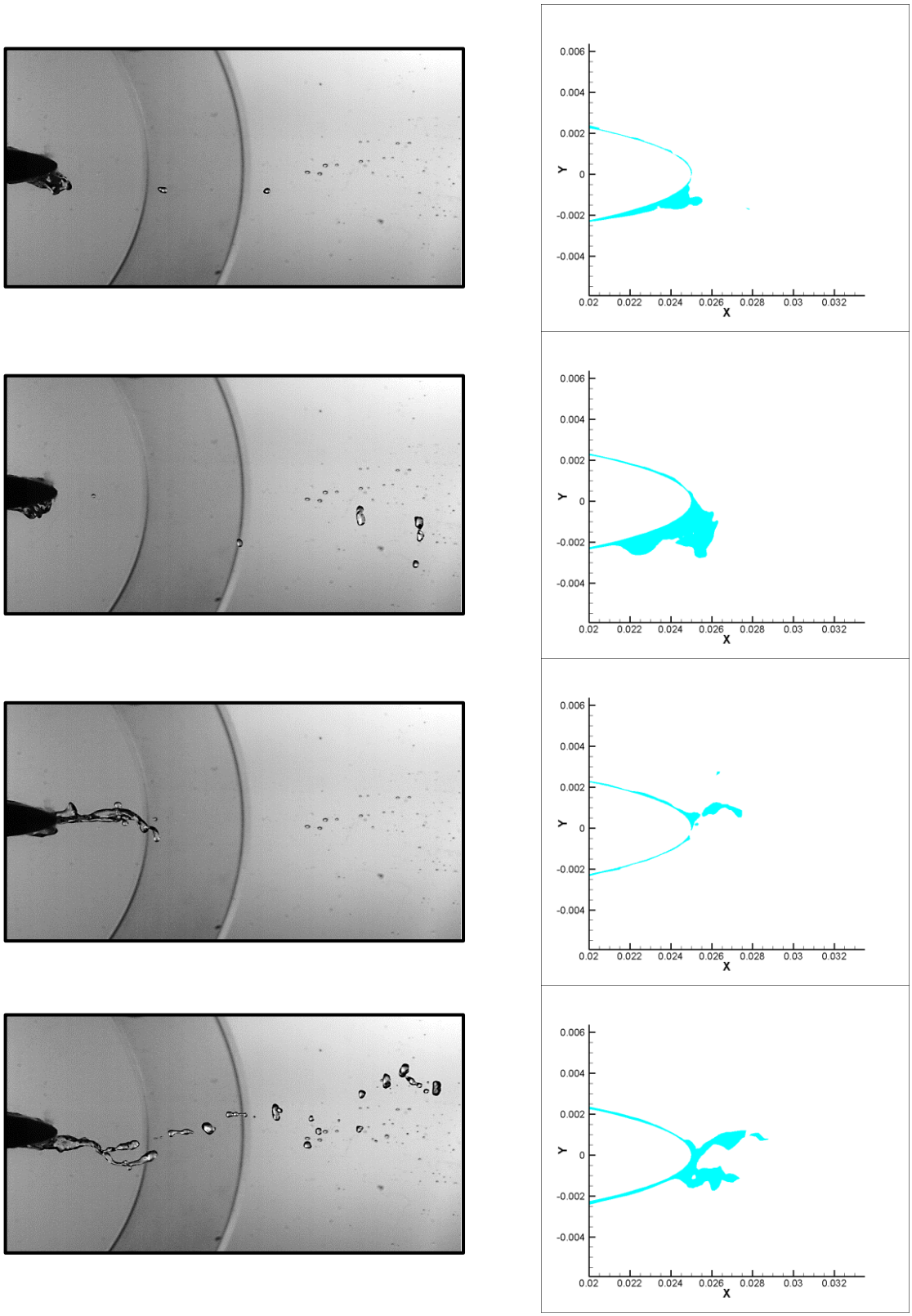

(a) Experimental (b) CIP-LSM

Figure D.10 – Comparison of experimental and numerical simulation (Case D - Air Velocity 20 m/sec) (1/2)

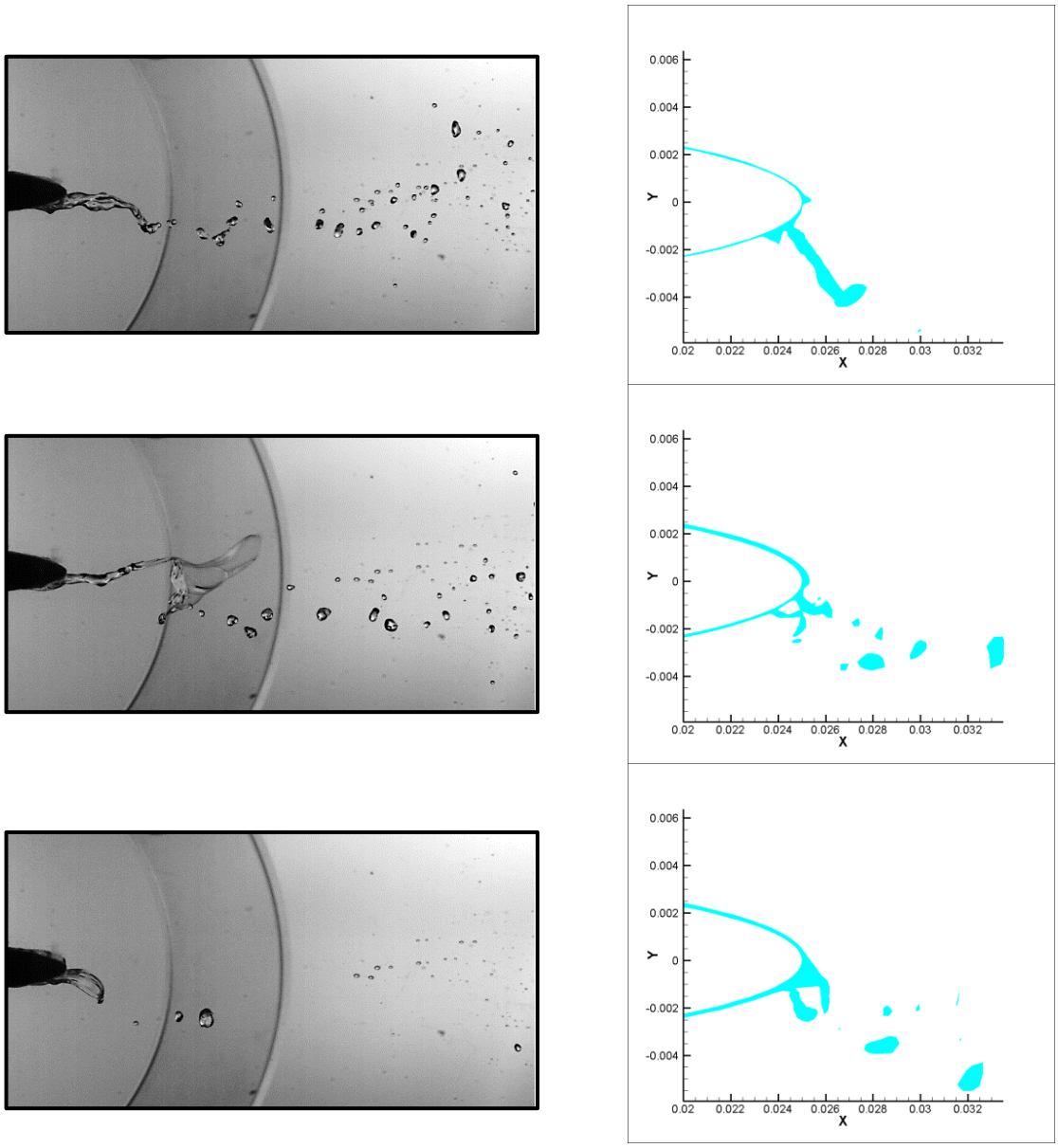

(a) Experimental (b) CIP-LSM

Figure D.10 – Comparison of experimental and numerical simulation (Case D - Air Velocity 20 m/sec) (2/2)